JOURNAL OF THE ELECTROCHEMICAL SOCIETY

ELECTROCHEMICAL
SCIENCE AND TECHNOLOGY

SOLID-STATE
SCIENCE AND TECHNOLOGY

REVIEWS AND NEWS

VOL. 124, NO. 9 SEPTEMBER 1977

JESOAN 124 (9) 1305-1464, 337C-356C

FUTURE MEETINGS
Of The Electrochemical Society

ATLANTA, GEORGIA—OCTOBER 9, 10, 11, 12, 13, & 14, 1977
Headquarters at the Hyatt Regency

The detailed Call for Papers published December 1976-April 1977 issues of **This Journal.** Final program published in August 1977 issue of **This Journal.**

Planned symposia for the Atlanta Meeting include the following Divisions and subjects:

Battery—Ambient Temperature Li Batteries, General Session; **Battery and Corrosion**—Corrosion of Battery Materials; **Battery, Industrial Electrolytic, and Energy Technology Group**—Load Leveling; **Corrosion**—Corrosion Inhibitors, General Session; **Corrosion and Energy Technology Group**—Materials for Fusion Reactors; **Dielectrics and Insulation**—Failure Mechanisms in Dielectric Materials, New Nonmetallic Materials for High Thermal Conductivity for Power Dissipation in Electrical and Optical Devices, Plasma Etching and Deposition Technology, General Session; **Dielectrics and Insulation and Electronics**—Charge Transport in Thin Film Insulators: Generation, Injection, Conduction, Trapping, Thin Film Phenomena: Interfaces and Interactions; **Dielectrics and Insulation, Electronics, and Electrothermics and Metallurgy**—Sixth International Conference on Chemical Vapor Deposition; **Electrodeposition**—General Session; **Electrodeposition and Electronics**—Plating Processes for the Electronic Application; **Electronics**—Devices in Amorphous and Polycrystalline Silicon, Highly Conducting Nonmetallic Materials, Semiconductors General Sessions, General Materials and Processes General Session; **Electronics and Electrothermics and Metallurgy**—Ohmic Contacts and Interconnect Technology; **Electrothermics and Metallurgy**—High Temperature Metal Halide Chemistry, General Session; **Energy Technology Group**—Materials and Processes for Photovoltaic Energy Conversion; **New Technology Subcommittee**—Fundamentals and Applications of Electrokinetic Phenomena.

SEATTLE, WASHINGTON—MAY 21, 22, 23, 24, 25, & 26 1978
Headquarters at The Olympic Hotel

The detailed Call for Papers published July-November 1977 issues of **This Journal.** Final program published in March 1978 issue of **This Journal.**

Planned symposia for the Seattle Meeting include the following Divisions and subjects:

Corrosion—General Session; **Corrosion and Electrothermics and Metallurgy**—Oxidation of Metals and Alloys; **Corrosion, Industrial Electrolytic, and Physical Electrochemistry**—Mathematical Modeling of Electrochemical Modeling of Electrochemical Processes; **Dielectrics and Insulation**—Solid-State Chemical Sensors, General Session; **Dielectrics and Insulation and Electronics**—Thin Films of Tunneling Dimensions; **Dielectrics and Insulation, Electronics, and Electrothermics and Metallurgy**—Defect Chemistry of Semiconductors and Dielectrics; **Dielectrics and Insulation and Electrothermics and Metallurgy**—Fundamentals of Film Growth Processes in Anodic and Thermal Oxides; **Electronics**—Multilayer Epitaxy, Semiconductor Materials and Device Characterization Techniques, Semiconductors General Sessions, Improved Energy Conversion Devices for Lighting: Fluorescent Lamps and Phosphors, Phosphor Screening, Luminescence General Session, General Materials and Processes General Session; **Electronics and Electrothermics and Metallurgy**—Eighth International Conference on Electron and Ion Beam Science and Technology; **Electrothermics and Metallurgy**—Electroslag Refining, General Session; **Industrial Electrolytic**—Chlorine and Chlorate Cell Technology, Industrial Water Electrolysis, General Session; **Organic and Biological Electrochemistry**—The Electrochemistry of Molecular Interactions in Biological Membranes, General Session; **Physical Electrochemistry**—Electrode Kinetics; **New Technology Subcommittee, Dielectrics and Insulation, Electrothermics and Metallurgy, and Industrial Electrolytic**—Source Reduction and Recycling in Industrial Processing.

NEW ORLEANS, LOUISIANA—OCTOBER 8, 9, 10, 11, 12, & 13, 1978
Headquarters at the Fairmont Hotel

The detailed Call for Papers published in December 1977-April 1978 issues of **This Journal.** Final Program published in August 1978 issue of **This Journal.**

Planned symposia for the New Orleans Meeting include the following Divisions and subjects.

Battery—Vehicle Propulsion; **Corrosion**—Atmospheric Corrosion, Fundamental Aspects of Cathodic and Anodic Protection, General Session; **Corrosion, Dielectrics and Insulation, and Electronics**—Corrosion of Electronic Materials; **Dielectrics and Insulation and Electronics**—Conductive Glass Technology, Double Dielectric Interfaces, Growth and Evaluation of Materials Prepared by Low Pressure CVD; **Electrodeposition**—Engineering Topics in Electrodeposition, General Session; **Electrodeposition and Physical Electrochemistry**—Electrocrystallization; **Electronics**—Passivation Techniques, Passive Display Devices, Reactive Ion Etching, Surface Preparation of Semiconductors, Semiconductors General Sessions, General Materials and Processes General Session; **Electrothermics and Metallurgy and Physical Electrochemistry**—Second International Symposium on Molten Salts; **Industrial Electrolytic**—Industrial Methods of Metal Extraction.

Deep in the heart of Poco Graphite lie the secrets of our success.

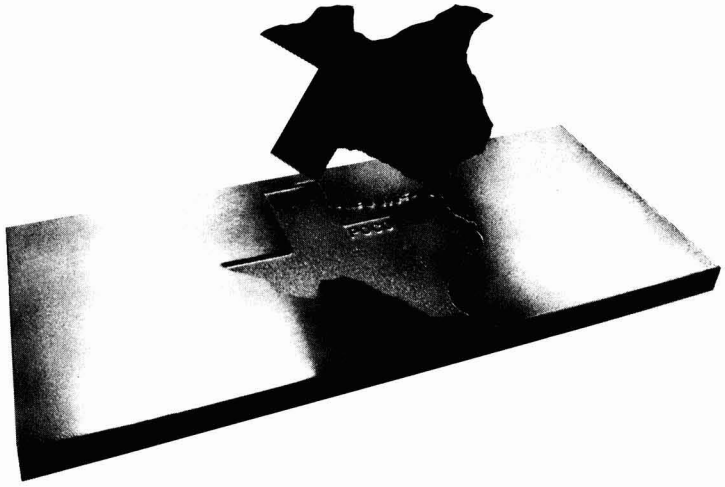

Poco is unique graphite. And we're uniquely involved with it—from technical materials to machining.

SECRET #1: There's none other like Poco graphite. Compared to ordinary premium grades of commercial graphite, Poco offers a unique combination of high strength, isotropic (non-directional) particle alignment and fine grain size homogenous structure. The result: Poco graphite consistently outperforms ordinary graphite. The material properties are controllable, uniform, and consistent batch to batch, grade to grade.

SECRET #2: Texas isn't the only thing unique about our company. We back up one of the world's most modern materials with some of the people who know the most about it. We're deeply involved with specialty graphite. So whether you have a question, a unique application, or a problem you're not solving with plastics, metals, or ceramics, give us a call at Poco. We offer the men, the materials and the machines to work with you from concept through completion.

SECRET #3: We specialize in specialty graphite. It's our business, and we know our business. When it comes to specialty graphite we believe we outperform. And in our business, that's no secret.

Poco Graphite: We outperform.

union 76 POCO

A Union Oil Company of California subsidiary
1601 South State Street, Dept. GT
Decatur, Texas 76234
(817) 627-2121
TWX 910-890-5724

THE ELECTROCHEMICAL SOCIETY BOOKS IN PRINT

Monograph Series

The following hardbound volumes are sponsored by The Electrochemical Society, Inc. and published by John Wiley & Sons, Inc., 605 Third Avenue, New York, N.Y. 10016. Members of the Society can receive a 33% discount by ordering from Society Headquarters. Books and invoice are mailed by publisher. Nonmembers (including subscribers) must order direct from the publisher. All prices subject to change without notice.

Corrosion Handbook, edited by Herbert H. Uhlig (1948). 1188 pages, **$37.25.**

Arcs in Inert Atmospheres and Vacuum, edited by W. E. Kuhn. A 1956 Spring Symposium (1956). 188 pages, **$12.25.**

The Electron Microprobe, edited by T. D. McKinley, K. F. J. Heinrich, and D. B. Wittry. A 1964 Fall Symposium (1966). 1035 pages, **$44.75.**

The Stress Corrosion of Metals, by Hugh I. Logan (1966). 306 pages, **$24.25.**

The Corrosion of Light Metals, by H. P. Godard, W. B. Jepson, M. R. Bothwell, and R. L. Kane (1967). 360 pages, **$22.00.**

High-Temperature Materials and Technology, edited by I. E. Campbell and E. M. Sherwood (1967). 1022 pages, **$45.50.**

Alkaline Storage Batteries, by S. Uno Falk and Alvin J. Salkind (1969). 656 pages, **$45.25.**

The Primary Battery, Volume I, edited by George W. Heise and N. Corey Cahoon (1971). 500 pages, **$37.25.**

Zinc-Silver Oxide Batteries, edited by Arthur Fleischer and John J. Lander (1971). 544 pages, **$38.75.**

The Corrosion of Copper, Tin, and Their Alloys, by Henry Leidheiser, Jr. (1971). 411 pages, **$47.50.**

Corrosion in Nuclear Applications, by W. E. Berry (1971). 572 pages, **$32.50.**

Handbook on Corrosion Testing and Evaluation, edited by W. H. Ailor (1971). 873 pages, **$54.50.**

Modern Electroplating, edited by Frederick A. Lowenheim. Third Edition (1974). 801 pages, **$33.50.**

Marine Corrosion, by Francis L. LaQue (1975). 332 pages, **$23.75.**

The Primary Battery, Volume II, edited by George W. Heise and N. Corey Cahoon (1975). 528 pages, **$42.25.**

Society Symposium Series

The following softbound symposium volumes are sponsored and published by The Electrochemical Society, Inc., P.O. Box 2071, Princeton, N.J. 08540. Orders filled at the list price given, subject to availability. Enclose payment with order.

Vacuum Metallurgy. J. M. Blocher, Jr., Editor. A 1954 symposium. 216 pages, **$5.00.**

High-Temperature Metallic Corrosion of Sulfur and Its Compounds. Z. A. Foroulis, Editor. A 1969 symposium. 276 pages, **$4.50.**

Electron and Ion Beam Science and Technology, Fourth International Conference. R. Bakish, Editor. A 1970 symposium. 680 pages, **$7.50.**

Fundamentals of Electrochemical Machining. C. L Faust, Editor. A 1970 symposium. 365 pages, **$4.50.**

Electron and Ion Beam Science and Technology, Fifth International Conference. R. Bakish, Editor. A 1972 symposium. 420 pages, **$5.50.**

Electrochemical Contributions to Environmental Protection. T. R. Beck, O. B. Cecil, C. G. Enke, J. McCallum, and S. T. Wlodek, Editors. A 1972 symposium. 173 pages, **$4.00.**

Oxide-Electrolyte Interfaces. R. S. Alwitt, Editor. A 1972 symposium. 312 pages, **$9.00.**

Electrets. Charge Storage and Transport in Dielectrics. M. M. Perlman, Editor. A 1972 symposium. 700 pages, **$18.00.**

Marine Electrochemistry. J. B. Berkowitz, M. Banus, M. J. Pryor, R. Horne, P. L. Howard, G. C. Whitnack, and H. V. Weiss, Editors. A 1972 symposium. 416 pages, **$15.00.**

Semiconductor Silicon 1973. H. R. Huff and R. R. Burgess, Editors. A 1973 symposium. 936 pages, **$15.00.**

Electrochemical Bioscience and Bioengineering. H. T. Silverman, I. F. Miller, and A. J. Salkind, Editors. A 1973 symposium. 268 pages, **$8.00.**

Chemical Vapor Deposition, Fourth International Conference. G. F. Wakefield and J. M. Blocher, Jr., Editors. A 1973 symposium. 608 pages, **$16.00.**

Fine Particles. W. E. Kuhn and J. Ehretsmann, Editors. A 1973 symposium. 352 pages, **$15.00.**

Chlorine Bicentennial Symposium. T. C. Jeffery, P. A. Danna, and H. S. Holden, Editors. A 1974 symposium. 404 pages, **$11.00.**

Electrocatalysis. M. W. Breiter, Editor. A 1974 symposium. 378 pages, **$12.00.**

Corrosion Problems in Energy Conversion and Generation. C. S. Tedmon, Jr., Editor. A 1974 symposium. 474 pages, **$12.00.**

Electron and Ion Beam Science and Technology, Sixth International Conference. R. Bakish, Editor. A 1974 symposium. 594 pages, **$16.00.**

Properties of Electrodeposits—Their Measurement and Significance. R. Sard, H. Leidheiser, Jr., and F. Ogburn, Editors. A 1974 symposium. 430 pages, **$13.00.**

Metal-Slag-Gas Reactions and Processes. Z. A. Foroulis and W. W. Smeltzer, Editors. A 1975 symposium. 1032 pages, **$20.00.**

Chemistry and Physics of Aqueous Gas Solutions. W. A. Adams, G. Greer, J. E. Desnoyers, G. Atkinson, G. S. Kell, K. B. Oldham, and J. Walkley, Editors. A 1975 symposium. 522 pages, **$11.00.**

Chemical Vapor Deposition, Fifth International Conference. J. M. Blocher, Jr., H. E. Hintermann, and L. H. Hall, Editors. A 1975 symposium. 848 pages, **$18.00.**

Thermal and Photostimulated Currents in Insulators. D. M. Smyth, Editor. A 1975 symposium. 215 pages, **$7.00.**

Energy Storage. H. P. Silverman and J. B. Berkowitz, Editors. A 1975 symposium. 258 pages, **$8.00.**

Etching. H. G. Hughes and M. J. Rand, Editors. A 1976 symposium. 203 pages, **$7.00.**

Electron and Ion Beam Science and Technology, Seventh International Conference. R. Bakish, Editor. A 1976 symposium. 632 pages, **$18.00.**

International Symposium on Solar Energy. J. B. Berkowitz and I. A. Lesk, Editors. A 1976 symposium. 372 pages, **$10.00.**

International Symposium on Molten Salts. J. P. Pemsler, J. Braunstein, K. Nobe, D. R. Morris, and N. E. Richards, Editors. A 1976 symposium. 632 pages, **$16.00.**

Properties of High Temperature Alloys. Z. A. Foroulis and F. S. Pettit, Editors. 851 pages, **$12.00.**

Semiconductor Silicon 1977. H. R. Huff and E. Sirtl, Editors. A 1977 symposium. 1100 pages, **$15.00.**

A History of The Electrochemical Society. R. M. Burns with E. G. Enck. 160 pages, **$5.00.**

7/77

ELECTROCHEMICAL PREPARATIVE AND ANALYTICAL EQUIPMENT

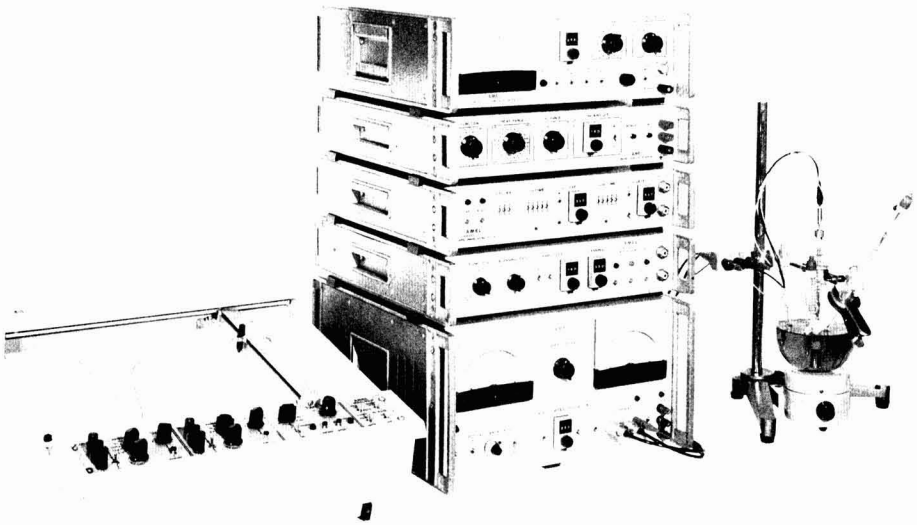

These are . . .
THE ADVANCED ALTERNATIVES

And we challenge you to compare the features, performance and value of these fine new instruments.

- **Cells for preparative organic chemistry**
- Electrometers/Ammeters
- Corrosion Testing Equipment
- Analog/Digital Function Integrators
- Multi-channel Scanners
- Signal Function Generators
- Polarographs
- **Potentiostats/Galvanostats**

For a copy of the current catalog describing these and other instruments, please write, or call Dr. Dennis Crouse at 617-661-8080.

ECO

ECO-CONTROL, INC.
FIFTY-SIX ROGERS STREET
CAMBRIDGE, MA 02142
Tel. 617-661-8080
TWX 710-320-6937

JOURNAL OF THE

September 1977

ELECTROCHEMICAL SCIENCE AND TECHNOLOGY

TECHNICAL PAPERS

Vol. 124 • No. 9

TECHNICAL NOTE

BRIEF COMMUNICATION

SOLID-STATE SCIENCE AND TECHNOLOGY

TECHNICAL PAPERS

Manuscripts submitted to the Journal should be sent, in triplicate, to the Editorial Office at P.O. Box 2071, Princeton, N.J. 08540. They should conform to the revised "Instructions to Authors" available from Society Headquarters. Manuscripts so submitted, as well as papers presented before a Society technical meeting, become the property of the Society and may not be published elsewhere in whole or in part without written permission of the Society. Address such requests to the Editor.

The Electrochemical Society does not maintain a supply of reprints of papers appearing in its Journal. A photoprint copy of any particular paper may be obtained from University Microfilms, Inc., 300 N. Zeeb St., Ann Arbor, Mich. 48106.

Inquiries regarding positive microfilm copies of volumes should be addressed to University Microfilms, Inc., 300 N. Zeeb St., Ann Arbor, Mich. 48106.

Walter J. Johnson, Inc., 355 Chestnut St., Norwood, N.J. 07648, have reprint rights to out-of-print volumes of the Journal, and also have available for sale back volumes and single issues, with the exception of the current calendar year. Anyone interested in securing back copies should correspond directly with them.

Published monthly by The Electrochemical Society, Inc., at 215 Canal St., Manchester, N.H.; **Executive Offices, Editorial Office and Circulation Dept.**, and **Advertising Office** at P.O. Box 2071, Princeton, N.J. 08540, combining the JOURNAL and TRANSACTIONS OF THE ELECTROCHEMICAL SOCIETY. Statements and Opinions given in articles and papers in the JOURNAL OF THE ELECTROCHEMICAL SOCIETY are those of the contributors, and The Electrochemical Society assumes no responsibility for them.

Claims for missing numbers will not be allowed if received more than 60 days from date of mailing plus time normally required for postal delivery of JOURNAL and claim. No claims allowed because of failure to notify the Circulation Dept., The Electrochemical Society, P.O. Box 2071, Princeton, N.J. 08540, of a change of address, or because copy is "missing from files." Subscription to members as part of membership service; subscription to nonmembers $60.00 plus $5.00 for postage outside U.S. and Canada. Single copies $3.25 to members, $5.00 to nonmembers. Second Class Postage Paid at Princeton, New Jersey, and at additional mailing offices. Printed in U.S.A.

SOLID-STATE SCIENCE (Cont.)

TECHNICAL NOTES

BRIEF COMMUNICATIONS

ACCELERATED BRIEF COMMUNICATION

REVIEWS AND NEWS

NEWS

JOURNAL OF THE ELECTROCHEMICAL SOCIETY

ELECTROCHEMICAL SCIENCE
— AND TECHNOLOGY —

SEPTEMBER
1977

The Hydrogen Electrode in Molten Carbonate

W. M. Vogel* and C. D. Iacovangelo*,[1]

United Technologies Corporation, Advanced Fuel Cell Research Laboratory, Power Systems Division, Middletown, Connecticut 06457

ABSTRACT

Open-circuit potentials are reported for the hydrogen (Au) electrode in molten carbonate at 650°C. The data, with few exceptions, agree with thermodynamic values calculated assuming simultaneous equilibrium of the shift and the methane reactions. The exceptions are those instances where methane has to be oxidized almost completely to reach equilibrium, and those where carbon can form during preheating of the gas.

The anodic activation polarization of the hydrogen electrode in alkali carbonate melts should be small because of the required high temperatures. This is evidently true because the nature of the electrode metal has no effect on the polarization (1). Ohmic losses can be estimated from the conductance of the electrolyte and should be generally small even in a porous gas diffusion electrode except when poorly conducting surface oxides are formed on the electrode metal. Thus, with negligible activation polarization and ohmic losses the anode polarization should consist, at potentials below the metal oxidation potential, of concentration overvoltages plus, possibly, some contribution from liquid junction potentials between anode and cathode.

Broers *et al.* (2) have found that the polarization of such anodes results primarily from the accumulation of reaction products (CO_2, H_2O) rather than from a lack of hydrogen. The anode reaction

$$H_2 + CO_3^{=} = H_2O + CO_2 + 2e^- \qquad [1]$$

produces CO_2 and H_2O both of which are acids in molten carbonates. Both enter into acid-base equilibria (3, 4) with the strongly basic $O^=$ ion

$$CO_2 + O^{=} = CO_3^{=} \qquad [2]$$

$$H_2O + O^{=} = 2\,OH^- \qquad [3]$$

The acidity constants, *i.e.*, the equilibrium constants of reactions [2] and [3] are of similar magnitude. Busson *et al.* (5) reported the values $K_{CO_2} = 10^{7.5}$ and $K_{H_2O} = 10^6$ for 600°C. The alkalinity of the melt, expressed as $pO \equiv -\log[O^=]$ in analogy to the pH of aqueous solutions (6), is therefore not determined by the CO_2 pressure alone but by both the pressures of H_2O and CO_2. Because of this simultaneous dependency of the oxygen ion concentration on both pressures, it appears more suitable to use the pO as the measure for acidity rather than the $PCO_2 \equiv -\log p_{CO_2}$ which was suggested by Janz *et al.* (7) for hydrogen-free systems.

A given melt can then be considered acidic if the pO is larger than a certain neutrality value, and alkaline if the reverse is true. Busson *et al.* (5) reported for the solubility of CO_2 the relationship $(CO_2) = 0.1\,P_{CO_2}$ (P_{CO_2} in atmospheres, (CO_2) in mole/liter). Together with the acidity constant of CO_2 we have, at 600°C

$$(CO_2)\,(O^=) = 10^{-8.5} \qquad [4]$$

We consider a melt to be neutral when $(CO_2) = (O^=)$, *i.e.*, at $pO = 4.25$. As long as the water pressure is not extremely high, the OH^- ions can be assumed to be dissolved in molten carbonate and we can use the same pO value for a neutral melt containing both acids, H_2O and CO_2. An equilibrium oxygen electrode can then be used as a pO indicator with the potential

$$E = E_o + \frac{RT}{4F} \ln P_{O_2} + \frac{2.3RT}{2F} \cdot pO \qquad [5]$$

The results of Broers *et al.* (2) indicate, in this terminology, a lack of buffer capacity of the electrolyte (8) as a main cause for the polarization of a hydrogen anode. This explanation assumes that the electrode reaction is, at all current densities, close to equilibrium, *i.e.*, the iR-free electrode potential is nearly identical with the equilibrium potential calculated with the activities of the reactants as they prevail at the metal/liquid interface. However, this explanation is in apparent contradiction to data in Ref. (5) which describes deviations from equilibrium even at open circuit. The discrepancies were as large as 100 mV with the largest differences observed in acidic and alkaline melts, *i.e.*, just where polarized molten carbonate electrodes are assumed to operate.

A number of factors can cause real or apparent discrepancies between calculated thermodynamic potentials and observed open-circuit potentials (ocp). The equilibrium potential of reaction [1] is given by

$$E = E^\circ + \frac{RT}{2F} \ln \frac{P_{H_2O} P_{CO_2}}{P_{H_2}} \qquad [6]$$

If arbitrary mixtures of H_2, CH_4, CO, and CO_2 are used we can calculate the equilibrium pressures of H_2O, CO_2, and H_2 provided that carbon is not formed.

* Electrochemical Society Active Member.
[1] Present address: General Electric Company, Research and Development Center, Schenectady, New York 12301.
Key words: molten carbonates, hydrogen electrode, open-circuit potentials.

However, the actual pressures at the electrode may be different, resulting in discrepancies between calculated and observed potentials.

It is also possible that observed differences are due to fundamental uncertainties which are introduced by the type of reference electrode used in previous studies. The H_2O and CO_2 pressures at a molten carbonate electrode cannot be changed without simultaneously changing the electrolyte composition (Eq. [2], [3]). As written, Eq. [6] assumes that E is measured against a reference in the same medium, and that the reference potential varies with the carbonate ion activity in the same way as that of the hydrogen electrode. An example is an oxygen reference electrode with the same H_2O and CO_2 pressures as the hydrogen electrode. In this case, E is simply the cell voltage for the water reaction and $E°$ can be calculated very accurately. Differences between such calculated values for E and observed ocp have to be due to nonequilibrium conditions of the working electrode. Such experiments are thermodynamically well defined but they are also cumbersome, requiring changes in the gas composition at the reference in concert with those at the working electrode.

It is more common to use a constant reference electrode. Such experiments are simpler to do but they are thermodynamically less well defined, *i.e.*, observed potentials cannot be compared with calculated values without additional assumptions. Assume that an oxygen electrode in a carbonate melt of fixed acidity (CO_2 pressure) is used as reference. Equation [6] can then be applied provided that liquid junction potentials and differences in the carbonate ion activities at the two electrodes are negligible. These conditions should be fulfilled except for very alkaline conditions at the working electrode. Similar restrictions apply to potentials referred to a metal/metal ion electrode such as that of Danner and Rey (9). With such a reference, furthermore, the standard potential $E°$ cannot be calculated from thermodynamic data but has to be determined empirically.

The present study was undertaken in an attempt to identify the reasons for previously reported deviations of ocp from thermodynamic values, and to determine how and under what circumstances the ocp can be calculated.

Experimental

The apparatus used in measuring the ocp is illustrated in Fig. 1. The electrolyte, which was a fused binary eutectic of 62 mole percent (m/o) Li_2CO_3 and 38 m/o K_2CO_3, was contained in a tapered crucible made of Degussit AL-23 (99.5% Al_2O_3, dense).

The working electrode (WE) was a 0.020 in. diam gold wire inside a 0.50 in. diam AL-23 tube with a 1 mm opening to the melt at the bottom. The tube was vented to the atmosphere through a 0.125 in. diam alumina tube.

The initial partial pressures of H_2 and CO_2 in the feed gas to the WE were regulated by flowing each gas through Gilmont Flowmeters (no. 1) connected by a tee to 0.25 in. diam tubing, 2 ft in length, where they were allowed to mix prior to entering the water saturator. The initial water pressure was established by flowing the gas mixture through a saturator maintained at the required temperature. The saturator efficiency was checked by absorbing the H_2O with Dri-Rite. The feed gas was subsequently preheated to 650°C by flowing at 200 ml/min through 0.25 in. diam 316 stainless steel tubing 7 ft in length. The latter was wrapped around the outside of the cell crucible.

The apparatus was heated in a Lindberg furnace. All experiments were done at 650° ± 0.5°C. The temperature was measured inside the cell with a thermocouple contained within an alumina tube.

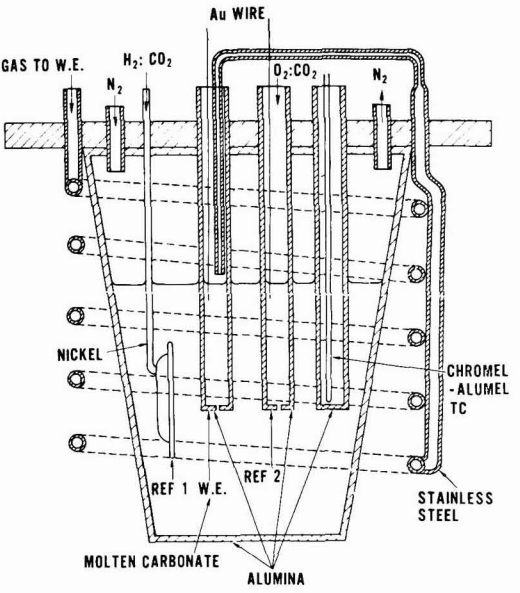

Fig. 1. Cell assembly

Cell voltages were measured with a Newport digital voltmeter having an input resistance of $10^9\Omega$.

For the present study a constant oxygen reference electrode was used [O_2, CO_2 (Au) with $P_{O_2} = 1/3$ and $P_{CO_2} = 2/3$ atm]. This choice of reference introduces fundamental inaccuracies which were described in the introduction. Significant errors of this nature should produce deviations of the ocp from theoretical values. As will be shown later, good agreement was observed which indicates that such errors were small for the range of compositions studied. The reference was checked against a CO/CO_2 electrode of similar melt composition ($P_{CO} = 0.382$ and $P_{CO_2} = 0.618$ atm). The difference between the observed and the calculated voltage of this cell [using data from Ref. (10)] was 2 mV which demonstrates the usefulness of our reference. Similar reliability in a ternary melt of alkali metal carbonates has been reported by Borucka *et al.* (11, 12).

Results and Discussion

The observed open-circuit potentials for initially dry mixtures of H_2 and CO_2 are listed in Table I. Included in this table are the pressures of H_2, H_2O, and CO_2 which were calculated assuming shift equilibrium ($K_p = 1.96$), and also simultaneous equilibrium of the shift and the methane reactions ($K_p = 2.68$). The data are plotted in Fig. 2. We see that neither assumption explains the experimental results.

One likely cause for the differences is carbon formation. If the gases are heated instantaneously to 650°C, carbon cannot form since the potential of the C/CO_2 reaction would be negative relative to the hydrogen potential if either shift or complete equilibrium is assumed. However, in our experiments the gas was heated gradually as it passed through the preheater tubing. At temperatures below 650°C the C/CO_2 potential becomes increasingly more anodic to the hydrogen potential assuming, *e.g.*, shift equilibrium, and carbon formation is likely.

The experiments were repeated with an addition of 14% H_2O vapor to the H_2-CO_2 mixtures. The re-

Table I. Initial (index°) and calculated pressures assuming equilibrium for the shift reaction only

Initially		Shift equilibrium				Shift and methane equilibrium					
$P_{H_2}°$	$P_{CO_2}°$	P_{H_2}	P_{CO_2}	P_{H_2O}	$E_{theor.}$	P_{H_2}	P_{CO_2}	P_{H_2O}	P_{CH_4}	$E_{theor.}$	$E_{expt.}$
0.05	0.95	0.005	0.905	0.045	−899	0.0045	0.905	0.045	3.4×10^{-8}	−894	−916
0.1	0.9	0.017	0.817	0.083	−927	0.017	0.817	0.083	1.7×10^{-6}	−926	−945
0.2	0.8	0.059	0.659	0.141	−964	0.059	0.659	0.141	7.7×10^{-5}	−964	−975
0.3	0.7	0.121	0.521	0.179	−993	0.120	0.523	0.179	6.4×10^{-4}	−992	−985
0.4	0.6	0.199	0.399	0.201	−1018	0.195	0.404	0.202	0.0027	−1017	−1000
0.5	0.5	0.292	0.292	0.208	−1045	0.279	0.301	0.214	0.0075	−1041	−1010
0.6	0.4	0.399	0.199	0.201	−1074	0.370	0.212	0.217	0.016	−1065	−1025
0.7	0.3	0.521	0.121	0.179	−1109	0.472	0.135	0.211	0.029	−1094	−1045
0.8	0.2	0.659	0.059	0.141	−1156	0.591	0.068	0.192	0.043	−1138	−1070
0.9	0.1	0.817	0.017	0.083	−1235	0.748	0.017	0.142	0.049	−1212	−1105

Table II. Initial (index°) and calculated pressures assuming equilibrium for shift reaction only, and assuming complete equilibrium

Initially			Shift equilibrium				Shift and methane equilibrium					
$P_{H_2}°$	$P_{CO_2}°$	$P_{H_2O}°$	P_{H_2}	P_{CO_2}	P_{H_2O}	$E_{theor.}$	P_{H_2}	P_{CO_2}	P_{H_2O}	P_{CH_4}	$E_{theor.}$	$E_{expt.}$
0.043	0.817	0.14	0.013	0.787	0.170	−890	0.013	0.787	0.170	1.4×10^{-7}	−890	−895
0.086	0.774	0.14	0.030	0.718	0.196	−921	0.030	0.718	0.196	2.7×10^{-6}	−921	−925
0.172	0.688	0.14	0.076	0.592	0.236	−958	0.076	0.552	0.236	6.4×10^{-5}	−958	−960
0.258	0.602	0.14	0.134	0.478	0.264	−985	0.133	0.479	0.264	3.9×10^{-4}	−984	−982
0.344	0.516	0.14	0.204	0.376	0.280	−1009	0.201	0.378	0.281	0.0014	−1008	−1010
0.430	0.430	0.14	0.285	0.285	0.285	−1032	0.277	0.289	0.289	0.0037	−1030	−1030
0.516	0.344	0.14	0.376	0.204	0.280	−1057	0.360	0.209	0.290	0.0076	−1053	−1050
0.602	0.258	0.14	0.478	0.134	0.264	−1086	0.451	0.139	0.284	0.0129	−1079	−1078
0.688	0.172	0.14	0.592	0.076	0.236	−1121	0.555	0.077	0.267	0.0185	−1113	−1112

sults are given in Table II, together with the pressures of H_2, H_2O, and CO_2 again calculated with the assumption that only the shift reaction is in equilibrium. The ocp and the thermodynamic potentials E, derived from these calculated pressures, are plotted in Fig. 3a against the activity term in Eq. [6]. The agreement is better than in Table I. However, at low potentials the experimental data still are more positive than the calculated values. The ocp appears to be a mixed potential with the hydrogen reaction being anodically polarized and some other reaction proceeding cathodically. This electrochemical description is being used because any of the possible chemical reactions (shift, Boudouard, etc.) can be considered as the neutral sum of electrochemical partial reactions. It does not matter, for the present purpose of determining equilibrium potentials, where these reactions occur, *i.e.*, at the metal/liquid interface or somewhere upstream from the electrode.

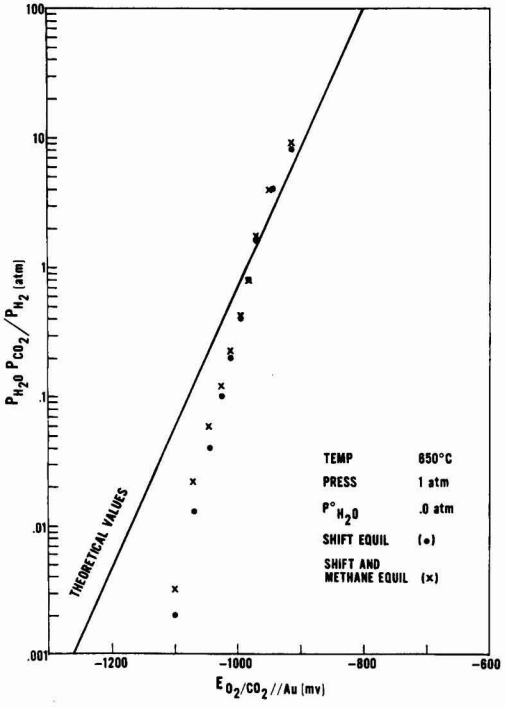

Fig. 2. Open-circuit potentials for dry mixtures of H_2 and CO_2. Partial pressures of H_2, CO_2, and H_2O calculated assuming equilibrium for the shift reaction only.

We have the following four reactions, combinations of which yield all other possible reactions (chemical or electrochemical)

$$H_2 + CO_3^{=} = CO_2 + H_2O + 2e^- \quad [7]$$

$$CO + CO_3^{=} = 2CO_2 + 2e^- \quad [8]$$

$$C + 2CO_3^{=} = 3CO_2 + 4e^- \quad [9]$$

$$CH_4 + 4CO_3^{=} = 5CO_2 + 2H_2O + 8e^- \quad [10]$$

Since, by adding 14% H_2O, we had raised the value of E for reaction [7] above that for reaction [9] no carbon formation was possible. Reaction [8] was accounted for by assuming equilibrium for the shift reaction which is the (electrically neutral) sum of reactions [7] and [8]. It was indicated, therefore, that the cathodic branch of reaction [10] was responsible for the remaining differences in Fig. 3a.

The equilibrium pressures for the gas mixtures in Table II were recalculated assuming that reactions [7], [8], and [10] were in equilibrium. Thus, in addition to the shift reaction, the methane formation, which results from a combination of reactions [10] and either [7] or [8], was assumed to be in equilibrium. The value

$$K = \frac{P_{CO}P_{H_2}^3}{P_{CH_4}P_{H_2O}} = 2.68 \quad [11]$$

was used. The results are given in Table II and Fig. 3b. Agreement between observed and theoretical potentials appears satisfactory.

In Fig. 4 and Table III the results are given for gas mixtures containing a constant initial amount of methane. The experimental and theoretical potentials agree with each other except for those gases for which complete equilibrium requires nearly complete oxidation of methane, *i.e.*, to pressures below approximately 0.0006 atm.

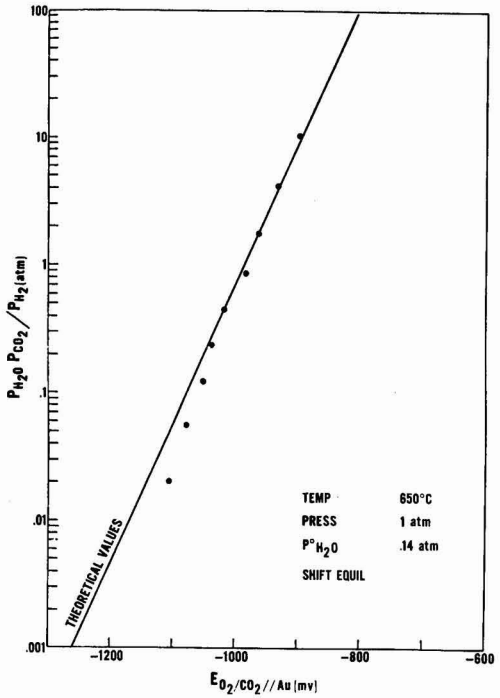

Fig. 3 (a, top; b, bottom) The ocp for humidified mixtures of H_2 and CO_2. Partial pressures of H_2, CO_2, and H_2O calculated assuming equilibrium for shift reaction only (a), and complete equilibrium (b).

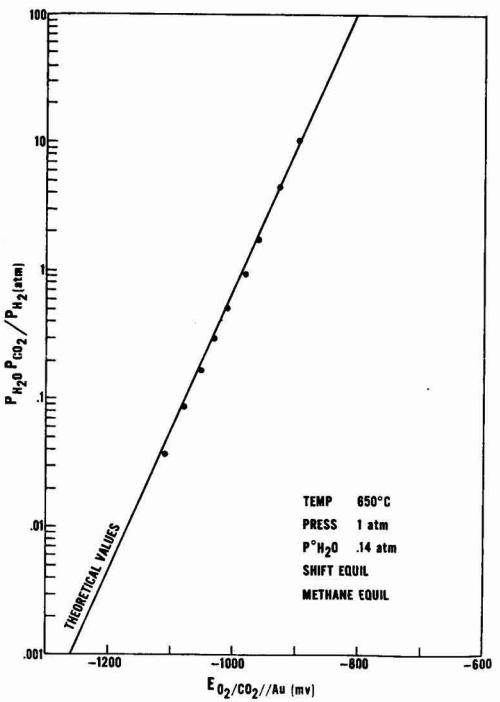

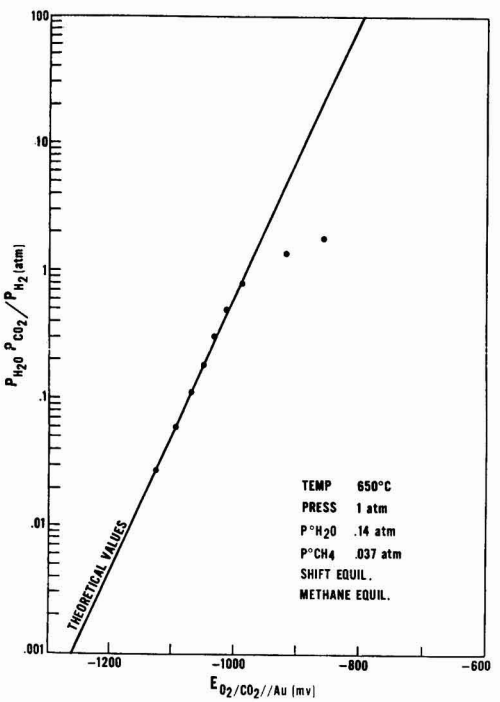

Fig. 4. The ocp for mixtures of H_2, CH_4, H_2O, and CO_2. Partial pressures calculated assuming complete equilibrium.

Conclusions

We conclude that, in calculating the ocp of a hydrogen electrode from the composition of the (initially cold) feed gas, the entire experimental setup has to be considered including the device used to preheat the gas. Large errors can result if complete equilibrium is not achieved. This is particularly true if the initial gas contains insufficient water to prevent carbon formation at lower temperatures encountered by the gas during heating. If, on the other hand, an equilibrium gas mixture is supplied, the ocp in most instances agrees accurately with the thermodynamic value. Exceptions are experiments in which equilibrium can be obtained only by nearly complete oxidation of excess methane in the feed gas.

Manuscript submitted Nov. 8, 1976; revised manuscript received April 21, 1977.

Any discussion of this paper will appear in a Discussion Section to be published in the June 1978 JOURNAL. All discussions for the June 1978 Discussion Section should be submitted by Feb. 1, 1978.

Publication costs of this article were assisted by United Technologies Corporation.

REFERENCES

1. L. P. Klevtsov, G. G. Arkhipov, and G. K. Stepanov, *Elektrokhimia*, **3**, 785 (1967).
2. G. H. J. Broers and M. Schenke, in "Hydrocarbon Fuel Cell Technology," B. S. Baker, Editor, Academic Press, New York (1965).
3. H. Lux, *Z. Elektrochem.*, **45**, 303 (1939).
4. H. Flood and T. Forland, *Acta Chim. Scand.*, **1**, 592 (1947); *ibid.*, **1**, 781 (1947); *ibid.*, **1**, 790 (1947).
5. N. Busson, S. Palous, J. Millet, and R. Buvet, *Electrochim. Acta*, **12**, 1609 (1967).
6. R. Littlewood, *This Journal*, **109**, 525 (1962).
7. M. D. Ingram and G. J. Janz, *Electrochim. Acta*, **10**, 783 (1965).
8. J. T. Lundquist and W. M. Vogel, *This Journal*, **116**, 1066 (1969).

Table III. Initial (index°) and calculated pressures assuming complete equilibrium

Initially				Shift equilibrium					Shift and methane equilibrium					
$P_{H_2}°$	$P_{CO_2}°$	$P_{H_2O}°$	$P_{CH_4}°$	P_{H_2}	P_{H_2O}	P_{CO_2}	P_{CH_4}	$E_{theor.}$	P_{H_2}	P_{H_2O}	P_{CO_2}	P_{CH_4}	$E_{theor.}$	$E_{expt.}$
0.0411	0.782	0.14	0.037	0.0125	0.169	0.753	0.037	−890	0.061	0.176	0.648	0.00005	−957	−860
0.082	0.741	0.14	0.037	0.029	0.193	0.688	0.037	−922	0.083	0.192	0.594	0.00014	−970	−920
0.165	0.658	0.14	0.037	0.073	0.231	0.567	0.037	−959	0.134	0.218	0.493	0.00061	−991	−991
0.247	0.576	0.14	0.037	0.129	0.258	0.459	0.037	−986	0.193	0.234	0.403	0.0018	−1011	−1015
0.329	0.494	0.14	0.037	0.196	0.273	0.361	0.037	−1010	0.258	0.244	0.321	0.0043	−1030	−1035
0.412	0.412	0.14	0.037	0.274	0.278	0.274	0.037	−1033	0.327	0.248	0.249	0.0084	−1049	−1050
0.494	0.329	0.14	0.037	0.361	0.273	0.196	0.037	−1058	0.403	0.246	0.183	0.0144	−1070	−1070
0.576	0.247	0.14	0.037	0.458	0.258	0.129	0.037	−1087	0.485	0.239	0.125	0.0220	−1093	−1096
0.658	0.165	0.14	0.037	0.567	0.231	0.073	0.037	−1122	0.578	0.223	0.073	0.0296	−1124	−1127
0.741	0.082	0.14	0.037	0.688	0.193	0.029	0.037	−1173	0.691	0.190	0.029	0.0331	−1174	−1175

9. G. Danner and M. Rey, *Electrochim. Acta*, 4, 274 (1961).
10. JANAF Thermodynamic Tables, 2nd ed., U.S. Dept. of Commerce, NSRDS-NBS 37 (1971).
11. A. Borucka and C. M. Sugiyama, *Electrochim. Acta*, 13, 1887 (1968).
12. A. Borucka and C. M. Sugiyama, *ibid.*, 14, 871 (1969).

Equilibrium Properties of Lithium/Niobium Selenide, Nonaqueous Secondary Cells

J. N. Carides and D. W. Murphy*

Bell Laboratories, Murray Hill, New Jersey 07974

ABSTRACT

Equilibrium-open-circuit potentials of Li/$LiClO_4$, PC/$NbSe_x$ (x = 2, 3, 4, 4.5) cells were measured as a function of the state of charge of these cells. For $NbSe_2$ the emf decreased monotonically from ~2.3 to 1.65V at full discharge (1 Li/Nb) and was independent of prior history. With $NbSe_3$ two distinct types of emf curves were found: (*i*) a constant emf of ~1.7V from 0-2Li/Nb followed by a monotonic decrease in emf to ~1.5V at 3Li/Nb, and (*ii*) a "stepped" form with breaks at 1 and 2Li/Nb. Neither type of curve was reproduced on cycling. The emf of $NbSe_4$ and $NbSe_{4.5}$ was nearly constant at 1.83V to ~4Li/Nb. The $NbSe_4$ exhibits a monotonic decrease in emf to ~1.6V at 5Li/Nb. The emf curves obtained on the first charge and subsequent cycles were higher in value. The implications of this data on the chemistry of cell discharge is discussed.

Interest in nonaqueous reversible cells of lithium with metal chalcogenides prompted a study on the equilibrium properties of these cells with the series of niobium selenides $NbSe_2$, $NbSe_3$, and $NbSe_{4+x}$ to determine equilibrium properties, and to better understand the chemistry in this series. The selenides of niobium were chosen because they exhibit a wide range of stoichiometries. Dynamic electrochemical results have been reported for $NbSe_3$ (1) and for $NbSe_{4+x}$ (x = 0-0.5) (2). The class of metal dichalcogenides has been suggested to form reversible cathodes with Li (3, 4), prompting the examination of $NbSe_2$.

Experimental

Materials.—Niobium powder (30 μm, 99.95% purity), selenium shot (5*N* purity), graphite powder (325 mesh), lithium foil (Foote Mineral Company), and polyethylene powder (Microthene 500, U. S. Industrial Chemicals) were used as received. Propylene carbonate (PC) and tetraglyme (TTG) were vacuum distilled from lithium. Lithium hexafluorophosphate (Ventron) and lithium perchlorate (Ventron) were vacuum dried at ~ 150°C. The selenides of niobium were prepared by direct reaction of the elements in sealed vitreous silica ampuls at 750°, 680°, and 450°C for $NbSe_2$, $NbSe_3$, and $NbSe_{4+x}$, respectively. X-ray diffraction patterns agree with those previously reported for these phases.

* Electrochemical Society Active Member.
Key words: batteries, intercalation, chalcogenides.

Construction of Test Cells

Except for $NbSe_3$, cathodes were prepared by hot pressing a mixture of 65-70% active powder (150 mesh), 30-25% graphite, and the balance polyethylene (PE). Pressing was done at ~123°C and 3.5 × 10^4 psi yielding samples of ~ 7 mil thickness that were cut to convenient sizes. The natural growth habit of $NbSe_3$ resulted in a conducting, feltlike material of interwoven fibers, which was cut into sections and used directly. All samples were sandwiched between nickel screen to provide support and external connection.

The cathodes were placed horizontally in a crystallizing dish together with a lithium electrode, separation provided by glass filter paper or glass wool.

With one exception, the electrolyte was 1.0*M* $LiClO_4$ in PC. One cell, using $NbSe_4$, was constructed with 0.1*M* $LiPF_6$ in TTG to determine the significance of the electrolyte.

Cells were constructed in an inert atmosphere box under argon, and were mounted in air-tight Mason jars fitted with electrical feed throughs.

Test Procedure

Voltages were measured using a Keithley 160B digital multimeter. Cells were discharged at low current densities for periods of 8-24 hr, representing a suitable fraction of the theoretical capacity. Typical current densities were of the order of 50 μA/cm². Following

discharge the cell was disconnected and allowed to equilibrate for periods of 16-48 hr. Approach to equilibrium was determined by periodic potentiometric readings during the time interval. When voltage readings indicated a change of 0.010V or less over an 8 hr sampling period, the cell was regarded as having attained equilibrium and the voltage at that point recorded; discharge to the next point was then resumed. The same procedure was followed on charging. All voltage readings were made at 24° ± 2°C.

Several cells of each type were tested and the curves derived were the best fit for all points.

At least one representative of each cathode material was cycled several times. Some cells were cycled within a range that represented only a fraction of the theoretical capacity.

After the tests were completed, each cell was dismantled and the cell components visually inspected. None of the electrodes showed any deterioration or other abnormalities.

Results and Discussions

$NbSe_2$.—Lithium is introduced into $NbSe_2$ according to $xLi + NbSe_2 \rightarrow Li_xNbSe_2$ $(0 \leq x \leq 1)$ (5, 6). Figure 1 shows a gradual decrease in emf indicating that Li_xNbSe_2 is single phase over the entire composition range. The shape may be understood to arise from a gradual filling of the metallic d band in $NbSe_2$, lithium inserting between Se layers in which only Van der Waals bonding exists. This result is similar to that previously discussed for TiS_2 (3, 7), whose equilibrium emf is compared in the same figure. Upon recharging $NbSe_2$ cells, the equilibrium voltage curve tracks the discharge curve within 3%, confirming that the same composition is obtained from charge or discharge.

These results were reproduced in several test cells and in each case the cells could be discharged to at least 95% of theoretical capacity (1 lithium) while still permitting recovery of at least 90% of the amount discharged.

Previous work (8) on $NbSe_2$ in Li cells containing I_2 suggested that $NbSe_2$ acted as a "host" for I. Reexamination of that cell data shows a substantial capacity in the voltage range observed here for lithium intercalation.

$NbSe_3$.—Results for $NbSe_3$ (Fig. 2) are ambiguous. In some cases the equilibrium emf was similar to that found for slow discharge (9), and OCV data for TiS_3 (3). Other cells behaved quite differently, sometimes even for material taken from the same sample preparation and with identical x-ray powder patterns. After cycling, all the $NbSe_3$ cells exhibited a gradual sloped emf. These differences in various $NbSe_3$ electrodes and the changes in emf on cycling imply that the structure is changing on cycling. Inspection of the structure of $NbSe_3$ (Fig. 3) (10) suggests the possibility that the complex arrangement of chains in the structure may not be unique. Such polytypism has been noted for a number of two-dimensional compounds involving coordination geometry and registry of the layers. The polytype formed at 680°C may not be the most stable at room temperature and also might change via lithiation and delithiation. We have been unable to detect

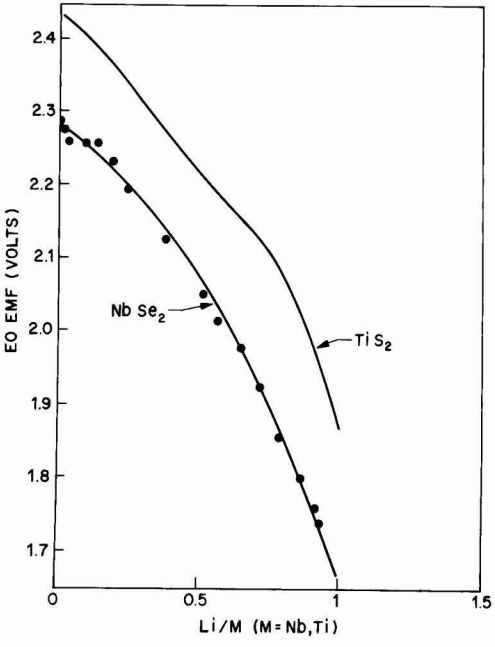

Fig. 1. Equilibrium voltage of $NbSe_2$ as a function of Li composition, compared with results given for TiS_2 (3).

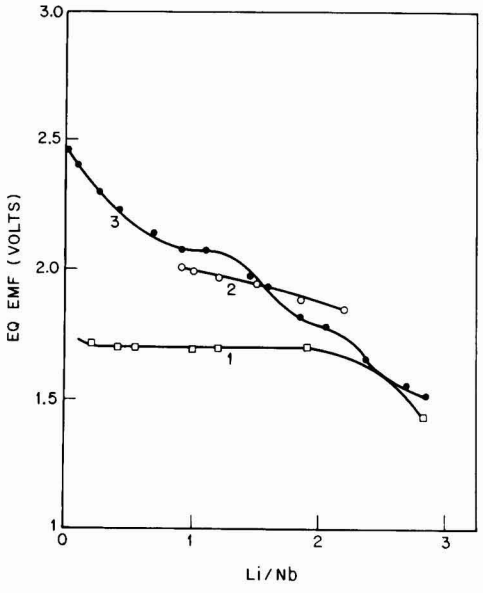

Fig. 2. Equilibrium voltage curves for $NbSe_3$ as a function of Li content. Curve 1 is first discharge curve for one type of behavior; curve 2 is the equilibrium curve for the same type on second discharge. Some $NbSe_3$ cells yielded a "stepped" voltage on first discharge, as shown by curve 3.

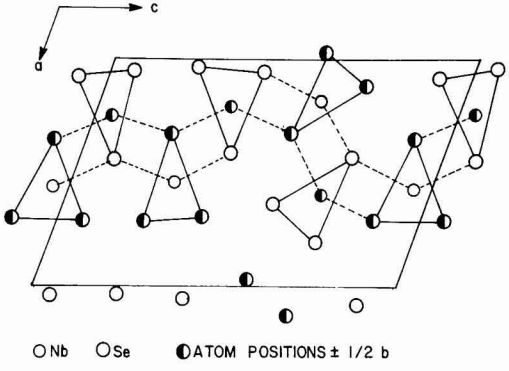

Fig. 3. Structure of $NbSe_3$ (10)

these changes by x-ray powder patterns, the patterns being quite complex, weak, and diffuse.

$NbSe_4$.—Cells were cycled to 2Li/Nb, 4Li/Nb, and 5Li/Nb. The equilibrium emf's are shown in Fig. 4. The curve is almost flat (slightly negative slope) from 1-3Li at about 1.83 ± 0.02V. This curve differs from that reported (2) under dynamic conditions in that a break appears beginning at about 3.5Li, with the voltage remaining above 1.5V at 5Li, as opposed to a sharp drop in voltage at 4Li in the dynamic study. This particular cell was recharged to ~ 84% of amount discharged.

Cells limited to 2 or 4Li showed better rechargeability, ~93% of amount discharged. In the initial part of the first recharge, the 0-4Li emf levels off at ~ 2.07V, and the 0-2Li emf merges with the 0-4Li emf near 1.5Li; therefore, these charge curves tracked each other. When both these types of cells were subsequently discharged (second discharge), they continued tracking each other closely, although at a higher but still flat emf (1.92 ± 0.02V) over the range 1.5-3.8Li. The second discharge curve for the 0-5Li cell started at higher voltages than the first discharge, but ultimately converged with the others in the range ~ 2.8-4Li. This phenomenon of different discharge curves converging to the same emf, and the relative flatness of the composite second discharge curve was true of the $NbSe_{4.5}$ series as well.

Another $NbSe_4$ cell using 0.1*M* $LiPF_6$ in TTG yielded a curve similar to that using $LiClO_4$/PC, but approximately 3% lower in emf, indicating any role played by the electrolyte is minimal.

$NbSe_{4.5}$.—Cells were cycled from 0 to 2Li, and 0 to 4Li. Recoverability was about 90% for all these cells. One cell was discharged to 4.3Li/Nb, but further discharge was not possible without a precipitous drop in the cell voltage below ~ 1.2V (recoverability for the cell was about 87%). The emf remained at 1.83 ± 0.01V to 4.3Li, thus there was no gradual decrease in emf as with $NbSe_4$. The initial equilibrium curve was nearly flat (1.83 ± 0.01V) over most of the range as shown in Fig. 4.

Except for the cell that was discharged beyond 4Li, the various initial charge and second discharge curves

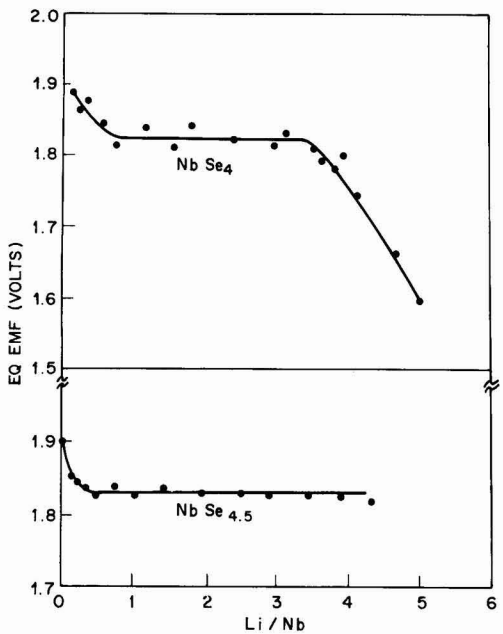

Fig. 4. Composite results for equilibrium voltages of $NbSe_4$ and $NbSe_{4.5}$, as a function of Li content; first discharge.

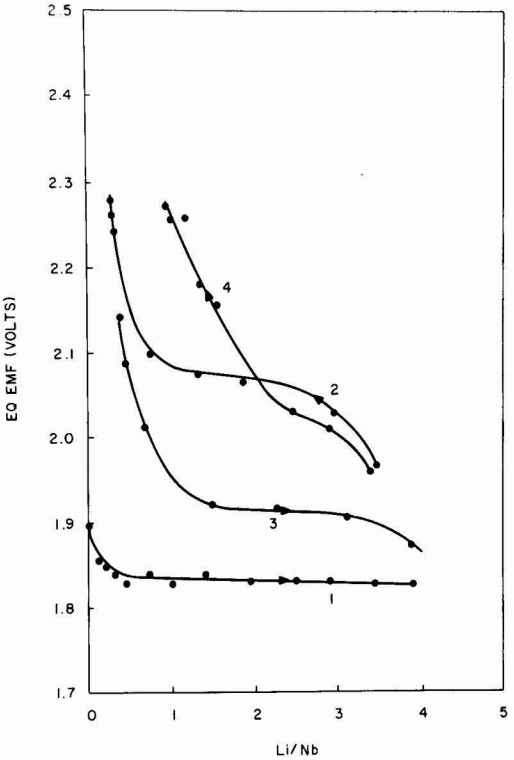

Fig. 5. Equilibrium voltages for two complete cycles of an $NbSe_{4.5}$ cell, as a function of lithium content.

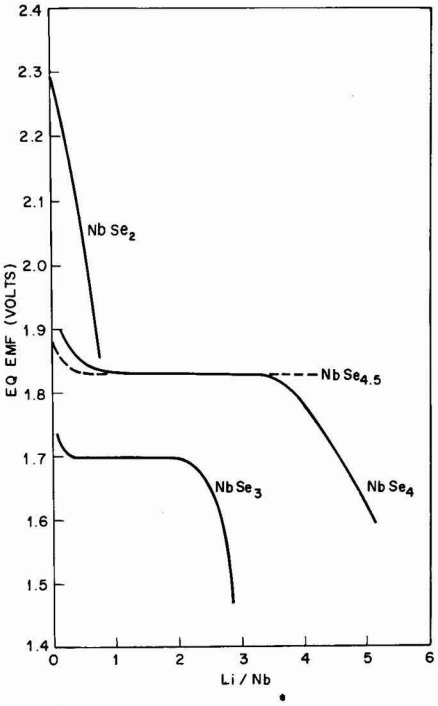

Fig. 6. Composite showing equilibrium voltages for cell $NbSe_x$ compounds studied in this series.

converged in a manner similar to that described for $NbSe_4$. The second discharge curve is flat at about 1.93 ± 0.02V over the range 1-3Li. Typical emf curves for 2 full cycles are shown in Fig. 5.

Discussion

All the initial discharge data are compared and summarized in Fig. 6. For $NbSe_3$ we observed varying initial discharge curves on samples giving identical x-ray patterns. We have included in Fig. 6 the curve resembling that previously published (9).

$NbSe_2$ is essentially fully reversible by the mechanism of lithium intercalation involving virtually no irreversible chemical changes, similar to TiS_2 (3). The shape of the equilibrium emf *vs.* composition curves confirm that a single phase is involved during cycling. The higher selenides of niobium were reversible in varying degrees, but the charge curves were significantly different than the discharge curves. Indeed, the equilibrium charge voltage exceeded the initial discharge voltages by at least 15%. In these cases, the chemistry is obviously more complex and significant changes take place within the first cycle. The very low current densities and long equilibration times minimized effects due to solvent incorporation. The test with 0.1*M* $LiPF_6$ in TTG supports this conclusion.

For $NbSe_3$ (curve 1, Fig. 2) the flat portion of the discharge curve is lost after the first cycle, while in $NbSe_4$ and $NbSe_{4.5}$ level, although higher than original, emf's persist and data points from cells having different cycle history tend to converge during some overlapping parts of the cycle span. This behavior is best reproduced when a composition of Li_4NbSe_{4+x} ($x = 0, 0.5$) is not exceeded.

The changing OCV curves on cycling the higher selenides $NbSe_3$ and $NbSe_{4+x}$ ($x = 0, 0.5$) seems to indicate a multiphase system or a gradual structure change in these cases. Further studies are needed to confirm and elucidate such changes.

Manuscript submitted March 7, 1977; revised manuscript received April 14, 1977.

Any discussion of this paper will appear in a Discussion Section to be published in the June 1978 JOURNAL. All discussions for the June 1978 Discussion Section should be submitted by Feb. 1, 1978.

Publication costs of this article were assisted by Bell Laboratories.

REFERENCES

1. J. Broadhead and F. A. Trumbore, Paper 178 presented at The Electrochemical Society Meeting, Chicago, Illinois, May 13-18, 1973.
2. D. W. Murphy, F. A. Trumbore, and J. N. Carides, *This Journal*, **124**, 325 (1977).
3. M. S. Whittingham, *ibid.*, **123**, 315 (1976).
4. G. L. Holleck, F. S. Shuker, and S. B. Brummer, Paper No. 759070, 10th International Energy Conversion Engineering Conference, 1975.
5. M. B. Dines, *Mater. Res. Bull.*, **10**, 287 (1975).
6. D. W. Murphy, F. J. Di Salvo, G. W. Hull, Jr., and J. V. Waszczak, *Inorg. Chem.*, **15**, 17 (1976).
7. M. S. Whittingham, *Science*, **192**, 1126 (1976).
8. J. Broadhead, in "Power Sources 4," D. H. Collins, Editor, p. 469, Oriole Press, Newcastle Upon Tyne, England (1973).
9. D. W. Murphy and F. A. Trumbore, *This Journal*, **123**, 960 (1976).
10. A. Meerschaut and J. Rouxel, *J. Less Common Metals*, **39**, 197 (1975).

The Allotropes of Dibasic Lead Oxide: A Quantitative X-Ray Diffraction Analysis

J. R. Dafler*[1]

ESB Incorporated, Technology Center, Yardley, Pennsylvania 19067

ABSTRACT

The allotropes of PbO are important in the formulation of positive and negative elements for lead-acid, SLI-battery systems. Recently, there has been renewed interest in making plates rich in tetrabasic lead sulfate [$(PbO)_4PbSO_4$] or tribasic lead sulfate [$(PbO)_3PbSO_4(H_2O)$], with special attention to which species predominates in the fully conditioned plate. The form is, characteristically, related to whether the starting oxide for paste formulation is rich in orthorhombic or tetragonal PbO. A quantitative technique, using x-ray diffractometry, to determine the amount of one allotrope in mixtures of both is given here, with a discussion of sources of probable error and the character of analyses based on linear calibration curves.

Dibasic lead oxide (PbO) occurs in two polymorphic forms: the tetragonal, t-PbO; and the orthorhombic, o-PbO; oxides. Both oxides are important in the lead-acid battery industry, and t-PbO is a major component of most commercial oxides used to make porous, pasted electrodes for storage batteries. The two oxides have slightly different densities and, according to Clark and Kern (1) and others (2-4), differing reactivities. Some battery manufacturers prefer to formulate pastes for electrode manufacture with oxide mixtures that contain no o-PbO. These oxides, the very low yellow (VLY) oxides, are considered by some to be superior for paste production and battery element fabrication. The presence of o-PbO is now considered desirable or undesirable only according to the crystal form sought in cured, pasted, unformed plates. If $(PbO)_4PbSO_4$ [tetrabase] is desired (5, 6), o-PbO rich oxides are selected, while the formation of $(PbO)_3PbSO_4(H_2O)$ [tribase] appears favored by the presence of t-PbO. Pavlov and Papazov (7) have recently summarized the results of a large amount of careful experimental work concerning the interplay of the divalent oxides in yielding the final form of battery plates. Their conclusions with respect to the morphologies of cured plate species disagree with ours, but their summaries of pasting and paste manufacturing do not.

* Electrochemical Society Active Member.
[1] Present address: Institute of Gas Technology, Chicago, Illinois 60616.

Key words: basic lead sulfates; lead oxides, dibasic; x-ray diffractometry.

Considerable battery practice has been devoted to developing cured plates rich in $(PbO)_3PbSO_4(H_2O)$, and Mrgudich (8), using VLY oxides found a modified or activated PbO that apparently was a distorted t-PbO. Moreover, in his work, mixing and pasting techniques that produced $(PbO)_4PbSO_4$ yielded little of the distorted species, suggesting a special propensity to incorporate into the tetrabase lattice. Clark and Tyler (3) had systematically studied the Pb(II) oxides and found an "active" PbO that had unusual properties which could be indexed by catalytically decomposing hydrogen peroxide, though some of their o-PbO:t-PbO mixtures also had unusual activity for H_2O_2 decomposition. Later Clark and Rowan (9) found that o-PbO could be converted to a distorted t-PbO by grinding. They attributed this to transformations taking place in imperfectly crystallized regions that were undergoing natural o-PbO → t-PbO transitions. Petersen (10) summarized much of the early effort devoted to preparation and identification of the allotropes of PbO.

In agreement with long standing experience, Pavlov and Iliev (11) established that $(PbO)_3PbSO_4(H_2O)$ is the preponderant phase in pastes made at temperatures below 80°C. They suggested that $(PbO)_4PbSO_4$ was formed at higher temperatures by reacting $(PbO)_3PbSO_4(H_2O)$ with t-PbO, but only if o-PbO was present. Pavlov and Papazov contend the necessary o-PbO will be generated by processes in paste mixing, and by oxidizing the metallic lead in commercial oxides when H_2SO_4 is present.

For reasons of older battery practice and craft, and evaluation of treated ores and commercial oxides for purchase, it was necessary to have a fast and reasonably simple technique to quantitatively determine o-PbO in a given oxide sample.

X-ray diffraction of Pb(II) oxides.—Orthorhombic and tetragonal PbO possess distinct, sharply defined x-ray diffraction spectra (12) and, moreover, their most intense diffraction maxima (I_{100}) occur quite close to one another in a spectrum of mixtures, making quantitative diffractometry appear a very promising method of analysis (13, 14). Mixtures of t-PbO and o-PbO, and commercial oxides for lead-acid battery manufacture represent quasi two-component systems in which the mass absorption coefficients, μ_{xi}, are the same, obviating the need to make absorption corrections to the measured intensities (15). Alexander and Klug have shown that the measured intensity, I_i, of a line in a mixture where $\mu_{xi} = \mu_{xj}$, is a linear function of the fraction of the ith component in an i-j mixture (14). Ores and commercial oxides sometimes contain metallic lead in quantities up to 30%, however, this component represents no difficulty, except as a relatively constant matrix diluent.

The method of standard additions is frequently used in atomic absorption spectrophotometry (16) and stripping voltammetry (17), and can be applied to any analytical problem in which matrix interference effects need to be minimized (18, 19). Klug and Alexander adumbrated the use of this method for quantitative diffraction analysis of very small samples (20).

Quantitative diffractometry by the method of standard additions is one depending on linear calibration curves, and the difficulties inherent in such analyses is discussed by Mandel and Linnig (21). The method and treatment of data derived using linear calibrations is treated in detail by Larsen, Hartmann, and Wagner (22). Basically what is done is the unknown matrix is scanned carefully and the ratio of the analyzed, I_{100}-line intensities is determined, preferably in a statistical fashion from several separate, discrete scans. The sample is then "spiked" or diluted with carefully measured amounts of the subject polymorph (in this case o-PbO) to produce two or three calibrating samples. These are mixed with extreme care and the x-ray intensity ratios, R_i, measured.

The standard addition samples are used to generate an analysis, or calibration curve, produced by plotting the appropriate R-values as a function of percent added o-PbO. Since linear regression analysis is available so casually through the use of hand-held calculators, a least squares line can usually be determined within minutes. The line will have a positive slope and a negative intercept on the abscissa. The absolute value of the x-intercept (percent added o-PbO concentration) will be the determined value of the unknown quantity. If the line is translated so that it includes the origin, a recalculation of all points must lie on a straight line parallel the original calibration curve.

The analytical possibilities inherent in the x-ray diffraction spectrum, apparently were first listed by Hull (23). The first practical analysis appears to be that of Clark and Reynolds (19), and since the work of Klug and Alexander and colleagues (14, 15, 20, 24) quantitative diffractometry has found widespread application.

Experimental Procedures

A commercial lead oxide was used for this study. It is a standard "leady" oxide used to prepare $(PbO)_3PbSO_4(H_2O)$-rich elements for positive plate manufacture. It contained 17.6% metallic lead, the rest being t-PbO. This was VLY oxide and contained no o-PbO. The o-PbO was a high purity litharge supplied by Johnson, Matthey and Company, Limited of London. An x-ray diffraction spectrum of a "nonleady" commercial oxide is shown in Fig. 1. The diffraction maxima useful in this analysis are noted.

Portions of the VLY oxide were carefully diluted with small amounts of o-PbO, the additions to represent, approximately 5, 10, 15, and 20%. The carefully measured chemicals were then mixed thoroughly in a SPEX shaker mill with a single alumina ball.

A Philips Electronics, Incorporated x-ray diffractometer, using Cu radiation was used for all intensity measurements. This unit has a curved crystal monochromator (LiF). For analytical measurements the scanning rate was 0.25°/min, with a 0.2° receiving slit, and beam settings of 42 kV:22 mA. These instrument settings yield a natural linewidth of ~0.2°.

Four spectra of the interesting regions were made for each sample. After each scan, the sample was discarded and the storage bottle once more shaken in the SPEX mill. Samples were back-filled into the holders to minimize possible orientation effects.

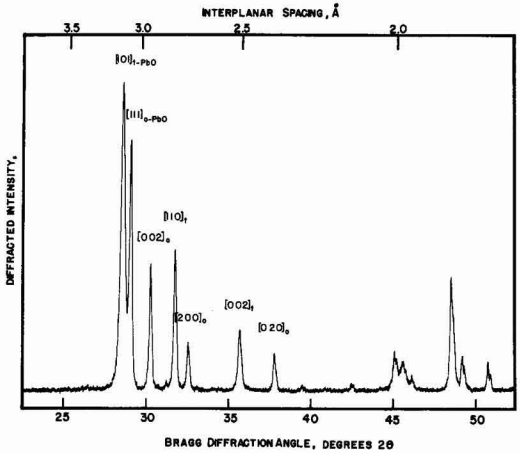

Fig. 1. X-ray diffraction spectrum of a "nonleady" commercial oxide. The principal x-ray diffraction maxima of t-PbO and o-PbO are indicated.

Commercial oxides for lead-acid battery plate manufacturing are generally very fine, and all but a very small fraction of the material used did not pass a 325 mesh ASTM sieve. Crystallite size and particle size in these oxides are so small, generally, that some line broadening is seen. This enhances the practicability of the analysis: Alexander, Klug, and Kummer (24) have shown that reproducibility of intensity measurements is highest if the average particle size is less than ~5μ. Wilchinsky has correlated the effects due to crystal, grain, and particle size on diffracted beam power (25).

To simulate unknown analysis and visually establish the linearity of the intensity ratio: percent added o-PbO calibration, all samples were scanned in serial order, After the initial remixing of the samples, each was scanned three more times in random order. The pooled data were then subjected to multiple linear regression analysis using a digital computer to establish the over-all "goodness" of the calibration line, and to obtain a statistically derived standard error of estimate, *Sr*. The data were also processed with a hand calculator that featured linear regression analysis (Texas Instruments SR-51A). The simulated analyses that follow were processed using the hand calculator.

Results and Discussion

The two x-ray diffraction maxima used in this determination are: o-PbO, the [111] line; 3.07Å at a Bragg angle of 29.06°; and t-PbO, the [101] line; 3.12Å at a Bragg angle of 28.58°. The base line for the intensity measurements was established between the steady background at 26.5° and the diffraction minimum at 29.8°. The relative intensity ratio, $R = I(\text{o-PbO}[111])/I(\text{t-PbO}[101])$, is obtained from the uncorrected peak height measurements. The method is illustrated in Fig. 2, which shows two typical scans for samples containing differing amounts of o-PbO.

The values of R calculated from four different "spiked" samples of the commercial oxide are summarized in Table I. The initial, serially obtained values are denoted with asterisks. They are discussed in another section as a simulated unknown analysis. The data in the table are listed in order of increase in R-value to facilitate initial statistical treatment. The line "added o-PbO" is used in a later section to discuss regular analysis of an unknown (in this case the first sample, 6.875% o-PbO, is the simulated unknown).

The sixteen data were subjected to linear regression analysis after examination for gross error. Of the two data that are questionable and do not fit their populations well (underlined in Table I) only the second, the 0.2595, point can be rejected by the ratio test of Crow *et al.* (26).

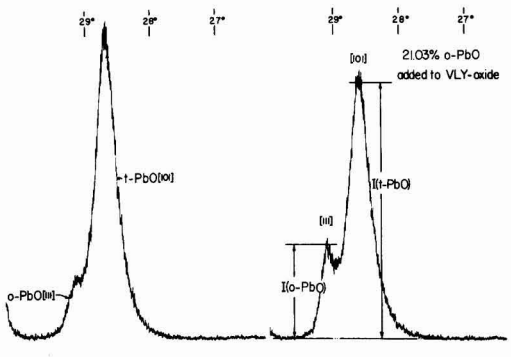

Fig. 2. Two analytical scans of the t-PbO/o-PbO region. The method of measuring line intensities is indicated on the right. The left-hand spectrum represents the simulated unknown.

Table I. Summary of intensity data for "spiked" oxides

Percent o-PbO (%)	6.876	9.128	14.58	21.03
Added o-PbO (%)	0.00	2.253	7.705	14.16
R-values	0.1341	0.1656	0.2595*	0.4003
	0.1365*	0.1729	0.2805	0.4012*
	0.1405	0.1764*	0.2812	0.4072
	0.1410	0.1794	0.2820	0.4097
Average *R*-values	0.1380	0.1736	0.2812	0.4046
Standard deviation	0.00330	0.00594	0.00075	0.00458
Range of *R*	0.0064	0.0138	0.0015	0.0094
Relative error	0.0239	0.0342	0.00267	0.0113

* Initial datum for each mixture.

Linearization: digital computer.—The program used yields a multiple linear regression analysis line that is weighed according to the density and distribution of observations about their mean value. The line obtained gave the percent o-PbO, Y, as a function of the intensity ratio, X. The F-value for the line was ~7000 with a sum of squares, attributable to the regression, of ~480. Statistically, this is a very good calibration curve, and indicates data linearization to be appropriate. The correlation coefficient was 0.9991. The equation is

$$Y = -0.10902 + 52.56X \qquad [1]$$

and the standard error of estimate, *Sr*, is 0.259, which indicates, or suggests that using this calibration will produce determinations, o-PbO = $(Y \pm 0.259)$%, 64% of the time, and o-PbO = $(Y \pm 0.518)$%, 90% of the time, etc.

Linearization: hand calculator.—To analyze the pooled data using the hand calculator, the averaged R-values were used, because multiple linear regression is not available on the instrument. The expression for percent o-PbO was

$$Y = -0.19620 + 52.53X \qquad [2]$$

The standard error of estimate calculated for this regression line for the four averaged values was 0.192. When calculated for all fifteen data, the value for *Sr* was 0.257. As expected, the linearization was very good, the correlation coefficient being 0.9997.

The error of estimate for both treatments is quite low but, of course, for low o-PbO contents (1-10%) would represent a fairly large relative error in the determination. For commercial ores and oxides that contain o-PbO this is a sufficiently precise and sensitive analysis.

As Klug (27) and others (28) have pointed out the sufficiency conditions for quantitative diffractometry (linearity in the analytical relationship) is met very well. The necessary conditions that the analytically interesting diffraction maxima intercept the same region of analyzing radiation (29) is, clearly, well met (cf. Fig. 2).

The analysis of an unknown.—To analyze an unknown, the R-values for the unknown and the "spiked" samples are plotted on any convenient axis; such as intensity ratio, R, *vs.* concentration added o-PbO. The unknown's R-value is plotted as 0.0% added o-PbO. To simulate analysis we plotted the values from Table I under the "added o-PbO" heading, on just such an axis. Since we know the correct, measured value of percent o-PbO in the simulated unknown we can discuss the precision and accuracy of this analytical method for the PbO allotropes.

To further simulate laboratory practice we will use the four initial readings only, then analyze the one-time analysis situation compared to the replicated analysis, using the pooled data. In the unknown determination, the R-values are treated as the dependent variables, functions of the percent of added o-PbO, P.

The data from Table I marked with asterisks were plotted on analysis axes, as shown in Fig. 3. One of the lines is a casual fit made by visually averaging the point splits, and may closely approximate real practice in the laboratory. The other line is the result of linear regression analysis by the hand calculator. The equation of the line is

$$R_{\text{Initial}} = 0.1320 + 0.01847P \quad [3]$$

with a P-intercept of -7.146 added o-PbO. We can generate a table of residuals and calculate Sr for this line. The standard error of estimate for this determination is 0.671, worse than for the replicated data (0.259 and 0.257). The analysis for o-PbO is in error by 3.94%, nearly twice the error of the answers derived using pooled data (2.20% for the computer linearization and 2.97% for the SR-51A linearization). It is interesting to note the casual, visual linearization led to a determination of 6.55% o-PbO, an error of 4.73%, not much worse than the answer calculated from Eq. [3].

The ordinary expectation is that precision and, presumably, the accuracy will be no worse than the error reflected in the distribution of the replicated data (Table I). The answer obtained in simulated analysis has a larger error than the replicated data, and the answers from pooled data indicate the relative error in the determination is larger than the error in the pooled data. The fact the computer linearization was outstanding (correlation coefficient = 0.9991) appears to offer us a paradox. The data are far better than the answer. This appears to be a property of the calibration line and its relationship to the data (21).

The solution lies in the fact that linear calibration lines are "best fits" of data that randomly fluctuate in the neighborhood of the line. It is, in fact, data scatter about the calibration curve that determines and defines the measure of precision and therefore the accuracy of this analysis (30) and it is always larger than the error in the replicated data. That is so, because, superimposed onto the replication error, as a source of scatter, are the ordinary experimental errors: in this case powder sample packing and mixing, peak height measurement, etc.

The reliability of the calibration line is a two-dimensional problem, and as Mandel and Linnig (21) and Lark (31) have shown, a complex one. The uncertainty in the slope and intercept of the least squares calibration line defines a two-dimensional confidence region, centered on the fitted (slope, intercept)-data pair (21, 26, 32). The area of the confidence region depends on the magnitude of the experimental errors that yielded the raw data, and the width of the confidence band, superimposed onto the linear calibration curve, defines the limits of precision and accuracy of such a method.

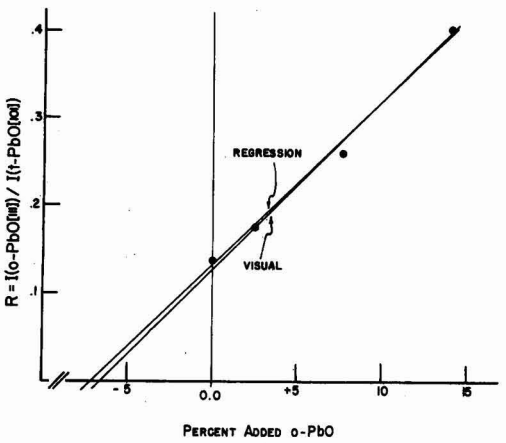

Fig. 3. Analysis plot for o-PbO determination. A casual, visual averaging of the initial points is shown compared to the least squares line.

A deeper analysis would yield the confidence band for any given selected confidence interval (σ, 2σ, 3σ . . .). That is unnecessary at this point, but it has been necessary to indicate how normal distribution of data can lead to unexpectedly large errors in analyses dependent on linear calibrations. This technique for the allotropes of PbO is a sound and useful method, providing normal care in preparation and experimental procedure is taken. The simulated analysis has shown that determinations without replication of observations leads to a less precise answer, with the decision whether or not to do data replication most likely to depend on the need to adjust formulated oxide mixtures for the presence or absence of one of the allotropes. The required degree of preciseness will depend on the required preciseness in the o-PbO analysis.

Acknowledgments

The author wishes to thank ESB Incorporated for support of this work, and thanks to Ted Blickwedel for computer analysis of data. Barbara Campbell assisted with x-ray diffraction measurements.

Manuscript submitted March 21, 1977; revised manuscript received April 28, 1977.

Any discussion of this paper will appear in a Discussion Section to be published in the June 1978 JOURNAL. All discussions for the June 1978 Discussion Section should be submitted by Feb. 1, 1978.

Publication costs of this article were assisted by ESB Incorporated.

APPENDIX

To investigate the expectation for accurate analyses from any set of four data we randomized the data pool with the 0.2595 point omitted, then wrote fifteen regressions using data sets made up by randomly selecting four R-values from the data pool. In each case we calculated the percent o-PbO of the "unknown," generated tables of residuals, and calculated the Sr-value for each of the fifteen lines (there are 192 possible combinations of data). These data are shown in Table II. The range in percent error in o-PbO and Sr are 11.44% and 0.435, respectively.

It is instructive to plot the signed percent error in o-PbO analysis as a function of the standard error of estimate of the fifteen lines. This can be seen as Fig. 4. The points from the computer and hand calculator analyses of the pooled data are also plotted. The distribution of the points in Fig. 4 appears strongly to indicate the presence of a systematic error that yields high values for o-PbO, giving regression lines that more frequently yield answers with a positive error. The source is probably a tendency to overestimate the intensity of the o-PbO[101] line, leading to high R-values.

Table II. Analysis of random data set linearization

Index	Intercept	Slope	o-PbO (%)	Sr	Error (%)	C_t
1	0.1333	0.01931	6.905	0.051	0.436	0.9999
2	0.1380	0.01852	7.452	0.160	8.39	0.9998
3	0.1371	0.01870	7.333	0.123	6.65	0.9999
4	0.1349	0.01927	7.004	0.331	1.88	0.9992
5	0.1319	0.01943	6.789	0.130	−1.25	0.9998
6	0.1315	0.01960	6.710	0.141	−2.41	0.9998
7	0.1372	0.01863	7.346	0.059	7.05	0.9999
8	0.1361	0.01848	7.475	0.171	8.73	0.9997
9	0.1369	0.01914	7.151	0.231	4.01	0.9995
10	0.1368	0.01898	7.207	0.214	4.83	0.9995
11	0.1380	0.01859	7.422	0.166	7.96	0.9958
12	0.1335	0.01890	7.061	0.494	2.70	0.9979
13	0.1367	0.01867	7.320	0.281	6.47	0.9993
14	0.1295	0.01917	6.758	0.335	−1.70	0.9990
15	0.1364	0.01863	7.325	0.264	6.54	0.9994

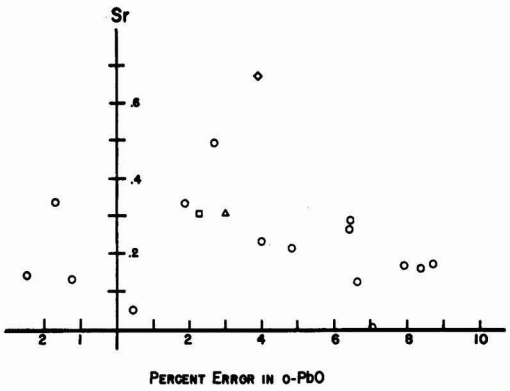

Fig. 4. Scatter diagram for standard error of estimate and signed error in o-PbO determination. The fifteen randomly generated regressions are shown as open circles: ◇ represents the visual averaging, while □ and △ are the computer and hand calculator values for the pooled data.

Figure 4 indicates the occurrence of very large error is coupled to small *Sr*-values, so that empirically the expectation of very large error is small. If we assume $Sr > 0.257$, the smallest value found for the treated, replicated data, then large errors correspond to *Sr*-values that are unrealistically small (outside the confidence band). The largest error in o-PbO analysis seen in this sampling, for $Sr > 0.26$ is ~6.65%.

REFERENCES

1. G. L. Clark and S. F. Kern, *J. Am. Chem. Soc.*, **64**, 1637 (1942).
2. H. Bode and E. Voss, *Electrochim. Acta*, **1**, 318 (1959).
3. G. L. Clark and W. P. Tyler, *J. Am. Chem. Soc.*, **61**, 58 (1939).
4. S. Ikari, S. Yoshizawa, and S. Okada, *J. Electrochem. Soc. Jpn.* (overseas ed.), **27**, E167 (1959).
5. R. V. Biagetti and M. C. Weeks, *Bell Syst. Tech. J.*, **49**, 1305 (1970).
6. C. W. Fleischmann and W. J. Schlotter, *This Journal*, **123**, 969 (1975).
7. D. Pavlov and G. Papazov, *J. Appl. Electrochem.*, **6**, 339 (1976).
8. J. M. Mrgudich, *Trans. Electrochem. Soc.*, **81**, 165 (1942).
9. G. L. Clark and R. Rowan, *J. Am. Chem. Soc.*, **63**, 1302 (1941).
10. M. Petersen, *ibid.*, **63**, 2617 (1941).
11. D. Pavlov and V. Iliev, *Elektrokhimiya*, **11**, 1735 (1975).
12. Joint Committee for Powder Diffraction Standards, Index to the Powder Diffraction File. No. 5-561 and 5-570.
13. U. W. Arndt, in "X-Ray Diffraction of Polycrystalline Materials," H. S. Peiser, H. P. Rooksby, and A. J. C. Wilson, Editors, chap. 7, p. 229, Chapman and Hall, London (1960).
14. H. P. Klug, L. E. Alexander, and E. Kummer, *Anal. Chem.*, **20**, 607 (1948).
15. L. Alexander and H. P. Klug, *ibid.*, **20**, 886 (1948).
16. R. Kunkel and S. E. Manhan, *ibid.*, **45**, 1465 (1973).
17. O. P. Bhargava, *Am. Lab.*, **7** (7), 11 (1975).
18. S. Sherken and E. J. Friedman, *Anal. Chem.*, **45**, 2399 (1973).
19. G. L. Clark and D. H. Reynolds, *Ind. Eng. Chem., Anal. Ed.*, **8**, 36 (1936).
20. H. P. Klug and L. E. Alexander, "X-ray Diffraction Procedures," Second ed., p. 553, John Wiley & Sons, Inc., New York (1974).
21. J. Mandel and F. J. Linnig, *Anal. Chem.*, **29**, 743 (1957).
22. I. L. Larsen, N. A. Hartmann, and J. J. Wagner, *ibid.*, **45**, 1511 (1973).
23. A. W. Hull, *J. Am. Chem. Soc.*, **41**, 1168 (1919).
24. L. Alexander, H. P. Klug, and E. Kummer, *J. Appl. Phys.*, **19**, 742 (1948).
25. Z. W. Wilchinsky, *Acta Cryst.*, **4**, 1 (1951).
26. E. L. Crow, F. A. Davis, and M. W. Maxfield, "Statistics Manual," pp. 102ff, 252, Dover Publications, Inc., New York (1960).
27. H. P. Klug, *Anal. Chem.*, **25**, 704 (1953).
28. R. A. Spurr and H. Myers, *Anal. Chem.*, **29**, 760 (1957).
29. L. E. Copeland and R. H. Bragg, *ibid.*, **30**, 196 (1958).
30. F. J. Linnig and J. Mandel, *ibid.*, **36** (13), 25A (1964).
31. P. D. Lark, *ibid.*, **26**, 1712 (1954).
32. M. G. Natrella, "Experimental Statistics," NBS Handbook No. 91, pp. 5-1ff, U.S. Government Printing Office, Washington, D.C. (1963).

Study by Auger Spectrometry and Cathodic Reduction of Passive Films Formed on Ferritic Stainless Steels

M. da Cunha Belo, B. Rondot, F. Pons, J. Le Héricy, and J. P. Langeron

National Center of Scientific Research, 94400 Vitry sur Seine, France

ABSTRACT

This paper deals with the passivation of ferritic stainless steels (26% Cr) in a 3.5% NaCl solution. The passive state was examined by Auger electron spectrometry and electrochemical reduction techniques. From the chemical composition profiles it appears that the passivation of these alloys is characterized by the formation of a thin oxide film and the development of a chromium-depleted zone in the metallic substrate near the metal-oxide interface. The composition of the passive film changes continuously with the depth. The number of atoms within a given layer of the film is lower than in the layers of the metallic matrix. The thickness and chemical composition of passive films change with the temperature of the corrosive medium. The study by cathodic reduction shows that molybdenum additions especially affect the properties of the inner layers of the passive film.

The great interest in the development of the passive state on iron-chromium steels is due both to the complexity of this phenomenon and to its practical importance. Despite numerous studies on this subject, there are still no definite conclusions relative to the nature and structure of the passive film formed on the surface of the alloys. There is some experimental evidence that the thickness of the oxide film varies from monolayer dimensions near the active-passive transition, up to dimensions of 10-50Å in the passive potential region. However, at present, it is not possible to identify the oxide phase as a single oxide, a duplex oxide, or an oxide not related to any known oxide.

It is obvious that an accurate and extended knowledge of the passivity phenomenon requires further experimentation, especially in connection with the factors affecting the ionic and electronic processes, the local electric potential, and the spatial variation of these through the film. In addition, more quantitative data must be obtained concerning chemical composition and structure.

Further investigation should take advantage of promising new techniques of surface analysis such as electron spectroscopy for chemical analysis (ESCA), low energy ion-scattering spectrometry (ISS), secondary ion mass spectroscopy (SIMS), Mössbauer spectroscopy, nuclear microanalysis, and activation analysis.

This work consists of a study by Auger electron spectrometry and coulometric techniques of passive films formed on very pure ferritic stainless steels exposed to a 3.5% NaCl (*p*H 2.5) solution. The influence of the passivation potential, alloy composition, and temperature of the corrosive medium were examined.

We have developed in a previous paper (1) some quantitative aspects of Auger electron spectrometry, and a general formalism has been given elsewhere (2). Up to now, determinations of surface concentrations have been carried out by resorting to standards. However, studies that have been published in the last 5 years (3-6) indicate the possibility of doing absolute measurements by taking an element of the matrix as a reference element. It is the purpose of this article to demonstrate the use of quantitative Auger analysis in the study of passivating films.

Experimental

Materials.—The alloys investigated were very high purity ferritic stainless steels prepared by plasma furnace melting (7). In these alloys the total content of metallic impurities is less than or equal to about 10 ppm by weight, and that of the nonmetallic impurities is also very low (typically: 10 ppm C, 7 ppm N, 10 ppm O).

The specimens were polished through 600 grade carborundum paper and then vacuum annealed for 1 hr at 900°C. Before introduction into the electrolytic cell the specimens were electropolished in a glacial acetic acid/perchloric acid mixture (3.2:1, by volume).

Electrochemical procedure.—Passivation experiments were carried out in 3.5% NaCl (*p*H 2.5) solution completely deaerated with pure nitrogen. Potentials are reported *vs.* the saturated calomel electrode (SCE). The specimen was polarized in the cathodic region at −700 mV/SCE for 2 min, and then submitted to a slight anodic dissolution: The specimen was put on open circuit for several seconds and then brought to the desired potential in the passive region. According to Frankenthal, this procedure gives the most reliable results (8). After passivation treatment, each specimen was rinsed in distilled water and dried in a stream of dry air.

The passivating films are formed at constant potential in the passive potential range. Passivation treatments correspond to a film growth stage where the log/log plots of the current *vs.* time give a straight line for periods of several hours. This stage occurs after about 30 sec of film growth. The study of the earlier stage of film formation during which the anodic current density decreases abruptly has not been considered here. Furthermore, it must be pointed out that the analytical and cathodic reduction study deals with films formed electrochemically with intermediate exposure to the atmosphere.

Passivation experiments were followed by analytical or coulometric measurements. The study of the cathodic reduction curve was conducted in 18*N* H_2SO_4 solutions deaerated with pure nitrogen (9). The passive film was cathodically reduced at a constant current of 5 $\mu A/cm^2$.

Analytical procedure.—The samples are introduced into the chamber of the Auger spectrometer a few minutes after formation of the passive film. The surface is bombarded under a vacuum of a few times 10^{-9} Torr with a beam of primary electrons having a kinetic energy of 2500 eV. The target current is 200 μA.

The Auger spectrometer operates with a conventional cylindrical mirror analyzer (CMA), *i.e.*, with a coaxial

Key words: passive films, Auger spectrometry, coulometry.

electron gun which bombards the surface of the sample at normal incidence. The emitted secondary electrons enter the CMA with an emission angle θ of 42°18′ with respect to the normal, and an angular aperture of the beam limited to ± 3°. Our spectrometer yields the differential energy distribution curve $dN(E)/dE$ of the secondary electrons emitted from the surface. We assume that the peak-to-peak amplitude of the Auger transition is due to the contribution of the atomic layers in the vicinity of the surface and proportional to the corresponding Auger current. From this hypothesis the peak-to-peak amplitude of the Auger signal due to an element I given by all the i layers, is

$$H_I = \sum_{i=0}^{\infty} h_I^{(i)} = \sum_{i=0}^{\infty} \alpha_I K_I^{(i)} N_I^{(i)}$$

where $N_I^{(i)}$ is the number of atoms I in the layer i, α_I is a sensitivity coefficient (characteristic of the element I), and $K_I^{(i)}$ is the contribution coefficient of the layer i to the total signal given by the whole specimen. (See the Appendix for the formalism leading to a quantization of Auger spectrometry and for more complete information relative to the physical meaning of the various factors.)

In the choice of the appropriate Auger peak for the assessment of the concentration of the various elements, the following conditions have been taken into account: The Auger peak should not involve valence electrons and should not be superimposed on another peak. In the case of iron, we chose the peak at 598 eV, and we converted it to an apparent peak at 703 eV by multiplying the measured height by a coefficient equal to the ratio of the peak heights at 598 and 703 eV, respectively, as determined on a pure iron matrix.

An approximate value of the sensitivity coefficients of iron, chromium, and molybdenum can be obtained from the study of the metallic matrix when the passive film has been completely removed by ion etching. This way the Auger signals are only related to the base elements of the alloy, the concentrations of which are well known. This assumes that sputtering is not selective, which seems to be verified by the constancy of the total number of atoms in every layer. By taking iron as a reference material, we obtain the sensitivity coefficients of the other elements I (I = A, B, C . . .), by satisfying the following relationship

$$\sum_{I=A}^{c} H^* = \sum_{I=A}^{c} \frac{H_I}{\alpha_I} = \text{constant}$$

where H^* is the corrected peak height.

The contribution coefficient K of iron has been calculated from Eq. [2] in the Appendix for different kinds of matrixes (metal or oxides). For the other elements the values of K are obtained by the same procedure (Table I).

Though a statistical approach enables one to show theoretically that the sputtering of atoms does not leave an atomically planar surface, we have nevertheless supposed for the sake of convenience that etching strips a complete layer before attack on the subsequent one. This approximation is more accurate when the number of layers removed is low. The focus of the ion beam is such that the irradiated area is much larger than the one sampled by the primary electrons.

To obtain the depth profile for the various elements, argon ions accelerated by a potential of 600V were used with the ionic current between the limits of 0.3×10^{12}–3×10^{12} ions cm^{-2} sec^{-1}. It has been derived (10) that

Table I

Elements	Fe	Cr	Mo	O	Cl
Energy, eV	598	529	186	510	181
α	1	0.9	3.1	2.1	1.9
K	0.73	0.70	0.57	0.70	0.57

the number n of argon ions impinging on a 1 cm^2 area of surface is proportional to the sputtering rate, *i.e.*, $n = \gamma(p \cdot t)$, in which p is the argon pressure in Torr, t is the sputtering time t in minutes, and the constant γ is equal to 4.1×10^{18} cm^{-2} $Torr^{-1}$ min^{-1}. If the sputtering rate of one Torr · min is taken as unity, and supposing that the atom density of a surface layer is nearly 10^{15} cm^{-2}, we obtain a sputtering rate of one monolayer for $p \cdot t \sim 0.2 \times 10^{-3}$ Torr · min. This is approximately the case for iron and chromium in the present study, the sputtering yields of which are, respectively, 1.25 and 1.26. This value for $p \cdot t$ is also compatible with the sputtering of monolayers obtained by thermal segregation.

Our method of quantifying the Auger spectra entails the measurement of the peak amplitude H_I of the characteristic Auger signals chosen for the various elements. The change of H_I as a function of the sputtering rate is plotted and this curve is cut by vertical and parallel lines corresponding to a separation equal to 0.2×10^{-3} Torr · min; this regular interval is consistent with the removal of a monolayer from the surface. The relevant abscissas of the points of intersection H_A^i and H_A^{i+1} permit the determination of the concentration of the element A in the layer i (*c.f.*, Eq. [4] in Appendix).

By applying Eq. [3] in the Appendix to each couple of successive vertical lines, we obtain, knowing the contribution coefficient k, the number of atoms of an element in the monolayer bounded by these lines.

From Table I it is seen that the carbon peak has not been taken into account. That element is only observed during the first sputtering period, and its concentration is considerably reduced in the second atomic layer. Nevertheless it represents the major constituent in the overlayer as the sample is taken from the electrolytic cell and is introduced into the spectrometer. Due to some difficulty in assigning an accurate sensitivity coefficient to carbon, it was decided to ignore that element, which has the drawback of leading to concentration values without physical meaning in the outermost layer of the sample, but does not significantly perturb the concentration profiles of the other elements in subsequent layers.

In addition to Auger electron technique, activation analysis was used to obtain in a quantitative manner the oxygen contained in the passive film; specimens are irradiated in a beam of tritons accelerated in a Van de Graaf generator. The following nuclear reaction has been used: ${}^{16}_{8}O(t,n){}^{18}_{9}F^*$ (T = 110 min). A detection limit of 0.004 $\mu g \cdot cm^{-2}$ may be obtained for a 10 min irradiation with 0.2 μA of tritons at 2 MeV (11, 12).

Results

Passive film formed electrochemically.—Figure 1 shows the composition profiles of the passive film on a ferritic 26% Cr-1% Mo steel that was passivated for 6 hr at a potential of + 650 mV/SCE in a 3.5% NaCl (pH 2.5) solution. Passivation of the ferritic steels is characterized by the formation of an oxide film 8-9 atomic layers in thickness, and by the development of a chromium-depleted zone inside of the matrix at the oxide-metal interface.

The diagram shows that the overlayer of the passive film is principally carbon, the concentration of which decreases abruptly and completely disappears beyond the fourth layer. Chlorine is also found in the first layers of the oxide. The depth of penetration of carbon and chlorine are similar.

From the depth profiles it can be seen that each atomic layer of the passive film has a particular composition. The internal layers of the oxide are richer in chromium than the matrix, while the iron concentration in the same layers is lower. There exist steep gradients of concentration near the metal-oxide and oxide-solution interfaces.

For the 26% Cr-1% Mo steel, the molybdenum concentration in the passive film is very low (Fig. 1 and 2). Nevertheless, the presence of that element in the

steel slightly modifies the depth profiles. Particularly, it appears that the maximum chromium content in passive films on the alloys without molybdenum (Fig. 3) is higher than that in films on alloys containing molybdenum (Fig. 2).

The thicknesses of passive films vary very slightly with potential and with the length of passivation (at least for times greater than 30 min). However, the depth of the chromium-depleted zone increases linearly

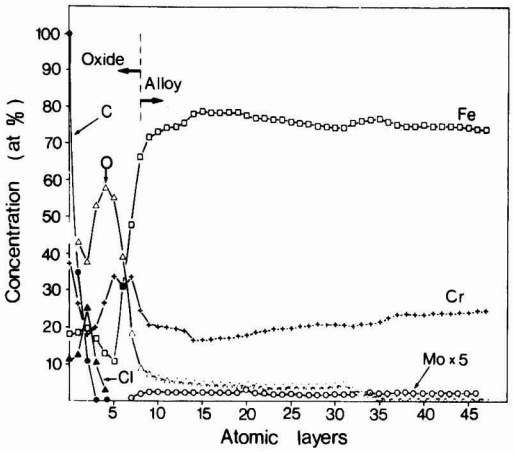

Fig. 1. Composition profiles of the principal elements in the passive film and in the alloy. (26% Cr-1% Mo steel) passivated for 6 hr at a potential of +650 mV/SCE in a 3.5% NaCl (pH 2.5) solution at 5°C.

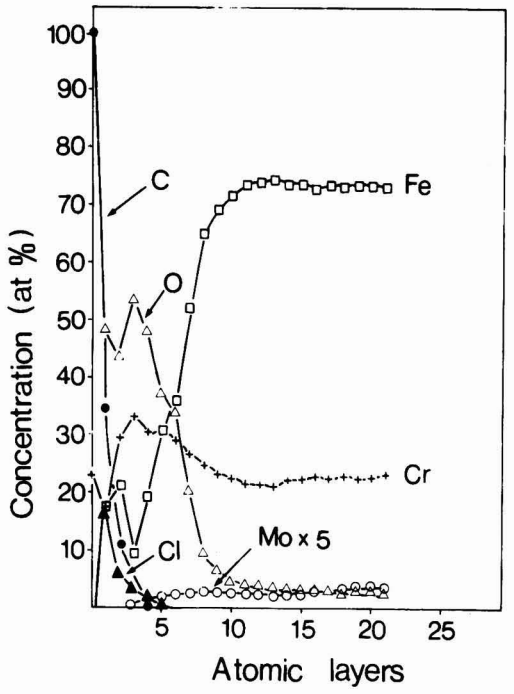

Fig. 2. Composition profiles of the principal elements in the passive film and in the alloy. (26% Cr-1% Mo steel) passivated for 6 hr at a potential of −250 mV/SCE in a 3.5% NaCl (pH 2.5) solution at 5°C.

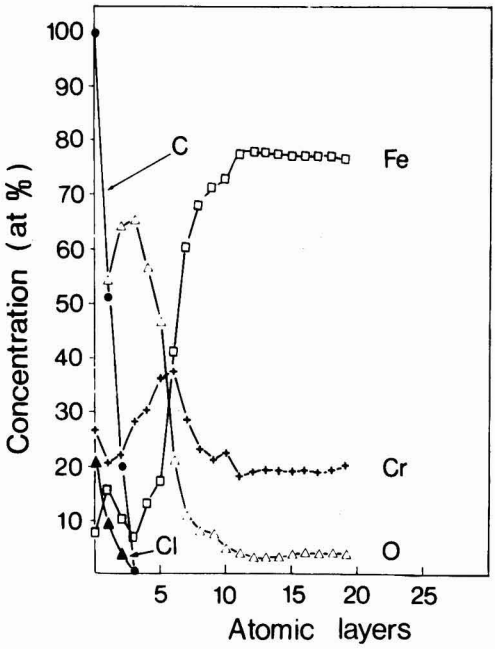

Fig. 3. Composition profiles of the main elements in the passive film and in the alloy. (26% Cr steel) passivated 6 hr at a potential of −250 mV/SCE in a 3.5% NaCl (pH 2.5) solution at 5°C.

with passivation time at all passivation potentials (Fig. 4).

The chromium concentration at the minimum of the composition profile is low for short passivation times (30 min), but rises progressively to a constant value as the time is increased. It appears that changes in alloy composition at the film-matrix interface can proceed long after the passive film has been formed.

Figures 5 and 6 show the influence of the temperature of the corrosive medium on the depth profiles of passive films. In the first example (Fig. 5), the potential of the sample was kept at −250 mV/SCE and the chloride solution was held at 98°C. In the second one (Fig. 6), the same alloy was passivated at a potential of +650 mV/SCE and removed from the solution when its temperature reached the critical pitting temperature, *i.e.*, the temperature beyond which localized attack is likely to occur. It can be seen that the films formed under these conditions are generally thicker. It also appears that the penetration of carbon and chlorine is more extensive. Both elements are detected in the film near the oxide-metal interface. In comparison with the experiments carried out at 5°C, the following differences are also noticed: the dip in the iron profile inside the passivating film is not as deep or broad and can hardly be seen for the experiment at 98°C; and the enrichment in chromium affects a much wider zone and is observed as a large hump in the concentration profile.

The curves giving the number of the atoms N_I^i of each element and those giving the total number of the atoms ΣN_I^i in each layer of the passive film are plotted in Fig. 7 as a percentage of the number of the atoms in a layer of the matrix. The number of atoms in each layer of the passive film is generally lower than in the layers of the matrix. This number is relatively low in the layers close to the oxide-solution interface, increases in the first layers, and then decreases at the oxide-metal interface. It also seems that the layers located in the chromium-depleted zone of the metallic matrix have a slightly smaller number of atoms than

in the deeper layers where the alloy reaches its true composition.

Hydrogen atoms are not detected by the Auger effect. This element could be present in the film in the form

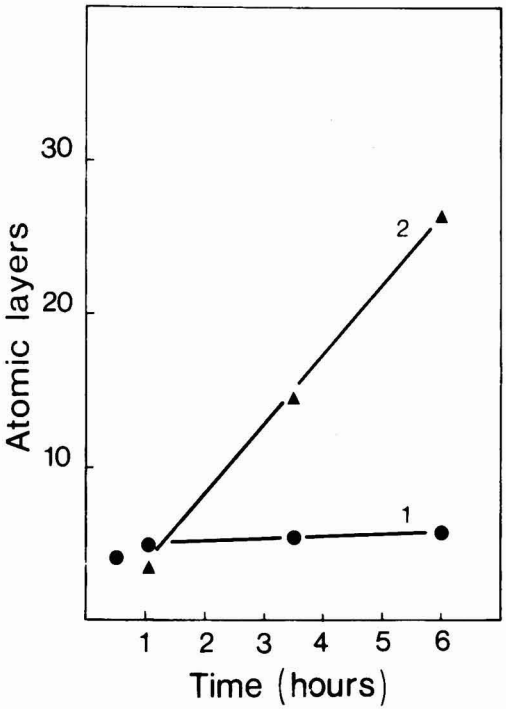

Fig. 4. Number of atomic layers in the passive film (curve 1) and in the chromium-depleted zone (curve 2) vs. the time of passivation. (26% Cr-1% Mo) steel passivated at a potential of +650 mV/SCE, in a 3.5% NaCl (pH 2.5) solution at 5°C.

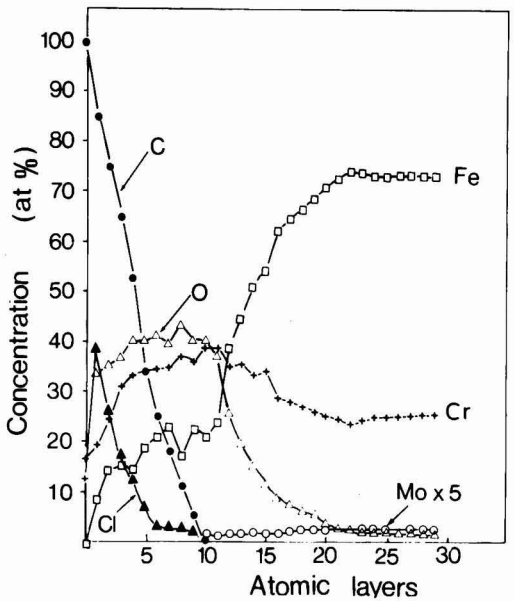

Fig. 5. Composition profiles of the principal elements in the passive film and in the alloy. (26% Cr-1% Mo) steel passivated for 1 hr at a potential of −250 mV/SCE in a 3.5% NaCl (pH 2.5) solution at 98°C.

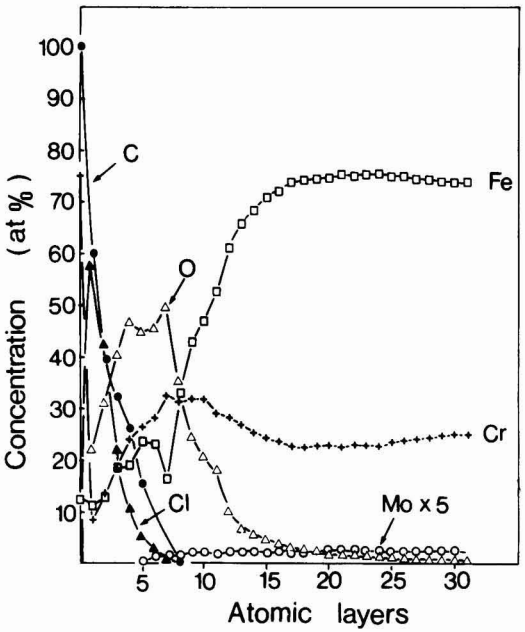

Fig. 6. Composition profiles of the principal elements in the passive film and in the alloy. (26% Cr-1% Mo) steel passivated for 1 hr at a potential of +650 mV/SCE, in a 3.5% NaCl (pH 2.5) solution at 34°C.

of water molecules, as has been suggested for the passive films formed on pure iron (13) and on stainless steels exposed to different solutions (14). Obviously, the presence of hydrogen can affect the total number of the atoms in each layer, and particularly near the oxide-solution interface.

The influence of the temperature of the corrosive environment upon the number of atoms of each element in an atomic layer appears very clearly: The films formed in a chloride solution heated at a temperature of 98°C (Fig. 7b) accommodate fewer atoms in a layer (lower ΣN_I^i) than those growing in the same medium at a temperature of 5°C (Fig. 7a).

Passive films formed in the air.—Passivation in air of a ferritic steel maintained for a fortnight in a desiccator at 25°C (Fig. 8) presents some analogies with that obtained in a chloride solution. The depth profiles show the presence of carbon and chlorine in the first layers of the film, chromium enrichment in the internal layers, and strong gradients of composition at the interfaces. In comparison with the passive films formed in an aqueous solution it appears that for the iron profile the minimum is much wider and its value is much higher. The external ridge of the well is also at a higher level. The concentration gradient for chromium is decreasing towards the surface. The molybdenum in the film is very low as in the films formed in aqueous solution. It is also observed that the number of atoms within a given layer of the film is lower than in the metallic matrix. Nevertheless, in the air-formed films the cations originating from the steel substrate tend to accumulate in the outer layers of the film, as a result of the absence of a dissolution process.

Activation analysis.—Activation analysis shows that oxygen content in the film varies only very slightly with the potential. For the 26% Cr-1% Mo steel passivated 1 hr in a 3.5% NaCl solution, the quantity of oxygen contained in the oxide varies from 0.40 to 0.45 $\mu g/cm^2$ when the potential is changed from −250 to +650 mV/SCE. However the oxygen content increases with the temperature of the solution (0.6 $\mu g/cm^2$ after

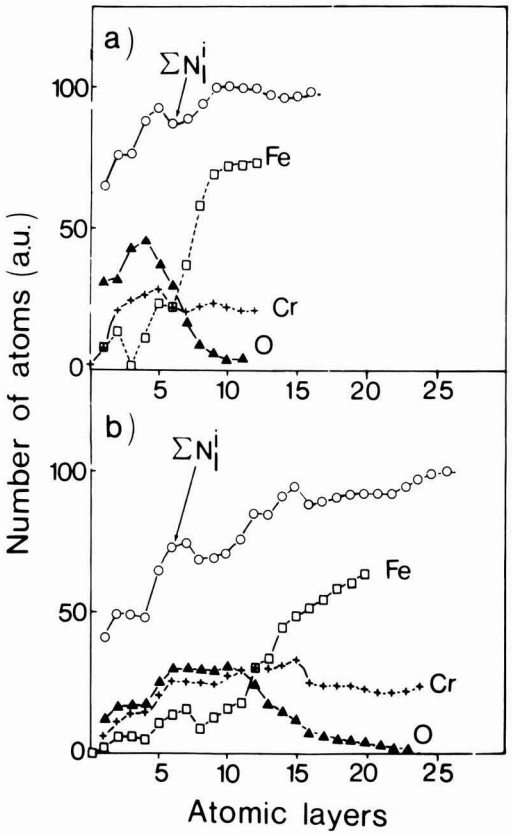

Fig. 7. Composition profiles giving the number of atoms of the principal elements within each layer of the passivated film and in the alloy. (26% Cr-1% Mo) steel passivated for 1 hr at a potential of +650 mV/SCE in a 3.5% NaCl (pH 2.5) solution. a. solution temperature 5°C; b. solution temperature 98°C.

passivation at −250 mV/SCE, when the solution is at 98°C).

Coulometric measurements.—The apparent coulombic thickness of the passivating films has been measured. Further, coulometric measurements have been made to learn more about the influence of molybdenum on the properties of the passive film.

Figure 9 shows the coulometric reduction results obtained with two different alloys (26% Cr and 26% Cr-1% Mo ferritic steels) for 1 hr polarization at a given potential. It appears that the quantity of charge used in the film reduction process increases with the passivation potential. Two different potential regions are indicated: the first is located at lower potentials and the second extends to the higher values. This behavior has been reported by many workers for the passivation of iron (15, 16) and stainless steel (14).

The efficiency of the cathodic process, measured as the quantity of charge required for reduction of the film decreases with molybdenum additions (Fig. 9 and 10). More precisely, the molybdenum content of the alloy has little influence on the reduction of the outer layer of the film (Fig. 9 and 10, curves a). However, the alloys with molybdenum require more charge for the reduction of the inner layers, particularly the layer next to the oxide-metal interface (Fig. 9 and 10, curves c). The quantity of charge for the reduction process increases with the temperature of the corrosive medium. It is also important to observe that the plateau in the potential-time curve disappears at the high temperature (Fig. 11).

Discussion

The analytical study by Auger electron spectrometry indicates that the composition of the passive film changes continuously with depth. This information supports recent ion-scattering spectrometry work for air-formed oxide film on a series of iron chromium alloys (17).

Previous ESCA studies (18) of films formed on chromium steels have shown that chromium is in a trivalent state in all zones of the passivating film, while iron is trivalent in the outer layers with a gradual transition to divalent state in the layers near the metal-oxide interface. These results can be correlated with the iron profile obtained by Auger-spectrometry. The minimum which can be observed in the concentration profile for iron (Fig. 1-3) leads us to consider two zones in the passive film: an inner nonporous oxide which exhibits good electronic conduction and in which cation transport could be expected, and an outer porous oxide in which anions can migrate. A difference between our results and those given by ESCA is worth noting: The

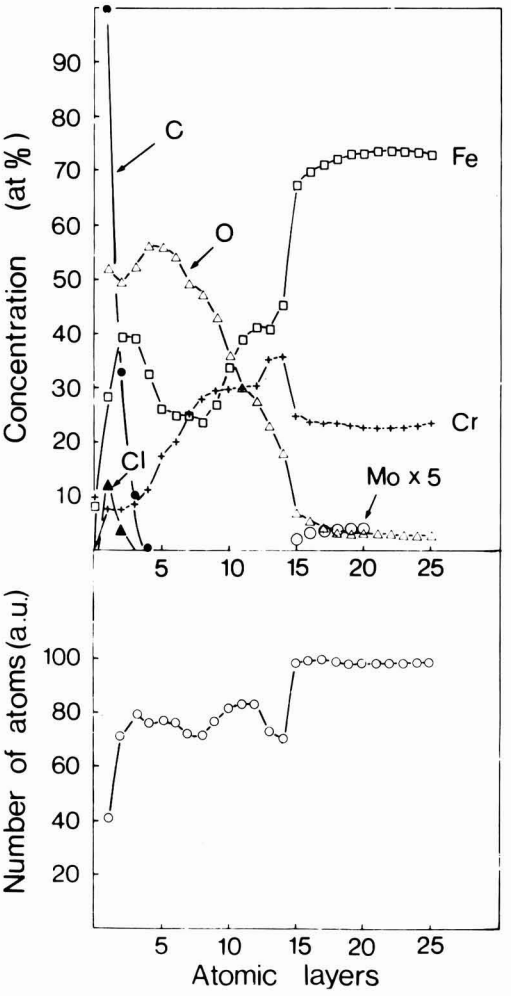

Fig. 8. Composition profile and number of atoms detected in the passive film. Ferritic 26% Cr-1% Mo steel maintained 15 days in a desiccator at 25°C.

chromium concentration gradient in the passive film formed on steels with 4-30% Cr at 25°C in oxygenated water is the inverse of that observed by Auger spectrometry in this work (except for the very first layers, where the sign of the slope is the same). Analytical results show that the thickness of the film does not depend directly on the electrode potential. However it must be recognized that changes in the defect structure probably occur with potential variations (15, 16).

The passive film formed on iron-chromium alloys appears to be a duplex oxide similar to that suggested for passivation of iron (19-23) and austenitic stainless steel (23a). Chlorine penetrates into the outer layers of the film at all potentials. Aggressive ions are stopped only by the inner layers of the film at all potentials. Aggressive ions are stopped only by the inner layers of the film, even when the temperature of the corrosive medium is increased.

In previous papers, the properties of films formed on stainless steels have been associated with an amorphous structure (14, 25). This gel-like structure may be more protective, because it offers a higher resistance to cation transport than crystalline structures (26). In our opinion the amorphous state is characteristic of the outer layers of the passive film. In this zone channels may be formed, and large ions can move (27-30). Further, if we assume that the outer layer forms a poor conductor, anion transfer may be assisted by a high field (16). The less dense matter of the outer zone implies a porous structure, and the presence of Cl^- in the outer layer is consistent with this model.

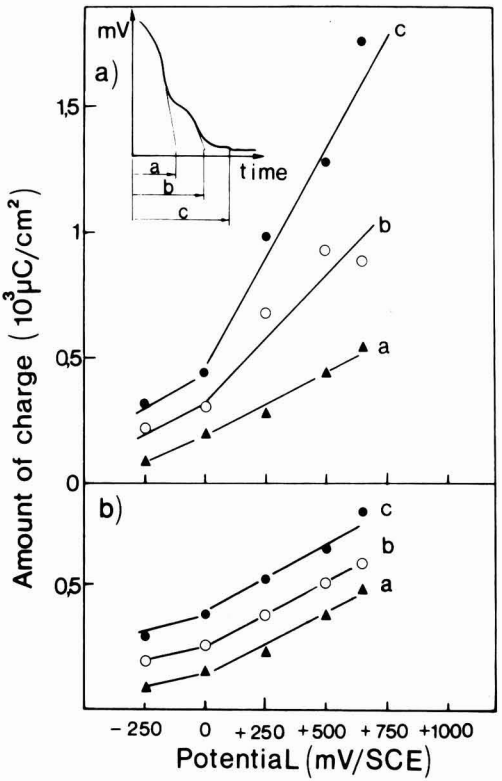

Fig. 9. Quantity of charge associated with the cathodic reduction process for each zone of the passivating film. Films were formed during polarization for 1 hr at different potentials in a 3.5% NaCl (pH 2.5) solution at 5°C. Curves a, b, and are related to the reduction of the outer, transition, and inner layer zones. Coulometric measurements were carried out in 18N H_2SO_4 solutions. a. Ferritic 26% Cr-1% Mo steel; b. ferritic 26% Cr steel.

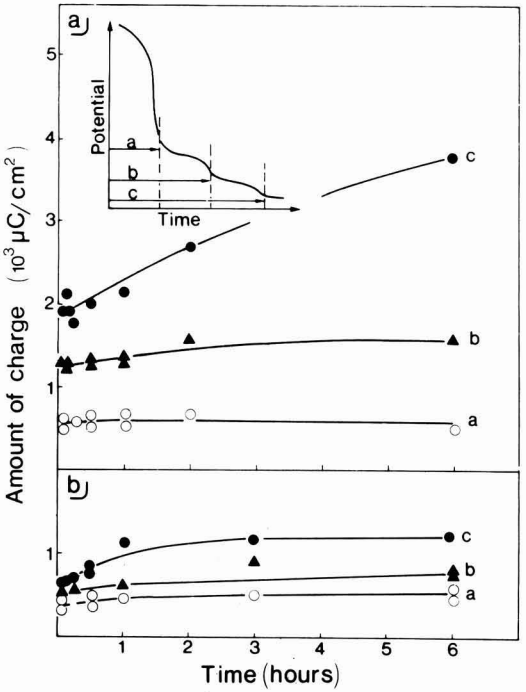

Fig. 10. Quantity of charge associated with each zone of the passivating film formed at +650 mV/SCE for different times of passivation (experimental conditions are the same as in Fig. 9). a. Ferritic 26% Cr-1% Mo steel; b. ferritic 26% steel.

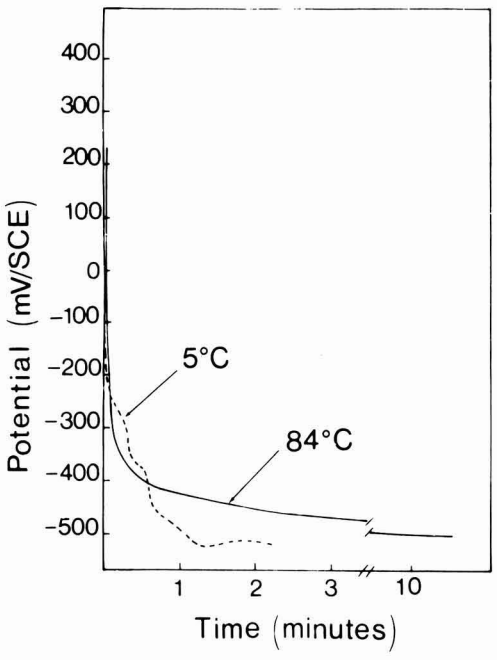

Fig. 11. Potential-time curves obtained during cathodic reduction. Films formed at −250 mV/SCE in a 3.5% NaCl (pH 2.5) solution at different temperatures (Ferritic 26% Cr-1% Mo steel).

The compositional analysis is in agreement with recent results (31), and shows that the molybdenum concentration in the passive films formed on ferritic stainless steels is very low (even in the case of an alloy with 3% Mo) and is only detectable in the inner part of the films. However, coulometric measurements indicate that the passive films formed on Fe-Cr-Mo alloys require a much greater quantity of charge for reduction than do the films formed on Fe-Cr alloys. This electrochemical behavior of the Mo alloys may be associated with their greater corrosion resistance (32-37). It should be pointed out that molybdenum additions have little effect on chromium depletion. This phenomenon, which occurs in high temperature oxidation of iron-chromium alloys (38-41), has not been mentioned as a possible process at low temperatures.

Conclusions

The passive film formed on iron-chromium alloys in NaCl solution is approximately 10 atomic layers thick. The film is enriched in chromium relative to iron. The composition profile of iron in the film shows a deep minimum with a value near to zero in the middle of the film, and a marked increase near the oxide-solution interface. There is a narrow zone inside the film which is only a chromium oxide, behind which molybdenum rises to a level equal to its concentration in the alloy. Further, we observe in the alloy chromium depletion at the oxide-metal interface. On the whole, the total number of atoms per layer is not the same in the oxide film as in the matrix. The less dense matter in the passive film implies a porous structure. Chlorine is always present in the outer zone of the film but does not penetrate into the inner zone. It appears that molybdenum additions increase the stability of the inner layers of the film near the oxide-metal interface.

Manuscript submitted Oct. 26, 1976; revised manuscript received May 11, 1977.

Any discussion of this paper will appear in a Discussion Section to be published in the June 1978 JOURNAL. All discussions for the June 1978 Discussion Section should be submitted by Feb. 1, 1978.

Publication costs of this article were assisted by the National Center of Scientific Research.

APPENDIX

Contribution of Each Atomic Layer to the Total Auger Signal: A Quantitative Approach

If we study a heterogeneous sample, the composition of which is a function of the depth in a direction normal to the surface but homogeneous within each atomic layer parallel to the surface, we may consider that the Auger current due to element A given by the whole specimen represents the sum of the contributions of each atomic plane. The peak-to-peak amplitude of the signal $h_A^{(i)}$ corresponding to the Auger current due to the layer i is expressed by the following relationship

$$h_A^{(i)} = \alpha_A k_A^{(i)} N_A^{(i)} \qquad [A\text{-}1]$$

where $N_A^{(i)}$ is the number of the atoms A in the layer i, a fraction of which are excited by the incident electron beam and yield Auger electrons. This proportion is taken into account in the α term. α_A is a sensitivity coefficient, characteristic of the element A, which includes the ionization cross-section, the probability of the Auger transition, as well as many constants of the spectrometer such as the intensity of the incident beam and the collection factor of the analyzer. This term has a fixed value provided the intensity of the beam and the energy of the primaries are well determined. Therefore, it is independent of the matrix insofar as there is no chemical binding resulting in a change of the Auger transition probability. $k_A^{(i)}$ is the contribution coefficient of the layer i to the total signal given by the whole specimen. It takes into account the escape depth of the Auger electrons in the layers before they reach the level i and the backscattering within the matrix.

Owing to these effects, it can be shown that the contribution coefficients are in geometrical progression: 1, K, K^2 ..., with the expression of K given by

$$K = \exp - \left(\frac{d}{D_x \cos\theta} + \frac{d}{D_p} \right) \qquad [A\text{-}2]$$

where d is the thickness of a monolayer, D_s the escape depth of the Auger electrons, D_p the depth of penetration of the primary electrons, and θ, the angle of acceptance of the Auger electrons in the cylindrical mirror analyzer.

If we designate by $H_I^{(0)}$ the initial Auger signal relative to the element I (I = A, B, C ...), when the zero layer is present we may write

$$H_A^{(0)} = \alpha_A (N_A^{(0)} + K_A N_A^{(1)} + K_A^2 N_A^{(2)} + \ldots + K_A^i N_A^{(i)} + \ldots)$$

$$H_B^{(0)} = \alpha_B (N_A^{(0)} + K_B N_B^{(1)} + K_B^2 N_A^{(2)} + \ldots + K_B^i N_B^{(i)} + \ldots)$$

$$H_I^{(0)} = \alpha_I (N_I^{(0)} + K_I N_I^{(1)} + K_I^2 N_I^{(2)} + \ldots + K_I^i N_I^{(i)} + \ldots)$$

and after removal of the zero layer, when layer one becomes the outermost layer, we may write

$$H_A^{(1)} = \alpha_A (N_A^{(1)} + K_A N_A^{(2)} + \ldots + K_A^{i-1} N_A^{(i)} + \ldots)$$

$$H_B^{(1)} = \alpha_B (N_B^{(1)} + K_B N_B^{(2)} + \ldots + K_B^{i-1} N_B^{(i)} + \ldots)$$

$$H_I^{(1)} = \alpha_I (N_I^{(1)} + K_I N_I^{(2)} + \ldots + K_I^{i-1} N_I^{(i)} + \ldots)$$

Hence, if we suppose a layer-by-layer ion etching, the number of the atoms of the element A in the "zero" layer can be deduced

$$N_A^{(0)} = \frac{H_A^{(0)} - k_A H_A^{(1)}}{\alpha_A} \qquad [A\text{-}3]$$

and those contained in layer "one" can be computed from the peak heights $H_A^{(1)}$ and $H_A^{(2)}$. More generally, for any element I (I = A, B, C ...), the number of atoms in the layer i is given by

$$N_I^{(i)} = \frac{H_I^{(i)} - k_I H_I^{(i+1)}}{\alpha_I}$$

The total number of the atoms present in layer i obviously is

$$\sum_{I=A}^{C} N_I^{(i)} = N_A^{(i)} + N_B^{(i)} + N_C^{(i)}$$

If it is certain that this quantity is the same in every layer, its value must be constant. It is therefore possible to choose the sensitivity coefficients α_A, α_B, α_C ... to verify that $\sum_{I=A}^{C} \frac{H_I^{(i)}}{\alpha_I}$ = constant. Inversely, if the values of α_A, α_B, α_C are known, the number of the atoms in each atomic layer can be deduced. The atomic fraction of the element A in layer i is given by

$$C_A^{(i)} = \frac{N_A^{(i)}}{\sum_{I=A}^{C} N_I^{(i)}} = \frac{\frac{H_A^{(i)} - k_A H_A^{(i+1)}}{\alpha_A}}{\sum_{I=A}^{C} \frac{H_I^{(i)} - k_I H_I^{(i+1)}}{\alpha_I}} \qquad [A\text{-}4]$$

REFERENCES

1. B. Rondot, F. Pons, J. Le Héricy, M. da Cunha Belo, and J. P. Langeron, Paper presented at the Second Colloquium of the Physics and Chemistry of Surfaces, France, May 27-30, 1975.
2. F. Pons, J. Le Héricy, and J. P. Langeron, *Surf. Sci.*, To be published.
3. P. W. Palmberg, *Anal. Chem.*, **45**, 549A (1973).
4. C. C. Chang, in "Characterization of Solid Surfaces," P. F. Kane and G. R. Larrabee, Editors, p. 509, Plenum Press, New York (1974).
5. R. Bouwman, L. H. Toneman, and A. A. Holscher, *Vacuum*, **23**, 163 (1973).

6. J. P. Coad and J. G. Cunningham, *J. Electron Spectrosc. Relat. Phenom.*, **3**, 435 (1974).
7. J. C. Durand, B. Rondot, and J. Montuelle, *Mem. Sci. Rev. Metall.*, **68**, 639 (1971).
8. R. P. Frankenthal, *This Journal*, **114**, 542 (1967); *ibid.*, **116**, 580 (1969).
9. P. Berge, *C. R. Acad. Sci.*, **245**, 1239 (1957).
10. F. Pons, Thesis, Paris XI (1976).
11. J. N. Barrandon and P. Albert, *Rev. Phys. Appl.*, **3**, 111 (1968).
12. G. Revel, M. da Cunha Belo, J. P. Mériaux, C. Schneider, M. Hilleret, and R. Bourguillot, *J. Radioanal. Chem.*, **17**, 101 (1973).
13. R. W. Revie, B. G. Baker, and J. O'M. Bockris, *This Journal*, **122**, 1460 (1975).
14. G. Okamoto, *Corros. Sci.*, **13**, 471 (1973).
15. N. Nagayama and M. Cohen, *This Journal*, **110**, 670 (1963).
16. J. Kruger and J. P. Calvert, *ibid.*, **114**, 43 (1967).
17. R. P. Frankenthal and D. L. Malm, *ibid.*, **123**, 186 (1976).
18. I. Olefjord, *Corros. Sci.*, **15**, 687 and 697 (1975).
19. K. G. Weil and K. F. Bonhoefer, *Z. Phys. Chem.*, **4**, 175 (1955).
20. H. Göhr and E. Lange, *Naturwissenschaften*, **43**, 12 (1956); *Z. Electrochem.*, **61**, 1291 (1957).
21. M. J. Pryor, *This Journal*, **106**, 557 (1959).
22. K. Hauffe, *Werkst. Korros.* **6**, 117 (1955).
23. K. H. Vetter, *This Journal*, **110**, 597 (1963).
23a. G. M. Bolman and A. C. C. Tseung, *Corros. Sci.*, **13**, 531 (1973).
24. C. L. Mc Bee and J. Kruger, *Electrochim. Acta*, **17**, 1337 (1972).
25. T. N. Rhodin, *Corrosion (NACE)*, **12**, 465t (1956).
26. T. P. Hoar, *This Journal*, **117**, 17C (1970).
27. H. Rawson, "Inorganic Glass Forming Systems," Academic Press, London (1967).
28. F. Ordway, *Science*, **143**, 800 (1964).
29. W. H. Zachariasen, *J. Am. Chem. Soc.*, **54**, 3841 (1932).
30. B. E. Warren, *J. Am. Ceram. Soc.*, **21**, 259 (1938).
31. J. B. Lumsden and R. W. Staehle, *Scr. Metall.*, **6**, 1205 (1972).
32. L. Colombier and J. Hochmann, "Aciers Inoxydables, Aciers Refractaires," 2nd ed., Dunod, Paris (1965).
33. E. A. Lizlovs and A. P. Bond, *This Journal*, **118**, 72 (1971).
34. A. P. Bond, *ibid.*, **120**, 630 (1973).
35. R. J. Brigham and E .W. Tozer, *Corrosion (NACE)*, **29**, 33 (1973).
36. R. Mayoud, *Bull. Cercle Etud. Met.*, **12**, 643 (1974).
37. M. B. Rockel, *Corrosion (NACE)*, **29**, 393 (1973).
38. D. P. Whittle, D. J. Evans, J. C. Scully, and G. C. Wood, *Acta Metall.*, **15**, 1421 (1967).
39. G. C. Wood, *Oxid. Met.*, **2**, 11 (1970).
40. G. C. Wood, M. G. Hobby and B. Vaszko, *J. Iron Steel Inst. (London)*, **202**, 685 (1964).
41. T. Heumann and H. Boehmer, *Arch. Eisenhuettenwes*, **31**, 749 (1960).

The Pb/Pb^{+2} Exchange Reaction in Perchlorate Acidic Solutions

A. S. Gioda, M. C. Giordano, and V. A. Macagno

Department of Physical Chemistry, National University of Córdoba, 5000 Córdoba, Argentina

ABSTRACT

The Pb/Pb^{+2} exchange reaction mechanism in acidic perchlorate solutions has been investigated. Tafel slopes of about 30 mV are found for both Pb dissolution and deposition under steady-state and nonsteady-state conditions, respectively. Empirical rate equations for electrodissolution and electrodeposition are

$$i_a = k_a F \exp \frac{2FE}{RT}$$

and

$$i_c = k_c F\, C^2_{Pb^{+2}} \exp -\frac{2FE}{RT}$$

respectively. A mechanism with a chemical step as the rds is proposed to explain the experimental results. Although there has been special interest in the study of lead electrodes as anode energy producers in acid and alkali media (1, 2), less is known about the anodic behavior of lead electrodes in acidic solutions without film formation.

The anodic dissolution of lead has been studied (3) in KNO_3, $Pb(Ac)_2$, and NH_4Ac solutions, and a mechanism involving Pb^+ ions was postulated. On the other hand, results of impedance and double impulse measurements (4) have shown that at low Pb^{+2} concentrations the exchange process was controlled by lattice growth and dissolution. A full account of kinetic parameters for the Pb/Pb^{+2} exchange reaction in the presence of different types of electrolyte solutions is compiled elsewhere (2). In $HClO_4$ acid solutions in particular (5) only the passivation time of polycrystalline lead anodes was studied as a function of current density. The authors concluded that the process of anodic passivation is controlled by mass transport in solution.

Recently (6) the anodic oxidation of solid Pb in H_2SO_4 has been investigated and compared with measurements on solid Pb in $HClO_4$ solutions. Although some interesting features are shown, a full account of kinetic parameters are missing. Nevertheless, they concluded that the slow step for surface area changes with $HClO_4$ solutions is located in the surface since the curves do not depend on rotation speed.

This paper reports the results of kinetic studies of the exchange reaction at polycrystalline lead electrodes in acidic perchlorate solutions containing different amounts of Pb^{+2} ions, using several electrochemical techniques under a wide range of experimental conditions.

Key words: electrodeposition, dissolution mechanism, adions.

Experimental

A common three-electrode Pyrex glass cell was used for this investigation. The electrolyte solutions were deareated with purified nitrogen before each run. Temperature was maintained at 25° ± 0.1°C.

Polarization curves were obtained with a fast rise time potentiostat. Linear potential sweep experiments were performed with a specially designed triangular pulse generator (7) provided with electronic ohmic compensation. Potential current curves were recorded with a X-Y EAI Variplotter or with a 545 B Tektronix oscilloscope. Potential/time curves were obtained with a specially constructed power supply of ±0.1% stability. Transients were recorded either with a Sargent MR register or with the oscilloscope. Rotating-disk electrode assembly was previously described (8).

A saturated calomel electrode was used as the reference electrode. It was conveniently isolated from the working solution by an agar plug and glass joint. The reference compartment was in contact with the electrolyte through a Haber-Luggin capillary.

Lead electrodes were prepared from a bar stock of 99.999% Koch-Light Limited. A Teflon electrode assembly was used (9) to support the piece of Pb bar. The seal is produced using the principle of a drill chuck. The collet was made in Teflon, while the truck and the chuck were made in Teflon charged with fiber glass to make it harder. The surface exposed to the solution was a disk of either 4×10^{-3} or 6.1×10^{-2} cm^2. The exposed surface was ground with carborundum paper 600A with distilled water, as the lubricant, washed with distilled water, and then placed immediately in the cell. The same procedure was repeated before each run. Although mechanical polishing for soft metals has been criticized (10), we found that the several electropolished electrodes tested were unable to give reproducible results. The auxiliary electrode was a Pt foil of about 6 cm^2.

Solutions were prepared from $NaClO_4$, Koch-Light crystallized from distilled water, and $HClO_4$ acid Merck pA. $Pb(ClO_4)_2$ was obtained from lead electrolytic dissolution in $HClO_4$-$NaClO_4$ solutions and standardized with EDTA. Concentration range was between 2×10^{-3} and 1.64M for ClO_4^- ions, from 10^{-5} to 10^{-1}M for H^+, and between 2.3×10^{-5} and 1.34×10^{-2}M for Pb^{+2}.

The steady-state rest potential was taken at open circuit until the drift in potential was 5 mV/hr or less, and it was measured with a pH Meter 4 Radiometer potentiometer. The time elapsed to reach the steady state depends on the type of solution and concentration.

Current efficiency for an exchange of two Faradays per mole was verified through quantitative determination of Pb^{+2}. Unless indicated otherwise, all potentials are quoted against the saturated calomel electrode.

Results

Potentiostatic polarization curves.—Two types of solution composition were studied: a mixture of $NaClO_4$-$HClO_4$, and the same mixture with addition of $Pb(ClO_4)_2$. The dependence of the steady-state rest potential with the different species involved are compiled in Fig. 1. It can be seen that E_r appears almost independent of ClO_4^- and H^+ species concentration. On the other hand, in the Pb^{+2} concentration range studied, a plot of E_r *vs.* log $C_{Pb^{+2}}$ shows a slope

$$\frac{\delta E_r}{\delta \log C_{Pb^{+2}}} = 0.03\text{V} \qquad [1]$$

and with an intersect at log $C_{Pb^{+2}} \simeq 0$ very close to $E°_{Pb/Pb^{+2}}$ electrode, indicating that a Nernst's equation for the process

$$Pb \rightleftharpoons Pb^{+2} + 2e \qquad [2]$$

is followed.

Figure 2 shows some of the anodic polarization behavior of Pb electrodes in the two types of solutions. A linear dependence of E *vs.* log i_a is observed over at least two decades of logarithm even for the most dilute solutions. The addition of different amounts of Pb^{+2} produces an increase on the exchange current, but it has no appreciable effect on Pb dissolution. The polarization data obtained with stationary and rotating-disk electrodes were similar except for the region near the rest potential where the effect for the backward reaction becomes important and at high overpotentials where mass transport interferes. Anodic Tafel slopes in both types of solutions are around 30 mV/decade. A similar value was also reported previously (6).

The experimental dependence of anodic dissolution current densities on ClO_4^-, H^+, and Pb^{+2} concentration gives the following results

$$\left(\frac{\delta \log i_a}{\delta \log C_{ClO_4^-}}\right)_{E,H^+,Pb^{+2}} = \left(\frac{\delta \log i_a}{\delta \log C_{H^+}}\right)_{E,ClO_4^-,Pb^{+2}} = \left(\frac{\delta \log i_a}{\delta \log C_{Pb^{+2}}}\right)_{E,ClO_4^-,H^+} = 0 \qquad [3]$$

Although ionic strength was not constant for the first relationship, the effect of ϕ_2 potential on i is minimal when the reaction is independent of the ion concentration, as it seems to be in this case.

The variation of exchange current density with Pb^{+2} concentration obtained by extrapolating the Tafel line to the rest potential is

$$\frac{\delta \log i_o}{\delta \log C_{Pb^{+2}}} = 1 \qquad [4]$$

as shown in Fig. 3. Also, from the dependence of the rest potential on Pb^{+2} concentration, a value of Pb^{+2} concentration at the surface could be calculated in the type solutions. This average exchange current is also included in Fig. 3.

On the other hand, i_o appears as almost independent on H^+ and ClO_4^- ions concentrations as it is shown in Table I. Thus

$$\left(\frac{\delta \log i_o}{\delta \log C_{H^+}}\right)_{Pb^{+2}} = \left(\frac{\delta \log i_o}{\delta \log C_{ClO_4^-}}\right)_{Pb^{+2}} = 0 \qquad [5]$$

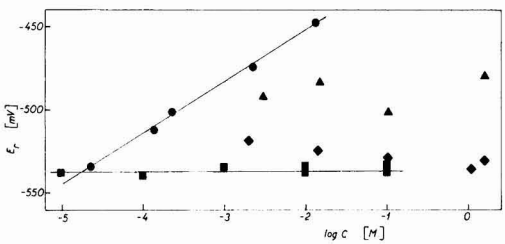

Fig. 1. Dependence of the steady-state rest potential with different species. ● *vs.* $C_{Pb^{++}} - C_{ClO_4^-} = 1.11$M, $C_{H^+} = 0.1$M; ■ *vs.* $C_{H^+} - C_{ClO_4^-} = 1.06$M; ▲ *vs.* $C_{ClO_4^-} - C_{Pb^{+2}} = 0.001$M, $C_{H^+} = 0.001$M; ♦ *vs.* $C_{ClO_4^-} - C_{H^+} = 0.001$M.

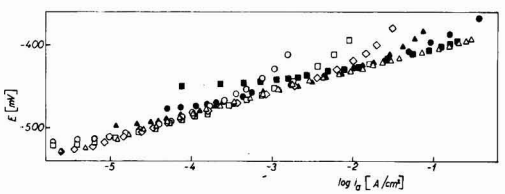

Fig. 2. Polarization curves for Pb electrodissolution. ○, □, ◇, △ $C_{H^+} = 0.001$M and $C_{ClO_4^-} = 0.002$, 0.014, 0.1, and 1.64M, respectively. ■ $C_{ClO_4^-} = 1.13$M, $C_{H^+} = 0.001$M, $C_{Pb^{+2}} = 0.013$M; ● $C_{ClO_4^-} = 1.64$M, $C_{H^+} = 0.001$M, $C_{Pb^{+2}} = 0.001$M; ▲ $C_{ClO_4^-} = 1.13$M, $C_{H^+} = 0.1$M, $C_{Pb^{+2}} = 0.0002$M.

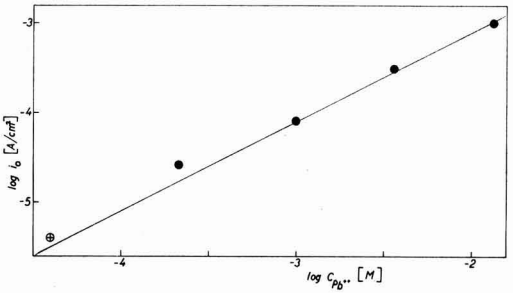

Fig. 3. Dependence of the exchange current density on log $C_{Pb}{}^{+2}$. ⊕ Concentration calculated as is indicated in the text.

Stoichiometric numbers (11) were experimentally obtained from current densities values at low overpotentials, as

$$\nu = \frac{i_o n\mathbf{F}}{RT}\left(\frac{\delta\eta}{\delta i_a}\right)_{\eta\to 0} \qquad [6]$$

Figure 4 gives typical η *vs.* i_a plots. The ν values obtained for the different types of solutions are compiled in Table I, and the average result is 0.5. In order to obtain reproducible results for the cathodic reaction, the electrode was rotated and the potential scanned at a constant rate of 5 mV/sec. Under this condition it is supposed that a quasisteady state is reached since no appreciable change in the E/i curves was found with potential sweep rates up to 20 mV/sec.

Figure 5 shows representative polarization curves for Pb deposition. Limiting currents are obtained which depend linearly on the square root of electrode rotation speed and Pb^{+2} concentration. Taking into account the Levich's equation (12)

$$i_L = 0.62\, n\mathbf{F}D^{2/3}\nu^{1-1/6}\omega^{1/2}C_b \qquad [7]$$

the diffusion coefficient can be evaluated. The average $D_{Pb^{+2}}$ is 4.8×10^{-6} cm² sec^{-1}.

The half-wave potential does not depend on rotation speed, this being an indication that the reaction behaves in a reversible way (13). On the other hand, a plot of η *vs.* log $[(i_L - i_c)/i_L]$ (12) gave a straight line with a slope of about 30 mV/decade.

Galvanostatic potential-time curves.—Representative potential-time curves for Pb^{+2} electrodeposition are shown in Fig. 6. Only one transition time is observed at all current densities studied. Nevertheless, an increase in the transition time was observed in repetitive runs performed at low current densities. This effect together with the increase of the $i_c\tau^{1/2}/C$ ratio as i_c is decreased, Fig. 7, could be attributed to an appreciable increase in the electrode area due to deposition. At moderate and high current densities a linear dependence of $i_c\tau^{1/2}/C$ *vs.* i_c is found.

By applying Sand's equation (14) to the linear region, the diffusion coefficient can be evaluated as

$$\frac{i_c\tau^{1/2}}{C_b} = \frac{n\mathbf{F}\pi^{1/2}D^{1/2}}{2} \qquad [8]$$

Table I. Kinetic parameters for Pb electrodissolution

$C_{ClO_4^-}$ (M)	C_{H^+} (M)	$C_{Pb^{+2}}$ (M)	b_a (V)	log i_o (A/cm²)	ν
			0.030	−5.48	—
		—	0 026	−5.32	—
			0.027	−5.44	0.40
			0.029	−5.44	0.54
1.64	0.001		0.028	−3.88	0.40
		0.001	0.027	−4.00	0.73
			0.027	−3.72	0.59
			0.029	−5 24	—
		—	0.030	−5.40	0.38
0.1	0.001		0.029	−3.88	0.46
		0.001	0.032	−3.92	—
			0.033	−5.72	0.54
		—	0.030	−5.27	—
			0.031	−5.60	—
0.014	0.001	0.001	0 030	−3.83	0.67
			0.028	−5.88	—
0.002	0.001	—	0.028	−5.20	0.49
0.003	0.001	0 001	0.029	−4.10	0.46
		0.002	0 025	−3.68	—
1.13	0.001	0.013	0.030	−2 36	—
		0.0002	0.026	−4.48	—

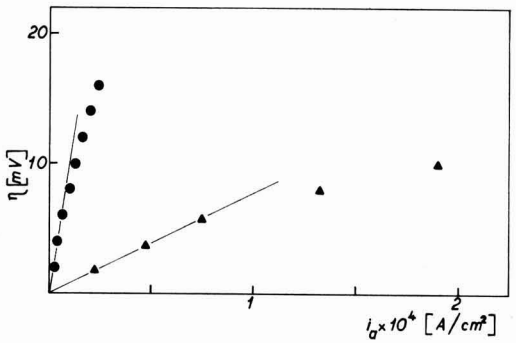

Fig. 4. Plots of overpotential *vs.* current density. $C_{ClO_4^-}$ = 1.64M, C_{H^+} = 0.001M. ● Without Pb^{+2}; ▲ $C_{Pb^{+2}}$ = 0.001M.

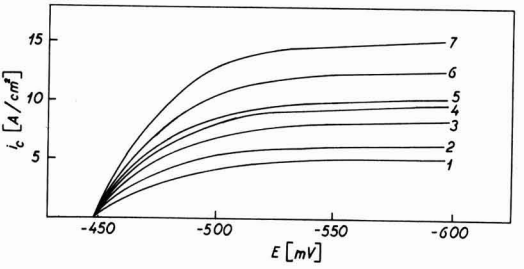

Fig. 5. Polarization curves for electrodeposition obtained at the RDE. $C_{Pb^{+2}}$ = 0.013M, $C_{ClO_4^-}$ = 1.64M, C_{H^+} = 0.1M. ω (rad/sec): 1 = 19.8; 2 = 40.2; 3 = 58.2; 4 = 77.4; 5 = 96.9; 6 = 128; 7 = 187.

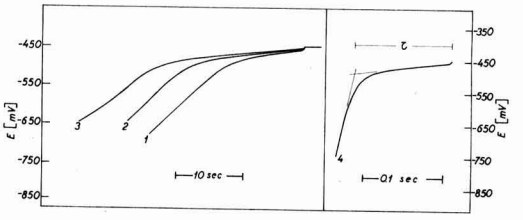

Fig. 6. Galvanostatic potential-time curves. $C_{ClO_4^-}$ = 1.13M, C_{H^+} = 0.1M. 1, 2, and 3 repetitive runs, $C_{Pb^{+2}}$ = 1.34 × 10^{-2}M, i_c = 2.05 × 10^{-3} A/cm², 4, $C_{Pb^{+2}}$ = 0.0036M, i_c = 4.60 × 10^{-3} A/cm².

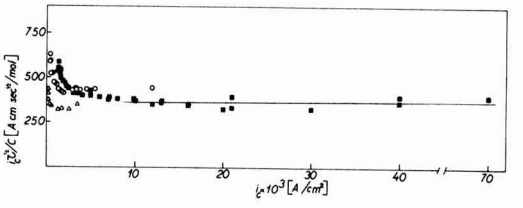

Fig. 7. Dependence of the chronopotentiometric constant on current density. $C_{ClO_4^-}$ = 1.13M, C_{H^+} = 0.1M; ○, ■, △ $C_{Pb^{+2}}$ = 0.0036, 0.013, and 0.0009M, respectively.

giving an average value of 4.5×10^{-6} cm^2 sec^{-1}. A plot of E *vs.* log $(\tau^{1/2} - t^{1/2})$ (14) gives a good straight line with a slope of 30 mV/decade.

Linear sweep voltammetry.—The dissolution curve appears as a typical process without film formation with a continuous increase in current as the potential is increased. On the reverse sweep a cathodic current appears near the rest potential. Voltammograms for Pb deposition are shown in Fig. 8. The cathodic i/E curves show a peak current that depends on sweep rate.

A plot of i_p *vs.* $v^{1/2}$, Fig. 9, shows a complex behavior. At low v there is a straight line dependence of i_p with $v^{1/2}$. As sweep rate is increased there is a transition to a lower slope. From the highest slope, the diffusion coefficient for a two electrons reversible process was calculated. The average value results 4.3×10^{-6} cm^2 sec^{-1}.

In Fig. 10, the behavior of E_p *vs.* log v is analyzed. Two different zones are observed depending on sweep rate. At low sweep rates, E_p remains constant independent of v, while after a certain v value the variation of E_p *vs.* log $v^{1/2}$ takes a slope of

$$\frac{\delta E_p}{\delta \log v^{1/2}} = 30 \text{ mV} \qquad [9]$$

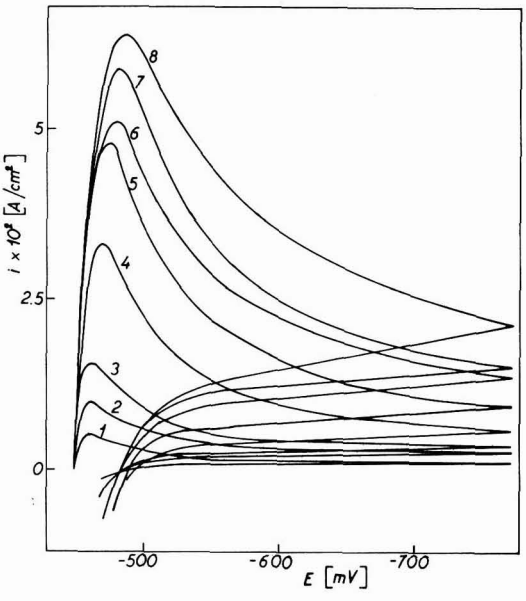

Fig. 8. Voltammograms for Pb^{+2} deposition. $C_{Pb^{+2}} = 0.013$M, $C_{ClO_4^-} = 1.13$M, $C_{H^+} = 0.1$M. Sweep rate (V/sec): 1 = 0.02; 2 = 0.1; 3 = 0.2; 4 = 0.8; 5 = 2; 6 = 4; 7 = 6; and 8 = 10.

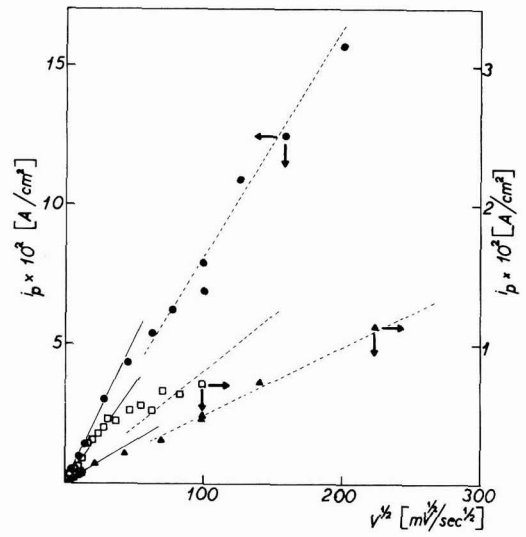

Fig. 9. Dependence of the peak current density on sweep rate for Pb^{+2} deposition. $C_{ClO_4^-} = 1.13$M, $C_{H^+} = 0.1$M. ●, □, ▲ $C_{Pb^{+2}} = 0.013$, 0.0036, and 0.0009M, respectively.

Discussion

From the experimental results given above, the rate for the anodic reaction can be derived from the theoretical expression (15)

$$i_a = \mathbf{F}k_a(\pi_s C_s Z_{a,s}) \exp(\alpha_a \mathbf{F}E/RT) \qquad [10]$$

With the experimental values of $\alpha_a = 2$ and Z_a for all species as zero, the empirical rate equation for the anodic reaction is obtained

$$i_a = \mathbf{F}k_a \exp \frac{2\mathbf{F}E}{RT} \qquad [11]$$

Introducing the overpotential in Eq. [10] as $\eta = E - E_r$, the theoretical rate equation is rewritten as

$$i_a = \mathbf{F}k_a(\pi_s C_s^{Z_{a,s}}) \exp[\alpha_a \mathbf{F}(\eta + E_r)/RT] \qquad [12]$$

when $\eta = 0$, $i_a = i_c = i_o$ and the exchange current results

$$i_o = \mathbf{F}k_a(\pi_s C_s^{Z_{a,s}}) \exp(\alpha_a \mathbf{F}E_r/RT)$$
$$= \mathbf{F}k_c(\pi_s C_s^{Z_{o,s}}) \exp(-\alpha_c \mathbf{F}E_r/RT) \qquad [13]$$

On the other hand, the Nernst equation can be written as

$$E_r = E_o - \frac{RT}{n\mathbf{F}} \ln \pi_s C_s^{m_s} \qquad [14]$$

which according to Eq. [2] takes the form

$$E_r = E_o + \frac{RT}{2\mathbf{F}} \ln C_{Pb^{+2}} \qquad [15]$$

Furthermore, the equilibrium constant of the total electrochemical reaction is related to the anodic and cathodic rate constants (15) as follows

$$\frac{k_a}{k_c} = K^{1/\nu} \qquad [16]$$

Taking into account the above equations, the following relations between kinetics parameters are found

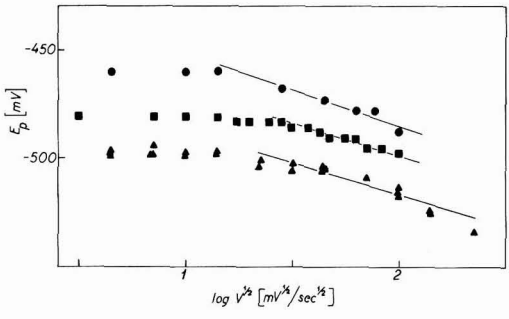

Fig. 10. Dependence of the peak potential on log $v^{1/2}$ for Pb^{+2} deposition. $C_{ClO_4^-} = 1.13$M, $C_{H^+} = 0.1$M. ●, ■, ▲ $C_{Pb^{+2}} = 0.013$, 0.0036, and 0.0009M, respectively.

$$n = \nu(\alpha_a + \alpha_c) \quad [17]$$

and

$$m_s = \nu(Z_a - Z_c) \quad [18]$$

Thus Eq. [13] for the exchange current can be transformed to

$$i_o = (k_c K^{1/\nu})\mathbf{F}\left[\pi_s C_s\left(\frac{m_s}{\nu} + Z_c\right)\right]\exp(\alpha_a \mathbf{F} E_r/RT) \quad [19]$$

Equation [19] shows that from a plot of ln i_o *vs.* ln $C_{Pb^{+2}}$ the cathodic reaction order can be found. Experimentally

$$\frac{\delta \ln i_o}{\delta \ln C_{Pb^{+2}}} = \left(\frac{m_s}{\nu} + Z_c\right) - m_s = 1 \quad [20]$$

hence, as $m_s = -1$ and $\nu = 0.5$, results are $Z_c = 2$. Also, according with Eq. [17], $(\alpha_a + \alpha_c) = n/\nu = 4$ and $\alpha_c = 2$; thus the rate equation for the cathodic reaction results in

$$i_c = \mathbf{F} k_c C^2_{Pb^{++}} \exp -\frac{2\mathbf{F}E}{RT} \quad [21]$$

Deposition of Pb^{+2} behaves as a rather reversible reaction under steady-state conditions. Nevertheless under linear sweep voltammetry a certain degree of irreversibility can be inferred from i_p *vs.* $v^{1/2}$ dependence, Fig. 9, and also from E_p *vs.* log $v^{1/2}$, Fig. 10, at high sweep rates giving a Tafel slope of about 30 mV/decade in agreement with the theoretical $\alpha_c = 2$.

By combining data represented in Fig. 9 and 10 the cathodic reaction order was obtained from log i_p *vs.* log $C_{Pb^{+2}}$ at constant E_p, Fig. 11. The experimental value is in agreement with the kinetic Eq. [21]. In a general case of a multistep reaction (16) the transfer coefficients α are denoted as

$$\alpha_a = \left(\frac{\gamma_a}{\nu} - \beta_r\right) \quad [22]$$

and

$$\alpha_c = \left(\frac{n - \gamma_a}{\nu} + \beta_r\right) \quad [23]$$

where γ's and r are the number of electrons transferred before and during the rds, respectively. β is usually taken as 0.5. On the bases of the kinetic parameters obtained, only one set of numbers of electrons transferred before and during the rds are possible. Thus, for $\alpha_a = 2$ and $\nu = 0.5$, with $\beta = 0.5$ results $\gamma_a = 1$ and $r = 0$.

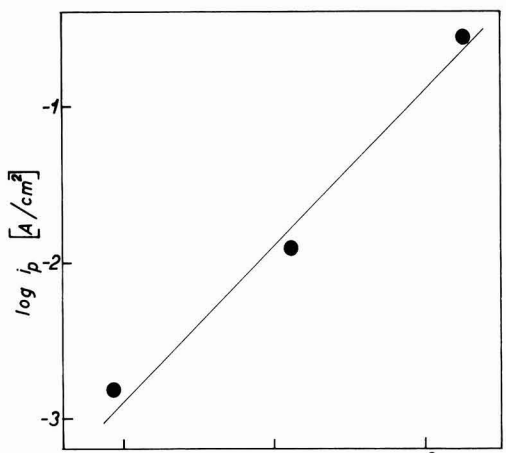

Accordingly a mechanism with a charge transfer in quasiequilibrium followed by a chemical step as the rate-determining step could be postulated as the most probable pathway for Pb/Pb^{+2} exchange reaction in acidic perchlorate solutions. Taking into account that Pb^{+2} concentration does not affect the anodic reaction rate, a loop-containing mechanism could be discarded in principle (17). On the other hand, the stoichiometric number of ½ experimentally obtained is an indication that for each occurrence of the rds the total reaction goes twice to completion. Hence, a quasiequilibrium one-electron charge transfer step to form species Pb(I) adion could be postulated for the first step (11). It is more difficult to assign a formal equation for the rds. Nevertheless, a chemical interaction between two Pb(I) adions to form a more suitable specie for the second charge transfer could be a plausible explanation for the $\nu = 0.5$ found experimentally. Formally, a sequence of steps

$$Pb \rightleftharpoons Pb(I) + 1e \quad [24]$$

$$2\,Pb(I) \xrightarrow{rds} [Pb(I)]_2 \quad [25]$$

$$[Pb(I)]_2 \rightleftharpoons 2Pb^{+2} + 2e \quad [26]$$

would be in agreement with the experimental data correlated by the empirical Eq. [11] and [21]. Much work is indicated in order to clarify the complex nature of the rds, but this investigation has shown that the behavior of the Pb/Pb^{+2} exchange reaction agrees with a series of previous results obtained with *sp* metals (18).

Acknowledgment

A. S. Gioda is grateful to the Consejo Nacional de Investigaciones of Argentina for the award of an Initiation Research Fellowship. This work was also supported in part by CONICET and CUI of Córdoba University.

Manuscript submitted Dec. 21, 1976; revised manuscript received May 16, 1977.

Any discussion of this paper will appear in a Discussion Section to be published in the June 1978 JOURNAL. All discussions for the June 1978 Discussion Section should be submitted by Feb. 1, 1978.

LIST OF SYMBOLS

A	amperes
b_a	anodic Tafel slope
C_b	concentration of diffusing specie in the bulk
C_s	concentration of *s* specie
D	diffusion coefficient
E	electrode potential
$E_{1/2}$	half-wave potential
E_o	standard potential
E_p	peak potential
E_r	steady-state rest potential
$\mathbf{F}$	Faraday's constant
i	current density
i_a	anodic net current density
i_c	cathodic net current density
i_L	limiting current density
i_p	peak current density
i_o	exchange current density
k_a	anodic specific rate constant
k_c	cathodic specific rate constant
K	equilibrium constant
m_s	stoichiometric coefficient of *s* specie in the overall reaction
n	number of electrochemical equivalents per mole
r	number of electrons transferred in the rds
R	gas constant

α_a anodic transfer coefficient
α_c cathodic transfer coefficient
β symmetry factor
γ_a number of electrons transferred before the rds
η overpotential
ν stoichiometric number
ν^1 kinematic viscosity
π_s productory over s
τ transition time
ϕ_2 potential at the outer Helmholtz plane
ω electrode rotation speed (radians/sec)

REFERENCES

1. G. Archdale and J. A. Harrison, *J. Electroanal. Chem. Interfacial Electrochem.*, **47**, 93 (1973).
2. T. F. Sharpe, "Encyclopedia of Electrochemical Elements," Vol. 1, Chap. 1-5 (1973).
3. J. W. Johnson, C. K. Wu, and W. J. James, *Corros. Sci.*, **8**, 309 (1968).
4. N. A. Hampson and D. Larkin, *Trans. Faraday Soc.*, **65**, 1660 (1969).
5. C. J. Bushrod and N. A. Hampson, *Br. Corros. J.*, **6**, 87 (1971).
6. A. N. Fleming and J. A. Harrison, *Electrochim. Acta*, **21**, 905 (1976).
7. G. Paus, A. J. Calandra, and A. J. Arvía, *Annales de la Soc. Cient. (Argentina)*, **192**, 35 (1971).
8. L. Sereno, V. A. Macagno, and M. C. Giordano, *Electrochim. Acta*, **17**, 561 (1972).
9. A. Capon and R. Parsons, *J. Electroanal. Chem. Interfacial Chem.*, **39**, 275 (1972).
10. C. V. D'alkaine, S. B. Estevez, and D. J. Schiffrin, *Metallurgical Journal No. 6*, Argentine Society of Metals, Buenos Aires, Argentina (1974).
11. J. O'M. Bockris, in "Modern Aspects of Electrochemistry," No. 1, J. O'M. Bockris, Editor, Chap. 4 Butterworths, London (1954).
12. A. C. Riddiford, in "Advances in Electrochemistry and Electrochemical Engineering," Vol. 4, P. Delahay and C. W. Tobias, Editors, Interscience, New York (1966).
13. G. Charlot, J. Badoz-Lambling, and B. Trémillon, Les Reactions Electrochimiques, Masson and Cie., Paris (1959).
14. P. Delahay, "New Instrumental Methods in Electrochemistry," Interscience, New York (1954).
15. T. Kodera, H. Kita, and M. Honda, *Electrochim. Acta*, **17**, 1361 (1972).
16. J. O'M. Bockris and A. K. N. Reddy, "Modern Electrochemistry," Vol. 2, Plenum Press, New York (1970).
17. A. R. Despić, Dj. Jovanović, and T. Rakić, *Electrochim. Acta*, **21**, 63 (1976).
18. T. Hurlen, *Acta Chem. Scand.*, **16**, 1337 (1962).

The Electrochemical Reduction of Carbon Dioxide, Formic Acid, and Formaldehyde

P. G. Russell,[1] N. Kovac,* S. Srinivasan, and M. Steinberg**

Brookhaven National Laboratory, Department of Applied Science, Upton, New York 11973

ABSTRACT

The prospects for the electrochemical reduction of carbon dioxide to methanol were examined by investigating the intermediate reactions. The reduction of carbon dioxide was carried out in a neutral electrolyte at a mercury electrode. The high overvoltage observed for carbon dioxide reduction to the formate anion reflects a low value for the efficiency of electric energy utilization for this process. Formic acid can be reduced to methanol in a perchloric acid electrolyte (at a lead electrode) or in a buffered formic acid electrolyte (at a tin electrode). The faradaic efficiency for methanol formation is close to 100% at the tin electrode in a narrow potential region corresponding to a low current density. The potential dependence of formic acid reduction to methanol suggests that the adsorption of formic acid on the electrode, near the pzc, may be the rate-controlling step in the over-all reaction. The reduction of formaldehyde to methanol occurs with a faradaic efficiency exceeding 90% in a basic solution. The Tafel slope decreases when either the formaldehyde concentration is increased (at constant pH) or when the pH of the solution is increased (at constant concentration). The polyoxymethylene glycols present as impurities in formaldehyde solutions may influence the mechanism of the electrode process through interaction with formaldehyde molecules and/or other adsorbed species resulting in small changes of the Tafel slope.

The prospects for electrochemical production of methanol from carbon dioxide.—With the increasing possibility of the unavailability of oil in 20-30 years, methanol will probably be the substitute liquid fuel (or fuel intermediate) in the future. New methods for the production of methanol should be economically competitive with existing technology. One approach for the production of methanol from nonfossil sources is by the electrochemical reduction of carbon dioxide. This will be feasible only with a potentially cheap source (*e.g.*, controlled thermonuclear generation) of electrical energy. Methanol may also be considered as a medium for the storage of hydrogen.

The purpose of this work is to evaluate the optimum conditions (electrode, electrolyte, pH, etc.) for the conversion of carbon dioxide to methanol. The high overpotentials observed for the reduction of carbon dioxide and its intermediates result in an over-all low energy efficiency. The reduction of carbon dioxide to formic acid has been studied extensively. However, few studies describe the further reduction of formic acid to methanol.

Previous studies on the electrochemical reduction of carbon dioxide.—The electrolytic reduction of carbon dioxide in aqueous solutions has been the subject of many investigations. According to the earlier papers (1-5) formic acid (or the formate ion) was found to be the principal product with the highest current efficiency being obtained at amalgamated electrodes (see Table I). The electrolyte, containing the alkali salt (bicarbonate, carbonate, or sulfate) was usually saturated with carbon dioxide gas [pressures of up to 50 atm were used in some experiments (4)]. High cur-

* Electrochemical Society Student Member.
** Electrochemical Society Active Member.
[1] Present address: Sprague Electric Company, Research and Development Laboratories, North Adams, Massachusetts 01247.

Table I. Results of some previous studies on carbon dioxide reduction in aqueous solution

Cathode	Anode	Separator	Electrolyte	Pressure of CO_2	Products other than HCOOH. Final conc. of HCOOH, g/liter	Percent faradaic efficiency for $HCOO^-$ production	Ref.
Zn electrodeposited on Cu, then amalgamated	Pb	Porous cell	Sat'd K_2SO_4	5 atm	—	98.6	(4)
Cu electrodeposited on Cu	Pb	Porous cell	Sat'd K_2SO_4	50 atm	—	86.4	
Zn (Hg)	Pb	Porous cell	Sat'd K_2SO_4	50 atm	96.4	49	
Rotating amalgamated Cu rod	Pb	Porous diaphragm	10% Na_2SO_4	Sat'd CO_2	1.8 as HCOONa	81.3	(12)
		Cation exchange membrane			From 190 to 200	80	
Hg						93 to 100	(13)
Ga(s)						34	
Ga(l)	Pt	Compartment Cell	0.5M $NaHCO_3$	Sat'd CO_2		34.9	
Cerrolow 136(s)						24.3	
Cerrolow 136(l)						36	
In							
Pb			1M Me_4NHCO_3			<80	(14)
Pb			1M $NaHCO_3$	Sat'd CO_2	Only H_2		
Hg							
Cd							
Carbon			1M Et_4NHCO_3	Sat'd CO_2	Some H_2 glycolic acid results from oxidation of carbon electrode		
Pt			pH = 8 in these solutions				
WC			1M Me_4NHCO_3	Sat'd CO_2	Only H_2		
Pb				1 atm		80	(15)

rent efficiencies for formate production (~ 99%) were obtained in short-term electrolysis experiments where the diffusion of the formate anion was negligible.

After long-term contact of a solution of sodium bicarbonate with sodium amalgam, appreciable concentrations of formate ion were detected (6). This result led some workers to believe that the bicarbonate and carbonate anions were electroactive species and that the reduction of carbon dioxide occurred on electrodes having high hydrogen overpotentials (2, 3). Polarographic waves observed in solutions containing carbon dioxide were interpreted as being due to the reduction of carbon dioxide (7-9). Later studies (10, 11) confirmed the above interpretation and showed that carbon dioxide, and not the bicarbonate or carbonate anion, is the electroactive species.

Intermediates are formed during the reduction of carbon dioxide. A number of studies have dealt with the properties of a "reduced carbon dioxide" species, $(CO_2)_r$, formed when carbon dioxide is reduced to formic acid in aqueous solution. The results of one study (16) carried out in acid solution show that carbon dioxide reacts with chemisorbed hydrogen (electrochemically formed) on bright platinum in the potential region 0 to +250 mV *vs.* the RHE to form $(CO_2)_r$. The rate of reaction is slow at room temperature, but increases rapidly with temperature. On platinized platinum at 90°C, chemisorbed hydrogen reacts rapidly with carbon dioxide. In another study (17), this reaction intermediate was produced at a platinum electrode and then oxidized at a constant current. The amount of carbon dioxide formed was determined by gas liquid chromatography. The results showed that two electrons are transferred during oxidation of each $(CO_2)_r$ species. In comparison with the results of similar experiments carried out using carbon monoxide, it was suggested that $(CO_2)_r$ is carbon monoxide, chemisorbed in the first layer on platinum.

Previous studies on the electrochemical reduction of formic acid.—The reduction of formic acid is more difficult and thus fewer studies have appeared in the literature. In one study, on the reduction of carboxylic acid esters (18), an ester of formic acid was found to be reduced with difficulty. In 1907, a patent was granted for an electrochemical method of reducing monobasic fatty acids to aldehydes and alcohols (19). Specific mention is made of formic acid reduction. In a 10% sulfuric acid electrolyte solution formic acid was reduced preferentially to formaldehyde at low current densities and to methanol at high current densities. In general, low current densities were recommended for carrying out the reduction. A number of metals were suggested for use as cathodes (lead, spongy nickel, iron, cobalt, and platinized platinum) but the coulombic efficiency for methanol production on the individual metals was not presented. In a recent two-part study (20, 13) tin was found to be a good electrocatalyst for formic acid reduction. In part I (20) formic acid was reported to be reduced to methanol with a 100% current efficiency at low current densities. A selective oxidation and titration scheme of the formic acid, formaldehyde, and methanol present was the analytical method used in the product analysis. However, in part II (13) of this work, significant analytical results showed that the current efficiency is quite low; polished tin (7%), electroplated tin (13%), and Cerrolow 136 (solid phase ~7.4%, liquid phase ~13.7%). The best results (for longer run tests) were obtained with the molten Cerrolow 136 (low melting point alloy containing tin) where the maximum effective current density was only 140 $\mu A/cm^2$.

Previous studies on the electrochemical reduction of formaldehyde.—The reduction of formaldehyde has been studied extensively in classical polarography [see Ref. (21) for a review of the earlier work]. The polarographic wave increases rapidly with the pH and temperature of the solution. The low kinetic current is attributed to the fact that formaldehyde is present predominantly in the electroinactive hydrated form, methylene glycol. The limiting current for reduction is governed by the reaction rate for methylene glycol dehydration to formaldehyde, which is the electroactive species. This dehydration appears to be a base catalyzed reaction. In solutions with a pH value greater than 12, the limiting current decreases with increase in the pH. This decrease probably results from the formation of an anion of methylene glycol, $H_2C(OH)O^-$, in high pH solutions which is the intermediate for formaldehyde formation. In a recent study (21) the presence of $H_2C(OH)O^-$ was observed through its u.v. absorption peak at 215 nm. The following mechanism (21, 22) has been proposed for formaldehyde formation in solution at a pH between 12 and 13

$$CH_2(OH)_2 + OH^- \underset{k_{-1}}{\overset{k_1}{\rightleftarrows}} CH_2(OH)^- + H_2O \qquad [1]$$

$$CH_2(OH)O^- \underset{k_{-2}}{\overset{k_2}{\rightleftarrows}} H_2C{=}O + OH^- \qquad [2]$$

Measurement of these rate constants using pulse polarography (22) can explain the sharp decrease ob-

served in the limiting current with an increase in pH above a value of 13.2. With lower pH values the rate of methylene glycol dehydration determines the available amount of formaldehyde.

In a previous study (23) on formaldehyde reduction evidence was found for a CECE mechanism in the pH region of 9 and below while a CEEC mechanism was suggested for the pH region of 13 and above. In cyclic voltammetry experiments with 5×10^{-2}M formaldehyde solutions an anodic peak (considered to be the oxidation of the radical anion intermediate resulting from the first electron transfer step) was obtained in a borate buffer (pH of 9) at a sweep rate of 100 V/sec. This peak was not observed in a solution of lower pH (phosphate buffer, pH = 6.8) and it disappeared at a pH above 9.5. These results, along with other evidence, suggested that in a neutral solution the chemical reaction following the first electron transfer step is fast enough so that no peak occurs. As the pH of the solution increases, this reaction becomes slower and an anodic peak occurs at fast sweep rates. In the absence of any appreciable dimerization of the adsorbed radical anion, the disappearance of this peak with a further increase of pH (greater than 9.5) indicated that a second electron transfer step, favored by the increase in the negative potential at the electrode surface due to the higher solution pH, occurs prior to the chemical step.

In addition to methylene glycol and a small amount of formaldehyde [$K \sim 10^{-4}$ for $H_2C(OH)_2 \rightleftarrows H_2CO + H_2O$], there are small amounts of polyoxymethylene glycols [$HO(CH_2O)_nH$ where $n \geq 2$], the concentrations of which depend on formaldehyde concentration (24). The amount (mole percent) of methylene glycol decreases while the amount of the polyoxymethylene glycols increases with increasing formaldehyde concentration. A number of equilibria can be written among the different species present in solution (the equilibria involving the anion of methylene glycol discussed above are not included here)

$$\begin{array}{ccc} H_2C(OH)_2 + HO(CH_2O)_nH & \rightleftarrows & HO(CH_2O)_{n+1}H + H_2O \\ \downarrow\uparrow & & \downarrow\uparrow \\ H_2CO + H_2O & & HO(CH_2O)_nH + H_2CO \end{array} \quad [3]$$

Previous studies (25) indicate that with increase in the pH of the solution, the amount of methylene glycol increases. Any mechanism study of formaldehyde reduction is complicated by the presence of these species.

Experimental

Types of studies.—Three types of experimental studies (carried out at 25° ± 3°C) were conducted: (*i*) current-potential relations obtained from steady-state potentiostatic experiments at a mercury electrode in electrolyte solutions containing either carbon dioxide or formaldehyde; (*ii*) current-potential relations obtained from nonsteady-state (cyclic voltammetric) experiments in electrolyte solutions at a hanging mercury drop electrode containing formaldehyde; and (*iii*) products formed in long-term electrolysis experiments with formic acid (carried out at both lead and tin electrodes) and formaldehyde (carried out at a mercury pool) as reactants were identified quantitatively, using gas chromatographic techniques.

Electrochemical instrumentation.—A PAR potentiostat (Model 173) and digital coulometer (Model 179) were used for the long-term electrolysis experiments on formic acid and formaldehyde. For the steady-state potentiostatic experiments a PAR potentiostat (Model 173) and a Keithley 160B digital multimeter were employed. The electronic instrumentation for the cyclic voltammetric studies consisted of the PAR potentiostat (Model 173), PAR universal programmer (Model 175), and a Hewlett Packard X-Y recorder (7047A) or Tektronix storage scope (702BA). The cyclic voltammograms obtained at a 10 mV/sec scan rate were displayed on the X-Y recorder while those obtained at faster sweep rates were recorded on the storage scope. The *IR* corrections (for the steady-state polarization curves) were made by the current interruptor method using a mercury relay switch and the storage scope.

Electrochemical cells.—The long-term electrolysis experiments with formaldehyde and the steady-state polarization measurements on formaldehyde and carbon dioxide were carried out in a Pyrex cell having a fine glass frit separating the working and counterelectrode compartments. The counterelectrode was platinized platinum. In these experiments the reference electrode (SCE) was placed 4-6 mm above (and in the center of) the 1 in. diam (5.06 cm^2) mercury pool. The reduction of formic acid was carried out in an enclosed glass cell in order to minimize the loss of any volatile products formed during electrolysis. The three anode compartments were symmetrically arranged and separated from the large cathode compartment (containing an electrode with geometric surface area of 50 cm^2) by fine glass frits each of which is covered with a layer of agar (containing either sodium or tetraethyl ammonium perchlorate). The sealed cell containing a nitrogen atmosphere above the oxygen-free electrolyte, is further isolated in a desiccator, (also containing a nitrogen atmosphere) during the electrolysis which lasted 40 hr or more.

Solutions and materials.—All solutions were made from reagent grade chemicals and distilled water which was redistilled in a Corning apparatus (Model AG-2). The buffer solutions were made in the following way: (*i*) pH 6.8, 0.05M KH_2PO_4 + 0.05M K_2HPO_4; (*ii*) pH 9.0, 0.1M $NaHCO_3$ + NaOH; (*iii*) pH 11.1, 0.1M Na_2CO_3 + NaOH; (*iv*) pH 13.0, 0.055M KCl + 0.145M NaOH. The stock formaldehyde solutions were prepared by bubbling the formaldehyde gas (obtained by heating paraformaldehyde) through water. The concentration was determined by the sulfite method (24). In the steady-state polarization experiments with carbon dioxide, good results were obtained with a commercial grade carbon dioxide gas. Reagent grade lead and tin and triply distilled mercury were used for the electrodes.

Gas chromatographic analysis of products.—A Carle analytical gas chromatograph with flame ionization detection modified with a catalytic converter (for reducing small molecules to methane) was used for the analysis of the products in the electrolyte solution. Matheson zero gas grade helium and hydrogen and ultra zero grade air were necessary for maximum sensitivity. A glass column (to minimize adsorption of formic acid) packed with Porapak QS was found to be best for the separation of formaldehyde, methanol, and formic acid in the presence of large amounts of water. Typical chromatograms run on a formaldehyde solution before and after electrolysis are shown in Fig. 1. The initial small amounts of methanol observed in the chromatograms are produced during preparation of the formaldehyde solution. A calibration curve to determine the quantity of methanol obtained during electrolysis is shown in Fig. 2. A similar calibration procedure was used to determine the quantity of methanol produced during the reduction of formic acid solutions.

Results and Discussion

Electrochemical reduction of carbon dioxide.—Detailed kinetic studies have been carried out on the reduction of carbon dioxide at a Hg-pool electrode by Eyring and co-workers (26, 27). Figure 3 shows the polarization curve for the reduction of carbon dioxide to the formate anion in a neutral solution where the faradaic efficiency is 100% (in acid solution the efficiency for formate production is much less because of a

parallel electrode reaction leading to the formation of molecular hydrogen). These results are in good agreement with previously published data (26). The galvanostatic charging curve experiments indicated that the coverage by an adsorbed intermediate is large ($\theta \rightarrow 1$) in region I (low overvoltage region with a Tafel slope of ~91 mV) and is small ($\theta \rightarrow 0$) in region II (with a Tafel slope of ~240 mV). The adsorbed intermediate was suggested to be the formate radical, $HCO_{2_{ads}}$. In addition the reaction order for the concentration of carbon dioxide was found to approach a value of zero and one in region I and II, respectively. The following mechanism best represents the experimental results (27)

$$CO_2 + e^- \rightarrow CO_{2^-_{ads}} \quad [4]$$

$$CO_{2^-_{ads}} + H_2O \xrightarrow{\text{fast}} HCO_{2_{ads}} + OH^- \quad [5]$$

$$HCO_{2_{ads}} + e^- \rightarrow HCO_2^- \quad [6]$$

In region I of the polarization curve, the step represented by Eq. [6] is considered to be rate determining while in region II the first step (Eq. [4]) is the rds. Water may be a reactant in the first step which then leads to the formation of $HCO_{2_{ads}}$. The variation of the reduction potential of carbon dioxide in DMSO with water content supports this hypothesis (28). For this case, the first step was proposed as the combination of Eq. [4] and Eq. [5] into a single step (26). When a more detailed analysis (which includes adsorption characteristics of the intermediate) is made, it is found that the experimental results (Tafel slope and reaction orders of carbon dioxide) are best explained when the intermediate is assumed to undergo activated adsorption according to the Temkin isotherm (26).

The intermediate may, however, not always be an adsorbed species with a large coverage. In another study (29) the intermediate (generated by a modulated cathode potential at a lead electrode) was found to be the carbon dioxide anion radical, CO_2^-. The technique of modulated specular reflectance spectroscopy was used to detect the presence of this radical by its optical absorption. The optical response of this radical indicated that it undergoes a rapid chemical reaction and that the amount calculated to be present would only form 2% of a monolayer.

The energy efficiency, ϵ, for the reduction of carbon dioxide to formic acid can be expressed in the following manner

$$\epsilon = \frac{\Delta H \times (\text{percent faradaic efficiency})}{n\mathbf{F}\{E_{rev} + \eta_c + \eta_a + \eta_{IR}\}} \quad [7]$$

where $\Delta H = 64.4$ kcal/mole and E_{rev} is 1.43V for the reaction $CO_2(g) + H_2O(l) \rightarrow HCOOH(aq) + \frac{1}{2} O_2(g)$. In a neutral solution (100% faradaic efficiency for formate production) a current density of 1 mA/cm² on mercury requires an overpotential, η_c, of 1.15V (see Fig. 3). Using a value of 0.5V for the value of the overpotential for oxygen evolution at the anode and neglecting all *IR* losses a value of 45% is obtained for ϵ. In a practical cell (with *IR* losses), the value of ϵ would be much less. The efficiency has been found to decrease with current density for a given electrode (12, 14, 30). In one series of experiments (12), a cell potential of 3.5V gave the highest coulombic efficiency (81.5%), at the lowest current density of 20 mA/cm². This yielded an energy efficiency of ~33%.

In order to improve the energy efficiency, it is necessary to test other electrode materials. Recently a number of sp metals (Zn, Pb, Sn, In, and Cd) have been tested as electrocatalysts for the reduction of carbon dioxide (30). The highest faradaic efficiency (92%) for formic acid production was obtained using an In electrode at a current density of 2.9 mA/cm² in 0.1*N* Li_2CO_3 electrolyte. On In, the overpotential is 400 mV lower than on a Hg electrode at the same current density.

Electrochemical reduction of formic acid.—The reduction of formic acid to methanol was carried out at both lead and tin electrodes. Product analysis revealed no detectable amounts of formaldehyde. Table II shows

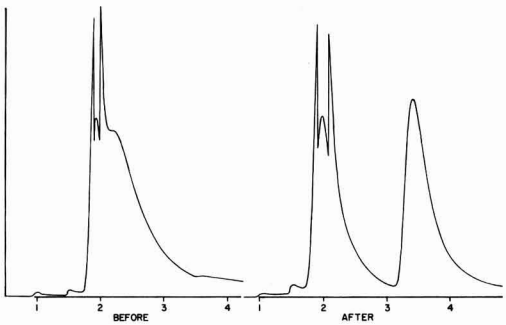

Fig. 1. Chromatograms of 0.1M formaldehyde and 0.1M sodium carbonate solution before and after electrolysis. The concentration of methanol in the solution is obtained from the area under the methanol peak and the calibration curve (Fig. 2).

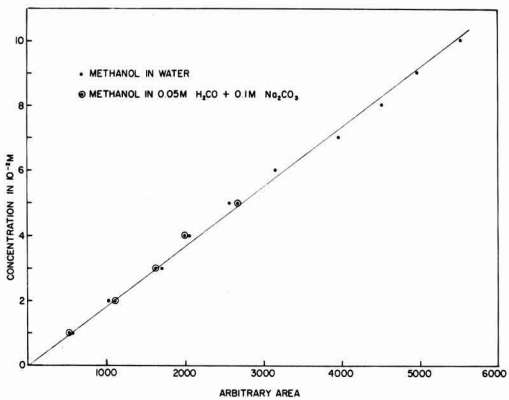

Fig. 2. Calibration curve for methanol detection in the electrolysis of formaldehyde solutions.

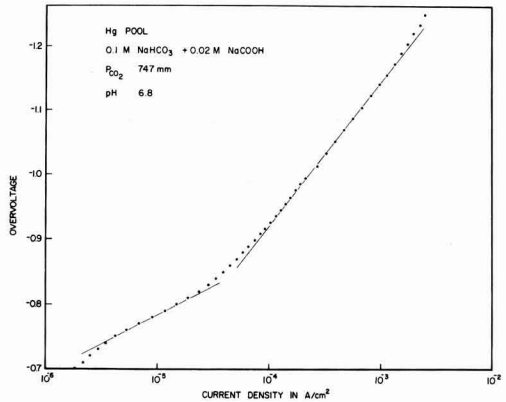

Fig. 3. Polarization curve for the reduction of carbon dioxide to the formate anion in a neutral solution. The overvoltage for the reduction of carbon dioxide is obtained by subtracting out the reversible potential which exists for the conditions of the experiment (26). The curve has been corrected for *IR* effects.

Table II. Faradaic efficiency for formic acid reduction to methanol on lead (area of electrode, 50 cm²) in 0.1N $HClO_4$ at 25°C

Experiment number	Range of working electrode potential, mV	Range of current, mA (average current density, μA/cm²)	Time, hr	Charge, C	Number of moles, methanol		Percent faradaic efficiency
					Maximum	Expt.	
1	−900 to −1000	20 to 5 (155)	68	1900	0.00491	0.00059	11.9
2	−900 to −1000	20 to 6 (185)	42	1403	0.00364	0.00001	0.28
3	−1320 to 1260	10 (200)	68	2440	0.00632	None	0
4	−900 to −1000	14-2 (151)	44	1245	0.00323	0.00007125	2.2
5	−900 to −1000	30-5 (346)	23	1435	0.00372	0.0000195	0.53

the results of the experiments at a lead electrode using 0.1M formic acid in 0.1M perchloric acid electrolyte. The current efficiency varied from zero to a maximum value of 12% for methanol production. In the potentiostatically controlled experiments, a low current density (for maximum efficiency) was maintained by making periodic adjustments to the working potential (*vs.* SCE) in the range −900 and −1000 mV. In a number of galvanostatic experiments (experiment 3 is an example) carried out at higher current densities, the working potential was always below −1000 mV and no methanol was produced during the electrolysis. The results on lead are not very reproducible. This may be due in part to variations in the chemical polishing procedure of the electrode surface prior to each experiment. In some experiments, an anodic potential was applied in a preelectrolysis step, but this procedure did not appear to stabilize the electrode surface in a way that would lead to consistent results.

Higher efficiencies and stable currents were obtained when the lead electrode was replaced with an electroetched tin electrode (Table III). The electrolyte (0.25M HCOOH + 0.1M $NaHCO_3$) is a formic acid/sodium formate solution buffered to a pH of about 3.8. In this case, good results (up to ~100% efficiency) are obtained only in a narrow potential region (with a lower limit of about −720 mV) where the average current density is less than 4.0 μA/cm² (experiments 5, 6, 7, and 9). In some of these potentiostatically controlled experiments, it was necessary to lower the potential occasionally in order to maintain a small electrolytic current density. In galvanostatic experiments (experiments 2, 3, and 4), where the working potential remained below −720 mV throughout most of the electrolysis (the initial potential is given in parentheses), no methanol was produced. In previous work (20), the 100% efficiency reported initially was obtained at a current density of 5 μA/cm², corresponding to a potential of −990 mV *vs.* SCE. In the present experiments, the lower end of the potential region for a high efficiency is more positive by about 270 mV. This discrepancy may be due in part to differences in the surface preparation of the electrodes (higher surface area).

The energy efficiency in an electrolysis cell for formic acid reduction to methanol will be low because of the large overvoltage required at a low current density. The overvoltage has been estimated for the conditions found in experiment 7 (Table III) assuming that $HCOOH_{aq} + 4H^+ + 4e^- \rightleftarrows CH_3OH_{aq} + H_2O$ is the half-cell reaction. The equilibrium potential (*vs.* SCE) obtained for this half-cell reaction after 31.4C has passed through a cell containing 20 ml of solution (pH ~3.8) is ~ − 0.3V. This corresponds to an overvoltage of ~420 mV at a current density of 3.6 μA/cm².

The present results on both lead and tin electrodes, along with previous results on tin, indicate that the reduction of formic acid occurs in a narrow potential region. On the other hand, the reduction of carbon dioxide and formaldehyde (see following section) occurs over wide potential regions (on a mercury electrode) and are activation-controlled processes. It may be only a coincidence that the reduction of formic acid occurs near the pzc which for lead and tin (*vs.* NHE) are −0.69 and −0.35V, respectively (31). Although these values change somewhat with the electrolyte composition, the maximum efficiency for formic acid reduction occurs at a potential slightly below the pzc (~ 0.1V) on both lead and tin. In this case, the adsorption of formic acid molecules (assuming these are the electroactive species) would appear to be a necessary and potential-dependent step in the reduction mechanism. Further studies (measurement of pseudocapacitance using impedance techniques, etc.) will be required before the role of adsorption in formic acid reduction can be determined.

A number of suggestions have been made (20) for increasing the current density of formic acid reduction: (*i*) increase in the real surface area; (*ii*) increase in the temperature of the reaction; (*iii*) increase in the reaction rate by using metals with lower pzc (a good choice here is cadmium); and (*iv*) application of a pulsed potential profile by which the molecules adsorbed at a potential near the pzc are reduced much faster at a more negative applied potential.

Electrochemical reduction of formaldehyde.—The electrolytic reduction of formaldehyde to methanol occurs, with a better than 90% faradaic efficiency, in a basic solution (pH ~11). In each experiment, a 100 ml sample containing 0.1M H_2CO in 0.1M Na_2CO_3 was electrolyzed (~1000C passed through the cell) in the limiting current region (current density ~10 mA/cm², see Fig. 10). Product analysis showed that the efficiency

Table III. Faradaic efficiency for formic acid reduction to methanol on tin (area of electrode, 50 cm²) in 0.1N $NaHCO_3$

Experiment number	Range of working electrode potential, mV	Range of current, mA (average current density, μA/cm²)	Time, hr	Charge, C	Number of moles, CH_3OH		Percent faradaic efficiency
					Maximum	Expt.	
1	−620 to −870	0.8 (16)	19.8	57	0.000148	0.00006	40.5
2	(600) −900 to −1000	1 (20)	67.7 23.6	195 85	0.0005062	0.00008 None	15.8 0
3	(600) −800 to −730	0.9 (18)	17.9	56.6		None	0
4	(620) −860 to −920	0.8 (16)	27	60.5		None	0
5	−680 to −700	(2.96)	46	24.4	0.0000632	0.0000608	96.2
6	−700	(1.6)	45	13.5	0.0000349	0.0000314	90
7	−680 to −720	(3.6)	48.5	31.4	0.000081	0.0000808	99.6
8	−690	(3.0)	90	48.8		None	0
9	−700	(3.2)	30.5	17.4	0.0000451	0.0000416	92.2

for methanol production was 103 ± 10%. This value includes a correction for the small amount of methanol produced in the initial formaldehyde solution (Fig. 1). No indication was found for the formation of a dimerization-type product such as ethylene glycol.

The energy efficiency in an electrolysis cell for formaldehyde reduction to methanol is low because of the large overvoltage at a moderate current density. The overvoltage was estimated for the conditions found in one electrolysis experiment assuming that $H_2CO_{aq} + 2H^+ + 2e^- \rightleftarrows CH_3OH_{aq}$ is the half-cell reaction. The equilibrium potential (*vs.* SCE) for this half-cell reaction, after 965C were passed through a cell operated in the limiting current region ($E_w = -1.8$V *vs.* SCE), is ~ -0.6V. This gives an overvoltage at the cathode of 1200 mV for a current density of ~10 mA/cm².

Cyclic voltammetry experiments have been carried out in 0.11M formaldehyde solutions buffered at different *p*H values (6.8, 9.0, 11.1, and 13.0) at sweep rates from 10 mV/sec to 1000 V/sec. The results of these experiments are in basic agreement with those in a previous study (23). A small anodic peak appears in each solution at sweep rates higher than a threshold value. In contrast to the previous results, however, this anodic peak is found in a solution having a *p*H of 6.8. In this solution it is more easily observed at lower sweep rates where the double layer charging current is less. In addition the anodic peak does not disappear in a solution having a *p*H value greater than 9.5 for fast sweep rates.

The *p*H dependence of this peak is shown in Fig. 4 for a sweep rate of 50 V/sec. It is observed in a solution with a *p*H of 6.8 and 9.0 but not in a solution with a *p*H of 13.0. The threshold sweep rates (in volts/second) are approximately 2, 10, 50, and 100 for solutions having *p*H values of 6.8, 9.0, 11.1, and 13.0, respectively. This peak, which has a longer lifetime in the neutral solution, is most likely due to the oxidation of the radical intermediate and/or its anion. Any methanol formed during the cathodic sweep will not be oxidized at the potential of the anodic peak. A log-log plot of the anodic peak current, I_{PA}, *vs.* the sweep rate, v (volts/second), (Fig. 5), shows that $I_{PA} \propto v^{1/2}$ and the reaction is, thus, diffusion controlled at a *p*H of 9 and below. For *p*H 11 and above, the slope is greater than 0.5 and the amount of intermediate available for oxidation appears to be no longer entirely diffusion controlled. The cathodic peak current appears to be diffusion controlled in a solution buffered at a *p*H of 6.8. The dehydration rate of methylene glycol is relatively slow at this *p*H and the amount of formaldehyde available for reduction can be considered to be fixed during the time interval of an experiment carried out at fast sweep rates (5-500 V/sec). The transfer of formaldehyde molecules across the interphase region to the electrode surface results in a diffusion-controlled current. In a solution of higher *p*H, where the reaction rate for the formation of formaldehyde (either from methylene glycol or its anion) is increased, the amount of formaldehyde available for reduction can no longer be considered constant throughout the lifetime of the cyclic sweep. Instead, it appears that the current is limited by the reaction kinetics of the reduction process at fast sweep rates (100-1000 V/sec). This results in a decrease or the slope (for log I_{PC} *vs.* log v) with increase in *p*H to a value approaching zero in a solution with a *p*H of 13.

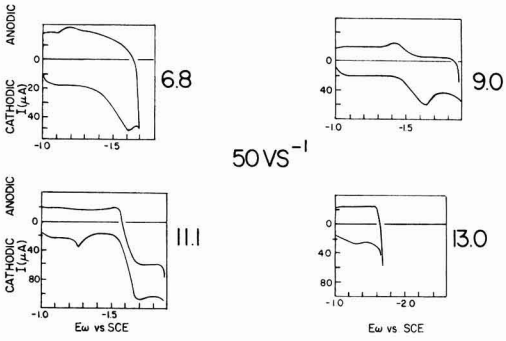

Fig. 4. Cyclic voltammograms obtained at a hanging mercury drop electrode (area ~0.22 cm²) in 0.11M formaldehyde showing the *p*H dependence of the anodic peak. (An impurity cathodic peak appears in the solutions having a *p*H value of 11.1 and 13.0 in the −1.2 to −1.3V region). In order to observe whether an anodic peak is present in the high *p*H (13.0) solution, the current sensitivity is the same as in two of the other buffer solutions. At this amplification only the current trace in the −1.0 to −1.6V region is shown.

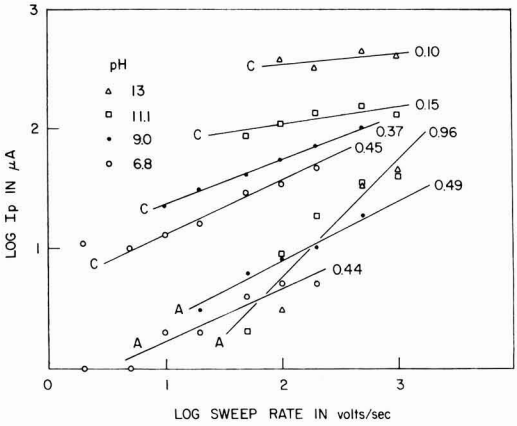

Fig. 5. Log-log plot of cathodic peak current, I_{PC}, and anodic peak current, I_{PA}, *vs.* sweep rate. The value of the slope is given to the right of each anodic line, A, and cathodic line, C. Any value of I_{PA} is one-tenth or less than the corresponding value of I_{PC} and is much less than the double layer charging current at higher sweep rates. As a result, there is more scatter in the data used for the anodic plots. For a *p*H of 11.1 and 13 a line with a slope of 0.96 is shown, whereas a lower value is probably more realistic.

The Tafel slope is observed to decrease with an increase in the *p*H of the solution (Fig. 6). In addition, it can be seen that the limiting current is not a simple function of the solution *p*H over the range of values examined here. In one solution (*p*H 13.0) the limiting current peaks and then it decreases somewhat at higher potentials. This observation may be explained by the mechanism (Eq. [1] and [2]) which accounts for the high *p*H behavior of the limiting current. The rapid generation of hydroxyl ions as the current density increases would momentarily increase the *p*H value in the double layer region. This causes a decrease in the amount of formaldehyde available for reduction (Eq. [2]).

The effect of *p*H on the Tafel slope, along with the cyclic voltammetry results, may be explained in terms of a mechanism change for formaldehyde reduction. The observed Tafel slopes fall in the range of 66-36 mV. The first electron transfer step is therefore not rate determining. A value of 60 mV is expected for the Tafel slope (under conditions of Langmuir adsorption) in the CECE mechanism (Fig. 7) if step 3 is rate determining. A value of 66 mV was observed for the Tafel slope in a neutral solution (*p*H = 6.8). However, step 4 may be the rds. In this case, the radical intermediate and its anion must be stabilized in order for the quasi-equilibrium condition to hold for all except the rds. A fast protonation reaction would produce an intermediate that is more easily stabilized than the

radical anion. Under these conditions, step 4 (with a 40 mV Tafel slope) would be the rds. Temkin adsorption could then account for the increase in Tafel slope observed here. The oxidation of the radical intermediate and/or its anion is controlled by the rate of diffusion of the radical species away from the electrode surface in solutions with a pH of 6.8 and 9.0. With increase in pH, a second charge transfer step, prior to the chemical reaction is favored due to the decrease in the hydrogen ion concentration and to an increase in the negative electrode potential. A charge transfer to the radical anion should occur at a slower rate since the radical already has a negative charge. However, the experimental results indicate that this electron transfer occurs at a relatively fast reaction rate. The anodic peak is more stable in a neutral solution, since it is observed at a slower sweep rate. The absence of this peak at the slow sweep rates (in the higher pH solutions) indicate that a second electron transfer can compete with the protonation reaction to produce a dianion of methanol. Although this species is not expected to be adsorbed at the electrode surface, it may be partially stabilized by one of the adsorbed species. This is necessary if the quasi-equilibrium condition is to hold for step 3 of the CEEC mechanism. In this case, the following chemical reaction (step 4 of the CEEC mechanism, Fig. 8) is the rds with a Tafel slope of 30 mV expected under conditions of Langmuir adsorption. A Tafel slope of 36 mV was observed in a solution with a pH of 13.0. The anodic peak current should then result from a diffusion-controlled process. The experimental results (Fig. 5) are not clear in the high pH solutions. If the reduction current is limited at fast sweep rates by the reaction kinetics, then a change in the slope, from a value of 0.5 of the I_{PA} *vs.* v plot would be expected. Interactions of the methanol dianion with adsorbed species and/or its repulsion from the double layer region could also affect the slope. In addition to the possibility that changes in the solution pH modify the reaction kinetics causing a change in mechanism, an indirect effect may result from a change in the composition of adsorbed species with pH. This can influence the Tafel slope through interactions with the electroactive species. The observed values of the Tafel slope are somewhat larger than the values expected under conditions of Langmuir adsorption. Evidence for Temkin adsorption, which could account for the larger values, was found in the steady-state measurements as discussed below.

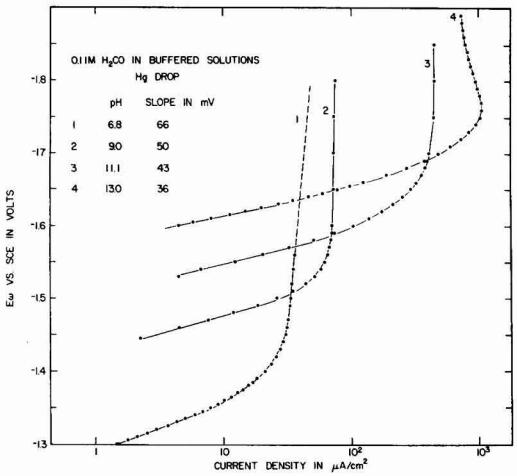

Fig. 6. Effect of pH on the Tafel slope. These polarization curves were obtained from the cyclic voltammetry experiments carried out at a 10 mV/sec sweep rate at a hanging mercury drop electrode where the hysteresis is small.

Steady-state polarization curves were obtained with solutions containing different formaldehyde concentrations (pH ~11.3). Some variation of the Tafel slope was observed in different runs on a given sample (Fig. 9). In the first run, the current stabilized quickly above −1.56V but at points below this potential, the current increased slowly for some time before reaching a steady value. Current readings obtained before steady-state conditions gave a low value for the Tafel slope. A 2-3 hr preelectrolysis, carried out prior to the first run, may have conditioned the electrode surface with various adsorbed species. Steady current values were obtained over the entire potential range in the second and third run. In these experiments, a 10% error can be expected in measuring the value of the Tafel slope under steady current conditions. The effect of concentration on the Tafel slope is shown in Fig. 10. Good agreement is obtained for the value of the Tafel slope in the 0.11M solution (47 mV) with the previous result (43 mV) near the same pH value at the mercury drop

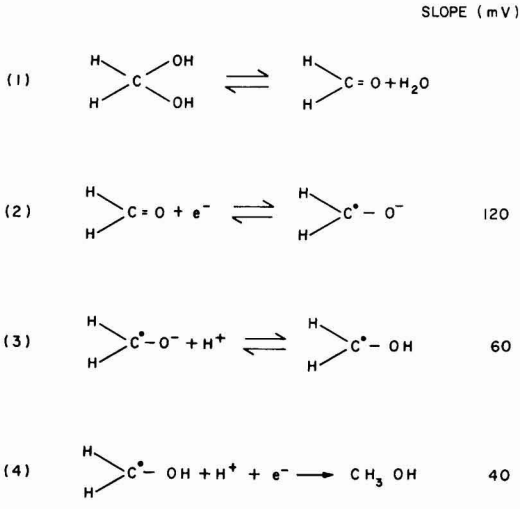

Fig. 7. Proposed mechanism for formaldehyde reduction in the pH region 6.8-9.

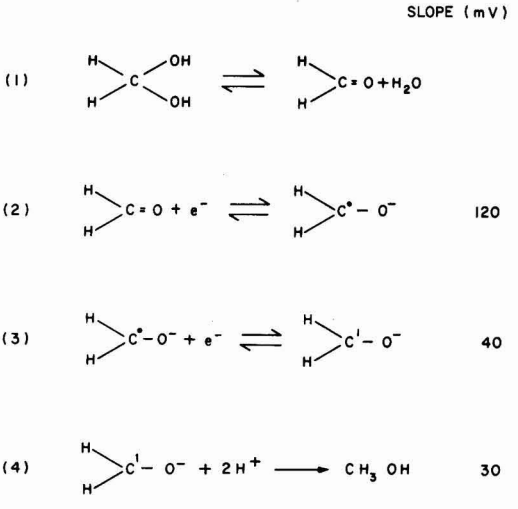

Fig. 8. Proposed mechanism for formaldehyde reduction in the pH region 11.1-13.0.

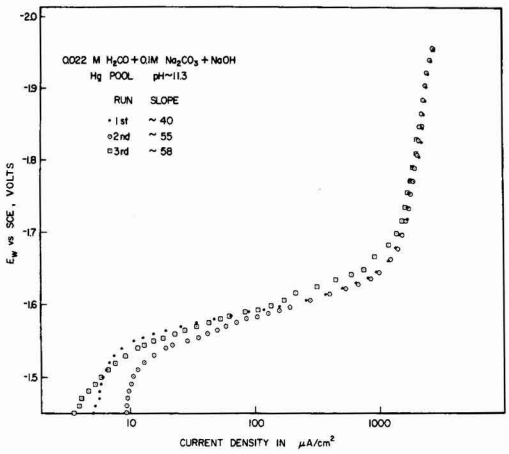

Fig. 9. Steady-state polarization curves for three runs made on a 0.022M formaldehyde solution. The limiting current is almost the same in each of the three runs. The curves have been corrected for *IR* effects.

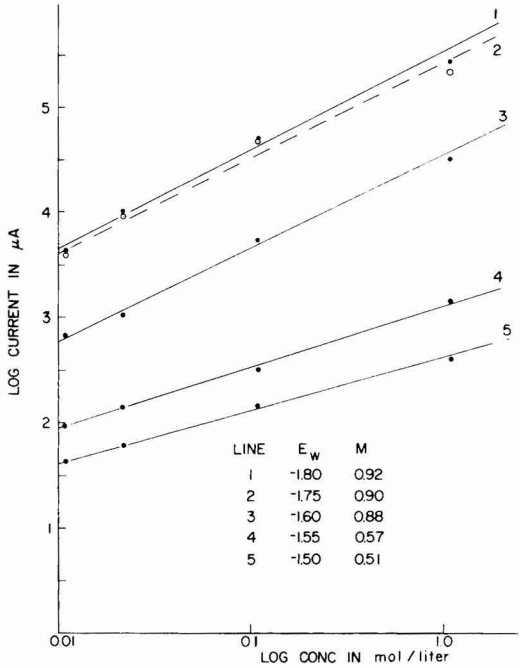

Fig. 11. Reaction order for formaldehyde reduction in the Tafel and limiting current regions obtained from steady-state polarization curves (Fig. 10).

electrode (Fig. 6). The value of the Tafel slope was found to decrease from 60 to 37 mV when the concentration of formaldehyde was increased by a factor of one hundred (0.011-1.09M). Adsorption effects may be partly responsible for this large decrease. A similar though smaller decrease in slope (9 mV) was observed in the reduction of acetophenone (32) at a mercury electrode in a methanol + sulfuric acid solution, containing a small amount of water when the concentration of acetophenone was increased by a factor of 10 (0.045-0.46M). The change in Tafel slope is attributed to adsorption effects.

The reaction order for formaldehyde reduction (Fig. 11) over the above concentration range is close to the expected value of one (0.92) in the limiting current region, but it aproaches a value of one-half in the Tafel region. A fractional reaction order indicates that the coverage, θ, by formaldehyde or an intermediate species is controlled by Temkin adsorption. The reaction order in the limiting current region should be independent of the reaction mechanism. It might be argued, however, that the decrease observed in the Tafel slope indicates a change in the reaction mechanism or a change in the rds (of a given mechanism) when the concentration is increased. Thus, it may not be valid to determine the reaction order over the entire concentration range. However the reaction order remains fractional and constant for a given working potential so that regardless of any mechanism change that might occur with increase of concentration the experimental results most likely indicate conditions for Temkin adsorption over the entire concentration range examined at a pH of 11.3. Temkin adsorption should occur over a wide range of pH values. Some evidence for this was given above.

Coverage by the adsorbed species, formaldehyde, and/or an intermediate, increases with the logarithm

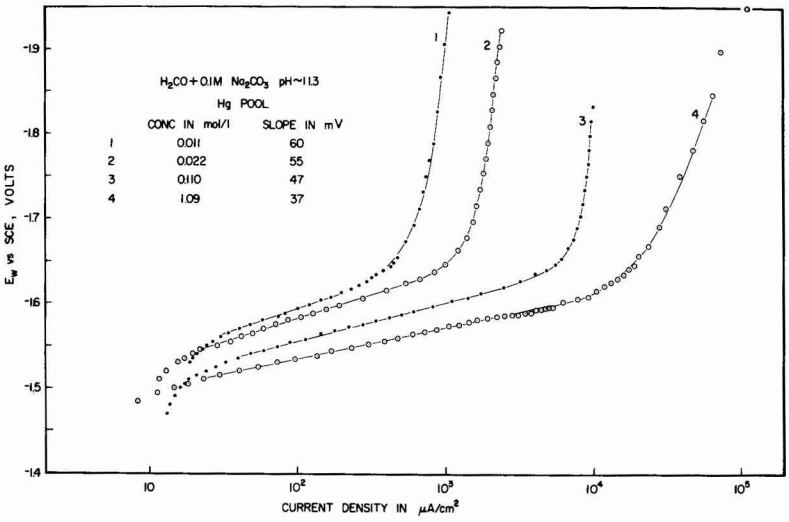

Fig. 10. Steady-state polarization curves for formaldehyde reduction showing the effect of formaldehyde concentration on the Tafel slope for solutions with a pH of 11.3. The curves have been corrected for *IR* effects.

of the concentration under conditions for Temkin adsorption. In addition, coverage by the much smaller amounts (mole percent) of the large species (polyoxymethylene glycols) present in solution may be increased at higher formaldehyde concentrations by preferential adsorption under Langmuir conditions, where the coverage is proportional to the concentration. Coverage by the adsorbed species will increase substantially as the formaldehyde concentration increases by a factor of 100. Normally, the Tafel slope would not be expected to change if this change in coverage remains within the Temkin region. The Tafel slope decreases almost linearly with the logarithm of the concentration (Fig. 12). If the coverage by formaldehyde molecules is predominant, then the decrease in the Tafel slope indicates an attraction between a formaldehyde molecule and nearby adsorbed species. However, the fractional reaction order, the presence of an anodic peak in cyclic voltammetry experiments, and the relatively low Tafel slope values suggest that coverage in the Temkin region is primarily due to an intermediate.

A change in coverage can affect the Tafel slope in a number of ways: (*i*) The adsorption kinetics may change with the increased coverage in such a way that a different step in the reaction mechanism becomes rate determining, and results in a lower value of the Tafel slope. (*ii*) A change in the energy of adsorption may accompany the increase in coverage. The standard free energy (for a coverage equal to θ) when an interaction occurs among the adsorbed species is given by

$$\Delta G^\circ_\theta = G^\circ_{\theta=0} + \alpha r\theta \qquad [8]$$

where r is the interaction parameter and $\alpha < 1$ for activated adsorption and $\alpha = 1$ for nonactivated adsorption (33). A decrease in Tafel slope, with an increase in coverage, requires that a change from activated to nonactivated adsorption occurs. (*iii*) A change in the number of water molecules displaced during the adsorption of the electroactive species will affect the Tafel slope (34). A decrease in Tafel slope requires that the number of water molecules displaced during the adsorption process decreases with increase in concentration (coverage). Small amounts of polyoxymethylene glycols adsorbed on the electrode surface could influence the adsorption process and hence the Tafel slope through interactions with formaldehyde and/or its intermediates. Measurement of double layer and adsorption capacitance will help determine the role of adsorption in the mechanism for formaldehyde reduction.

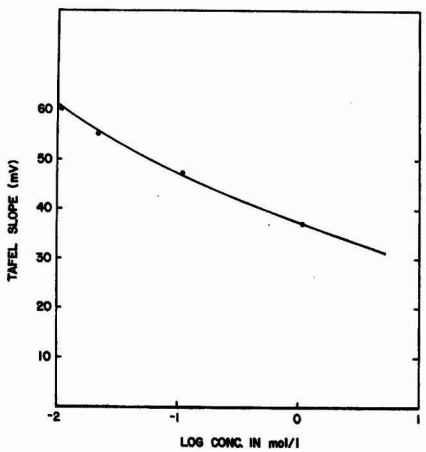

Fig. 12. Change in Tafel slope with formaldehyde concentration

Conclusions

Some conclusions can be made based on the results of this study: (*i*) It is difficult to find conditions for the direct electrochemical reduction of carbon dioxide to methanol. The reduction of carbon dioxide and formaldehyde occur readily in neutral and basic solutions, respectively, while formic acid reduction (assuming the molecule to be the electroactive species) requires an acid or buffered acid solution. (*ii*) The reduction of carbon dioxide to formic acid can be carried out quantitatively on sp-metals having high overpotential for hydrogen evolution at an estimated maximum energy efficiency of ~45% (on Hg). (*iii*) The reduction of formic acid to methanol is difficult to carry out simultaneously at a high faradaic efficiency and high current densities due to the limited potential region for formic acid reduction. (*iv*) The reduction of formaldehyde to methanol was carried out quantitatively on Hg at a current density of ~10 mA/cm^2. The Tafel slope was observed to decrease with an increase in concentration (at constant pH) and with an increase in pH (at constant concentration). The adsorption of polyoxymethylene glycols, which is both concentration and pH dependent, may cause changes to occur in the Tafel slope through interactions with formaldehyde and/or intermediate species.

Acknowledgments

The authors acknowledge the assistance of Mr. George Kissel in the solution of a number of experimental problems that occurred during this work. We would like to thank Drs. Stephen Feldberg and Shimshon Gottesfeld for a number of suggestions that were useful in the interpretation of our results. We would also like to express our gratitude to Professor Brian Conway for a number of stimulating discussions and for his continued interest throughout the course of this work. The authors are grateful to the referees of the original manuscript. Their critical comments were valuable in the preparation of the revised version. This work was performed under the auspices of the U.S. Energy Research and Development Administration.

Manuscript submitted Dec. 27, 1976; revised manuscript received May 2, 1977. This was Paper 286 presented at the Washington, D.C., Meeting of the Society, May 2-7, 1976.

Any discussion of this paper will appear in a Discussion Section to be published in the June 1978 JOURNAL. All discussions for the June 1978 Discussion Section should be submitted by Feb. 1, 1978.

Publication costs of this article were assisted by Brookhaven National Laboratory.

REFERENCES

1. M. E. Royer, *C. R. Hebd Seances Acad. Sci.*, **70**, 731 (1870).
2. A. Cohen and S. Jahn, *Ber. Dtsch. Chem. Ges.*, **37**, 2836 (1904).
3. R. Ehrenfeld, *ibid.*, **38**, 4138 (1905).
4. F. Fischer and O. Prziza, *ibid.*, **47**, 256 (1914).
5. M. Rabinowitsch and A. Maschowetz, *Z. Elektrochem.*, **36**, 846 (1930).
6. A. Lieben, *Monatsh.*, **16**, 211 (1895).
7. P. Van Rysselberghe, *J. Am. Chem. Soc.*, **68**, 2047 (1946).
8. P. Van Rysselberghe and G. J. Alkire, *ibid.*, **66**, 1801 (1944).
9. P. Van Rysselberghe, G. J. Alkire, and J. M. McGee, *ibid.*, **68**, 2050 (1946).
10. T. E. Teeter and P. Van Rysselberghe, *J. Chem. Phys.*, **22**, 759 (1954).
11. T. E. Teeter and P. Van Rysselberghe, Proceedings of the 6th Meeting of the International Committee on Electrochemical Thermodynamics and Kinetics, p. 538 (1955).
12. K. S. Udupa, G. S. Subramanian, and H. V. K. Udupa, *Electrochim. Acta*, **16**, 1593 (1971).
13. F. H. Meller, Final Report (Phase II), Contract no. NOOO14-66-CO139 (1968).

14. V. Kaiser and E. Heitz, *Br. dB. Gesellschaft*, **77**, 818 (1973).
15. T. N. Andersen, B. A. Miner, E. Bibble, and H. Eyring, *Stud. Trop. Oceanogr.*, **5**, 229 (1965).
16. J. Giner, *Electrochim. Acta*, **8**, 857 (1963).
17. M. W. Breiter, *ibid.*, **12**, 1213 (1967).
18. J. Tafel and G. Friedrichs, *Ber. Bunsenges. Phys. Chem.*, **37**, 3187 (1904).
19. C. Ellis and K. P. McElroy, U.S. Pat. 867,575 (1907).
20. F. B. Leitz and H. I. Viklund, Final Report (Phase I), Contract no. NOOO14-66-CO139 (1967).
21. D. Barnes and P. Zuman, *J. Electroanal. Chem.*, **46**, 323 (1973).
22. J. M. Los, A. A. A. Brinkman, and B. J. C. Wetsema, *ibid.*, **56**, 187 (1974).
23. S. Clarke and J. A. Harrison, *ibid.*, **36**, 109 (1972).
24. J. F. Walker, "Formaldehyde," Van Nostrand-Reinhold, New York (1974).
25. R. Sauterey, *Ann. Chim. (Paris)*, **12**, 7, 1 (1952).
26. J. Ryu, T. N. Andersen, and H. Eyring, *J. Phys. Chem.*, **76**, 3278 (1972).
27. W. Paik, T. N. Andersen, and H. Eyring, *Electrochim. Acta*, **14**, 1217 (1969).
28. L. V. Haynes and D. T. Sawyer, *Anal. Chem.*, **39**, 332 (1967).
29. A. W. B. Aylmer-Kelly, A. Bewick, P. R. Cantrill, and A. M. Tuxford, *Discuss. Faraday Soc.*, **56**, 96 (1973).
30. K. Ito, T. Murata, and S. Ikeda, *Bull. Nagoya Inst. Technol.*, **27**, 369 (1975).
31. E. Gileadi, Editor, "Electrosorption," Plenum Press, New York (1967).
32. E. J. Rudd and B. E. Conway, *Trans. Faraday Soc.*, **67**, 440 (1971).
33. B. E. Conway, "Theory and Principles of Electrode Processes," The Ronald Press Co., New York (1965).
34. T. Bejerano, Ch. Forgacs, and E. Gileadi, *J. Electroanal. Chem.*, **27**, 69 (1970).

The Application of Concentration Jump and Impedance Measurements to the Mechanistic Study of the Fluoride Solid-State Electrode

P. Van den Winkel and J. Mertens

Farmaceutisch Instituut, Vrije Universiteit Brussel, Paardenstraat 67, B-1640 St. Genesius-Rode, Belgium

T. Boel

Hoger Rijksinstituut voor Technisch Onderwijs, Welvaarstraat, B-9300 Aalst, Belgium

and J. Vereecken*

Laboratorium voor Metallurgie en Electrochemie, Vrije Universiteit Brussel, Campus Oefenplein, Gebouw G, B-1050 Brussel, Belgium

ABSTRACT

This study describes the combined use of a-c impedance and fast flow techniques to elucidate the mechanism of the fluoride solid-state electrode. By describing fast flow data in the complex frequency Laplace plane and correlating it with a-c impedance data, it has been possible to separate interfacial and mass transport contributions to over-all electrode behavior; and describe the manner in which the electroactive species modifies individual reaction steps. Using this, a preliminary mechanism for the fluoride solid-state electrode involving heterogeneous F^- exchange reactions at two types of sites, one involving electronic and the other ionic conduction, is presented.

Various experimental methods are described for the study of electrode processes of ion-sensitive electrodes. These methods may be classified according to the type of input function applied to an electrochemical cell built up from the electrode of interest and a suitable nonpolarizable reference electrode immersed in an appropriate test solution.

As shown in Table I, two types of experiments may be used. One type of experiment deals with the study of the response signal measured as a function of time when a well-known electrical signal (the driving force or excitation function) is applied to the cell. For example, phase and impedance measurements using small sinusoidal input voltages were employed in this study. The system frequency response is usually represented in a Cole-Cole diagram in the complex plane. From experimental data in a frequency range from 10^{-3} up to 10^5 Hz for various concentrations of the electroactive species an equivalent circuit for the test electrode is obtained. The transfer impedance for this equivalent circuit can be calculated and so the behavior of the system with regard to a specified input is characterized. Physicochemical phenomena associated with the electrode processes are then interpreted in terms of diffusion, double layer, and space charge impedances (1-6).

The second type of experiment deals with the measurement of the transient signal caused by a rapid concentration change of the electroactive species around the sensor surface using fast flow techniques. From these experiments a dynamic response equation for the sensor is obtained. Based on experimental data, rate-limiting processes, as for instance solvation-desolvation (7), adsorption (8), and diffusion (9), were proposed. However, it should be pointed out that the mathematical form of the semiempirical response equation may lead to an erroneous interpretation of the rate-limiting process (10).

As the electrochemical behavior of a sensor is characterized by its transfer function, both types of experiments must supply information about the rate-limiting

* Electrochemical Society Active Member.
Key words: selective electrode, impedance measurements, fluoride.

Table I. Study of electrode processes: mechanistic studies

Method	Driving force	Example	Result
1	Electrical signals of small amplitude excursion	Phase-impedance measurements (10^{-3}-10^{5} Hz)	Linearized electrical equivalent model and transfer impedance
2	Concentration gradients of the electroactive species	Dynamic response studies (fast flow injection experiments)	Transfer function and transfer impedance

process. Nevertheless, fast flow experiments should supply information only about the interfacial process. Indeed, due to the high linear flow rates, the thickness of the hydrodynamic layer is reduced to a minimum (11). Therefore little or no data concerning a Warburg-type process are available from kinetic measurements under these conditions. Moreover, time constants associated with macroscopic electrode kinetics are large compared with those obtained from impedance measurements in a higher frequency range and which are related mainly to space charge impedances. Therefore, a comparison and/or correlation of the results of both kinetic and impedance measurements is valid only in the time constant range obtained in fast flow experiments.

The present paper deals with the equivalent model and rate-limiting processes of the ORION 94-09A electrode. Fast flow studies (11) and impedance measurements (12) were performed. By conversion of the dynamic response equation from fast flow studies into the Laplace domain, the transfer function for this sensor will be calculated. As the transfer function arising from linear networks must be rational, a rational approximation of the experimental and irrational transfer function will be made so that a reasonable comparison of fast flow and impedance data can be made. Making then simple assumptions about the excitation function applied in fast flow studies allows the transfer impedance for the intermediate frequency range to be calculated.

Both transfer impedances or equivalent circuits, one obtained from impedance measurements, the other from fast flow kinetics, contribute to the physicochemical interpretation of the interfacial sensor process.

Experimental Results from Fast Flow Kinetics and Impedance Measurements

The results of kinetic fast flow experiments were reported in a previous paper (11). They revealed that the dynamic response of new fluoride electrodes with an internal reference system of the wick type can be represented by a hyperbol

$$E_t = \frac{t}{a + bt} \qquad [1]$$

where a and b are constants and $t_{50} = a/b$ (*i.e.*, the time required to reach 50% of the steady-state potential); E_t = potential as function of time; $E_{t=0} = 0$, $E_{t=\infty} = 1/b = S \log a_2/a_1$; S = slope of the indicator electrode; and a_1 and a_2 = initial and final concentration of the jump.

The striking discrepancy in rate of response between fast flow and continuous auto analyzer systems (11) is attributed to a rate-limiting film diffusion process in the hydrodynamic layer when the sensor is mounted in a sample processor. In fast flow experiments this layer is reduced to a minimum and hence the response is fast.

From impedance measurements in a range 10^{-3} up to 10^{5} Hz, the locus for the same electrode was obtained (12). It is shown in Fig. 1. Three parts can be distinguished. The high frequency and perfect semicircle is due to space charge and to geometrical and wiring impedances. The lowered semicircle is attributed to a slow interfacial charge transfer represented by a time constant related to an apparent transfer resistance and a double layer capacitance. The influence of the concentration of the potential-determining ion on this part of the complex plane plot is obvious. Egorov and Novell'skii (13) proved that a depressed semicircle is also obtained for a series of two parallel networks with R and C of the same order of magnitude.

The very low frequency part of the complex plane plot is characteristic for a film diffusion process. If the slope equals one, it can be interpreted as a Warburg impedance. Deviations from unity slope are attributed to adsorption of intermediate species or to a nonlinear diffusion path at the interface. The latter is related to the surface structure of the membrane, which is far from ideal as was shown by microscopic examination.

Mathematical Treatment of the Dynamic Response Equation

Laplace transform of the dynamic response $r(t)$ of an electrical network to a known excitation function $x(t)$ yields

$$R(s) = G(s) \cdot X(s) \qquad [2]$$

where $R(s)$ = response in the s-domain, s = Laplace variable; $G(s)$ = transfer function of the network; and $X(s)$ = excitation in the s-domain.

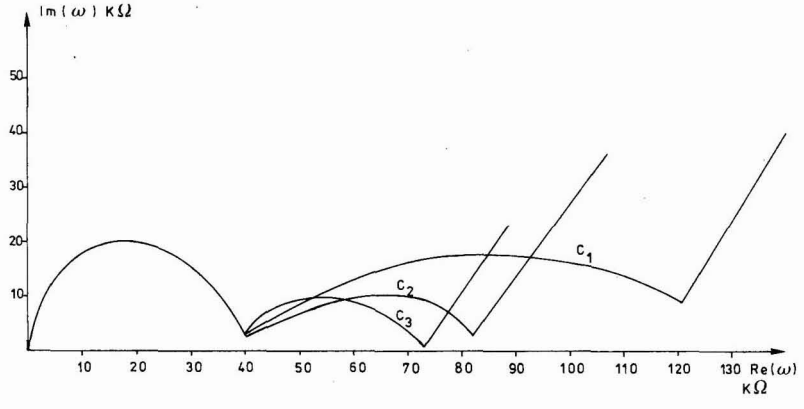

Fig. 1. Indication of the fluoride electrode (Orion 94-09A), influence of the concentration.

With Eq. [1], one obtains

$$R(s) = \mathcal{L}\left\{\frac{t}{a+bt}\right\} = \frac{1}{bs}\cdot\left\{1 - \frac{as}{b}\cdot e^{as/b}\cdot E_1\left(\frac{as}{b}\right)\right\} \quad [3]$$

where $E_1(as/b)$ is the exponential integral.

As $1/bs$ represents a step input excitation with amplitude $1/b$, one may put

$$X(s) = \frac{1}{bs} \quad [4]$$

and

$$G(s) = 1 - \frac{as}{b}\cdot e^{as/b}\cdot E_1\left(\frac{as}{b}\right) \quad [5]$$

As the transfer function must be rational, an appropriate rational approximation of Eq. [5] must be applied. According to Hastings (14) and with $x = as/b$

$$x\cdot e^x\cdot E_1(x) = \frac{x^2 + a_1x + a_2}{x^2 + b_1x + b_2} + \epsilon(x) \quad [6]$$

where $|\epsilon(x)| < 5\cdot 10^{-5}$; $a_1 = 2.334733$; $a_2 = 0.250621$; $b_1 = 3.330657$; and $b_2 = 1.681534$.

Neglecting the correction term $\epsilon(x)$ and introducing the numerical values for a_1, a_2, b_1, and b_2 yields

$$G(s) \cong K\cdot\frac{(s+\alpha)}{(s+\beta)(s+\gamma)} \quad [7]$$

with $K = b/a$, $\alpha = 1.43\ b/a$, $\beta = 0.63\ b/a$, and $\gamma = 2.71\ b/a$.

As β and γ are positive, $G(s)$ is the transfer function of a stable network. $G(s)$ is a function of a/b, the half-time potential, *i.e.*, the time required to reach 50% of the steady-state potential $1/b$, and which is an experimental datum. In Fig. 2 the relation between the irrational transfer function and its rational approximation is represented. The agreement is excellent.

Equation [7] may be used either to evaluate an exponential form of the hyperbolic response (Eq. [1]) or to calculate the frequency response of the sensor. The first is accomplished by multiplying Eq. [7] by $1/bs$ (for a step input excitation) and applying an inverse Laplace transform

$$E_t = \frac{t}{a+bt} \cong \mathcal{L}^{-1}\left\{\frac{1}{bs}\left(\frac{K(s+\alpha)}{(s+\beta)(s+\gamma)}\right)\right\} \quad [8]$$

$$= K_0 - K_1e^{-\beta t} - K_2e^{-\gamma t} \quad [9]$$

and $K_0 = 0.851$, $K_1 = 0.226$, $K_2 = 0.625$, $1/\beta = 0.369\ a/b$, and $1/\gamma = 1.613\ a/b$.

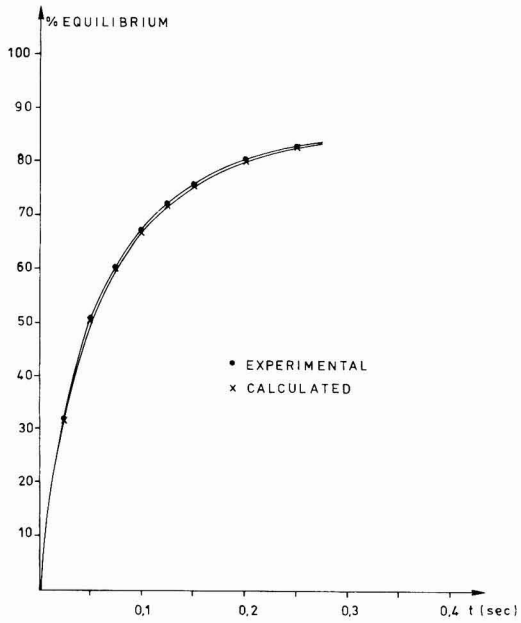

Fig. 3. Concentration jump $10^{-5} \rightarrow 10^{-3}$M F^- in 1/3 TISAB

In Fig. 3 the experimental hyperbolic dynamic response and its calculated exponential approximation for a concentration jump 10^{-5}-10^{-3}M NaF in 1/3 TISAB (total ionic strength adjustment buffer) is shown. As the thickness of the hydrodynamic layer is practically zero in the experimental conditions, the existence of two time constants $1/\beta$ and $1/\gamma$ of the same order of magnitude are most likely associated with interfacial processes. The transfer function $G(s)$ (Eq. [7]) suggests two parallel first-order processes as rate-limiting phenomena. These could be, for instance, exchange reactions of F^- anions at the interface at two types of exchange sites. For LaF_3 crystals doped with Eu(II), these might be

1. $(EuF_2)_c + F^-_s \rightarrow (EuF_3)_c + e^-$ (electronic conduction) [10]
2. $(LaF_3)_c + [\ ] \rightarrow (LaF_2)^+_c + [F^-]$ (ionic conduction) [11]

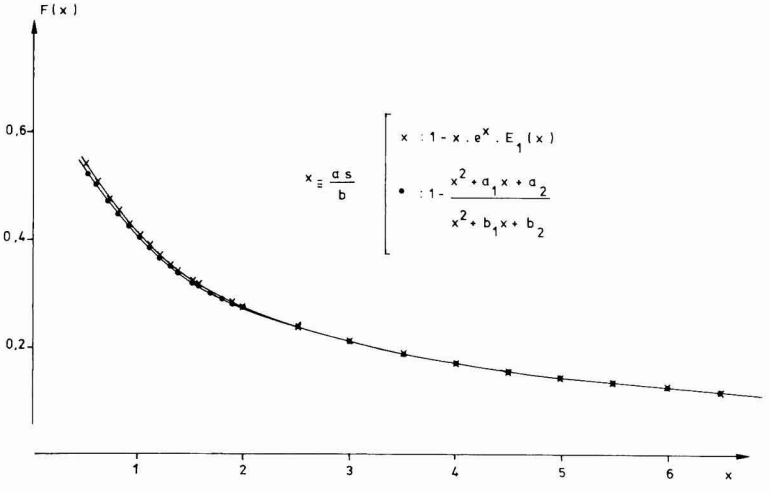

Fig. 2. Rational approximation of the transfer function.

$$(LaF_2)^+_c + F^-_s \rightarrow (LaF_3)_c \qquad [12]$$

where c = crystal, s = solution, and [ ] = lattice vacancy.

The first can be interpreted as a semiconductor behavior with a deep donor level of Eu(II), *i.e.*, 0.41 eV energy gap between donor and conduction levels (12). The second reaction involves a crystal F^- anion to jump into a lattice vacancy near the crystal surface followed by the exchange of a F^- with the solution. The fluoride initially trapped in the vacancy then contributes to the ionic conduction of the crystal. To the credit of this mechanism is the remarkable coincidence that the hyperbolic response also holds for other electrodes, *i.e.*, the Ag_2S electrode (15), which exhibit both ionic and electronic conduction (16). Resistance measurements as a function of increasing temperature show increasing conductance in both cases. Therefore the contribution of both types of conduction can be possibly evaluated by Hall effect measurements as a function of frequency or by the square wave method applied by Koebel *et al.* (16).

The calculation of the frequency response of the electrode at lower frequencies can also be done by means of the transfer function $G(s)$ (Eq. [7]), obtained from kinetic fast flow experiments.

Writing the excitation function $1/bs$ as

$$\frac{1}{bs} = \frac{i}{s} \cdot R \qquad [13]$$

i.e., the step input voltage excitation is formally treated as the product of a step input current i/s multiplied by a resistor R. Therefore

$$R(s) = \frac{i}{s} \cdot \frac{K \cdot R \cdot (s+\alpha)}{(s+\beta)(s+\gamma)} \qquad [14]$$

and the transfer impedance $Z(s)$ is given by

$$Z(s) = \frac{K \cdot R \cdot (s+\alpha)}{(s+\beta)(s+\gamma)} \qquad [15]$$

which means that the response in the s-domain is given by the product of a step input current i/s and the transfer impedance $Z(s)$. For low frequencies $s = j\omega \cong 0$. Therefore, neglecting the influence of the concentration change on the transfer resistance

$$Z(o) = \frac{K \cdot R \cdot \alpha}{\beta \cdot \gamma} = R_t \qquad [16]$$

with R_t the total transfer resistance. As $K\alpha/\beta \cdot \gamma \simeq 1$, R equals the total transfer resistance as obtained from impedance measurements (see Fig. 1). As a lowered semicircle is the result of two parallel RC networks in series, the components of these networks can be evaluated by identifying the corresponding terms in the expressions [15] and [17]

$$Z(s) = \frac{C_A + C_B}{C_A \cdot C_B} \cdot \left\{ \frac{S + \dfrac{R_A + R_B}{R_A \cdot R_B (C_A + C_B)}}{\left(S + \dfrac{1}{R_A C_A}\right)\left(S + \dfrac{1}{R_B C_B}\right)} \right\} \qquad [17]$$

For the given example, the result is represented in Fig. 4. Moreover, the dynamic response to a current step input is a hyperbola and in addition, the values of R_t, K, α, β, and γ allow the complex plane response to be calculated by means of the well-known formulas for phase angle $\phi(j\omega)$ and magnitude $|Z(j\omega)|$

$$\phi(j\omega) = \tan^{-1}\left(\frac{\omega}{\alpha}\right) - \left[\tan^{-1}\left(\frac{\omega}{\beta}\right) + \tan^{-1}\left(\frac{\omega}{\gamma}\right)\right] \qquad [18]$$

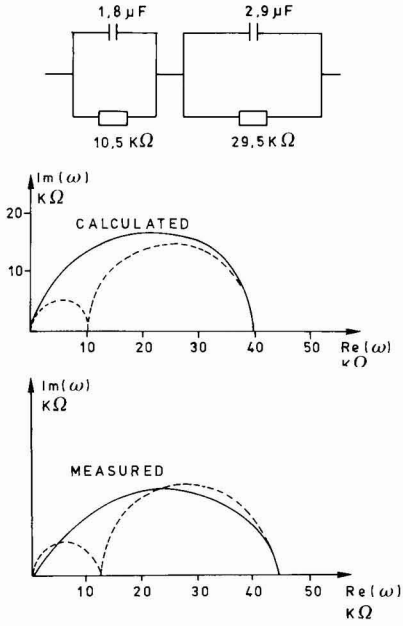

Fig. 4. (a, top) Equivalent circuit. (b, center) (c, bottom).

$$|Z(j\omega)| = R_t \cdot K \cdot \frac{\sqrt{\omega^2 + \alpha^2}}{\sqrt{\omega^2 + \beta^2} \cdot \sqrt{\omega^2 + \gamma^2}} \qquad [19]$$

The result is a lowered semicircle which is known to be the result of two perfect semicircles.

Conclusion

From impedance measurements (12) in a frequency range 10^{-3}-10^5 Hz we concluded that the equivalent circuit of the 94-09A fluoride electrode involves: (*i*) a parallel RC network representing space charge and geometrical impedances (R = 100 kΩ, C = 100 pf), (*ii*) a diffusion impedance which is not a pure Warburg impedance due to complex diffusion at the surface, and (*iii*) a series of two parallel RC networks representing double layer capacitance and transfer resistance at both sides of the membrane.

From the present discussion it is obvious that both kinetic fast flow studies and a-c impedance measurements do inform about the rate-limiting process at the electrode-solution interface as evidenced by the lowered semicircle of the complex plane response. Mathematical treatment of kinetic fast flow data allows the evaluation of double layer capacitance and charge transfer resistors and hence allows the elucidation of the electrode process to a greater extent.

Manuscript submitted Dec. 27, 1976; revised manuscript received April 21, 1977.

Any discussion of this paper will appear in a Discussion Section to be published in the June 1978 JOURNAL. All discussions for the June 1978 Discussion Section should be submitted by Feb. 1, 1978.

Publication costs of this article were assisted by Vrije Universiteit Brussel.

REFERENCES

1. R. P. Buck, *Electroanal. Chem. Interfacial Electrochem.*, **18**, 363 (1968).
2. R. P. Buck and I. Krull, *ibid.*, **18**, 387 (1968).
3. J. R. Sandifer and R. P. Buck, *ibid.*, **56**, 385 (1974).
4. M. J. D. Brand and G. A. Rechnitz, *Anal. Chem.*, **10**, 1185 (1969).
5. M. J. D. Brand and G. A. Rechnitz, *ibid.*, **41**, 1788 (1969).

6. M. J. D. Brand and G. A. Rechnitz, *ibid.*, **42**, 478 (1970).
7. K. Toth and E. Pungor, *Anal. Chim. Acta*, **64**, 417 (1973).
8. R. P. Buck, *Anal. Chem.*, **48**, 23R (1976).
9. W. E. Morf, E. Lindner, and W. Simon, *ibid.*, **47**, 1596 (1975).
10. J. Mertens, Ph.D. Thesis, University of Brussels (V.U.B.) (1976).
11. J. Mertens, P. Van den Winkel, and D. L. Massart, *Anal. Chem.*, **48**, 272 (1976).
12. J. Mertens, P. Van den Winkel, and J. Vereecken, To be published.
13. L. Ya Egorov and I. M. Novosel'skii, *Electrokhimiya*, **5** (3), 274 (1969); (U.D.C. 541.138: 621.3.0218).
14. C. Hastings Jr., "Approximations for Digital Computers," Princeton University Press, Princeton N.J. (1955).
15. R. H. Müller, *Anal. Chem.*, **41** (12), 113A (1969).
16. M. Koebel, N. Ibl., and A. M. Frei, *Electrochim. Acta*, **19**, 287 (1974).

An Electrochemical Study of Flavin Adenine Dinucleotide

Robert D. Braun*[1]

Department of Chemistry, Vassar College, Poughkeepsie, New York 12601

ABSTRACT

Flavin adenine dinucleotide (FAD) is examined using polarography, cyclic voltammetry, and controlled potential coulometry. At pH less than 6.5 and at pH greater than 10, the reaction proceeds in two single electron steps through the semiquinone. At intermediate pH the reaction consists of a preceding hydrogen ion addition followed by a two-electron transfer which in turn is followed by a second hydrogen ion addition.

The flavins are an important class of biochemical compounds which are found in both plants and animals. Due to their importance, most of the flavins have been the subject of many studies. In particular isoalloxazine, lumichrome, lumiflavin, riboflavin, and flavin mononucleotide (FMN) have been thoroughly investigated and excellent reviews of these studies are available (1, 2). Although flavin adenine dinucleotide (FAD) occupies a key position in the respiratory transport chain (2), relatively few electrochemical studies of this compound are available (3, 4). These electrochemical studies consisted entirely of polarographic examinations at the dropping mercury electrode (DME). No successful attempt has been made to unravel the electrochemical reaction mechanism or to examine the kinetics of the reaction. In the present study polarography, controlled potential coulometry, cyclic voltammetry, and voltammetry at a rotating platinum disk electrode have been used to study the electrochemical reaction mechanism of FAD throughout a broad pH range in aqueous solution.

Experimental

Chemicals.—FAD was obtained from the Sigma Chemical Company and used without further purification. The manufacturer's assay listed the purity of the FAD as 95%. Spectrophotometric analysis at 450 nm assuming a molar absorptivity of 1.13×10^4 l mole^{-1} cm^{-1} (5) resulted in a calculated purity of 92% (14 trials). Any impurity in the FAD was not electroactive within the potential region used in this study. All other chemicals were reagent grade.

Buffer solutions were prepared to be 0.1*M* in their minor constituent except for the pH 2.1 HCl solution and the pH 11 or greater sodium hydroxide solutions. The ionic strength of each buffer solution was adjusted to 0.5M with KCl except for the pH 7.5 Tris buffer and the pH 10.0 and 10.2 carbonate buffers which had ionic strengths of 0.8, 0.8, and 1.3*M*, respectively. The buffer solution components were HCl at pH 2.1, acetic acid and sodium acetate at pH 4-5.1, potassium hydrogen phthalate and sodium hydroxide at pH 5.9, potassium dihydrogen phosphate and dipotassium hydrogen phosphate at pH 6-8, tris (hydroxymethyl) aminomethane (Tris) and HCl between pH 7.5 and 9.2, potassium hydrogen carbonate and potassium carbonate between pH 8 and 10.2, and NaOH at pH greater than 11.

Apparatus.—Experiments were performed using a Beckman electroscan 30 in its controlled potential mode equipped with an electroscan 30P integrator which was used to integrate the area under controlled potential coulometry current-time curves. The output pulses from the integrator were counted with a Heathkit IM-4100 counter.

Rotating platinum disk electrode (RPDE) studies were performed at 1800 rpm (Sargent synchronous rotator). Cyclic voltammetry experiments were carried out at a hanging mercury drop electrode (HMDE). Polarographic studies were carried out at a conventional dropping mercury electrode (DME). The reference electrode was a saturated calomel electrode (SCE). The auxiliary electrode was made of platinum foil.

All experiments were carried out at 25° ± 0.5° in either a water-jacketed, three-compartment cell, or in a commercially available water-jacketed cell with accompanying cell top (Princeton Applied Research 9300 and 9350). In either case separation between the compartments was effected by medium porosity glass frits and salt bridges containing saturated KCl in agar gels.

Solutions were deaerated prior to examination with Linde high purity dry grade nitrogen which was passed through two wash towers containing acidic ammonium metavanadate and amalgamated zinc, and a final wash tower containing distilled water (6a). All pH measurements were made with a Radiometer PHM62 pH meter.

Results and Discussion

A cursory polarographic examination of FAD shows a single cathodic wave throughout the pH range 2-13. A plot of $E_{1/2}$ *vs.* pH yields three straight-line portions corresponding to Eq. [1], [2], and [3] for the acidic, neutral, and basic regions, respectively. The two inflection points in the

* Electrochemical Society Active Member.
[1] Present address: Department of Chemistry, University of Southwestern Louisiana, Lafayette, Louisiana 70504.
Key words: polarography, cyclic voltammetry, coulometry.

$$E_{1/2} = -0.010\text{-}0.0646\,pH \quad [1]$$

$$E_{1/2} = -0.205\text{-}0.0342\,pH \quad [2]$$

$$E_{1/2} = 0.056\text{-}0.0604\,pH \quad [3]$$

plot occurred at pH of 6.4 and 10.0 in fair agreement with previously reported values (3, 4). The first inflection point in the $E_{1/2}$-pH curve has been attributed to the acid dissociation constant of the reduced form of FAD and the second inflection point to the dissociation constant of the oxidized form (1, 3). In the acidic region the slope of the $E_{1/2}$-pH curve was found to be −0.065 V/pH unit. Between the two inflection points in the curve the slope was −0.034 V/pH unit, and at pH greater than 10.1 the slope was −0.060. These values compare to slopes of −0.06, −0.03, and −0.06 reported earlier (3).

Controlled potential coulometry was carried out at several pH's and the results are shown in Table I. In each case the potential was adjusted to a position on the plateau of the polarographic wave and the electrolysis carried out to completion. Throughout the entire pH range a coulometrically calculated value of $n_{\text{redn.}}$ of 2 was obtained. The resulting reduction products were examined polarographically and in a few instances the potential was adjusted on the plateau of the reduced FAD anodic wave and exhaustive electrolysis carried out. The coulometrically calculated values of $n_{\text{oxdn.}}$ obtained in these oxidations are also listed in Table I. After each oxidation the products were examined polarographically and found to have exactly the same $E_{1/2}$ and i_d as did the original FAD sample, *i.e.*, the original FAD was regenerated with no loss to other possible products.

The values of $n_{\text{oxdn.}}$ obtained in basic solutions varied from 0.7 at pH 9.25 to a high value of 1.7 at pH 8.18. These values are all less than the expected coulometric value of 2.0, apparently as a result of air oxidation of the FAD reduction products. Even with nitrogen flowing through the cell it was found that in basic solution the reduced FAD reverts to FAD at a rate that is significant with respect to the relatively long times (about 1 hr) used for the controlled potential oxidations. The pseudo first-order rate constant for the conversion of the reduction products to FAD under the experimental conditions at pH 8.18 was estimated by measuring the increase in the diffusion current of the FAD wave with time and found to be 1.1×10^{-4} sec^{-1}. Consequently after 1 hr about 40% of the reduced substance reverts to FAD.

Table I. Controlled potential coulometry data obtained on FAD and reduced FAD samples

Initial FAD conc, mmole	pH	Working electrode	Reduction potential, −V	$n_{\text{redn.}}$	Oxidation potential, −V	$n_{\text{oxdn.}}$
1.20	4.1	Hg	0.60	1.82		
0.46	4.1	Hg	0.40	2.3	0.20	2.04
0.57	4.1	Hg	0.40	1.74		
0.52	8.2	Pt	0.60	1.98		
0.84	8.2	Pt	0.60	1.92		
1.11	8.2	Pt	0.60	1.98		
0.40	8.2	Hg	0.60	2.16		
0.66	8.2	Hg	1.00	2.04		
1.17	8.2	Hg	1.00	2.02		
0.45	8.2	Hg	1.00	1.99		
0.55	8.2	Hg	0.80	2.03	0.20	1.0*
0.59	8.2	Hg	0.80	1.92	0.30	1.4*
1.54	8.2	Pt	0.80	1.96	0	1.7*
0.68	9.3	Hg	0.60	1.97		
0.21	9.3	Hg	0.60	2.13		
0.42	9.3	Hg	0.60	2.02	0.20	0.72*
0.51	10.2	Hg	0.90	2.09		
0.97	10.2	Hg	0.90	2.05		
			Average	2.01		

* The low $n_{\text{oxdn.}}$ values reported here are apparently due to relatively rapid air oxidation of the reduced FAD in alkaline solutions.

Rapid air oxidation of reduced FAD was not observed in solutions of pH 4.08. For convenience the remainder of this report is divided into sections corresponding to the pH range throughout which a particular reaction mechanism takes place

pH 6.6-8.6.—Careful polarographic examination (DME) of the FAD wave in this pH range revealed only a single cathodic wave. The "anomalous" wave at a potential more negative than the main wave observed by Ke (3) was not observed in this study.

A requirement of a reversible electrode reaction is that the half-wave potential of the oxidized species must be identical to that of the reduced species (6b). Half-wave potentials were obtained for the FAD reduction waves from plots of E *vs.* log $(i/i_d - i)$ at the point where the log term was zero. Half-wave potentials for the oxidation of reduced FAD were similarly obtained from plots of E *vs.* log $(i_d - i/i)$. Throughout the remainder of this paper these plots are referred to as log plots. In each case in this pH region the log plots were linear. The average difference between the half-wave potentials of FAD and reduced FAD at the pH's in this range was 0.012 ± 0.006V for five trials at differing pH. The uncertainty is expressed as the standard deviation. A "t" test for significance indicated that at the 90% probability level the confidence limit was identical to the standard deviation. Since the oxidized and reduced forms of FAD do not have identical $E_{1/2}$'s, this system cannot be classified as reversible in this pH range as has been done previously (3). The cathodic FAD wave does overlap with the anodic reduced FAD wave however and consequently this system is best described as quasireversible. A typical FAD cathodic wave and the corresponding reduced FAD anodic wave are shown in Fig. 1.

Slopes of log plots for reversible systems at 25° are given by Eq. [4]. The slopes of log plots obtained

$$\text{slope} = -0.059/n \text{ V/decade} \quad [4]$$

with FAD solutions are listed in Table II. The average

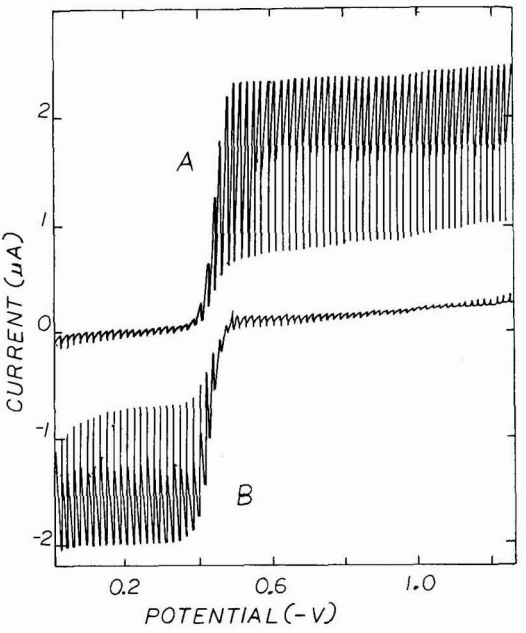

Fig. 1. Polarograms obtained in pH 8.2 Tris buffer. A, 0.41 mmole FAD; B, 0.41 mmole reduced FAD.

Table II. Slopes obtained from log plots* of various FAD solutions at differing pH values

FAD conc, mmole	pH	Slope, −V/decade
0.208	6.82	0.036
0.208	6.96	0.037
0.208	7.92	0.039
0.208	8.09	0.037
0.208	8.13	0.038
0.59	8.18	0.039
0.78	8.18	0.035
0.59	8.18	0.037
0.208	8.59	0.034
0.51	9.13	0.040
0.42	9.25	0.043
0.68	9.25	0.034
0.208	9.25	0.034
0.51	9.26	0.034
0.51	9.28	0.035

* Log plots are defined as plots of E vs. log $(i/i_d - i)$ on the rising portion of the cathodic wave.

slope throughout this pH range was −0.037. This value is closer to the value expected for a two-electron reversible process (−0.030) than to the value for a one-electron reversible process (−0.059). It should be noted that the values of the log plot slopes obtained in this study differ significantly from the value of 0.06 obtained at pH 7.4 by Ke (3). A similar examination of the anodic wave of reduced FAD at pH 8.2 revealed the slope to be 0.030 ± 0.003 (four trials) where the uncertainty is expressed as the standard deviation.

At pH 8.2, i increased linearly with increasing $h^{1/2}_{corr.}$, and $i_d/h^{1/2}_{corr.}$ decreased slightlly with increasing $h^{1/2}_{corr.}$ for solutions of FAD and reduced FAD thereby apparently indicating diffusion control of both the cathodic and anodic FAD reactions (6c). A plot of i_d as a function of FAD concentration was linear and when extrapolated passed through the origin. From the slope of the plot, the diffusion current constant ($I = i_d/Cm^{2/3}t^{1/6}$) was found to be 3.0. The values of m and t used in this calculation were measured in the supporting electrolyte-buffer solution on the plateau of the wave at −0.8V and the diffusion current was measured as the maximum drop current using no recorder damping. This same data was used to calculate the FAD diffusion coefficient from Eq. [5]. The terms in parentheses in Eq. [5] were set equal

$$i_d = (708nD^{1/2}m^{2/3}t^{1/6})C \qquad [5]$$

to the slope of the $i_d - C$ plot and the coulometric value of n of 2.0 used to obtain a value of D of 4.5×10^{-6} cm^2 sec^{-1}. As expected this value is slightly less than the average D of 6.5×10^{-6} which has been calculated for the lighter riboflavin at pH 7.4 (7). Between pH 6.8 and 13, the ratio of diffusion current to concentration never varied by more than 5% (solutions at 10 different pH's examined) and consequently the value of D given above may be assumed to be approximately constant throughout this entire pH range. There was no noticeable variation in $E_{1/2}$ with FAD concentration at the pH's examined.

Similar behavior was observed at the RPDE. A single wave was observed throughout the pH range from 2 to 10. The $E_{1/2}$ of the wave varied with pH in a manner similar to that observed at the DME. The RPDE wave occurred about 0.11V negative of the corresponding DME wave. At pH 8.2 the limiting current increased linearly with increasing FAD concentration. Since the RPDE wave was not as well formed as the DME wave, accurate potential measurements at the RPDE were impossible. Consequently the RPDE offered no particular advantage in studying the FAD system and its use was abandoned after the pH study and an examination of the variation of limiting current with concentration.

Cyclic voltammetry studies were carried out at both the HMDE and at a platinum disk. In order to remove the platinum oxide coating on the platinum disk it was necessary to pretreat the electrode by dipping it in concentrated nitric acid, rinsing with distilled water, and reducing the oxide coating by controlled potential electrolysis at a potential on the platinum oxide peak. Even this procedure was not always adequate at the relatively high current sensitivities used in this study, however, and as a result, after the studies in this pH region, the use of the platinum disk was abandoned.

Between pH 6.8 and 8.6, a single cathodic-anodic peak couple was observed at both the platinum disk and the HMDE (Fig. 2). Application of the diagnostic criteria of Nicholson and Shain (8) to the cathodic peaks resulted in plotted curves (Fig. 3) with shapes characteristic of an electrochemical mechanism consisting of a reversible first-order or pseudo first-order preceding reaction followed by a reversible electron transfer. Since the equilibrium constant for the preceding reaction is not known, it is not possible to use the method of Nicholson and Shain to obtain the rate constant for the preceding chemical reaction.

Reduced FAD in the pH 6.8-8.6 region had a single cyclic voltammetry anodic-cathodic peak pair. Application of the diagnostic criteria to the anodic peak resulted in curves similar in shape to those shown in Fig. 3 for the cathodic peak. This appears to indicate that the oxidation of reduced FAD also follows an electrochemical mechanism consisting of a first-order reaction followed by a reversible electron transfer.

All of the studied flavin compounds have been shown to undergo an over-all reduction to the dihydroflavin compounds (1, 2) as shown in Eq. [6]. As has been previously suggested by Ke (3)

$$F + 2H^+ + 2e = FH_2 \qquad [6]$$

this apparently is also the case for FAD. Between pH 6.8 and 8.6 the cyclic voltammetry data indicate a chemical reaction prior to the electron transfer. For a fast acid-base reaction prior to the electron transfer (Eq. [7] and [8]), if the unprotonated species, O, predominates in this pH range, then the slope of the

$$O + pH^+ = H_pO^{p+} \qquad [7]$$

$$H_pO^{p+} + ne = RH_p \qquad [8]$$

polarographic $E_{1/2}$ − pH curve is given by $-0.059p/n$ (6d). Since n has been shown by both controlled-potential coulometry and by the slope of the log plots to be 2 in this region, and the slope of the $E_{1/2}$ − pH

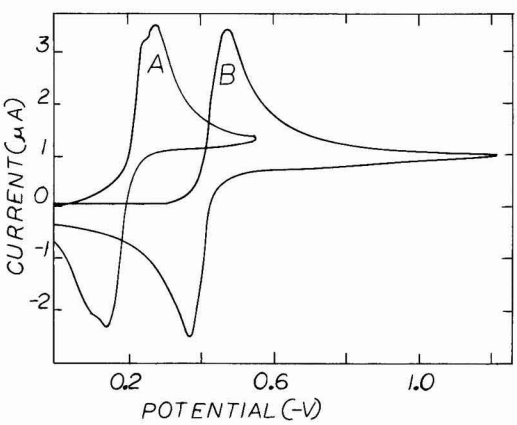

Fig. 2. Cyclic voltammograms obtained at a HMDE. A, 0.53 mmole FAD in pH 4.08 acetate buffer at 0.2 V sec^{-1}; B, 0.72 mmole FAD in pH 8.2 Tris buffer at 0.10 V sec^{-1}.

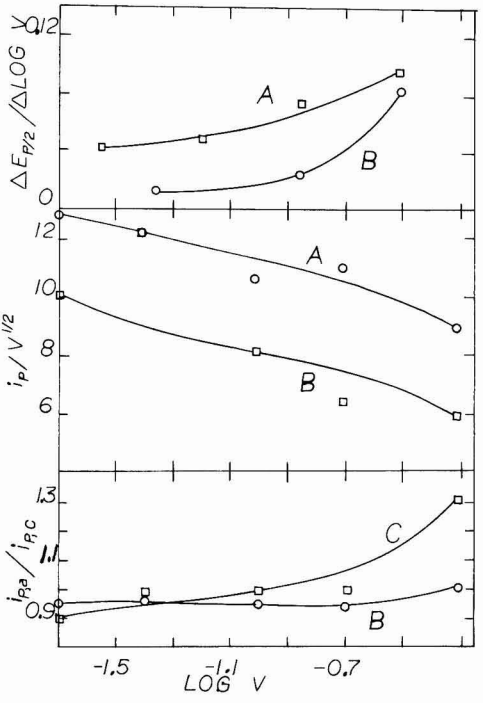

Fig. 3. Application of the diagnostic criteria of Nicholson and Shain (8) to cyclic voltammograms of FAD in pH 8.2 Tris buffer. A, 0.55 mmole at the HMDE; B, 0.87 mmole at the Pt disk; C, 0.87 mmole at the HMDE.

curve was −0.034, then p must be equal to 1. Cyclic voltammetry data also indicates a chemical step prior to oxidation of reduced FAD. The electrochemical mechanism which appears to best explain all of these observations is the three-step mechanism shown in Eq. [9], [10] and [11] where Eq. [9] is the rate-determining step for FAD reduction and Eq. [11] is the rate-determining step for FADH oxidation. In this pH range the present study contains no evidence for semiquinone formation. Semiquinone formation is clearly indicated, however

$$FAD + H^+ = FADH^+ \quad [9]$$

$$FADH^+ + 2e = FADH^- \quad [10]$$

$$FADH^- + H^+ = FADH_2 \quad [11]$$

in other pH ranges (see the following discussion). It should be noted that Eq. [9], [10], and [11] are not meant to imply a specific acidity state of FAD. The K_a values of various flavin compounds are listed elsewhere (1, 9).

Although the reaction apparently does not proceed in the single step indicated by Eq. [6], it is informative to calculate the rate constant for this over-all reaction. The rate constant can be calculated from cyclic voltammery data at the HMDE (10) by assuming n is the coulometrically determined value of 2 and D of FAD is the polarographically calculated value of 4.5×10^{-6} cm^2 sec^{-1}. Several calculated values of the rate constant (k_s) for a 0.21 mmole FAD solution are listed in Table III. The rate of the reaction decreases with increasing pH as would be expected if Eq. [9] were the rate-determining step for FAD reduction.

pH 2.1-6.5.—Polarographic examination at the DME of FAD in this pH region revealed a single cathodic wave at pH above about 6 which split into two overlapping waves of equal height (Fig. 4) at lower pH's. If a slow scan rate is not employed while recording the polarogram, the split into two waves can be easily overlooked, as was apparently done in the earlier study (3). In this instance a scan rate of 0.5 mV sec^{-1} was used. At pH 2.2 the proximity of the adsorption prewave (11) to the main FAD wave made it impossible to determine whether one or two waves were present.

Table III. Calculated values of the pseudo first-order rate constant (k_s) for the over-all electrochemical reduction of 0.21 mmole FAD

pH	Scan rate, V sec^{-1}	ΔE_p*xn, mV	k_s, cm sec^{-1} × 10^{-3}
6.96	0.020	84	4.7
6.96	0.040	100	3.8
8.09	0.040	104	3.4
8.13	0.020	100	2.7
8.59	0.040	110	3.0

* $\Delta E_p = E_{p,anodic} - E_{p,cathodic}$.

Log plots at pH 4.08 yielded straight lines from which the half-wave potentials of the two waves could be determined. In drawing the lines through the log plot points it was necessary to neglect those points at potentials on wave I_c which were more than one-fourth of the way up the wave and those points on wave II_c which were less than three-fourths of the way up the wave. The overlapping of the waves in the intermediate region caused the log plots to curve away from the straight line. Using this method the $E_{1/2}$ of wave I_c was found to be 8 mV less negative than the $E_{1/2}$ of wave II_c. The average slopes (three trials) of the log plots were −0.055 V/decade for wave I_c and −0.052 V/decade for wave II_c. Both of these values are only slightly less than the −0.059 V/decade expected for a reversible one-electron process.

At pH's of 6.43, 6.20, and 6.04 the single cathodic FAD waves yielded log plots which were linear but which had two segments of slightly differing slope (Fig. 5). This can be interpreted to mean that two cathodic waves were present which overlapped to an extent which made separate wave identification impossible.

FAD which had been reduced by electrolysis showed only a single anodic wave in the acidic pH region unlike the behavior of FAD prior to reduction. Apparently two waves were not observed since the $E_{1/2}$'s of the waves were too close to each other to allow differentiation. Log plots of reduced FAD at pH 4.08 were linear with a slope of −0.041 V/decade. The

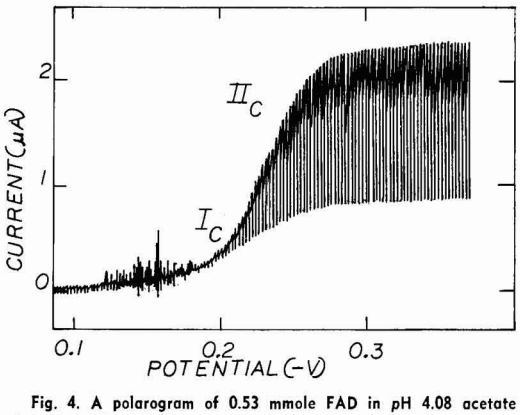

Fig. 4. A polarogram of 0.53 mmole FAD in pH 4.08 acetate buffer. I_c, the first cathodic wave; II_c, the second cathodic wave.

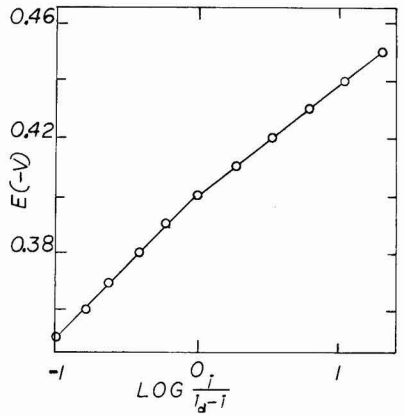

Fig. 5. A log plot of 0.19 mmole FAD in pH 6.04 phosphate buffer

average $E_{1/2}$ of the anodic wave (three trials) was −0.232V. In each case the diffusion current of the reduced FAD anodic wave equaled the total diffusion current of the two cathodic waves of the FAD starting material.

At pH 4.08 the total diffusion current ($i_{d,tot.}$) for the two FAD waves increased linearly with increasing $h^{1/2}_{corr.}$ and $i_{d,tot.}/h^{1/2}_{corr.}$ decreased slightly with increasing $h^{1/2}_{corr.}$ apparently indicating diffusion control of the electrode process. The diffusion current for the reduced FAD anodic wave behaved similarly.

A plot of $i_{d,tot.}$ as a function of FAD concentration at pH 4.08 was linear with a slope of 3.78 μA mmole^{-1}. The single reduced FAD wave behaved identically. From the slope of these straight lines and the measured values of m and t on the plateaus of the cathodic and anodic waves, the diffusion current constants (maximum drop currents used throughout) for FAD and reduced FAD at pH 4.08 were found to be 2.35 and 2.32, respectively. The diffusion coefficients were calculated from Eq. [5] using the coulometrically determined n of 2 and found to be 2.75×10^{-6} cm^2 sec^{-1} and 2.68×10^{-6} cm^2 sec^{-1}, respectively.

Cyclic voltammetry experiments were performed at the HMDE. At slower scan rates in the acidic pH range two overlapping cathodic peaks and two overlapping anodic peaks were observed (Fig. 2). At scan rates above about 0.25 V sec^{-1} the two cathodic and the two anodic peaks merged into a single cathodic-anodic peak pair. Cyclic voltammograms of reduced FAD showed two overlapping anodic peaks which did not completely merge even at 0.50 V sec^{-1}. Scan reversal at potentials cathodic of the anodic peak revealed two overlapping cathodic peaks at scan rates up to 0.05 V sec^{-1} and a single cathodic peak at higher scan rates. Since the cathodic peaks (and the anodic peaks) overlap each other it is impossible to apply the diagnostic criteria used earlier in the neutral pH range.

Controlled potential coulometry data has shown the total n for the over-all reduction of FAD to be 2. Since the polarograms of FAD in acidic solutions exhibit two waves of equal height, FAD must be reduced in two, one-electron steps. The slope of the $E_{1/2}$-pH curve in this pH range has been shown to be −0.065. For a fast acid-base reaction prior to the electron transfer (if the unprotonated FAD species predominates) or for a simultaneous addition of hydrogen ion and an electron, the slope of the polarographic $E_{1/2}$-pH curve is given by $-0.059p/n$ (see earlier discussion). Since n for each individual step is 1, then for each cathodic FAD wave the number of hydrogen ions added (p) is also 1. The electrochemical reaction mechanism which appears to best explain these results as well as the two cathodic cyclic voltammetry peaks is the stepwise reduction of FAD first to the semiquinone and finally to $FADH_2$ (Eq. [12] and [13]). It is not possible from the present data to determine when the hydrogen ions

$$FAD + H^+ + e = FADH\cdot \quad [12]$$

$$FADH\cdot + H^+ + e = FADH_2 \quad [13]$$

are added. The data may be interpreted to indicate either H^+ addition prior to or simultaneous with the addition of each electron.

pH 9-13.—Between pH 9.13 and 9.28 a single FAD cathodic wave was observed at the DME which yielded a linear log plot with an average slope of −0.037 V/decade (Table II). Between pH 9.34 and 9.89 the single polarographic wave resulted in a log plot with two linear portions of slightly differing slopes (similar to Fig. 5). Both portions had slopes of about −0.035 V/decade. The more cathodic portion always had the slightly greater negative slope. At pH's of 10.0 or greater two close polarographic waves were observed. By using the log plot method discussed earlier the separation between the $E_{1/2}$'s of the two waves at pH 10.2 (0.97 mmole solution) was found to be 24 mV.

At pH 10.2, 0.51 mmole FAD which had been exhaustively reduced by electrolysis showed two overlapping anodic waves of equal height. The difference in $E_{1/2}$ of the waves was 26 mV. The $E_{1/2}$ of the more positive anodic wave was 6 mV more positive than the $E_{1/2}$ of the more positive cathodic wave of the original FAD. Likewise the $E_{1/2}$ of the more negative anodic wave was 5 mV more positive than the $E_{1/2}$ of the more negative cathodic wave of the FAD starting material. This appears to indicate the presence of two quasireversible electrode reactions. The total diffusion current of the two anodic reduced FAD waves equaled the total diffusion current of the two cathodic waves of the original FAD.

At pH 9.25 i_d increased linearly with increasing $h^{1/2}_{corr.}$ and $i_d/h^{1/2}_{corr.}$ decreased slightly with increasing $h^{1/2}_{corr.}$ for solutions of FAD and reduced FAD. This is normally considered to be evidence of diffusion control of the electrode process.

At pH 12.3 the polarogram of FAD revealed two small waves at −1.1 and −1.4V and two small maxima at about −1.6 and −1.7V in addition to the main FAD wave (Fig. 6). With time the main FAD wave was observed to decrease in height while the wave at about −1.1V grew. The waves at −1.4 and −1.7V also became slightly more prominent (Fig. 6). Apparently the small waves observed in the original FAD polarogram in basic solution were due to FAD decomposition products. The identity of the decomposition products is presently unknown. The "anomalous" postwave observed by Ke (3) may have been due to one of these decomposition products.

Throughout the entire pH 9-13 range, cyclic voltammograms of FAD obtained at the HMDE revealed two overlapping cathodic peaks (*i.e.*, a major peak with a shoulder) and, upon scan reversal, two overlapping anodic peaks (similar to Fig. 2, curve A). In some cases the two cathodic peaks and the two anodic peaks merged to give a single cathodic-anodic peak pair at a scan rate of 0.5 V sec^{-1}. At scan rates of 0.02 and 0.04 V sec^{-1} the cyclic voltammetry traces were erratic making meaningful observations at these scan rates impossible. The overlapping of the peaks made it impossible to apply the diagnostic criteria of Nicholson and Shain to either of the cathodic peaks. Cyclic voltammograms obtained on solutions of reduced FAD showed two overlapping anodic peaks and, after scan reversal, two overlapping cathodic

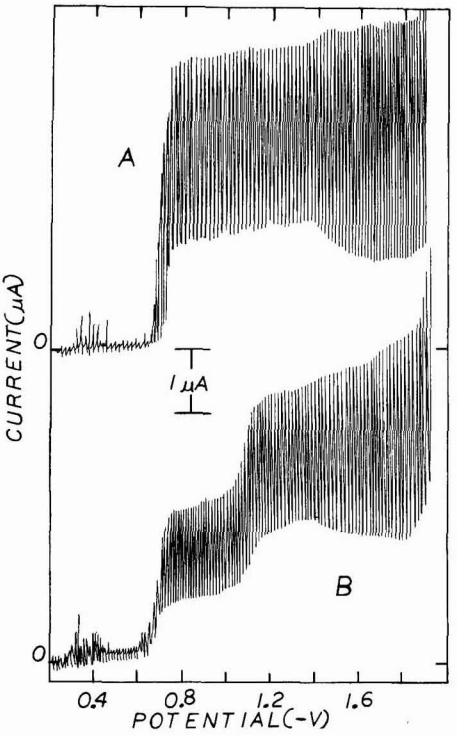

Fig. 6. Polarograms of 0.92 mmole FAD at pH 12.3. A, Immediately after solution preparation; B, 43 hr after solution preparation.

peaks. As with FAD, these peaks often merged into a single anodic-cathodic pair at a scan rate of 0.5 V sec^{-1}.

In the pH 10-13 range, reasoning completely analogous to that used in the acidic pH region leads to the conclusion that FAD is reduced in two single-electron steps first to the semiquinone and finally to $FADH_2$ (Eq. [12] and [13]). Information concerning the order in which the hydrogen ions are added is not available. In the pH region between 9 and 10, the two cyclic voltammetry cathodic peaks indicate two single-electron transfers, however, the single polarographic wave and the slope of the log plots indicate a single two-electron transfer. It appears likely that in the pH 9-10 region the actual electrochemical reaction mechanism is a combination of that given by Eq. [9], [10], and [11] and that given by Eq. [12] and [13], *i.e.*, in this pH region the reaction mechanism is switching from the mechanism observed at neutral pH to the one observed in basic solution.

Acknowledgments

The author gratefully acknowledges the assistance of Professor Philip J. Elving in providing the three-compartment water-jacketed cell and of the Society of Sigma Xi for a Grant-In-Aid-of-Research which was used to partially support this study.

Manuscript submitted Feb. 2, 1977; revised manuscript received *ca.* May 1, 1977.

Any discussion of this paper will appear in a Discussion Section to be published in the June 1978 JOURNAL. All discussions for the June 1978 Discussion Section should be submitted by Feb. 1, 1978.

Publication costs of this article were assisted by Vassar College.

REFERENCES

1. B. Janik and P. J. Elving, *Chem. Rev.*, **68**, 295 (1968).
2. A. L. Underwood and R. W. Burnett, "Electroanalytical Chemistry," A. J. Bard, Editor, p. 60, Marcel Dekker, New York (1973).
3. B. Ke, *Arch. Biochem. Biophys.*, **68**, 330 (1957).
4. Y. Asahi, *J. Pharm. Soc. Jpn.*, **76**, 378 (1956).
5. L. G. Whitby, *Biochem. J.*, **54**, 437 (1953).
6. L. Meites, "Polarographic Techniques," 2nd ed., Interscience, New York (1965): a, p. 89; b, p. 218; c, pp. 132-133; d, p. 282.
7. R. Brdicka, *Z. Elektrochem.*, **48**, 686 (1942).
8. R. S. Nicholson and I. Shain, *Anal. Chem.*, **36**, 706 (1964).
9. L. Michaelis, M. P. Schubert, and C. V. Smythe, *J. Biol. Chem.*, **116**, 587 (1936).
10. R. S. Nicholson, *Anal. Chem.*, **37**, 1351 (1965).
11. A. M. Hartley and G. S. Wilson, *ibid.*, **38**, 681 (1966).

The Rate of the Photoelectrochemical Generation of Hydrogen at p-Type Semiconductors

J. O'M. Bockris* and K. Uosaki[1]

School of Physical Sciences, Flinders University, Adelaide, Australia 5042

ABSTRACT

The current-potential relations with and without illumination, quantum efficiency-wavelength relations at several potentials, the flatband potentials, the transient behavior, and the stability of seven p-type semiconductors, *i.e.*, ZnTe, CdTe, GaAs, InP, GaP, SiC, and Si, have been measured in 1*N* NaOH and 1*N* H_2SO_4. The position of the photocurrent-potential relations are related to the flatband potential and the energy gap of the semiconductor. The existence of the maximum in quantum efficiency-wavelength relation is analyzed by considering surface recombination. The stability and the transient behavior are analyzed.

Photoelectrochemical production of hydrogen was envisaged by Fujishima and Honda in 1972 (1). To obtain hydrogen, either a pH gradient or an external power source in the cell was required (2-4). However, homogenization of the solution would inevitably occur on prolonged functioning in such an arrangement.

The lack of need for single crystals in the photoelectrochemical approach to energy conversion (5, 6) gives the prospect of favorable economics in purely photoelectrochemical hydrogen production from water. The primary aim is the development of a suitable cathode, so that light may be directed both onto the cathode and anode, with the objective of obtaining stable photoelectrolysis in a cell with a uniform pH. A previously reported photocathode is unstable (7). We report investigations concerning the stability and efficiency of certain new photocathodes.

Experimental

Apparatus.—The photoelectrochemical cell is shown in Fig. 1. Stopcocks and taps were Teflon. To avoid contact of the metal used to form an ohmic contact with the solution, the back face and side of the electrode were covered with epoxy resin. To minimize contact of this with the solution, a Teflon electrode holder was used. The absence of a leak was verified by the small magnitude of the dark current. All photoelectrode areas were 0.125 cm^2.

A PAR Model 173 potentiostat/galvanostat, with a Model 176 current-potential converter, was used to control the potential. The electrode potential was swept by a Wenking SMP 69 potential stepping motor control. The current-potential relationship was recorded by a Hewlett-Packard Model 7004B X-Y recorder. The time dependence of the photocurrent was recorded by means of a Hitachi QD25 recorder.

A 900W xenon lamp (Canrad-Hanovia 538C1) was used as a light source and a Jarrell-Ash quarter-meter grating monochrometer (Cat. no. 82-410) was employed to obtain monochromatic light. An *IR* absorbing filter (Oriel G-776-7100) was placed between the cell and the light house, when current-potential measurements were carried out without the monochrometer. However, a quartz lens (d = 5 cm, f = 5 cm) was employed to concentrate the light on the electrode surface when the photocurrent was measured under monochromatic light. In this case, two long pass filters (Oriel G-772-3900 and Oriel G-772-5400) were used with an *IR* absorbing filter to eliminate second-order diffraction. The conditions used in this respect were: 3000 ~ 5000Å, *IR* absorbing filter only; 5000 ~ 7000Å, *IR* absorbing filter + G-772-3900 filter; 7000 ~ 7500Å, *IR* absorbing filter + G-772-5400 filter; 7500Å, G-772-5400 filter only.

The intensity of light was measured by means of a Hewlett-Packard Model 8334 radiant flux meter with either a 8334A radian flux detector or a Carl Zeiss vacuum thermocouple (VT Q3/A) with a Keithley 149 millimicrovoltmeter. The error in relative intensity measurement was < 5%. However, absolute intensity measurements had an uncertainty of ± 20% error.

The electrochemical cell and the optical system were set up on an optical bench.

Impedance measurement.—The cell for impedance measurements had a working electrode surrounded by a cylindrical platinized platinum counterelectrode, apparent area 60 cm^2. Hydrogen gas was passed into the solution before and during measurement.

The direct method was employed (8, 9). The circuit contained a dry cell (6V) as a d-c source and the potential was controlled by a ten-turn variable resistor

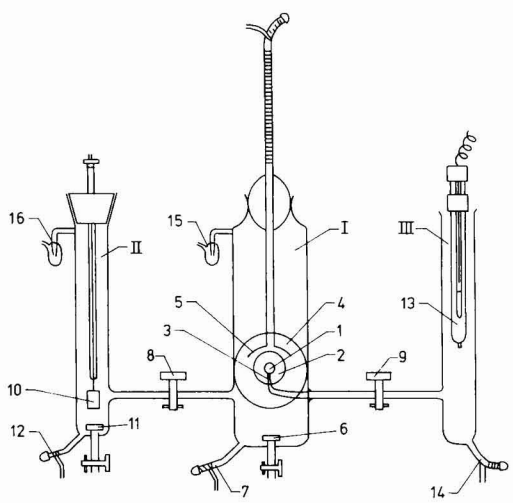

Fig. 1. The photoelectrochemical cell (front view). I, Working electrode compartment (*d* = 50 mm); II, counterelectrode compartment (*d* = 25 mm); III, reference electrode compartment (*d* = 20 mm). 1, Working (semiconductor) electrode; 2, Teflon electrode holder; 3, Luggin capillary; 4, quartz optical flat; 5, gas collector; 6, 11, frits (gas inlets); 7, 12, 14, drains; 8, 9, Teflon stopcocks; 10, Pt counterelectrode; 13, reference electrode (SCE); 15, 16, gas bubbler.

* Electrochemical Society Active Member.

[1] Present address: Mitsubishi Petrochemical Company, Limited, Ami, Ibaraki, Japan.

Key words: hydrogen production, photoelectrochemical reaction, p-type semiconductors, photocathodes.

while being monitored by means of a Keithley 616 digital electrometer. The a-c source was a Mini-Lab Model 603A (B.W.D. Electronics). A capacitor (10 μf) and a choke coil (35 H) were in the circuit. The resistor, the value of which was several hundred times larger than the cell impedance, Z_{cell}, was connected in series to the cell so that the alternating current, I, became constant, and independent of the cell voltage. The impedance of the choke was at least one hundred times larger than that of the cell.

Signals taken from two points in the circuit and applied to the X and Y inputs of a cathode ray oscilloscope (Tetronix 5103N with 5A20N and 5A2IN differential amplifiers) displayed Lissajou's figures. Since the X and Y inputs showed I ($Z_{cell} + R$) and IZ_{cell}, respectively, and $R >> Z_{cell}$, the absolute value of the cell impedance, and phase difference due to the cell, could be ascertained. Assuming a series equivalent circuit (measurements were carried out under nearly ideally polarized conditions), the cell capacitance, which is effectively the space charge capacitance of the semiconductor electrode, can be obtained.

The accuracy of the direct method is low compared with that of the bridge method (8, 9). At metal electrodes the phase difference is small, and hence determination of C is inaccurate by this method.

However, at semiconductor electrodes, capacitance is low so that the phase difference can be measured accurately.

Semiconductors chosen.—Cathodes were selected on the basis of sufficiently low values of energy gap (2.574 $E_G < 1.3$ eV) and electron affinity ($E_a < 4.0$ eV) (28).

Zinc telluride (ZnTe).—A ZnTe single crystal (Ag doped), grown by the Bridgeman method, was cut parallel to the cleaved face (100). After being etched in $K_2Cr_2O_7$-HNO_3 aqueous solution, the specimen was dipped in $HAuCl_4$ solution to make an ohmic contact (10). It was masked with paraffin, later removed in trichloroethylene. The contact was ohmic and the specific resistance was 0.2 $\Omega \cdot$ cm. The face of the specimen was polished by means of emery paper to 600 grade. The electrode was etched in HF-HNO_3 (11) solution.

Cadmium telluride (CdTe).—A CdTe single crystal (undoped) grown by the Bridgeman method was cut parallel to the cleaved face (100). The specimen was heated in Te vapor at 500°C for 8 hr to increase nonstoichiometry. Thereafter, the crystal was etched in $K_2Cr_2O_7$-HNO_3 (12), dipped into $AgNO_3$ solution, and heated at 200°C for 30 min. Finally, a gold film was grown on the crystal by dipping it into aqueous $HAuCl_4$ (13). During the processes of etching and dipping into $AgNO_3$ and $HAuCl_4$ solutions, the crystal was covered with paraffin except for the spots where it was intended to make a contact. The specific resistance was 10^3 $\Omega \cdot$ cm and the ohmic character of the contact good. The face to be used was polished by emery paper, 400 to 600 grade, and the surface etched in HF-HNO_3 solution.

Gallium arsenide (GaAs).—The GaAs was a single crystal in wafer form, (100) face; Zn doped; carrier density = 2×10^{19} cm^{-3}; 0.5 mm thick. It was etched (12) by dipping into CH_3OH-Br_2 (5%) solution, for 1 min before an ohmic contact was made by soldering with indium (14). The I-V relation was ohmic. The specific resistance was 0.2 $\Omega \cdot$ cm.

Indium phosphide (InP).—The InP was a single crystal wafer (100) face, Zn doped; carrier density 5.6×10^{18} cm^{-3}; 0.8 mm thick. Treatment was as for GaAs except that the ohmic contact was by means of an In-Zn alloy (15). The specific resistance was 0.21 $\Omega \cdot$ cm.

Gallium phosphide (GaP).—The GaP was a single crystal wafer, Zn doped; carrier density 6.7×10^{17} cm^{-3}; (111) face; 0.4 mm thick. A HNO_3-HCl mixture was used for etching (12). An ohmic contact was obtained by the use of an In-Zn alloy (7). The specific resistance was 2.0 $\Omega \cdot$ cm.

Silicon carbide (SiC).—The silicon carbide was a single crystal; (000$\bar{1}$) face; Al doped; carrier density 4×10^{18} cm^{-3}; 0.2 mm thick. "Acme" conductive adhesive gave an ohmic contact if heated in hydrogen at 300°C for 2 hr. The specific resistance was 0.31 $\Omega \cdot$ cm. The electrode was dipped in HF for 1 min before each experiment.

Silicon (Si).—The silicon was a single crystal wafer, (100) face; B doped; 0.2 mm thick. An In-Zn alloy was used to obtain an ohmic contact. The specific resistance was 1.2 $\Omega \cdot$ cm. The crystal was etched in HF solution before each experiment.

Results

The current-potential relations.—The current-potential relations with and without illumination by means of a 900W Xe lamp were measured in 1N NaOH and in 1N H_2SO_4. The relations found can be divided into two groups. Results typical of the first group (ZnTe, CdTe, GaP,[2] SiC, and Si) are exemplified in Fig. 2 (ZnTe). Dark curents are low. Typical results of the second group (GaAs and InP) are in Fig. 3 (GaAs).[2] The degree of displacement of the current-potential

[2] In the measurements of Gerischer *et al.* (16), GaAs showed saturation photocurrents at −1.0V, but such saturation was not observed in our work, probably due to a lower intensity of illumination. The current-potential curves observed for GaP were similar to those reported earlier by other workers (17-19).

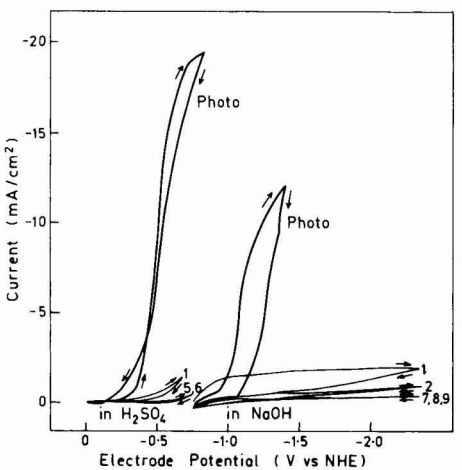

Fig. 2. The current-potential relations of ZnTe in 1N NaOH and 1N H_2SO_4 with and without illumination by a 900W Xe lamp. Sweep rate: 1.5 V/min. Intensity of light 0.08 W/cm². Arrows show the direction of the polarization. 1, 1st sweep in dark; 2, 2nd sweep in dark. 5, 6, 7, 8, 9, 5th, 6th, 7th, 8th, and 9th sweeps in dark.

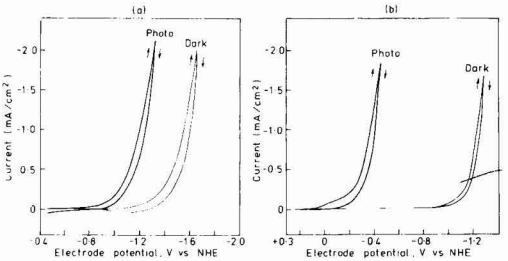

Fig. 3. The current-potential relations of GaAs with and without illumination by a 900 Xe lamp in 1N NaOH (a) and 1N H_2SO_4 (b). Sweep rate: 1.5 V/min. Intensity of light: 0.08 W/cm².

curves in H_2SO_4 and NaOH respectively is shown in Table I.

At CdTe in NaOH no photocurrent was observed at a potential more positive than −0.75V, when the oxygen concentration in the solution had been sufficiently diminished.

A white film was observed on the InP electrode after measurements in 1*N* H_2SO_4. Mayumi *et al.* (20) observed such white films: Irreproducibility due to them may account for the fact that the critical potential observed by Mayumi was 0.5V more negative than that reported here. No films were observed in 1*N* NaOH.

Photocurrents at SiC electrodes were $< 10\ \mu A\ cm^{-2}$.

Quantum efficiency-wavelength relations at several potentials.—Photocurrents were measured under monochromatic light at several potentials. Quantum efficiencies were calculated by using measured values of the photocurrents and the light intensity. Typical results are shown in Fig. 4 (GaP).[3] The spectral response of the quantum efficiency in 1*N* NaOH of the semiconductors examined in this work except for GaP and SiC are shown in Fig. 5. Those in 1*N* H_2SO_4 are as in 1*N* NaOH. Quantum efficiencies at SiC in 1*N* NaOH (Fig. 6) are low.

The flatband potential.—The flatband potentials were determined by using Mott-Schottky plots. A typical plot is shown in Fig. 7 (SiC). Table II shows the flatband potential of the semiconductors in 1*N* NaOH and 1*N* H_2SO_4 and the slopes of the corresponding Mott-Schottky plot. The flatband potentials of InP in 1*N* H_2SO_4 and Si in 1*N* NaOH and 1*N* H_2SO_4 could not be measured due to the instability of these materials in solution.

Gleria and Memming reported (22) difficulties in respect to the Mott-Schottky plot on SiC but none were noted here.

Transient measurement.—Current-time relations at fixed potentials following illumination and interruption of light were measured in 1*N* NaOH and 1*N* H_2SO_4. Typical results are in Fig. 8. When the potential is relatively negative, the current becomes stable just after the light was on or off, but when the electrode potential became relatively positive, it took time to attain a steady state (Fig. 8d).

Stability.—The photocurrents at fixed potentials were measured as a function of time (1-20 hr) at all semiconductors mentioned above in 1*N* NaOH and 1*N* H_2SO_4. Results are listed in Table III in terms of $(1/i)\ (di/dt)$, which is a measure of the instability.

Discussion

By analogy to well-known behavior at the metal-vacuum interface, the electrode potential corresponding to the commencement of electron emission ("the critical potential") would have been expected to vary with change of the frequency of the exciting source. That the critical potential is not thus dependent for the semiconductor-solution interface is demonstrated in Fig. 9 (ZnTe). An interpretation is that electron-phonon collisions in the semiconductor cause the electrons photogenerated within the semiconductors at various energies (depending on the wavelength of the incident light) to fall to the bottom of the conduction band before they have reached the electrode surface.

The i_{photo}-V relations are Tafel-like (Table IV), whereas, at metals, $i^{0.4}$ is linear with V. Thus, in metals, nearly all the photoactivated electrons decay before the surface is reached. The small fraction ($< 10^{-2}\%$) of photoactivated electrons which reach the surface and emit have an energy distribution which is a function of the energy of the exciting source. In the semiconductor, a greater fraction ($\sim 1\%$) of the photogenerated electrons reaches the surface but the energy of nearly all of them is that of the conduction band, Fig. 10. (See above). The variation of the electrochemical photocurrent with potential then becomes subject to the reasoning [*e.g.*, Ref. (23)] which relates the thermal current to potential at metals.

The saturation part of the photocurrent-potential relation can be understood from Fig. 11. When the electrode potential is such that the energy of the emitting electrons is equal to that of the ground state of the acceptor levels in H_3O^+, no further increase in the availability of acceptor levels in solution occurs as the potential is made more negative (24).

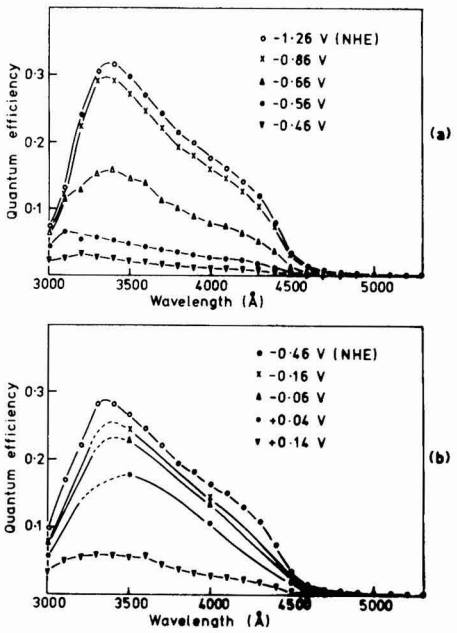

Fig. 4. The quantum efficiency-wavelength relations of GaP in 1*N* NaOH (a) and 1*N* H_2SO_4 (b) at several electrode potentials.

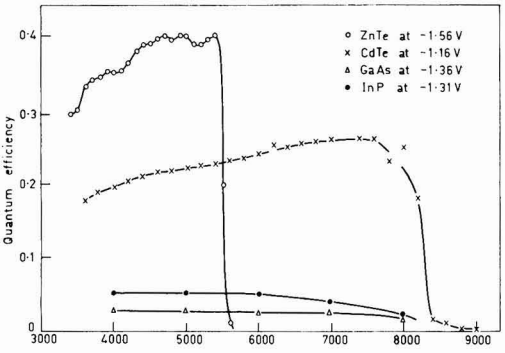

Fig. 5. The quantum efficiency wavelength relations for ZnTe, CdTe, GaAs, and InP in 1*N* NaOH.

[3] Reasonable agreement was observed with the results of Yoneyama *et al.* (21), but the maximum in the quantum efficiency-wavelength relation was at 4500Å in their measurement and at 3500Å in ours. In the Yoneyama work, published data on xenon lamps (instead of calibration) was used.

Table 1. The difference in the range of potentials (volts) for photocurrent-voltage relations in NaOH and H_2SO_4

ZnTe	0.6
CdTe	0.5
GaAs	0.8
InP	0.5
GaP	0.6
SiC	Not applicable
Si	0.5

The "critical potential".—$\Delta H'(e)$ (Fig. 12) at the flatband potential is given by (23)

$$\Delta H'(e) = -L_o + E_a - J + A + R + ({}^{S.C}\Delta^S\phi)_{fbp} \quad [1]$$

where L_o, E_a, J, A, R, and $({}^{S.C}\Delta^S\phi)_{fbp}$ are the hydration energy of the proton, electron-affinity of the semiconductor, ionization energy of hydrogen, adsorption energy of hydrogen, H-H_2O repulsive force, and the potential drop in the electric double layer at the flatband potential.

$({}^{S.C}\Delta^S\phi)_{fbp}$ can be estimated as follows.

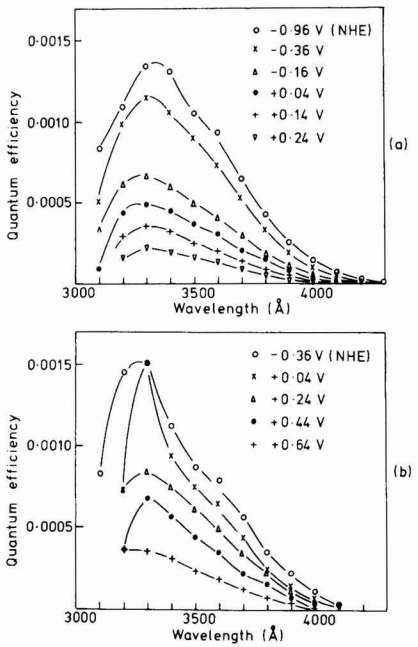

Fig. 6. The quantum efficiency-wavelength relations of SiC in 1*N* NaOH (a) and 1*N* H_2SO_4 (b).

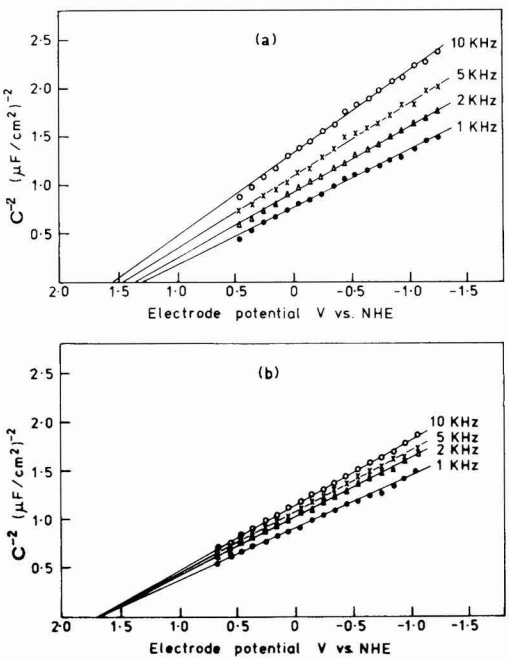

Fig. 7. The Mott-Schottky plots of SiC in 1*N* NaOH (a) and 1*N* H_2SO_4 (b) at several frequencies.

Table II. The flatband potential and slope of Mott-Schottky plots of semiconductors

Semiconductors	1*N* NaOH		1*N* H_2SO_4	
	Flatband potential, V, NHE	Slope ($\mu F/cm^2)^{-2}/V$	Flatband potential, V, NHE	Slope ($\mu F/cm^2)^{-2}/V$
ZnTe	−0.79	28	0.04	150
CdTe	0.21	6000	−0.35	2200
GaAs	−0.04	0.12	0.43	0.22
InP	−0.07	0.48	—	—
GaP	0.18	6.0	1.13	4.6
SiC	1.38	0.86	1.68	0.7

The flatband potential, V_{fbp}, with respect to normal hydrogen electrode (NHE) is given by

$$V_{fbp} = {}^{Pt}\Delta^{S.C}\phi + ({}^{S.C}\Delta^S\phi)_{fbp} + ({}^S\Delta^{Pt}\phi)_{\substack{p_{H_2}=1 \\ C_{H^+}=1}} \quad [2]$$

where ${}^{Pt}\Delta^{S.C}\phi$ is the potential difference between the semiconductor and the Pt wire, $({}^S\Delta^{Pt}\phi)_{\substack{p_{H_2}=1 \\ C_{H^+}=1}}$ is the potential drop in the electric double layer of the semiconductor at the flatband potential and $({}^S\Delta^{Pt}\phi)_{\substack{p_{H_2}=1 \\ C_{H^+}=1}}$ is the potential drop in the electric double layer at the Pt electrode in the presence of 1 atm of hydrogen gas and with $C_{H^+} = 1$. (See Fig. 12).

Since

$$\mu_e{}^{-Pt} = \mu_e{}^{-S.C} \quad [3]$$

where $\mu_e{}^{-Pt}$ and $\mu_e{}^{-S.C}$ are the electrochemical potentials of electrons in Pt and the semiconductor, respectively. Hence

$${}^{Pt}\Delta^{S.C}\phi = (\mu_e{}^{Pt} - \mu_e{}^{S.C})/F \quad [4]$$

where $\mu_e{}^{Pt}$ and $\mu_e{}^{S.C}$ are the chemical potentials of Pt and the semiconductor, respectively. Therefore

$$V_{fbp} = \{({}^{S.C}\Delta^S\phi)_{fbp} - \mu_e{}^{S.C}/F\} - [({}^{Pt}\Delta^S\phi)_{\substack{p_{H_2}=1 \\ C_{H^+}=1}} - \mu_e{}^{Pt}/F] \quad [5]$$

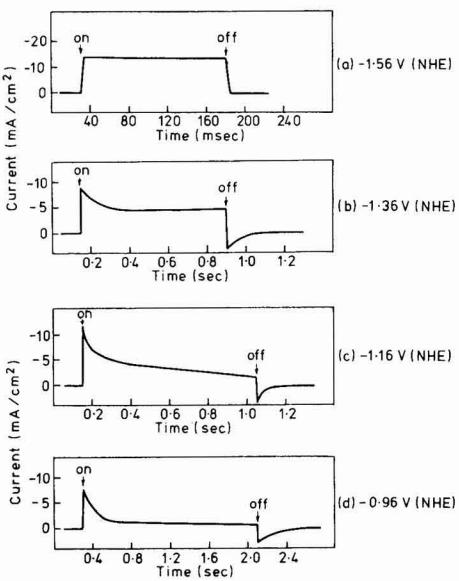

Fig. 8. The transient behavior of the current of ZnTe after illumination and interruption of light in 1*N* NaOH at several potentials. The current before illumination is taken as zero. Intensity of light: 0.08 W/cm².

Table III. The stability of photocathodes, as measured by their change with time at various potentials (given)

Semiconductor	Value of $\frac{1}{i}\frac{di}{dt}$ (sec^{-1})	
	1*N* NaOH	1*N* H_2SO_4
ZnTe	6×10^{-4} (−1.26V)	5×10^{-5} (−0.56V)
CdTe	2.5×10^{-6} (−1.16V)	1×10^{-6} (−0.76V)
GaAs	2×10^{-4} (−1.36V)	3×10^{-4} (−0.76V)
InP	2×10^{-5} (−1.36V)	2×10^{-4} (−0.46V)
GaP	5×10^{-6} (−0.76V)	5×10^{-5} (−0.26V)
SiC	0* (−1.16V)	0* (−0.76V)
Si	5×10^{-6}** (−1.06V)	1.7×10^{-4}** (−0.41V)

* Current is very small 9 $\mu A/cm^2$ in 1*N* NaOH and 3 $\mu A/cm^2$ in 1*N* H_2SO_4.
** After 10 hr in dark, almost no photocurrent was observed.

Thus, the potential drop in the electric double layer of the semiconductor at the flatband potential is given by

$$({}^{S.C}\Delta^{S}\phi)_{fbp} = V_{fbp} + [\,({}^{Pt}\Delta^{S}\phi)_{\substack{p_{H_2}=1 \\ C_{H^+}=1}} - \mu_e{}^{Pt}/F] + \mu_e{}^{S.C}/F$$
$$= V_{fbp} + [\,({}^{Pt}\Delta^{S}\phi)_{\substack{p_{H_2}=1 \\ C_{H^+}=1}} - \mu_e{}^{Pt}/F] - (\Phi/F - \chi^{S.C}) \quad [6]$$

where Φ is the work function of the semiconductor and $\chi^{S.C}$ is potential drop in the semiconductor.

$$[({}^{Pt}\Delta^{S}\phi)_{\substack{p_{H_2}=1 \\ C_{H^+}=1}} - \mu_e{}^{Pt}/F]$$

was calculated by Trasatti (25) using a method suggested by Bockris and Argade (26), as 4.3V. Therefore

$$({}^{S.C}\Delta^{S}\phi)_{fbp} = 4.3/F + V_{fbp} - (\Phi/F - \chi^{S.C}) \quad [7]$$

A schematic of the energy levels of a semiconductor which has surface states in a vacuum is shown in Fig. 13. From this figure, $\chi^{S.C}$ is given by

$$F\chi^{S.C} = \Phi + \Delta E - E_a - E_g \quad [8]$$

where ΔE is the energy difference between the Fermi level and the top of the valence band in the bulk. Hence, Eq. [7] becomes

$$({}^{S.C}\Delta^{S}\phi)_{fbp} = 4.3/F + V_{fbp} - (E_a + E_g - \Delta E)/F \quad [9]$$

As a first approximation, ΔE is assumed to be zero for all p-type semiconductors concerned.

The values of $({}^{S.C}\Delta^{S}\phi)_{fbp}$ were calculated from Eq. [9] for semiconductors listed in Table V. $({}^{S.C}\Delta^{S}\phi)_{fbp}$ is negative in all cases, ${}^{S.C}\Delta^{S}\phi$ in NaOH is more negative than that in H_2SO_4 for most electrodes except CdTe.

From Eq. [1] and [9]

$$\Delta H(e) = -L_o + E_a - J + A + R + 4.3/F + V_{fbp} - (E_a + E_g - \Delta E)/F$$
$$\simeq -L_o - J + A + R + 4.3/F + \underline{V_{fbp}} - E_g/F + \Delta E/F \quad [10]$$

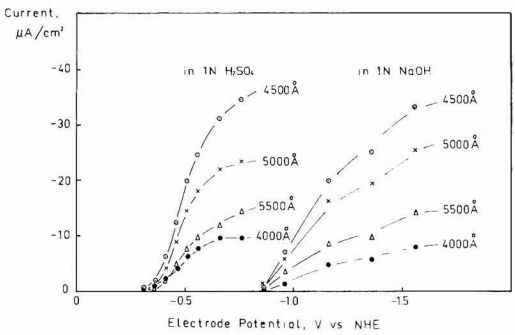

Fig. 9. The photocurrent-potential relations of ZnTe in 1*N* NaOH and in 1*N* H_2SO_4 for light of several wavelengths.

Table IV. Slope of log i_p-V relations

	1*N* NaOH	1*N* H_2SO_4
ZnTe	0.165	0.13
GaAs	0.3	0.25
GaP	0.1	0.18
CdTt	Not available because of high resistance	
Si	0.17	0.21

where L_o, J, and R do not depend on semiconductor and the dependence of A on the semiconductor is less than 0.1 eV (27), Therefore, $\Delta H(e)$ is given by

$$\Delta H(e) \simeq \text{const.} + V_{fbp} - E_g/F \quad [11]$$

The probability of the existence of acceptors at energy E, $G(E)$, is given by

$$G(E) = \exp(H(e) - E_v)/kT \quad [12]$$

where E is the energy of the electrons at the surface at a potential V.

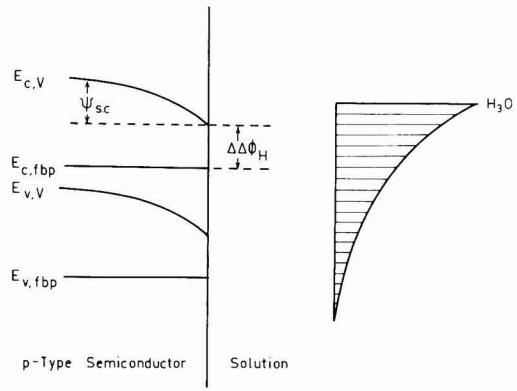

$$\begin{cases} V - V_{fbp} = \psi_{s.c} + \Delta\Delta\phi_H \\ \Delta\Delta\phi_H = ({}^{SC}\Delta^{S}\phi)_V - ({}^{SC}\Delta^{S}\phi)_{fbp} \end{cases}$$

Fig. 10. The schematic diagram of energy levels of the valence band and conduction band of a semiconductor and of an acceptor.

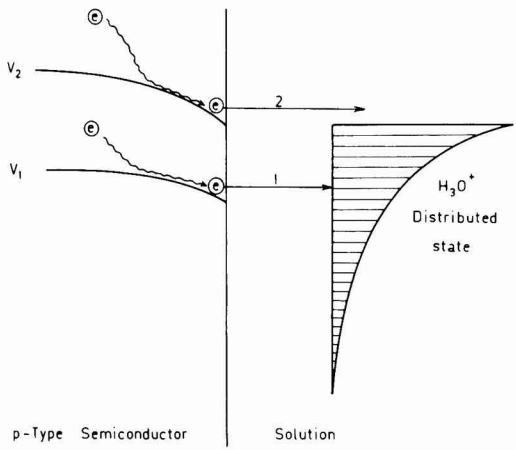

Fig. 11. Schematic illustration of the model proposed to describe the observed photocurrent behavior of semiconductor electrodes.

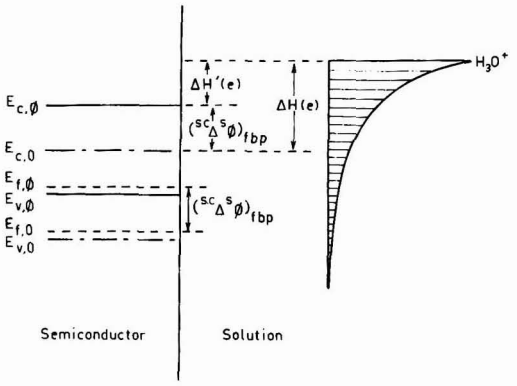

Fig. 12. The energy levels at a semiconductor solution interface

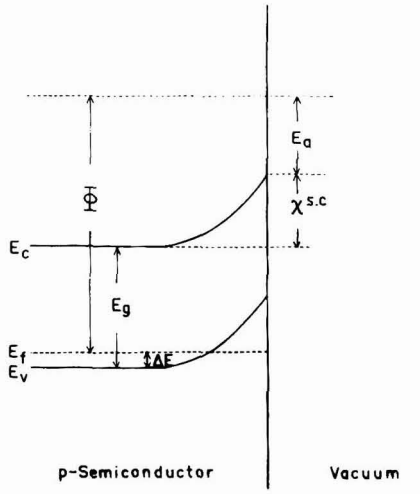

Fig. 13. Schematic diagram of the energy levels of a semiconductor with surface states in a vacuum.

E_v is given by

$$E_v = -F(V - V_{fbp}) \qquad [13]$$

where each of these potentials is on (*e.g.*) the N.H. scale. Therefore, E_v at the critical potential E_{crit} is given by

$$E_{crit} = -F(V_{crit} - V_{fbp})$$

At the critical potential, it can be assumed that $G(E)$ corresponds to an energy value of 0.1-0.2 eV from the ground state of H_3O^+.

Therefore

$$\Delta H(e) \simeq -F(V_{crit} - V_{fbp}) \qquad [14]$$

From Eq. [12] and [14], a linear relation between $(V_{fbp} - E_g/F)$ and $(V_{crit} - V_{fbp})$ is expected. Figure 14 shows this relation. The relation shows the importance of any energy gap in respect to the critical potential. Although a small energy gap is required from the point of solar energy absorption, the smaller the energy gap, the more negative the critical potential (with respect to the flatband potential) and, therefore, the smaller the efficiency of the hydrogen production.

Table V. Calculated values of the potential drop (volts) in the electric double layer at the flatband potential (see Eq. [10])

Semiconductor	1*N* NaOH $^{s.c}\Delta^{s}\phi$, V	1*N* H_2SO_4 $^{s.c}\Delta^{s}\phi$, V
ZnTe	−2.25	−1.42
CdTe	−1.27	−1.83
GaAs	−1.20	−0.77
InP	−1.42	—
GaP	−2.07	−1.12

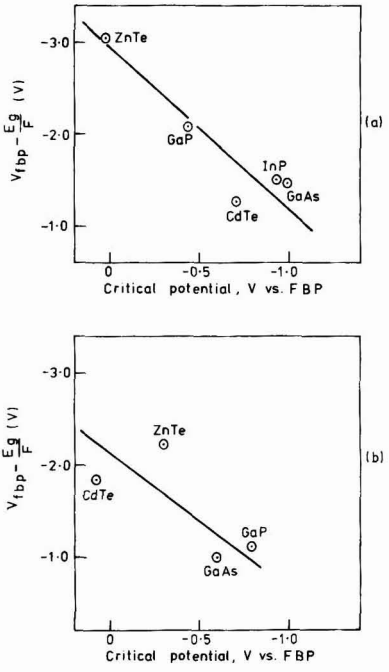

Fig. 14. The relations between $V_{fbp} - E_g/F$, and the critical potential with respect to the flatband potential in 1*N* NaOH (a) and 1*N* H_2SO_4 (b).

The quantum efficiency-wavelength relation.—Quantum efficiency-wavelength relation shown in Fig. 4-6 exhibit two features. (*i*) The quantum efficiency wavelength relation passes through a maximum. (*ii*) The height of the maximum decreases as the potential becomes more positive and therefore nearer to the flatband potential.

The position of the maximum can be interpreted by considering the photocurrent (i_p) as a function of the surface recombination.

Thus, i_p is given by

$$i_p = f(i_{\text{electron arriving at surface}}) - f(v_{\text{surface recombination}}) \qquad [15]$$

As the wavelength decreases, the photon absorption increases and the number of electrons created per average photon increases and therefore the quantum efficiency. At sufficiently small wavelengths, the position of the average absorption of photons gets nearer to the surface. Hence, the effect of surface recombination will become more important and decrease the net current or quantum efficiency.

Stability.—The most outstanding differences in stability (Table III) are for ZnTe and CdTe.

Figures 15 and 16 (drawn for us by Dr. T. Ohashi) show the equilibrium potentials for several reactions relevant to ZnTe and CdTe. For CdTe, the equilibrium potential of hydrogen evolution at pH = 14 is more negative than that of the decomposition of CdTe. Hence, CdTe will not decompose in the potential range of hydrogen evolution. For ZnTe, the equilibrium potential of hydrogen evolution is close to that of ZnTe decomposition.

Transient behavior.—Surface recombination.—The transient behavior may be due to either a process in the semiconductor or a process in the surface of the electrode, or a process in solution.

In the former case, the behavior would be due to time dependence of the electron concentration at the surface. The time constant is 10^{-3} sec and could arise from the recombination process. Then, the number of excess electrons t sec after illumination, $N(t)$, is

$$N(t) = N(1 - e^{-t/\tau}) \quad [16]$$

where N represents excess electrons at the steady state and τ is the lifetime of the excited electron. The number of electrons t sec after illumination is turned off, $N'(t)$, is

$$N'(t) = Ne^{-t/\tau} \quad [17]$$

The time constant of diffusion is less than that of recombination process, so that

$$N_o(t) = N_o(1 - e^{t/\tau}) \quad [18]$$

when the light is on and

$$N'_o(t) = N_o e^{-t/\tau} \quad [19]$$

when the light is off, where N_o is the steady-state concentration of excess electrons at the surface.

Since the photocurrent, $i_p(t)$ is

$$i_p(t) \alpha N_o(t) \quad [20]$$

the time dependence of the photocurrent is

$$i_p(t) = i_{st.}(1 - e^{-t/\tau}) \quad [21]$$

with illumination on, where $i_{st.}$ is the steady-state photocurrent. Also

$$i_p(t) = i_{st.}e^{-t/\tau} \quad [22]$$

when the light is off.

The photocurrent according to Eq. [21] and [22] is shown in Fig. 17. The result of the behavior found in the present work was quite different from these predictions, especially when the electrode potential was near to the flatband potential (Fig. 17).

Hence, since the lifetime of excited electrons is $<10^{-3}$ sec, the transient behavior observed is due to surface electrochemical processes, such as the reduction of oxygen. Thus

$$\begin{aligned} i_p &= i_{p,H_2} + i_{p,red} \\ &= k_{H_2}C_{H_3O^+} + k_{red}C_{red} \end{aligned} \quad [23]$$

where k_{H_2} and k_{red} are the rate constant for hydrogen evolution reaction and for some other reduction reaction, respectively.

Using Faraday's laws

$$i_p(t) = i_{p,H_2}C_{H_3O^+} + k_{red}C_{o,red} \exp\left(-\frac{M}{\mathbf{F}}k_{red}t\right) \quad [24]$$

where $C_{o,red}$ is the concentration of the species to be reduced at time zero.

From Eq. [24], $\log \dfrac{i(t) - i(\infty)}{i(o)}$ should be proportional to time, as shown in Fig. 18 [see also Ref. (28)].

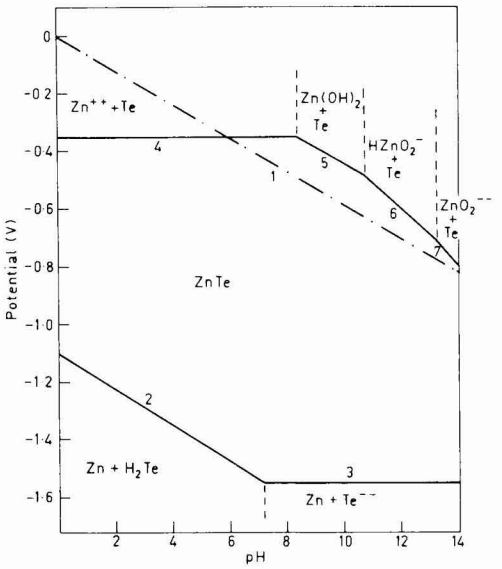

Fig. 15. Potential-pH equilibrium diagram for the system ZnTe-water at 25°C.

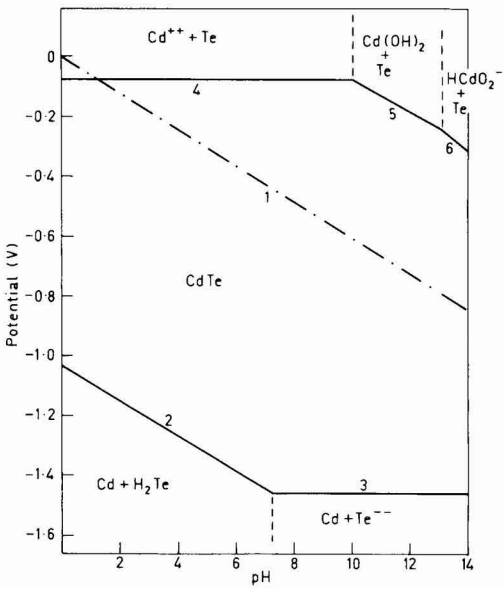

Fig. 16. Potential-pH equilibrium diagram for the system CdTe-water at 25°C.

Acknowledgments

We thang Mr. H. Kimura of Mitsubishi Electric Company Limited, Dr. O. Mizuno of Nippon Electric Company Limited, Dr. K. Akita of Fujitsu Laboratory

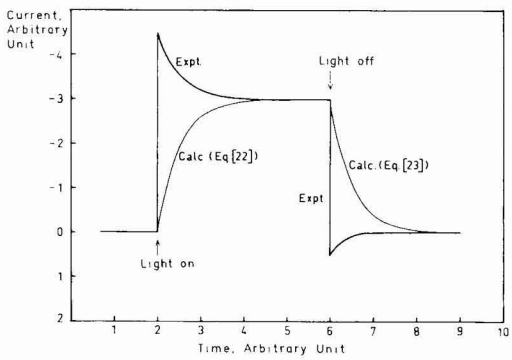

Fig. 17. Schematic diagram of the transient behavior of the current after illumination and interruption of light. 1, Equations [21] and [22]; 2, experimental.

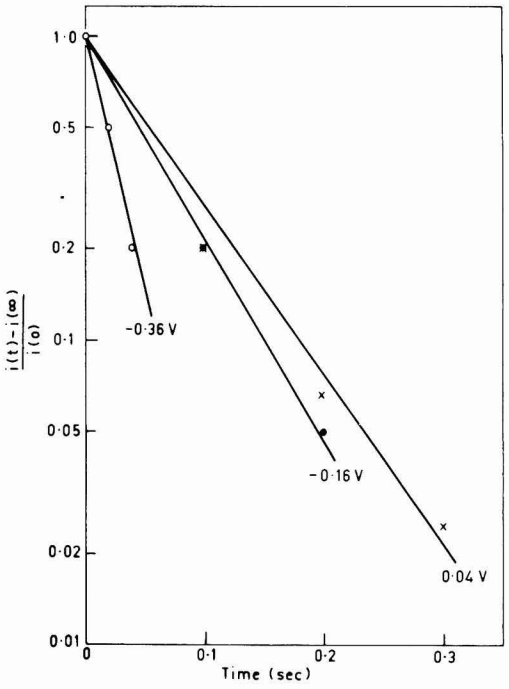

Fig. 18. The relation between $\frac{i(t) - i(\infty)}{i(0)}$ and time for GaP in 1*N* H_2SO_4.

Limited, Professor von Munch of Technical University of Hannover, and Toyo Silicon Company Limited for their donation of semiconductor single crystals. Thanks are due to Dr. K. Ohashi for discussion. One of us (K.U.) thanks Flinders University for its Flinders University Research Scholarship.

Manuscript submitted Dec. 13, 1976; revised manuscript received April 1, 1977.

Any discussion of this paper will appear in a Discussion Section to be published in the June 1978 JOURNAL. All discussions for the June 1978 Discussion Section should be submitted by Feb. 1, 1978.

Publication costs of this article were assisted by Flinders University of South Australia.

REFERENCES

1. A. Fujishima and K. Honda, *Nature (London)*, **238**, 37 (1972).
2. W. Gissler, P. L. Lensi, and S. Pizzini, *J. Appl. Electrochem.*, **6**, 9 (1976).
3. A. J. Nozik, *Nature (London)*, **257**, 383 (1975).
4. M. S. Wrighton, D. S. Ginsley, P. T. Wolczauski, A. B. Ellis, D. L. Morse, and A. Lind, *Proc. Natl. Acad. Sci., U.S.A.*, **72**, 1518 (1975).
5. K. L. Hardee and A. J. Bard, *This Journal*, **122**, 75 (1975).
6. A. Fujishima, K. Kohayakawa, and K. Honda, *ibid.*, **122**, 1487 (1975).
7. H. Yoneyama, H. Sakamoto, and H. Tamura, *Electrochim. Acta*, **20**, 341 (1975).
8. H. Gerischer, *Z. Elektrochem.*, **59**, 9 (1954).
9. M. Sluyters-Rehbach and J. H. Sluyters, "Electroanalytical Chemistry: A Series of Advance," Vol. 4, A. J. Bond, Editor, chap. 1, Marcel Dekker, Inc., New York (1970).
10. W. D. Baker and A. G. Milnes, *This Journal*, **119**, 1269 (1972).
11. V. I. Sapritskii and N. G. Bardina, *Elektrokhimiya*, **18**, 655 (1972).
12. H. C. Gatos and M. C. Lavine, *Prog. Semiconductors*, **9**, 1 (1965).
13. M. Aven and W. Garwacki, *This Journal*, **114**, 1063 (1967).
14. J. Lowen and R. H. Rediker, *ibid.*, **107**, 26 (1960).
15. O. Mizuno, Private communication.
16. H. Gerischer and I. Mattes, *Z. Phys. Chem. (N.F.)*, **49**, 112 (1966).
17. K. H. Beckmann and R. Memming, *This Journal*, **116**, 368 (1969).
18. R. Memming and G. Schwandt, *Electrochim. Acta*, **13**, 1299 (1968).
19. R. Memming, *This Journal*, **116**, 785 (1969).
20. S. Mayumi, C. Iwakura, H. Yoneyama, and H. Tamura, *Denki Kagaku*, **44**, 339 (1976).
21. H. Yoneyama, H. Sakamoto, and H. Tamura, *Electrochim. Acta*, **20**, 341 (1975).
22. M. Gleria and R. Memming, *J. Electroanal. Chem.*, **65**, 163 (1975).
23. J. O'M. Bockris and A. K. N. Reddy, "Modern Electrochemistry," Vol. 2, chap. VII, Plenum Press, New York (1970).
24. A. R. Despic and J. O'M. Bockris, *J. Chem. Phys.*, **32**, 389 (1960).
25. S. Trasatti, *J. Electroanal. Chem.*, **52**, 313 (1974).
26. J. O'M. Bockris and S. O. Argade, *J. Chem. Phys.*, **49**, 5133 (1968).
27. J. O'M. Bockris and K. Uosaki, *Adv. Chem. Ser.*, Am. Chem. Soc., In press (1976).
28. K. Uosaki, Ph.D. Thesis, The Flinders University of South Australia (1976).

Chemical Action of Glow Discharge Electrolysis on Ethanol in Aqueous Solution

M. A. Almubarak and A. Wood

Chemistry Department, Liverpool Polytechnic, Liverpool L3 3AF, United Kingdom

ABSTRACT

The action of anodic glow discharge electrolysis (gde) on ethanol in neutral aqueous phosphate buffer gave acetaldehyde, butan-2,3-diol, hydrogen peroxide, and acid. The yields of these products were found to vary substantially with the presence or absence of oxygen and in particular with oxygen flow rate and substrate concentration. A mechanism has been proposed for the reaction of substrate in both the presence and absence of oxygen.

Ethanol vapor and water vapor, over aqueous ethanol solutions, were subjected to glow discharge electrolysis (gde) by Klemenc (1), who examined the gaseous products only. Gde has been performed also on pure methanol (2), with a variety of supporting electrolytes; products were a complex mixture of simple breakdown species. Scholes and co-workers (3) studied the effects of x-rays (200 kV) on ethanol in aqueous solution and found that in the presence of oxygen the products were hydrogen peroxide and acetaldehyde alone. Using deaerated solutions they found acetaldehyde and butan-2, 3-diol, with traces of hydrogen peroxide (under acid conditions). Seddon and Allen (4) studied the hydrogen yields arising from the γ-radiolysis of neutral aqueous solutions of ethanol both in the presence and in the absence of oxygen. Recently Schultze and Schulte-Frohlinde (5) studied the effects of the γ-irradiation of dilute aqueous ethanol under a gaseous mixture of oxygen and nitrous oxide. The products were acetaldehyde, acetic acid, glycolaldehyde, ethylene glycol, and hydrogen peroxide.

A careful study was made of the total yields in the present work to determine the ultimate fates of all the radicals generated by gde: As will be seen, we have accounted for G(OH) in terms of our products. We also studied carefully the proportion of acetaldehyde and hydrogen peroxide since this gives valuable evidence about the reaction possibilities, and we were able to show that in gde under oxygen flow rates high enough to scavenge all the 1-hydroxyethyl radicals (CH_3CHOH) and at ethanol concentrations high enough to scavenge all the hydroxyl radicals, there is a particularly straightforward interaction between the 1-hydroxyethylperoxyl radicals (CH_3CHOH with O_2) yielding acetaldehyde and hydrogen peroxide in 2:1 proportions.

Experimental

The ethanol solutions were prepared by dissolving the correct amounts of pure absolute ethanol in neutral phosphate buffer solution, except for runs on acid determination under oxygen where very dilute alkali was used. The solutions after gde were analyzed for hydrogen peroxide (6), acetaldehyde (7), butan-2, 3-diol, and acid. since these compounds were the products of x-irradiation of phosphate buffer/ethanol solutions (3). Other species sought by the workers who used x-irradiation were acetic acid, ethylene glycol, glycolaldehyde, ethyl hydroperoxide, diethyl peroxide, peracetic acid, and ethyl acetate, but no evidence was found for any of these. The acetaldehyde determination is essentially colorimetric: the absorbance, which declined rapidly, was recorded as a function of time and extrapolated backward to the point of preparation of the final solution. Butanediol was determined by reaction with potassium periodate at about pH 9 (bicarbonate); the unreacted periodate was determined, as I_3^-, by addition of excess potassium iodide.

The acid produced in gde was measured in separate experiments using very dilute alkali to carry the current and also to measure the acid formed as a fall in the pH of the solution during the gde.

The equipment required for rectification and control at the high currents and high voltages required was constructed specially and has been described elsewhere (8). The gde cell and vacuum line were of conventional design (9). The quantity of electricity was obtained by using a sampling digital voltmeter together with the electric clock. Typical run conditions used a current of 30 mA, a vacuum main pressure of 10 cm Hg, a stirring rate of "9" (ideally about 1500 rpm), and an oxygen flow rate of 900 $cm^3\ min^{-1}$. Run times varied from 30 to 300 sec, typically, the quantities of electricity passed being of the order of 10-100 μf. Substrate solutions were degassed with argon or saturated with oxygen, as required. When using argon it was usual to close the system so as to have no gas flow, since the argon flow did not affect the processes (argon not being involved chemically) except at very high flow rates where some arc instability occurred. Manostat gas flow regulation (9) was not always satisfactory and in later runs manual control was used.

Results

Gde on ethanol in neutral aqueous solution produces acetaldehyde, hydrogen peroxide, butan-2, 3-diol, and acid. The yields (in moles per faraday) of these products were found to vary substantially with the presence or absence of oxygen and with its flow rate and with ethanol concentration. Other factors which would affect the yields of the above products are the stirring rate, the gas pressure, the current, and the quantity of electricity.

The original work on the oxygen flow rate effect was reported by Almubarak (10). It was found from preliminary results here that the hydrogen peroxide yield increased with increasing oxygen flow rate. Hence oxygen is involved in the reaction and in the formation of hydrogen peroxide, and the hydrogen peroxide yield was used, therefore, as a convenient measure of the degree of mass transfer of oxygen from gas phase to liquid phase and as an indication of solution-oxygen content. (It was later shown that the hydrogen peroxide comes from two sources: ethanol, involving reactions, and preliminary processes, the first of these being the major source at sufficiently high ethanol concentrations.) This measure of oxygen availability in the solution was confirmed by measurements of

Key words: glow discharge electrolysis, ethanol, mechanism.

the butanediol yield which decreased to zero at very high oxygen flow rates (indicating total scavenging by oxygen of reaction intermediate CH_3CHOH).

Flow rate experiments were repeated, using argon, but no change in hydrogen peroxide yield was observed except at high flow rate values where some discharge instability may be expected.

Increasing the current at a given oxygen flow rate caused the hydrogen peroxide yield to fall (suggesting that the oxygen flow rate was not sufficient to scavenge all the 1-hydroxyethyl radicals): However, the yield could be restored to its original value by increasing the oxygen flow rate. In gde, increases in the discharge current cause increases in the glow spot area; the current density and the radical concentration tend to remain constant. Hence an increase in current at constant hydrogen peroxide yield increases the demand for oxygen. There was a limit, however, to the extent to which the hydrogen peroxide yield could be maintained at its high value by increases in oxygen flow rate; this limit arose from the instability of the discharge at very high gas flow rates. In practice, therefore, a low current (30 mA) was used, together with an oxygen flow rate which was high enough to scavenge most of the 1-hydroxyethyl radicals but not high enough to introduce discharge instability.

Hydrogen peroxide yields varied a little with stirring rate, a fairly rapid rate appearing to be the most suitable. Pressure changes did not affect the peroxide yield significantly at high oxygen flow rates, though it is possible that sufficiently high pressures would improve the mass transfer of oxygen from the gaseous to the solution phases at low oxygen flow rates.

Gde on aqueous ethanol in neutral phosphate buffer at the oxygen flow rate selected produced hydrogen peroxide, acetaldehyde, some diol (none at the highest oxygen flow rates where, however, some arc instability occurs), and acid. The yields of hydrogen peroxide related linearly to the quantity of electricity, showing that there were no peroxide-destruction reactions under the conditions used in this work. Linearity of butanediol yield with quantity of electricity was assumed, when required, since this product is nonvolatile. Acid appeared only in the combined presence of oxygen and substrate.

Under argon, low or zero flow rates were used and the products were acetaldehyde, hydrogen peroxide, and butan-2, 3-diol. It was verified that the yields of the nonvolatiles were linear functions of the quantity of electricity.

The graphs of yield *vs.* quantity of electricity and the results of the acetaldehyde work, whether under oxygen or argon, showed a tendency of the acetaldehyde yield to show a possible stationary state. The effect may arise from chemical decomposition of the acetaldehyde (*e.g.*, reaction with the aqueous electron) but it seems more likely to arise from vaporization because of the high temperature of the arc and the low boiling point of the acetaldehyde. A mathematical analysis, in essence, obtained the initial slopes of the plots of number of moles of acetaldehyde *vs.* quantity of electricity.

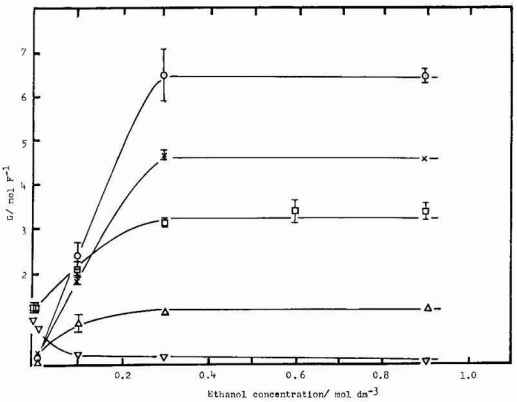

Fig. 1. G *vs.* ethanol concentration: ○, G(CH_3CHO, O_2); ×, G(CH_3CHO, Ar); □, G(H_2O_2, O_2); △, G($C_4H_{10}O_2$, Ar); ▽, G(H_2O_2, Ar).

Discussion

Plots of G-values *vs.* substrate concentration for each of the products are given in Fig. 1 and Table I.

Taking the argon runs first, G(H_2O_2) falls as the ethanol concentration increases, becoming very small. It is possible that at least some of this residual hydrogen peroxide corresponds to the generation of hydroxyl radicals at a rate (represented by 30 mA) slightly too high to permit total scavenging by ethanol within the concentration range used here. G(CH_3CHO) increases sharply, eventually leveling off. G($C_4H_{10}O_2$) increases in a like manner, the plateau value being about 1.16 mole F^{-1}.

In general gde of aqueous solutions may be regarded as producing the following species from the primary reaction zone (9, 11, 12)

$$H_2O \rightsquigarrow e_{aq}^-, H, OH, H^+, OH^-, H_2O_2, H_2, H_2O \quad [1]$$

In the absence of oxygen and in the presence of sufficient ethanol, the initial main reaction was OH + C_2H_5OH. Other radicals, H and e_{aq}^-, undergo slower reactions, under our conditions. The reactions of hydrogen and hydroxyl radicals with ethanol are well known. The hydroxyl radicals abstract hydrogen atoms from ethanol to form CH_3CH_3O (2.5%), CH_2CHOH (84.3%), and CH_2CH_2OH (13.2%) (13). The hydrogen radical abstracts a hydrogen atom primarily from the CH_2 group (14). The rate of reaction of the hydrogen radicals is about 1% of the rate of reaction of the hydroxyl radicals and may be neglected. In the same way reactions between hydrogen radicals and other substrates here are likely to be much slower than reactions between hydroxyl radicals and the same substrates. The CH_3CH_2O radicals pick up hydrogen atoms from ethanol molecules. The CH_2CH_2OH radicals may undergo a similar reaction, so improving the conversion of the hydroxyl radicals to 1-hydroxyethyl radicals, since separate measurements of G(OH, ferrocyanide) agree well with a G(OH) calculated from

Table I. Variation of G-values for acetaldehyde, butan-2,3-diol, and hydrogen peroxide with ethanol concentration and gas

[C_2H_5OH]/ mole dm^{-3}	G(H_2O_2)/mole F^{-1}		G(CH_3CHO)mole F^{-1}		G($C_4H_{10}O_2$)/mole F^{-1}
	Oxygen	Argon	Oxygen	Argon	Argon
0	1.24 ± 0.08	0.89 ± 0 03	0		0
0.01	1.25 ± 0.08	0.79 ± 0.04	0.18 ± 0.02	0.25 ± 0 01	0.05 ± 0.09
0.1	2.11 ± 0.17	0.21 ± 0.05	2.39 ± 0 29	1.83 ± 0 08	0.90 ± 0.19
0.3	3.12 ± 0 08	0.17 ± 0.02	6.47 ± 0.60	4.67 ± 0.11	1.14 ± 0.07
0.6	3.38 ± 0.26	—	—	—	—
0.9	3.39 ± 0.16	0.10 ± 0.01	6.44 ± 0.13	4.56 ± 0.04	1.20 ± 0.05

the product yields discussed here, under both argon and oxygen. Thus the main species formed from ethanol in the secondary reaction zone are 1-hydroxyethyl radicals. We assumed that the reactions of hydroxyl radicals with butan-2, 3-diol [$k = 8.1 \times 10^8$ dm^3 mole^{-1} sec^{-1} (15)] and acetaldehyde (possibly of similar rate constant) do not affect the yields of these two products significantly: The ethanol concentration was much higher than the concentration of these two products, there was no deviation from linearity in the plots of yields of nonvolatile products *vs.* quantity of electricity (suggesting therefore insignificant destruction reactions) and G(OH), ferrocyanide (see below) agrees well with G(OH) calculated from product yields. The reaction of hydrogen atoms with ethanol constitutes the fastest process involving these radicals, but it is still much slower than the rate of reaction of hydroxyl radicals with ethanol.

The products of the gde of aqueous ethanol in neutral phosphate buffer, under argon, are hydrogen peroxide, butanediol, and acetaldehyde, formed according to the following proposed reactions.

$$OH + OH \rightarrow H_2O_2 \qquad [2]$$

$$2CH_3CHOH \rightarrow C_4H_{10}O_2 \qquad [3]$$

$$2CH_3CHOH \rightarrow CH_3CHO + CH_2OH \qquad [4]$$

Formation of acetaldehyde by additional radical/1-hydroxyethyl radical reactions seems unlikely. However, we do know that two 1-hydroxyethyl radicals interact to form butan-2, 3-diol, so we propose that under argon this interaction can yield acetaldehyde also, by disproportionation (reaction [4]).

Of the possible reactions of the aqueous electrons, those with peroxide and acetaldehyde (16) are the most probable

$$e_{aq}^- + CH_3CHO \rightarrow CH_3CHO^- \qquad [5]$$

$$CH_3CHO^- + H_2O \rightleftharpoons CH_3CHOH + OH^- \qquad [6]$$

$$e_{aq}^- + H_2O_2 \text{—} OH + OH^- \qquad [7]$$

Under oxygen, G(H_2O_2) and G(CH_3CHO) increase with increasing ethanol concentration and level off. G(CH_3CHO, O_2) was always greater than G(CH_3CHO, Ar). No butanediol is detectable at sufficiently high oxygen flow rates. These two facts point to a change of mechanism. Under oxygen G(CH_3CHO) is almost exactly double G(H_2O_2). The actual peroxide:acetaldehyde ratio under oxygen is 3.39:6.46. In the absence of oxygen, and persisting even at the highest ethanol concentrations, there is a small residue of hydrogen peroxide; if we assume that this residue also occurs in the runs under oxygen we can subtract it from G(H_2O_2, O_2), leaving 3.25 mole F^{-1}. The hydrogen peroxide:acetaldehyde ratio is then 3.25:6.46, which is very close to 1:2. Reactions of the 1-hydroxyethyl radicals other than those giving acetaldehyde and hydrogen peroxide in the correct proportions can be neglected. We assume that the 1-hydroxyethyl radicals are scavenged completely by oxygen, under the high gas flow rate

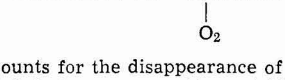

$$CH_3CHOH + O_2 \rightarrow CH_3\underset{\substack{|\\O_2}}{CHOH} \qquad [8]$$

and this accounts for the disappearance of the butanediol. The 1:2 hydrogen peroxide:acetaldehyde ratio can be accounted for by

$$2CH_3\underset{\substack{|\\O_2}}{CHOH} \rightarrow 2CH_3CHO + H_2O_2 + O_2 \qquad [9]$$

Because of the 1:2 hydrogen peroxide:acetaldehyde ratio we can assume also that the aqueous electron does not react significantly with products (reactions [5]-[7]). However, it could be argued that reactions [5] and [6] regenerate the 1-hydroxyethyl radical and hence, regenerate acetaldehyde. Nevertheless any cyclic process involves losses and the total hydroxyl radical yield, as estimated from the reaction products, would be less than G(OH, ferrocyanide). Reaction [7] would constitute clear loss of hydrogen peroxide also, since the hydrogen peroxide/hydroxyl radical scheme would mean loss of at least half a molecule of hydrogen peroxide at each cycle.

The peroxyl radical, HO_2, is of importance in radiation chemistry

$$H + O_2 \rightarrow HO_2 \qquad [10]$$

$$e_{aq}^- + O_2 \rightarrow O_2^- \qquad [11]$$

O_2^- is in equilibrium with HO_2. The peroxyl radical could take part in the main acetaldehyde-hydrogen peroxide-generating processes by reactions such as the following

$$2HO_2 \rightarrow O_2 + H_2O_2 \qquad [12]$$

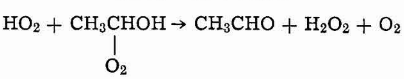

$$HO_2 + CH_3\underset{\substack{|\\O_2}}{CHOH} \rightarrow CH_3CHO + H_2O_2 + O_2 \qquad [13]$$

Both these reactions would upset the 1:2 hydrogen peroxide:acetaldehyde ratio and therefore are not important here.

An alternative reaction scheme for the 1-hydroxyethylperoxyl radicals is as follows and involves formation of ethanol hydroperoxide (1-hydroxyethyl hydroperoxide) (15)

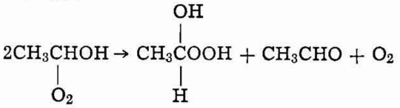

$$2CH_3\underset{\substack{|\\O_2}}{CHOH} \rightarrow CH_3\overset{\substack{OH\\|}}{\underset{\substack{|\\H}}{C}}OOH + CH_3CHO + O_2 \qquad [14]$$

Ethanol hydroperoxide undergoes various possible reactions, in particular a rapid base-catalyzed decomposition to acetaldehyde and hydrogen peroxide (17)

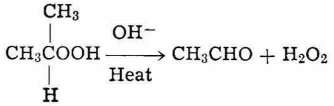

$$CH_3\overset{\substack{CH_3\\|}}{\underset{\substack{|\\H}}{C}}OOH \xrightarrow[\text{Heat}]{OH^-} CH_3CHO + H_2O_2 \qquad [15]$$

This reaction requires an elevated temperature, as is found under the glow spot (18). Reactions [14] and [15], therefore, are alternatives to reaction [9].

Ethanol hydroperoxide also tends to convert to the di-peroxide in aqueous systems (19). No evidence could be found (3) for this di-peroxide in x-irradiation studies.

The exactness of the hydrogen peroxide:acetaldehyde ratio shows that little, if any, of the product is locked up in the form of organic peroxides. It is possible, on the other hand, that the organic peroxides reacted as mixtures of hydrogen peroxide and acetaldehyde, since time was always allowed for the analytical processes to reach completeness, but the balance of the evidence is against significant organic peroxide formation.

A further possibility is the elimination of the hydroperoxyl radical from the 1-hydroxyethylperoxyl radical, followed by disproportionation of the former species

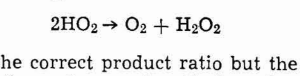

$$CH_3\underset{\substack{|\\O_2}}{CHOH} \rightarrow CH_3CHO + HO_2 \qquad [16]$$

$$2HO_2 \rightarrow O_2 + H_2O_2 \qquad [12]$$

This gives the correct product ratio but the possibility of side reactions of peroxyl radicals makes the above scheme less probable. Reaction [12] was investigated

in the absence of ethanol and using dilute aqueous alkali: No change in pH was observed after gde, so no hydrogen peroxide formation was inferred.

Reactions such as

$$CH_3CHOH + HO_2 \rightarrow CH_3CHO + H_2O_2 \quad [17]$$

or

$$CH_3CHOH + HO_2 \rightarrow CH_3\overset{\displaystyle OH}{\overset{|}{C}}HOOH \quad [18]$$

followed by

$$CH_3\overset{\displaystyle OH}{\overset{|}{C}}HOOH \xrightarrow[\text{Heat}]{OH} CH_3CHO + H_2O_2 \quad [15]$$

can be discounted, since they give an unambiguously incorrect product ratio.

If the oxygen flow rate is not high enough the 1-hydroxyethyl radicals are incompletely scavenged and some butanediol appears, possibly with some disproportionation also. The ethanol scavenges most, but not all, of the OH radicals as deduced from our G(OH, ferrocyanide) work and from the small residual peroxide in the argon runs. It was found that the total nonacid yield corresponded very closely to G(OH, ferrocyanide): see Table II. The gde work on neutral and also on alkaline ferrocyanide gave closely similar ferricyanide yields, and no hydrogen peroxide, indicating total scavenging of the hydroxyl radicals by ferrocyanide.

Schultze and Schulte-Frohlinde (5) also postulated the decomposition of ethanol hydroperoxide to acetic acid and water

$$CH_3 - \overset{\displaystyle OH}{\overset{|}{C}}HOOH \xrightarrow{H^+} CH_3COOH + H_2O \quad [19]$$

The reaction is acid-catalyzed. Our G-values for acid were very high (of the order of 9 mole F^{-1}). Acid formation as proposed above must involve a chain process, starting from ethanol, since G(acid) is so large: Such a process might involve acetaldehyde, as an intermediate or by-product, and this would upset the 1:2 hydrogen peroxide:acetaldehyde ratio and also the correlation between G(OH, ferrocyanide) and total yields. If acetaldehyde were the source of the acid, then, in order to preserve the acetaldehyde yield, another chain process would be required, consuming ethanol. The gain in acid does not correlate with the loss in acetaldehyde. Further, the acid yield *vs.* quantity of electricity curve flattens off with increasing run time, suggesting some kind of saturation. Acid was found also in gde studies on aqueous isopropanol, involving either a combustion process (yielding carbon dioxide) or C-C bond fission. Acid formation involves the simultaneous presence of oxygen and substrate. The observed hydrogen peroxide:acetaldehyde ratio is consistent with the mechanism proposed above but does not account for the acid. If other reactions occur they must somehow produce acid and the proper product ratio. It is concluded tentatively that the acid arises from combustion processes.

Table II. Total yields under oxygen

	G/mole F^{-1}
G(OH, ferrocyanide)	7.19 ± 0.66
$G(CH_3CHO, O_2)$	6.44 ± 0.13
$2G(C_4H_{10}O_2, O_2)$ (trace)	0.45 ± 0.05
$2G(H_2O_2, Ar)$ (trace)	0.19 ± 0.02
	7.08 ± 0.14

The total yield calculation was repeated for the argon runs, G(OH) being estimated to be 7.145 ± 0.149 mole F^{-1}. It seems we have accounted for all the hydroxyl radicals. Other species may compete, but at a much lower level. We did not find any need to assume loss of products (except for acetaldehyde): Decomposition of products is a main feature of Seddon and Allen's radiolysis work (4).

In the absence of ethanol and in the absence of oxygen, under established conditions, the product-destroying reactions

$$H + H_2O_2 \rightarrow OH + H_2O \quad [20]$$

and

$$OH + H_2O_2 \rightarrow HO_2 + H_2O \quad [21]$$

might occur, but the extent is not clear. The main product under argon and in the absence of ethanol is hydrogen peroxide and possible reactions are

$$H + H \rightarrow H_2 \quad [22]$$

$$H + OH \rightarrow H_2O \quad [23]$$

$$OH + OH \rightarrow H_2O_2 \quad [2]$$

In the presence of oxygen and in the absence of ethanol oxygen/radical or oxygen/aqueous electron reactions compete with radical/radical processes. Perhydroxyl radical formation may be possible, giving some additional peroxide by self-reaction.

It is possible that some or all of the aqueous electrons which may be generated in gde may react with hydrogen ions also generated or with those from water. There seems to be no need to include this species in the yield analyses: For example, under oxygen the aqueous electron has an opportunity to partake via reaction [11] but there is no evidence for this.

The radiation and gde chemistry of aqueous ferrocyanide has been reviewed by Denaro and Owens (20) and further work carried out by others, especially Almubarak and Wood (21). It was found (21) that G(ferricyanide) was independent of pH (from pH 7 upward). In alkali, inorganic peroxide is expected to reduce ferricyanide, *i.e.*, reducing G(ferricyanide); it was concluded that at sufficiently high ferrocyanide concentrations no peroxide occurs and all the hydroxyl radicals are scavenged by the substrate. The absence of any oxygen flow rate effect suggests that reactions involving the hydroperoxyl radical or its anion can be neglected here also. For similar reasons contributions by hydrogen radicals and by aqueous electrons to the reaction system were discounted also. It was concluded that G(ferricyanide) represented G(OH). It is hoped to publish details of this work shortly.

Further work on the gde of aqueous ethanol in selected buffers is proposed in order to investigate the mechanism at various pH values and also to examine the possibility that ethanol itself is decomposed directly by the bombardment processes. This latter may be achieved by analysis for other products, such as ethylene glycol and 1,3-propanediol, arising from C-C fission. The ultimate fate of the hydrogen radicals and the aqueous electrons requires further study also, and substrates likely to show improved reactivities toward these species have been selected.

Manuscript submitted Jan. 20, 1977; revised manuscript received April 23, 1977.

Any discussion of this paper will appear in a Discussion Section to be published in the June 1978 JOURNAL. All discussions for the June 1978 Discussion Section should be submitted by Feb. 1, 1978.

REFERENCES

1. A. Klemenc, *Z. Electrochem.*, **53**, 694 (1953).
2. G.-A. Mazzochin, G. Bontempelli, and F. Magno, *Electroanal. Chem. Interfacial Electrochem.*, **42**, 243 (1973).

3. G. G. Jayson, G. Scholes, and J. Weiss, *J. Chem. Soc.*, **1957**, 1358.
4. W. A. Seddon and A. O. Allen, *J. Phys. Chem.*, **71**, 1914 (1967).
5. H. Schultze and D. Schulte-Frohlinde, *J. Chem. Soc. Faraday Trans. 1*, **71**, 1099 (1975).
6. J. Brode, *Z. Phys. Chem.*, **37**, 257 (1901).
7. G. R. A. Johnson and G. Scholes, *Analyst*, **79**, 217 (1954).
8. N. J. Davies, A. R. Denaro, A. Wood, and M. A. Almubarak, *J. Appl. Chem. Biotechnol.*, **26**, 715 (1976).
9. A. Hickling, in "Modern Aspects of Electrochemistry," Vol. VI, J. O'M. Bockris, Editor (1971).
10. M. A. Almubarak, M.Sc. Thesis, University of Aberdeen (1972).
11. G. Hughes, "Radiation Chemistry," (1973).
12. A. R. Denaro and G. G. Jayson, "Fundamentals of Radiation Chemistry," (1972).
13. K.-D. Asmus, H. Möckel, and A. Henglein, *J. Phys. Chem.*, **77**, 1218 (1973).
14. A. Appleby, G. Scholes, and M. Simic, *J. Am. Chem. Soc.*, **85**, 3891 (1963).
15. M. Anbar and P. Neta, *Int. J. Appl. Rad. Isotopes*, **18**, 493 (1967).
16. D. W. Johnson and G. A. Salmon, *J. Chem. Soc. Faraday Trans. 1*, **71**, 583 (1975); K.-D. Asmus, A. Henglein, A. Wigger, and G. Beck, *Ber. Bunsenges. Phys. Chem.*, **70**, 756 (1966); M. Simic, P. Neta, and E. Hayon, *J. Phys. Chem.*, **73**, 3794 (1969).
17. D. Swern, "Organic Peroxides," (1970).
18. A. Reiche and R. Meister, *Ber. Dtsch. Chem. Ges.*, **68**, 1465 (1935); A. Reiche, *Angew. Chem.*, **70**, 251 (1958).
19. A. Rieche, *Ber. Dtsch. Chem. Ges.*, **64**, 2328 (1931); P. L. Kooijman and W. L. Ghijsen, *Rec. Trav. Chim.*, **66**, 205 (1947).
20. A. R. Denaro and P. A. Owens, *Electrochim. Acta*, **13**, 157 (1968).
21. M. A. Almubarak and A. Wood, To be published.

X-Ray Photoelectron Spectroscopic Studies of Tin Electrodes after Polarization in Sodium Hydroxide Solution

R. O. Ansell, T. Dickinson,* A. F. Povey,[1] and P. M. A. Sherwood

School of Chemistry, The University, Newcastle upon Tyne, NE1 7RU, United Kingdom

ABSTRACT

The surface of tin electrodes after potentiostatic polarization in 0.50 mole dm^{-3} sodium hydroxide solution has been examined by x-ray photoelectron spectroscopy. Stannous oxide and hydroxide are shown to be present in the prepassive region. At higher potentials stannic oxide and hydroxide are formed. The thickness of the layer is evaluated over the potential range −0.95 to +0.40V using various models and is in the range 30-86Å.

X-ray photoelectron spectroscopy (XPS) has been shown to be a valuable tool in the study of electrode surfaces (1-6). Information on the species present and quantitative information on thickness of layers and their distribution may be established. These may lead to proposed mechanisms being disproved or substantiated (7).

In this study tin electrodes have been examined after potentiostatic polarization in 0.5 mole dm^{-3} sodium hydroxide solution. Much of the previous electrochemical work on this system involved galvanostatic methods (8-13) but some workers have adopted a potentiostatic approach (14-18). The anodic polarization curve shows two peaks in the active-passive region. The occurrence of the first passivation has been attributed to the formation of a layer of SnO or $Sn(OH)_2$ by a dissolution precipitation mechanism (13, 15). The second region of passivity has been attributed to the presence of SnO_2 (13, 15).

In this study we have investigated the effect of potentiostatic polarization over a wide potential range. The existence of Sn II and Sn VI species is confirmed.

Experimental

All the spectra were run on an AEI ES200B spectrometer using Mg $K_{\alpha_1\alpha_2}$ radiation. Both the analyzer entrance and exit slits were set at their minimum values to give maximum resolution conditions. The electron gun was operated at 120W power for all the studies to give a relatively low x-ray flux [and thus minimize any x-ray reduction (19)] and to enable the intensities of the photoelectron peaks to be compared. No time dependence of the spectra was observed. The spectrometer was operated in the fixed retardation ratio mode for the recording of all the photoelectron peaks. The scan speed used was either 0.05 or 0.02V sec^{-1} depending on the absolute intensity of the peaks. The binding energies are calibrated with respect to the C1s electron peak at 284.6 eV due to residual pump oil on the sample surface. This gave a value of 484.1 eV for the Sn(metal) 3d5/2 electron peak. This was subsequently used to calibrate the spectra where such a peak was clearly observed. The pressure in the sample chamber was, typically, 10^{-8} Torr. This was achieved rapidly after the insertion of the sample probe with the aid of a titanium sublimation pump. The temperature of the samples was maintained at 10°C.

Curve resolution was carried out on a du Pont Model 310 curve resolver using a 50:50 Gaussian-Lorentzian shape fit. For both the tin and oxygen spectra curves were fitted to be within ±0.3 eV of the binding energy quoted and ±0.2 eV of the separation from the tin metal 3d5/2 electron peak where this is observed. In the case of the tin spectra the separation of the 3d5/2 electron peaks due to Sn II and Sn IV from that due to tin metal (when this was observed) was within ±0.2 eV of the difference between their quoted binding energies.

A current-voltage curve was recorded (Fig. 1a), using a triangular voltage sweep at a sweep rate of 10 mV sec^{-1} before any other measurements were made to ensure the system was behaving satisfactorily.

* Electrochemical Society Active Member.
[1] Present address: Central Electricity Research Laboratories, Leatherhead, Surrey, KT22 7SE, United Kingdom.
Key words: photoelectron, tin, oxide, passivation.

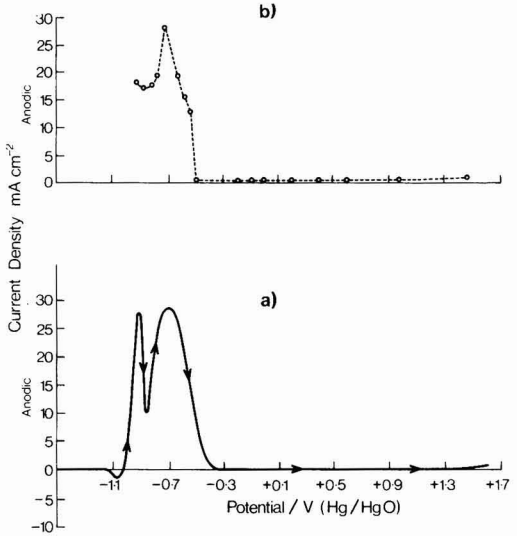

Fig. 1. (a) A current-voltage curve for the tin electrode in 0.50 mole dm^{-3} sodium hydroxide solution at a sweep rate of 10 mV sec^{-1}. Ordinate: Current density mA cm^{-2}. Abscissa: Potential/V (Hg/HgO). (b) The steady-state current-voltage curve for tin electrodes polarized in 0.50 mole dm^{-3} sodium hydroxide solution and subsequently examined by XPS. Ordinate: Anodic current density mA cm^{-2}. Abscissa: Potential/V (Hg/HgO).

Fresh electrodes were used for each measurement to eliminate the possibility of inadequate removal of the electrochemically formed oxide. Ventron (Alpha Products) tin foil (m5N) was used for the electrode studies. The electrodes were degreased in acetone and rinsed copiously before introduction into the cell. They were prepolarized initially for 10 min at −2.00V, the potential was slowly turned to −1.50V, and allowed to rest there for 1 min to allow the hydrogen gas bubbles to disperse. The potential was then either pulsed to the required value or adjusted to the required potential over a few seconds. The electrodes were polarized for 10 min at each potential studied; the current having become steady within this time. These steady-state currents are shown in Fig. 1b.

The electrochemical cell has been described before (7). In this case the electrode was carefully positioned next to the Luggin capillary tip to minimize effects of *iR* drop in the solution. The cell was housed in a nitrogen-filled glove box to enable anaerobic transfer of the electrode to the spectrometer as described previously (5).

All potentials in these experiments were measured and are quoted with respect to the mercury-mercuric oxide electrode in 0.5 mole dm^{-3} sodium hydroxide solution.

Table I

	Binding energy (eV)*		
	Sn 3d5/2	O1s	Na2s
SnO	485.8	529.8	—
SnO_2	486.3	530.4	—
Sn (foil) (21) "as received"	485.8	531.2	—
Sn(m) (metal) (21)	484.1	—	—
NaOH	—	531.5	63.7
Na_2SnO_3	487.0	531.3	63.9

* With respect to C1s = 284.6 eV.
— Not present.

Results

The tin 3d5/2, oxygen 1s and sodium 2s electron peaks were studied for the treated electrodes, and were compared with spectra obtained from tin compounds (Table I). The tin 3d5/2 electron peak observed with treated electrodes could be resolved in all cases into two or three peaks at binding energies of 484.1, 485.8, and 486.3 eV corresponding to tin metal, stannous oxide and/or hydroxide, and stannic oxide and/or hydroxide, respectively (Table II). Representative spectra are shown in Fig. 2.

The oxygen 1s electron peak could be resolved into two or three peaks at binding energies of 532.3, 531.4, and 529.9 eV (Table II, Fig. 3). The peak at 532.3 eV is present on all samples introduced into the spectrometer and may be shown to be due to a surface species by angular variation experiments (21). This peak is therefore assigned to adsorbed oxygen or water. In those cases in which the proportion of the total peak area assignable to these species is <5% this peak has not been shown in Fig. 3. The peak at 529.9 eV may be assigned to oxide oxygen by comparison with the tin oxides studied (Table I). A hydroxyl oxygen species would, on a simple basis of charge, be expected to have a higher binding energy and this has been the case for many hydroxide species studied [Table I and previous work (3-7)]; thus the peak at 531.4 eV is assigned to hydroxyl oxygen.

Table II

	Proportions of photoelectron peaks assigned to each species						Absolute intensity of sodium 2s electron peak
Potential	Tin 3d5/2 electron region			Oxygen 1s electron region			
vs. Hg/HgO	SnO_2/ $Sn(OH)_4$	SnO/ $Sn(OH)_2$	Sn(metal)	O_2 ads/ H_2O	OH^-	O^{2-}	Na2s
−0.95	—	65	35	25	59	16	0.15
−0.90	—	60	40	21	52	29	—
−0.85	—	57	43	19	63	19	—
−0.80	—	67	33	—	>95	—	—
−0.75	~10	58	32	—	76	24	0.09
−0.70	16	50	34	—	61	39	0.46
−0.60	21	44	35	—	64	36	—
−0.55	30	38	32	—	62	38	—
−0.50	75	~10	15	—	64	37	—
−0.20	80	—	20	—	58	42	0.18
−0.10	83	—	17	—	57	43	0.05
0.00	84	—	16	—	66	34	0.28
+0.20	92	—	8	—	45	55	0.08
+0.40	>95	—	~5	—	48	52	—
+0.60	>95	—	—	—	47	53	0.13
+1.00	>95	—	—	—	35	65	—
+1.50	>95	—	—	—	30	70	0.10
+2.40	>95	—	—	—	28	72	—

— Not detectable.

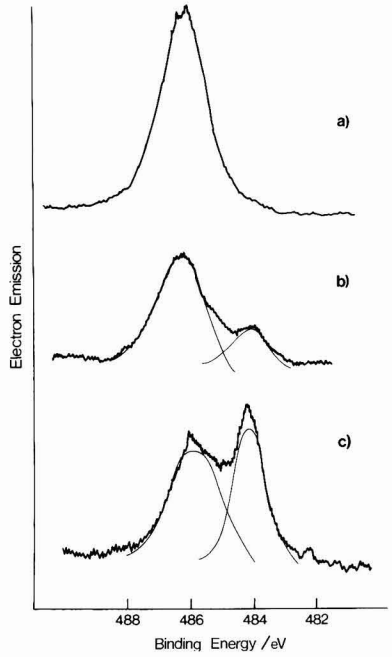

Fig. 2. Representative spectra of the tin 3d5/2 electron region of the tin electrodes after polarization at a potential of (a) −0.90V, (b) −0.10V, (c) +1.50V. Ordinate: Electron emission. Abscissa: Binding energy/eV.

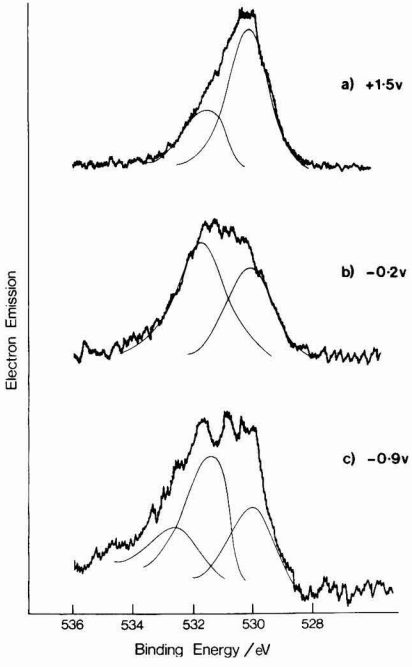

Fig. 3. Representative spectra of the oxygen 1s electron region of the tin electrodes after polarization at a potential of (a) −0.90V, (b) −0.10V, (c) +1.50V. Ordinate: Electron emission. Abscissa: Binding energy/eV.

A single peak at 63.5 eV could be detected at many potentials due to sodium incorporation in the layer. The absolute intensity of this peak in the spectrum of the treated electrodes is given in Table II.

In spite of the precaution taken in transferring the electrode to the spectrometer, even after pretreatment at −2.00V for 10 min the presence of some stannous hydroxide could be detected. Since similar results were obtained after polarizing in the active region no useful information could be deduced from them. At more positive potentials, however, significant differences were observed in the spectra.

Characterization of the layer.—It has been demonstrated previously how the relative intensities of the photoelectron peaks from the surface oxide and substrate metal may be used to derive the thickness of the layer (3-5, 7). When two oxides/hydroxides possibly of different valence states are present a more comprehensive study may reveal how the species are distributed over the surface and thus explain more fully the nature of the passivation process (20).

In this case in order to analyze the intensity data it is convenient to divide the potential range into four sections. The region from −0.95 to 0.80V in which Sn II species are present, from −0.75 to −0.50V in which both Sn II and Sn IV species are present, and −0.20 to +0.40V in which Sn IV species are present. In these three regions the metal substrate is also detectable. In the fourth region, +0.60 to +2.40V the substrate is no longer detectable; this implies the layer is greater than *ca.* 90Å thick (see Table III).

The first and third regions have been analyzed assuming the electrode is completely covered by an oxide/hydroxide layer. The relevant equation is then

$$\frac{I_{ox}}{I_m} = K\frac{(1 - \exp(-x\sigma_{ox}))}{\exp(-x\sigma_{ox})} \qquad [1]$$

where the symbols have the same meaning as before (4, 5, 7). Taking values of 1.81 and 27.7Å for K and $1/\sigma_{ox}$, respectively, arising from our previous angular variation study (21) the thickness of the layer can be evaluated (Table III).

In the second region where two different valency states of tin are present in the surface layer the data may be analyzed in various ways. The results are given in Table IV and discussed below.

Discussion

Assignment of the photoelectron peaks.—The spectra show that oxide/hydroxide species are present on the electrode over the total potential range studied. Assignment of the tin species is based partly on a comparison with the spectra of stannous oxide and stannic oxide. The total Sn 3d5/2 electron peak envelope can be satisfactorily resolved into peaks due to these two species and tin metal. There is no evidence for a chemical shift between stannous oxide and hydroxide in the Sn 3d5/2 electron peak. Thus for the tin foil as received the tin 3d5/2 electron peak is at the same bind-

Table III

Potential *vs.* Hg/HgO	Thickness,* Å
−0.95	35
−0.90	32
−0.85	30
−0.80	37
−0.20	51
−0.10	56
0.00	57
+0.20	75
+0.40	86

The thickness of the layer in the regions where only one oxide is present.

* Assuming $\lambda_{SnO} = \lambda_{SnO_2} = 27.7$Å, and D_{SnO} and D_{SnO_2} are the atom densities of the bulk species.

Table IV

Model	A patchy layer, Substrate covered but detectable under both oxides		Homogeneous mixture. Substrate covered but detectable		Two distinct layers. Substrate covered but detectable			
					$\lambda_1 = \lambda_2$, $D_1 = D_{SnO}$, $D_2 = D_{SnO_2}$			
Assumptions made*	Thickness of patches is same $\lambda_1 = \lambda_2$ $D_1 = D_{SnO}$, $D_2 = D_{SnO_2}$		$\lambda_1 = \lambda_2$, $D_1 = D_{SnO}$, $D_2 = D_{SnO_2}$		Sn IV on top of Sn II		Sn II on top of Sn IV	
					Thickness, A		Thickness, A	
Potential *vs.* Hg/HgO	Thickness, A	Coverage of surface by Sn II	Thickness, A	Fraction of atoms as Sn II	Sn IV layer	Sn II layer	Sn IV layer	Sn II layer
−0.75	38	0.85	38	0.85	3.1	35	11	27
−0.70	36	0.75	36	0.75	5.2	31	15	21
−0.60	35	0.68	36	0.67	7.1	29	18	18
−0.55	38	0.55	38	0.55	11	28	24	14
−0.50	59	0.11	59	0.11	40	19	56	2.6

* Subscript 1 refers to Sn II species. Subscript 2 refers to Sn IV species.

ing energy as that for SnO although the oxygen peaks are shifted. Similarly the spectra of the electrode after polarization at −0.80V show only hydroxide oxygen species and the Sn 3d5/2 peak can be readily resolved into peaks at 485.8 and 484.1 eV. Neither is there any evidence for a chemical shift of the Sn 3d5/2 electron peak between stannic oxide and hydroxide. At very high potentials where there is a high proportion of oxide the tin 3d5/2 electron peak is virtually identical to that at lower potentials where a considerably higher proportion of hydroxide is present.

The assignment of the oxygen 1s electron peak at 531.4 eV to hydroxyl species is based on previous work (5, 7). There is no doubt that there are at least two different oxygen-containing species present in the layer and it seems reasonable to assign one to oxide and one to hydroxide.

The amount of sodium present shows no correlation with potential or with any of the other species present. This is probably due to a small amount of sodium incorporation in the layer and/or some residual NaOH being left on the surface after washing.

Characterization of the layer.—The analysis of the positions and intensities of the photoelectron peaks suggest that in the prepassive region only Sn II species are present.

Both oxide and hydroxide are present in this region and the total thickness is in the range 20-26Å. We have found, previously, that metal dissolution may proceed at a high rate even when the electrode surface is covered by thick layers of oxide/hydroxide (5).

Both Sn II and Sn IV species are present in the region −0.25 to −0.50V. The oxygen 1s electron spectra show only hydroxide is present at −0.80V but at all higher potentials both oxide and hydroxide are present. The total layer thickness is in the range 38-59Å for each of the models chosen for the analysis (Table IV).

In the region −0.20 to +0.40V there is a steady increase in the thickness of the layer which is composed solely of Sn IV species. The oxide/hydroxide ratio also shows an increasing trend with increasing potential (Tables II and III). This trend continues at higher potentials where the substrate is no longer detectable. The film becomes visible at very high potentials suggesting the thickness has increased further.

Correlation with the electrochemical data.—It is important to see if the species identified, the layer thickness, and the distribution of the species can be correlated with the electrochemical data; in particular the current-potential curve (Fig. 1b). In the prepassive region only stannous oxide and hydroxide are present. The current is $\geq$ 15 mA cm^{-2} throughout this region indicating that this layer is not strongly passivating.

The fall in current between −0.95 and −0.90V is probably due to the increased proportion of oxide in the surface layer (Table II). The subsequent increase in current may be tentatively correlated with the decrease in proportion of stannous oxide and of course the more positive potentials.

The true passivation correlates with an increasing proportion of the tin 3d5/2 electron envelope being due to Sn IV species. The intensities have been analyzed using four different models (Table IV). A satisfactory model must explain a slowly decreasing current from −0.75 to −0.55V, followed by a very abrupt decrease at −0.50V to a value of 0.05 mA cm^{-2}. The model must also give a total thickness of about 35Å from −0.75 to −0.55V, since the proportion of the tin 3d5/2 electron envelope due to the metal is approximately constant from −0.80 to −0.55V. A considerably thicker layer (*ca.* 50Å) must be present at −0.50V because, at this potential, the proportion of the tin peak due to the metal falls to a value similar to that observed in the potential range −0.20 to 0.00V.

All models give values for the total thickness which satisfy the requirements described above. This is, indeed, to be expected since, lacking the appropriate data, it has been necessary to assume that $\lambda_1 = \lambda_2$. The slow decrease in current could be explained, by the patchy layer model, as due to an increasing coverage by Sn IV species; as discussed above the Sn II species are not strongly passivating. A fivefold increase in the coverage by Sn IV species (from −0.55 to −0.50V) does not, however, seem a sufficient change to account for the very large fall in the current.

It is difficult to decide whether a homogeneous layer is physically realistic, what properties it would have, and how changes in its composition would affect the degree to which it passivated the electrode.

Both the models involving two distinct layers predict an increase in the thickness of the Sn IV layer with potential, as seems to be necessary to account for the decreasing current. If the lower layer is composed of Sn IV species, it appears that this would have a thickness corresponding to that of at least two unit cells, even at −0.75V (SnO_2 has a tetragonal structure with unit cell dimensions of a = 4.74Å and c = 3.19Å). Since the electrode undergoes rapid dissolution at this potential, whereas Sn IV species appear to be strongly passivating, it seems unlikely that such a relatively thick film would be present. If the upper layer consists of Sn IV species, the thicknesses involved are more acceptable and the fourfold increase in the thickness of this layer between −0.55 and −0.50V would account for the dramatic fall in the current which accompanies this change in potential.

So far as it is possible to analyze this situation, therefore, the balance of evidence suggests that, in the potential range between −0.75 and −0.50V, two distinct layers are present on the electrode surface. It also appears, as is to be expected on thermodynamic

grounds, that the layer nearest the electrode is that of lowest oxidation state.

When the electrode is fully passivated, there is very little dependence of the current on potential (between −0.5 to +0.60V). This can be explained in terms of both the increasing thickness of the layer (22) (Table III) and its progressive dehydration; the oxide/ hydroxide ratio shows a generally increasing trend as the potential is made more positive (Table II). At still more positive potentials the thickness continues to increase but the current rises somewhat. This may be due to the onset of oxygen evolution or to imperfections in the layer.

Acknowledgments

A.F.P. would like to thank I.C.I. for the award of a fellowship and R.O.A. would like to thank the Science Research Council for the award of a research associateship.

Manuscript submitted Jan. 21, 1977; revised manuscript received April 28, 1977.

Any discussion of this paper will appear in a Discussion Section to be published in the June 1978 JOURNAL. All discussions for the June 1978 Discussion Section should be submitted by Feb. 1, 1978.

REFERENCES

1. K. S. Kim, A. F. Gossman, and N. Winograd, *Anal. Chem.*, **46**, 197 (1974).
2. G. C. Allen, P. M. Tucker, A. Capon, and R. Parsons, *J. Electroanal. Chem.*, **50**, 335 (1974).
3. A. F. Povey, Ph.D. Thesis, University of Newcastle-upon-Tyne (1975).
4. T. Dickinson, A. F. Povey, and P. M. A. Sherwood, *J. Chem. Soc., Faraday Trans. 1*, **71**, 298 (1975).
5. T. Dickinson, A. F. Povey, and P. M. A. Sherwood, *ibid.*, **73**, 327 (1977).
6. R. O. Ansell, T. Dickinson, and A. F. Povey, *Corros. Sci.*, In press.
7. T. Dickinson, A. F. Povey, and P. M. A. Sherwood, *J. Chem. Soc. Faraday Trans. 1*, **72**, 686 (1976).
8. A. W. Hothersall, S. G. Clarke, and D. J. Macnaughton, *J. Electrodep. Tech. Soc.*, **9**, 101 (1934).
9. F. F. Oplinger and C. J. Wernlund, U.S. Pat. 1,919,000 (1933).
10. R. Kerr, *J. Soc. Chem. Ind.*, **57**, 405 (1938).
11. H. Barbre, C. Bagger, and E. Maahn, *Electrochim. Acta*, **16**, 559 (1971).
12. D. Eurof Davies and S. N. Shah, *ibid.*, **8**, 663 (1963); *ibid.*, **8**, 703 (1963).
13. N. A. Hampson and N. E. Spencer, *Br. Corros. J.*, **3**, 1 (1968).
14. M. N. Anwar, *U.A.R.J. Chem.*, **13**, 109 (1970).
15. B. N. Stirrup and N. A. Hampson, *J. Electroanal. Chem.*, **67**, 45 (1976).
16. B. N. Stirrup and N. A. Hampson, *ibid.*, **67**, 57 (1976).
17. D. R. Gabe and P. Sripatr, *Trans. Inst. Met. Finish.*, **51**, 141 (1973).
18. T. Dickinson and S. Lotfi, In preparation.
19. A. F. Povey and P. M. A. Sherwood, *J. Chem. Soc., Faraday Trans. 2*, **70**, 1240 (1974).
20. A. F. Povey, Submitted to *J. Electron Spectrosc. Rlat. Phenom.*
21. R. O. Ansell, T. Dickinson, A. F. Povey, and P. M. A. Sherwood, *ibid.*, **11**, 301 (1977).
22. K. J. Vetter, *Electrochim. Acta*, **16**, 1923 (1971).

Diffusion and Charge Transfer Parameters for the Ag/AgCl Electrode

Hiram Gu* and Douglas N. Bennion*

Energy and Kinetics Department, School of Engineering and Applied Science, University of California, Los Angeles, California 90024

ABSTRACT

Galvanostatic formation and potentiostatic reduction of silver chloride on silver have been studied. Experiments were conducted in 0.5, 1.0, 1.5, 2.0, and 3.0*N* KCl solutions. The effective mass transfer coefficient, k_m^o, for the transport of complex silver ions from AgCl crystals to reaction sites on the silver surface was found to depend on KCl concentrations in the form

$$k_m^o = 1.808 \times 10^3 \, [\exp(-1.519 \times 10^3 c_e)] \text{ cm/sec}$$

with c_e in mole per cubic centimeter. The apparent cathodic charge transfer coefficient, α_c, was determined to be 0.30, and the exchange current density

$$i_o = 0.15 \, (c_R^{sat}/10.1 \times 10^{-8})^{0.70} \text{ A/cm}^2$$

with c_R^{sat} (mole per cubic centimeter) being the saturated concentration of complexed silver ions in the KCl solution.

In addition to being used as reference electrodes, silver/silver chloride electrodes have found use as porous electrode plates in batteries such as the seawater battery. Previous studies on porous Ag/AgCl electrodes (1, 2) have indicated that the electrode may be used successfully in secondary storage batteries.

The silver/silver chloride electrode is an electrode with a sparingly soluble reactant, AgCl. Numerous studies have been conducted on the thermodynamics of Ag/AgCl electrodes (3) and the mechanism of AgCl formation and reduction at silver electrodes (4-11). The studies of Kurtz (4) and Lal *et al.* (5) suggested that electrolytically formed AgCl films are porous in nature. Briggs and Thirsk (6) studied the galvanostatic reduction of silver chloride films on silver at different current densities and KCl concentrations. They found that an increase in the initial AgCl layer thickness reduces the number of reduction centers visible at a given percentage reduction. Jaenicke *et al.* (7) found that if a pore-free AgCl layer is reduced by a cathodic current, pores soon appear. Fleishmann and Thirsk (8) studied the growth of AgCl on Ag and concluded that the growth of AgCl is two dimensional. Giles (9), however, believed that the formation of AgCl is by progressive nucleation and growth of three-dimensional centers and that the diffusion of $AgCl_{n+1}^{-n}$ may

* Electrochemical Society Active Member.
Key words: porous electrodes, batteries, exchange current.

be rate determining. The value of n for the complex may be 0, 1, 2, or 3. Katan *et al.* (10) studied the reduction of silver ions from potassium chloride solutions saturated with AgCl. A rotating disk silver electrode was used. Their results also indicate that the formation and reduction of silver chloride involves the solution diffusion of $AgCl_{n+1}^{-n}$. Aleskovskii *et al.* (11) studied the structure of silver deposits with respect to electrode potentials at which the reduction of AgCl takes place. They also suggested that the reduction is via a solution diffusion path.

No information regarding the charge transfer overvoltage of Ag/AgCl electrodes was found in the literature. The absence of charge transfer studies on Ag/AgCl electrodes is probably due to two reasons. First, the overvoltage in the case of solid silver electrodes consists mainly of crystallization and diffusion overvoltage with large exchange current density according to Gerischer and Tischer (12, 13) and Bockris *et al.* (14, 15). Second, the coverage of silver surface by silver chloride adds complexity to the analysis of experimental data.

The present study was conducted with the intention of determining apparent diffusion and charge transfer parameters for the Ag/AgCl system. These parameters are to be used in the mathematical modeling of Ag/AgCl porous electrodes.

The potentiostatic reduction of porous silver chloride films on silver was analyzed. As the silver chloride is being converted to silver, the silver area available for charge transfer increases. The cathodic current increases to a maximum and decreases as the silver chloride is being depleted. The maximum current density reached during potentiostatic reduction was used to construct the current-overpotential curves. From the i-η curves, values of four parameters were deduced. They are: the cathodic charge transfer coefficient, α_c; the mass transfer coefficient of complexed silver ions, k_m^o, for solution phase transport between Ag surface and AgCl surface; the exchange current density, i_o; and the order of dependence of i_o on silver ion concentration, γ.

Qualitative results observed on the galvanostatic formation of AgCl are also presented.

Experimental

The experimental arrangement is shown in Fig. 1. The electrode studied was a circular silver disk 1/8 in. in diameter embedded in Lucite. Another Lucite piece that consisted of the counterelectrode compartment, a 1/8 in. diam tunnel, and a small branch tunnel approximately 1/32 in. diam was spring pressed against the working electrode piece. The 1/8 in. tunnel was aligned with the silver disk allowing uniform primary current distribution on the electrode surface. A thin film of electrolytic solution approximately 10 μm thick existed between the two Lucite pieces which provided a solution connection between the main cell and the reference electrode compartment. The reference electrode was a Ag/AgCl electrode. The same KCl concentration as the main cell was used in the reference electrode compartment. A tube pump was used to circulate the electrolyte so as to maintain a constant electrolyte concentration near the electrode surface. The electrolyte flow rate used during experimental runs was 3.5 cm^3/sec.

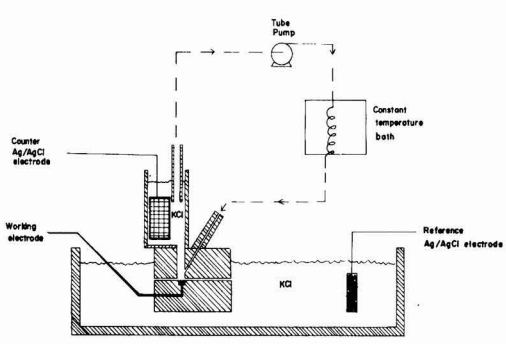

Fig. 1. Experimental arrangement

The KCl solutions used were prepared from doubly distilled water and reagent grade KCl. The initial silver surface was mechanically finished with 4/0 emery polishing paper purchased from Buehler Limited.

The experiments were conducted at 25° ± 1°C in 0.5, 1.0, 1.5, 2.0, and 3.0N KCl solutions. The electrode was galvanostatically charged at 5 mA/cm^2 and subsequently reduced potentiostatically. A PAR Model 173 potentiostat/galvanostat was used to impose the experimental current or voltage.

The overpotential, η, reported in this communication is the potential measured or imposed between the working electrode and the Ag/AgCl reference electrode.

Results

Galvanostatic formation of AgCl.—Typical η-t (overpotential-time) curves for the galvanostatic charging (passage of constant anodic current) of silver electrodes in KCl solutions are shown in Fig. 2. Curve a was obtained when silver chloride was formed on an electrode with a freshly polished silver surface. The curve shows a close to linear rise in potential with time. After the electrolytically formed silver chloride was totally reduced back to silver (either galvanostatically or potentiostatically), galvanostatic recharging of the electrode exhibited a different η-t curve (curve b). The η-t curve has a rather flat portion at the beginning followed by a rapid rise. Additional cycling (charged and discharged) did not seem to have further effect on the η-t curves for galvanostatic charging nor was there any observable dependence (based on scanning electron microscope observation) of the electrode surface roughness on the number of cycles. However, it was observed that the flat portion of the η-t curve was usually lower and the rapid rise in potential was usually earlier (shorter t_p as defined in Fig. 2) when higher concentrations of KCl solutions were used. Figure 3 shows the equivalent amount of charge, Q^* (equal to it_p), at t_p with respect to KCl concentrations. The time t_p is time at which rapid rise in potential begins as defined in Fig. 2. Galvanostatic charging in 1N KCl with current densities from 2.5 to 100 mA/cm^2 indicated that the value of Q^* is independent of the charging current in the range studied.

Scanning electron microscope pictures of the electrode surfaces at positions 1, 2, and 3 as indicated in

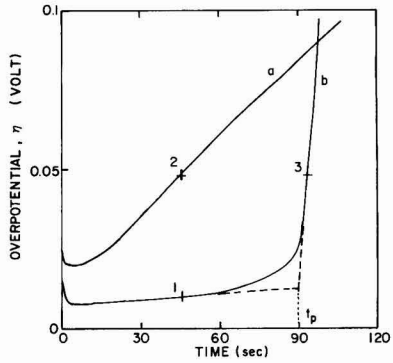

Fig. 2. Overpotential vs. time curves for the galvanostatic formation of silver chloride at 5 mA/cm^2 in 1.5N KCl solution. Curve a, initial freshly polished silver surface; curve b, cycled silver surface.

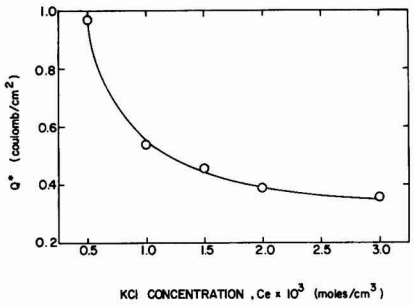

Fig. 3. Dependence of Q* on KCl concentrations. Anodic charging current was 5 mA/cm².

Fig. 2 are shown in Fig. 4. Figures 4a and 4b give comparison of the surfaces (fresh and cycled) at the same state of charge while Fig. 4b and 4c give comparison of the surfaces at the same electrode potential. The small particles between the AgCl crystallites in Fig. 4c are silver.

Potentiostatic reduction of AgCl.—The current flow during the reduction of AgCl depends on the rate of diffusion of complexed silver ions from the silver chloride surface to the silver surface. As an approximation, one can say that the silver area is θA and the silver chloride area is $(1 - \theta)A$. Here A is the total electrode area and θ is the fraction of silver area exposed. By assuming a linear concentration profile between the AgCl area and Ag area, the reaction rate, based on the area A, can be written as (16)

$$i = n\mathbf{F}k_m^{\circ}(\theta)^{1/2}(1-\theta)^{1/2}(c_R^{s} - c_R^{sat}) \quad [1]$$

where c_R^s is the concentration of complexed silver ions at the silver surface where charge transfer reaction takes place and c_R^{sat} is the saturation concentration of complexed silver ions which prevails at the AgCl surface. **F** is the Faraday constant and n is the number of electrons involved in the charge transfer reaction. The mass transfer coefficient, k_m°, is equal to D/δ where D is the complexed ions diffusion coefficient and δ is the average diffusion length. One can also define an over-all mass transfer coefficient, k_m, such that

$$k_m = k_m^{\circ}(\theta)^{1/2}(1-\theta)^{1/2} \quad [2]$$

The over-all mass transfer coefficient thus varies with the amount of surface coverage by AgCl.

The maximum current density reached during potentiostatic reduction was found to depend on the initial coverage of silver surface by AgCl. If the initial coverage, $1 - \theta$, was above 0.5 and below about 0.8 (state of charge in the flat portion of curve b in Fig. 2), the maximum current remained the same over a wide range of initial charge. However, if the electrode was initially heavily covered by AgCl (state of charge corresponding to rising portion of curve b in Fig. 2), lower maximum currents were obtained. Typical i-t curves are shown in Fig. 5. Curve a was obtained with an initially porous silver chloride film. Curves b and c were obtained from initially heavily charged electrodes. Curve c had a more dense coverage of AgCl compared to curve b.

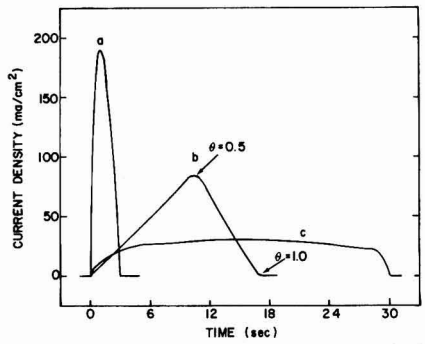

Fig. 5. Current-time curves for the potentiostatic reduction of AgCl at −100 mV in 1N KCl solution. Curve a, initial porous coverage of AgCl; curve b, heavy initial coverage of AgCl; and curve c, nonporous initial coverage of AgCl with few reduction centers.

Surface morphology of the electrode at the cathodic current maximum for the cases corresponding to curves a and c in Fig. 5 are shown in Fig. 6. For the case with initial heavy coverage, there were few reduction centers, and the boundaries of the centers expanded in a circular manner as AgCl was being reduced (Fig. 6 d and e). For the case where the initial AgCl film was quite porous, there were many more reduction centers dispersed among the silver chloride crystallites (Fig. 6 a, b, and c). Figure 6c shows the structure of reduced silver after the remaining silver chloride had been removed by sodium thiosulfate. Similar surface morphology was also reported by Briggs and Thirsk (6).

Cathodic i-η curves obtained for KCl concentrations of 0.5, 1.0, 1.5, 2.0, and 3.0N are shown in Fig. 7. Experiments were performed on a cycled electrode with the surface undisturbed between runs. Before each potentiostatic reduction run, the electrode was charged galvanostatically at 5 mA/cm² to approximately 85% of t_η (see Fig. 2). This assured that the AgCl film was porous and the surface coverage was approximately the same for each run. Data points in Fig. 7 correspond to maximum currents reached during potentiostatic reductions. At the maximum current, the fraction of ex-

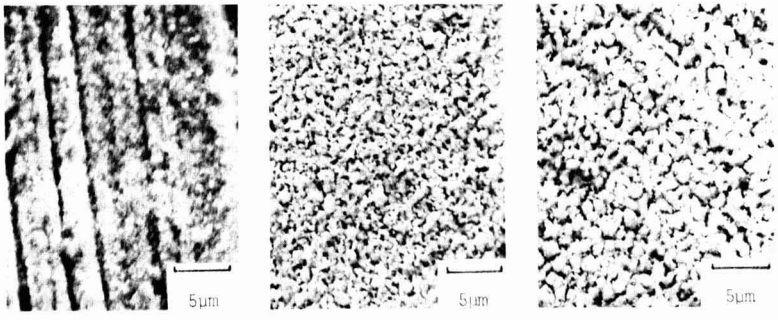

Fig. 4. Scanning electron microscope pictures of the electrode surface during galvanostatic formation of AgCl. Pictures a, b, and c correspond to positions 2, 1, and 3 in Fig. 2, respectively.

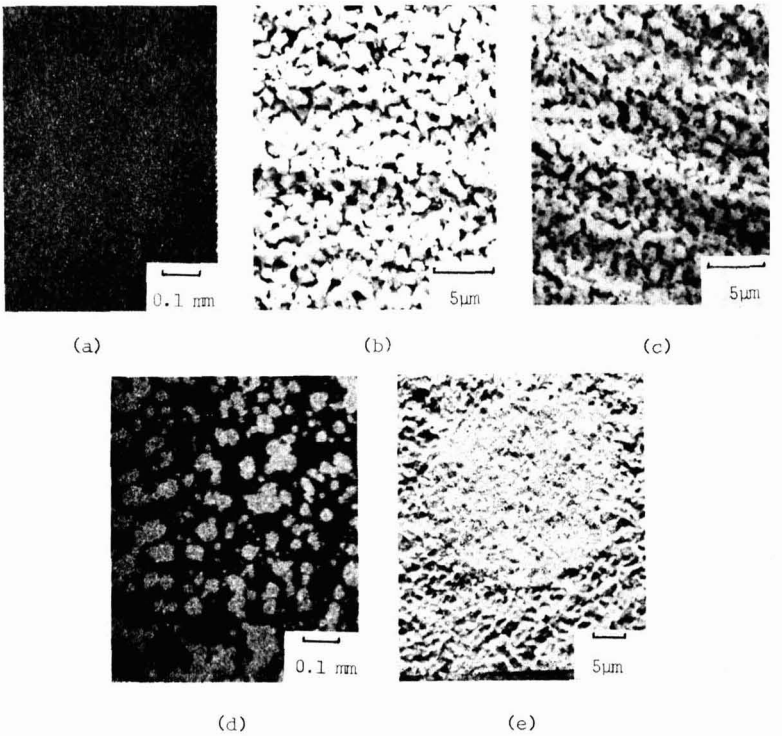

Fig. 6. Pictures showing electrode morphology at the maximum cathodic current. a, b, and c correspond to curve a in Fig. 5. a, Optical microscope picture of the surface; b, SEM picture of the surface; c, SEM picture of the surface after the remaining AgCl has been removed by sodium thiosulfate; d, e, correspond to curve c in Fig. 5 with d, optical microscope picture showing large reduction centers, and e, SEM picture showing circular growth of the reduction center.

posed silver area, θ, was 0.5 as determined from microscope pictures.

No limiting current plateau was observed in the 0.5*N* KCl solution. From the limiting current plateaus in 1.0, 1.5, 2.0, and 3.0*N* KCl solutions, the over-all mass transfer coefficients for the transport of $AgCl_{n+1}^{-n}$ (at $\theta = 0.5$) were calculated using the following equation

$$\kappa_m = \frac{-i_{lim}}{\mathbf{F} c_R^{sat}} \qquad [3]$$

Values of c_R^{sat} were obtained from experimental results (17). The mass transfer coefficient, k_m^o, was then calculated from Eq. [2] where k_m^o is $2k_m$ at $\theta = 0.5$.

The mass transfer coefficient was found to depend on KCl concentrations (Fig. 8). Examination of Fig. 8 shows that the dependence follows the relationship

$$k_m^o = B \exp(Ec_e) \qquad [4]$$

with $B = 1.808 \times 10^3$ cm/sec and $E = -1.519 \times 10^3$ cm^3/mole.

The kinetic rate expression applied to the present system can be written as

$$i = \theta i_o \left[\left(\frac{c_R^s}{c_R^{sat}} \right)^{\gamma - \alpha_a} \exp\left(\frac{\alpha_a \mathbf{F} \eta}{RT} \right) - \left(\frac{c_R^s}{c_R^{sat}} \right)^{\gamma - \alpha_c} \exp\left(\frac{-\alpha_c \mathbf{F} \eta}{RT} \right) \right] \qquad [5]$$

where γ is the order of dependence of i_o on the complexed silver ion concentration; α_a and α_c are the anodic and cathodic charge transfer coefficients, respectively; R is the gas constant; and T is the absolute temperature. The exchange current density i_o can be written as

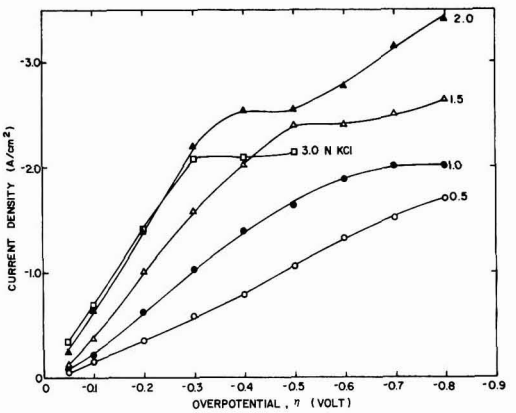

Fig. 7. Current-overpotential curves for the reduction of silver chloride. The current is the maximum current from the *i-t* curves.

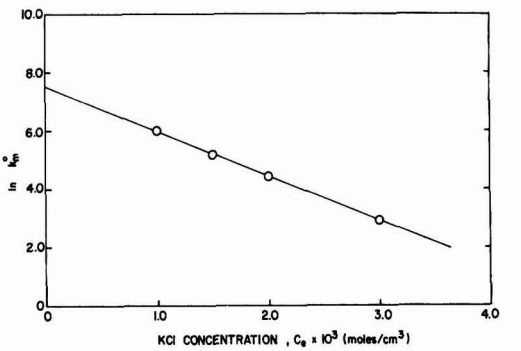

Fig. 8. Dependence of the mass transfer coefficient on KCl concentrations.

$$i_o = i_o^o \left(\frac{c_R^{sat}}{c_R^*} \right)^{\gamma} \quad [6]$$

where i_o^o is the exchange current density corresponding to the concentration of complexed silver ions, c_R^*. In the present investigation, c_R^* was selected as the saturated concentration of $AgCl_{n+1}^{-n}$ in 1*N* KCl solution, *i.e.*, $c_R^* = c_R^{sat}$ in 1*N* KCl.

It is believed that the silver dissolution and deposition involves a one-electron transfer elementary step. Therefore, Eq. [5] can be rearranged, with $\gamma = \alpha_a$ and $\alpha_a + \alpha_c = 1.0$, to read

$$\ln \frac{i}{\left[\left(\frac{c_R^{sat}}{c_R^s} \right) \exp \left(\frac{\mathbf{F}\eta}{RT} \right) - 1 \right]} - \ln \left(\frac{c_R^s}{c_R^*} \right) = \ln \theta i_o^o - \alpha_c \left[\frac{\mathbf{F}\eta}{RT} + \ln \left(\frac{c_R^{sat}}{c_R^*} \right) \right] \quad [7]$$

Using the results from Fig. 7 and 8, values of c_R^s were first calculated from Eq. [1]. The left-hand side of Eq. [7] was then plotted against the terms in the bracket on the right-hand side as shown in Fig. 9. The slope of the plot allowed the detemination of α_c and the intercept gives the value of θi_o^o with $\theta = 0.5$ (since the peak current was used). The values of α_c and i_o^o were determined to be 0.3 and 0.15 A/cm^2, respectively.

The current density, i, can be calculated with respect to θ at a fixed η by solving Eq. [1] and [7] simultaneously. Calculations of i *vs.* θ for several different η indicate that the maximum currents occur at θ around 0.75 instead of 0.5 as was experimentally observed. The solubility of AgCl is quite low and thus the distance from silver chloride sites where $AgCl_{n+1}^{-n}$ ions are reduced is probably quite small. It is possible that the effective charge transfer silver area for the reduction of $AgCl_{n+1}^{-n}$ was actually less than the total exposed silver area when the electrode surface was less than 50% covered by AgCl.

A model was developed to calculate the effective silver reacting area. The model assumes that the effective silver area per silver chloride center is a ring extending a fixed distance from the perimeter of the silver chloride-silver interface. The effective width of the ring is calculated by assuming that all the exposed Ag is effective at θ equals 0.5. At $\theta \leq 0.5$

$$\theta_{eff} = \theta \quad [8a]$$

and at $\theta \geq 0.5$

$$\theta_{eff} = (1 - \sqrt{0.5})[2\sqrt{(1 - \theta)} + (1 - \sqrt{0.5})] \quad [8b]$$

An effective silver chloride area was also assumed for the supply of complexed silver ions at $\theta < 0.5$. Similar to the treatment in obtaining effective silver area at $\theta < 0.5$, the effective silver chloride area per center at $\theta < 0.5$ was also assumed to be a ring extending a fixed distance from the silver chloride-silver interface; the distance being calculated by assuming that all the silver chloride area is effective at $\theta = 0.5$. Therefore, at $\theta \leq 0.5$

$$(1 - \theta)_{eff} = 2\sqrt{1 - \theta}\sqrt{0.5} - 0.5 \quad [9a]$$

and at $\theta \geq 0.5$

$$(1 - \theta)_{eff} = 1 - \theta \quad [9b]$$

According to the model, θ and $(1 - \theta)$ in Eq. [1], [2], [5], and [7] should now be replaced by θ_{eff}, and $(1 - \theta)_{eff}$, respectively. The k_m in Eq. [2] is thus in the form, at $\theta \leq 0.5$

$$k_m = k_m^o [2\sqrt{1 - \theta}\sqrt{0.5} - 0.5]^{1/2}[\theta]^{1/2} \quad [10a]$$

and at $\theta \geq 0.5$

$$k_m = k_m^o [1 - \theta]^{1/2}[2\sqrt{1 - \theta}(1 - \sqrt{0.5}) + (1 - \sqrt{0.5})^2]^{1/2} \quad [10b]$$

Applying this revised form of the model, a maximum in current was obtained mathematically at $\theta = 0.5$.

To obtain the variation of θ with respect to Q (accumulated charge) for application in porous battery electrode modeling, the i-θ profiles were first calculated at various η using revised Eq. [1] and [5] for KCl concentration of 1.0*N*. From the experimental potentiostatic i-t curves at the corresponding η, a set of i-Q curves were then obtained approximately by graphical integration. Comparison of the calculated i-θ curves with the corresponding i-Q curves gave the variation of θ with respect to Q. It was found that the best fitted relationship is of the form

$$\theta = (0.25)^{Q/Q^*} \quad [11]$$

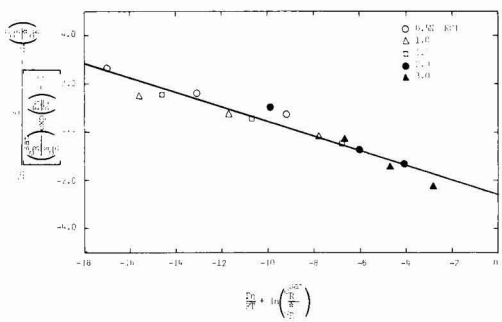

Fig. 9. Plot corresponding to Eq. [7]

Discussion

The two differently shaped η-t curves obtained on two different silver surfaces have also been observed separately by previous investigators. Briggs and Thirsk (6) obtained curves similar to curve a in Fig. 2 on their freshly polished silver surface while Katan *et al* (10) obtained curves similar to curve b on their cycled silver surface. The exchange current densities on a freshly polished silver surface and a cycled silver surface are probably different. The growth of AgCl on the two different surfaces is also different as can be seen from Fig. 4. On a freshly polished silver surface, there are a large number of AgCl nucleation centers formed at the beginning. As more charge is passed, the porous AgCl film thickens with a slow decrease in porosity. On a cycled surface, there are less nucleation centers and more crystal growth of silver chloride (Fig. 4 b and c). In addition, the true silver surface area of a cycled electrode is larger, as has been reported by Giles (9), and can be seen from Fig. 4 b and c. As a result, there is more silver surface available for charge transfer to occur for a longer duration and the overpotential is smaller. Finally, as anodic charging continues on the cycled Ag electrode, the AgCl crystallites begin to grow together, blocking off the silver surfaces, and the rapid rise in overpotential results. These observations support the fact that the formation of AgCl is mainly via solution phase diffusion of $AgCl_{n+1}^{-n}$ followed by crystal growth from a supersaturated solution.

For cycled surfaces, higher KCl concentrations produced lower overpotentials. This is attributed to higher $AgCl_{n+1}^{-n}$ solubility and resulting smaller concentration overpotentials. The shorter time to surface coverage, t_p, at higher KCl concentrations seems to indicate earlier coverage of the silver surface by AgCl in solutions of higher Cl^- content. The earlier coverage can be due to the increase in nucleation sites. Briggs and Thirsk (6) have also observed the earlier surface coverage in higher KCl concentrations. From their η-t curves (which are similar to curve a of Fig. 2), one

can see that the slopes of the curves are steeper in higher KCl concentrations.

The initial higher overpotential of the galvanostatic η-t curves of Fig. 2 are probably due to slow nucleation leading to a "nucleation overpotential" (18).

An electrolyte flow rate of 3.5 cm²/sec was used to keep the KCl concentration near the electrode surface constant. No dependence of current densities on the flow rate was observed during potentiostatic reduction within the flow rate range of 2.0-7.4 cm³/sec. With no circulation of the electrolyte, the measured current densities were higher as a result of the increase in KCl concentrations near the electrode surface as the AgCl was being converted to silver, the increase in KCl concentrations increases the solubility of the silver chloride.

The fact that no limiting current was observed during potentiostatic reduction in 0.5*N* KCl solution can be explained by nonuniform secondary current distributions and nonuniform concentration distributions of complexed silver ions at the silver surface. The experimental arrangement was designed for uniform macroscopic primary current distribution. However, due to the roughness of the electrode surface and because the reactants are supplied from the silver chloride crystallites, the secondary current distribution and the reactant concentration on a micro scale on the order of 1 μm at the silver surface are not uniform with respect to distance from AgCl crystals. This is especially true in 0.5*N* KCl, where the solubility of AgCl is lower and the microscale nonuniformity becomes more pronounced. As a result, the diffusion limiting current of silver deposition was not separable from the onset of another reaction (possibly hydrogen evolution) for the 0.5*N* KCl run.

An increase in silver chloride coverage reduces the number of reduction centers. The lesser number of reduction centers resulted in larger area per reduction center at $\theta = 0.5$ during discharging. For the case with heavy initial coverage of silver chloride, i-η curves similar to those reported by Katan *et al.* [Fig. 7 of Ref. (10)] were obtained. As can be expected, no limiting currents were observed due to the large area per reduction center at $\theta = 0.5$ (see Fig. 6 d and e), which resulted in very nonuniform microscale distribution of complexed silver ions and secondary reaction current across the exposed silver surface. The total effective silver area (boundaries of reduction centers) for the reduction of complexed silver ions was very small as compared to the total exposed silver area. Again, the limiting diffusion current was obscured by the onset of another reaction. The total effective area for the case with a large area per reduction center is also smaller than that for the case with a large number of reduction centers, and resulted in lower currents at $\theta = 0.5$ during potentiostatic reduction (Fig. 5, curve c).

The almost order of magnitude difference in maximum currents between curve a and curve c in Fig. 5 supports the solution diffusion mechanism in the electrochemical formation and reduction of silver chloride. If significant solid phase transport had occurred, there should have been less differences in the magnitude of the maximum currents.

The decrease in k_m^o at higher concentrations of KCl is due to the increased portion of $AgCl_4^{-3}$ present as can be shown from calculations using stability constants (19). The complexed $AgCl_4^{-3}$ has a larger ionic radius and thus a smaller diffusion coefficient than the other complexes. The measured k_m^o which includes all $AgCl_{n+1}^{-n}$, is therfore smaller at higher concentrations of KCl. Katan *et al.* (10), from their rotating disk experiments, also obtained a smaller effective diffusion coefficient for complexed silver ions in 4*N* KCl compared to that obtained in the 2*N* KCl solution.

The overpotential η, as measured, includes concentration overpotential, η_c as well as the charge transfer overpotential, η_s. At high overpotentials, η_c becomes important. The terms involving c_R^s/c_R^{sat} were introduced in Eq. [5] to correct for the concentration overpotential. At low overpotentials (less than −60 mV), surface diffusion of adions may become rate determining as was indicated by Bockris *et al.* (14, 15) in their studies of the dissolution and deposition of silver from solutions of silver perchlorate in aqueous perchloride acid. The effect of adion surface diffusion was not included in Eq. [5]. Therefore, in obtaining the slopes and intercepts according to Eq. [7], only data points above cathodic overpotential of 100 mV were used. In addition, since kinetic parameters were to be determined, data in the range where reaction rates might be predominantly solution phase mass transfer limiting were also excluded when constructing Fig. 9. The data excluded were $|\eta| > 0.4$V in 0.5, 1.0, and 1.5*N* KCl, $|\eta| > 0.3$V in 2.0*N* KCl, and $|\eta| > 0.25$V in 3.0*N* KCl.

It might be emphasized that the data in Fig. 7 and 9 are the same with the exceptions noted. The combination of Eq. [1] and [5] correlate the data as shown in Fig. 9. Since Fig. 7 presents the same data, it follows that these same equations yield approximately the curves shown in Fig. 7. The curves in Fig. 7 can be seen to be S shaped, the lower portions being near the inflection point of the S. The data at low η are in the region of exponential dependence of i on η shown in Eq. [5]. However, at larger η the curve in Fig. 7 bends downward due to a decrease in c_R^s as described by Eq. [1].

The overpotential as measured by the reference electrode also contained a small IR or ohmic resistance contribution which was considered negligible. The KCl solutions served as supporting electrolytes with high conductivity. Calculations showed, for example, at a current density of 2.0 A/cm², in 1*N* KCl, the maximum IR drop was about 20 mV, approximately 3% of the total observed overpotential, η.

Current densities as reported in this communication are based on the apparent electrode area. As mentioned earlier, the true surface area increases after the electrode has been cycled in KCl solutions. To account for the surface roughness based only on scanning electron microscope observations would not be very accurate. It was decided, therefore, that the results should be reported based on the apparent electrode area, keeping in mind that the experiment was performed on cycled electrode surfaces.

The true surface area also varied slightly between runs. Random checks showed that the current densities reported are reproducible to within ±10%.

It must also be pointed out that the variation of θ with accumulated charge shown in Eq. [11] is quite approximate. The variation of θ is actually potential dependent. This is because the growth of silver deposits is potential dependent as has been indicated by Aleskovskii *et al.* (11). The result also varied somewhat with the KCl concentration. However, the results shown in Eq. [11] appear to be suitable for purposes of mathematical modeling of porous Ag/AgCl battery electrodes.

Conclusions

The electrochemical behavior of a Ag/AgCl electrode is highly dependent on the surface coverage by AgCl during galvanostatic charging. The η-t (overpotential-time) curves differ widely in shape depending on whether the silver surface is freshly polished or previously cycled.

The number of silver chloride nucleation centers increases with increasing KCl concentrations during galvanostatic charging.

Experimental observations support previous conclusions that the formation and dissolution of AgCl on silver is via solution diffusion of complexed silver ions, $AgCl_{n+1}^{-n}$, with $n = 0$, 1, 2, or 3.

The maximum current density during potentiostatic discharge depends highly on the number of reduction centers. The number of reduction centers in turn depends on the degree of initial coverage by silver chloride. A heavier initial coverage gives lesser number of reduction centers during discharge. A larger number of small reaction sites leads to lower overpotentials at comparable current densities.

The mass transfer coefficient, k_m^o, for the diffusion of $AgCl_{n+1}^{-n}$ was found to depend on KCl concentrations in the form

$$k_m^o = B \exp(Ec_e)$$

with $B = 1.808 \times 10^3$ cm/sec and $E = -1.519 \times 10^3$ cm^3/mole.

The exchange current density was determined to be

$$i_o = 0.15 \left(\frac{c_R^{sat}}{10.1 \times 10^{-8}} \right)^{0.70} \text{A/cm}^2$$

The units of c_R^{sat} are mole per cubic centimeter.

The cathodic charge transfer coefficient, α_c was determined to be 0.30.

Acknowledgment

This work was supported by the Office of Naval Research under Contract no. N0014-75-C-0794 and the University of California, Los Angeles, California.

Manuscript submitted Oct. 18, 1976; revised manuscript received April 23, 1977.

Any discussion of this paper will appear in a Discussion Section to be published in the June 1978 JOURNAL. All discussions for the June 1978 Discussion Section should be submitted by Feb. 1, 1978.

Publication costs of this article were assisted by the University of California.

LIST OF SYMBOLS

A	electrode surface area, cm^2
c_e	electrolyte concentration, mole/cm^3
c_R^s	complexed silver ions concentration at the silver surface mole/ cm^3
c_R^{sat}	saturated concentration of complexed silver ions in the KCl solution mole/cm^3
c_R^*	saturated concentration of complexed ions in 1N KCl solution, mole/cm^3
D	effective diffusion coefficient of complexed silver ions, cm^2/sec
$\mathbf{F}$	Faraday constant, 96,487 C/equiv.
i	current density, A/cm^2
i_o	exchange current density, A/cm^2
i_o^o	exchange current density based on saturated concentrations of complexed ions in 1N KCl solution, A/cm^2
k_m	surface coverage dependent mass transfer coefficient, cm/sec
k_m^o	effective mass transfer coefficient of complexed silver ions (equal to $2k_m$ at $\theta = 0.5$), cm/sec
n	number of electrons transferred in electrode reaction; or number of charge on complexed silver ions
Q	charge, C/cm^2
Q^*	charge parameter, equal to it_p, C/cm^2
RT	gas constant multiplied by absolute temperature, J/mole
α_a, α_c	anodic and cathodic charge transfer coefficients
γ	exponent in composition dependence of the exchange current density
δ	effective diffusion path, cm
η	overpotential, $\eta = \eta_c + \eta_s$, V
η_c	concentration overpotential, V
η_s	charge transfer overpotential, V
θ	fraction of silver surface not covered by silver chloride

REFERENCES

1. H. Gu, D. N. Bennion, and J. Newman, *This Journal*, **123**, 1364 (1976).
2. T. Katan, H. Gu, and D. N. Bennion, *ibid.*, **123**, 1370 (1976).
3. G. J. Janz, in "Reference Electrodes," D. J. G. Ives and G. J. Janz, Editors, chap. 4, Academic Press, New York (1961).
4. L. J. Kurtz, C. R. URSS, **11**, 283 (1935).
5. H. Lal, H. R. Thirsk, and W. F. K. Wynne-Jones, *Trans. Faraday Soc.*, **47**, 70 (1951).
6. G. W. D. Briggs and H. R. Thirsk, *ibid.*, **48**, 1171 (1952).
7. W. Jaenicke, R. P. Tischer, and H. Gerischer, *Z. Elektrochem.*, **59**, 448 (1955).
8. M. Fleischmann and H. R. Thirsk, *Electrochim. Acta*, **1**, 146 (1959).
9. R. D. Giles, *J. Electroanal. Chem.*, **27**, 11 (1970).
10. T. Katan, S. Szpak, and D. N. Bennion, *This Journal*, **120**, 883 (1973).
11. V. B. Aleskovskii, E. V. Bairashnyi, E. G. Ivanov, and V. A. Nikoshii, *Sb. Rab. Khim. Istochnikam*, **4**, 241 (1969).
12. H. Gerischer and R. P. Tischer, *Z. Electrochem.*, **61**, 1159 (1957).
13. H. Gerischer, *ibid.*, **62**, 256 (1958).
14. W. Mehl and J. O'M Bockris, *J. Chem. Phys.*, **27**, 818 (1957).
15. A. R. Despic and J. O'M Bockris, *ibid.*, **32**, 389 (1960).
16. H. Gu, Ph.D. Thesis, School of Engineering, University of California, Los Angeles (1977).
17. W. F. Kinke, "Solubilities (Seidell)," 4th ed., Vol. I, p. 67, D. Van Nostrand Co., Inc., New York (1958).
18. M. Fleischmann and H. R. Thirsk, in "Advances in Electrochemistry and Electrochemical Engineering, III," P. Delahay, Editor, p. 168, Interscience Publishers (1963).
19. L. G. Sillen and A. E. Martell, "Stability Constants," Spec. Pub. No. 17, The Chemical Society, London (1964).

Statistical Analysis of Electrode Kinetics Measurements–Copper Deposition from $CuSO_4$-H_2SO_4 Solutions

Reinaldo Cabán[1] and Thomas W. Chapman*

Department of Chemical Engineering, University of Wisconsin, Madison, Wisconsin 53706

ABSTRACT

The kinetics of electrochemical copper deposition from copper sulfate-sulfuric acid solutions have been studied by measuring polarization curves with a rotating-disk electrode. Kinetics models are evaluated and their parameters determined by nonlinear regression analysis of 87 data points. The data are fit within experimental error by a five-parameter model which includes the effects of both copper sulfate and sulfuric acid concentrations. The statistical analysis is made feasible by the rapid simulation of the experimental system by orthogonal collocation. The simulation involves computation of current distribution below limiting current at a specified applied potential for a given kinetics model.

The determination of quantitative electrode kinetics expressions is difficult because of the large number of variables and parameters involved and because of the complicated nonlinear form of the electrochemical kinetics relationships. As a result most kinetic studies focus on only a subset of parameters such as the exchange current density or a reaction order, and do not attempt often to cover a wide range of experimental conditions. For engineering calculations, however, it is necessary to have a fairly complete kinetics expression which can predict local current density over a range of composition and potential.

It is risky to construct a kinetics expression for a given reaction by taking an exchange current density from one experiment and a Tafel slope from another experiment, etc., because there is no guarantee that such parameters are truly independent and that the composite expression will represent properly the behavior of a particular experimental system. For example, the metal surface formed in copper electrowinning probably has quite different catalytic properties from one prepared in the laboratory for a basic mechanistic study. It would be preferable for engineering purposes to determine a complete, empirical kinetics expression with all of its parameters estimated simultaneously from a set of experimental data which cover the ranges of variables to be encountered in a system of practical interest.

Statistical Treatment of Complex Systems

The problem of estimating multiple parameters of nonlinear models from data has been studied in some detail by statisticians (1-3), and methods have been developed for treating many complex phenomena, for example, heterogeneous catalysis (4). The appropriate statistical procedures are indicated in Fig. 1. The form of a kinetics model is postulated and incorporated in a simulation of the experimental system behavior. The parameters of the model are adjusted to make the simulation match the experimental data within experimental accuracy. Figure 1 indicates that least squares fitting of the data yields not only a set of parameters for a given kinetics model but also quantitative measures of goodness of fit and a parameter-estimate correlation matrix. The former may be compared with experimental error as determined by experimental replication to inspect whether or not a postulated kinetics model is adequate to fit the data. The latter indicates whether various parameters characterize independent effects or whether some are superfluous.

In most electrochemical experiments the data are some sort of current-potential relationship, and the simulation of the system behavior requires consideration of mass transfer and potential distribution effects in addition to the specific kinetics model. The major difficulty in applying nonlinear least squares regression analysis to fitting such electrochemical polarization data with a set of parameters is that the data analysis is an iterative procedure in which trial values of the parameters are repeatedly revised until the variance between the observed and predicted data is minimized. At each iteration one must generate not only a simulation or prediction of the experimental system output for each data point but also derivatives of the predicted output with respect to each parameter value, which are used in revising the parameter estimates.

Because electrochemical systems are so complicated these requirements imply a large and expensive computational effort. Recently we have described an approximate procedure for simulating electrochemical cell polarization which is significantly faster in computation time than alternative methods (5). The method known as orthogonal collocation is well suited to the repetitive calculations of nonlinear least squares analysis of electrochemical kinetics data. In this paper we demonstrate the combination of system simulation by collocation with nonlinear least squares estimation of electrochemical kinetics parameters by analyzing

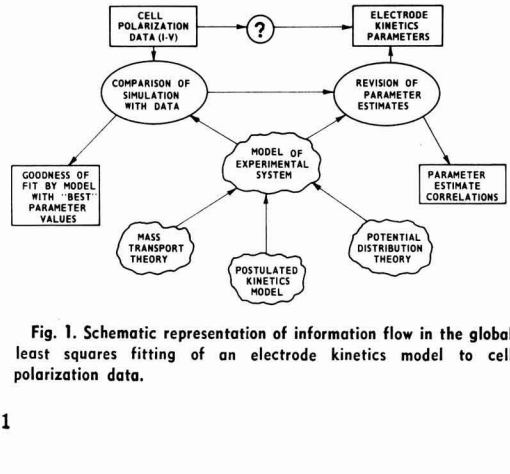

Fig. 1. Schematic representation of information flow in the global least squares fitting of an electrode kinetics model to cell polarization data.

* Electrochemical Society Active Member.

[1] Present address: Department of Chemical Engineering, University of Puerto Rico, Mayaguez, Puerto Rico 00708.

Key words: copper sulfate, sulfuric acid, rotating disk, current distribution, orthogonal collocation.

steady-state polarization measurements on a rotating-disk electrode. Measurements have been made with copper sulfate in sulfuric acid, and the kinetics parameters determined here are compared with earlier results.

Simulation of the Rotating-Disk Electrode

The problem of current distribution on a rotating-disk electrode below limiting current was first solved by Newman (6) in one of the earliest analyses of moderately complicated electrochemical transport problems. The problem was made tractable by a thin diffusion-layer approximation so that potential distribution and mass transfer effects could be treated separately (7). Since the solution to Laplace's equation for the potential in this geometry can be expressed as a series of Legendre functions, a summation of Legendre polynomials was used to describe the current distribution on the electrode. A second series was postulated for the concentration, and the two were matched by relating the current density to the flux of reactant at the surface. It was not recognized at the time that a formal solution for the concentration can be obtained as a superposition integral over the current density, but a later communication clarifies the point (8). Ten approximating functions were required to describe a metal deposition reaction, and a solution to the system of algebraic equations was obtained by repetitive substitution. Numerous convergence and precision difficulties were reported.

It is our purpose to show here how the incorporation of orthogonal collocation concepts in the solution of this problem can result in a faster and more stable computational algorithm. It is important to recognize that we are more interested in computing total current rather than computing detailed current distributions. Since the method of orthogonal collocation renders the solution at Gaussian quadrature points, estimates of the average current density can be obtained with considerably more accuracy than the detailed current distribution at any given order of approximation. Consequently, fewer approximating functions are required, and precision difficulties are minimized. Furthermore, it will be seen that the numerous integrals needed in the nonlinear regression calculations can be evaluated easily by Gaussian quadrature.

Mathematical formulation of the problem.—Newman (7) has presented the mathematical formulation for the current distribution problem for a disk electrode of radius r_0 embedded on an infinite rotating disk with a counterelectrode placed at infinity. According to the usual boundary layer arguments, concentration gradients can be neglected in the bulk of the solution such that Laplace's equation for the potential holds. A solution to the Laplace equation in rotational elliptical coordinates is (7, 9)

$$\phi(\xi,\rho) = \frac{RT}{|n|\mathbf{F}} \sum_{k=0}^{\infty} D_k P_{2k}(\rho) M_{2k}(\xi) \qquad [1]$$

where $y = r_0\xi\rho$, $r = r_0\sqrt{(1+\xi^2)(1-\rho^2)}$, y is the normal distance from the electrode, r is the radial distance, P_{2k} is a Legendre polynomial $[-1, 1]$ of degree $2k$, and M_{2k} is a Legendre function of imaginary argument, zeroeth order, and degree $2k$ (10). The latter is subject to the condition $M_{2k}(0) = 1$ and can be expressed formally as

$$M_{2k}(\xi) = \frac{(-1)^k (k!)^2 i}{(2k)!\pi} \int_{-1}^{+1} \frac{(1-t^2)}{(i\xi - t)^{2k+1}}\, dt \qquad [2]$$

The multiplicative constant in Eq. [1] is included for convenience. For large ξ, far from the disk, the first term in a series solution of Eq. [2] provides a useful approximation

$$M_{2k}(\xi) = \frac{(k!)^2}{\pi(2k)!\xi^{2k+1}} \frac{\Gamma(2k+1)\Gamma(1/2)}{\Gamma(2k+3/2)} \qquad [3]$$

The potential in the solution extrapolated to the surface of the electrode is given by

$$\phi_0(\rho) = \phi(0,\rho) = \frac{RT}{|n|\mathbf{F}} \sum_{k=0}^{\infty} D_k P_{2k}(\rho) \qquad [4]$$

Thus, the normal current density at the electrode is given by

$$\frac{i}{\kappa_\infty} = -\frac{\partial\phi}{\partial y}\bigg|_{y=0} = \frac{-1}{r_0\rho}\frac{\partial\phi}{\partial\xi}\bigg|_{\xi=0}$$

$$= \frac{-RT}{r_0\rho|n|\mathbf{F}} \sum_{k=0}^{\infty} D_k P_{2k}(\rho) M_{2k}'(0) \qquad [5]$$

where

$$M_{2k}'(0) = -\frac{2}{\pi}\frac{\{2^k k!\}^4}{\{(2k)!\}^2} \qquad [6]$$

We restrict our discussion to systems with an excess of supporting electrolyte so that the effect of ionic migration may be neglected. The equation of convective diffusion for every minor species in solution reads

$$v_r\frac{\partial c_i}{\partial r} + v_y\frac{\partial c_i}{\partial y} = \mathcal{D}_i\frac{\partial^2 c_i}{\partial y^2} \qquad [7]$$

in cylindrical coordinates, where $\mathcal{D}_i$ is the pseudobinary diffusion coefficient. An analytical solution to Eq. [7] may be obtained for the thin diffusion layer case where the first terms in the small y expansions of Von Kármán's velocity profiles may be used (11, 12). The appropriate approximations for the radial and axial velocity components are

$$\left.\begin{aligned} v_r &= ary\Omega\sqrt{\Omega/\nu} \\ \text{and} \qquad v_y &= -ay^2\Omega\sqrt{\Omega/\nu} \end{aligned}\right\} \qquad [8]$$

with $a = 0.51023$ (13). The solution to Eq. [7] corresponding to the limiting current ($c_R(0,r) = 0$) is

$$i_{lim} = \frac{n\mathbf{F}\mathcal{D}_R c_\infty}{s_R\Gamma(4/3)}\left(\frac{a\nu}{3\mathcal{D}_R}\right)^{1/3}\left(\frac{\Omega}{\nu}\right)^{1/2} \qquad [9]$$

Below limiting current we find it convenient to express the surface concentration as a superposition integral over the prevailing current density which is to be determined. For each reacting species

$$c_i(0,r) = c_{i0}(r) = c_{i\infty} + \frac{n\mathbf{F}\mathcal{D}_i}{s_i\Gamma(2/3)}\left(\frac{3\mathcal{D}_i}{a\nu}\right)^{1/3}\left(\frac{\nu}{\Omega}\right)^{1/2}\int_0^r \frac{i_y(\zeta)\zeta d\zeta}{[r^3-\zeta^3]^{2/3}} \qquad [10]$$

which can be obtained as shown in Section 58 of Levich (11) or, more easily, by applying Eq. [40] in a paper by Stewart (13).

Equations [5] and [10] relate the potential and concentration distributions on the electrode to the current distribution function. Another relationship among these quantities is needed, specifically a kinetics expression. Let us consider an electrode reaction

$$\sum_i s_i M_i^{z_i} \rightleftharpoons ne^- \qquad [11]$$

which follows kinetics of, say, the Butler-Volmer type. Many reactions have been shown to follow such a rate expression, which in general can be written as

$$i(r) = {}^0i_0\left[\prod_i c^{\gamma_{i0}i}(r)\right]\left[e^{\alpha_a\frac{\mathbf{F}\eta_s(r)}{RT}} - e^{-\alpha_c\frac{\mathbf{F}\eta_s(r)}{RT}}\right] \qquad [12]$$

where ${}^0i_0$ is the standard exchange current density ($c_{i0} = 1M$, all i), η_s is the surface overpotential, and α_a and α_c are the anodic and cathodic transfer coefficients, respectively. According to the simplified activated complex analysis from which Eq. [12] follows, one should have for a single step redox reaction ($0 + e^- \rightleftharpoons R$) following first-order kinetics, $\alpha_a = \alpha_c = \gamma_0 = \gamma_R = 1/2$.

The surface overpotential in Eq. [12] is related to other contributions to the cell potential by

$$V = U(c_\infty) + \phi_0(r) + \eta_s(r) + \eta_c(r) \qquad [13]$$

where V is the potential applied to the working electrode, $U(c_\infty)$ is the equilibrium cell potential for the conditions prevailing in the bulk of the solution, and η_c is the concentration overpotential given by

$$\eta_c = \frac{-RT}{n\mathbf{F}} \sum_i s_i \ln \frac{c_{i0}}{c_{i\infty}} \qquad [14]$$

In order to reduce the number of independent parameters we define the following dimensionless variables

$$E^* = E\frac{|n|\mathbf{F}}{RT} \qquad E = (V, \eta_s, \eta_c, U, \phi) \qquad [15]$$

$$i^* = \frac{i}{|i_{\lim}|} \qquad [16]$$

$$c_i^* = c_{i0}/c_{1\infty} \qquad [17]$$

$$x = r/r_0 \qquad [18]$$

$$\alpha = \alpha_a/|n| \qquad [19]$$

$$\beta = \alpha_c/|n| \qquad [20]$$

and

$$\Upsilon = \frac{|i_{\lim}n|r_0\mathbf{F}}{\kappa_\infty RT} \qquad [21]$$

Consequently, the basic equations [4], [5], [10], and [12-14] become

$$\phi_0^*(x) = \sum_{k=0}^{\infty} D_k P_{2k}(\rho) \qquad [22]$$

$$i^*(x) = -\frac{1}{\Upsilon\rho} \sum_{k=0}^{\infty} D_k P_{2k}(\rho) M'_{2k}(0) \qquad [23]$$

$$c_i^*(x) = c_{i_\infty}^* + \left(\frac{\mathcal{D}_1}{\mathcal{D}_i}\right)^{2/3} \frac{3\sqrt{3}}{2\pi} \left(\frac{s_i}{s_1}\right) \int_0^x \frac{i^*(\xi)\xi d\xi}{[x^3 - \xi^3]^{2/3}} \qquad [24]$$

$$i^* = {}^0i_0^* \left[\Pi(c_i^*(x)/c_{i\infty}^*)^{\gamma_i}\right]\left[e^{\alpha\eta_s^*(x)} - e^{-\beta\eta_s^*(x)}\right] \qquad [25]$$

$$V^* = U_\infty^* + \phi_0^*(x) + \eta_c^*(x) + \eta_s^*(x) \qquad [26]$$

and

$$\eta_c^* = \sum_i s_i \ln \frac{c_i^*}{c_{i\infty}^*} \qquad [27]$$

where $\rho^2 = 1 - x^2$. Simulation of polarization of a rotating-disk electrode requires solution of these equations for the current distribution for given values of V^* and system parameters.

Solution by orthogonal collocation.—We implement the orthogonal collocation procedure by postulating a trial solution as a finite summation of orthogonal polynomials $Q(x)$; that is

$$\overset{(N)}{i^*}(x) = \sum_{k=0}^{N-1} A_k Q_{2k}(x) \qquad [28]$$

for the Nth approximation. The polynomials Q_{2k} are orthogonal over $[-1, 1]$; since $i^*(x)$ is an even function only even polynomials of order 0, 2, . . . , $2N$-2 are included. At this stage the selection of particular polynomials need not be specified. If Eq. [22] and [23] are truncated to the first N terms, and Eq. [28] is substituted into Eq. [24], yielding a finite series of integrals which can be evaluated, the problem is reduced to solving a set of algebraic equations with N unknown coefficients A_k. We obtain a solution by requiring Eq. [22-27] to be satisfied exactly at N discrete points x_i which are selected as the roots of Q_{2N}. The rationale for this choice is that the error contributed by the first neglected term in the truncated series [28] is made identically zero. Also, because such a choice of collocation points corresponds to Gaussian quadrature abscissas, the average error in the approximation is minimized, and the evaluation of integrals involving any of the functions arising in the basic equations can be made with considerable accuracy by quadrature, even with small N. For example, it will be necessary to compute the total current, which is given by an integral. In this problem we take Q_{2k} to be a Legendre polynomial, P_{2k}, defined as (14)

$$\left.\begin{aligned} &P_{2k} = \sum_{m=0}^{k} a_{km} x^{2k-2m} \\ \text{where} \quad &a_{km} = \frac{(-1)^m}{2^{2k}} \binom{2k}{2m} \binom{4k-2m}{2k} \end{aligned}\right\} \qquad [29]$$

This choice is natural because these functions have already arisen in solving the Laplace equation. The total current can now be computed by

$$I = 2\pi r_0^2 \int_0^1 i(x)x\,dx \doteq 2\pi r_0^2 \sum_{k=0}^{N-1} w_i x_i i(x_i) \qquad [30]$$

where x_i and w_i are the points and the weights, respectively, of Gaussian Legendre quadrature (14). The quadrature in Eq. [30] will be exact for current distributions which can be represented by polynomials of degree $4N$-2 or less. The choice of a different quadrature formula may result in a more accurate approximation. For example, Tchebychev quadrature would be more accurate for highly nonuniform current distributions because it would give more weight to the function values near the edge of the disk than does the Legendre quadrature. Depending on the choice of quadrature formula, the polynomials $Q_k(x)$, the points x_i, and the weights w_i are chosen accordingly.

If we consider the reaction $O + e \rightleftharpoons R$ and take O as the reference species, substitution of Eq. [28] into [24] gives

$$\left.\begin{aligned} &c_O^*(x) = 1 + \frac{3\sqrt{3}}{2\pi} \sum_{k=0}^{N-1} A_k E_k(x) \\ \text{and} \quad &c_R^*(x) = c_{R_\infty}^* - \frac{3\sqrt{3}}{2\pi} \left(\frac{\mathcal{D}_R}{\mathcal{D}_O}\right)^{2/3} \sum_{k=0}^{N-1} A_k E_k(x) \end{aligned}\right\} \qquad [31]$$

where

$$E_k(x) = \int_0^x \frac{P_{2k}(\xi)\xi d\xi}{[x^3 - \xi^3]^{2/3}} = \Gamma(4/3) \sum_{m=0}^{k} a_{km} \frac{\Gamma\left(\frac{2k-2m+2}{3}\right)}{\Gamma\left(\frac{2k-2m+3}{3}\right)} x^{2k-2m} \qquad [32]$$

The coefficients in the potential distribution can be related to those in the trial function in the manner suggested by Newman (7), that is, by requiring Eq. [28] and [23] to be equal, multiplying both sides of the equality by $\rho P_{2s}(\rho)$, and integrating with respect to ρ

$$\sum_{k=0}^{N-1} A_k \int_0^1 \rho P_{2k}(x) P_{2s}(\rho)\, d\rho = \frac{-1}{\tau} \sum_{k=0}^{N-1} D_k M'_{2k}(0) \int_0^1 P_{2s}(\rho) P_{2k}(\rho)\, d\rho \quad [33]$$

By virtue of the orthogonality condition Eq. [33] becomes

$$D_k = \frac{-\tau(4k+1)}{M'_{2k}(0)} \sum_{l=0}^{N-1} A_l G_{lk} \quad [34]$$

where

$$G_{kl} = G_{lk} = \int_0^1 \rho P_{2k}(x) P_{2l}(\rho)\, d\rho = \sum_{m=0}^{l} a_{lm} \sum_{p=0}^{k} a_{kp} \sum_{q=0}^{l-m} \left\{ \frac{(-1)^q \binom{l-m}{q}}{2q+2k-2p+2} \right\} \quad [35]$$

These coefficients need be calculated only once for a given order of approximation.

Computational procedure and results.—The unknown coefficients A can be obtained by requiring the trial current distribution function to match the current density as given by the kinetic rate expression. That is

$$f(x_i) \equiv \sum_{k=0}^{N-1} A_k P_{2k}(x_i) - {}^0i_0{}^* \left[\frac{c_O{}^*(x_i)}{c_{O_\infty}{}^*} \right]^{\gamma_1} \cdot \left[\frac{c_R{}^*(x_i)}{c_{R_\infty}{}^*} \right]^{\gamma_2} \cdot \{ e^{\alpha \eta_s{}^*(x_i)} - e^{-\beta \eta_s{}^*(x_i)} \} = 0 \quad [36]$$

at all x_i ($i = 1, 2, \ldots, N$) which are the positive roots of $P_{2N}(x)$. The values of A may be obtained by a Newton-Raphson iteration about an appropriate initial guess. The following order of computation is convenient:

1. Given τ, V^* and all kinetic parameters adopt an initial guess for A. For example, obtain the leading coefficient A_0 from the zeroeth order solution (constant current distribution) and set the remaining coefficients to some small number.

2. Calculate $c_O{}^*(x)$ and $c_R{}^*(x)$ from Eq. [31], where x represents the set of N points x_i.
3. Calculate $\eta_c{}^*(x)$ from Eq. [27].
4. Calculate $\phi_0{}^*(x)$ from Eq. [22].
5. Calculate $\eta_s{}^*(x)$ from Eq. [26].
6. Calculate the residuals $f(x)$ from Eq. [36] and the Jacobian matrix of elements $\partial f(x_i)/\partial A_k$. New coefficient values are obtained as

$$A^{(n+1)} = A^{(n)} - [J^{(n)}]^{-1} f^{(n)} \quad [39]$$

where the superscript is an iteration index.

7. Return to step two with the $A^{(n+1)}$ if the rms of the normalized residuals is not less than some specified tolerance, that is, if

$$\left\{ \frac{1}{(N-1)} \sum_{i=1}^{N} \left(\frac{f(x_i)}{i^*(x_i)} \right)^2 \right\}^{1/2} \leq \epsilon$$

is not satisfied. We have used $\epsilon = 10^{-3}$.

In principle, the procedure outlined above must be repeated for increasing values of N until a characteristic quantity, say $\langle i^* \rangle = I^*/\pi r_0{}^2$, converges to a stationary value. A value of $N = 6$ has been found to be sufficient here to achieve not only a stationary $\langle i^* \rangle$ but also a satisfactory distribution $i^*(x)$. This small number of terms alleviates the numerical precision problems encountered by Newman (7) in dealing with Legendre polynomials of degree 20. The results of our calculations appear to be comparable to those presented by Newman (7). The principle difference in the two computational procedures is that our method exploits the accuracy of Gaussian quadrature in evaluating the integrals involved and allows us to work with fewer unknown coefficients and a small number of discrete points x_i on the electrode.

The complete solution of the current distribution problem for a given set of parameters at $N = 6$ required from 3 to 7 iterations and less than 0.25 sec of computing time on a Univac 1110 computer. Complete polarization curves could be generated economically, and extensive simulations made to study the sensitivity of the polarization curve to the kinetic parameters in the Butler-Volmer kinetics, Eq. [12]. As an example, Fig. 2 shows cathodic polarization curves computed for a redox reaction at various values of $i_0{}^*$ and α_c. It is apparent that the experimental discrimination of ${}^0i_0$ and α_c from experimental polarization curves of this sort requires analysis of data at values of $\langle i^* \rangle$ where variations in the surface concentrations become significant and must be accounted for in the data treatment. With the collocation simulation of the experimental system written for any postulated kinetics model and provided as a computer subroutine, nonlinear least squares regression routines can be used to determine kinetic parameters from a set of cell polarization data.

Statistical Analysis of Polarization Data

A common practice in the study of electrode kinetics is to postulate Butler-Volmer kinetics (Eq. [12]) with a symmetry factor $\beta = 1 - \alpha = 1 - \gamma_1 = \gamma_2$. The two parameters ${}^0i_0$ and β are obtained by comparing data at different degrees of polarization with limiting forms of the model, corresponding to linear and Tafel kinetics, respectively (15). It is also common to fix the value of β at 0.5, thus leaving ${}^0i_0$, or the rate constant, as the only independent parameter. A more reliable approach, at least for engineering purposes, will be to start with a rate expression of the form of Eq. [12] including the possibility that all the parameters are independent. A complete statistical analysis will involve the simultaneous estimation of all parameter values for a postulated kinetic model and an assessment of how well the model describes the data. Investigation of the parameter correlations and the variations of residuals in the experimental space guides one in revising the kinetic model to obtain a better fit of the data.

Consider a set of experimental data consisting of an array of observable quantities y and an array of independent or state variables ζ. A mathematical model is proposed to relate the two in terms of some system parameters θ, namely

$$\hat{y} = g(\zeta; \theta) \quad [40]$$

where $\hat{y}$ is the array of predicted responses. The statistical problem is to obtain estimates of the param-

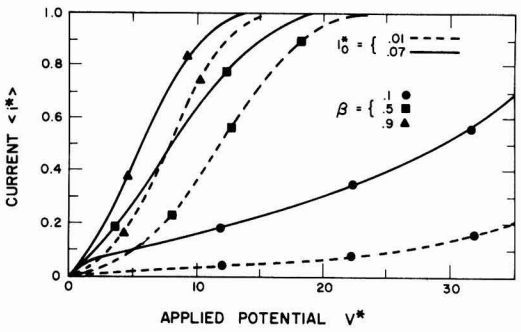

Fig. 2. Simulated cathodic polarization curves for a redox reaction on a rotating-disk electrode for $\tau = 7$ and various values of ${}^0i^*_0$ and β. $\gamma_O = \gamma_R = \frac{1}{2}$; $\alpha = 1 - \beta$; $n = 1$ (see Eq. [25]).

eters θ such that the best predictions of the observable quantity are obtained according to some optimality criterion. A common approach is to minimize the sum of squares of the errors. That is, values of θ are determined which minimize the quantity

$$\text{SSQ} \equiv \left\{ \sum_{\text{observations}} u_i (y_i - \hat{y}_i)^2 \right\} \quad [41]$$

where u_i is some suitable weighting function which reflects the distribution of experimental accuracy (4). In polarization experiments, the total current is the observable quantity, and Eq. [40] may be written as

$$\hat{y} = \int_0^1 i^*(x, \Upsilon, V^*; \theta)\, x\, dx \quad [42]$$

where the kinetic model for i^* might be of the form of Eq. [12], so that $\theta = (\alpha, \beta, i_0, \gamma_1, \gamma_2)$.

In the least squares fitting of such a model to a set of data, one starts with initial guesses for the parameters θ and computes from the simulation procedure a prediction $\hat{y}_i$ for each experimental point. Then SSQ can be computed according to Eq. [41], and some standard computer algorithm, such as Marquardt's method (16), can be used to find the values of θ which minimize SSQ. Such minimization programs require evaluation of a Jacobian or covariance matrix of partial derivatives of $\hat{y}$ with respect to each of the parameters. It is clear from the form of Eq. [42] that the elements of such a matrix will contain integrals. For example, we would have from Eq. [25] and [42]

$$\frac{\partial \hat{y}}{\partial \gamma_1} = {}^0i_0{}^* \int_0^1 c_O{}^{*\gamma_1} \ln (c_O{}^*)\, c_R{}^{*\gamma_2} [e^{\alpha \eta_s{}^*} - e^{-\beta \eta_s{}^*}]\, x\, dx \quad [43]$$

and

$$\frac{\partial \hat{y}}{\partial \beta} = {}^0i_0{}^* \int_0^1 c_O{}^{*\gamma_1} c_R{}^{*\gamma_2} \eta_s{}^* e^{-\beta \eta_s{}^*}\, x\, dx \quad [44]$$

Now, since the collocation simulation generates the value of every term in these integrands at Gaussian quadrature points, the integrals can be evaluated quite rapidly and accurately. An alternative procedure, computing the derivatives by finite differences, would require the complete solution of the current distribution problem at perturbed values of the parameters, and would increase the computation time considerably.

Experimental Measurements and Data Analysis

To demonstrate the application of these methods to electrochemical kinetics, we have studied copper deposition from aqueous $CuSO_4$-H_2SO_4 solutions onto a rotating-disk electrode. This system was chosen because of its industrial importance and because published results (15, 17-19) provide a good basis for comparison.

In order to discriminate the effects of the various parameters in Eq. [12], operation at high overpotentials, and hence at appreciable fractions of the limiting current, is necessary. The collocation method allows the appropriate interpretation of polarization curves in that region by expedient solution of the complete current distribution problem.

Experimental.—Potentiostatic measurements were made on an ESB Research Depak rotating-disk electrode assembly by means of a Princeton Applied Research Model 170 electrochemistry system. Although the ESB Depak indicates rotation speed on a digital meter, more accurate measurement of rotation speed was made by use of a stroboscope.

The working electrode was a 0.1 cm^2 platinum disk embedded in the end of a 1.6 cm diam Teflon shaft. The platinum electrode was covered with copper by deposition from the solution A (see Table I) at 0.2 mA for 2 min.

The cell was made of glass and had a cylindrical shape, 6.4 cm diam and 7.4 cm deep, and was blanketed with nitrogen. The reference electrode was a copper wire placed at 4.5 cm from the disk on the axis. The counterelectrode was a loop of copper wire, 6 cm diam, placed at the bottom of the cell. The reference and the counterelectrodes were covered with fresh deposits of copper from solution A. The solutions were prepared by weight from twice distilled water and reagent grade copper sulfate and sulfuric acid. The temperature was 21° ± 0.5°C. The solutions were thoroughly deaerated with nitrogen before each experiment.

Measurements were made for different levels of metal and acid concentration, the applied potential and disk rotation speeds were varied to obtain currents between 0.45 and −4.25 mA/cm^2, and concentrations were chosen to avoid complications due to varying physical properties and ionic migration. Table I shows the concentrations of the 6 solutions studied and the rotation speeds used. Limiting currents shown are those measured experimentally. Copper diffusivities were estimated from the compilation given by Selman (20). Using the latter, we verified the linear dependance of i_{lim} on $\Omega^{1/2}$ (21). Conductivities were calculated from the correlation given by Hsueh (22)

$$\kappa_\infty = 0.011163 + 0.030798\ (CuSO_4) + 0.423553\ (H_2SO_4) - 0.045224\ (H_2SO_4)^2 - 0.135359\ (H_2SO_4)\,(CuSO_4) \quad [45]$$

where molar analytical concentrations are used.

Smooth traces of current *vs.* potential were obtained for each of the 16 cases indicated in Table I by scanning the potential from anodic to cathodic at 5 mV/sec. Repeated scans on the same surface provided reproducible traces. The maximum noise was observed at limiting current, where fluctuations were less than 5% of the measured current. Replicate experiments, in which complete cell preparation was repeated, were conducted with solution A. Reproducibility of the current measurements between replicates was within 10%.

Sampled data points from the 16 polarization curves are given in Table II, where the observed currents have been divided by the measured limiting current.

Data analysis.—It has been verified (19) that the copper (II) deposition-dissolution reaction in acid sulfate systems takes place in two steps

Table I. Experimental conditions for Cu(II) deposition studies*

Concentration of $CuSO_4$ (M) \ Concentration of H_2SO_4 (M)	2.0	0.70	0.20
0.100	A 64 (911) 45 (400) 40 (295) 39 (300) $\mathcal{D}_{Cu^{+2}} = 3.82$	x	x
0.0316	B 27.5 (1757) 18.0 (596) $\mathcal{D}_{Cu^{+2}} = 4.41$	D 28.0 (1462) 17.5 (443) $\mathcal{D}_{Cu^{+2}} = 5.24$	x
0.0100	C 11.6 (2340) 9.4 (1592) 4.8 (430) $\mathcal{D}_{Cu^{+2}} = 4.67$	E 8.0 (995) 5.0 (313) $\mathcal{D}_{Cu^{+2}} = 5.35$	F 11.7 (1815) 8.0 (834) 6.8 (466) $\mathcal{D}_{Cu^{+2}} = 6.0$

* Entries are limiting current densities in mA/cm^2 and corresponding rotation speeds Ω (rpm). Copper diffusivities are in $cm^2/sec \times 10^6$.

$$\left.\begin{array}{ll} Cu^{2+} + e^- \rightleftharpoons Cu^+ & \text{(slow)} \\ Cu^+ + e^- \rightleftharpoons Cu & \text{(fast)} \end{array}\right\} \quad [46]$$

The assumption of Butler-Volmer kinetics with a symmetry factor $\alpha_c = 1/2$ for the slow reaction and of equilibrium for the fast reaction yields

$$i = {}^0i_0(CuSO_4)^\gamma \left[e^{\alpha_a \frac{F\eta_s}{RT}} - e^{-\alpha_c \frac{F\eta_s}{RT}} \right] \quad [47]$$

Table II. Summary of experimental results

Solution identification	Limiting current (mA/cm²)	Applied potential (V)	Observed current $\langle i^* \rangle_{OBS}$	Predicted current $\langle i^* \rangle_{PRED}$	Error $\frac{\langle i^* \rangle_{PRED} - \langle i^* \rangle_{OBS}}{\langle i^* \rangle_{OBS}}$
A	4.65	0.025	0.097	0.073	0.244
		−0.100	−0.118	−0.136	−0.153
		−0.200	−0.473	−0.420	0.111
		−0.300	−0.549	−0.785	0.076
A	3.25	−0.100	−0.154	−0.186	−0.207
		−0.200	−0.554	−0.519	0.063
		−0.300	−0.8..2	−0.852	0.045
		−0.040	−0.068	−0.076	−0.120
A	2.35	−0.100	−0.2.8	−0.242	0.098
		−0.150	−0.481	−0.411	0.146
		−0.200	−0.702	−0.609	0.133
		−0.250	−0.851	−0.783	0.080
		−0.025	−0.055	−0.070	−0.273
A	4.50	−0.100	−0.167	−0.140	0.158
		−0.200	−0.489	−0.423	0.122
		−0.300	−0.800	−0.792	0.010
		−0.400	−0.944	−0.962	−0.019
A	3.90	−0.100	−0.141	−0.159	−0.127
		−0.200	−0.410	−0.468	−0.141
		−0.300	−0.756	−0.820	−0.085
		−0.400	−0.936	−0.970	−0.037
B	1.80	0.030	0.133	0.119	0.109
		−0.010	−0.022	−0.020	0.085
		−0.020	−0.039	−0.037	0.056
		−0.050	−0.083	−0.078	0.070
		−0.100	−0.172	−0.160	0.069
		−0.150	−0.275	−0.293	−0.054
		−0.200	−0.472	−0.476	−0.009
		−0.250	−0.733	−0.673	0.082
		−0.300	−0.861	−0.829	0.037
B	3.00	−0.050	−0.067	−0.048	0.282
		−0.100	−0.133	−0.102	0.236
		−0.150	−0.240	−0.196	0.185
		−0.200	−0.433	−0.344	0.206
		−0.300	−0.750	−0.724	0.035
		−0.400	−0.873	−0.942	−0.078
C	0.48	−0.050	−0.135	−0.128	0.056
		−0.100	−0.229	−0.252	−0.101
		−0.150	−0.396	−0.427	−0.080
		−0.200	−0.625	−0.628	−0.005
		−0.250	−0.813	−0.799	0.016
		−0.300	−0.953	−0.908	0.052
C	0.94	0.030	0.106	0.106	0.000
		−0.050	−0.069	−0.069	−0.001
		−0.100	−0.128	−0.145	−0.132
		−0.150	−0.245	−0.268	−0.097
		−0.200	−0.415	−0.447	−0.077
		−0.250	−0.628	−0.647	−0.030
		−0.300	−0.798	−0.812	−0.017
		−0.350	−0.894	−0.915	−0.024
D	1.75	−0.050	−0.114	−0.121	−0.056
		−0.100	−0.234	−0.238	−0.016
		−0.150	−0.400	−0.403	−0.008
		−0.200	−0.611	−0.538	0.022
		−0.300	−0.886	−0.892	−0.007
		−0.350	−0.943	−0.957	−0.015
D	2.80	0.030	0.096	0.115	−0.188
		−0.010	−0.018	−0.021	−0.149
		−0.020	−0.029	−0.037	−0.301
		−0.050	−0.068	−0.079	−0.158
		−0.100	−0.168	−0.161	0.041
		−0.150	−0.296	−0.290	0.023
		−0.200	−0.500	−0.466	0.069
		−0.300	−0.857	−0.814	0.050
		−0.350	−0.936	−0.915	0.022
E	0.50	−0.050	−0.200	−0.184	0.079
		−0.100	−0.340	−0.344	−0.013
		−0.200	−0.700	−0.730	−0.042
		−0.300	−0.900	−0.944	−0.049
E	0.80	0.020	0.094	0.105	−0.121
		−0.010	−0.044	−0.033	0.249
		−0.020	−0.069	−0.059	0.140
		−0.030	−0.086	−0.082	0.067
		−0.040	−0.106	−0.102	0.036
		−0.050	−0.125	−0.123	0.018
		−0.150	−0.363	−0.413	−0.138
		−0.250	−0.700	−0.785	−0.122
		−0.350	−0.888	−0.961	−0.083
F	0.62	−0.020	−0.097	−0.086	0.111
		−0.030	−0.145	−0.118	0.185
		−0.070	−0.242	−0.233	0.038
		−0.100	−0.355	−0.329	0.074
		−0.200	−0.758	−0.706	0.069
F	1.17	0.020	0.162	0.143	0.117
		−0.100	−0.231	−0.201	0.131
		−0.200	−0.573	−0.530	0.074
		−0.300	−0.872	−0.852	0.023

with $\gamma = (2 - \alpha_c/2) = 0.75$ and $\alpha_a = 2 - \alpha_c = 1.5$. Equation [47] may not apply very precisely to the dissolution process because it does not account for diffusion of Cu(I) away from the electrode (23).

Statistical regression analyses of our data with Eq. [47] and several other models were performed with 87 discrete points selected from the 16 polarization curves. Simulation was accomplished by using the algorithm described above with two collocation points ($N = 4$). For lack of a better criterion, these were selected at potential intervals of 0.05 or 0.10V to get about 4 or 5 points from each curve as indicated in Table II. Some observations on the anodic side were necessary for the independent estimation of the anodic transfer coefficient, but these were taken only at currents small compared to the cathodic limiting current. The variable used in the statistical analysis was dimensionless average current density $\langle i^* \rangle = \langle i \rangle / i_{lim}$, and a weighting factor u_i of $1/\langle i^* \rangle^2_{obs}$ was used. This renders the residuals on a percentage basis which is representative of the error distribution in the instrument.

Table III summarizes the parameters estimated from the data for four kinetics models which were tested and their respective sums of squares. Models I and II correspond to those used by the investigators cited earlier. Model II, in which the two transfer coefficients are estimated independently, gives a better fit. However, neither model fits the data within experimental accuracy, and an investigation of their residuals reveals a correlation with sulfuric acid concentration.

To account for the acid concentration effect, we devised semiempirical models III and IV. Because of the precautions taken in selecting the relative concentrations of acid and metal, we can safely neglect the effect of the acid on copper migration. On the other hand, the scant data available on activity coefficients for aqueous $CuSO_4$-H_2SO_4 solutions point to a strong dependence of copper sulfate activity on the concentration of sulfuric acid (24, 25). In view of the large excess of sulfuric acid present, a first-order approximation of the activity coefficient variation should be obtained with an expression of the form $e^{-\delta(H_2SO_4)}$ (26). It is apparent from the results in Table III that the inclusion of such a term reduces the sum of squares considerably, with the model which allows the independent estimation of transfer coefficients, Model IV, being the more likely. Note that the term $\theta_1 e^{-\delta(H_2SO_4)}$ represents the standard exchange current densities for Models III and IV.

In Table II we have listed with the data the residuals corresponding to Model IV. It is seen that the largest percentage deviations occur for very small potentials and that there is no apparent correlation of errors between runs at different concentrations.

The standard deviation obtained for Model IV, about 11%, is roughly equal to that obtained from the replicate runs with solution A, so that within the limits of experimental reproducibility, Model IV describes our experimental observations adequately.

Figure 3 compares two representative experimental curves with the results of the simulation with Model IV shown as discrete points. The results shown here are typical of those obtained for all 16 experimental curves. Although the largest relative error occurs at small currents, the largest absolute discrepancy in the current appears in the intermediate range. In all cases, however, the error is less than 0.3 mA, which should be satisfactory for most practical purposes.

Discussion of Results

It has been found that Model IV in Table III describes our data within the accuracy of the experimental measurements, that is, with a standard deviation of about 11%. On the other hand, Model I with the parameters listed in Table III exhibits a standard deviation of 22% and is not considered to be a satisfactory model for reproducing the data. It appears that sulfuric acid

Table III. Models for Cu (II) deposition and dissolution kinetics

Model*	Parameters					SSQ (87 observations)
	$^0i_0$ or θ_1 (mA/cm^2)	γ	α_A	α_c	δ (M^{-1})	
I $i = {}^0i_0(\mathrm{Cu})^\gamma \left[e^{(2-\alpha_c)\eta \frac{F}{RT}} - e^{-\alpha_c \eta \frac{F}{RT}} \right]$	5.51	0.62	—	0.42	—	4.231
II $i = {}^0i_0(\mathrm{Cu})^\gamma \left[e^{\alpha_A \eta \frac{F}{RT}} - e^{-\alpha_c \eta \frac{F}{RT}} \right]$	6.78	0.58	1.09	0.36	—	3.051
III $i = \theta_1(\mathrm{Cu})^\gamma e^{-\delta(H_2SO_4)} \left[e^{(2-\alpha_c)\eta \frac{F}{RT}} - e^{\alpha_c \eta \frac{F}{RT}} \right]$	14.5	0.72	—	0.43	0.40	2.117
IV $i = \theta_1(\mathrm{Cu})^\gamma e^{-\delta(H_2SO_4)} \left[e^{\alpha_A \eta \frac{F}{RT}} - e^{-\alpha_c \eta \frac{F}{RT}} \right]$	15.6	0.67	1.08	0.39	0.37	1.123

* Concentrations are analytical concentrations in moles/liter.

concentration has a measurable effect on copper deposition kinetics.

The principal purpose of this work has been to develop a systematic methodology for obtaining kinetic data for practical engineering purposes. Thus, we were content to take our example data at room temperature (21°C) rather than at 25.0°C, and to prepare electrode surfaces in a rather arbitrary way. Nevertheless, it is interesting to compare our experimental results with those of earlier workers.

For the description of kinetic behavior in a solution of fixed composition, the kinetics expression may be written

$$i = i_o \left[e^{\alpha_a \eta F/RT} - e^{-\alpha_c \eta F/RT} \right] \qquad [48]$$

where the preexponential factor is called simply the exchange current density. By comparison with Model IV, the exchange current density i_o should be

$$i_o = 1.58\,(\mathrm{Cu})^{0.67} e^{-0.36(H_2SO_4)} \mathrm{mA/cm^2} \qquad [49]$$

where the concentrations are expressed in moles/liter. Table IV compares kinetic parameters i_o, γ, α_a, and α_c indicated by this work with results reported by earlier workers. Specific concentrations have been chosen in each case to make the i_o comparison possible. It is gratifying that the i_o values predicted from Eq. [49] agree so well with the results of the earlier workers, particularly considering the wide ranges of composition involved. Better agreement could hardly be expected among workers who prepared electrodes differently and made different types of measurements. Also, the temperature differences should affect i_o.

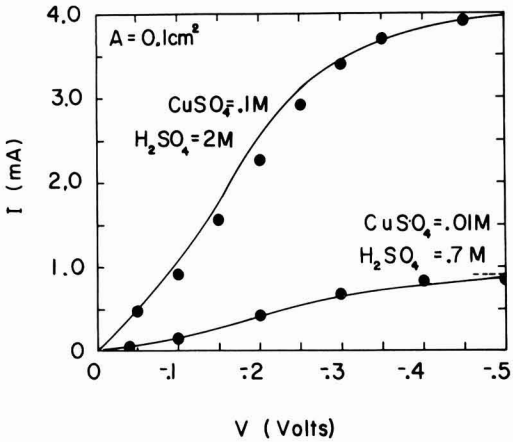

Fig. 3. Comparison of two experimental polarization curves with point values predicted by Model IV and the collocation simulation.

The reaction order γ is also in good agreement with earlier work. On the other hand, it is somewhat distressing that our transfer coefficients are significantly lower than those obtained previously. We see no obvious explanation of this discrepancy, but we note that in Models I and III, where $\alpha_a = 2 - \alpha_c$, the statistical analysis yields a larger value for α_c.

Table V shows the correlation matrix for the parameters of Model IV. It is seen that the correlation coefficients are generally small, which means that each parameter is characterizing a different aspect of the kinetics law. The largest correlation, 0.843, is between θ_1 and γ. This probably means that the model is not accounting as well as it might for the dependence of the rate on the copper concentration. Clearly, the use of γ is not redundant as shown by the range of i_o in Table IV, but the assumed form of the copper dependence may not be satisfactory. For example, a factor for the copper dependence of the activity coefficient might be appropriate.

It should not be surprising that the best empirical parameters for the models tested do not agree with the theoretical values of Eq. [47]. Copper sulfate-sulfuric acid solutions are quite nonideal with $CuSO_4$ ion pair formation likely (24). For engineering purposes it is necessary to obtain experimental kinetics data measured under conditions similar to those where the data will be applied. Measurement on a rotating disk with proper analysis of transport effects satisfies this requirement in the sense that the boundary layer phenomena on the disk should be similar to those in electrolysis cells (27).

It should be noted that the data analysis presented here can be simplified by using a one-point approximation ($N = 1$). In that case, $i^* = A_0$, $c_0^* = 1 + A_0$, $c_R^* = 1 - A_0$, $\phi_0 = \Upsilon\pi A_0/4$, etc., and the statistical parameter determination can be done quite easily. An important point, however, is that this first approximation of the complete model does not correspond to the simple one-dimensional model commonly used.

Summary

Nonlinear regression analysis can be used to determine empirical parameters for a postulated electrode kinetics expression. All parameters are estimated simultaneously from a set of polarization data to obtain an optimal fit of the data. Accordingly, the resulting kinetics model should be useful for engineering analysis of experimental systems where the same range of conditions is encountered.

Practical implementation of the regression analysis requires rapid simulation of the experimental system. Approximate computation of current distribution by orthogonal collocation fulfills this requirement and

Table IV. Comparison of Model IV parameter estimates with published results for copper electrode kinetics in acidic sulfate solutions

Source	$CuSO_4$ (M)	H_2SO_4 (M)	i_o (mA/cm²)	i_o predicted by Eq. [49] (mA/cm²)	γ	α_a	α_c
Mattsson and Bockris (15)	0.075	0.5	2.2-3.7	2.3	0.6	1.3	0.49
Hurlen (17) (extrapolated)	1	0.05	23.6	15.5	0.73	1.5	0.50
Karasky and Linford (18)	0.75	0.25	11.4	11.9	—	—	0.59
This work					0.672	1.07	0.38

Table V. Parameter estimate correlation matrix for Model IV

	θ_1	α_a	α_A	γ	δ
θ_1	1				
α_a	0.29	1			
α_A	−0.18	0.52	1		
γ	0.84	0.64	0.15	1	
δ	−0.70	−0.42	−0.04	−0.51	1

facilitates the iterative calculations which yield the parameter values.

We have demonstrated the application of these methods to the rotating-disk system. Because of the flexibility and efficiency of the collocation method it can be applied to other geometries and extended to multiple reaction cases as well (21).

Acknowledgments

Reinaldo Cabán has been supported by the University of Puerto Rico at Mayaguez. This work has been funded in part by the National Oceanic and Atmospheric Administration's Office of Sea Grant, Department of Commerce, through an institutional grant to the University of Wisconsin.

Manuscript submitted Aug. 16, 1976; revised manuscript received May 17, 1977.

Any discussion of this paper will appear in a Discussion Section to be published in the June 1978 JOURNAL. All discussions for the June 1978 Discussion Section should be submitted by Feb. 1, 1978.

LIST OF SYMBOLS

A_k coefficients defined by Eq. [28]
a coefficient in Eq. [8]
a_{km} coefficients defined by Eq. [29]
c^* dimensionless concentration
c concentration, mole/m³
D_k coefficients defined by Eq. [1]
$\mathcal{D}_i$ pseudobinary diffusion coefficient of species i in solution, m²/sec
E_k functions defined by Eq. [32]
$\mathbf{F}$ Faraday's constant, 96,487 C/equiv.
f residual defined by Eq. [36]
G_{kl} coefficients defined by Eq. [35]
I total current, A
i current density, A/m² or mA/cm² in numerical results
$\langle i \rangle$ average current density, A/m²
i_o exchange current density, A/m²
$^0i_0$ standard exchange current density, A/m²
i_{lim} limiting current density, A/m²
i^* dimensionless current density, normal component at electrode
M_i chemical species i
M_{2k} Legendre function defined by Eq. [2]
N number of collocation points
n number of electrons produced by electrode reaction
P_i Legendre polynomial of degree i
Q_{2k} polynomial of order $2k$, members of an orthogonal set
R universal gas constant, 8.3143 J/mole-°K
r radial position, m
r_0 radius of disk electrode, m
s_i stoichiometric coefficient of species i
SSQ sum of squares, defined by Eq. [41]
T temperature, °K
u_i weight factor in Eq. [41]
U equilibrium cell potential, V
v velocity, m/sec
w_i quadrature weights
x_i collocation abscissas
x dimensionless radial position on electrode surface, r/r_0
y normal distance from electrode, m
$\hat{y}$ predicted experimental response
z_i charge number of species i

Greek letters

α_a anodic transfer coefficient
α scaled anodic transfer coefficient, $\alpha_a/|n|$
α_c cathodic transfer coefficient
β scaled cathodic transfer coefficient, $\alpha_c/|n|$
β_0 derivative of axial velocity at the wall, sec^{-1}
γ a kinetic parameter, reaction order
$\Gamma(x)$ Gamma function of x
δ parameter in kinetics model, $(mole/liter)^{-1}$
ϵ error tolerance
ζ dummy integration variable
η_s, η surface overpotential, V
η_c concentration overpotential, V
θ kinetic parameters
κ conductivity, $\Omega^{-1}m^{-1}$
ν kinematic viscosity, m²/sec
ξ a rotational elliptical coordinate defined below Eq. [1]
ρ a rotational elliptical coordinate defined below Eq. [1]
Υ dimensionless parameter defined by Eq. [21]
ϕ potential in the solution, V
Ω rotation speed, rad/sec

Common subscripts

i of species i or evaluated at collocation point x_i
0 evaluated at the surface of the electrode
∞ evaluated in the bulk of the solution
R reactant or reduced species
O oxidized species

Common superscripts

$*$ dimensionless variable
(N) refers to the Nth approximation
(n) refers to nth iteration

REFERENCES

1. G. E. P. Box and W. G. Hunter, *Technometrics*, **4**, 301 (1962).
2. G. E. P. Box and W. J. Hill, *ibid.*, **9**, 57 (1967).
3. N. R. Draper and H. Smith, "Applied Regression Analysis," John Wiley & Sons, New York (1966).
4. J. R. Kitrell, W. G. Hunter, and C. C. Watson, *AIChE J.*, **12**, 5 (1966).
5. R. Cabán and T. W. Chapman, *This Journal*, **123**, 1036 (1976).
6. J. Newman, *This Journal*, **13**, 1236 (1966).
7. J. Newman, "Electrochemical Systems," Prentice-Hall, Inc., Englewood Cliffs, New Jersey (1973).
8. J. Newman, *This Journal*, **114**, 239 (1967).
9. J. Newman, "The Fundamental Principles of Current Distribution and Mass Transfer in Electrochemical Cells," *UCRL-20547*, University of California, Berkeley (1971).
10. P. M. Morse and H. Feshbach, "Methods of Theoretical Physics," McGraw-Hill Book Co., New York (1953).
11. V. G. Levich, "Physicochemical Hydrodynamics," Prentice Hall, Inc., Englewood Cliffs, New Jersey (1962).
12. G. K. Batchelor, "An Introduction to Fluid Dynamics," Cambridge University Press, Great Britian (1970).
13. W. E. Stewart, *AIChE J.*, **9**, 528 (1963).

14. "Handbook of Mathematical Functions," M. Abramowitz and I. Stegun, Editors, National Bureau of Standards, Washington, D.C. (1964).
15. E. Mattsson and J. O'M. Bockris *Trans. Faraday Soc.*, **55**, 1586 (1959).
16. D. L. Marquardt, *J. Soc. Ind. Appl. Math.*, **2**, 431 (1963).
17. T. Hurlen, *Acta Chem. Scand.*, **15**, 630 (1961).
18. L. Karasyk and H. B. Linford, *This Journal*, **110**, 895 (1963).
19. O. R. Brown and H. R. Thirsk, *Electrochim. Acta*, **19**, 383 (1965).
20. J. R. Selman, Ph.D. Dissertation, University of California, Berkeley (UCRL-20557) (1971).
21. Reinaldo Cabán, Ph.D. Thesis, University of Wisconsin, Madison (1976).
22. L. Hsueh, Dissertation, UCRL-18597, University of California, Berkeley, California (1968).
23. C. Wagner, *Electrochim. Acta*, **14**, 971 (1969).
24. R. A. Robinson and R. H. Stokes, "Electrolyte Solutions," 2nd ed., Butterworths Publications Ltd., London (1959).
25. T. W. Chapman, Unpublished research.
26. E. A. Guggenheim, "Thermodynamics," 5th ed., North-Holland Publishing Co., Amsterdam (1967).
27. J. Newman, *Int. J. Heat Mass Transfer*, **10**, 983 (1967).

Double Layer Capacitance and Charging Rate of Ultramicroporous Carbon Electrodes

J. Koresh and A. Soffer

Atomic Energy Commission, Nuclear Research Centre-Negev, Beer-Sheva, Israel

ABSTRACT

Adsorption of ions from aqueous solutions into pores, as narrow as 3.7Å was observed, using linear sweep cyclic voltametry. The conductivity of the solution in pores of less than 7Å diameter is several orders of magnitude lower than that of a free 0.1*N* NaCl solution in contact with the carbon electrode. It seems negligibly slow in pores of less than 3.7Å diameter, which are still completely filled with water. Highly oxidized ultramicroporous carbons show much lower double layer capacitance at positive potentials than nonporous carbon surfaces. This is interpreted as repulsive ion-dipole interaction of the anion with the dipole of the chemisorbed oxygen. Ions can penetrate the tiny pores after depletion of the hydration sheath. The double layer charging rate is therefore much slower if 0.1*N* NaCl is replaced by 0.1*N* LiCl. A brief discussion is presented in order to confirm that the electroactive surface groups can be treated in terms of (capacitative) double layer charging.

One of the fundamental requirements of electrochemical power sources are low overvoltage electrodes. Optimization of the physical design of the electrode is partially achieved by increasing the ratio of internal, S_i, to geometrical, S_g, surface area; this lowers the real current density. The S_i/S_g can be increased by using a thicker electrode and/or by increasing the porosity of the electrode. However, since the porous matrix serves as sink for the electrical charge, and due to the resistivity of the solution in the pores, the current decays rapidly on moving away from the counterelectrode. This imposes a limit for the thickness of a practical electrode. The question now is whether the increased active surface area of the porous electrode has also theoretical limitations. Ion mobility in the narrow pores of high internal surface area electrodes may rule out the availability of this surface for the electrode process.

Extensive studies were published on the transport properties of porous electrodes (1, 2), where models of continuous electrode media were used, but the role of pore structure was mostly neglected Only recently has the simplest of these models been satisfactorily matched with experiment (3, 4).

Another property of high surface porous electrodes is their probable usefulness as high capacity electroadsorbent. This idea, which was first put forward by Garten and Weiss (5), was examined experimentally by Murphy *et al.* (6). Much later, the electrosorptive properties were attributed to the electric double layer (7, 8), but again the influence of the fine structure was still disregarded. The pore structure which is characterized by a solid-gas system is being investigated, and several techniques for the characterization of mean pore diameter and pore diameter distribution have been developed (9). The kinetics of adsorption of neutral molecules from solution into porous solids have also been studied (10).

Key words: double layer charging, ultramicropores, carbon electrode.

In the present work pore structure of various carbons and graphites are characterized by means of the well-established methods of gas adsorption, and then the double layer capacitance (C_d) and ion transport through the pore are examined.

An ultramicroporous carbon, with pore size comparable to that of small molecules, is studied. Because of their electrical charge, the rate of transport and adsorbability of ions into narrow pores may have some special features which are encountered neither in solid-gas adsorption systems nor in solid-nonelectrolytic liquid interfaces. As carbon and graphite have polar oxygen surface groups (11), short range ion-dipole interactions influence the behavior of ions in ultramicroporous carbon, unlike flat or wide pore carbon electrodes.

Experimental

The porous carbon electrode was TCM 128 carbon cloth and TGM 389 served as nonporous reference carbon, both supplied by Le Carbonne Loraine, France. Both electrode materials are composed of fibers of cylindrical cross sections of approximately 3 μm for TGM 389, and 6-10 μm for TCM 128 (Fig. 1 and 2). A special feature of TCM 128 and of some other nonactivated fibrous carbons is the complete absence of pores larger than ultramicropores. The diameter of the pores was less than 3.7Å (12). This is the reason that almost all of the surface area results from ultramicropores and only a very small part from the outer surface area of the fibers. The geometrical surface area, S_g, of TGM 389, calculated from an average diameter of 3.2 μm, is

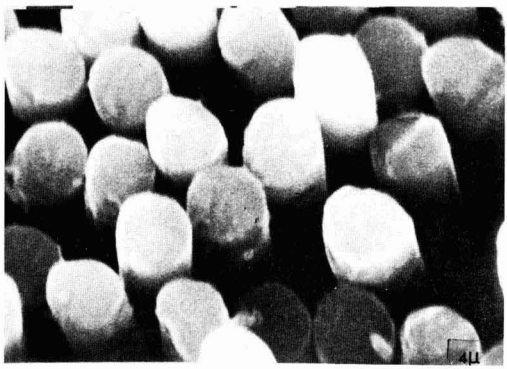

Fig. 1. SEM micrograph of the graphitized carbon fibers TGM 389.

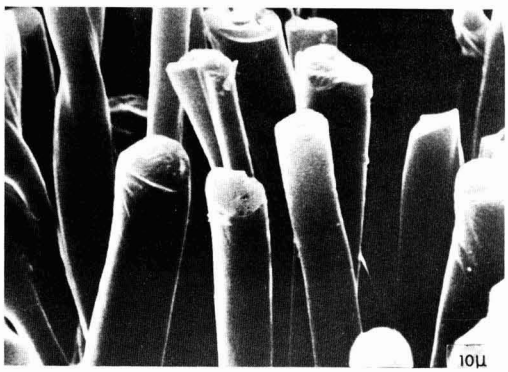

Fig. 2. SEM micrograph of the ultramicroporous carbon fibers TCM 128.

approximately 0.3 m^2/g. The BET surface area (S_{BET}) of TGM 389, measured on a 3g sample, was 1.2 m^2/g. This corresponds to a roughness factor of $S_{BET}/S_g = 4$.

The ultramicropores of the as-received TCM 128 carbon were too narrow to accommodate N_2 molecules (12), therefore the BET surface area obtained from nitrogen adsorption isotherms gave the outer surface area (as for TGM 389) 0.95 m^2/g. From an average diameter of 8 μm we have approximately 0.12 m^2/g for the geometrical surface. This corresponds to a roughness factor of 8. These rough outer surface areas are negligible compared to the much larger (> 250 m^2/g) area of the ultramicropores of TCM 128 (12).[1] Some of the manufacturers' specifications of the carbons are given in Table I.

The electrolytes were sodium chloride and lithium chloride, analar grade. Water was triply distilled.

The electrochemical cell.—Through the openings in the cover of a standard Metrohm cell, three electrodes, deaeration tubes, and a gas outlet were introduced. The reference electrode was a 0.1*N* NaCl calomel electrode half-cell. The auxiliary electrode was a platinum and later a silver rod, enclosed in a glass tube with a sintered base containing the solution. The carbon cloth, working electrode ($\sim 3 \times 3$ cm^2) was stretched across the opening of another glass tube and tightened with gold wire which also served as current collector. The reference electrode was mostly introduced into this tube so that the *IR* drop was screened off by the carbon cloth. At currents below 50 μA the reference electrode was transferred to the main compartment of the cell, since otherwise its complete freedom from *IR* drop at the first mode resulted in an oscillatory response of the potentiostat. This is because the *R-C* impedance of the working electrode in the double layer range produces a delay in the potential response at the solution compartment opposite the counterelectrode (4). The electrolytic solution used mostly was sodium chloride 0.1*N*. The maximum value of the *IR* drop was evaluated by interrupting the charging current and measuring the sudden change in potential. It was never above the millivolt range and had thence been neglected.

Instrumentation.—An electromechanical ramp generator, driven by a synchronous motor, was used to obtain very slow voltage sweep rates for following the slow charging rates of the ultramicroporous carbons. For fast voltage sweep a Hewlett Packard function generator, Model 3300 A, was used, and the voltammogram was recorded on a Tektronix, Type 549, storage oscilloscope. A Kepco bipolar operational amplifier power supply was used as potentiostat. Figure 3 is a diagram of the circuitry.

Methods of measurement.—Evaluation of pore diameters and pore surface.—The treatment of the carbon cloth, TCM 128, and the estimation of pore diameters by probe molecules are described elsewhere (12). The probe molecules were H_2 (d = 3.7Å), N_2 (d = 4.3Å), and SF_6 (d = 5.6Å). The molecular diameter was calculated by the equation $d = 2^{1/6}V_L$, where V_L is the molecular volume of a single molecule in the liquid phase, assuming hexagonal packing of spherical molecules. It is well known that pores, almost impermeable to a given molecule at a certain temperature, can become permeable at higher temperatures (13). This was taken into consideration when the various pore diameter ranges were estimated. The amount of chemisorbed oxygen was changed to a certain extent by high temperature, stepwise, evacuation (12) or by limited O_2 chemisorption on oxygen depleted samples.

The internal surface area of TCM 128 was estimated as needed, by BET, Langmuir, and Polanyi-Dubinin models (14).

Evaluation of double layer capacitance (C_d) and kinetic parameter.—Considering the porous electrode as an *R-C* network, it can be easily deduced that the application of a constant potential sweep dv/dt starting at time $t = 0$, results in a current transient which decays to the pure capacitor behavior

$$i_x = C_d\, dv/dt \qquad [1]$$

where C_d is the total capacitance of the *R-C* network. A current transient should similarly occur after the inversion of the linear potential sweep at each end of

[1] A discrimination between roughness and porosity has to be made. Roughness is a property of the outer geometrical surface. It results from shallow pores of a depth not much greater than the diameter. Porosity is a property of the entire solid where the pore length is several orders of magnitude more than their diameter.

Table I. General characteristics of carbon and graphite textiles

Characteristics	Unit	TCM 128	TGM 389
Diameter of thread	mm	0.2-0.4	—
Thickness	mm	0.25	0.2-0.25
Weight per m^2	g	60	120
Electrical resistance of a square	ohm	1-1.5	0.8-0.9
Carbon content	%	92-96	99-100
Ashes	%	0.3-1	<0.1
Volatile material	%	4-7	<1

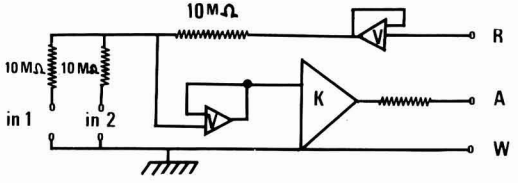

Fig. 3. The potentiostat circuitry. K, Kepco operational power supply amplifier; V, voltage follower (bias current < 10^{-11}A).

the cyclic voltametry half-cycle. This should result in distortion of the symmetry of the voltamogram *vs.* the potential axis (Fig. 4). The distortion is more pronounced by the edges of the voltamogram when the former transient is well relaxed as compared to the new one produced after the potential inversion. This transient behavior has been thoroughly studied by Austin and Gagnon (15) for the specific model of undimensional distribution of capacitance and resistivity. It can, however, be easily recognized that the same behavior holds qualitatively for any ideally polarized electrode model with resistive restrictions.

Cyclic voltametry on a wide potential range, appeared to be a fast and sensitive method of measuring C_d and for evaluating the double layer relaxation time. It is, however, quite complex for quantitative analysis unless C_d and/or the charging relaxation time are independent of potential, as was the system studied by Austin and Gagnon (15). The slower and less convenient measurements of current transients resulting from small potential steps, are easier to interpret quantitatively, since the C_d and the relaxation time can be assumed to be constant.

The experimental results of cyclic voltametry are given in this work in terms of apparent differential capacitance, C_d via Eq. [1], rather than in terms of the directly measured current. This was found more informative since C_d is the fundamental property which rules the current. One should, however, keep in mind that Eq. [1] is valid only after the decay of the transient, *i.e.*, at the symmetrical portions of the voltamogram. The various plots of C_d are given in two scales: farad per gram (f/g) and microfarad per square centimeter (μf/cm^2) of total surface area. The first unit (f/g) does not take into account the surface area measurements while the second enables comparison of ultramicroporous (3-10Å), with microporous (10-30Å) (8) or nonporous carbon electrodes and also with the classical mercury electrode interface.

Results and Discussion

Nonporous graphitized carbon TGM 389 was investigated in order to have a reference for nonporous carbon surface behavior. The apparent differential capacity obtained from cyclic voltametry is given in Fig. 5 for two very different sweep rates, 1000 and 1 mV/sec. It can be seen that the inversion of the linear sweep produces a very fast current reversal. A slight asymmetry, corresponding to a contribution of slowly charging sites, can be observed at the slower sweep rate. These slow sites are attributed (16) to "slow" electronic surface states which are isolated from the bulk conduction band of graphite by a potential barrier.

The roles of pore diameter and of concentration of oxygen surface groups have been examined in TCM 128 carbon, using thermal treatments under vacuum and in the presence of oxygen or air. The various samples used are given in Fig. 6. The C_d *vs.* potential plot is given in Fig. 7 for carbon I. This sample was activated for 2 hr in air at 450°C in order to obtain relatively large ultramicropores. The slow current inversion indicates a considerably low charging rate com-

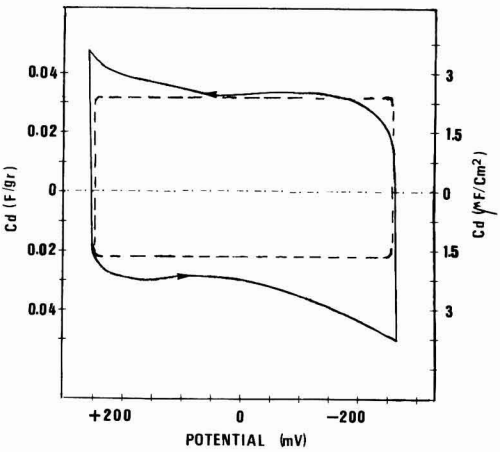

Fig. 5. C_d *vs. V* curve of TGM 389, ----, 1000 mV/sec; ——, 1 mV/sec. Potential *vs.* 0.1*N* NaCl C.E. The μf/cm^2 scale stands for the outer surface area of the fiber.

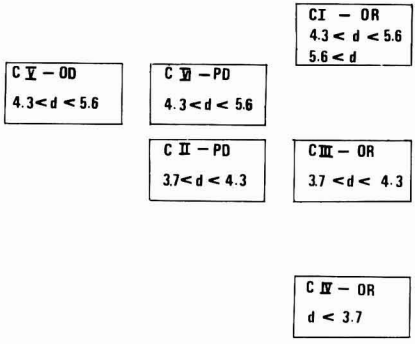

Fig. 6. Diagram of the various carbons according to their pore diameter and surface oxidation state. Moving to the right: samples with higher surface oxygen concentration. Moving to the bottom: samples with lower pore diameter. OD, oxygen depleted; OR, oxygen rich; PD, partly oxygen depleted.

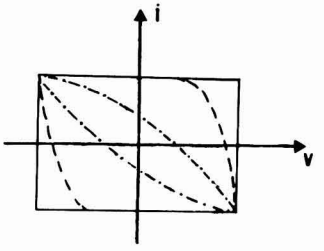

Fig. 4. Illustration of the response of the current to the reversal of potential linear sweep for a constant ideally polarized electrode. a, "Fast" electrode; b, "slow" electrode; relaxation during half-cycle time; c, "very slow" electrode, relaxation time greater than the half-cycle time.

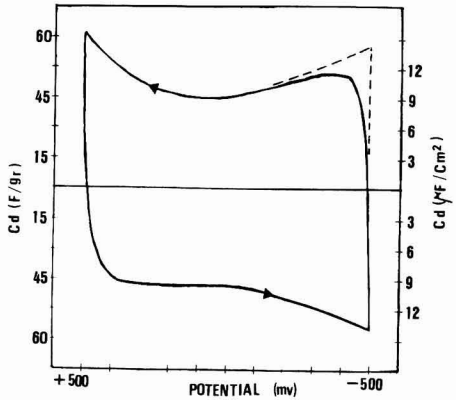

Fig. 7. C_d *vs. V* curve of carbon CI-OR in 0.1*N* NaCl; potential *vs.* 0.1*N* NaCl C.E.; 0.5 mV/sec. Dotted line is the symmetrical image of the lower curve for calculating the relaxation time.

pared to the nonporous TGM 389 (Fig. 5), but it is three orders of magnitude higher in capacitance per gram, thereby indicating that the high surface ultramicropores take part in double layer charging and in ion transport.

The carbon II samples were prepared by evacuation at 200°C during 2 days. This caused a slight depletion of chemisorbed oxygen which was removed as CO_2 (18). The lower pore diameter range resulted in a great decrease of C_d. No potential range could be found at which C_d from the increasing voltage sweep is equal to C_d of the decreasing sweep, because the charging rate slowed to such an extent that the C_d-V curve (Fig. 8) was completely distorted. This implies that the relaxation time of double layer charging is considerably greater than the half-cycle time of the cyclic voltamogram. The higher capacitance at negative potentials is connected with chemisorbed oxygen. The role of chemisorbed oxygen is well demonstrated by carbon III in Fig. 9. The pore diameter range of this carbon is much the same as the slightly oxygen depleted carbon II; it was obtained by widening the pores of the original TCM 128 by oxidation in air at 450°C for 1 hr, rather than by prolonged evacuation at 200°C. This is known to result in a highly oxidized surface (19). The C_d retains the high values of carbon I at negative potentials. It corresponds also to the C_d values of microporous (10-30Å) carbons (8). However, unlike these examples, where C_d changes only slightly with potential, it gradually decreases in carbon III by two orders of magnitude at +500 mV (Fig. 10).[2]

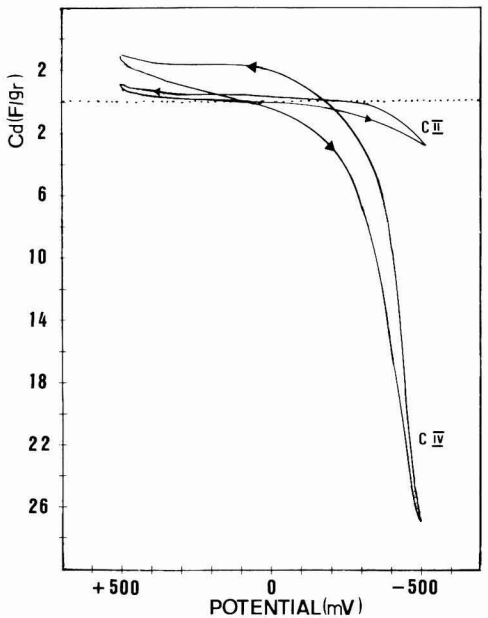

Fig. 8. C_d *vs.* V curve of the carbons C II-PD and C IV-OR in 0.1*N* NaCl; potential *vs.* 0.1*N* NaCl C.E.; 0.5 mV/sec.

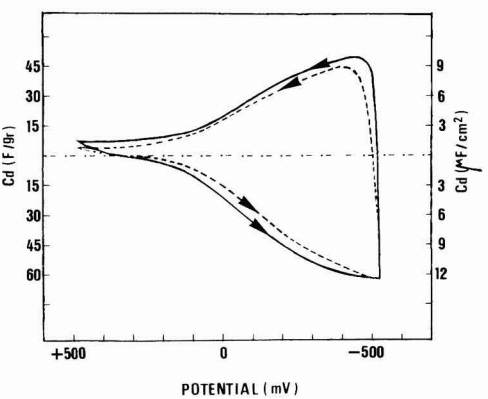

Fig. 9. C_d *vs.* V curve of carbon C III-OR in 0.1*N* NaCl. ----, 0.5 mV/sec; ——, 0.166 mM/sec; potential *vs.* 0.1 NaCl C.E.

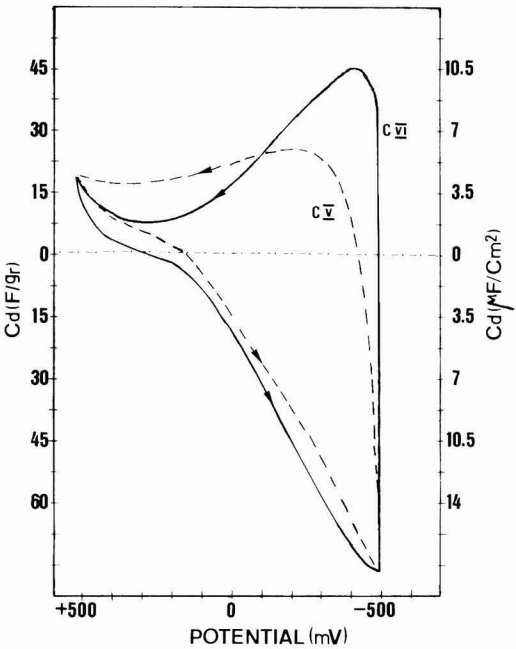

Fig. 10. C_d *vs.* V curve of the carbons C V-OD and C VI-PD in 0.1*N* NaCl; potential *vs.* 0.1*N* NaCl C.E., which shows the influence of reoxidation on double layer behavior; 0.5 mV/sec.

To our knowledge no such extreme change in C_d has been found, with the exception of peaks in C_d for some organic molecules (20). Moreover, the negative branch is almost symmetrical with respect to the potential axis, showing equilibration of the double layer during the half-cycle time, while at positive potentials the C_d-V curve resembles the extremely slow charging rate of carbon II. The fact that the C_d-V curve at a sweep rate of 0.5 mV/sec (Fig. 9) is very similar to that of the threefold slower sweep rate, indicates that the difference in C_d between the positive and negative potentials is due to equilibrium properties and not to different charging rates. A previous study (8) shows that at potentials greater than −190 mV *vs.* 0.1 NCE, cations are repelled from the interface of an oxidized microporous carbon electrode, resulting in a negative cation surface excess. At more negative potentials, anions are repelled similarly. This behavior can be explained by elementary electrostatic considerations, provided there is no specific ion adsorption (21).

Assuming that the oxidized carbon III has a pzc close to that found in a previous work (8), we deduce that the very low capacity at positive potentials originates from repulsive interaction of the anions with the negative dipoles of the surface oxides which, up to +500 mV, is not compensated by the attractive positive electronic charge. The opposite is obviously deduced for cations which penetrate and adsorb into the 3.7-4.4Å pores of the oxidized surface of carbon III. The adsorp-

[2] The capacitance which corresponds to the sweep rates of Fig. 10 is taken to be half the distance between the upper and lower curve.

tion is virtually nonexistent at the slightly less oxidized surface of carbon II, which has the same pore diameter range. The fact that anions are "normally" adsorbed at the carbon I oxidized surface (Fig. 7) is attributed to the larger pores which allow greater ion-interface distance. Here anion adsorption becomes possible again, since the repulsive ion-dipole potential decreases quicker than the attractive ion point charge or the ion-distributed surface charge of the carbon electrode.

The effect of surface oxides can be further demonstrated by starting from the oxygen depleted carbon V and inducing oxygen chemisorption at 300°C which will result in carbon VI, while the pore diameters remain essentially unchanged. The C_d-V curves for these two samples are given in Fig. 10. It can be seen that the charging rate and, to a lesser extent, the C_d increases at negative potentials for the oxidized carbon VI and decreases at positive potentials. This shows that the direct chemisorption of oxygen is the cause of the different double layer behavior. It also shows that the oxidized electrodes favor cation adsorption at the larger diameter (4.3-5.6Å) as well.

A further reduced pore diameter was studied in the original TCM 128 fiber (designated carbon IV). The narrow pores of this carbon could still accommodate water up to 16% w/w. This enabled a minute penetration and adsorption of solvated ions (Fig. 8), resembling the behavior of carbon II. The higher capacitance as compared to carbon II, especially at negative potentials, is due to the slightly larger amount of chemisorbed oxygen. Here again the charging rate is much slower than the potential sweep rate.

The role of the hydration sheath.—The experimental results lead to the conclusion that when the pore diameter is reduced to less than 5.6Å, slowing down of charging rate and dependence of C_d on the amount of surface oxides becomes significant. Since below 5.6Å and especially below 4.7Å (carbons II, III, and IV) ions can penetrate the pores only after partial depletion or distortion of the hydration sheath (22) different behavior could be expected from the various ions. Preliminary results are given in Fig. 11 which shows the effect of exchanging Na^+ by Li^+ on a carbon III ($3.7 < d < 4.3$) electrode. The charging rate of the extensively hydrated Li^+ ion is considerably slower at negative potentials. This is seen by comparing Fig. 9 and 11. Upon a tenfold reduction of the sweep rate, the shape of the C_d curve of LiCl (Fig. 11b) retains the C_d-V curve of NaCl (Fig. 9). This indicates that the equilibrium behavior of Li^+ on carbon III is similar to that of Na^+, but their charging rates differ considerably. This is unlike the difference in equilibrium behavior of cation and anion (negative and positive branches), demonstrated by the two curves in Fig. 9. The apparent selectivity, when accommodating the less hydrated cations, is common to other systems which have molecular size cages, *i.e.*, crown-ether complexes (23), and to highly cross-linked cation exchanger resins (24). In the first case the cation is held by ion-dipole forces, while in the second, interaction with the resin's negative charge takes place. The negatively charged ultramicroporous carbon comprises both types of interaction.

Influence of concentration and voltage sweep rate.—The higher concentration of the electrolyte seems to increase both the charging kinetics and C_d, as is shown in Fig. 12. The effect of the very high 5N NaCl concentration needs more study, as there is evidence of pore enlargement during slow charging cycles.

The above porous carbons have at least two different surface areas, that of the ultramicropores which is very large and always charged slowly, and that of the outer surface of the fibers, which should be compared to the nonporous graphite TGM 389 (Fig. 5), concerning C_d and charging rate. Figure 13 shows that the increase of the sweep rate excludes contribution of the micropores to C_d. The remaining much lower capacitance at the

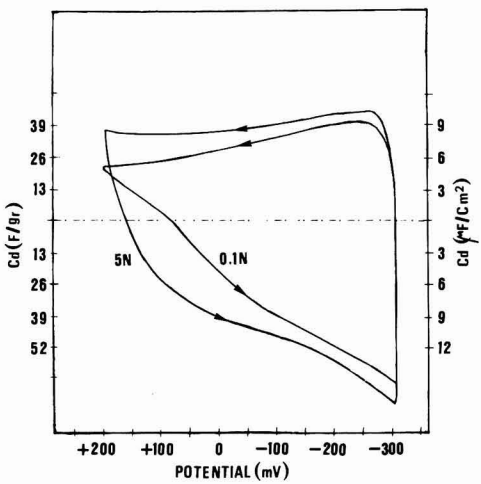

Fig. 12. The influence of increasing concentration on kinetics and C_d of carbon C V-OD in 0.1N NaCl and 5N NaCl. Potential *vs.* 0.1N NaCl C.E.; 0.15 mV/sec.

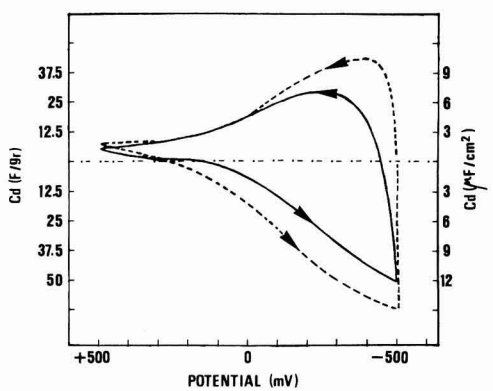

Fig. 11. C_d *vs.* V curve of carbon C III-OR in LiCl 0.1N. ----, 0.05 mV/sec; ——, 0.5 mV/sec; potential *vs.* 0.1N NaCl C.E.

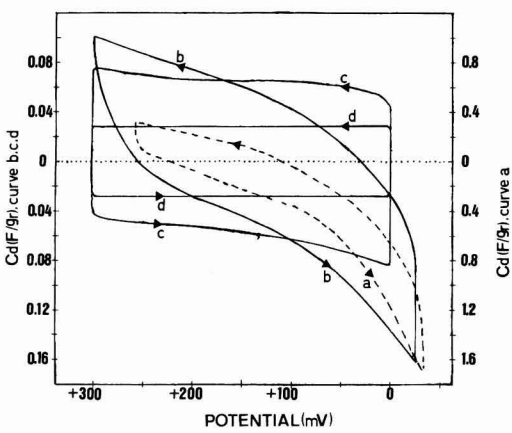

Fig. 13. The influence of potential sweep rate on C_d of carbon C IV-OR in 0.1N NaCl, potential *vs.* 0.1N NaCl C.E. a, 0.5 mV/sec; b, 10 mV/sec; c, 60 mV/sec; d, 600 mV/sec.

sweep rate of 600 mV/sec (Fig. 13d) corresponds to $2.8 \cdot 10^{-2}$ f/g. A doubled value of C_d, observed at 60 mV/sec (Fig. 13c), and a third charging process was observed (Fig. 13b) at an intermediate sweep rate of 10 mV/sec. All three curves were symmetrical and the current changes sign very fast by inversion of the voltage sweep. They are clearly distinct from the much slower and unsymmetrical ultramicropore charging process (Fig. 13a). The difference in C_d for Fig. 13(d, c, and b) is probably due to the difference between the geometrical and the BET surface area of the fibers. The same shallow micropores which cause the roughness factor might also be responsible for the intermediate rate charging process exhibited by Fig. 13b.

Estimation of ionic conductivity into the pores.—The delay of the current inversion after reversal of the sweep rate may be considered as a measure of restricted transport of ions into the pores. A characteristic relaxation time, τ, of the system could thus be the retention time of the symmetry between the upper and lower C_d-V curves. This value is deduced from Fig. 7 and 9. It could not be obtained from other curves, where no symmetry was achieved, with respect to the potential axis, during the voltametric cycle time. Regarding the porous electrode impedance as an R-C combination, we can write

$$\tau = RC_d \qquad [2]$$

from which the order of magnitude of the specific resistivity ρ_P of the solution into the pores can be derived. Considering the radial symmetry of the current flow, the porous fiber is viewed as a solution conductor of a cross-sectional area A and length l. The area A is given by

$$A = A'P \qquad [3]$$

where A' is the geometric surface area per gram of the fibrous material and P is the porosity in volume percent, which is about 30% for carbon I and III (12). The approximate length (l) of the ion pathway is expressed by

$$l = \frac{r}{2} \cdot T \qquad [4]$$

where r is the average fiber radius and T is tortuosity factor of the conductance path, taken as 2 (4), thus $l \simeq r$. The cylindrical geometry of the fiber is thus approximated to be linear by means of Eq. [4]; therefore

$$R = \frac{\rho_R l}{A} \qquad [5]$$

Substituting Eq. [4] and [2] in [5] and substituting the corresponding C_d values from the C_d-V curves at the negative inversion potentials of Fig. 7 and 9, we obtain $\rho_P^{I} = 1.1 \cdot 10^{11}$ Ω-cm and $\rho_P^{III} = 10^{11}$ Ω-cm for carbon I and III, respectively. This is several orders of magnitude larger than the resistivity of the bulk of 0.1*N* NaCl solution ($\rho \simeq 100$ Ω-cm).

The rough approximation applied renders ρ_P accurately only within the order of magnitude. It is still of value because of the great deviation of ρ_P from ρ. Extension of such studies over wider pore diameter ranges and to solutions used in practical porous electrode systems could provide information about the availability of the tiny pores for electrochemical reactions.

Faradaic and double layer currents.—On studying the electrochemical properties of carbon surfaces, discrimination between faradaic and double layer processes has to be made regarding the various surface groups existing on carbon. Recognizing that electrochemical reactions of surface groups involve the adsorption or desorption (in the thermodynamic, Gibbsian sense of surface excesses) of "aqueous components" (17) such as H^+, OH^-, H_2O_2 as well as electronic charge, we consequently deduce that surface groups fall within the generalized double layer concept. This concept has been put forward by Frumkin and coworkers (25) and later by Soffer (17). It is valid for both ideally polarized and reversible electrodes and makes no fundamental discrimination between them. The surface groups are simply considered as part of the components of the interface or the generalized double layer.

Putting the above argument into more experimental terms: The capacitor behavior of the double layer will not be imparted by the presence of the surface group in the sense that the interface should still acquire, for a finite potential change, a finite electronic charge which corresponds quantitatively with surface coverage constraints. This is unlike true faradaic processes which require an amount of charge according to the concentration and amount of redox components in the solution, regardless of surface coverage constraints.

The differential capacitance C_d (or the current) *vs.* potential function may, however, exhibit certain peaks due to specific surface groups if they are electroactive in a sufficiently narrow potential range. We have not encountered this behavior in sodium chloride solutions here and elsewhere (8, 16), nor in H_2SO_4 solution (26) in the range 0-650 mV *vs.* NHE. Peak-shaped voltamograms have been observed, however, in hot concentrated phosphoric acid (27) and in dilute HCl (28) and it may obviously depend on the type of carbon and surface treatment. In light of the above considerations, however, peak behavior is not necessarily an indication of faradaic response. It may simply be a hump in the C_d-V function.

In this work the electrode potential was always kept far from the thermodynamic potential of water decomposition. The *p*H was frequently monitored in order to assure, as has been done in a former work (8), that *p*H changes, if they occur at all, are too small to account for the charge delivered. We found, in fact, that the ultramicroporous electrodes were more immune to capacitance increase and *p*H changes at extreme potentials, than open structure electrodes.

Last but not least, no conceivable amounts of redox impurities could account for the delivered charges. On the other hand, these charge densities did correspond always to reasonable double layer charge values.

Conclusion

This work is restricted to ultramicropores of dimensions from close to those of water molecules up to 6Å. Qualitative evaluation, using constant sweep cyclic voltametry, showed that the mobility of ions into ultramicropores is several orders of magnitude smaller than in the free solution outside the pores. The surface dipoles have a stronger effect on adsorption and mobility into ultramicroporous carbons than on flat surfaces.

Manuscript submitted Jan. 11, 1977; revised manuscript received April 25, 1977.

Any discussion of this paper will appear in a Discussion Section to be published in the June 1978 JOURNAL. All discussions for the June 1978 Discussion Section should be submitted by Feb. 1, 1978.

REFERENCES

1. R. De Levie, in "Advances in Electrochemistry and Electrochemical Engineering," Vol. 6, P. Delahay and C. W. Tobias, Editors, Interscience Publishers, London, New York (1966).
2. See Ref. 3-10, 16, 17 in Ref. (4).
3. E. C. Gagnon, *This Journal*, **121**, 512 (1974).
4. M. Yaniv and A. Soffer, *ibid.*, **123**, 506 (1976).
5. G. W. Garten and D. E. Weiss, *Rev. Pure Appl. Chem.*, **7**, 69 (1957).
6. G. W. Murphy *et al.*, Demineralization of Saline Water by Electrically Induced Adsorption on Porous Carbon Electrodes, Annual Rep. U.S. Dept. of the Interior (1958).
7. J. Newman, *This Journal*, **118**, 510 (1971).
8. A. Soffer and M. Folman, *J. Electroanal. Chem.*, **38**, 25 (1972).
9. C. Orr and J. M. Dallavalle, "Fine Particle Measurement" MacMillan, New York (1960).

10. J. J. Kipling, "Adsorption from Solutions of Non-Electrolytes," chap. 13, Academic Press, London and New York (1965).
11. B. R. Puri, in "Chemistry and Physics of Carbon," Vol. 6, P. L. Walker Jr., Editor, p. 191, Marcel Dekker, Inc., New York (1970).
12. J. Koresh and A. Soffer, To be published.
13. S. J. Gregg and K. S. Sing, "Adsorption, Surface Area and Porosity," p. 214, Academic Press, London and New York (1967).
14. S. J. Gregg and K. S. Sing, *ibid.*, p. 223
15. L. G. Austin and E. G. Gagnon, *This Journal*, **120**, 251 (1973).
16. M. Yaniv, M.Sc. Thesis, Weizman Institute of Science, Rehovot, Israel (1974).
17. A. Soffer, *J. Electroanal. Chem.*, **40**, 153 (1972).
18. S. S. Barton and B. H. Harrison, *Carbon*, **10**, 245 (1972).
19. B. G. Linsen, "Physical and Chemical Aspect of Adsorbent and Catalyst," p. 458, Academic Press, London and New York (1970).
20. P. Delahay, "Double Layer and Electrode Kinetics," chap. 5, Interscience Publishers, London and New York (1956).
21. D. C. Graham and B. A. Soderberg, *J. Chem. Phys.*, **22**, 449 (1954).
22. E. Glueckauf, in "The Structure of Electrolyte Solution," W. J. Hamer, Editor, John Wiley & Sons, Inc. New York (1959).
23. H. K. Frensdorff, *J. Am. Chem. Soc.*, **93**, 600 (1971).
24. E. Riand, in "Physics of Electrolytes," Vol. 1, J. Hladik, Editor, Academic Press, London and New York (1972).
25. A. N. Frumkin, O. S. Petrii, and B. B. Damaskin, *Elektrokhimiya*, **6**, 614 (1970).
26. E. Keren and A. Soffer, *J. Electroanal. Chem.*, **44**, 53 (1973).
27. K. Kinoshita and J. A. S. Bett, *Carbon*, **11**, 403 (1973).
28. C. Tobias and A. Soffer, Unpublished results.

Technical Note

A Method for Direct, Real-Time Display of Q-$t^{1/2}$ Chronocoulometric Data

K. Keiji Kanazawa and R. K. Galwey

IBM Research Laboratory, San Jose, California 95193

In single step chronocoulometry, the time dependence of the charge Q passing through the working electrode in an electrochemical cell due to a step function of applied potential is recorded and studied. This technique was introduced many years ago (1). Even then, the utility of a Q *vs.* $t^{1/2}$ plot was recognized and discussed. The variety of information which can be obtained using this and related techniques has been reviewed by Murray (2).

A linear Q-$t^{1/2}$ dependence is a limiting case of a more general time dependence. To examine the generalized time dependence of charge, the data should be processed using digital computation. This can be done on line, and such systems have been described (3). For less demanding applications however, the necessary time and money investment required for laboratory automation is not warranted. This is particularly true when the functional time dependence is specified and only that dependence is examined. This note describes the technique which we have used to implement a real-time display of Q-$t^{1/2}$ data, permitting a quick assessment of the experimental conditions and eliminating the time, tedium, and possible error involved in manual plotting.

A block diagram of the experimental arrangement is shown in Fig. 1. An analog current-follower potentiostat was used for these measurements. Such instruments have been discussed in detail by Harrar (4). The output of the current follower in the potentiostat is a voltage e_I which is proportional to the cell current. Analog integration of this voltage yields a voltage e_Q which is proportional to the charge Q. Such circuitry is common (5), although special care must be taken in certain coulometric applications (6). Essentially, we want to plot e_Q against a voltage e_T which varies as the square root of time. One could conceivably have used analog techniques to generate this particular function of time. However, to provide maximum flexibility a stored waveform digital generator was used to produce e_T (7). The block diagram for this generator is shown in Fig. 2.

Key words: chronocoulometry, digital function generation, instrumentation.

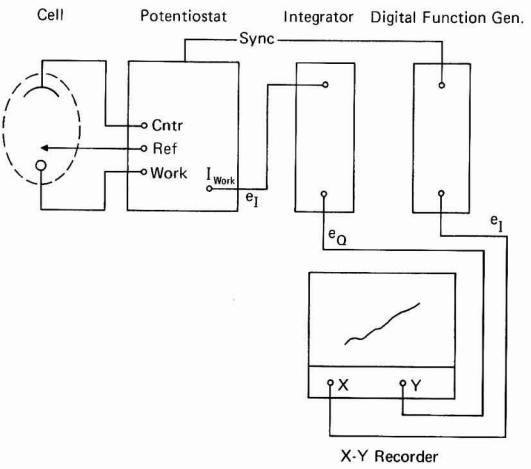

Fig. 1. A block diagram, showing the arrangement of the basic modules.

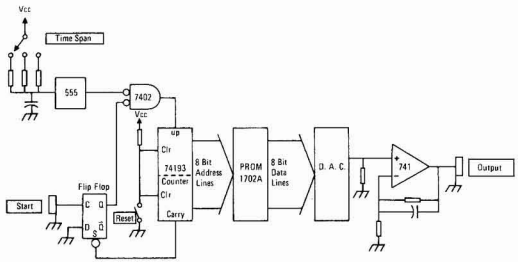

Fig. 2. A functional schematic diagram of the digital function generator.

The requirement on the circuitry is to produce an analog, time-dependent waveform which is digitally derived. The fundamental concepts for this circuit are described below. The digital equivalent of the waveform is stored in an erasable programmable read-only memory (Intel 1702A, 8×256 PROM). By sequentially addressing the PROM, the contents are sensed by the digital to analog converter (Hybrid Systems 371-8, DAC), and converted to the appropriate analog value. The amplifier provides proper scaling and filtering of the DAC output. The filtering is chosen commensurate with the instrument used for recording. In our particular case, where an X-Y recorder was used, the amplifier had a gain of 5 and was rolled off at 40 Hz. The PROM addresses are derived by incrementing an 8 bit binary counter. A clock provides the periodic pulses which increment the counter. We used an NE 555 timer because of ease of operation, simplicity, and cost. Depending on the specific application's needs, different timers may be selected.

Application of the clock signal is controlled by the NAND and the D flip-flop. The intent of these logical elements is to cause the counter to first be reset to address zero (or count zero) when the reset button is momentarily depressed. Simultaneous with the application of the step function voltage to the potentiostat, a "start" pulse must be received by the clock (C) input of the flip-flop. Its "Q" output will then go to a zero state. This zero state is NANDed by the negative-going clock pulses, resulting in positive-going pulses being sent to the counter. The counter will then begin incrementing, causing updated values to be sent to the DAC at the clock rate. When 256 clock pulses (the capacity of the PROM) have been received by the counter, a carry pulse will be generated by the counter. This pulse is received by the flip-flop, causing the "Q" output of the flip-flop to go to a "1" state. This "1" state inhibits any further pulses from incrementing the counter. Thus the cycle is complete.

There are two principal sources of error from the digital function generator. The 8 bit resolution introduces a digitization error. The maximum percentage error is 2% occurring near the beginning of the scan. After the first five points, this error is less than 1%. Since data reduction involves slope and/or intercept determination using a sizable fraction of the sweep data, the error introduced by this is much less than 1%. When the clock is an R-C controlled timer, as in this circuit, a larger uncertainty exists in the clock rate. Use of trimming techniques allows this error source to be reduced to less than 1%. This error is acceptable, being smaller than the 5-10% uncertainties introduced by other sources, such as cell geometry, incomplete IR compensation, and instrument and recorder calibration.

An example of a Q-$t^{1/2}$ plot obtained by us is shown in Fig. 3. This is an actual recording of the signal obtained in a cell using a 0.2 cm^2 Pt button working electrode in a solution containing 0.1M tetraethylammonium fluoborate in acetonitrile. The active species was methoxy pyrazoline, present at 0.001M concentration.

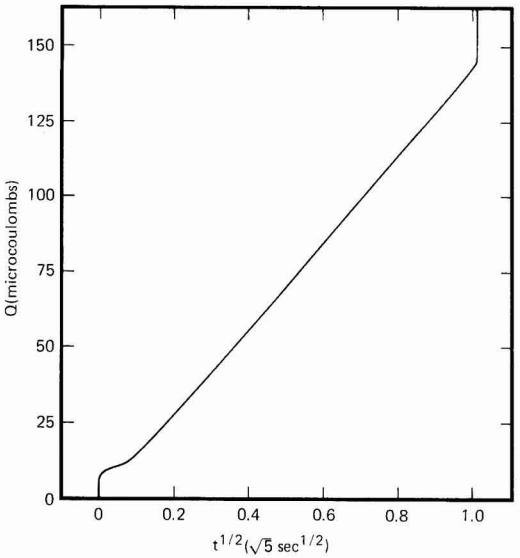

Fig. 3. An example of a direct display of Q-$t^{1/2}$ coulometric data.

For detailed work, the effective electrode area should be evaluated using a known electrochemical system, as was done, for example, by Bacon and Adams (8). The data were plotted using a Hewlett-Packard 7040A X-Y recorder. The hump at the beginning of the plot is due to overshoot in the potentiostat-cell system.

It is clear that this same technique could be used to examine other time dependencies. In fact, any waveform which can be stored with sufficient accuracy in the PROM can be used to drive the recorder X axis. For example, we have generated a $t^{-1/2}$ voltage function to compare these coulometric studies with a direct display of current *vs.* $t^{-1/2}$. We found the Q-$t^{1/2}$ technique to be superior, primarily because it was much less demanding of the recorder response time. We are finding this technique increasingly useful and feel that the versatility of this technique will permit the study of other interesting time behaviors.

Acknowledgments

The authors thank J. Gordon and A. Diaz for their insights and expertise. We are indebted to H. Seki for his support and encouragement.

Manuscript submitted March 2, 1977; revised manuscript received April 20, 1977.

Any discussion of this paper will appear in a Discussion Section to be published in the June 1978 JOURNAL. All discussions for the June 1978 Discussion Section should be submitted by Feb. 1, 1978.

Publication costs of this article were assisted by IBM Corporation.

REFERENCES

1. J. H. Christie, G. Lauer, R. A. Osteryoung, and F. C. Anson, *Anal. Chem.*, **35**, 1979 (1963).
2. Royce R. Murray, in "Physical Methods of Chemistry," Vol. I., Part IIA, Chapter VII, A. Weissberger and B. W. Rossiter, Editors, Wiley Interscience, New York (1971).
3. G. Lauer, R. Abel, and F. C. Anson, *Anal. Chem.*, **39**, 765 (1967).
4. J. E. Harrar, in "Electroanalytical Chemistry," Vol. 8, p. 43, A. J. Bard, Editor, Marcel Dekker, Inc., New York (1973).

5. "Operational Amplifiers, Design and Applications," pp. 213-218, J. G. Graeme, G. E. Toby, and L. P. Huelsman, Editors, McGraw-Hill Book Co., New York (1971).
6. W. S. Woodward, T. H. Ridgway, and C. N. Reilley, *Anal. Chem.*, **46**, 1151 (1974).
7. "Analog-Digital Conversion Handbook," pp. I-(68-79), D. H. Sheingold, Editor, Analog Devices, Inc., Norwood, Massachusetts (1972).
8. J. Bacon and R. N. Adams, *Anal. Chem.*, **42**, 524 (1970).

Brief Communication

n-Butyllithium–An Effective, General Cathode Screening Agent

M. Stanley Whittingham* and Martin B. Dines

Exxon Research and Engineering Company, Linden, New Jersey 07036

Currently, high energy density lithium storage systems are the focus of intense interest and expectation (1,2). In order to scan and characterize oxidants as potential cathodes, it would be very useful to have a reliable chemical reagent which could, in effect, mimic the half-cell reaction under consideration. Although reagents formed by dissolving alkali metals in ammonia, polyamines, polynuclear aromatic solutions in ethers, or hexamethyl phosphoramide (3) might be used, they have a number of shortcomings. Their reactions are difficult to run, since they involve extremely reactive materials, very dark opaque media, their polar solvents can also partake in the reaction, and it is difficult to separate the product from residual reagent. It would be preferable to have instead an agent whose lithium activity is more on the order of a volt or so below the alkali itself. We report that n-butyl lithium serves as such an agent.

The use of butyllithium to chemically mimic an electrochemical reaction was first mentioned by Armand (4) in connection with work on chromium oxide/graphite compositions. Dines (5, 6) then discovered that the lithium intercalates of the lamellar transition metal dichalcogenides were readily afforded without any of the degradation of their crystalline form previously seen, for instance, with lithium naphthalide (7) or lithium in ammonia, for which it is necessary to subsequently remove, by heating to 250°C, the coincorporated solvent (8). This latter effect, the coinsertion of solvating neutral molecules, has even been observed during electrochemical discharge in organic electrolytes (1). No such complications accompany the inclusion of lithium from butyllithium-hydrocarbon solutions. Because the solution is light and clear, the effect of the reagent on the oxidant can be visually [even microscopically (9)] observed during the process of lithiation.

n-butyl lithium, previously extensively used as an alkylating agent (3), is commercially available as a 1.5-2.0 molarity solution in hexane. In a typical experiment, a known quantity (~100 mg) of the candidate solid oxidant (Ox) was placed in contact with an excess of butyl lithium solution in a dry box and allowed to react for several days at room temperature, after which the solid was filtered, washed with hexane, and examined by x-ray diffraction. The reaction, which is shown schematically (10)

$$C_4H_9Li + (Ox) \rightarrow Li^+ (Ox)^- + (C_4H_9) \rightarrow \tfrac{1}{2}\, C_8H_{18}$$

was followed by acid-base titration of the unreacted butyl lithium and by monitoring the octane formed using gas chromatography. The latter is less reliable because of the possible formation of butene and butane from the butyl radicals. The results are summarized in Table I. A number of materials were found not to react at all, including graphite, aluminum, and antimony.

These results indicate that the reaction is indeed a general one, and that where battery discharge capacity data are available, excellent agreement is obtained. Thus, the carbon fluorides react with the stoichiometric quantity of lithium (11), and cupric sulfide takes up almost two equivalents as expected for formation of lithium sulfide and copper. Tetracyanoquinodimethane (TCNQ) reacts with one lithium to form $TCNQ^-$, in agreement with previous cell data (12). The oxides of vanadium and molybdenum reacted with about 2, and 1.5 equivalent of lithium, respectively, as previously reported (13, 14), and in both cases x-ray analysis indicated that two new phases were being formed. With TiO_2 (anatase form), butyllithium reacted vigorously forming first a blue, then a black compound. The degree of reaction was much higher than that reported by Johnson (19) for rutile, however, preliminary NMR results suggest that the lithium atoms are mobile just as he found them to be. The observed low level of reaction of CuF_2 could be related to the presence of a

Table I. Summary of results

Oxidant	Equivalent BuLi consumed	Oxidant	Equivalent BuLi consumed
$CF_{1.1}$	1.10	TiS_2(Se)	1.0
CuF_2	0.17	ZrS_2(Se)	1.0
CuS	1.72	HfS_2(Se)	1.0
TCNQ	1.00	NbS_2(Se)	0.8 (1)
$Ni(CN)_2$	2.00	TaS_2(Se)	1.0
FeS_2 (natural)	1.70	MoS_2(Se)	>1.5
SnO_2	0.09	WS_2(Se)	0.3 (>1.5)
Bi_2Te_3	1.26	VSe_2	>1.5
GaS	0.30	TiS_3	3.0
TiO_2	0.60	ZrS_3(Se)	3.0
Cr_2O_3	0.12	HfS_3(Se)	2.8
Ta_2O_5	3.70	NbS_3(Se)	3.0
V_2O_5	2.00	VS_4	~2.0
MoO_3	1.55	SnS_2	0.25
WO_3	0.00		

* Electrochemical Society Active Member.

Key words: cathode chemistry, n-butyllithium, screening agent, redox reactions, chalcogenides, oxides, titanium disulfide, lithium cells.

product film of LiF which prevented further reaction. The trichalcogenides, first studied in cells by Broadhead *et al.* (16), all reacted with about 3 moles of butyllithium, and have recently been extensively studied (17, 18). The reactivity of materials such as WO_3 might be enhanced by going to elevated temperatures to overcome kinetic barriers.

The use of butyllithium solutions also allows the rate of the process to be derived. This can be accomplished either by titrating aliquots of the supernatant reagent at appropriate time intervals, thereby following its consumption by the oxidant, or, as depicted in Fig. 1, by measuring the temperature rise of a reaction of the solid on addition to an excess of a molar solution of the reagent. The more rapid the temperature rise, the greater the reaction rate (and the potential discharge current density). As the figure shows, of TiS_2, MoO_3, and V_2O_5, the sulfide holds the greatest rate capability; this is consistent with our finding that current densities of 10 mA/cm^2 and greater can be attained in practical cell configurations (19, 20). In principle, the area under such curves can give a relative measure of the potential energy densities; strictly speaking it is the heat of the reaction which is measured, rather than the free energy. Thus, in the example given in the figure, V_2O_5 would promise the highest energy density. By carrying out the reactions in a calorimeter, a quantitative determination of the heat of reaction could be obtained for those cases where the reaction is rapid (such as TiS_2 and V_2O_5). However, in these qualitative studies, care must be taken in drawing conclusions of comparative behavior, since properties such as particle size obviously influence the results.

A problem in the discharge of cells is that conductive diluents, or other binding agents such as Teflon, must often be utilized in order to allow for the function of the cathode, but these additives are not necessary with the chemical reaction. Thus the butyllithium technique has allowed for the formation of the discharge product of a cell in a form readily amenable to x-ray analysis (21) and other physical measurements (22-24) without the complications of any possible side reactions or additional phases as might be present after disassembly of a battery. X-rays showed that these products were the same as those formed in cells.

That the effective cutoff of the voltage of butyllithium is on the order of *ca.* 1.4V below lithium itself is gathered from the behavior of $NbSe_3$. It has been found that on discharge the triselenide takes up 3 lithiums, with a final open-circuit voltage of above 1.4V (18). This sets an upper limit to the difference in activity between lithium and butyllithium, since the latter also yields Li_3NbSe_3. An approximate lower limit to the activity difference can be inferred from the observation that antimony does not react with butyllithium, and has a voltage relative to lithium of about 1V (25). Therefore, we can say that butyllithium is less active than lithium by 1-1.4V. Since the free energy of formation of octane is +4 kcal/mole (26), one infers a value for the free energy of formation of butyllithium of about 25 kcal/mole (±5 kcal/mole).

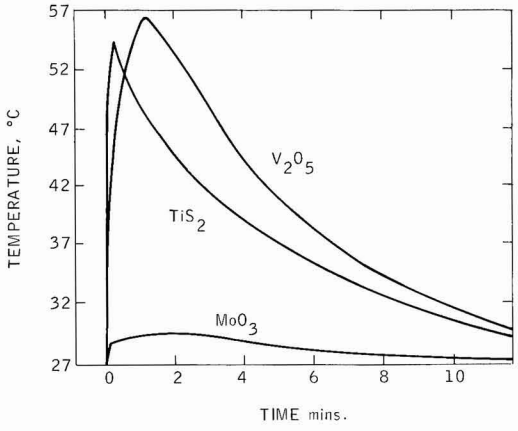

Fig. 1. Effect of the addition of excess butyllithium to equivalent slurries of V_2O_5, TiS_2, and MoO_3.

Manuscript submitted March 21, 1977; revised manuscript received April 11, 1977. This was Paper 31 presented at the Dallas, Texas, Meeting of the Society, Oct. 5-9, 1975.

Any discussion of this paper will appear in a Discussion Section to be published in the June 1978 JOURNAL All discussions for the June 1978 Discussion Section should be submitted by Feb. 1, 1978.

Publication costs of this article were assisted by Exxon Research and Engineering Company.

REFERENCES

1. M. S. Whittingham, *This Journal*, **123**, 315 (1976).
2. J. O. Besenhard and G. Eisenger, *J. Electroanal. Chem. Interfacial Chem.*, **77**, 1 (1976).
3. E. Bayer and W. Rudorff, *Z. Naturforsch.*, **27b**, 1336 (1972).
4. M. B. Armand, in "Fast Ion Transport in Solids," W. Van Gool, Editor, North-Holland (1973).
5. M. B. Dines, U.S. Pat. 3,933,688 (1976).
6. M. B. Dines, *Mater. Res. Bull.*, **10**, 287 (1975).
7. W. Rudorff, *Chimia*, **19**, 489 (1965).
8. A. Leblanc-Soreau, M. Danot, L. Trichet, and J. Rouxel, *Mater. Res. Bull.*, **9**, 191 (1974).
9. R. R. Chianelli, *J. Cryst. Growth*, **34**, 239 (1976).
10. B. J. Wakefield, "The Chemistry of Organolithium Compounds," Pergamon Press, Inc., New York (1974).
11. M. S. Whittingham, *This Journal*, **122**, 526 (1975).
12. F. Gutmann, A. M. Hermann, and A. Rembaum, *ibid.*, **114**, 323 (1967).
13. C. R. Walk and J. S. Gore, Paper 27 presented at The Electrochemical Society Meeting, Toronto, Canada, May 11-16, 1975.
14. F. W. Dampier, *This Journal*, **121**, 656 (1974).
15. O. W. Johnson, *Phys. Rev.*, **A136**, 284 (1964).
16. J. Broadhead and F. Trumbore, Paper 178 presented at The Electrochemical Society Meeting, Chicago, Illinois, May 13-18, 1973; U.S. Pat., 3,864,167.
17. R. R. Chianelli and M. B. Dines, *Inorg. Chem.*, **14**, 2417 (1975).
18. Papers 443 RNP and 26 presented at The Electrochemical Society Meeting, Toronto, Canada, May 11-16, 1975; Paper 31 presented at The Electrochemical Society Meeting, Dallas, Texas, October 5-9, 1975. To be published by Chianelli *et al.* and Murphy *et al.*
19. M. S. Whittingham, *Science*, **192**, 1126 (1976); U.S. Pat. 4,009,052.
20. L. H. Gaines, R. W. Francis, G. H. Newman, and B. M. L. Rao, Proceedings of the 11th Intersociety Energy Conversion, p. 418 (1976).
21. M. S. Whittingham and F. R. Gamble, *Mater. Res. Bull.*, **10**, 363 (1975).
22. B. G. Silbernagel, *Solid State Communications*, **13**, 1911 (1975).
23. B. G. Silbernagel and M. S. Whittingham, *J. Chem. Phys.*, **64**, 3670 (1976).
24. D. W. Murphy, F. J. DiSalvo, G. W. Hull, and J. V. Waszczak, *Inorg. Chem.*, **15**, 17 (1976).
25. H. P. Fritz and J. Besenhard, U.S. Pat. 3,960,594 (1976).
26. N. A. Lange, "Handbook of Chemistry," Revised 10th ed., p. 1655, McGraw-Hill Book Co., New York (1967).

JOURNAL OF THE ELECTROCHEMICAL SOCIETY

SOLID-STATE SCIENCE
—AND TECHNOLOGY

SEPTEMBER
1977

Electrochemical Properties of Dopants and the D-C Dynamic Scattering of a Nematic Liquid Crystal

H. S. Lim,* J. D. Margerum, and A. Graube

Hughes Research Laboratories, Malibu, California 90265

ABSTRACT

Flow of liquid crystal from one electrode to the other was observed during dynamic scattering of a phenyl benzoate nematic liquid crystal. The direction of the flow depended upon the electrochemical properties of dopants. The flow was from cathode to anode when the dopant was an electron acceptor, and vice versa when the dopant was a donor. A redox dopant gave distinctively different d-c dynamic scattering patterns from a salt dopant, and did not give the Williams domain pattern which was observed with a salt dopant. Charge conduction mechanisms through the liquid crystal are discussed in terms of the electrode reactions of the liquid crystal components and the dopants.

Dopants are commonly used to improve the properties of nematic liquid crystals (LC) for dynamic scattering (DS) displays (1). The conductivity anisotropy (2-4) of a LC depends very much on the dopants which are used. The a-c dynamic scattering characteristics depend strongly on the conductivity anisotropy. Lower threshold voltages (3, 4) and higher scattering levels (4) were observed as the value of the anisotropy was increased. The conductivity anisotropy depends on the structure of the dopant as well as on the liquid crystal material itself (4). The d-c-DS characteristics also depend on the electrochemical properties of the dopant; redox dopants consisting of electron acceptors, donors, or a combination of both, give a low threshold voltage (5, 6) and a high scattering level (6). A combination of an electron acceptor and a donor gives good electrochemical stability (6-8) for long-term d-c-DS of liquid crystals. Redox dopants which can be reduced and oxidized much more easily than the LC compounds minimize the participation of the LC compounds in the electrode reactions which are responsible for their decomposition (6, 9).

In a recent preliminary report (9), we showed that the charge injection and LC flow direction as well as the scattering patterns in a d-c activated LC depended upon the dopants that were used. Earlier, Heilmeier *et al.* (10) reported that in anisylidene-*p*-aminophenylacetate the DS was initiated from the negative electrode and was propagated to the positive electrode. However, they used geometrically dissimilar electrodes and they did not specify the dopants responsible for the observed conductivity and DS of their Schiff base. Lacroix and Tobazeon (11) carried out studies on N-(*p*-methoxybenzylidene)-*p*-*n*-butylaniline (MBBA) in a special cell in which the electrodes were coated with anion-permeable membranes. They observed that the LC motion started at the negative (anion-injecting) electrode and spread toward the positive (collector) electrode, giving a "finger"-type flow pattern followed by a turbulent region spreading toward the collector.

In the present paper we first report studies on the electrode reactions of various dopants and of 4 ester liquid crystal components in solutions of acetonitrile or dimethyl formamide. Then we report studies of the hydrodynamic flow patterns and dynamic scattering effects of these dopants dissolved in the nematic ester liquid crystal mixture when d-c voltages are applied.

Experimental

The LC used was a phenyl benzoate mixture designated as HRL-2N10. It was a four-component mixture of *p*-butylphenyl *p*-toluate, *p*-butoxyphenyl *p*-butoxybenzoate, *p*-butoxyphenyl *p*-hexyloxybenzoate, and *p*-butoxyphenyl *p*-octyloxybenzoate in a weight ratio of 15:5:9:9, respectively. It had a nematic range of about 20°-55°, a dielectric anisotropy of $\Delta\epsilon = -0.12$ (25°C, 500 Hz), and a birefringence of $\Delta n = 0.14$ (25°C, 545 nm). Before dopants were added, the resistivity of the LC at 25°C was greater than 10^{11} Ω-cm at 100 Hz. The resistivity of the LC after doping ranged from 4×10^8 to 1×10^{10} Ω-cm. The individual components of the LC were prepared by the reactions of the corresponding substituted benzoyl chloride and the substituted phenol in pyridine. The reaction products were recrystallized several times. Three types of dopants were used: (*i*) electrochemically inactive salts, tetrabutylammonium perchlorate (TBAP), and tetrabutylammonium trifluoromethanesulfonate (TBATMS); (*ii*) electron acceptors, 7,7',8,8'-tetracyanoquinodimethane (TCNQ), and (2,4,7-trinitro-9-fluoroenylidene)malononitrile (TFM); and (*iii*) electron donors, di-*n*-butylferrocene (DBF) and tetrathiofulvalene (TTF). The acceptor and donor dopants are called "redox" dopants throughout this paper. TBATMS was prepared (12) by reaction of trifluoromethanesulfonic acid and

* Electrochemical Society Active Member.

Key words: redox dopant, salt dopant, liquid crystal, electrohydrodynamic motion, dynamic scattering.

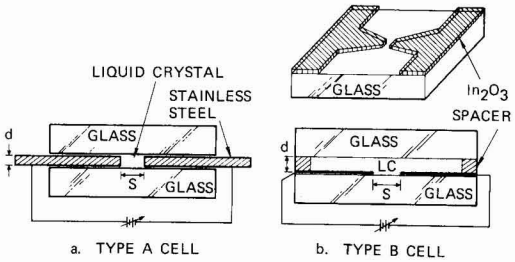

Fig. 1. Schematic drawings of test cells

tetrabutylammonium bromide. The crude product was recrystallized from water and dried. TBAP was the polarographic grade from Southwestern Analytical Chemicals, Incorporated. It was vacuum dried at 50°C before use. TCNQ (from either Aldrich Chemical Company or Eastman Organic Chemicals) was recrystallized more than twice from acetonitrile (AN). TFM (Aldrich Chemical Company) was recrystallized from AN. DBF (Research Organic Chemical Company) was purified by vacuum distillation. The TTF sample was donated by Dr. Fred G. Yamagishi.[1] The solvents AN (Burdick and Jackson Laboratories Incorporated) and spectrophotometric grade dimethyl-formamide (DMF) (J. T. Baker Chemical Company) were used as purchased for electrochemical studies.

The electronic apparatus employed for the cyclic voltammetry was similar to that described earlier (13). The cyclic voltammograms were recorded on an Omnigraphic Model 2000 X-Y recorder (Houston Instrument) using a conventional two-compartment cell. The electrodes used for cyclic voltammetry were either commercially available hanging mercury drop electrodes or a platinum ball attached to a fine platinum wire sealed in glass. Potentials were measured against a saturated calomel electrode (SCE), and solution resistance was not compensated. All experiments were carried out at room temperature.

Two different types of test cells for liquid crystals were used for the microscopic study. Schematic diagrams of type A and B cells are shown in Fig. 1. The LC was restricted to a small interelectrode space in the type A cell. The purpose of the type B cell was to allow enough space so that the liquid crystal could move from one electrode to the other without generating a compensating flow in the area under observation. The electrode separations (S) were varied from 180 to 600 μm, and the thickness of the liquid crystal layer (d) from 25 to 200 μm. The liquid crystal was aligned either perpendicular or parallel to the electric field and parallel to the surface of the glass substrates by manually rubbing the substrate with Kimwipes. The perpendicular alignment was obtained by bonding long alkyl chains onto the surface of the substrates. The microstructure of the DS was observed from a direction perpendicular to the direction of the applied electric field using a Zeiss standard WL polarizing microscope.

Results and Discussion

Electrode reactions in solvents.—The electrode reactions of the liquid crystal components were studied by cyclic voltammetry using platinum and mercury electrodes. The cyclic voltammograms of the LC components in AN are shown in Fig. 2. Anodic oxidations of the compounds occurred at potentials more positive

[1] Preparation of TTF: 1,3-dithiole-2-thione (Strem Chemicals Incorporated) was oxidized with peracetic acid [E. Klingsberg, *J. Am. Chem. Soc.*, 26, 5240 (1964)], and the resulting salt was converted to 1,3-dithialium perchlorate with perchloric acid [D. Leaver *et al.*, *J. Chem. Soc.*, 5104 (1962)]. Deprotonation of this compound with triethylamine [D. L. Coffen *et al.*, *J. Am. Chem. Soc.*, 93, 2258 (1971)] gave TTF in quantitative yield. After recrystallization from hexane, the product was gradient-sublimed (75°C, 10^{-5} Torr) [A. R. McGhie *et al.*, *J. Cryst. Growth*, 22, 295 (1974)] to give orange prisms, mp 118°-119.5°C.

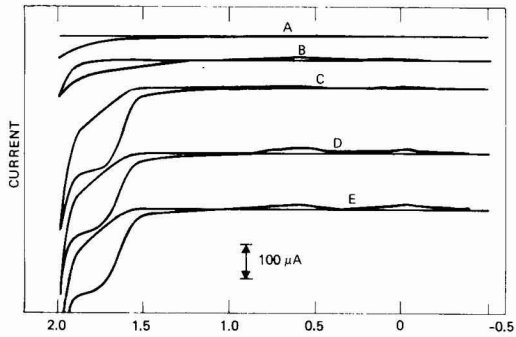

Fig. 2. Cyclic voltammograms of the LC components in 0.1M TBAP solution of AN. Electrode, platinum ball; voltage scan rate, 100 mV/sec; (A) blank solution; (B) 2 mM *p*-butylphenyl toluate; (C) 2 mM *p*-butoxyphenyl *p*-butoxybenzoate; (D) 2 mM *p*-butoxyphenyl *p*-hexyloxybenzoate; and (E) 2 mM *p*-butoxyphenyl *p*-octyloxybenzoate.

than 1.5V *vs.* SCE. A coupled reduction peak of the anodic peak (Fig. 2) of the compounds was not observed, indicating that the oxidation products were not readily rereduced in the experimental conditions. Typical cyclic voltammograms are shown in Fig. 3 of one of the LC components in DMF for the cathodic process. A cathodic reduction of *p*-butylphenyl *p*-toluate (not shown in Fig. 3) occurred at more negative potentials than −2.0V *vs.* SCE, while the reduction of the other three compounds occurred at more negative potentials than −2.1V *vs.* SCE, as in Fig. 3. No coupled oxidation peaks to the reduction peaks were observed at low voltage scan rates [Fig. 3(A)]. As the scan rates were increased above a certain value (*e.g.*, about 100 mV/sec for *p*-butoxyphenyl *p*-hexyloxybenzoate), an oxidation peak which appeared to be coupled with the reduction peak was observed [Fig. 3(B) and (C)]. This observation indicated that a chemical reaction of the primary reduction product might be followed by the cathode reaction to give a reaction product which was not easily oxidizable at the electrode. Primary reaction products of both cathodic and anodic processes would probably be radical ions (14, 15) of the LC esters, which would be unstable in the experimental conditions.

The cyclic voltammograms of the dopants in 0.1M TBAP solution of AN using the platinum electrode are shown in Fig. 4. The cathodic and anodic peaks of all the redox couples in Fig. 4 were separated by about 70-100 mV. The separation of the cathodic and anodic peaks (70 or 80 mV) of the two one-electron reduction steps of TFM appeared to indicate that the electrode reactions were reversible. The values of the peak potential separation (slightly larger than the theoretical

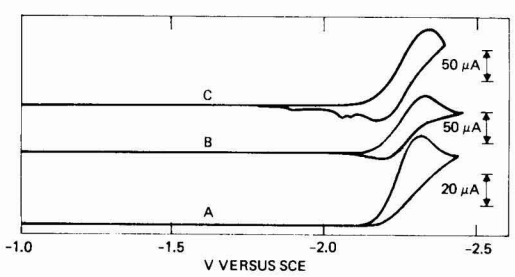

Fig. 3. Cyclic voltammograms of 1 mM *p*-butoxyphenyl *p*-hexyloxybenzoate in 0.1M TBAP solutions of DMF. Hanging drop mercury electrode. Voltage scan rates: (A) 20 mV/sec; (B) 100 mV/sec; and (C) 200 mV/sec.

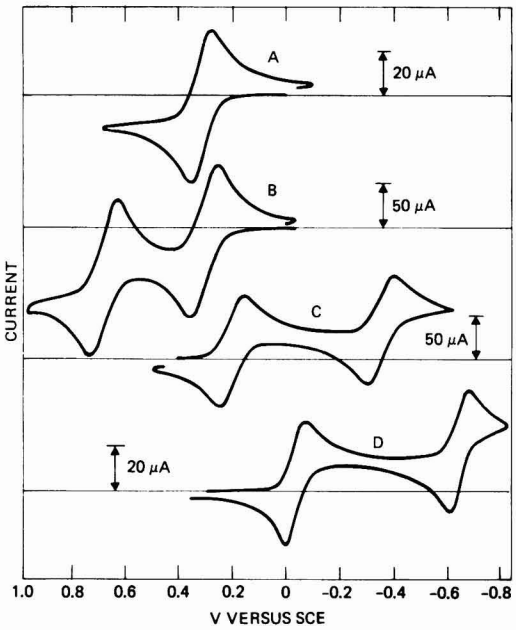

Fig. 4. Cyclic voltammograms of the redox dopants in 0.1M TBAP solution of AN. Electrode, platinum ball; voltage scan rate, 100 mV/sec; (A) 1.0 mM DBF; (B) 3 mM TTF; (C) 2.5 mM TCNQ; and (D) 1.1 mM TFM.

value of 58 mV) might be due to the uncompensated resistance of the electrolyte in the test cell.

Reversible electrode reactions in AN have been reported for the two one-electron oxidations of TTF (16) and also for the first one-electron reduction step of the two one-electron reduction steps of TCNQ (17, 18). Such reversibility has not been reported for TFM and DBF, but in the latter case a similar structure [1,1'-diethylferrocene (19)] was reported to show a reversible one-electron oxidation step.

The redox potentials of the dopants indicate that the electron acceptors such as TFM and TCNQ and donors such as DBF and TTF are expected to dominate cathodic and anodic processes, respectively, in the LC if they are present in sufficient concentrations.

Liquid crystal studies.—The dominating effects of the electrode reactions of dopants on the electrohydrodynamics of the LC have been observed during the microscopic study of DS with applied d-c fields. The characteristic microscopic patterns of DS with various types of dopants are shown in Fig. 5 and 6. Salt dopants [Fig. 5(B) and 6(A)] and redox dopants [Fig. 5(B-D) and 6(B-F)] showed distinctly different DS patterns. When the dopant was salt type and the liquid crystal alignment was perpendicular to the electric field and parallel to the glass substrate, the scattering pattern had a line or channel structure [Fig. 5(A) and 6(A)] which was asymmetric with respect to the polarity of the field but otherwise similar to that previously observed by Chang (20) with MBBA subjected to an a-c signal. (When the alignment was parallel to the electric field, the line structure was spatially very irregular; otherwise, the appearance was similar to the perpendicular case.) Thin flow lines of liquid crystal [Fig. 5(A)] were initiated from both electrodes visibly at the same time and propagated toward the opposite electrodes. The initiation of these flow lines alternated regularly from one electrode to the other. Dust particles moved in one direction along the flow lines originating at one electrode, and in the opposite direction along the flow lines originating at the other electrode, indicating that the lines were caused by LC flow. These particles moved back and forth along the flow channels. This observation is consistent with earlier observations on Williams domain patterns (21). There appeared to be little or no net flow of liquid crystal from one electrode to the other, even with type B cells in which room for net flow was provided.

When the dopant was a redox-type, *i.e.*, an electron acceptor or an electron donor, the general appearance of the scattering pattern was quite different from that observed with the salt dopants. Turbulent motions of liquid crystal were observed at lower voltages, without formation of the regular line or channel structure discussed above. The turbulence was initiated from one electrode and propagated to the other at a visible rate. Except at very high voltages, the turbulence did not reach the opposite electrode and remained localized near the electrode where it was initiated [Fig. 5(B-D) and 6(B-E)]. A surprising observation was that the turbulence was initiated from the cathode when the dopant was an electron donor and from the positive when the dopant was an electron acceptor, *i.e.*, the turbulence was observed at the opposite electrode of

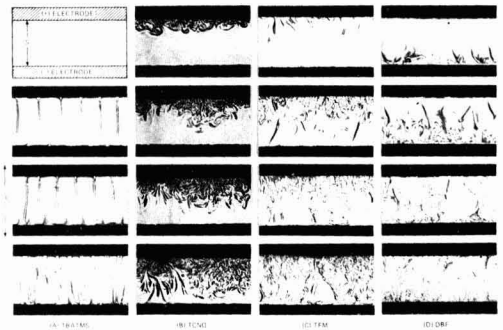

Fig. 5. Photographs of the microscopic patterns of DS using type A cells. A single polarizer parallel to the direction of LC alignment was used. The alignment of LC was perpendicular to the electric field and parallel to the surface of the glass substrate. d = 51 μm. (A) 0.03%, $\rho \sim 4 \times 10^8$ Ω-cm; (B) saturated, $\rho \sim 10^{10}$ Ω-cm; (C) 0.5%, $\rho \sim 10^{10}$ Ω-cm; and (D) 1%, $\rho \sim 10^{10}$ Ω-cm.

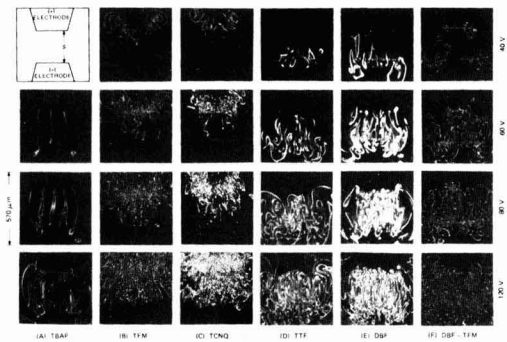

Fig. 6. Photographs of the microscopic patterns of DS using type B cells. Crossed polarizers are used with one polarizer parallel to the direction of LC alignment. The alignment of LC was perpendicular to the electric field and parallel to the surface of the glass substrate. d = 51 μm. (A) 0.02% TBAP, $\rho \sim 2 \times 10^9$ Ω-cm; (B) 0.2% TFM, $\rho \sim 10^{10}$ Ω-cm; (C) saturated TCNQ, $\rho \sim 10^{10}$ Ω-cm; (D) 0.5% TTF, $\rho \sim 9 \times 10^{10}$ Ω-cm; (E) 0.2% DBF, $\rho \sim 10^{10}$ Ω-cm; and (F) 0.1% DBF-TFM, $\rho \sim 10^{10}$ Ω-cm.

the electrode from which the charge injection was expected through the faradaic reaction of the dopant.

The flow of LC under the influence of the applied d-c field was also observed with the redox dopants. A unidirectional flow from one electrode to the other was observed with these dopants, unlike the case of salt dopants. The direction of the flow was always from the anode to the cathode when the dopant was a donor, and from the cathode to the anode when the dopant was an acceptor. Figure 7 shows an example of microscopic flow patterns with a donor dopant (DBF). As indicated by arrows in the figure, average dust particles moved from the back side of the electrode from which charge injection is expected through the faradaic reaction of the dopants toward the opposite electrode, traveled across the electrode boundary and came back to the starting point by the periphery of the electrodes where the electrical field was weak. The dopant-dependent flow of LC was confirmed by another independent method using a test cell which is shown schematically in Fig. 8. The field was applied across two metal screen electrodes and a net liquid flow in a given direction introduced a pressure which changed the height of the liquid crystal in the capillaries. When voltage was applied to the cell, the LC column was displaced from the anode side to the cathode side when the dopant was an electron donor, and vice versa when the dopant was an acceptor. When the dopant was either a salt or an equimolar mixture of the donor (DBF) and the acceptor (TFM), the displacement was much smaller than previous cases.

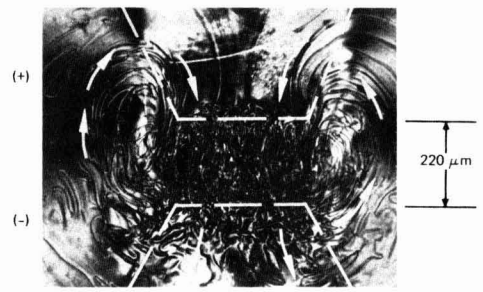

Fig. 7. Flow pattern of LC in a type B cell. Alignment of LC was perpendicular to the surface of the glass substrate. Photographs were taken with crossed polarizers. Dopant: 0.2% DBF. Applied voltage: 120V.

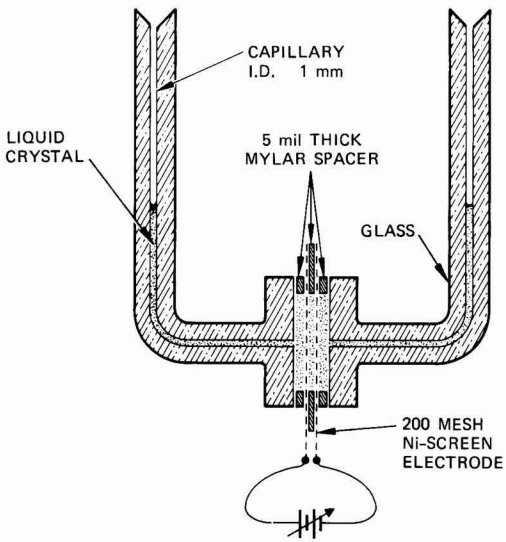

Fig. 8. Liquid crystal flow detection cell.

The dopant-dependent flow of LC under the influence of the d-c field clearly indicated that the electrode reactions of the dopants played the dominant role in the electrohydrodynamics of the LC. The observation with the redox dopants appears to be consistent with the charge conduction mechanisms, as shown in Fig. 9(a) and (b), which involve a unipolar charge injection through the faradaic reaction of the dopant at our electrode followed by space charge (11) migration to the opposite electrode where the charge is neutralized by the reverse electrode reaction. The space charge should be associated with the radical ions of the dopants. When the dopant is an electron acceptor [Fig. 9(a)], negative charge injection occurs at the cathode ($A + e \rightarrow A^-$), the charge migrates to the anode in the form of a space charge to be neutralized at the anode ($A^- \rightarrow A + e$), and vice versa when the dopant is a donor [Fig. 9(b)]. The LC flow is caused by the migration of ions through it. The alternative mechanisms shown in Fig. 9(c-f) which do not require space charge formation do not explain the unidirectional flow of the LC.

When the redox dopant was a mixture of an electron acceptor and a donor, the direction of the net flow of LC depended on relative amounts of each component. Microscopic studies showed that the over-all flow pattern of the LC was a mixture of regions which were similar to the pattern with an acceptor dopant and those with donor dopant rather than those of a salt dopant with a flow line structure. The patterns contained regions of turbulence which were similar to those with an acceptor dopant and regions which were similar to those with a donor dopant [Fig. 6(F)]. This observation was also supported by the motion of dust particles which moved from one electrode to the other in one region and in the opposite direction in the adjacent region. The charge conduction mechanism appears to involve regions where the mechanism shown in Fig. 9(a) operates, and other regions where the mechanism shown in Fig. 9(b) operates. These two

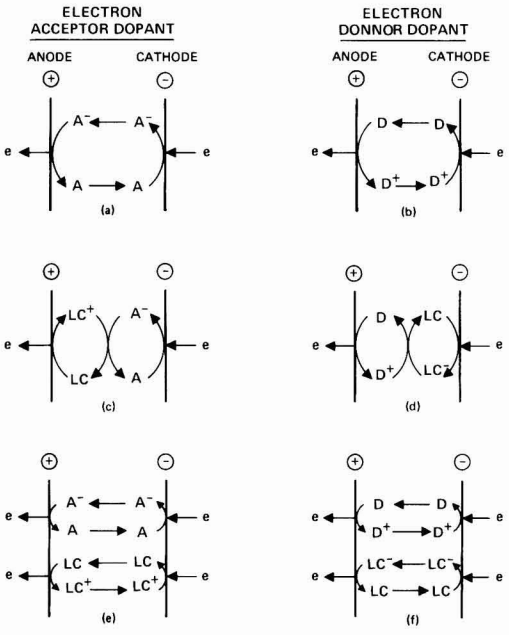

Fig. 9. Charge conduction mechanisms through LC when the dopant is a redox type.

different regions are randomly distributed throughout the conduction area.

When the dopant is a salt, the charge conduction mechanism is probably as shown in Fig. 10(a). The LC components are reduced at the cathode to give a radical anion ($LC + e \rightarrow LC^-$), and oxidized at the anode to give a radical cation ($LC \rightarrow LC^+ + e$). At the same time, channels of cation and anion space charge regions are formed during the charge migrations to the opposite electrodes, and the charge is neutralized at the opposite electrodes by reverse reactions. An alternate mechanism (22) [Fig. 10(b)] which includes a reaction of the cation and anion in the bulk of LC does not explain the alternating flow channels of LC which are observed with the salt dopant.

The hydrodynamic instability of LC with the salt dopants to form the flow channel structure has been theoretically analyzed previously (23). However the reason, why the turbulence pattern is formed during dynamic scattering of LC when the dopant is a redox type and why the turbulence is localized at one particular electrode are not known presently. The reason why two different turbulence regions are formed when the dopant is a mixture of an electron acceptor and a donor, instead of giving the flow channel structure, remains also to be explained.

The turbulent LC flow patterns observed in Fig. 5 and 6 correspond to the dynamic scattering (DS) effects observed in display cells. The DS threshold voltage is considerably higher in the present test cells than in conventional sandwich-type display cells because of the surface boundary conditions. Comparison of the microscopic patterns of salt-doped LC in Fig. 5(A) and 6(A) (no DS was observed at 30 and 40V, respectively) with those of redox-doped LC in Fig. 5(B-D) and 6(B-F) showed that the redox dopants gave lower DS threshold voltage than the salt dopants. Threshold voltages of 2.0-2.1V for a redox dopant and 3-5V for a salt dopant were observed (6) in a comparable resistivity range of the LC in conventional 13 μm thick display cells in which the LC was sandwiched between 2 flat transparent electrodes. The comparison of the microscopic patterns also indicated that the LC doped with a redox dopant would give a higher DS level than the LC with a salt dopant. The scattering levels in a given voltage in the display cells were always higher with the redox dopants than the salt dopants (6).

Our observations (6) of long d-c operational lifetimes of LC with redox dopants as compared to short lifetimes with salt dopants are consistent with the present charge conduction mechanism. In 13 μm thick display cells an operational lifetime of more than 18,000 hr with continuous 20V d-c operation has been achieved when the LC was doped with 0.5% DBF and 0.5% TFM, while the lifetime was shorter by more than two orders of magnitude when the LC was doped with a salt dopant. The shorter lifetime with a salt dopant was probably due to the formation of LC radical ions which are unstable, while in the presence of redox dopants such LC radical ions were not formed.

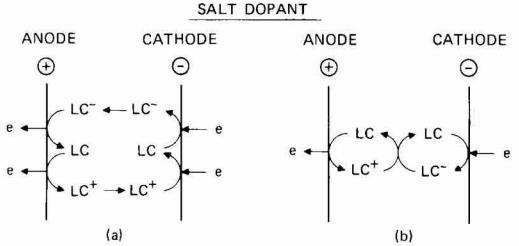

Fig. 10. Charge conduction mechanisms through LC when the dopant is a salt.

Conclusions

1. Discretely different d-c-activated hydrodynamic instabiltities were observed with a redox dopant than with a salt dopant in the same ester liquid crystal. At voltages just above the threshold the liquid crystal with salt dopants showed a flow pattern with periodically arrayed flow channels, while the liquid crystal with redox dopants showed turbulence motion.

2. A unidirectional flow of LC from one electrode to the other has been observed during the DS of the LC which was doped with either an electron acceptor or a donor. The direction of the flow depended on the dopants. The flow was from the positive electrode to the negative when the dopant was an electron donor and vice versa when the dopant was an acceptor.

3. The observations of the flow appeared to be consistent with the charge transport mechanisms which involved a unipolar injection of charge at the anode when the dopant was a donor and at the cathode when the dopant was an acceptor through the faradaic reaction of the dopants and migration of the injected space charge toward the opposite electrode to be neutralized by the reverse electrode reactions.

4. When the dopant was a redox type, dynamic scattering appeared to be initiated and localized (at lower voltages) at the opposite electrode of charge injection.

5. The higher d-c scattering levels (6) of the present liquid crystal with redox dopants rather than with salt dopants appeared to be due to the distinctively different hydrodynamic instability patterns.

Acknowledgment

We are indebted to the Directorate of Chemical Sciences, Air Force Office of Scientific Research, Contract F44620-72-C-0075 for partial financial support of this research. We also wish to thank Mrs. Anna M. Lackner for her help in cyclic voltammetric experiments, Mr. Michael J. Little for helpful discussions on the experimental setup, and Dr. Leroy J. Miller and Mr. John E. Jensen for the synthesis of the liquid crystal materials.

Manuscript submitted Nov. 5, 1976; revised manuscript received May 20, 1977.

Any discussion of this paper will appear in a Discussion Section to be published in the June 1978 JOURNAL. All discussions for the June 1978 Discussion Section should be submitted by Feb. 1, 1978.

Publication costs of this article were assisted by Hughes Research Laboratories.

REFERENCES

1. G. H. Heilmeier, L. A. Zanoni, and L. A. Barton, *IEEE Trans. Electron Devices*, **17**, 22 (1970).
2. R. Chang, in "Liquid Crystals and Ordered Fluids," Vol. 2, J. F. Johnson and R. S. Porter, Edtors, p. 367, Plenum Publishing Corp., New York (1974).
3. M. I. Barnik, L. M. Blinov, M. F. Grebenkin, S. A. Pikin, and V. G. Chigrinov, *Phys. Lett.*, **51A**, 175 (1975); *Zh. Eksp. Teor. Fiz.*, **69**, 1080 (1975).
4. J. D. Margerum, H. S. Lim, P. O. Braatz, and A. M. Lackner, *Mol. Cryst. Liq. Cryst.*, **38**, 219 (1977).
5. A. I. Baise, J. Teucher, and M. M. Labes, *Appl. Phys. Lett.*, **21**, 142 (1972).
6. H. S. Lim and J. D. Margerum, *ibid.*, **28**, 478 (1976).
7. Y. Ohnishi and M. Ozutsumi, *ibid.*, **24**, 213 (1974).
8. S. Barret, F. Gaspard, R. Hernio, and F. Mondon, *J. Appl. Phys.*, **47**, 2375 (1976).
9. H. S. Lim and J. D. Margerum, *This Journal*, **123**, 837 (1976).
10. G. H. Heilmeier, L. A. Zanoni, and L. A. Barton, *Proc. IEEE*, **56**, 1162 (1968).
11. J. C. Lacroix and R. Tobazeon, *Appl. Phys. Lett.*, **20**, 251 (1972).
12. K. Rousseau, G. C. Farrington, and D. Dolphin, *J. Org. Chem.*, **37**, 3968 (1972).
13. G. Lauer, Ph.D. Thesis, California Institute of Technology (1967).
14. A. Lomax, R. Hirasawa, and A. J. Bard, *This Journal*, **119**, 1679 (1972).

15. A. Denat and B. Gosse, *Chem. Phys. Lett.*, **22**, 91 (1973).
16. S. Hünig, G. Kiesslich, H. Quast, and D. Scheutzow, *Justus Liebigs Ann. Chem.*, **1973**, 310.
17. D. S. Acker and W. R. Hertler, *J. Am. Chem. Soc.*, **84**, 3370 (1962).
18. L. R. Melby, R. J. Harder, W. R. Hertler, W. Mahler, R. E. Benson, and W. E. Mochel, *ibid.*, **84**, 3374 (1962).
19. T. Kuwana, D. E. Bublitz, and G. Hoh, *J. Am. Chem. Soc.*, **82**, 5811 (1960).
20. R. Chang, *J. Appl. Phys.*, **44**, 1885 (1973).
21. P. A. Penz, *Phys. Rev. Lett.*, **24**, 1405 (1970); *Phys. Rev. A*, **10**, 1300 (1974).
22. M. Voinov and J. S. Dunnett, *This Journal*, **120**, 922 (1973).
23. W. Helfrich, *J. Chem. Phys.*, **51**, 4092 (1969).

Chemical Mechanisms in Photoresist Systems

I. Photochemical Cleavage of a Bisazide System

Shigeki Shimizu[1] and George R. Bird

School of Chemistry, Rutgers University, New Brunswick, New Jersey 08903

ABSTRACT

We have investigated the familiar photoresist system of cyclized polyisoprene + bis(4-azidobenzal)cyclohexanone by the methods of infrared and u.v. spectroscopy, solvent extraction, and thin layer chromatography. The principal photoreaction is the simultaneous cleavage of both azido groups on a single molecule by absorption of a single photon with 43% quantum yield. The observed traces of monoazides and or other materials are insufficient to justify a biphotonic mechanism. The reacted bisazide (bisamine and/or by-products) acts as a quencher for neighbor bisazide molecules, producing a complicated kinetic behavior which may simulate a second-order (biphotonic) reaction.

Among the practical photoresist systems used to fabricate printed microcircuits or lithographic plates, symmetrical bisazides have been widely used as the photoactive, cross-link-forming element.[2] It is obvious from the wide acceptance of this class of materials that the quantum yield for formation of cross-links must be high. In describing these systems, Kosar (1) makes repeated mention of the thermal stability of the azide group, a stability which may be contrasted with the relative thermal instability of most photochemical initiators and cross-linking agents (2). Since single-cross-links suffice to bind and immobilize large polymer molecules, a photoresist system must be considered as a chemical image amplifier with a gain roughly proportional to the degree of polymerization of the parent polymer. This amplification applies equally to the desired image of actinic photons and to the undesired thermal initiation of cross-linking reactions.

The high sensitivity of bisazide photoresist systems was called to our attention by John Weigl (3), who indicated that the system described by Clecak, Cox, and Moreau (4) was "a extraordinary fast system described in the literature." This system involves partially cyclized polyisoprene as the starting polymer and 2,6-bis(4-azidocinnamylidene)cyclohexanone as the cross-linking agent (I). Related initiators involving cyclopentanone and methyl substituted cyclic ketones have been described (5). We were initially interested in the question of thermal instability of the cinnamylidene bisazide, but soon discovered that the question of instability could not be approached without a satisfactory understanding of the mechanism of the primary photoreactions of these systems. Conversations with Dr. Moreau indicated that a commercially available material, 2,6-bis(4-azidobenzal)cyclohexanone (II), would be a much more suitable material for investigation, so we began a mechanistic investigation on this compound as a photo-cross-linking agent for partially cyclized polyisoprene.

The scientific literature is ambiguous as to the initial step in the photoreaction of a variety of bisazides. It is clear that N_2 is split off and nitrene formed as a highly reactive intermediate, but it is not at all clear whether absorption of a single photon results in the cleavage of one or both of the azido groups. Reiser *et al.* (6, 7) have analyzed the photoreactions of a number of bisazides in frozen matrixes at 70°K, and reported quantum yields for 2 separate steps in the formation of the bisnitrene (stable only in the frozen matrix). One very notable exception in this investigation is the listing of the compound p,p′-diazidobenzophenone at the end of the table of the quantum yields with the single entry $\Phi = 1.00$ and no indication as to whether this refers to the quantum yields of 2 discrete steps or to the simultaneous cleavage of both azido groups by absorption of a single photon. Trozollo *et al.* (8) have reported on the ESR spectra of some bisnitrenes in frozen matrixes, and suggested in the text that these may be formed by simultaneous single photon cleavage in some cases.

In an attempt to settle the distinction between simultaneous, monophotonic cleavage and stepwise two-photon cleavage, we examined the details of light sensitivities reported by Clecak *et al.* (4). Although these workers write an explicit biphotonic equation, their system sensitivity suggests simultaneous cleavage. Thus, the absorption of some 5.0×10^{14} photons/cm^2 suffices to insolubilize over 90% of a film of polymer containing 8.7×10^{14} molecules/cm^2. One could appeal to thermal reactions to make up the difference to at least one reacted azido group per bisnitrene molecule, but such extensive thermal reaction would imply instability on storage, which is not observed.

[1] Present address: Mitsubishi Chemical Industries, Research Laboratory, Midori-ku, Yokohama, Japan.

Key words: cross-linking, energy transfer, infrared spectrometry.

[2] Since the bisazide systems form cross-links and become resistant to solution in exposed areas, they are described as "negative photoresists" by analogy to a photographic negative.

We observed the photoreaction of bisazide (II), monitoring azido group absorption at room temperature in the polyisoprene matrix by infrared spectrometry. This observation was made directly on the actual photoresist composition as coated on high resistivity Si wafers, which allowed us to take advantage of the infrared transparency of pure Si. Photoreaction of quinone diazide (III) which makes a positive[3] photoresist system was also observed by infrared spectroscopy to illustrate the difference of the photoreaction mechanisms between these positive and negative photoresists. In particular, the quinone diazide is a monofunctional reagent, in contrast to the bisazide crosslinking agent. It forms no quenchers in the course of photoreaction, and thus gives uncomplicated kinetic behavior.

(I)

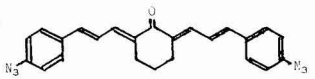

(II)

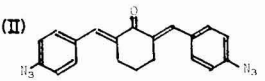

(III)

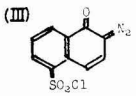

Results and Discussion

Photoreaction characteristic of positive and negative resists.—Figures 1 and 2 show the plot of logarithms of infrared absorbance *vs.* photodosing time at constant intensity. In the case of the positive photoresist (Fig. 1), the logarithmic plot is linear, indicating that the photoreaction is a simple first-order reaction in terms of unreacted quinone diazide (9, 15).[4] No quenching by reaction products is observed, nor was any expected.

In the case of the bisazide photoresist (Fig. 2), the decrease of azide absorbance shows a sharp retardation as the photoreaction proceeds. The reaction curve is more complicated than a simple second-order reaction. We first tried to explain this phenomena by a sequential two-photon process, as proposed by Reiser *et al.* (6). As will be seen, this proved to be impossible to do.

Simulation of photoreaction of bisazide by a sequential two-photon process.—If the bisnitrene is formed through a sequential two-photon process, the decrease of bisazide and increase of intermediate azidoamine can be expressed in Eq. [1] and Eq. [2]. Also, their concentrations (A and B) can be expressed by Eq. [3] and Eq. [4], where K_1 and K_2 are the first-order reaction rate constants for the first and second step, respectively, and are given by products of quantum yields and rates of absorption of photons.

Sequential two-photon mechanism

$$\text{bisazide (A)} \quad h\nu \downarrow K_1 \qquad \frac{dA}{dt} = -K_1 A \qquad [1]$$

$$\text{azido amine (B)} \quad h\nu \downarrow K_2 \qquad \frac{dB}{dt} = K_1 A - K_2 B \qquad [2]$$

$$\text{bisamine} \qquad A = e^{-K_1 t} \qquad [3]$$

$$B = \frac{K_1}{K_2 - K_1}\left(e^{-K_1 t} - e^{-K_2 t}\right) \qquad [4]$$

By assuming that the infrared azido absorption coefficient of azidoamine is half of that of bisazide, we can plot the expected azido absorbance ($2A + B$) *vs.* photodosing time at different K_2 values. The dotted line in Fig. 3 shows the experimental data from a 3% wt. bisazide (II) photoresist coated on NaCl. Other solid lines represent simulated data from Eq. [3] and Eq. [4] in which K_1 was determined to be 0.48 min^{-1} from the observed decrease during the first 1 min, and from the assumption that the initial reaction rate involves only cleavage of a single azido group. Figure 4 shows the simulated concentration of the intermediate azidoamine under the same conditions as Fig. 3.

We had searched carefully with a high resolution infrared spectrometer (PE 521) for the expected shift of the infrared band shape and position upon formation of increasing monoazide, and observed none (Fig. 5). The experimental conditions for Fig. 5 are completely the same as Fig. 3.

Extraction of azide from photoresist films.—When it became clear that the observations could not be fitted to a sequential two-photon mechanism, we made a careful analysis of the reaction products in photoresist films. Several mixtures of methanol and benzene were tested to find the conditions for extracting only starting bisazide and low molecular weight reaction products from the photoresist film without removing appreciable

[3] In this system, exposure forms solubilizing groups, so the polymer is removed in exposed areas. Such a system is described as a "positive photoresist".

[4] First-order kinetics are observed when a reaction proceeds at constant quantum yield in an optically dilute sample.

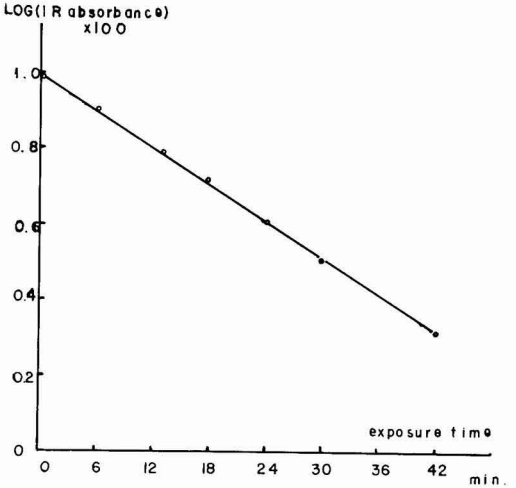

Fig. 1. Disappearance of diazo absorption of positive photoresist (quinone diazide-novolac). Dosing condition, 365 nm, 6.1 mJ/cm² min; photoresist coating, 0.96 μm on Si.

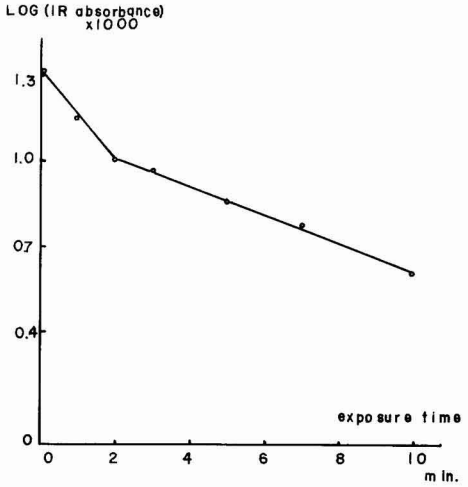

Fig. 2. Disappearance of azido absorption of negative photoresist (bisazide-polyisoprene). Dosing condition, 365 nm, 5.8 mJ/cm² min; photoresist 3 w/o bisazide based on polymer, 1.2 μm coating on Si.

polymer. After extracting the photoresist for 3 min, we analyzed the remaining azide and polyisoprene by the infrared N_3 band and CH band absorbances, respectively. As shown in Fig. 6, an equal volume mixture of methanol and benzene will extract only low molecular weight materials from the polymer layer. All of the uncross-linked polyisoprene is found to dissolve in benzene, so pure benzene can be used for "development" of the exposed photoresist.

We performed extractions from photoresists coated on silicon wafers after different exposure times. The azide remaining in the film was observed by infrared spectrometry. The extracts were separated by TLC (E. Merck, Silica Gel 60 F-254, $CHCl_3$ solvent) and starting bisazide ($R_f = 0.6$) and other colored products ($R_f = 0.0$-0.2) were detected. The R_f (0.6) and u.v. spectrum of the principal extracted material matched the unreacted bisazide (II).

The low mobility colored products were difficult to characterize. They are proved not to be azidoamine (azidonitrene-polyisoprene adducts), but rather by-products of nitrene-bisazide coupling side-reaction from the following observations:

1. The TLC spots of these products can be moved to the solvent front ($R_f = 1.0$) by using polar solvents ($MeOH/CHCl_3 = 5/2$), while cyclized polyisoprene (not cross-linked) does not move at all ($R_f = 0.0$).

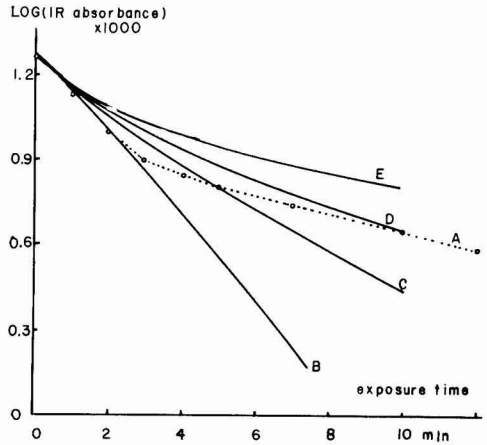

Fig. 3. Simulation of total azido absorbance by sequential two-photon process. Dosing condition, 365 nm, 5.8 mJ/cm² min. A, observed from 3% bisazide photoresist, coated 1.2 μm thick on NaCl; B, simulated from $K_1 = 0.48$ min^{-1}; $K_2 = 0.48$ min^{-1}; C, simulated from $K_1 = 0.48$ min^{-1}, $K_2 = 0.16$ min^{-1}; D, simulated from $K_1 = 0.48$ min^{-1}, $K_2 = 0.096$ min^{-1}; E, simulated from $K_1 = 0.48$ min^{-1}, $K_2 = 0.048$ min^{-1}. K_1 is fixed by observation.

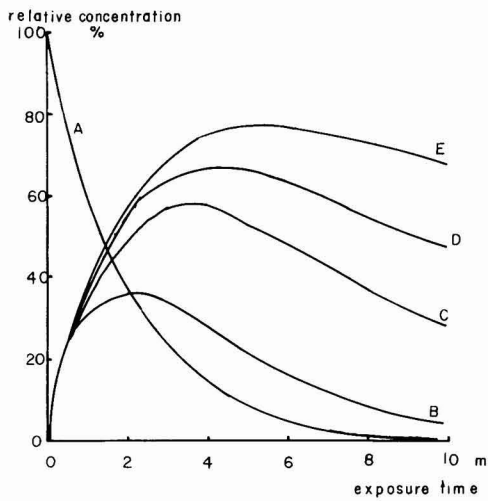

Fig. 4. Simulation of azidoamine and bisazide concentration by sequential two-photon process. A, bisazide simulated from $K_1 = 0.48$ min^{-1}; B, azidoamine simulated from $K_1 = 0.48$ min^{-1}, $K_2 = 0.48$ min^{-1}; C, azidoamine simulated from $K_1 = 0.48$ min^{-1}, $K_2 = 0.16$ min^{-1}; D, azidoamine simulated from $K_1 = 0.48$ min^{-1}, $K_2 = 0.096$ min^{-1}; E, azidoamine simulated from $K_1 = 0.48$ min^{-1}, $K_2 = 0.048$ min^{-1}. K_1 is fixed by observation.

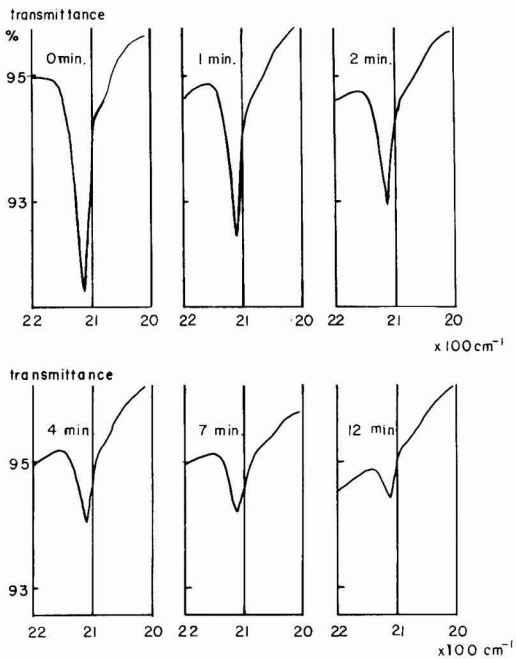

Fig. 5. Infrared spectra (expansion times 10) of photoresist at different photodosing times. Dosing condition, 365 nm, 5.8 mJ/cm² min; photoresist, 3% bisazide, 1.2 μm coating on NaCl.

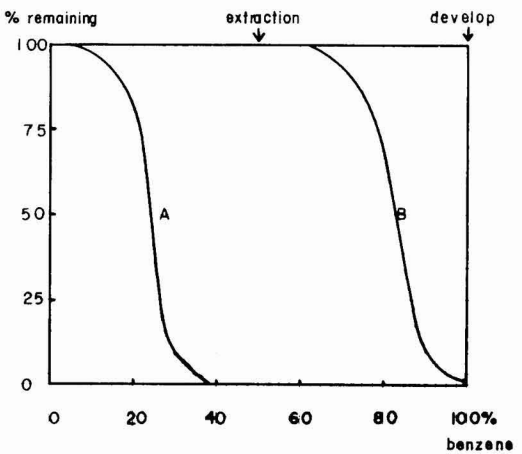

Fig. 6. Extractability of unexposed bisazide and cyclized polyisoprene by methanol-benzene acting for 3 min on a 1.2 μm film containing 3% bisazide. A, bisazide; B, cyclized polyisoprene.

2. The shape, frequency, and especially the relative strength of infrared CH-stretching absorptions are very different from those of cyclized polyisoprene. The ratio of total CH to N_3 absorptions is very low.

3. The low mobility colored spots increased with photodosing time, and never decreased, precluding monoazide intermediates.

4. The infrared spectrum of the mixture of colored products extracted from the low mobility TLC spots by methanol/benzene (1/1) showed a weak azido absorption.

The bisazide spots (R_f = 0.6, $CHCl_3$) were scraped from the TLC plate, extracted again by methanol/benzene (1/1), and analyzed by u.v. spectrometer. The results of the extractions are summarized in Table I. In every case almost all the azido compound can be extracted from the polymer layer, as shown by the disappearance of the infrared azido absorption after extraction.

Discussion on the simultaneous single photon mechanism and the sequential two-photon mechanism.— Azidonitrene, which is supposed to be the intermediate product of the two-photon mechanism, is expected to react almost instantaneously with polyisoprene to form polymer adducts (azidoamine) which cannot then be extracted by polar solvent (methanol/benzene = 1/1). These adducts should show an infrared azido absorption, which we have not observed. We can compare the absence of observed azido absorption after extraction with the calculated minimum absorption required to support a sequential two-photon mechanism. The relation between any first-order photochemical reaction rate constant K (min^{-1}) and quantum yield (Φ) and fraction of incident light absorbed (A) can be expressed as follows

$$K = \frac{\Phi \times \text{photon flux for 1 min} \times A}{\text{starting bisazide molecular concentration}}$$

The parameters for a hypothetical biphotonic decomposition (Φ, A) can be approximated from observed infrared and u.v. data which are summarized in Table II.

Φ_1, which is the quantum yield of the hypothetical first process, can be calculated by assuming equal infrared absorbance for all azido groups. Table II shows an infrared absorbance decrease from 0.0179 to 0.0136 for the first 1 min, which would have to mean that 2.46×10^{15} bisazide molecules/cm^2 were decomposed to monoazide. U.V. absorbance shows that the average absorbance is 0.306 at 365 nm for the first 1 min, so the fraction of light absorbed (A_1) is 50.6%, which means that 5.3×10^{15} photons/cm^2 were absorbed in the first 1 min. Therefore the quantum yield (Φ_1) can be calculated at 46.4% in this particular 3% film.

The fraction of light absorbed by half-reacted bisazide existing as monoazide-monoamine (A_2) can be calculated by taking the mean of initial and final u.v. absorption coefficient of bisazide upon exposure. Table II shows that the absorbance of photoresist at 365 nm decreased to 54% of the initial value when almost all the azido groups are decomposed after a massive 50 min dosing. By taking the mean of 100% and 54%, the average absorbance of the photoresist film can be estimated as $0.306 \times 0.77 = 0.236$, which would mean that A_2 is 41.8%.

When the quantum yield of the hypothetical second step (Φ_2) is assumed to be high, smaller amounts of azidonitrene adducts are to be expected in the photoresist after extraction. In the limiting case with Φ_2 = 100%, K_2 can be estimated as follows

$$K_2 \approx \frac{1.00(\Phi_2) \times 0.418\ (A_2) \times 0.48\ (K_1)}{0.464\ (\Phi_1) \times 0.506\ (A_1)} = 0.85\ \text{min}^{-1}$$

Figure 7 shows the minimum azido absorbance required to agree with a two-photon mechanism in which the infrared absorption coefficient of azidoamine is half that of bisazide. This is a conservative approximation because it has been reported that the infrared absorption coefficient of the azido group increases when conjugated electron-accepting groups are replaced by electron-donating groups, as would be the case if one azido group were converted to a secondary or tertiary amine (10). An azidonitrene would react with polymer to form azidoamine, which can thus be expected to increase the absorption coefficient per azido group.

Figure 8 shows the infrared azido band before and after extraction. The minimum amount of absorbance allowable for a sequential two-photon process is shown aside. The observed absorbance in the polymer after

Table I. Analysis of extracted photoresist and extracts after different amount of photodosing (365 nm)

Photoresist; 3% bisazide, 1.2 μm coating on Si
Extraction; dissolving in methanol-benzene(1/1) solvent for 3 min

Remaining N_3 absorbance after exposure (%)	Remaining N_3 absorbance after extraction (%)	Recovered bisazide from TLC spot of extracts (%)
78	≦4.0	61
67	≦5.5	
65	≦5.0	54
61	8 ± 3	45
51	6 ± 3	
47		28
46		24
40	10 ± 4	19
38	6 ± 4	
32	10 ± 3	22

* The notation ≦ indicates that there appears to be a trace of azide absorption, but the quantity present could range from zero to the stated upper value.

Table II. Observed infrared and u.v. absorbance of bisazide and photoresist

Photoresist; 3% bisazide, 1.2 μm coating on NaCl
Dosing condition; 365 nm, 1.04×10^{16} photon/cm^2 min

	Infrared (2110 cm^{-1})	U.V. (365 nm)
Molar absorption coefficient of bisazide (II)	2.1×10^3 $mole^{-1} \cdot l \cdot cm^{-1}$	3.73×10^4 $mole^{-1} \cdot l \cdot cm^{-1}$
Absorbance of photoresist upon exposure		
t = 0	1.79×10^{-2}	3.32×10^{-1}
t = 1 min	1.36×10^{-2}	2.80×10^{-1}
t = 50 min	$\leq 0.15 \times 10^{-2}$	1.80×10^{-1}

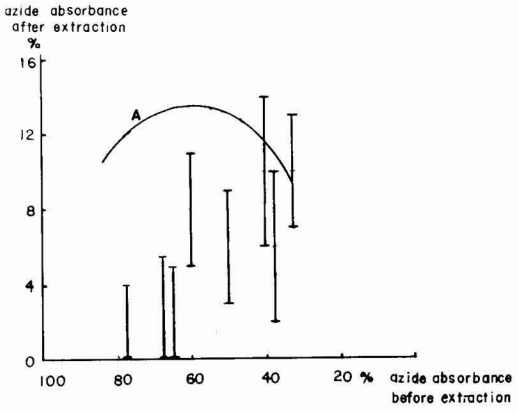

Fig. 7. Comparison of azido absorbance between observed and calculated (two-photon process). A, calculated minimum absorbance for sequential two-photon process, Φ_2 = 100%; I, observed data of photoresist, 3% bisazide based on polymer, 1.2 μm coating on Si, methanol-benzene (1/1) extraction for 3 min.

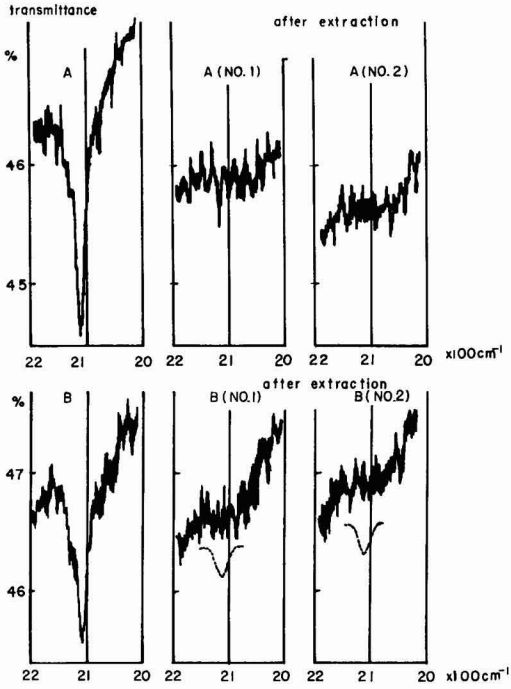

Fig. 8. Infrared spectra (times 20 expansion) of photoresist before and after extraction. A, no exposure, 3% bisazide, 1.2 μm coating on Si; B, partial exposure (remaining azido absorbance is 66%), 3% bisazide, 1.2 μm coating on Si, no. 1 and 2 refer to repeated observations. Note that much of the fine structure (as seen especially clearly in spectrum A-1), is the interference pattern imposed by the high refractive index of the Si wafer (n = 3.4). Fortunately, the azide absorption band is considerably broader than the repeat period of this pattern.

extraction is considerably less than the calculated absorbance.

Thus the two-photon mechanism is inadequate to explain the results and products above mentioned; instead, the simultaneous one-photon mechanism seems much more reasonable. The small amount of azido absorption detected after extraction in Fig. 8 can be attributed in part to unextracted bisazide, because repeated extraction further lowers the intensity of the azido absorption in the polymer while the intensity of the CH absorption is unchanged. Perhaps the over-all cross-linking makes the extraction of bisazide more difficult. The increase in the retained azide with photodosing time (Fig. 7) is thus assigned to cross-linking and reduced swelling of the polymer in the methanol/benzene (1/1) extraction.

The one-photon mechanism also suggests that effective cross-linking occurs at the early stages of photodosing. By measuring the film thickness after development (dissolve in benzene for 3 min), we can estimate the extent of the cross-linking. The results, shown in Table III, give a satisfactory fit for a one-photon mechanism.

Energy transfer.—If we accept a simple one-photon mechanism, the reduced photodecomposition rate of bisazide after *ca.* 50% of photoreaction is still to be explained. We made several coatings with different azide concentration, and observed their azido absorbance decrease upon photodosing. The results are shown in Fig. 9. The decrease of rate with increasing concentration suggests some inhibition of the primary photoreaction by its products. At highest concentration (7% bisazide based on polymer), quenching is observed from the earliest stages and reaction is completely quenched after about 50% of completion. On the other hand, low concentration photoresist layers (1% bisazide based on polymer) show higher initial rate and only slight quenching.

Table III. Fraction of cross-linked polymer after different amount of photodosing

Photoresist; 3% bisazide, 1.2 μm coating on Si
Exposure; 365 nm
Development; dissolve in benzene for 3 min

Decreased amount of N_3 absorbance upon exposure (%)	Remaining polyisoprene after development (%)
43	43
47	49
55	67
71	82

Figure 10 shows the u.v. absorption of negative photoresist before exposure, after complete photodosing, and after development. During photo exposure, a new long-wavelength absorption around 410 nm appears

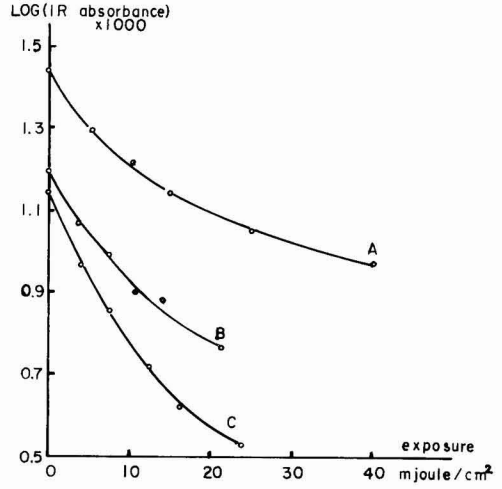

Fig. 9. Rate of disappearance of azido absorbance. Dosing, 365 nm, photoresist A, 7% bisazide, 0.8 μm coating on Si; photoresist B, 3% bisazide, 1.0 μm coating on Si; photoresist C, 1% bisazide, 2.3 μm coating on Si.

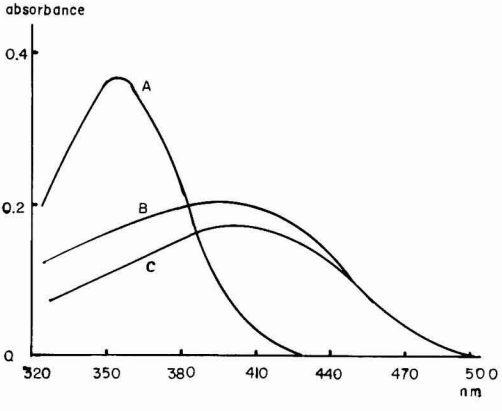

Fig. 10. U.V. spectra of negative photoresist. Photoresist, 3% bisazide, 1.2 μm coating on NaCl, dosing condition, 365 nm, 5.8 mJ/cm² min. A, before exposure; B, after 50 min exposure; C, after development of exposed film.

and remains fixed in the cross-linked polymer after development. We assign this absorption to reacted bisnitrene, presumably bisamine,[5] which forms the actual cross-links. The absorption decrease (curves B and C in Fig. 10) around 350 nm is due to extractable low molecular weight by-products which have been discussed (the low mobility spots).

For the moment we can only note that both of the absorption spectra (bisamine and byproducts) lie at longer wavelength than the spectrum of the starting material. Thus, direct singlet-singlet intermolecular energy transfer can occur. Further, this is a very concentrated system, and the potential donors and acceptors are nearly in contact. Triplet-triplet transfer may also occur (11), but we have no indication supporting or disproving it. The bisamine appears to be inert to direct photoreaction and to reaction by energy transfer. Thus the retardation of decomposition in this system is explicable in terms of energy transfer to the reaction product.

The u.v. absorption of the positive photoresist shows no long-wavelength absorption in the course of photodosing. The absorbance of every peak decreases according to simple first-order reaction kinetics and no quenching is observed (15). The contrast between the complicated concentration dependence shown by the bisazide system and the single first-order dependence of the quinone diazide system can be examined to emphasize the importance of energy transfer in the bisazide system.

The highest quantum yield of bisazide decomposition observed was 43% (one-photon process). The conditions were as follows: bisazide concentration, 0.56% based on polymer; film coating, 3.5 μm on NaCl; photon flux, 8.22×10^{15} photon/cm^2 min; fraction of light absorbed, 29.7%; decomposed bisazide after 1 min dosing, 1.06×10^{15} molecule/cm^2. An even higher quantum yield is to be expected from shorter exposure times and lower azide concentrations, but these conditions lie beyond the accuracy of the infrared observations.

Experimental

The negative-type photoresist was made by dissolving bis(4-azidobenzal)-cyclohexanone(II) and cyclized polyisoprene in Kodak KTFR Thinner.[6] Cyclized polyisoprene was prepared by refluxing a solution of toluene, cis-1,4-polyisoprene (MW 110,000-150,000, Goodyear NATSYN-200) and p-toluenesulfonic acid for 6 hr (12). Cyclicity (1.7-2.3) and uncyclized isoprene unit (4-6%) were characterized by NMR (Varian T-60). Cyclized rubber was dissolved to 10-15 weight percent (w/o) in KTFR Thinner, and bisazide(II) was added 1-7 w/o based on polymer.

The positive-type photopolymer was prepared by condensing pheno-formaldehyde polymer (Union Carbide, NOVOLAC BRN-5834) with 50 w/o of o-naphthoquinone diazide sulfonyl chloride (III) in the presence of sodium carbonate (13). About 20% of the hydroxyl groups were substituted by the quinone diazide sulfonyl group. The photoresist was made by dissolving this photopolymer to 25 w/o in Shipley AZ-1350 Thinner.[7]

The photoresist films were spincoated on silicon wafers and prebaked at 80°C for 20 min in an oven before use. The film thickness was calculated from the interference pattern obtained by measurement of specular reflectance, using the Model 1413 reflectance attachment of a Cary 14 spectrophotometer.

A medium pressure mercury lamp (100W, GE 100A4/T) was used as the u.v. light source. Specific wavelengths were selected using interference filters (365 nm, 405 nm). During photodosing, light intensity was monitored with an EMI S-10 photomultiplier, which was calibrated by a potassium ferrioxalate actinometer (14). Nitrogen gas was flushed through the photoreaction box during photodosing.

The reactions of bisazide and quinone diazide were monitored by observing the infrared absorption of the azido (2110 cm^{-1}) and diazo (2120 cm^{-1}) group using the scale expansion attachment of the Perkin Elmer 521 spectrophotometer (Fig. 11).

P-doped silicon wafers with a high infrared transmittancy of 45-55% at 2100 cm^{-1}, resistance of 300Ω cm^{-1}, diam of 2 in., thickness of 0.27 mm were obtained from Monsanto Chemical Company, and they were used without further heating. A silver bromide window (blue and u.v. absorbing) was placed in front of the photoresist to protect the bisazide and quinone diazide from any actinic light emitted by the infrared light source. When both infrared and u.v. information was needed, the photoresist layers were coated on sodium chloride plates instead of the silicon wafers.

Conclusions

From the infrared study of azido absorption of photoresist upon exposure, and from the analysis of low molecular weight compounds extracted from exposed photoresists, we obtained the following conclusions:

1. The cleavage of both azido groups of the starting bisazide is brought about by absorption of a single photon. This is established by the following observations: (*i*) Azidoamine, which is considered to be the intermediate of the two-photon process, is not observed in partially exposed photoresists; and (*ii*) bisazide is the principal azido compound still existing after any amount of photodosing.

2. The photodecomposition rate of bisazide is reduced as cross-linking proceeds. This is probably due to energy transfer from unreacted bisazide to reacted bisazide (bisamine cross-link and/or byproducts).

Acknowledgments

The authors gratefully thank Dr. W. M. Saltman of Goodyear Corporation for supplying cis-polyisoprene, Mr. B. Herbert of Monsanto Company for supplying Si

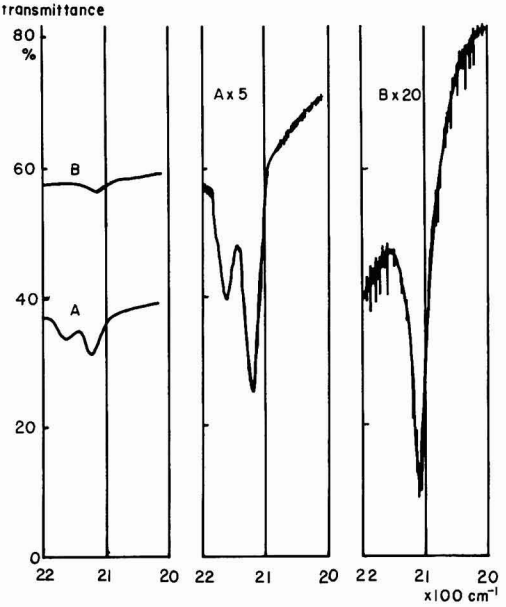

Fig. 11. Infrared spectra of photoresists and their expansion. A, positive-type resist, 0.96 μm coating on Si; B, negative-type resist, 3% bisazide, 1.2 μm coating on Si.

[5] This assignment was confirmed by the absorption spectrum of a related bisamine, bis(4-dimethylaminobenzal)-cyclohexanone, which showed an almost identical absorption band (425 nm) to reacted bisazide (Fig. 10C).

[6] This material is observed by infrared and NMR to be substantially o-xylene.

[7] This material is analyzed by GC to be cellosolve acetate (90%), butyl acetate (5%), and xylene (5%).

wafers, Mr. Harding of Union Carbide Corporation for supplying Novolac, and Dr. F. Hessert of Fairmount Chemical Company for supplying bisazides. Stimulating discussions with Dr. W. Moreau of IBM Corporation and Dr. J. Weigl of Xerox Corporation are gratefully acknowledged.

Manuscript submitted Feb. 22, 1977; revised manuscript received April 15, 1977. This was Paper 75 presented at the Philadelphia, Pennsylvania, Meeting of the Society, May 8-13, 1977.

Any discussion of this paper will appear in a Discussion Section to be published in the June 1978 JOURNAL. All discussions for the June 1978 Discussion Section should be submitted by Feb. 1, 1978.

REFERENCES

1. J. Kosar, "Light Sensitive Systems," p. 336, John Wiley & Sons, Inc., New York (1965).
2. W. D. Pandolfe and G. R. Bird, "Unconventional Photographic Systems Symposium," p. 19, SPSE (1975).
3. Private communication, Xerox Corp.
4. N. J. Clecak, R. J. Cox, and W. M. Moreau, *Polym. Eng. Sci.*, **14**, 491 (1974).
5. H. F. Mark and N. M. Bikales, "Encyclopedia of Polymer Science and Technology," Supplement Vol. 1, p. 401, Wiley-Interscience, New York (1976).
6. A. Reiser, H. M. Wagner, R. Marley, and G. Bowes, *Trans. Faraday Soc.*, **63**, 2403 (1967).
7. A. Reiser and R. Marley, *Trans. Faraday Soc.*, **64** 1806 (1968).
8. A. M. Trozzolo, R. W. Murray, G. Smolinsky, W. A. Yager, and E. Wasserman, *J. Am. Chem. Soc.*, **85**, 2526 (1963).
9. J. Kosar, "Light Sensitive Systems," p. 342, John Wiley & Sons, Inc., New York (1965).
10. Y. N. Sheinker and L. B. Senyania, *Izv. Akad. Nauk SSSR, Ser. Khim. Nauk*, 2113 (1964).
11. T. Tsunoda, T. Yamaoka, and G. Nagamatsu, *Photogr. Sci. Eng.*, **17**, 390 (1973).
12. R. K. Agnihotri, D. L. Falcon, F. P. Hood, L. G. Lesoine, C. D. Needham, and J. A. Offenbach, *Photogr. Sci. Eng.*, **16**, 443 (1972).
13. S. Amakawa, Japan Pat. SHO-459610.
14. J. G. Calvert and J. N. Pitts, "Photochemistry," p. 780, John Wiley & Sons, Inc., New York (1966).
15. D. Ilten and R. J. Sutton, *This Journal*, **119**, 539 (1972).

On the Use of X-Ray Screens in Mammography

A. L. N. Stevels

Philips Research Laboratories, Eindhoven, The Netherlands

and F. Pingault

Massiot-Philips, 80690 Ailly-Le-Haut-Clocher, France

ABSTRACT

Measurements on $CaWO_4$ screen/film combinations show that in mammography significant speed gains compared with the no-screen film technique can be realized. However, the resolution of such high speed systems is poor. Calculations on recently developed powder phosphors like $BaFCl:Eu^{2+}$, LaOBr: Tb^{3+}, $Y_2O_2S:Tb^{3+}$, and $Gd_2O_2S:Tb^{3+}$ show that there are prospects of even faster mammography screens, but the resolution obtained with thinner layers of such new phosphors is expected to be only marginally better. Measurements of the sharpness of imaging phantoms indicate that indeed the resolution is hardly improved by employing new phosphors. The speed gains with respect to $CaWO_4$ are about a factor 2 lower than the calculated ones. New screen technologies have to be found to eliminate the resolution bottleneck. It is found that vapor-deposited CsI: Na and CsI: Tl layers would be very promising candidates for use in mammography. However, hygroscopy is at present a serious obstacle to their application, especially in the CsI: Na case.

The use of x-ray intensifying screens in film radiography is always in the nature of a compromise. On the one hand the speed of the system is increased, so that x-ray exposure can be reduced. On the other hand the quality of the image obtained is reduced by insertion of such an intensification device in the x-ray system.

The choice of an optimum trade-off between speed and image quality depends in the first instance on the type of radiological examination involved. From a technical point of view, not only do all these trade-off points have to be covered by the availability of the corresponding screen-film systems, but also a continuous effort is needed to extend the limits of the system.

As far as the last aspect is concerned, encouraging progress has been made in the last decade. Basically these improvements originate from the availability of new x-ray phosphors (1) which have the potential to replace traditional phosphors like $CaWO_4$ in certain radiological techniques. CsI: Na, CsI: Tl have largely replaced (Zn,Cd) S: Ag in the input screens of image intensifier tubes. For some of the new phosphors (CsI: Na, CsI: Tl) new screenmaking technologies can be applied. Vapor-deposited layers of these materials give rise to less image blurring than comparable ones prepared by the usual powder sedimentation techniques (1-4).

Meanwhile, mainly theoretically (1, 5, 6) and mainly practically oriented (2-4, 7-11) studies have been devoted to the use of new phosphors in x-ray intensifying screens. Almost all of them pertain to the "normal" radiological range, that is to x-rays with energies between 30 and 100 keV.

The present paper pays attention to the use of screens in mammography. Usually in these examinations x-ray films with high silver content are directly exposed to "soft" x-rays with energies between 6 and 30 keV. The main purposes of employing intensifying screens are x-ray dose reduction and economizing on the use of silver in the x-ray film.

First, we compare the properties of $CaWO_4$ screen-film combinations with those of "no-screen" films. After that we calculate what improvements can be

expected from the use of new phosphors and discuss some practical realizations. The results obtained here for soft x-rays are compared with those for the harder x-rays of the 30-100 keV range.

Experimental

The x-ray source used in this investigation was a Rotalix type with W-anode operated at 30 kV. The focus was 0.3 × 0.3 mm², the focus-film distance 1m. No radiation filter was used.

When a double-coated x-ray film is employed, the screen/film combination consists of a front and a back screen with the film in between. With a single-coated film, the screen is placed (with respect to the x-ray source) at the back.

The screens investigated were prepared at our own laboratories or commercially obtained from various sources. For their characterization we use plots of relative speed against resolution. The relative speed is defined as the exposure needed to obtain unit film density above the fog, the mammography no-screen film Kodak PE 4006 being the standard of comparison. All films used in this investigation were processed for 90 sec. The resolution of the system is characterized by the frequency in line pairs per centimeter at which the amplitude of the square wave response of a test grid, consisting of lead strips at varying distances apart, had dropped to 30% of its value at zero frequency. Again the PE 4006 film was used as a standard.

Some Properties of $CaWO_4$ Screen-Film Combinations

In Fig. 1 we have plotted relative speed against resolution for $CaWO_4$ screen/film combinations. The upper curve refers to screens used in combination with double-coated film, type Agfa-Geveart RP3, the lower curve to combinations with a single-coated film, type du Pont "Lo-dose." The points labeled by the subscript 1 represent a standard $CaWO_4$ screen, the Philips Universal type. It is seen that under mammography

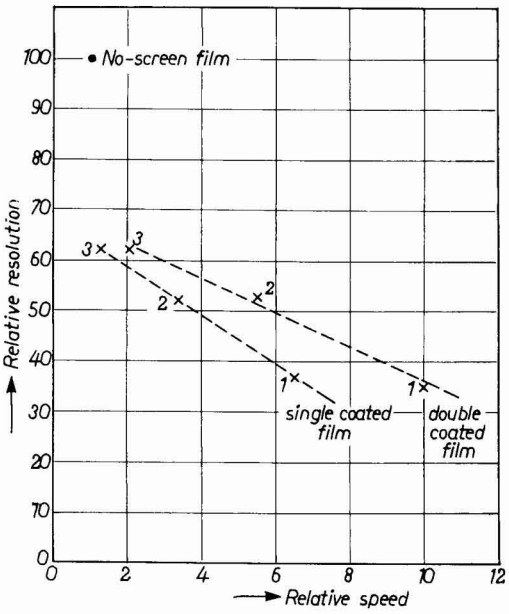

Fig. 1. Relative resolution against relative speed for various screen/film combinations. The no-screen film has a speed equal to unity and a resolution equal to 100. The x-ray source (W-anode) was operated at 30 kV. 1 = $CaWO_4$ standard screen, 2 = $CaWO_4$ high resolution screen, 3 = $CaWO_4$ very high resolution screen (see text also).

conditions its speed is 6.5 (single-coated film) or 10 times (double-coated film) higher than a no-screen film system. The resolution, however, has dropped to about 35% of that of the last-named system. In the literature (12-15) such a deterioration of image quality is stated to be completely unacceptable in mammography. Hence we conclude that with $CaWO_4$ screens maximal speed gains can be achieved which, while preserving a resolution acceptable for mammography, are definitely lower than 6.5× for single-coated film systems and 10× for double-coated film systems.

When a Philips "Micro" screen (points indicated by 2) is used instead of a Universal one the speed is reduced by a factor of about 2, whereas the resolution gain is only a factor of 1.5. It should be noted here that the thickness of the phosphor layer and its packing density are equal to that of a Universal one (≈120 μm and ≈55%). The different properties of the Micro screen have been achieved by adding to the binder some paint which absorbs laterally spread light more than directly escaping light. This method to increase the resolution is more attractive than making the phosphor layer thinner, because in the last-named case the intrinsic x-ray quantum noise of the system increases.

Returning now to Fig. 1, we conclude that also a further reduction of the speed of the system does not result in a compensating increase in resolution: the very high resolution MCD screen (laboratory-made, more heavily colored than Micro), labeled by 3, shows a speed reduction of about 2.5× with respect to the Micro screen, whereas the gain in resolution is only some 20%. Figure 1 suggests that for both types of film there is a limit in resolution of about 65% compared to no-screen film. There are several reasons for this "resolution gap":

1. To a limited extent this gap is due to the fact that the RP3 and the "Lo-dose" films used in combination with the screens contain less silver than the no-screen PE 4006 one. The resolution of the three films is found to be essentially identical. This implies that in Fig. 1 the reference point might shift a bit to the left. In connection with this we note that the speed and the resolution of PE 4006/screen combinations are found to be about equal to those of the RP3/screen combination. Apparently the screen is the limiting factor of the system. This conclusion is also supported by the observation (see Fig. 1) that systems with double-coated films have a speed which is approximately 1.5× that of the ones with single-coated films, whereas the resolution is about equal.

2. A large contribution to the resolution gap is due to geometrical reasons. If, for instance, measurements are made on screens without a plastic protective layer in between the phosphor and the film, the resolution figures are about a factor of 1.2 higher than those given in Fig. 1. If the focus-film distance is increased the resolution gain is small, however.

3. The above-mentioned factors do not bridge the resolution gap indicated in Fig. 1. It is obvious to think that the remaining part is due to the very fact that the $CaWO_4$ phosphor considered is used in the form of a light scattering powder.

On basis of the foregoing section we now formulate several conclusions regarding the use of x-ray screens in mammography:

1. Whatever speed increases can be realized, a resolution drop has to be accepted. Among other things this drop is due to geometrical factors, such as the presence of a protective layer between phosphor and film and the fact that the focus-film distance is not infinite.

2. The use of light scattering powder phosphors gives rise to an additional resolution drop. This makes the image quality marginal in cases where substan-

tial speed gains can be achieved. The impact of laterally scattered light of powder phosphors might be reduced by decreasing the mean grain size of the phosphor and by making the phosphor layer thinner. Regarding the first suggestion we note that in the $CaWO_4$ screens discussed the mean grain size is already low (2.3 μm). Further reduction would entail serious technological problems as well as substantial losses in light output. Thinner phosphor layers would give rise to less x-ray absorption in the screens and hence to increased quantum mottle ("noise") on the film.

3. Screen/single-coated film combinations are disadvantageous from a speed point of view. At present there are no indications that such systems would give a substantially better resolution than those with double-coated films.

4. The use of new powder phosphors instead of $CaWO_4$ gives additional degrees of freedom regarding the realization of screens. Whether this only implies increases of speed or whether it also reduces the resolution drop is a question to be studied. For instance, if a phosphor has higher x-ray absorption per unit length than $CaWO_4$ the phosphor layer thickness can be diminished without increasing the quantum noise above the $CaWO_4$ level.

Calculated Properties of New Phosphors in the Mammography (6-30 keV) Energy Range

A few years ago we studied extensively the properties of new x-ray phosphors in the 30-100 keV energy range (1). We now extend the calculations made in Ref. (1) to the 6-30 keV "mammography" energy range. In order to link up as closely as possible to practical conditions we give data for 100 μm thick powder phosphors screens in contact with u.v./blue sensitive "standard" film or with green sensitive film. We consider 100 μm thick vapor-deposited screens only for CsI:Na (or Tl).

We now discuss the following new materials: $Gd_2O_2S:Tb^{3+}$, CsI:Na (or Tl), $LaOBr:Tb^{3+}$, $Y_2O_2S:Tb^{3+}$, $BaFCl:Eu^{2+}$, and (Zn,Cd)S:Ag. Brief particulars of these phosphors and references to original literature are given in Ref. (1). For $BaFCl:Eu^{2+}$ see also Ref. (8).

The inclusion of $LaOBr:Tb^{3+}$ deserves some special comment. Some two years ago it seemed that this phosphor was not practical because of its hygroscopy and afterglow properties. However, these obstacles to its application now seem to have been eliminated. It should further be noted that the $Gd_2O_2S:Tb^{3+}$, CsI:Tl, and (Zn,Cd)S:Ag phosphors cannot be used in combination with standard x-ray film; green-sensitive films have to be employed instead.

In Fig. 2 we present data on the calculated relative x-ray absorption of the new phosphors, taking a 100 μm thick $CaWO_4$ powder layer as a reference.[1]

Data from tables published by Storm and Israel (16) were used. For the 100 μm powder layers a packing density of 50% was assumed, for the CsI evaporated layers the density was taken to be 100%.

It is seen in Fig. 2 that in the complete 6-30 keV range the x-ray absorption of all the new phosphors considered does not much exceed that of $CaWO_4$. In the case of some well-known candidates for application in standard intensifying screen like $BaFCl:Eu^{2+}$ and $Y_2O_2S:Tb^{3+}$ the absorption in the main part of the mammography range is even substantially lower than that of $CaWO_4$. It is also noted that CsI evaporated layers, which show a superior x-ray absorption in the 40-100 keV range due to their high packing density, need this high density here to have a performance comparable to that of the tungstate.

The fact that, at equal screen thicknesses, the x-ray absorption of the new phosphors is not better than

[1] For reasons of simplicity we have smoothed the curves between 10.2 and 12.1 keV. They would otherwise show small jumps due to L transitions in W at 10.2, 11.5, and 12.1 keV.

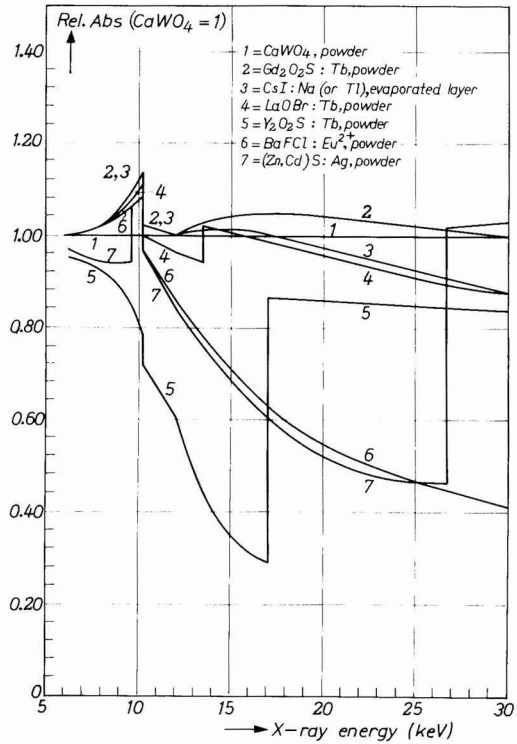

Fig. 2. Calculated relative x-ray absorption ($CaWO_4$ = 1) of various phosphors in the 6-30 keV range. The curves between 10.2 and 12.1 keV have been smoothed (see text).

that of $CaWO_4$ make us conclude that it is probably not possible to improve the resolution of mammography powder screens by decreasing their thickness. The main reason behind this is that the absorption-related [see Ref. (1)] noise properties of the new phosphors are not better and in some cases even inferior to those of $CaWO_4$. At present, the only candidates for mammography screens with improved resolution seem to be those phosphors for which screen technology can be changed, as for instance CsI:Na or CsI:Tl. However, as will be discussed in more detail below, these phosphors have the serious drawback of being hygroscopic, especially in the CsI:Na case.

The speed gains to be expected are shown in Fig. 3, where the relative quantum detection efficiency *QDE* is plotted against x-ray energy. As in Ref. (1) and (6) *QDE* is defined as

$$QDE_E = A_E \cdot \eta \cdot \lambda_{Em} \cdot C_E \cdot D_\lambda$$

where A_E is the x-ray absorption of the screen (as a percentage), η is the luminescence radiant efficiency under cathode-ray excitation of the phosphor[2] (as a percentage), λ_{Em} is the mean wavelength of the detected emission, C_E is a factor representing the energy losses in the screen, and D_λ is the efficiency for detection of the screen luminescence, I_λ, by a detector with response R_λ. D_λ is defined as $\int I_\lambda R_\lambda d\lambda / \int I_\lambda d\lambda$. Details of the calculations are given in Ref. (1).

In Fig. 3, the *QDE* curves of CsI:Na with standard film and of CsI:Tl with green emitting film happen to coincide within 5%. We have drawn data for these two combinations as one curve. As in Fig. 1, the curves have been smoothed between 10.2 and 12.1 keV.

[2] In contrast to efficiencies under x-ray excitation, these are fairly accurately known.

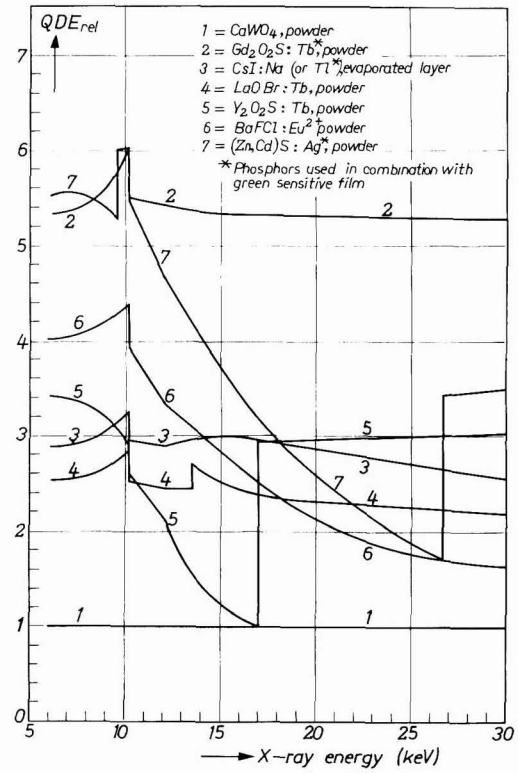

Fig. 3. Calculated relative quantum detection efficiency ($CaWO_4$ = 1) of various phosphors in the 6-30 keV range. The curves between 10.2 and 12.1 keV have been smoothed (see text).

It is concluded from Fig. 3 that the highest *QDE* figures are found at low x-ray energies. In this region the differences in x-ray absorption are small (see Fig. 2) so that the suggested gains almost completely originate from differences in luminescence conversion efficiency and in the match between the spectral distribution of the generated light and spectral sensitivity of the film. Green-emitting phosphors perform especially well in this region, the main reason being that these materials yield more quanta per percent energy efficiency than blue-emitting materials.

The drop in *QDE* above 10 keV is due to the absorption properties of the phosphors. In the most important region for mammography, 15-20 keV (17), the *QDE* lies between 1 and 3 for blue emitting phosphors and between 2.5 and 5.5 for materials to be used in combination with green-sensitive film. In the blue, evaporated layers of CsI:Na are considered to be the best proposal, followed by $BaFCl:Eu^{2+}$ and LaOBr: Tb^{3+} powders. $Y_2O_2S:Tb^{3+}$ performs well above 17 keV but not below that energy. The best phosphor in the green seems to be $Gd_2O_2S:Tb^{3+}$ powder, whereas the promising candidate from a resolution point of view, (see introduction) seems to be CsI:Tl. However, these calculated speed gains with respect to $CaWO_4$ are not as impressive for mammography screens as for screens used at higher x-ray energies. Table I lists some QDE_{rel} data at 15 and 20 keV (100 μm thick screens) and at 60 keV [200 μm thick screen, see Ref. (1)]. It is seen that in most cases the ratio $QDE_{15\ keV}/QDE_{60\ keV}$ or $QDE_{20\ keV}/QDE_{60\ keV}$ is below 1. The more promising candidates even score ratios below 0.5.

Application of the New Phosphors; Measured Properties of Some New Mammography Screens

As concluded in the section on properties of $CaWO_4$ screen-film combinations, an inprovement of the resolution of mammography screens is more urgently needed than a further increase of speed. Therefore CsI:Na and CsI:Tl vapor-deposited screens seem to be the most obvious candidates to replace $CaWO_4$ screens. Impressive resolution gains have in fact been realized for CsI:Na screens used as input screens in an image intensifier tube (1, 3, 4). Good agreement between calculated and measured *QDE* has also been found (6). However, this material can only be used in vacuum devices like the image intensifier tube. Up to now no plastic covers have been found that protect CsI:Na screens sufficiently against moisture, which makes this material unattractive for mammography application.

CsI:Tl is much less hygroscopic than the Na-activated material. A drawback of such screens is, however, that a special green sensitized film should be used in combination with the screen to realize substantial speed gains. In many cases this requires adaptation of existing "dark room" lighting. The strong afterglow of CsI:Tl (1) observed for x-rays with energies of the usual radiological range, might also be a serious application disadvantage. We have found, however, that the soft x-rays used in mammography give rise to a negligible amount of afterglow.

It is concluded that vapor-deposited CsI:Tl layers are candidates for application in mammography screens. We hope to report more details on their properties in the near future.

Regarding powder phosphors, Fig. 4 shows some results of measurements on $BaFCl:Eu^{2+}$ (Philips "Bfc") and $LaOBr:Tb^{3+}$ (Agfa "MR") screens. These screens have thicknesses comparable to those of $CaWO_4$ Universal or Micro screens discussed above. $Gd_2O_2S:Tb^{3+}$ screens, which have to be used with green sensitive films have not yet been considered by us. It is seen in Fig. 4 that, at equal resolution, the speed gains with respect to $CaWO_4$ are only marginal, namely about a factor of 1.2 or 1.3 for use in combination with double-coated film and 1.1 or 1.2 for use in combination with single-coated film. These gain factors are about half of the calculated ones. This result corroborates our conclusion (6) that the screen technology for these new powder phosphors still lags behind the well-established technology for $CaWO_4$.

Table I. Relative x-ray quantum efficiencies (*QDE*) of x-ray screen/film combinations

Screen phosphor	Film	*QDE* at x-ray energies of: (100 μm thick layers) 15 keV	(100 μm thick layers) 20 keV	(200 μm thick layer) 60 keV	ratio $\frac{QDE_{15\ keV}}{QDE_{60\ keV}}$	ratio $\frac{QDE_{20\ keV}}{QDE_{60\ keV}}$
$CaWO_4$	standard (u.v./blue sensitive)	1.0	1.0	1.0	1.00	1.00
$Gd_2O_2S:Tb^{3+}$	green sensitive	5.3	5.3	12.0	0.44	0.44
CsI:Na	standard	3.0	2.9	14.6	0.21	0.20
CsI:Tl	green	2.9	2.8	14.0	0.20	0.19
$LaOBr:Tb^{3+}$	standard	2.4	2.3	5.2	0.46	0.44
$Y_2O_2S:Tb^{3+}$	standard	1.2	3.0	3.5	0.34	0.86
$BaFCl:Eu^{2+}$	standard	2.8	2.1	5.2	0.54	0.40
(Zn,Cd)S:Ag	green	3.9	2.8	3.2	1.21	0.87

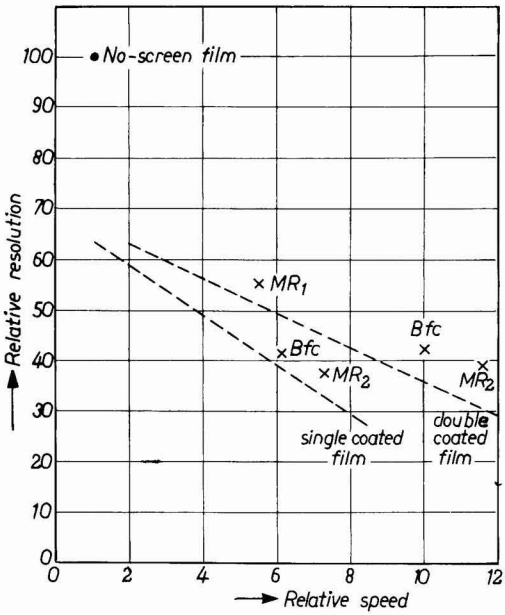

Fig. 4. Relative resolution against relative speed for BaFCl:Eu^{2+} (Bfc) and LaOBr:Tb^{3+} (MR) screen/film combinations. The no-screen film has a speed equal to unity and a resolution equal to 100. The dashed line represents results for $CaWO_4$ screen/film systems, taken from Fig. 1. The x-ray source (W-anode) was operated at 30 kV.

Conclusions

The use of x-ray screens in mammography can give rise to substantial speed gains and hence to x-ray dose reduction. The simultaneously occurring deterioration of the image quality as established by physical measurements, makes the benefits rather questionable. Whether this also holds true from a clinical point of view needs further investigation. Replacement of $CaWO_4$ by more recently developed x-ray powder phosphors like BaFCl:Eu^{2+} or LaOBr:Tb^{3+} does not drastically change these conclusions.

New screen technologies have to be found to give mammography screens better properties. Improvement of the screen resolution is a primary prerequisite, although the resulting improvement of the system may be limited by geometrical factors.

Manuscript submitted March 2, 1977; revised manuscript received May 13, 1977. This was Paper 150 presented at the Philadelphia, Pennsylvania, Meeting of the Society, May 8-13, 1977.

Any discussion of this paper will appear in a Discussion Section to be published in the June 1978 JOURNAL. All discussions for the June 1978 Discussion Section should be submitted by Feb. 1, 1978.

Publication costs of this article were assisted by Philips Research Laboratories.

REFERENCES

1. A. L. N. Stevels, *Med. Mundi*, **20**, 12 (1975).
2. C. Bates, *Adv. Electron. Electron Phys.*, **28A**, 451 (1969).
3. A. L. N. Stevels and A. D. M. Schrama-de Pauw, *Philips Res. Rep.*, **29**, 353 (1974).
4. A. L. N. Stevels and W. Kühl, *Med. Mundi*, **19**, 3 (1974).
5. G. W. Ludwig, *This Journal*, **118**, 1152 (1971).
6. A. L. N. Stevels and A. D. M. Schrama-de Pauw, *ibid.*, **123**, 887 (1976).
7. J. G. Rabatin, Abstract 102, p. 250, The Electrochemical Society Extended Abstracts, Spring Meeting, San Fransisco, Calif., Vol. 74-2 (1974).
8. A. L. N. Stevels and F. Pingault, *Philips Res. Rep.*, **30**, 277 (1975).
9. R. V. Alves and R. A. Buchanan, *IEEE Trans. Nucl. Sci.*, **19**, 415 (1972).
10. R. A. Buchanan, S. I. Finkelstein, and K. A. Wickersheim, *Radiology*, **105**, 187 (1972).
11. G. W. Ludwig and J. S. Prener, *IEEE Trans. Nucl. Sci.*, **19**, 3 (1972).
12. J. C. Price and P. D. Butler, *Br. J. Radiol.*, **43**, 251 (1970).
13. O. Camby and W. Gordenn, *J. Belge. Radiol.*, **56**, 237 (1973).
14. E. Deichgräber, S. Reichmann, and M. Burén, *Acta Radiol. Diagn.*, **15**, 93 (1974).
15. J. L. Lamarque, *J. Radiol. Electrol.*, **52**, 797 (1971).
16. E. Storm and H. I. Israel, U.S. Nat. Techn. Information Service Rep. La 3753 (1967).
17. K. Kyser, *Fortschr. Röntgenstr.*, **116**, 818 (1972).

Auger Analysis of Thermally Oxidized GaAs Surfaces

Ikuo Shiota, Nobuo Miyamoto, and Jun-ichi Nishizawa*

Research Institute of Electrical Communication, Tohoku University, Sendai, Japan 980

ABSTRACT

We have investigated in-depth composition profiles of the GaAs crystals with thermally oxidized (100) and (111) surfaces by Auger electron spectroscopy during Ar sputter etching. The Ga depletion is found at two different positions when the oxide thickness is less than about 250 and about 140Å for the closed- and the open-tube oxidation, respectively. One of the positions is within the oxide layer and is always accompanied by the increase in As concentration, while the other is at the oxide-GaAs interface and appears upon the formation of Ga_2O_3 thicker than ~50Å. It is found that the oxide growth rate, the transition layer width, and the composition ratio between As and Ga near the interface strongly depend upon the surface orientation. It turns out that there are three different oxidation kinetics as functions of oxide thickness: the reaction of oxygen with GaAs at the interface, and in- and out-diffusions of oxidizing species and Ga.

GaAs is an important semiconducting material for various optoelectronic and high frequency devices. At the present stage, however, it is still difficult to control the surface properties of GaAs. The difficulty lies in the fact that the surface composition of GaAs easily deviates from its stoichiometry by heating even at lower temperatures and by any chemical treatments. This is due to the high equilibrium vapor pressure of As (1) and the different reactivities of Ga and As with the oxidizing species and chemical reagents (2). This situation does correspond to the thermal oxidation of GaAs surfaces.

The detailed mechanism of thermal oxidation of binary semiconductors (3) such as GaAs (4-9), particularly in relation to the role of As atoms in the oxide, has not been accounted for. In this work, we have investigated the in-depth profiles of thermally oxidized GaAs (100) and (111) surfaces by Auger electron spectroscopy during Ar sputter etching. It has turned out that As plays an important part in the formation of oxide films and exhibits a peculiar compositional distribution in the case of the lower temperature oxidation.

Experimental

Undoped GaAs (100) and (111) wafers were cut from the same boatgrown ingot with a carrier concentration of 1×10^{16} cm^{-3} and an etch pit density of 5000 cm^{-2}. After mechanical polishing, the surfaces were thoroughly degreased using trichlorethylene and methanol cycles in an ultrasonic bath, and then the damaged surface layer was etched off in a solution of 4 parts H_2SO_4, 1 part H_2O_2, and 1 part H_2O, followed by dipping in a concentrated HF solution for 5 min after rinsing with deionized water. The wafers were finally rinsed with doubly distilled methanol.

In the open-tube oxidation system, the flow rate of oxygen gas was about 500 cm^3/min, while in the closed-tube system with the closed inlet and outlet valves of the quartz reaction tube, oxidation took place in a stationary oxidizing atmosphere. The wafers oriented to (100) and (111) were simultaneously oxidized in a resistance heating furnace under identical experimental conditions.

The Auger transitions used for in-depth profiling of the oxide-GaAs system are those in the higher energy states of 1087 and 1228 eV $L_3M_{4,5}M_{4,5}$ for Ga and As, respectively, in order to avoid peak overlapping as observed in the lower energy range (< 100 eV) and also to obtain precise peak-to-peak values of their Auger signals. A 510 eV $KL_{2,3}L_{2,3}$ transition was monitored for oxygen profiling. An accelerating voltage of 4 kV was employed as the primary electron beam to excite the higher energy Auger electrons, the beam current used being 1 μA. The modulation amplitude of the phase-sensitive detector was set at 5 eV, the time constant at 1 sec, and the scanning rate at 6 eV/sec. The peak-to-peak Auger signals were monitored automatically by a physical electronics multiplex control system.

In taking the lower energy part of the Auger spectrum, an excitation voltage of 2 kV was used to avoid sample charging. Furthermore a modulation amplitude of 2 eV, a time constant of 1 sec, and a scanning rate of 1 eV/sec were employed to increase the resolution of the spectrum.

Simultaneous sputter etching was made at a sputtering voltage V_{sp} of 1 or 2 kV, and an emission current of 30 mA under a 5×10^{-5} mm Hg Ar atmosphere. The sputtering rate of the Ga oxide formed in a series of experiments was determined to be 20 and 55 Å/min for $V_{sp} = 1$ and 2 kV, respectively. In this evaluation the oxide thickness measured by a multiple-beam interferometer was divided by the sputtering time when the Auger peak ratio, O/Ga, started to decrease from the value of 1.75 for the bulk oxide. Once the sputtering rate was calibrated, the oxide thickness was determined from the sputtering time defined above. This method was also applied to the oxide in which the interface with the GaAs substrate was not clearly defined and which contained a considerable amount of As.

Results and Discussion

A characteristic compositional distribution in which the amount of Ga is depleted at two different positions has been found in the thermal oxide-GaAs system for the oxides, less than about 250 and 140Å in thickness, formed in the closed- and the open-tube system, respectively. Typical examples are shown in Fig. 1 and 2. Figure 1 shows the GaAs (100) surface oxidized at 500°C for 20 min in the closed-tube system, and Fig. 2 shows the same surface oxidized at 450°C for 60 min in the open-tube system. Two Ga valleys, *i.e.*, the two Ga depletion regions, were observed not only in the (100) surfaces but also in the (111) A and B surfaces. One valley was within the oxide layer 50Å off from the oxide surface [hereafter called the outer (Ga) valley], and the other at the oxide-GaAs interface [hereafter called the inner (Ga) valley]. At the outer valley the amount of As took a peak value and O acted like Ga; that is, the Ga and O distributions showed a tendency opposite to that of the As distribution. It should be further noted that the amounts of Ga and O in the region between the outer and the inner valley are

* Electrochemical Society Active Member.

Key words: composition profile, inner and outer Ga depletion, oxidation kinetics.

smaller than those of the surface layer of the oxide, and that the coexistence of a considerable amount of As is observed between the two valleys. These observations suggest that the total amount of Ga oxide and As remains constant throughout the oxide, and that the close packing of Ga oxide up to its maximum density is impeded by the presence of As. The oxide with the two Ga valleys was more easily created in the closed-tube oxidation than in the open-tube one. For instance, the two valleys were formed by oxidation at 600°C for 10 min or 500°C for 30 min in the closed-tube system, while the outer valley disappeared even by oxidation at 550°C for 10 min in the open-tube system. The inner valley was always observed when the oxide thickness became more than 50Å, as is the case with the oxide formed by violent chemical etching of GaAs surfaces (8, 10). This would mean that the occurrence of Ga depletion at the oxide-GaAs interface is a fundamental phenomenon in the formation of a native Ga oxide on the GaAs substrate by thermal oxidation.

The Auger spectra corresponding to the points indicated by the numbered arrows in Fig. 1 are shown in Fig. 3. The Ga $M_2M_4M_4$ peak and the Ga M_2M_4V peak made chemical shifts of 5 and 5.5 eV toward the lower energy side from their original energies of 54 and 81 eV for the clean GaAs surface. It is obvious that the spectrum at point 1 has a closer resemblance to that at point 3 than the spectrum at point 2. It is evident that at the outer valley (at point 1), a weak but unchemically shifted Ga peak was observed, and the chemical shift of the As Auger peak is much smaller (< 1 eV) throughout the oxide layer compared with that of Ga. These facts indicate the presence of a small amount of the unoxidized Ga at the outer valley, and the presence of the unoxidized As throughout the oxide layer except the uppermost surface layer.

As the oxidation proceeded, the outer valley became shallower, flattened out, and finally disappeared. Thus, only the inner valley remained. With further oxidation, the amounts of Ga and O gradually increased inward from the oxide surface, accompanied by a decrease of the As content in the oxide. Finally the oxide became homogeneous Ga_2O_3. In the single valley oxide formed above 700°C the unchemically shifted Ga Auger peak was observed.

The Auger peak ratio, O/Ga, showed a constant value of 1.75 ± 0.05 throughout the oxide regardless of whether the oxide system had one or both of the Ga valleys, although in the latter case a considerable amount of As was present between the two Ga valleys. It can be inferred from this result that the O atoms around a Ga atom are identical in coordination throughout the oxide layer and only the Ga oxide density varies in it, and that the O atoms are preferentially bound with Ga atoms rather than As atoms. This

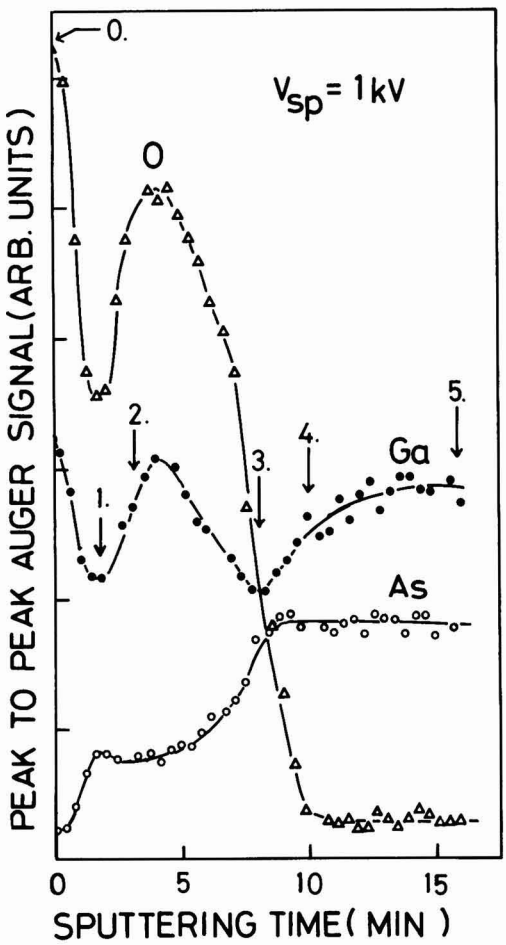

Fig. 1. Composition profile of a thermally oxidized GaAs (100) surface in the closed-tube system at 500°C for 20 min.

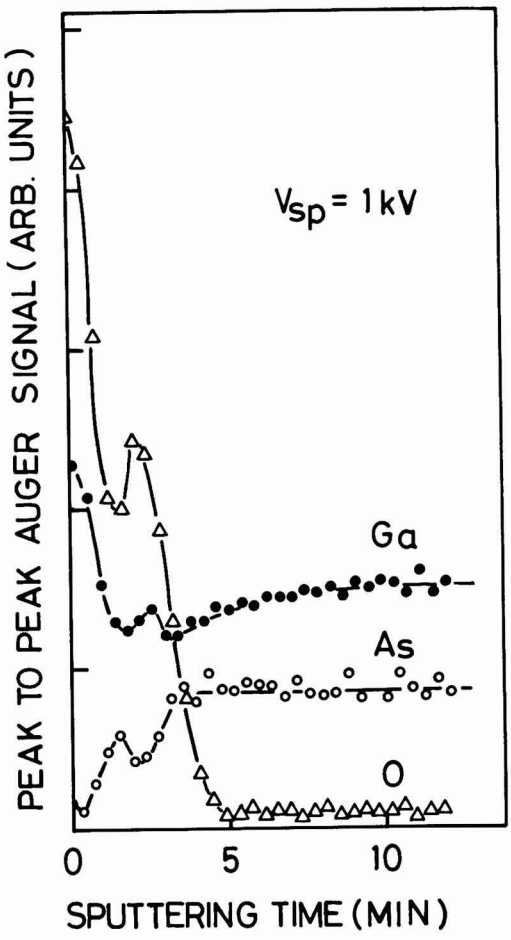

Fig. 2. Composition profile of a thermally oxidized GaAs (100) surface in the open-tube system at 450°C for 60 min.

conception can well explain the previously described result that the chemical shift of the As Auger peak is negligibly small.

The composition profile at the interface shows a large dependence on the crystal orientation and the oxidation condition. Typical examples for the orientation dependence of composition profiles of the (100), (111) B, and (111) A surfaces are shown in Fig. 4, 5, and 6, respectively. Each surface was oxidized at 700°C for 10 min in the open tube. In these figures, the ratios of O and As to Ga Auger peaks are also shown. In the (111) B surface the O penetrated very deeply into the GaAs bulk and the interface was elongated, while in the (100) and (111) A surfaces the interfaces were clearly defined. A remarkable As accumulation appeared only at the (100) interface and increased up to approximately 700°C, beyond which it disappeared. There occurred a weaker As accumulation in the closed-tube oxidation at the (100) interface.

Figures 7 and 8 show the dependence of oxide thickness and Δt on the reciprocal oxidation temperature, where the oxidation was performed for 10 min at each temperature. The quantity Δt is the duration of sputtering time for a half recovery of the Ga Auger peak to the value of the bulk GaAs as indicated in the insert of Fig. 8, and gives a measure of the thickness of the transition layer at the interface. The oxide growth rate is equal between the (100) and the (111) faces below 500°C, but it is greater for the (111) face than that for

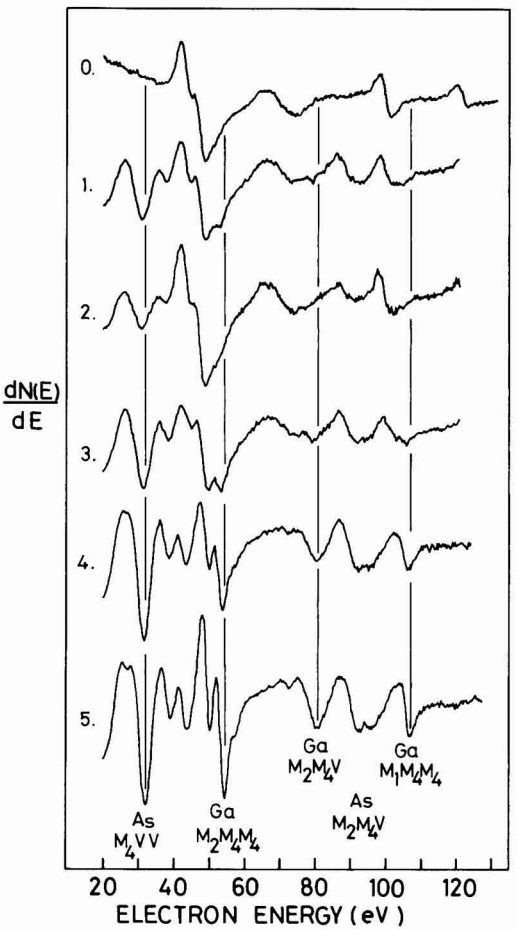

Fig. 3. Auger spectra corresponding to the points indicated by the numbered arrows in Fig. 1.

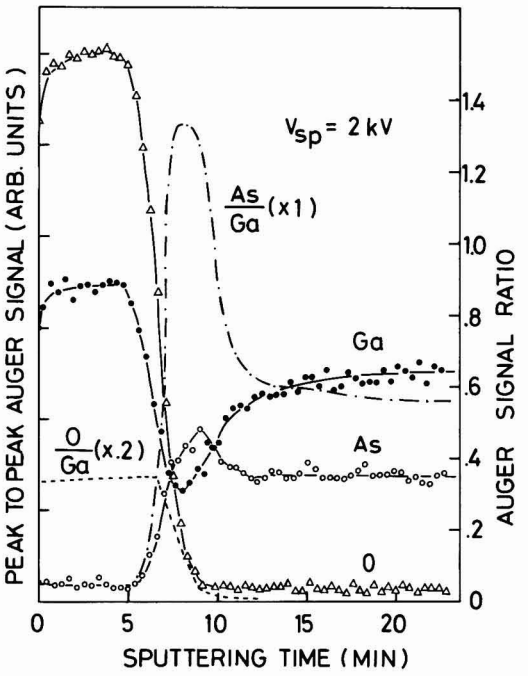

Fig. 4. Composition profile of a thermally oxidized GaAs (100) surface in the open-tube system at 700°C for 10 min.

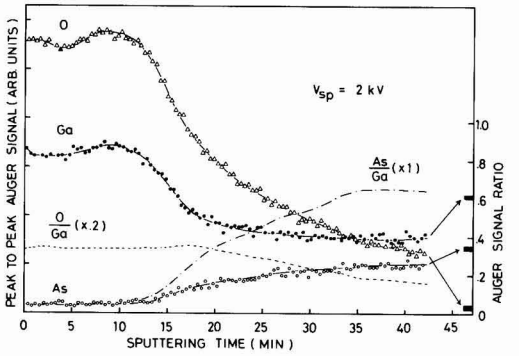

Fig. 5. Composition profile of a thermally oxidized GaAs (111) A surface. Other conditions are the same as used in Fig. 4.

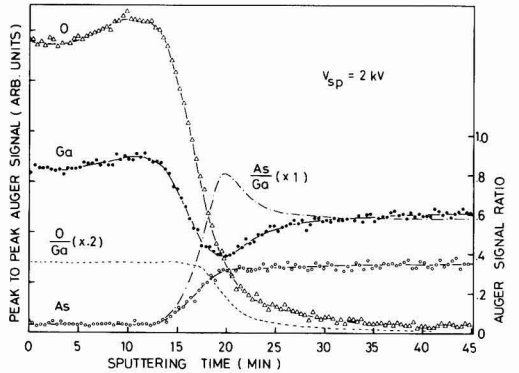

Fig. 6. Composition profile of a thermally oxidized GaAs (111) A surface. Other conditions are the same as used in Fig. 4.

the (100) face above 500°C. From Fig. 7 and 8, it is obvious that the thermal oxidation has three different rate-limiting processes, depending on the values of activation energy E_a. For the (100) faces, E_a is approximately 0.4 eV between 500° and 700°C, and E_a = 1.3 ~ 1.4 eV at both sides out of that temperature range. For the (111) faces, the temperature range with E_a = 0.4 eV starts from about 550°C.

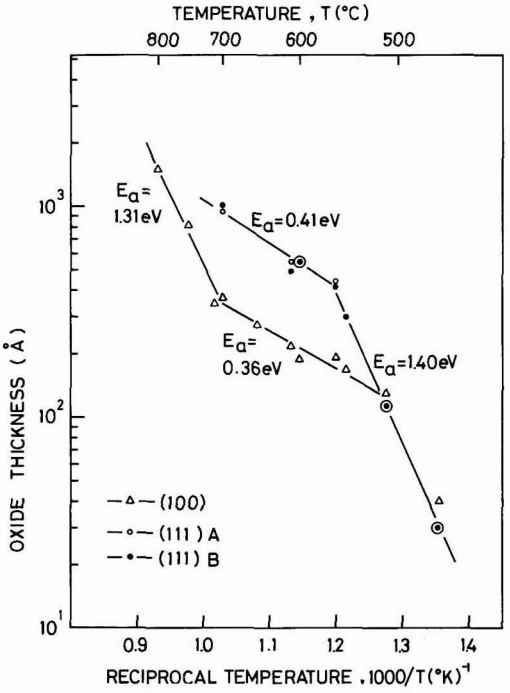

Fig. 7. Oxide thickness as a function of reciprocal temperature. Oxidation was made for 10 min at the specified temperatures.

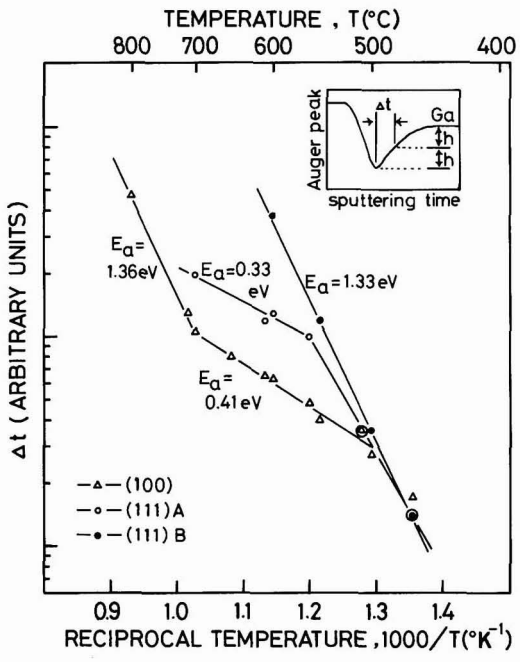

Fig. 8. Δt, the duration of sputtering time for a half recovery of the Ga Auger peak to the value of the bulk GaAs, as a function of reciprocal temperature for the same samples as used in Fig. 7.

In the oxidation at 510°C where E_a falls on 1.3 ~ 1.4 eV for the (111) and 0.4 eV for the (100) face, the relation between oxide thickness and oxidation time is linear for the (111) A and B faces and is parabolic for the (100) face. However, the oxidations at 600° and 730°C with E_a = 0.4 and 1.3 ~ 1.4 eV, respectively, obey an identical parabolic law for both (100) and (111) faces. These results lead to the conclusion that the oxidation in the temperature range where a linear law holds, and E_a = 1.3 ~ 1.4 eV is controlled by the reaction of O with GaAs at the interface. Thus, the remaining As will be distributed in the oxide and near the interface. In the other temperature ranges the oxidation will be controlled by the in- and outdiffusion of oxidizing species such as water and Ga with E_a = 0.4 and 1.3 ~ 1.4 eV, respectively. The diffusion of water is inferred from the analogy with the thermal oxidation of Si in an atmosphere containing water vapor (11). The Δt data plotted in Fig. 8 also show a similar behavior to the oxide thickness for the reciprocal temperature; above 500°C the transition layer at the interface is wider in the (111) surface than in the (100) one. It should be noted here that the width of the transition layer in the (100) surface is narrower than in the (111) surface, but the inner valley is deeper in the (100) than in the (111) surface.

From Fig. 7 and 8, it is apparent that for the same oxide thickness in the range of less than approximately 300Å, the value of Δt is nearly the same regardless of the difference in surface orientation. This suggests that Δt depends solely on the oxide thickness in such a thickness range, and hence the orientation dependence of sputtering may safely be ignored. In the oxide thickness range of more than 300Å, however, Δt becomes dependent not only on the oxide thickness, but on the surface orientation; that is, in the (111) B face Δt is greater than that of the (100) and (111) A faces when the oxide thickness is the same. It is very difficult to understand these results only in terms of such artifacts as selective sputtering and the implantation effect, because the former seems to give the same effect on Δt regardless of the difference in surface orientation when the oxide thickness is the same, and the latter should give an equivalent effect on Δt for the identical surface orientation regardless of the difference in oxidation temperature. Therefore, some other fundamental explanation is indispensable to the understanding of the observed phenomena at the interface. The occurrence of the inner Ga depletion cannot be related to the oxidation kinetics because the inner Ga valley appears inevitably whenever the oxide thickness is in excess of 50Å. Therefore, the cause of the depletion should be sought from the oxide formation itself. A possible explanation may be given as follows. As described above, Ga is preferentially oxidized and consequently As atoms accumulate around the interface, resulting in a relative decrease of the Ga to As ratio in that region. That is to say, the inner Ga depletion is caused by a selective oxidation of Ga and the resulting As accumulation at the interface.

Conclusions

We have obtained new results on the thermal oxidation of GaAs surfaces by measuring in-depth profiles of the compositional distribution by Auger electron spectroscopy during Ar sputter etching. The thermal oxide films can be classified in two groups. One is the oxide with two Ga valleys and the other is the oxide with a single Ga valley. The Ga depletion at the oxide-GaAs interface appears inevitably upon the formation of the oxide layer thicker than ~ 50Å. The Ga depletion in the oxide near the outer surface is always accompanied by the increase in As. The close packing of the Ga oxide up to its maximum density is hindered

by the presence of As. It has been made clear for the first time that the behavior of As plays an important role in the formation of the Ga oxide by thermal oxidation of GaAs surfaces.

Three different oxidation kinetics have been proposed: The first is the reaction of O with GaAs at the interface and dominates the formation of thin oxide films characterized by the two Ga valleys; the second and the third correspond to the indiffusion of oxidizing species, such as water, and to the outdiffusion of Ga. For the (100) surfaces, the second mechanism holds for the temperature range between 500° and 700°C, and the third does above 700°C. In these temperature ranges, the growth rate, the transition layer width, and the composition ratio strongly depend on the crystal orientation.

Manuscript submitted Aug. 31, 1976; revised manuscript received May 1, 1977.

Any discussion of this paper will appear in a Discussion Section to be published in the June 1978 JOURNAL. All discussions for the June 1978 Discussion Section should be submitted by Feb. 1, 1978.

Publication costs of this article were assisted by Tohoku University.

REFERENCES

1. J. Nishizawa, H. Ohtsuka, S. Yamakoshi, and K. Ishida, *Jpn. J. Appl. Phys.*, **13**, 46 (1974).
2. D. R. Wood and D. V. Morgan, *This Journal*, **122**, 773 (1975).
3. A. J. Rosenberg, *J. Phys. Chem.*, **64**, 1135, 1143 (1960).
4. H. T. Minden, *This Journal*, **109**, 733 (1962).
5. M. Rubenstein, *ibid.*, **113**, 540 (1966).
6. K. Navrátil, *Czech. J. Phys.*, **B18**, 266 (1968).
7. S. P. Murarka, *Appl. Phys. Lett.*, **26**, 180 (1975).
8. I. Shiota, S. Yamakoshi, N. Miyamoto, and J. Nishizawa, Paper presented at the second research meeting Surface Electronics, Ministry of Education of Japan, Sendai, Japan, October 13, 1975.
9. T. Sugano *et al.*, Technical Digest of the Meeting of Japan Society of Applied Physics, Fukuoka, Japan, November 23, 1975.
10. I. Shiota, K. Motoya, T. Ohmi, N. Miyamoto, and J. Nishizawa, *This Journal*, **124**, 155 (1977).
11. G. L. Holmberg, A. B. Kuper, and F. D. Miraldi, *ibid.*, **117**, 677 (1970).

The Properties of Silica Diffusion Sources under Oxidizing Ambient Conditions and Their Application to Solar Cell Fabrication

T. C. Chandler, Jr.,[1] R. B. Hilborn, Jr., and J. W. Faust, Jr.*

College of Engineering, University of South Carolina, Columbia, South Carolina 29208

ABSTRACT

In this paper a technique for the design and fabrication of silicon solar cells using spin-on silica doping sources is discussed. This technique involves the use of an oxidizing ambient during diffusion which limits the diffusion flux and yields lower surface concentrations of impurities and shallow p-n junctions. It is shown that the uniformity of the film thickness is an important factor in maintaining a uniform surface concentration of impurities in a diffused substrate. Data are given to demonstrate the effects of such silica film thickness variations on solar cell performance.

During the past four years industry and government interest in silica films as diffusion sources in electronic device applications has grown immensely (1, 2). The silica film itself has been in small scale use for some time, but the recent interest in developing inexpensive solar cells has renewed interest in this technology. Doped silica diffusion sources may reduce the cost of solar cell processing and have the advantage of better over-all process control (3).

Silica sources (or doped SiO_2) exist in a variety of forms. Owen and Schmidt (4) have reported on the use of thin anodic silicon dioxide films as diffusions sources, but their analysis is hampered by experimental conditions which are difficult to control. Reactive sputtering has also been investigated (5) but results have not been consistent enough for applications in photovoltaics. A more recent development is the paint-on or spin-on silica film. These films when applied properly, yield excellent p-n junction uniformity, surface concentration of impurities, and minimal surface damage. The silica solutions consist of organic silicates and the appropriate dopant elements dissolved in an alcohol solution. These types of solutions have a typical room temperature viscosity of 25 cp making them well suited for standard photoresist spinning apparatus. Herein lies a primary advantage of the spin-on silica film. The simplicity of the technique and equipment makes this an inherently cheaper process than the anodized or sputtered films mentioned above.

In this paper we describe the diffusion theory and technique used to fabricate p-n junction silicon solar cells using doped, spin-on films. Experimental data are presented to demonstrate the controllability obtained from spin-on silica films.

Diffusion Theory

In a recent paper Barry (3) has demonstrated that in a nonoxidizing ambient, diffusions from doped silicon dioxide films agree with the solutions to Fick's second law to within experimental error and that the surface concentrations of impurities resulting from such diffusions are functions of the silica dopant concentration. It was shown that the surface concentration was independent of diffusion time and temperature for surface concentrations less than or equal to 1.0×10^{20} cm^{-3}. This limitation in Barry's model is an important point. Other studies (6-8) show that for surface concentrations greater than 1.0×20^{20} anomalous diffusion profiles result, leading to regions near the surface of constant impurity concentration having

* Electrochemical Society Active Member.
[1] Present address: U.S. Air Force Materials Laboratory, Electromagnetic Materials Division (LPO), WPAFB, Ohio 45433.
Key words: silicon dioxide, diffusion flux, phosphorus.

a very high diffusion-induced density of dislocations and consequently low minority carrier lifetimes. These are the regions described in the literature as "dead layers" (9). Hence, if one wishes to manufacture silicon solar cells with the highest obtainable efficiencies one must limit the surface concentration to values less than 2×10^{20} cm^{-3} so that the dead layer is eliminated.

Flux limiting.—A method of maintaining a surface concentration at the proper level is to introduce oxygen into the ambient during diffusion (6). The presence of sufficient quantities of oxygen allows oxidation to take place at the silicon surface thus limiting diffusion at the oxide-silicon interface. By proper control of the thermal oxidation rate, one can control the diffusion-limiting process and consequently, the surface concentration. The use of an oxidizing ambient causes deviations from Fick's laws of diffusion resulting in shallow p-n junction depths and, unlike Barry's model, surface concentrations that are functions of the diffusion temperature.

Intuitively, one sees that diffusion in the presence of a retarding mechanism (diffusion limiting due to oxidation) requires changing the boundary conditions of the diffusion model, since the physical boundary (oxide-oxide interface) is in motion.

This moving boundary can be described by two coordinate axes (Fig. 1) X and X'. X is fixed with its origin at the oxide-silicon interface. X' has its origin at the oxide-oxide interface. X and X' are related by

$$X' = X - \frac{R\sqrt{t}}{N} \qquad [1]$$

Where R is the oxidation rate constant in cm/sec$^{1/2}$ and N is the volume ratio of silicon dioxide to silicon (equal to 2.30). (Notice that this formulation of the moving boundary condition is relative in nature. It is just as correct to assume that the oxide-oxide interface is fixed and to allow the oxide-silicon interface to move.) It can be demonstrated by Eq. [1] that in the oxidizing ambient, diffusion is a function of the oxidation rate and not the oxide thickness. It was assumed in this study that the oxide growth followed the parabolic law[2] (5)

$$\alpha = (\alpha_0^2 + R^2 t)^{1/2} \qquad [2]$$

where α is the total oxide thickness, and in practice α_0, the initial oxide thickness, is zero.

Fick's second law can be written for region B and C of Fig. 1 yielding

$$\frac{\partial C_B}{\partial t} = D_B \frac{\partial^2 C_B}{\partial X'^2} \qquad [3]$$

[2] This is a good approximation for temperatures falling in the range 950°C $\leq T \leq$ 1250°C) (5).

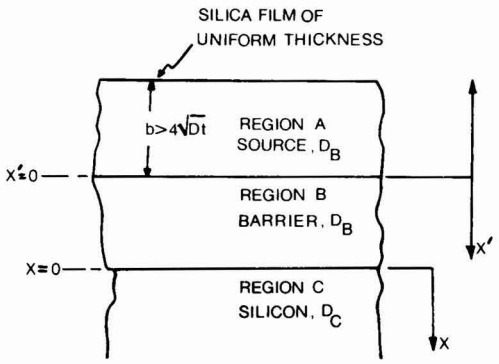

Fig. 1. The three layer diffusion system showing the origin of the X and X' axis.

and

$$\frac{\partial C_c}{\partial t} = D_C \frac{\partial^2 C_c}{\partial X^2} \qquad [4]$$

The solution (10) to Eq. [4] is

$$C_c(X, t) = \gamma C_o \operatorname{erfc} \frac{X + \dfrac{R\sqrt{t}}{N}}{2\sqrt{D_c t}} \qquad [5]$$

where

$$\gamma \simeq \frac{1}{1 + \sqrt{\dfrac{D_c}{D_B}}} \qquad [6]$$

and C_o is the concentration of dopant (atoms/cm^3) in the source material. Evaluating Eq. [5] at $X = 0$ the surface concentration is found to be

$$C_s = \gamma C_o \operatorname{erfc} \frac{R}{2N\sqrt{D_c}} \qquad [7]$$

These equations show that unlike Barry's fixed boundary model, C_s is a function of temperature and also the junction depth is shallower by the quantity $R\sqrt{t}/N$.

Theoretical limitations.—The theory given above is dependent on two basic assumptions. The first assumption is that the oxidation rate constant, R, is independent of time and is only a function of temperature. This assumption is only valid when the silica film is of uniform thickness. Experiments show that oxidation constants for localized regions of thin silica film ($<<$200Å) have somewhat higher values of R and oxidation in these regions is not independent of time. Figure 2 shows a plot of R *vs.* temperature for two different silica layers. Notice that the thin SiO_2 film has a slightly higher R value. This behavior is not completely understood but from microscopic examina-

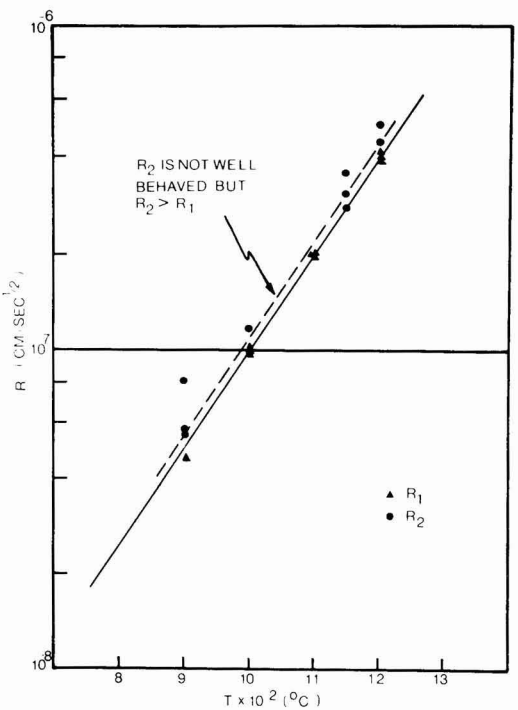

Fig. 2. Plot of R *vs.* temperature. R_1 is measured for thin silica regions and R_2 is measured for thick regions.

tion of such thin regions it is felt that the film has poor oxide integrity, *i.e.*, there are regions which are cracked and porous so that the migration of oxygen ions necessary for the oxidation is somewhat enhanced, unlike the regions of thick SiO_2 coverage (see Fig. 3) which display a reasonably constant R.

The problem of thin regions in the silica film is inseparably linked with the second limitation of the foregoing theory. To maintain the constant source condition of a silica (or deposited SiO_2) film, its thickness must equal or exceed the diffusion length of a dopant atom in the oxide (3, 10), *i.e.*, the silica thickness b must obey the inequality

$$b^2 > 4D_B t \qquad [8]$$

When inequality [8] is not satisfied, the film is quickly depleted of dopant; and, over the extended period during which an ideal erfc profile would have resulted, the profile for such a nonconstant source would be gaussian with a reduced value of C_s. Figure 4 shows the source thickness necessary for a given temperature. Satisfying conditions [8] might seem like a formidable problem, but fortunately the thickness of a spin-on source can be easily controlled by the spin speed and duration.

Solar Cell Processing

Given below is the general procedure for fabricating a silicon solar cell using silica films. The process can be divided into four major segments, prediffusion cleaning, application and examination, diffusion, and metallization. Both prediffusion cleaning and metallization are covered adequately in the literature (1, 5). Application and diffusion are discussed here because they involve implicitly the silica film.

Application.—It has been found by trial and error that silica films, utilizing an alcohol carrier liquid, spin on best at temperatures from 20°C up to 25°C. Spin speeds can vary but the best range is between 2500 and 3500 rpm. Best results are obtained when the substrate is the same temperature as the source liquid; however it cannot have a temperature above the source liquid temperature.

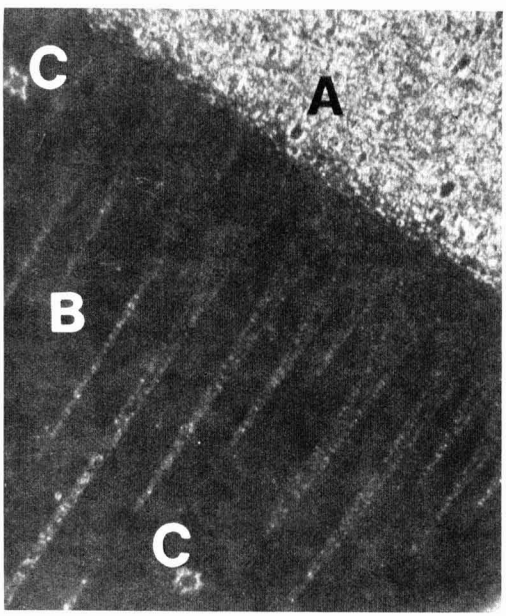

Fig. 3. Purposely induced thin regions of a spun-on silica film. Notice that the thin regions (A) provide poor coverage as opposed to the thick regions (B). C is due to bubble damage. (Magnification 160X.)

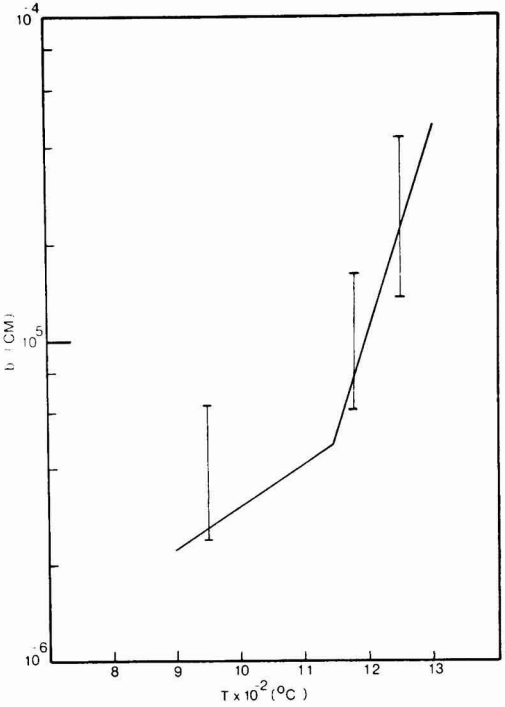

Fig. 4. Plot of source thickness necessary for maintaining constant source conditions as a function of temperature.

To prepare a liquid solution for application, it should be placed in a container so that it fills it completely, with no empty space, and allowed to come slowly to some temperature less than 25°C. If the source liquid is stored for this period in a large partially filled container, evaporation of the alcohol will generate bubbles which can degrade the uniformity of the film, see Fig. 3 and 6.

After the film has been spun on the substrate, it should be examined to see if the source layer is uniform, or if it has thickness variations (12) similar to Fig. 3. (This step is necessary because the properties of commercially available films differ from type to type, batch to batch, etc. Once satisfied that these guidelines are adequate, this step may be deleted.) These variations in thickness can yield thin spots on the order of 200Å or less. The cause is improper film application as described by Chandler *et al.* (12). Similar bad results occur when particles of dust or debris touch the silica film. It has been observed in this laboratory that a particle 1μ in diameter can result in poor silica coverage for a distance of 50μ around the particle. Elimination of these thin areas is essential in view of the theoretical limitation described previously. The silicon beneath a thin area oxidizes faster and the forming oxide, in effect, dilutes the source diffusion. More importantly, one can see from Fig. 4 that a silica thickness of 200Å is far from satisfying inequality [8] for common diffusion temperatures. The cumulative effect is the dilution of a source which itself is growing smaller with time. It has been experimentally confirmed that extremely shallow junctions, if present at all, will form under these thin layers.

If the deposited films have thickness variations, holes, or striation (12), the poor results discussed above will occur; hence the application procedure,

however different from the recommended process, must be altered to insure a uniform silica film. Figure 5 illustrates a ripple formation of the type encountered. During the bakeout cycle the organic compounds are driven off, the film becomes rigid, and the variations are frozen into the silica layer. Hence one means of reducing the thickness variations is to delay the bakeout until the wet film can flow to a more uniform layer. This technique works best below 25°C where evaporation of the alcohol is slow. Delaying the bakeout cycle will not eliminate thickness variations but it will allow thin areas to change sufficiently to satisfy the inequality [8].

Once the film integrity has been established, the substrate should be baked in dry nitrogen at 200°C for 4 hr. This step drives off the organic carrier liquids, leaving a doped silica film on the wafer.

Diffusion.—Diffusion of the substrate was carried out in an ambient mixture of 50% nitrogen and 50% oxygen at a temperature of 1000°C. The doping element was phosphorus at a concentration, C_o, of 4×10^{20}. The values of the oxidation constant R were determined experimentally. These conditions were chosen because they yield a uniform shallow junction.

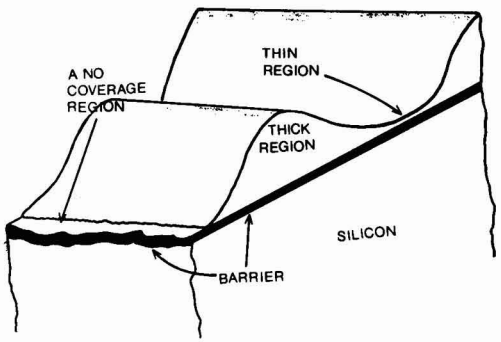

Fig. 5. Artist's conception of a ripple formation in a silica film. The thin regions of the film produce poor p-n junction characteristics.

Fig. 6. Photograph of a silica film with bubbles trapped in the film. If these bubbles remain in the film when it is drying, the damage shown in Fig. 3 results. (Magnification 100X.)

Results

Four series of solar cells were fabricated. Table I gives some data on each series. Each substrate had a background resistivity of 1 Ω cm and a thickness of 200μ. The contact pattern utilized is a common type having a center bar with six fingers. The contact metal was aluminum and the contacts were sintered in an N_2 ambient at 450°C for 10 min. No antireflection coatings were applied. The light source was the sun and the incident solar power was determined by pyranometer measurements.

The first two series were done with no control of the silica film uniformity. The third run utilized the simple temperature/spin guideline given above, and the fourth series was fabricated making sure that the silica film was more uniform by delaying the bakeout. Difference in cell performance is obvious from Table I. Runs 1 and 2 are not encouraging.

The nonuniformity of the film allowed diffusion to take place in a nonuniform fashion so that some regions of the cell display extremely high sheet resistances. In some areas where doping levels were not degenerate, the p-type contact on the n-type diffused region formed p-n junctions. It was found that the level of photon-generated current in the poorly diffused region was low also. Steps were taken to minimize these flaws so run 3 showed that when the uniformity of the silica film improved so did the characteristics of the solar cells.

Series 3 cells were moderately efficient, having fill factors averaging 0.60, but this was greatly improved in series 4.

The solar cells of series 4 were designed using the theory presented in this paper. The diffusion model defined by Eq. [1] through [7] allows the diffusion to take place at a higher temperature and achieve the same surface concentration and junction depth as for the low temperature diffusion. It has been found that diffusion from silica sources is more uniform for temperatures of 1000°C. The results were significant. By eliminating the diffusion inhomogeneities, the series resistance was reduced to tolerable levels. The results of junction depth and surface concentration measurements show good agreement between the theory and the diffused region of the cells.

Figure 7 shows the theoretical junction depth for a surface concentration of 1.2×10^{20} cm^{-3}, and a background concentration of 1×10^{16} cm^{-3}, at various diffusion times. The experimental points show that agreement with theory is good except at very short intervals (less than 5 min). This is probably due to the presence of an unavoidable oxide on the substrate before the source application, such that there is an initial oxide layer which has to be penetrated in a finite amount of time.

In Fig. 8 is an evaluation of the surface concentration for various diffusion times. This figure demonstrates that C_s is not time dependent for periods longer than 5 min and less than 60 min. Inside this time interval the curve of Fig. 8 is in agreement with Eq. [7]. The deviation from simple theory seen here can be explained. The low C_s seen for short diffusion times can be attributed to the residual oxide layer that was evidenced in the junction depth data. Deviations seen for

Table I. $X_j = 4000$Å

Series	I_{SC} (mA)	V_{OC} (V)	R-sheet (Ω/□)	R_S (Ω)	Fill factor (avg)
1	50	0.44	750	3	0.30
2	51	0.45	710	2.8	0.31
3	110	0.56	120	0.5	0.60
4	140	0.57	85.0	0.3	0.70

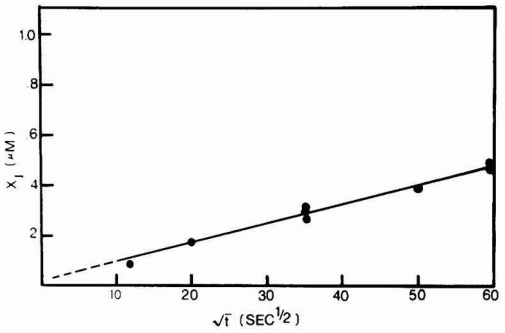

Fig. 7. Plot of junction depth vs. $\sqrt{t}$ for diffusion at 1000°C in an atmosphere of 50% O_2 and 50% N_2.

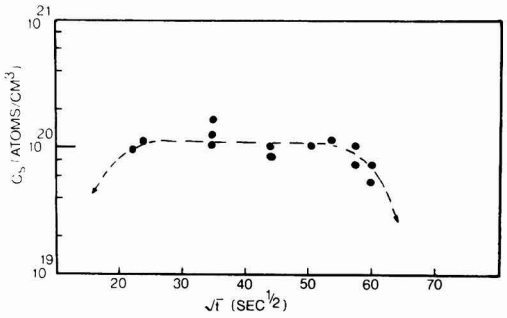

Fig. 8. Plot of surface concentration vs. $\sqrt{t}$ for 1000°C and an atmosphere of 50% O_2 and 50% N_2. $C_o \simeq 4 \times 10^{20}$ cm^{-3}.

periods greater than 60 min indicate that the source material is becoming depleted of its dopant.

Solar cells processed by this technique and described here have better characteristics than those previously reported (12); their series resistances are comparable to standard, commercially diffused cells. These improvements are due to the uniformity of the silica film which results in a homogeneous surface concentration approximately equal to 1×10^{20} cm^{-3} and a shallow, uniform junction.

The uniformity of the degenerate surface concentration is the most important factor. To test qualitatively for uniformity of surface concentration a staining etchant which turns n^+ regions dark (5) was applied. Results show that when the film is uniform the surface concentration of impurities is uniform.

The junction depth was also established by the standard method involving angle lapping and staining (5, 11). The results were consistent with theory.

Conclusions

A model and general technique for fabricating solar cells using silica films is presented. This technique yields predictable, uniform shallow junctions, and acceptable surface concentrations for most diffusion cycle times. Calculations show also that for a given value of C_O and temperatures between 950° and 1250°C, C_s varies little with the diffusion temperature. This technique is further simplified by the fact that excellent process control can be achieved by varying C_O and the percent of oxygen in the ambient. It is obvious from the test data that moderately efficient solar cells can be fabricated using spin-on silica sources, and, when care is taken to insure proper film thickness and uniformity, cells comparable to those produced by standard, more expensive diffusion techniques can be manufactured.

The most important feature of this technique is that by introducing an oxidizing ambient, the resulting diffusion retardation allows the diffusion of impurities to be carried out at temperatures exceeding 1000°C while maintaining junction depths which are less than 0.5μ. This is significant because spin-on silica films yield more uniform junctions for temperatures greater than or equal to 1000°C. Although this uniformity could be obtained by using a nonoxidizing ambient, without the benefit of the diffusion retardation, deeper (>0.5 μm) p-n junctions would result. Because this technique also yields degenerate surface concentrations with no dead layer, the resulting solar cells have low series resistance and high blue response.

In view of the data presented in this paper, it seems that there is only one problem related to the full scale use of doped silica films, the rather long bake-out times required for these films. It is felt that the advantages of using silica films probably outweigh this minor difficulty. The original wafer diameters utilized in this research range from less than 2 cm to over 5 cm. No variation in film quality due to wafer size was observed, indicating that the silica films might be applied economically to larger diameter slices. It was also found that once the proper procedure was established for applying these films, the analytical procedures given in this paper could be eliminated. This reduced the somewhat tedious procedures outlined here to mere routine.

Manuscript submitted Dec. 16, 1976; revised manuscript received April 18, 1977.

Any discussion of this paper will appear in a Discussion Section to be published in the June 1978 JOURNAL. All discussions for the June 1978 Discussion Section should be submitted by Feb. 1, 1978.

Publication costs of this article were assisted by the University of South Carolina.

REFERENCES

1. R. H. Hopkins, J. R. Davis, P. Rai-Choudhury, and P. D. Blais, First Quarterly Report, Silicon Materials Task of the Low Cost Solar Array Project (Part 2), October-December 1975, NAS-100.
2. J. A. Becker, Solid-State Electron., **17**, 87 (1974).
3. M. L. Barry and P. Olofsen, **116**, 854 (1969).
4. A. E. Owen and P. F. Schmidt, *This Journal*, **116**, 548 (1969).
5. R. M. Burger and R. P. Donovan, "Fundamentals of Silicon Integrated Device Technology," pp.36-105, p. 175, Prentice Hall, Englewood Cliffs, N.J. (1967).
6. R. A. McDonald, G. G. Ehlenberger, and T. R. Huffman, *Solid-State Electron.*, **9**, 807 (1966).
7. P. A. Iles and B. Leibenhaut, *ibid.*, **5**, 331 (1962).
8. E. Tannenbaum, *ibid.*, **2**, 123 (1961).
9. J. Lindmayer, *Comsat Tech. Rev.*, **2**, 105 (1972).
10. D. Kahng, Ph.D. Dissertation, Ohio State University (1959).
11. C. S. Fuller and J. A. Ditzenberger, *J. Appl. Phys.*, **27**, 544 (1956).
12. T. C. Chandler, R. B. Hilborn, Jr., and J. W. Faust, Jr., Presented at IEEE/ERDA 12th Photovoltaics Specialists Conference, Baton Rouge, La. (Nov. 1976).

The Effect of Growth Rate and Temperature on the Incorporation of Sn in GaAs during LPE

Ulf König[1]

Institüt für Halbleitertechnik Sonderforschungsbereich 56, Technische Hochschule, Aachen, Germany

ABSTRACT

A growth rate dependence of the impurity incorporation has been measured for the first time: average carrier n, donor $\overline{N}_D$, and acceptor $\overline{N}_A$ concentrations of heavily Sn-doped GaAs layers grown by liquid phase epitaxy (LPE) increase in the range $0.2 < \overline{V}/\mu m/min < 6$. At faster growth rates, the concentrations tend to be constant ($1.4 \cdot 10^{19}$ cm^{-3} for donors, $3.5 \cdot 10^{18}$ cm^3 for acceptors). Growth rates between 0.2 and 35 μm/min have been adjusted by varying the cooling rates of the epitaxial processes between 0.04° and 100°C/min. It can be reported that the relation between $\overline{N}_{D/A}$ and $\overline{V}$ corresponds to the theoretical predictions under surface equilibrium conditions. The most important parameter is the barrier height of the system melt and semiconductor, modified by a concentration-dependent barrier lowering in the case of heavy doping. Based on the same assumptions, the temperature dependence of the measured incorporation $\overline{N}_{D/A}$ (T) is explained. This results from a comparison of the possiole incorporation theories surface and bulk equilibrium.

During epitaxial growth from the liquid phase, the interface between melt and semiconductor can be regarded as a metal semiconductor contact because of the great density of conduction electrons in the melt. The Schottky model is then applicable to the surface. Merten and Hatcher (1) have pointed this out. Later on Zschauer and Vogel (2) and Casey *et al.* (3) used this model. As a consequence of such an electrical model, the thermodynamic equation for the impurity incorporation will have electrical properties like the Fermi level or the barrier height (3, 4).

According to the growth conditions, two aspects have to be distinguished: the bulk equilibrium and the surface equilibrium. If the growth rates of the crystal are slow compared with the impurity diffusion in the semiconductor, there exists a thermal equilibrium between the two phases, melt and semiconductor bulk (bulk equilibrium). This model explains the impurity incorporation of Zn (5, 6) and Cu (7) in GaAs. Where the ratio of the growth rate to the solid diffusion constant is large, the melt is in equilibrium with the surface of the growing crystal only. The important parameter of the surface equilibrium theory is represented by the height of the Schottky barrier. The validity of this theory has been shown for the incorporation of Te (8) and for the Sn donor (4, 9). Panish has found that the incorporation of Sn in GaAs can be better explained if one also assumes a Sn acceptor complex $Sn_{As}2V_{Ga}$ using the surface equilibrium theory again (4). The concentration in the case of bulk equilibrium is almost proportional to the square root of the atomic fraction of tin X_{Sn} in the melt, while in the case of surface equilibrium it is directly proportional to X_{Sn}. In spite of the principal agreement Panish obtained with the surface equilibrium theory, for high Sn concentrations above $4 \cdot 10^{17}$ cm^{-3} there exists a discrepancy between theory and experiment: Experimentally evaluated concentrations indicate a weaker slope with higher X_{Sn} data than expected (4). This can probably be interpreted as a concentration dependence of the barrier height, resulting in a lowering of the barrier (10).

Some authors (11, 12) suspect an additional manifestation of the barrier height or the Fermi level in a cooling rate dependence of the Sn segregation coefficient during liquid phase epitaxy (LPE). As the cooling rate influences the growth rate, this amounts to a growth rate dependence of the impurity concentration. Panish (4), however, did not detect such a dependence of the Sn doping when slightly varying the cooling rate. There is no record of systematic experiments. Zschauer and Vogel (2) predicted a quantitative dependence of the impurity incorporation on the growth rate. Experimental proof has not yet been obtained, partly because the cooling rates, or growth rates, respectively, have not been varied over an extended range large enough to observe this effect. Such a variation is possible, using the epitaxial apparatus and the experimental procedure described in this paper.

Experimental

Crystal growth process.—The heavily tin-doped GaAs layers are grown in a horizontal crucible of high purity graphite, with a fixed chamber for the GaAs-Sn melt and a movable graphite slider for the substrate (13). A radiation heating furnace is used. For the desired experiments, the low heat capacity of the furnace, the small crucible (length 6 cm, diam 2.2 cm), and the small melt (2.5g) in addition, are preferable to allow fast heating and cooling rates. For the rest, this setup corresponds to conventional equipment.

During heating at a constant temperature the GaAs pieces dissolve in the liquid tin. This forms a saturated solution with the liquidus composition of the binary Sn-GaAs cut of the ternary system for the respective saturation temperature. The boat is cooled down to room temperature. The substrate is then positioned in the boat. After a few minutes at saturation temperature, the system is cooled at a constant rate R between 0.04° and 100°C/min. The cooling rate is established by actual measurement of the boat temperature. 2°-10°C below the saturation temperature, the substrate is brought into contact with the melt. As there occurs no spontaneous crystallization during this initial cooling, the result is a supercooled melt of 2°-10°C, or according to the solution diagram of GaAs in Sn, a supersaturation of approximately 2-10%. The cooling continues during the growth period. The growth is terminated by removing the graphite with the substrate from the melt. To avoid strong annealing effects on the average electron concentration during the epitaxial process, the growth times of the examined layers do not exceed 20 min (14).

Two kinds of experiments have been carried out: variation of the cooling rate at an initial process temperature of 650°C, and variation of the initial process

[1] Present address: Forschunginstitut AEG Telefunken, D7900 Ulm, Germany.

Key words: liquid phase epitaxy, impurity concentration, growth rate, gallium arsenide.

temperature from 570° to 710°C. For the later experiments, the cooling rates have to be varied between 0.7° and 1.7°C/min to make sure that the temperature dependence of the growth rate is compensated. The average growth rates of the layers are then approximately 0.6 μm/min for each process temperature.

Growth rate and doping measurements.—The (100) orientated crystals are cleaved in (110) directions, and the cross-sections are etched under illumination with a $HF-H_2O_2-H_2O$ solution. The thickness L of the epitaxial layer grown during the time t is measured optically. An average growth rate of the epitaxial layer is defined as $\overline{V} = L/t$. As it is preferable to grow the layers at an initial supersaturation, actual and average growth rates (V and $\overline{V}$) of a layer decrease with time of growth. $\overline{V}$ is varied over an extended range for the experiments reported here. In a small range, this is attained by varying the growth time at constant cooling rate, in an extended range, however, by varying the cooling rate. [$\overline{V}$ increases approximately linearly with cooling rate R and is a function of temperature (15).] Although it would be better to describe the doping studies in terms of the actual growth rate V, the average growth rate $\overline{V}$, when combined with average doping parameters, is also informative.

The doping data for the epitaxial layers are measured by the Van Der Pauw method. The thicker edges of the layers are removed to avoid errors in the measurements. Ohmic contacts are made by alloying Sn in forming gas at about 400°C. Even the layers grown at 100°C/min are smooth enough to guarantee an accurate measurement of the doping properties.

As the GaAs layers are grown out of a Sn-rich GaAs solution, the expected electron concentration will be in the range of 10^{18} cm^{-3}. Where the materials are heavily doped, the donor and acceptor concentrations can be estimated by the equations of Kressel and Nelson (16), using the measured $\overline{n}$ and $\overline{\mu}$ data at room temperature, and the mobility μ_u of uncompensated material. For μ_u, the highest reported values, extrapolated to carrier concentrations of 10^{19} cm^{-3}, are used (16). To consider the geometrical effects of a nonideal Van Der Pauw structure, a systematic error of +5% for μ and −5% for n was taken into account (17).

Results and Discussion

Growth rate dependence of the Sn concentration.—The average values of carrier concentration $\overline{n}$ (300°K) and mobility $\overline{\mu}$ (300°K) *vs.* the cooling rate R of layers grown at an initial process temperature of 650°C are shown in Fig. 1. The cooling rate varies from 0.04° to 100°C/min. $\overline{n}$ and $\overline{\mu}$ are constant for cooling rates greater than 10°C/min, and decrease or increase, for lower cooling rates. Mobility values of 1200-1400 cm²/Vsec are typical of heavily tin-doped GaAs (4, 18) grown at cooling rates less than 1°C/min. For the higher cooling rate range, no comparable data are available in print. The increase of $\overline{\mu}$ with decreasing $\overline{n}$ is similar to that given by Sze (19), but weaker than that found by Panish (4) with various liquidus compositions of Sn. This can be attributed to a decreasing compensation ratio with $\overline{n}$ or the growth rate, as shown in Fig. 2.

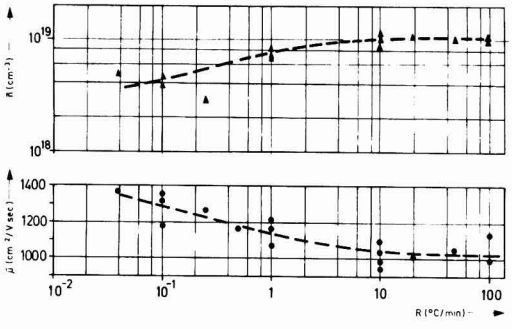

Fig. 1. Average carrier concentration $\overline{n}$ and average carrier mobility at room temperature of several heavily Sn-doped GaAs layers, grown at different cooling rates R.

With the Van Der Pauw data of Fig. 1, the average donor and acceptor concentrations are calculated. As the cooling rate is a process specific parameter only, it is better to use the growth-specific parameter; the average growth rate $\overline{V}$. $\overline{N}_D$, $\overline{N}_A$, and $\overline{N}_A/\overline{N}_D$ are drawn *vs.* the average growth rate $\overline{V}$ in Fig. 2, now showing the uncertainty of the measurements. In spite of a scatter in the experimental data, a significantly steeper increase of $\overline{N}_D$ than $\overline{N}_A$ is observed at slow growth rates. This results in a decreasing compensation ratio with increasing growth rate.

A growth rate dependence can be caused by the redistribution of dissolved Sn in the melt in front of the growing interface because of its small segregation coefficient ($\approx 10^{-4}$). To avoid this effect, $V \cdot L/D_{Sn(m)} < 10^{-1}$ has to be fulfilled (2). This is best guaranteed by the self-diffusion of tin $D_{Sn(m)} \geq 10^{-4}$ cm²/sec (20), the measured epitaxial layers $L < 20$ μm, and growth rates $\overline{V} < 40$ μm/min.

Another possible way of describing a growth rate dependence follows from the surface equilibrium theory. It can be explained qualitatively with the scheme in Fig. 3: in case of surface equilibrium the donor concentration is a function of the electron concentration n_S in the thin surface layer. According to the Schottky theory, n_S depends on the barrier height Φ_{Bn} and the temperature T. It amounts to a varying donor concentration with the parameter Φ_{Bn}/kT at fast growth rates or high ratios of growth rate and diffusion constant (see Fig. 3). For slow rates,

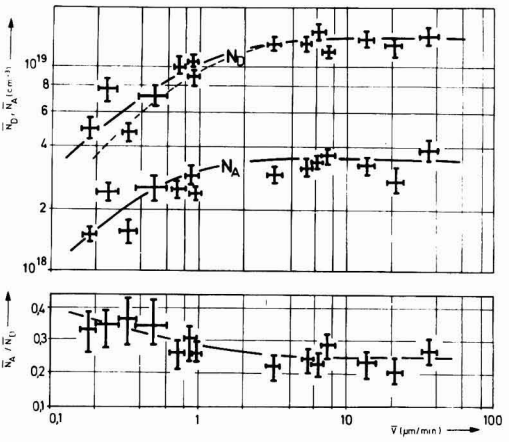

Fig. 2. + Experimental average data $\overline{N}_D$ or $\overline{N}_A$ or $\overline{N}_A/\overline{N}_D$ *vs.* average growth rate $\overline{V}$. —— Theoretical curves N_D or N_A or N_A/N_D vs. constant growth rate V. Parameter $\Phi_{Bn}(650°C) = 0.51$ eV for donors and $\Phi_{Bp}(650°C) = 0.61$ eV for acceptors at low concentrations. A concentration-dependent barrier lowering is taken into account (*cf.* Table I). Fitting parameter; $\overline{N}_{D/A}$ ($\overline{V} > 6$ μm/min) and $D_{Sn\,D/A} = 3 \cdot 10^{-14}$ cm²/sec. ---- Theoretical curve $N_D(V)$, to demonstrate the sensitivity of the theory for a larger barrier height $\Phi_{Bn}(650°C) = 0.61$ eV or a 0.1 eV smaller barrier lowering.

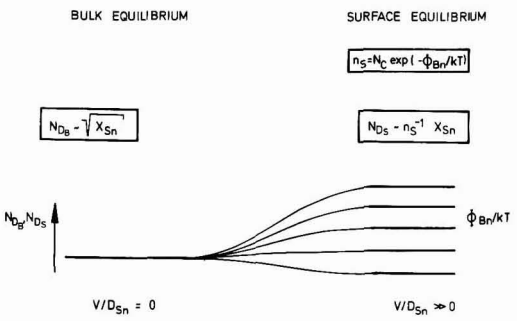

Fig. 3. Scheme for qualitative explanation of the growth rate dependence of the concentration using bulk equilibrium ($V/D_{Sn} \approx 0$) and surface equilibrium ($V/D_{Sn} >> 0$).

on the other hand, in the case of bulk equilibrium such dependence does not exist. Then such transitions as drawn for intermediate V/D_{Sn} values will certainly be possible. Zschauer and Vogel (2) have formulated the corresponding theoretical relationship between impurity concentration N_D, N_A, or in the case of an amphoteric impurity ($N_D + N_A$) and a temporal constant growth rate, on the premises of an intrinsic semiconductor at the epitaxial process temperature. These equations have been derived by Zschauer for donors on Ga and acceptors on As vacancies. In the case of Sn it is not considered that the Sn acceptor is likely to have the more complex structure $Sn_{As}2V_{Ga}$.

For Sn, Zschauer's equation of ($N_D + N_A$) ought to be applicable. Nevertheless, it would be better to regard the growth rate dependence of N_D and N_A separately; by this it is avoided that a characteristic slope of N_A (*cf.* Fig. 2) disappears in the experimental uncertainties of the slope of ($N_D + N_A$). In this case, no mutual influence of donors and acceptors during the incorporation process is assumed. The theory, originally valid for low doping, is modified for heavy doping studied here. The concentration dependence of some properties has to be taken into account (*cf.* Appendix I).

The computation with the equations of Zschauer and Vogel modified with respect to heavy doping, details of which are described in Appendix I, results in the growth rate dependence of donors and acceptors plotted in Fig. 2. (solid and dashed curves). The different slopes of the experimental $\overline{N}_D$ and $\overline{N}_A$ can be fitted by the theoretical curves for N_D and N_A. Consequently, the theory agrees with the increasing compensation ratio at decreasing growth rate (Fig. 2). Satisfactory explanation of the experimental $\overline{N}_D$ and $\overline{N}_A$ by independent theoretical equations points to a separate incorporation of donors and acceptors during the epitaxial growth process.

The fitting parameters for the calculated growth rate dependence are the solid diffusion constants D_{SnD} and D_{SnA} for the Sn donor and the Sn acceptor (see Eq. [1] in Appendix I). The same value for D_{SnD} and D_{SnA} has been found by the fitting. With $3 \cdot 10^{-14}$ cm²/sec, the diffusion constants are relatively large compared with data at 650°C in older literature (21). But new measurements by Peart (22) yield a Sn solid diffusion constant between 10^{-13} and 10^{-14} cm²/sec in the temperature range of 650°-750°C. This confirms the validity of the fitting.

The established growth rate dependence of the concentration does not indicate the transition to constant concentration at slow growth rates (compare Fig. 2 and 3). The bulk equilibrium in this case is not reached before approximately 0.02 μm/min, as it is calculated theoretically. Strictly speaking, the surface equilibrium ($N_{D/A}$ = constant at fast growth rates) is valid only for growth rates above 6 μm/min (Fig. 2), but because of the extended transition region up to bulk equilibrium, it is approximately applicable for some slower growth rates, too.

The transition region is changed at lower doped layers. The equations of Zschauer and Vogel can then be used in their unmodified form. As Zschauer stated, the surface equilibrium theory ought to be applicable for growth rates which fulfil $V/D_{SnD/A} \cdot \lambda_i > 10$ (λ_i intrinsic reciprocal Debye length). Using the fitting parameter D_{SnD} of this work, it is estimated that in the case of low doping the Sn incorporation ought to follow from the surface equilibrium theory already for growth rates above 0.7 μm/min. A possible concentration dependence of the diffusion constant has not been considered. The decrease of the concentration in the transition between surface equilibrium and bulk equilibrium is also much weaker in the case of intrinsic-doped layers. Probably this is the reason why the growth rate influence established for heavily Sn-doped layers has not yet been observed in the case of low-doped layers.

It should be emphasized that the theoretical relationship between temporal constant growth rate V (presumption of Zschauer's equations) and the concentrations $N_{D/A}$ has been compared with the corresponding experimental relationship $\overline{N}_{D/A}(\overline{V})$ for average properties. Strictly speaking this is correct for completely constant doping and mobility within the layer. But this is not valid here because of the established growth rate dependence of concentration and mobility (Fig. 1, 2) and a temporal varying growth rate during the LPE process with a supersaturated melt. In the ideal case of constant profiles, the experiments would have yielded a similar structure, but shifted to faster growth rates and higher concentrations. In addition, the concentration profiles are slightly influenced by the respective process temperature during extended cooling periods, especially at fast cooling rates. To eliminate this effect a constant growth temperature has to be assumed. It is estimated that for this ideal case the expected concentration at fast cooling rates would only be 15% above the experimental value established. For these reasons, the comparison between theory and experiment may be regarded as a first approximation only.

Temperature dependence of the Sn concentration.— The relation between N_D, N_A, and the atomic fraction of tin in the melt X_{Sn} can be described using the surface equilibrium theory at different temperatures above 700°C (4). In this section, however, the temperature dependence $N_{D/A}(T)$ at large X_{Sn} data is deduced. The respective working points for each temperature considered are then positioned on the quasi-binary Sn-GaAs cut of the ternary phase diagram. Experimental data $\overline{N}_D$, $\overline{N}_A$ are compared with the ones expected at surface and bulk equilibrium to examine the validity of the surface equilibrium theory for the heavily Sn-doped layers reported here. All the temperature-dependent values have to be considered, partly computed and partly from literature, while in the case of the $N_{D/A}(X_{Sn})$ dependence, most of the temperature-dependent properties can be comprehended in a normalization constant at each temperature considered (4).

For both possible incorporation theories, surface and bulk equilibrium (S.EQ. and B.EQ.), the theoretically expected concentrations for the Sn donor on Ga vacancies and the Sn acceptor [which is possibly the complex Sn_{As} $2V_{Ga}$ (4)] are plotted in Fig. 4. The essential steps for its calculation are presented in Appendix II. N_D and N_A are normalized on the established concentrations $\overline{N}_D$ or $\overline{N}_A$ at the lowest experimental temperature T_i = 843°K. In the case of surface equilibrium (S.EQ.), an increase in N_D of about 70% is expected. In the case of bulk equilibrium (B.EQ.) a more distinct temperature dependence between 843° and 983°K with an increase of about 400% is estimated.

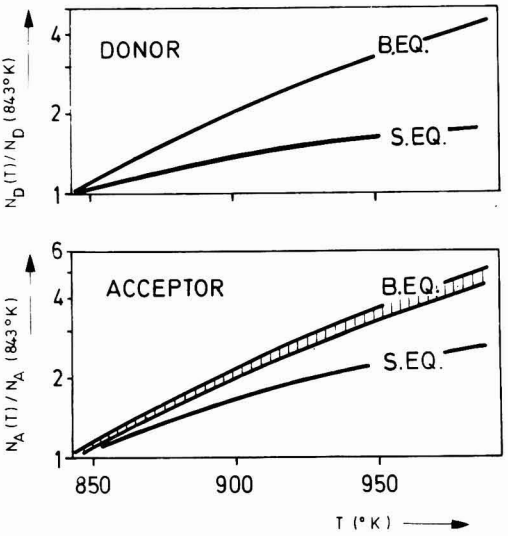

Fig. 4. Semiquantitative computation of the temperature dependence for the Sn donor and the Sn acceptor, normalized at the lowest experimental concentration $\overline{N}_{D/A}$(843°K). B.EQ.: curve for bulk equilibrium; S.EQ.: curve for surface equilibrium.

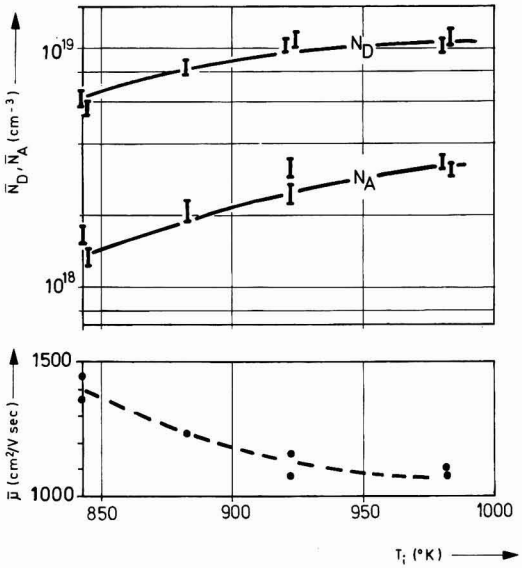

Fig. 5. I Experimental average concentrations $\overline{N}_D$ and $\overline{N}_A$, and ● experimental average mobility vs. process temperature T_i. —— Theoretical curves for N_D and N_A in the case of surface equilibrium.

For the acceptor concentrations calculated with bulk equilibrium, the shaded area has to be plotted in Fig. 4 because of an uncertainty in the transition of the hole activity coefficient between unity and the calculated values at high concentrations (*cf.* Table II in Appendix II). Comparing the curves S.EQ. and B.EQ., a steeper slope was found for the bulk equilibrium both for the donor and for the acceptor.

Experiments at several process temperatures T_i for high Sn contents in melt and solid, for which the calculations are made, are carried out. The layers have been grown at approximately the same growth rate to avoid the influence of different growth rates on the concentrations (see Experimental section). The average donor and acceptor concentration $\overline{N}_D$, $\overline{N}_A$, and the average mobility $\overline{\mu}$ in the range 843°-983°K are shown in Fig. 5. The experimental concentrations are compared with the respectively calculated concentrations in the case of surface equilibrium, as shown in Fig. 4 (solid curves in Fig. 5). Considerable agreement with the temperature behavior expected can then be established. The curves B.EQ. of Fig. 4 instead would be too steep to fit the experiments. According to these experiments at several temperatures, it can be concluded that the bulk equilibrium cannot be responsible for the incorporation of Sn. This conclusion is consistent with the results of $N_{D/A}$ (X_{Sn}) experiments by Panish (4).

As the experimental compensation ratio $\overline{N}_A/\overline{N}_D$ increases, the average Hall mobility decreases with temperature. The measured value of $\overline{N}_A/\overline{N}_D = 0.32$ at 983°K agrees with the one Panish applied to his $N_A(X_{Sn})$ calculations at 973° and 1073°K. According to the increase of the compensation ratio with temperature dealt with in this paper, however, at 1073°K a larger compensation ratio ought to be better. The above values for the compensation ratio may be used for cooling rates of approximately 1°C/min. Otherwise, the cooling rate or growth rate dependence, shown in Fig. 2, has to be considered. The above statements of the compensation ratio reported at high atomic fractions of Sn in the melt should be approximately valid for lower doping, too, if one considers the theoretical results of thermodynamic calculations that the X_{Sn} dependence of N_A is similar to that of N_D and therefore the compensation ratio is independent of X_{Sn}. This is only approximately correct. Regarding the donor and acceptor concentrations found at large X_{Sn} values, different barrier lowerings for donors and acceptors are to be expected which result in different slopes of $N_D(X_{Sn})$ and $N_A(X_{Sn})$ (10). Therefore, the experimental compensation ratio can change slightly in the upper X_{Sn} range.

Summary

The behavior of the concentrations $\overline{N}_D$ and $\overline{N}_A$ for heavily Sn-doped layers indicates the transition region between surface equilibrium and bulk equilibrium, *i.e.*, between fast and slow growth rates of the LPE layers. Donor and acceptor seem not to interact. The increase of the experimental concentrations with the epitaxial process temperature could be explained by surface equilibrium only, in spite of relatively slow average growth rates $\overline{V} \approx 0.6$ μm/min in this kind of experiment. Surface equilibrium, consequently, ought to be applicable for most of the reported epitaxial layers. The barrier height of the system melt-solid is an important property. Attention is drawn to an additional influence of barrier lowering in the high concentration range.

Acknowledgments

I am indebted to Dr. K. Heime for many valuable discussions. I am grateful to Dr. K. H. Zschauer (Siemens, Munic) for suggesting that his calculations might be applicable and for stimulating discussions. I wish to thank A. Dierick for computer programming. Financial support provided by the Deutsche Forschungsgemeinschaft, Sonderforschungsbereich Festkörperelektronik is gratefully acknowledged.

Manuscript submitted May 28, 1976; revised manuscript received March 25, 1977. This was Paper 263 RNP presented at the New York, New York, Meeting of the Society, Oct. 13-17, 1974.

Any discussion of this paper will appear in a Discussion Section to be published in the June 1978 JOURNAL. All discussions for the June 1978 Discussion Section should be submitted by Feb. 1, 1978.

Publication costs of this article were assisted by Sonderforschungsbereich 56.

APPENDIX I

Details of the semiquantitative computation process for the growth rate dependence with heavy Sn doping and the important parameters tabulated are presented. No interdependence of donors and acceptors during the incorporation process is presumed. This allows the separate consideration of the carriers in the solid.

The growth rate dependence of donors and acceptors $N_{D/A}(\bar{V})$ normalized at very slow growth rates $N_{D/A}(V \approx 0)$ were formulated by Zschauer and Vogel for an intrinsic semiconductor

$$\frac{N_{D/A}(V)}{N_{D/A}(V \approx 0)} = \frac{D_{Sn\,D/A}}{V}\left[\int_0^\infty \exp\left(\mp \psi_{D/A}[l]\right) \exp\left(-\frac{V}{D_{Sn\,D/A}}\right) dl\right]^{-1} \quad [A\text{-}1]$$

The minus sign stands for donors and the plus sign for acceptors ($l = 0$ the moving interface between melt and semiconductor; dl, differential layer increase; $D_{Sn\,D/A}$, solid diffusion of the donor and acceptor Sn). $\psi_{D/A}[l]$ represents the normalized potentials of the Schottky barrier, only temperature dependent. It contains the intrinsic reciprocal Debye length and the built-in potential.

In heavy doping, however, the concentration dependence of some properties has to be taken into account; the "quadratic" approximation for the Schottky barrier potential

$$\psi_{D/A}(l) = \pm 0.5([2\psi_{D/A}(l=0)]^{1/2} - \lambda_{D/A}l)^2 \quad [A\text{-}2]$$

and the built-in potentials

$$kT\,\psi_{oD} = kT\,\psi_D(l=0) = (\Phi_{Bn} - \Delta\Phi_n) - (E_G - E_{FD})$$
$$kT\,\psi_{oA} = kT\,\psi_A(l=0) = E_{FA} - (\Phi_{Bp} - \Delta\Phi_p) \quad [A\text{-}3]$$

have to be used now (E_G, bandgap), with the concentration-dependent reciprocal Debye lengths $\lambda_{D/A}$ and the Fermi levels E_{FD} (N_D) and E_{FA} (N_A.) The important parameters are the barrier heights Φ_{Bn}, Φ_{Bp} of donors and acceptors. The currently available room temperature barrier height $\Phi_{Bn} = 0.83$ eV for Sn on GaAs (19, 23) seems to be a satisfactory approach for the experimental situation of a Sn-GaAs melt containing 92 atomic percent (a/o) of Sn. The respective barrier heights at the process temperature $T = 923$°K are evaluated with (18, 24)

$$E_G(T) = \Phi_{Bn}(T) + \Phi_{Bp}(T) \quad \text{and}$$
$$E_G(T) - \Phi_{Bn}(T) = \text{constant} \quad [A\text{-}4]$$

i.e., the position of the Fermi level at the surface remains at a fixed energy above the valence band as the temperature varies. The above assumptions that the barrier heights are only metal and temperature dependent is correct for low solid concentrations. In the concentration range of this work, a barrier lowering probably due to a dipole layer at the interface between metal and semiconductor ought to be considered as well for donors ($\Delta\Phi_n$) as for acceptors ($\Delta\Phi_p$). Calculations of Crowell *et al.* (25) for n-Si Schottky diodes lead to a constant barrier height up to a doping level of approximately 10^{16} cm^{-3}, and a decrease of 0.23 eV at $N_D = 10^{18}$ cm^{-3} or 0.33 eV at $N_D = 10^{19}$ cm^{-3}. But these authors also feel that the calculated falling off at large N_D is too rapid. For GaAs Schottky diodes, however, such a distinct concentration dependence is not expected because of a larger density of surface states compared with Si. There are some hints for quantitative values of the Sn barrier heights (10), as already mentioned in the introductory section of this work.

Due to the $N_{D/A}$ dependence of $\lambda_{D/A}$, $E_{F\,D/A}$ and $\Delta\Phi_{n/p}$ at heavy doping, a semiquantitative calculation is performed. According to Eq. [1], [2], and [3], the growth rate dependence is computed for a lot of values of N_D or N_A, respectively (for several concentrations the values used in the calculation are presented in Table I). The highest concentrations, the computations of which are made, are the characteristic experimental data at fast growth rates $N_{D/A}(V > 6\ \mu$m/min) (see Fig. 2). Each curve of the calculated family is presumed to be approximately valid in a small concentration range around the respective values of $N_{D/A}$. A graphical approximation follows. This procedure results in the solid and dashed curves of Fig. 2, evaluated now having taken into account the concentration dependence of all parameters.

APPENDIX II

The important equations for calculating the temperature dependence of the donor and the acceptor concentration with heavy Sn doping (N_D and N_A) and the temperature dependent properties tabulated are shown. The donor on Ga vacancies can be calculated in the case of surface equilibrium with

$$N_{DS} = A_{DS}\,X_{Sn}\,n_S^{-1}\,\gamma_n^{-1} \quad [A\text{-}5]$$

and in the case of bulk equilibrium with

$$N_{DB} = \left(\gamma_n^{-1}\left(1 + \frac{n_i^2}{A_{DB}\,X_{Sn}}\right) A_{DB}\,X_{Sn}\right)^{1/2} \quad [A\text{-}6]$$

Each property depends on the temperature (see Table II). A_{DS} and A_{DB} are the product of the mass-action constant K, the As activity $\gamma_{As}X_{As}$, the activity constant γ_{Sn}, as well as the normalization constants K_{DS} and K_{DB} for surface and bulk equilibrium. K_{DS} and K_{DB} contain a factor, usually temperature dependent, between the atomic fraction of the liquid and the concentration of the solid, that is essentially the segregation coefficient. But in the case of high Sn concentrations in melt and semiconductor the segregation coefficient was found to be approximately independent of the process temperature in the low temperature range (15). This corresponds to theoretical calculations of the segregation coefficient by Stringfellow (26). The normalization constant is evaluated with the lowest experimental concentration $\bar{N}_D$ (843°K). The temperature-dependent properties γ_{As}, γ_{Sn}, X_{As}, and X_{Sn} are determined by the working points on the quasibinary Sn-GaAs cut of the ternary phase diagram (27), where heavily Sn-doped solids are concerned. The other temperature-dependent data, the Schottky barrier concentration

Table I. Parameters for calculating $N_D(V)$ and $N_A(V)$ at the process temperature 923°K

Temperature T (°K)	Carrier type	Bulk concentration $\bar{N}_D$ / $\bar{N}_A$ (10^{18} cm^{-3})	Reciprocal Debye length λ_D / λ_A (10^6 cm^{-1})	Barrier height $\Phi_{Bn}(300)$ / $\Phi_{Bp}(300)$ (eV)	Barrier height $\Phi_{Bn}(T)$ / $\Phi_{Bp}(T)$ (eV)	Barrier lowering $\Delta\Phi_n(\bar{N}_D)$ / $\Delta\Phi_p(\bar{N}_A)$ (eV)	Fermi level $E_F(\bar{N}_D)$ / $E_F(\bar{N}_A)$ (eV)	Built in potential $\psi_{oD}(T,\bar{N}_D)$ / $\psi_{oA}(T,\bar{N}_A)$	Solid diffusion constant $D_{Sn\,D}$ / $D_{Sn\,A}$ (10^{-14} cm^2/sec)
923	D	14	5.05	0.83	0.51	0.220	1.29	5.8	3
		10	4.27			0.190	1.26	5.8	
		6	3.31			0.155	1.21	5.6	
		4	2.70			0.130	1.14	5.4	
		2	1.91			0.085	1.11	5.2	
		1	1.35			0.050	1.04	4.8	
	A	3.5	2.53	0.61	0.61	0.115	0.23	−3.3	
		2.0	1.91			0.085	0.27	−3.2	
		1.0	1.35			0.050	0.33	−2.9	
		0.6	1.05			0.035	0.38	−2.5	
		0.4	0.85			0.025	0.41	−2.2	
		0.1	0.43			0.005	0.53	−0.9	

Table II. Parameters for calculating $N_D(T)$ and $N_A(T)$ in the case of surface (S.EQ.) and bulk (B.EQ.) equilibrium

Temperature T (°K)	Mass-action constant K (10^{-4})	Activity product $\gamma_{As}\gamma_{Sn}$ $X_{As}X_{Sn}$ (atomic fraction^2)	Equilibrium type	Carrier type	Normalization concentration $\overline{N_D}(843°K)$ $\overline{N_A}(843°K)$ (10^{18} cm^{-3})	Barrier height $\Phi_{Bn}(300)$ $\Phi_{Bp}(300)$ (eV)	Barrier height $\Phi_{Bn}(T)$ $\Phi_{Bp}(T)$ (eV)	Barrier lowering $\Delta\Phi_n(N_D)$ $\Delta\Phi_p(N_A)$ (eV)	Schottky barrier concentration $n_S(T,N_D)$ $p_S(T,N_A)$ (10^{18} cm^{-3})	Activity constant $\gamma_n(n_s$ resp. $N_D)$ $\gamma_p(p_s$ resp. $N_A)$
843	1.67	0.038	S.EQ.	D	6.0	0.83	0.55	0.155	0.89	1.00
				A	1.5	0.61	0.61	0.055	2.02	1.00
			B.EQ.	D	6.0					0.2
				A	1.5					0.7-1.0
883	3.03	0.05	S.EQ.	D	6.0	0.83	0.53	0.165	1.76	0.98
				A	1.5	0.61	0.61	0.075	3.96	1.00
			B.EQ.	D	6.0					0.19
				A	1.5					0.6-1.0
923	5.18	0.07	S.EQ.	D	6.0	0.83	0.51	0.175	3.51	0.97
				A	1.5	0.61	0.61	0.095	7.42	1.00
			B.EQ.	D	6.0					0.18
				A	1.5					0.52-0.95
983	9.98	0.095	S.EQ.	D	6.0	0.83	0.48	0.192	8.75	0.89
				A	1.5	0.61	0.61	0.110	14.3	1.00
			B.EQ.	D	6.0					0.17
				A	1.5					0.47-0.8

$$n_S = N_C \exp\left[(\Phi_{Bn} - \Delta\Phi_n)/kT\right] \quad [7]$$

including the conduction band concentration N_C and the barrier height Φ_{Bn}, the intrinsic concentration n_i, and the activity coefficient of the electrons γ_n (which is a function of n_S/N_C with surface, or N_{DB}/N_V with bulk, equilibrium), have been computed using published data (19, 23, 28, 29). (As to the concentration dependent barrier lowering $\Delta\Phi_n$, see Appendix I and Table II.)

Equations similar to [5], [6], and [7] are used for the Sn acceptor, which is possibly the complex Sn_{As} $2V_{Ga}$. As Panish stated (4), both equations for the donor can be used for the respective acceptor concentrations N_{AS} and N_{AB}; only N_C is substituted by N_V, Φ_{Bn} by Φ_{Bp}, γ_n by γ_p, besides the normalization constants $K_{DS/B}$ by $K_{AS/B}$. Taking into account Eq. [4] of Appendix I, the barrier height for the acceptor in GaAs is found to be independent of temperature. A small barrier lowering $\Delta\Phi_p$, the value of which depends on the respective acceptor concentration N_A in the bulk of the solid, is used. There are some suggestions of a barrier lowering for acceptors with the same value as the one for donors at corresponding concentrations (10).

The properties $\Delta\Phi_n$, $\Delta\Phi_p$, and γ_n, γ_p on the right side of Eq. [5], [6], and [7], and the respective ones for the acceptor depend on the bulk concentrations $N_{DS/B}$ or $N_{AS/B}$. This allows a semiquantitative calculation only. Starting from the properties obtained with the experimentally established bulk concentrations at the normalization temperature 843°K, an iterative calculation for the temperatures considered yields to the parameters listed in Table II and the theoretical concentrations plotted in Fig. 4.

LIST OF SYMBOLS

A_{DS}, A_{DB} constants in the case of surface, bulk equilibrium incorporation

D, A symbols for donors, acceptors

D_{Sn}, $D_{Sn\ D/A}$, $D_{Sn\ D}$, $D_{Sn\ A}$ diffusion constants of Sn in the solid (cm^2/sec)

$D_{Sn(m)}$ diffusion constant of Sn in the melt (cm^2/sec)

$E_{F\ D/A}$, E_{FD}, E_{FA}, $E_F(N_D)$, $E_F(N_A)$ Fermi level of donors, acceptors (eV)

E_G bandgap energy (eV)

k Boltzmann constant

K mass-action constant

$K_{D\ S/B}$, K_{DS}, K_{DB}, $K_{A\ S/B}$ normalization constants of surface, bulk equilibrium for donors, acceptors

l direction into substrate or LPE layer (μm)

L total epitaxial layer thickness (μm)

n experimental average carrier concentration of a layer (cm^{-3})

n_i intrinsic concentration (cm^{-3})

n_S electron concentration in the Schottky surface (cm^{-3})

$N_{D/A}$, N_D, N_A theoretical donor, acceptor concentrations (cm^{-3})

$N_{D\ S/B}$, N_{DS}, N_{DB}, $N_{A\ S/B}$, N_{AS}, N_{AB} theoretical donor, acceptor concentrations in the case of surface, bulk equilibrium (cm^{-3})

$\overline{N_{D/A}}$, $\overline{N_D}$, $\overline{N_A}$ experimental average donor, acceptor concentrations (cm^{-3})

N_C, N_V effective concentration of states in conduction, valence band (cm^{-3})

p_S hole concentration in the Schottky surface (cm^{-3})

R cooling rate of the LPE process (°C/min)

t growth time of a LPE layer (min)

T, T_i temperature, initial process temperature (°K)

V momentary growth rate (μm/min)

$\overline{V}$ average growth rate of a LPE layer (μm/min)

X_{As}, X_{Sn} atomic fraction of arsen, tin in the melt (at. fr.)

γ_{As}, γ_{Sn} activity coefficients of arsen, tin

γ_n, γ_p activity coefficients of electrons, holes

$\Delta\Phi_n$, $\Delta\Phi_p$ barrier lowering of Φ_{Bn}, Φ_{Bp} (eV)

$\lambda_{D/A}$, λ_D, λ_A reciprocal Debye length of donors, acceptors (cm^{-1})

λ_i intrinsic reciprocal Debye length (cm^{-1})

$\bar{\mu}$ average mobility of a LPE layer (cm^2/V sec)

μ_u mobility of uncompensated GaAs (cm^2/V sec

$\Phi_{Bn/p}$, Φ_{Bn}, Φ_{Bp} barrier height of donors, acceptors (eV)

$\psi_{D/A}$, ψ_D, ψ_A normalized Schottky barrier potential of donors, acceptors (eV)

ψ_{oD}, ψ_{oA} normalized built-in potential of donors, acceptors (eV)

REFERENCES

1. U. Merten and A. P. Hatcher, *J. Phys. Chem. Solids*, **23**, 533 (1962).
2. K. H. Zschauer and A. Vogel, Gallium Arsenide and Related Compounds, Proceedings of the Third International Symposium, Institute of Physics and the Physics Society, p. 100, London (1971).
3. H. C. Casey Jr., M. B. Panish, and K. B. Wolfstirn, *J. Phys. Chem. Solids*, **32**, 571 (1971).
4. M. B. Panish, *J. Appl. Phys.*, **44**, 2659 (1973).
5. M. B. Panish and M. C. Casey Jr., *J. Phys. Chem. Solids*, **29**, 1719 (1968).
6. A. S. Jordan, *This Journal*, **118**, 781 (1971).
7. Y. Furikawa and C. D. Thurmond, *J. Phys. Chem. Solids*, **26**, 1535 (1965).
8. M. C. Casey and M. B. Panish, *J. Cryst. Growth*, **13/14**, 818 (1972).
9. U. König, Paper presented at the DGKK Meeting, Freiburg, Germany (1972).
10. U. König and F. Schwocula, To be published.
11. R. H. Saul and W. H. Hackett Jr., *This Journal*, **117**, 921 (1970).
12. F. E. Rosztoczy, This was Paper 526 presented at The Electrochemical Society Meeting, Montreal, Quebec, Canada, Oct. 6-11, 1968.
13. H. Beneking, P. Mischel, and G. Schul, *Electron. Lett.*, **8**, 16, (1972).

14. E. Falkenberg, U. König and K. Heime, Paper presented at the DPG Meeting, Münster, Germany (1975).
15. U. König, Ph.D. Thesis, Technische Hochschule Aachen, Germany (1973).
16. H. Kressel and H. Nelson, *J. Appl. Phys.*, **40**, 3720 (1969).
17. R. Ehret, FTZ, 18, TBr 6, Darmstadt, Germany (1974).
18. E. Grobe and H. Salow, FTZ, A65, TBr. 2, Darmstadt, Germany (1969).
19. S. M. Sze, "Physics of Semiconductor Devices," Wiley-Interscience, New York, (1969).
20. "Gmelins Handbuch der anorganischen Chemie," Zinn, Teil B, 152 Gmelin Institut der MPG, Springer Verlag, Berlin (1971).
21. D. L. Kendall, in "Semiconductor and Semimetals IV," p. 163, Willardson, Beer, Academic Press, New York (1968).
22. R. F. Peart, Paper presented at the Meeting of the Institute of Physics, London (1974).
23. G. B. Seiranyan and Yu. A. Tkhorik, *Phys. Status Solidi A*, **13**, K115 (1972).
24. Y. Nannichi and G. L. Pearson, *Solid-State Electron.*, **12**, 341 (1969).
25. C. R. Crowell and G. J. Roberts, *J. Appl. Phys.*, **40**, 3726 (1969).
26. G. B. Stringfellow, *J. Phys. Chem. Solids*, **35**, 775 (1974).
27. M. B. Panish, *J. Less-Common Met.*, **10**, 416 (1966).
28. A. Dierick, Wahlarbeit, Technische Hochschule Aachen, Institut für Halbleitertechnik (1974).
29. C. J. Hwang and J. R. Brews, *J. Phys. Chem. Solids*, **32**, 837 (1971).

Silicon Nitride Coatings on Molybdenum by RF Reactive Ion Plating

Masao Fukutomi, Masahiro Kitajima, Masatoshi Okada, and Ryoji Watanabe

National Research Institute for Metals, 2-3-12, Nakameguro, Meguroku, Tokyo, Japan

ABSTRACT

Rf reactive ion plating technique has been applied to the preparation of protective silicon nitride coating on molybdenum. All the deposits prepared at deposition temperature of less than 1000°C were amorphous. Silicon in deposits was found to be present as nitride by Auger electron spectroscopic, infrared absorption spectroscopic, and x-ray diffraction analyses. Nearly stoichiometric silicon nitride deposits were obtained at a deposition rate of as high as 1 μm/min. Several factors affecting the stoichiometry of the silicon nitride were discussed. Oxidation test of the coated specimens showed that the silicon nitride layer obtained under optimum conditions protected the molybdenum substrate from oxidation in Ar-1% O_2 gas mixtures up to approximately 1200°C. Typical pitting corrosion was observed in the coating film at the higher temperatures.

Silicon nitride films have received much attention especially for applications in the semiconductor industry because of their excellent chemical stability and resistance to diffusion of impurities. Many authors have studied the preparation of silicon nitride films and their structural and electrical properties. Most of the existing studies are, however, mainly concerned with thin films formed by sputtering (1-4) or chemical vapor deposition (5, 6). Little work on the ion-plated silicon nitride film has been reported in the literature except by Chin *et al.* (7), who dealt with the silicon nitride coatings for thermoelectric couples. On the other hand, the applications of molybdenum as a high temperature material are limited by its severe oxidation at temperatures above 800°C. Considerable effort, therefore, has been made to develop various high temperature protective coatings for molybdenum such as metallic, disilicide-based diffusion, and ceramic overlay coatings (8). The present paper describes a preparation technique of silicon nitride by reactive ion-plating, and the structural and compositional characteristics of the film obtained. An attempt to apply this silicon nitride film to the high temperature oxidation resistant coating for molybdenum is also described.

Experimental

Apparatus.—The apparatus shown in Fig. 1 is specially designed for the rf reactive ion plating of silicon nitride. The rf ion-plating technique was basically the same as that described by Murayama (9). The rf coil electrode (7 turns and 10 cm in spiral coil diam) was placed directly above the evaporation source and connected to a 13.56 MHz, 300-VA rf power supply to make a glow discharge region for the ionization and activation of the reactants. The 6 kW electron beam gun has a 180° bent beam whose spot was swept over the entire source surface for the uniform melt and evaporation rate. The vacuum chamber is separated by the conductance baffle to maintain pressures of less than 10^{-3} Torr around the EB gun, while pressures are as high as 2×10^{-2} Torr in the deposition side. The substrate holder was constructed such that a bias from 0 to −3 kV d.c. could be applied to the substrate for the acceleration of ionized particles toward it. The source-to-substrate distance was approximately 14 cm for all experiments. The substrate was heated by radiation from a tantalum resistance heater to a desired temperature between 400° and 1000°C. The temperature was measured with a Chromel-Alumel thermocouple placed in contact with the back side of the substrate. Gas pressure was measured with a Schulz-Phelps and a Bayard-Alpert ionization gauge and controlled to a desired level by a high vacuum leak valve.

Evaporation source, substrate, and reactive gas.—Semiconductor-grade silicon was used as the evaporation source. Substrate for deposition was prepared from sintered molybdenum sheet and electrochemically polished prior to mounting on the substrate holder. The source for nitrogen was ammonia, supplied by Mathieson Gas Products with a purity of 99.99%. The ultra-high purity argon was also used for the sputter cleaning of substrate.

Coating procedures.—In a typical coating experiment, the vacuum chamber was evacuated to approximately 5×10^{-6} Torr or lower. Prior to each deposi-

* Key words: silicon nitride, ion plating, protective coating, molybdenum.

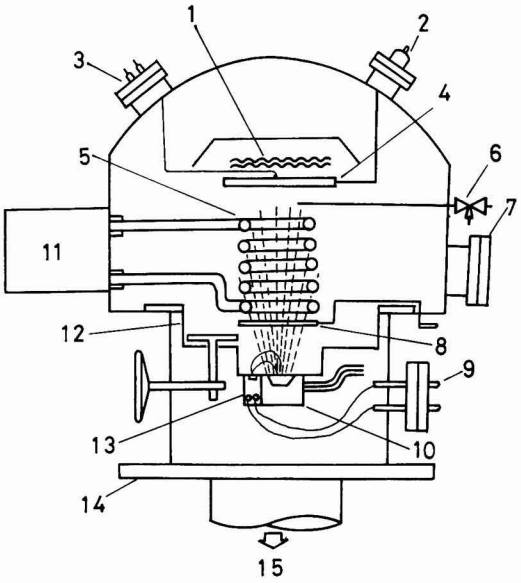

Fig. 1. Ion plating apparatus: 1, substrate heater; 2, high voltage feedthrough (—d.c. power); 3, thermocouples; 4, substrate holder; 5, rf coil; 6, variable leak valve; 7, view port; 8, shutter; 9, electrical feedthrough (EB power); 10, water-cooled copper hearth; 11, impedance matching box; 12, conductance baffle; 13, sweep, focus coils, and EB gun; 14, base plate; 15, pumping system.

tion, the substrate was sputter cleaned for about 10 min under argon pressure of 2×10^{-2} Torr. As for the evaporation of silicon, uncontrolled splatting of the silicon frequently occurred during melting even after the electron beam power inputs were limited to a low enough level. The same trouble was already reported by Chin *et al.* (7). After examining the vaporization technique, we found that silicon was vaporized significantly without any splatting when it was melted together with several pieces of tantalum sheet. Emission spectroscopic analysis of the deposits obtained by this technique showed traces of tantalum in the film deposited around the crucible but not in the deposited film on the substrate. This is probably due to the very low vapor pressure of tantalum compared with that of silicon. After initiating the evaporation of silicon, the ammonia gas was introduced into a chamber and the rf power supply was increased until a steady glow was observed in the chamber. No apparent changes in the deposited film were observed depending upon the distance between the outlet of ammonia gas feed pipe and the substrate. The shutter was then opened to begin the deposition of nitride under various conditions as given in Table 1. The coating was 7-10 min for most experiments.

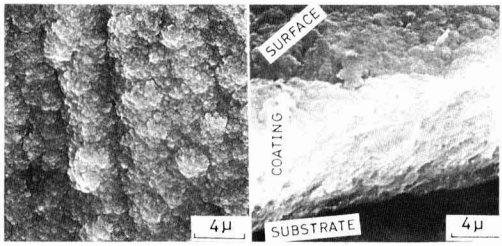

Fig. 2. Scanning electron micrograph of silicon nitride coating (left; coating surface, right; fracture cross section for the same deposit). Deposition rate was 1 μm/min at a substrate temperature of 950°C.

Results

Analysis of ion-plated silicon nitride.—Visual and scanning electron microscopic observations.—The silicon nitride deposits were obtained at a deposition rate of from 0.1 to 1.2 μm/min depending upon the coating conditions. Most deposits showed a dark green color, but some were gray and/or red brown. Figure 2 shows typical scanning electron microphotographs of silicon nitride coatings. Although large primary grains composed of many small grains were observed in the coating surface, no clear grain boundaries in cross-sectional structure were visible. This vitreous structure seems to be characteristic of the deposits obtained in the present work.

Auger electron spectroscopic analysis.—The chemical compositions of the deposited silicon nitride films were determined by means of Auger spectroscopic analysis (Cylindrical Mirror Analyzer, PHI Incorporated). Concentrations were calculated from the peak-to-peak Auger signal height by using relative elemental sensitivity factors given in the literature (10). Table I summarizes the chemical composition representative of the various deposits together with their coating conditions. For comparison, electron probe microanalysis (EMX-SM Shimazu Seisakusho, Limited) was also carried out by using BN as the standard sample for nitrogen. The results are also shown in parentheses in Table I. In certain cases, the results show considerable discrepancy between the two. This can be considered due to the difficulty of quantitative analysis of nitrogen in thin film by electron probe microanalyzer. As for the effect of the deposition temperature, no apparent composition changes in the film were observed in the temperature range from 400° to 1000°C. Nitrogen contents in the film varied over a wide range depending upon the deposition conditions. It should be noted that nearly stoichiometric deposits were obtained in runs 73, 76, and 78, in which silicon was vaporized with EB gun power of about 2 kW under reactant gas pressure of as high as 10^{-2} Torr. Further discussions on this point are made later. Oxygen and carbon were prominent con-

Table I. Deposition conditions and chemical analyses of silicon nitride films formed on molybdenum

Run no.	Reactant gas pressure (Torr)	Electron beam gun power (kW)	RF power (W)	Substrate voltage (−kV)	Substrate temperature (°C)	Composition (weight percent)			
						Si	N	O	C
18	9.0×10^{-3}	1.0	190	0.5	—[b]	49	45	0	5.9
39	5.5×10^{-3}	1.0	200	0.3	—	61	37	0.8	1.2
69	5.0×10^{-3}	1.2	150	0.3	800	97	2.6	0	—[c]
72	5.0×10^{-3}	1.5	150	0.3	—	68 (58)[a]	29 (42)	1.0 (0)	2.0 (—)
73	1.5×10^{-2}	2.0	210	0.3	700	51 (51)	42 (49)	3.0 (0)	4.0 (—)
76	1.0×10^{-2}	1.8	200	0.4	950	62 (42)	35 (56)	1.0 (2.0)	2.0 (—)
78	8.0×10^{-3}	1.8	220	0.4	—	59	39	1.0	2.0

[a] Value obtained by EPMA analysis is in parenthesis.
[b] Not heated but the temperature rises to ~400°C because of ion bombardment.
[c] Not analyzed.

taminants in these deposits. Presumably, they come from the impurities in the reactant gas. As the formation of nearly stoichiometric silicon nitride has been so far ascertained by the compositional data in Table I, the chemical state of silicon in deposits is hereafter examined in some detail. Figure 3 shows an example of Auger spectra for the silicon nitride coatings obtained in this study. After 3 min Ar-sputtering (removing ~300Å), AES signals from silicon and nitrogen increased in intensity, while those from oxygen and carbon became very weak, with an additional peak from argon atoms implanted during sputter cleaning. A detailed comparison of our Auger electron spectra with published data (10-12) revealed that the chemical shift and Auger electron peak shape from silicon in the spectra given in Fig. 3 are completely different from those of elemental Si and SiO_2, but showed a significant agreement with those from silicon in Si_3N_4 and in $Si_{0.54}N_{0.46}$ (10, 12).

Infrared spectroscopic analysis.—Infrared absorption of the deposits was measured by using a double-beam spectrophotometer (JASCO A-3, Japan Spectroscopic Company Limited). The silicon nitride layer removed from the molybdenum substrate was ground to microsize with potassium bromide and the mixture was pressed into a pellet. In a typical infrared absorption profile shown in Fig. 4, a strong, broad band with its center at 830 cm^{-1} was observed and was identical with the Si-N stretching band reported by many other investigators (1-3, 5). The very weak absorption peaks for N-H and Si-H also were discernible. This hydrogen contamination seems to come from ammonia gas used.

X-ray analysis.—In the as-coated condition, all the coatings obtained in this study proved to be amorphous because no peaks except for the molybdenum substrate were obtained. For further confirmation of the formation of silicon nitride, the coating layer removed mechanically from the substrate was heat-treated at 1400° and 1500°C for about 2 min under 10^{-6} Torr. This caused the crystallization of amorphous deposits. Figure 5 shows the x-ray diffraction profile obtained with Ni-filtered CuKα radiation. All peaks corresponded to those of silicon and Si_xN reported in the ASTM powder diffraction data. The latter substance was originally obtained by Decker (13) together with free silicon when commercial silicon nitride was arc melted. It is obvious from this and previous studies already described that silicon in ion-plated films is present as the nitride. In addition, the deposits were nearly stoichiometric compounds.

Oxidation test of silicon nitride coated molybdenum.—The oxidation resistance of coated specimens was examined by thermogravimeter. Coated specimens of about 1 × 0.5 × 0.07 cm were heated at a rate of 20°C/min in the Ar 1% O_2 gas mixtures with a flow rate of ~200 ml/min. Figure 6 shows the results of oxidation tests for typical coated specimens. Uncoated specimens which were oxidized under the same conditions show a drastic weight decrease at about 790°C. This is because the MoO_3 formed begins to melt at this temperature and has a high vapor pressure. In this test, the edges of the specimens were painted with Al_2O_3 slurry to protect the cut edges and the film defect in the vicinity of edges in specimens. Observation of specimens after oxidation test, however, showed that film failure ascribed to the unprotected cut edges still existed. The oxidation test profiles shown in Fig. 6, therefore, give a rough estimation for the oxidation resistance of silicon nitride coatings. In the coated specimens which showed a marked decrease in weight at relatively low temperature, typical pitting corrosion shown in Fig. 7 was observed. On the other hand, the film adherence to the substrate generally plays an important role in

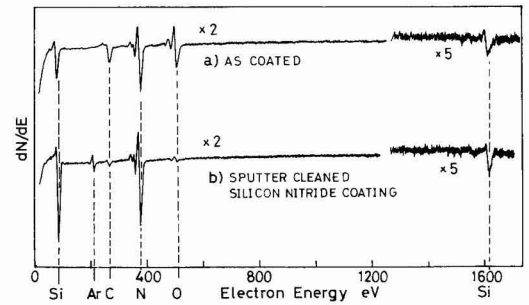

Fig. 3. Auger spectra from a) as coated surface; b) sputter-cleaned surface of silicon nitride coating (Run no. 76).

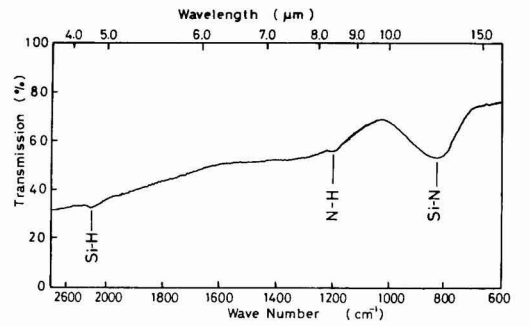

Fig. 4. Typical infrared spectrum of ion-plated silicon nitride film. (Run no. 72), the decrease of transmission in shorter wavelengths is ascribed to the difference in particle size between the sample and KBr reference.

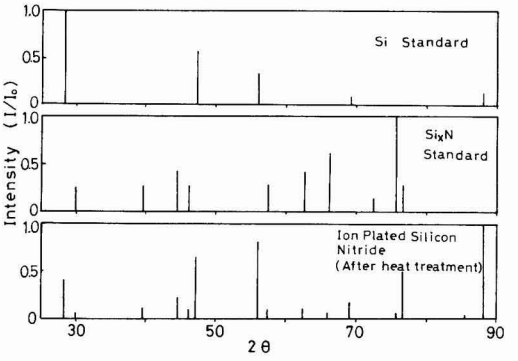

Fig. 5. X-ray diffraction pattern of the silicon nitride deposit (heat-treated at 1400°C for 2 min under 10^{-6} Torr).

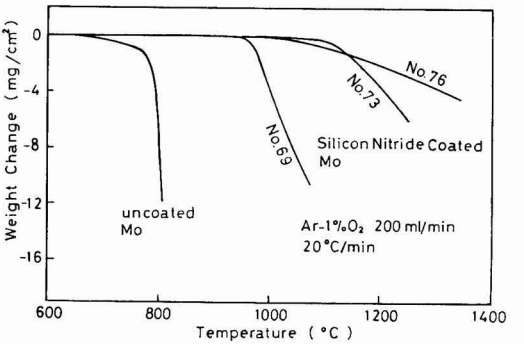

Fig. 6. Weight change vs. temperature of uncoated and silicon nitride coated molybdenum.

Table II. Variation of Si/N (atomic ratio) in deposit with EB power and the deposition site

Run no.	Electron beam gun power (kW)	Evaporation rate of Si (g/min)	A		B		C	
			Si/N	μ	Si/N	μ	Si/N	μ
51	1.2	0.07	0.9	2.5	1.0	~1	1.6	~1
53	1.1	0.1	1.4	3.5	1.9	~1.5	3.9	~1
78	1.8	0.3	0.7	9.9	0.6	6.8	1.3	2.3

protective coating technology. On this point, silicon nitride layer obtained in this study showed comparatively poor adherence to molybdenum substrate. The bonding was improved to some extent when the substrate was heated during coating. It can still, however, be removed by bending the specimens, even though not as easily as in specimens obtained without the substrate heating. Further investigations concerning the pitting corrosion and the film adherence are needed to obtain more protective silicon nitride coatings for molybdenum.

Discussion

Table I indicates that the ion-plated films vary considerably in their chemical composition, depending upon the coating conditions. For the purpose of examining the several factors affecting the stoichiometry of deposits, another ion-plating experiment was undertaken using a long strip-shaped molybdenum substrate. As shown schematically in Fig. 8, the substrate length is large enough compared with the diameter of rf coil. Evaporation rates of silicon were varied from 0.07 to 0.3 g/min. After the coating experiment, silicon nitride deposits from three different places on the substrate were analyzed by Auger electron spectroscopy. The atomic ratio between silicon and nitrogen in the deposits and the coating thickness measured by scanning electron microscopy are summarized in Table II. A, B, and C in Table II correspond to the three places on the substrate, *i.e.*, directly above the center, close to, and outside of the rf coil, respectively. In each run, as the deposition site was moved closer to the center of the rf coil, namely site A, a smaller value of Si/N was obtained and the deposit became nearly stoichiometric. This is probably because the concentration of ionized reactants is largest in the center of rf coil. On the other hand, when the EB gun power input was increased to as high as 1.8 kW, the deposition rate noticeably increased. Furthermore, the film became close to stoichiometric silicon nitride. This result is consistent with those of run 73 and 76 in Table I. This high rate deposition of nearly stoichiometric silicon nitride can be attributed to the fact that the power of EB gun as well as that of rf discharge is highly effective for the ionization or activation of reactants. The advantage of the use of electron beam evaporation technique for ion plating which was introduced by Chambers and Carmichael (14) has been pointed out by other investigators too (15, 16). From the fact mentioned above, it is concluded that nearly stoichiometric silicon nitride can be ion plated with a rather high speed, as long as the reactants are sufficiently ionized or activated.

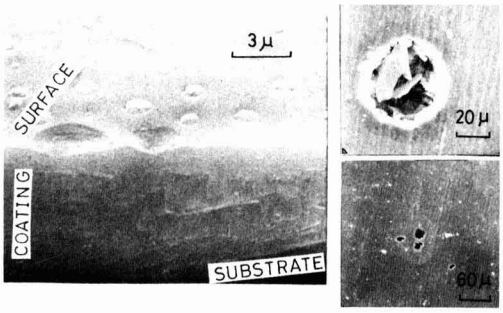

Fig. 7. Scanning electron microphotograph of typical film failure after oxidation test.

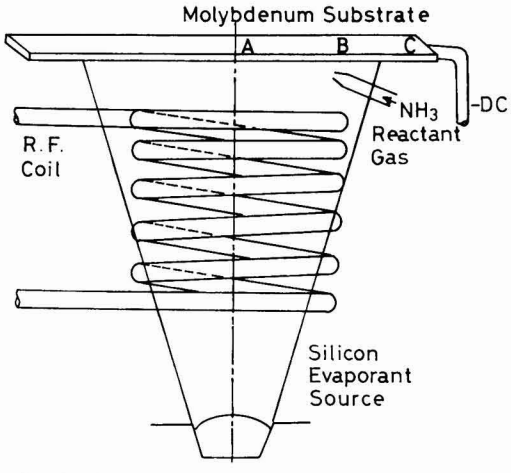

Fig. 8. Schematic illustration of ion-plating experiment using a long strip-shaped substrate.

Conclusions

Nearly stoichiometric silicon nitride coatings on molybdenum can be prepared by rf reactive ion plating from Si and NH_3. The most important factors affecting the stoichiometry of the deposit seemed to be an electron beam power into the Si evaporation source and the condition of rf glow discharge region, where most of the ionized or activated species of the reactants might be produced. The oxidation tests performed on coated specimens showed that the silicon nitride layer restrained the oxidation of molybdenum up to approximately 1200°C, but typical pitting-like failure in the deposited film occurred at the higher temperature.

Acknowledgments

The authors would like to express their appreciation to Dr. K. Yoshiwara and Dr. M. Kurahashi for the Auger electron spectroscopy measurements. The cooperation of the Physical and Chemical Analysis Departments of the National Research Institute for Metals is gratefully acknowledged.

Manuscript received March 18, 1977.

Any discussion of this paper will appear in a Discussion Section to be published in the June 1978 JOURNAL. All discussions for the June 1978 Discussion Section should be submitted by Feb. 1, 1978.

Publication costs of this article were assisted by the National Research Institute for Metals.

REFERENCES

1. G. J. Kominiak, *This Journal*, **122**, 1271 (1975).
2. S. M. Hu and L. V. Greger, *ibid.*, **114**, 826 (1967).
3. C. J. Mogab, P. M. Petroff, and T. T. Sheng, *ibid.*, **122**, 815 (1975).
4. S. I. Raider, R. Flitsch, J. A. Aboaf, and W. A. Pliskin, *ibid.*, **123**, 560 (1976).
5. J. A. Aboaf, *ibid.*, **116**, 1736 (1969).

6. R. C. G. Swann, R. R. Mehta, and T. P. Cauge, *ibid.*, **114**, 713 (1967).
7. J. Chin and N. B. Elsner, *J. Vac. Sci. Technol.*, **12**, 821 (1975).
8. High Temperature Oxidation-Resistant Coatings, Committee on Coatings, National Research Council, National Academy of Sciences, Washington D.C., p. 99 (1970).
9. Y. Murayama, *J. Vac. Sci. Technol.*, **12**, 818 (1975).
10. L. E. Davis, N. C. MacDonald, P. W. Palmberg, G. E. Riach, and R. E. Weber, "Handbook of Auger Electron Spectroscopy," 2nd ed., Physical Electronics Industries, Inc. (1976).
11. P. H. Holloway and H. J. Stein, *This Journal*, **123**, 723 (1976).
12. P. H. Holloway, *Surf. Sci.*, **54**, 506 (1976).
13. Index to the X-ray Powder Data File (1962).
14. D. L. Chambers and D. C. Carmichael, *Research/Development Magazine*, **22**, 32 (1971).
15. L. B. Leder, *Met. Finish.*, **72**, 41 (1974).
16. R. F. Bunshah and A. C. Raghuram, *J. Vac. Sci. Technol.*, **9**, 1385 (1972).

Precipitation-Induced Currents and Generation-Recombination Currents in Intentionally Contaminated Silicon P$^+$N Junctions

H. H. Busta[1] and H. A. Waggener

Teletype Corporation, Skokie, Illinois 60076

ABSTRACT

The effects of impurities such as gold, iron, copper, nickel, tantalum, and tungsten on junction reverse *I-V* characteristics were investigated using DLTS (deep level transient spectroscopy), TSCAP (thermally stimulated capacitance), *I-V*, *C-V*, and *I-T* measurements. In almost all cases, the reverse *I-V* characteristics consisted of two components; a normal Shockley-Read-Hall (SRH) generation component and a soft leakage component which dominates the SRH component above a given onset voltage. Only the SRH component can be detected with the DLTS and TSCAP methods. The soft leakage currents were ascribed to the presence of impurity precipitates lying near the metallurgical junction of the devices. Soft leakage currents measured at 80°K were fitted to a Fowler-Nordheim field-emission model. Localized electric field values near the precipitates of the order of 10^6-10^7 V/cm were obtained by this analysis. These values could be correlated with the possible shape of the precipitates. The distribution of the SRH generation centers within the active regions of the devices and the activation energies of the emission rates of above-mentioned impurities were measured using the DLTS technique. The following results were obtained: Au 0.55 eV (*c*), Fe 0.57 eV (*c*); Cu 0.2 eV (*c*), 0.49 eV (*v*), 0.41 eV (*v*); Ni 0.19 eV (*c*), 0.36 eV (*c*); Ta 0.21 eV (*c*); and W 0.25 eV (*c*), 0.28 eV (*c*), respectively. Here *c* and *v* represent measurements from the conduction band and valence band, respectively.

It is well known that point defects distributed in the bulk or at the surface of pn junctions can act as generation centers for electron-hole pairs and thus cause diode leakage. These defects can be process-induced defects, dislocations, radiation-induced defects, or impurities such as gold, iron, copper, manganese, nickel, sulfur, etc. They are characterized by activation energies which lie within the forbidden bandgap of the semiconductor, and by their thermal capture and emission rates for minority and majority carriers, respectively. Their contribution toward diode leakage is governed by the Shockley-Read-Hall generation-recombination theory (1). The most effective centers, in terms of the generation component, lie near the midgap of the semiconductor.

Detection of these defects can be achieved, for instance, by using thermally stimulated current (TSC) (2, 3) measurements. Identification of a given generation center with the above techniques can be achieved in certain cases. Complications arise due to the fact that for some impurities such as gold, iron, copper, sulfur, manganese, etc., the near midgap energy levels are separated by only a few millielectronvolts, which in terms of temperatures, corresponds to only a few degrees difference in the position of the measurement signals. When using the TSC and TSCAP methods, the position of the signals is strongly dependent on heating rates. Therefore, for identification purposes, these rates have to be known precisely. Lang has recently published a paper on deep level transient spectroscopy (DLTS) measurements (4). The advantage of this method is that it is heating rate independent. For a given fixed emission rate window, the position of the signals occurs at the same temperature. Another advantage of the DLTS method is that it is spectroscopic in nature, which means that it has a zero base line. However, this can also be achieved by using the differential TSCAP method (5)

The intention of this work was to identify leakage mechanisms of some diodes fabricated in our facilities using DLTS, TSCAP, *I-V*, *C-V*, and *I-T* measurements. These measurements were performed on planar diodes, gate-controlled diodes, and MOS capacitors. In the course of this work, some devices with known characteristics (6) were intentionally contaminated with gold, iron, copper, nickel, tantalum, and tungsten. It was found that for gold- and tungsten-doped diodes the generation components increased by three orders of magnitude as compared to the precontamination level. This gave rise to large DLTS signals ($N_t \simeq 10^{14}$ cm^{-3}). The reverse *I-V* characteristics of these diodes were almost ideal over the entire voltage range, with *I* varying as $V^{1/2}$. For all the other elements, the generation components increased only moderately, giving rise to weak DLTS signals ($N_t \simeq 10^{11}$-10^{13} cm^{-3}). However,

[1] Present address: Gould Laboratories, Rolling Meadows, Illinois 60008.

Key words: junction leakage, defects in pn junctions, field emission, tunneling, deep level transient spectroscopy.

these diodes showed soft characteristics. In some extreme cases, the onset of the soft current component occurred at voltages as low as 1V. Goetzberger and Shockley (7) attributed this softness to the formation of metallic precipitates, and conjectured that Zener tunneling at localized high field points was responsible for the observed soft leakage currents. They reported leakage currents proportional to V^n, with n ranging from 3 to 7. However, no attempts were made to explain the exponent n in terms of a physical model.

In this paper, the soft component of leakage current is modeled in two ways and experimental results are compared to these models. First, a tunnel or field-emission model is considered. From analysis of the data, values of the electric field at localized high field spots, information about the shape of the precipitates, and estimates of the local extension of the emission sites are obtained. The information gained from this analysis has to be considered more qualitatively than quantitatively, since the expression used for the tunneling current density is only applicable to direct gap tunneling. In the indirect case, such as silicon, effects due to momentum conservation and multiple band effective masses should be included. Second, the possibility that these currents arise from SRH centers is presented. There are other mechanisms which might explain soft leakage currents. Charge multiplication due to impact ionization at localized areas of high electric fields might be one possibility. The reason why a tunneling approach is chosen in this work is due to the experimentally observed fact that leakage currents have a negative temperature coefficient, *i.e.*, at a given voltage the current increases with increasing temperature. Also, in all cases, a temperature-independent component was observed at liquid nitrogen temperatures. Impact ionization has a positive temperature coefficient, *i.e.*, at a given voltage the ionization rate increases with decreasing temperature (8).

Device Fabrication

The diodes were fabricated using Czochralski-grown n-type (111) wafers having an uncompensated phosphorus concentration of approximately 1×10^{15} cm^{-3}. BN disks were used for the p$^+$ diffusion. Diodes from different stages during the common p-channel MOS process were used for this experimentation. Before testing, all devices were either nitrogen annealed or forming gas annealed at 450°C in order to reduce the surface component of the leakage.

Before the devices were subjected to the impurity diffusion, reverse I-V control measurements were performed. After appropriate cleaning of the slices, the elements under investigation were either filament or electron beam evaporated on the back of the wafers, and diffused in a nitrogen atmosphere. In most cases, a new quartz furnace tube was used for each element. Diffusion temperatures ranged from 800° to 1150°C.

Experimental Results

Leakage mechanisms.—Figure 1 shows the current-reverse voltage characteristics of two diodes. The measurements of Fig. 1 were taken at room temperature and 80°K, respectively. The room temperature plots consist of two distinct regions: a region where the current varies approximately as $V^{1/2}$, followed by a region of very strong voltage dependence. For both junctions, the leakage currents below the onset of the soft knees are governed by Shockley-Read-Hall generation centers. At low temperatures, these currents decrease, due to the exponential temperature dependence of the electron-emission and hole-emission rates (1, 2). The soft component of diode A is almost temperature independent in the range from 80° to 300°K. Diode B does show some temperature dependence of its soft characteristics, however, measurements showed that from 80° to 130°K this component is also temperature independent. Experimentally, it was observed that for a given impurity, both type A and B behavior were present for

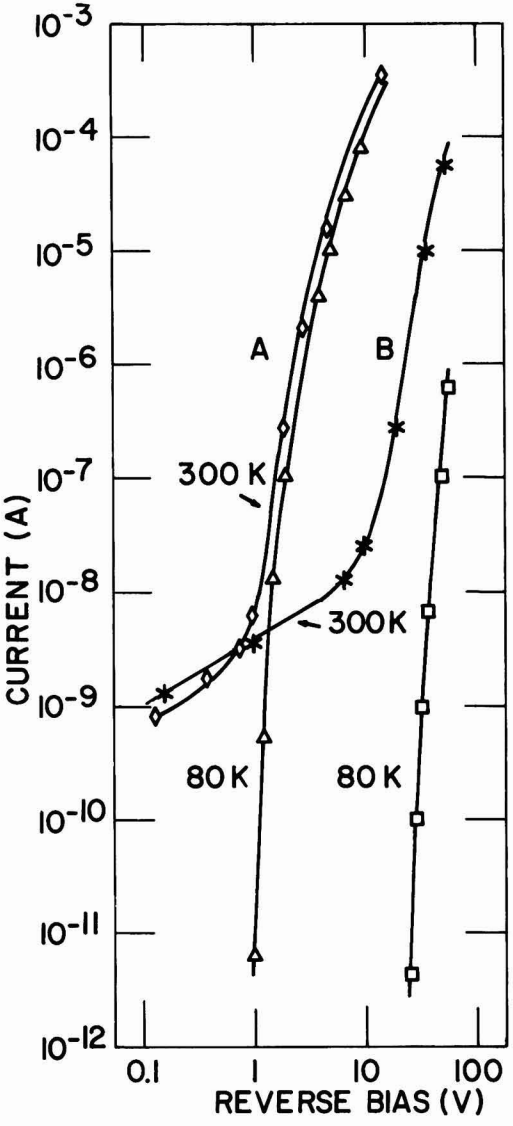

Fig. 1. A: I-V_R characteristics of the tantalum-doped diode C-4 of lot 4521, W-8, chip J-7 measured at 300° and at 80°K, respectively. B: I-V_R characteristics of the tungsten-doped diode C-4 of lot 4521, W-7, chip G-13 measured at 300° and at 80°K, respectively.

a given wafer. Also, the onset voltages of the soft knees varied over wide ranges. In some cases values ranging from 1 to 40V were observed. Due to these reasons, no attempt was made to rank order the influence of the individual impurities upon diode leakage. However, based upon the limited sample size which was investigated, some general comments can be made. Iron, nickel, copper, and tantalum gave rise to the formation of soft diodes with low SRH generation components. The concentrations of generation centers ranged from 10^{11} to 10^{13} cm^{-3}. Tungsten-doped diodes showed softness occurring at voltages of larger than 20V. A large generation component was observed with a concentration of generation centers larger than 10^{14} cm^{-3}. No softness was observed for gold-doped diodes. Their concentration of SRH centers was approximately 10^{14} cm^{-3}. As mentioned, the existence of a temperature-

independent soft leakage component and of a negative-temperature coefficient led to the consideration of a tunnel or field-emission mechanism.,

Tunnel or field emission.—Before discussion of the data, some of the expressions which are used in the analysis of the data are summarized. In this work, only the temperature-independent components of soft leakage currents are analyzed.

The basic law governing field emission is given by the Fowler-Nordheim equation. The current density at temperature $T = 0$ is given by (9)

$$J = \frac{q^3E^2}{16\pi^2\hbar\, q\, \Phi_B t^2(y)} \exp\left(-\frac{4(2m^*)^{1/2}(q\Phi_B)^{3/2}\, v(y)}{3\hbar\, qE}\right) \quad [1a]$$

with t and v being tabulated functions of the argument y, which is given by

$$y = (q^3E)^{1/2}/q\Phi_B \quad [1b]$$

Here E is the applied electric field, $q\Phi_B$ is the barrier height, and m^* is the tunneling effective mass. The function $t(y)$ in Eq. [1a] is almost independent of y. It monotonically increases from 1.00 to 1.11 as y varies from 0 to 1. The barrier-lowering factor $v(y)$ decreases monotonically from 1 to 0 as y varies from 0 to 1. To test if a field-emission process can be used to describe soft leakage currents, the data is plotted in the form $\ln J/E^2$ *vs.* E^{-1} (Fowler-Nordheim plot). A straight line should be obtained, the slope of which is given by

$$-\frac{4(2m^*)^{1/2}(q\Phi_B)^{3/2}\, v(y)}{3\hbar\, q}. \quad [2]$$

Near a precipitate it is assumed that the electric field E is enhanced by a factor of β above the unperturbed background field of the junction. A similar assumption was made in Ref. (10), where Fowler-Nordheim field emission from protruding whiskers on nickel cathodes was considered. The electric field is then given by

$$E = \beta E_{\text{unperturbed}} \quad [3]$$

Using the abrupt junction approximation (11)

$$E_{\text{unperturbed}} = E_{\max} = \left(\frac{2qN_D}{\epsilon_s}\right)^{1/2} (V_{bi} + V_R)^{1/2} \quad [4]$$

Here N_D is the donor-doping concentration, ϵ_s is the dielectric constant of the semiconductor, V_{bi} is the built-in voltage, and V_R is the reverse bias voltage. Two further conditions are invoked. It is assumed that one end of the precipitate is located near the maximum field, while the other end of the precipitate extends into the heavily doped region. Therefore, only a small voltage drop can exist between the precipitate and the heavily doped region. With these conditions, the unperturbed field at the tip of the precipitate is the maximum field in the junction, $E_{\max}$. Since under these conditions E is proportional to $(V_{bi} + V_R)^{1/2}$, a Fowler-Nordheim plot should be of the form $\ln J/(V_{bi} + V_R)$ *vs.* $(V_{bi} + V_R)^{-1/2}$ with a slope of

$$-\frac{4(2m^*)^{1/2}(q\Phi_B)^{3/2}}{3\hbar\, q\left(\frac{2qN_D}{\epsilon_s}\right)^{1/2}} \frac{v(y)}{\beta} \quad [5]$$

By using Eq. [5], it is possible to obtain estimates of the field-enhancement factors at the precipitates. From these values, information about the shape of the precipitates can be deduced.

Since the devices were contaminated with metals, it is assumed that the precipitates are either metallic or in the form of conductive silicides such as CuSi, Ni_2Si, FeSi, $TaSi_2$, WSi_2, etc. Assuming a spherical precipitate imbedded in a dielectric medium, the field inside the sphere is zero; the field outside the sphere is given by (12)

$$\hat{E}(r, \theta) = E(1 + 2a^3/r^3)\cos\theta\hat{r} - E(1 - a^3/r^3)\sin\theta\hat{\theta} \quad [6]$$

Here E is the uniform background field, a is the radius of the sphere, r and θ are the polar coordinates, and $\hat{r}$ and $\hat{\theta}$ are the unit vectors. For $r = a$ and $\theta = 0$, $\hat{E}(a, 0) = 3E$. This means that the field-enhancement factor at the precipitate has a value of 3. As can be seen from Eq. [6] the field-enhancement factor has a strong spatial dependence. In the case of a conducting prolate spheroidal-shaped precipitate, the field-enhancement factor depends strongly on the c/b ratio (10). Here c is the extension of the precipitate in the direction of the field, and b is the diameter. For $c/b = 1$, β reduces to 3, the value of the field-enhancement factor for a sphere. It should be mentioned that field enhancement also occurs for noncontacting precipitates. For instance, the field enhancement for a spherical SiO_2 precipitate is approximately 1.5 (12).

Fowler-Nordheim plots of the temperature-independent components of the two diodes shown in Fig. 1, as well as of one other diode, are shown in Fig. 2 where $V_R^{-1/2}$ is used as the abscissa. From the slopes corresponding to large reverse voltages, (*i.e.*, $V_R + V_{bi} \simeq V_R$), values of $\beta' = (m_e/m^*)^{1/2}v^{-1}\beta$ can be obtained. Here m_e is the free electron mass. Using Eq. [5] and taking for $q\Phi_B = 0.5$ eV and for $N_D = 1 \times 10^{15}$ cm^{-3}, these values ranged from 9.4 to 114 for the diodes shown in Fig. 2. Similar values were obtained for iron-, nickel-, and copper-doped diodes. Using Eq. [3] and [4] and assuming that $m^* \simeq m_e$, and $v(y) \simeq 1$, values of the electric field at the precipitates of 0.82×10^6 V/cm for $-V_R = 25$V and of 1.33×10^6 V/cm for $-V_R = 65$V were obtained for diode B of Fig. 1 and 2. This is close to the reported value of 10^6 V/cm for silicon where currents due to tunneling become significant (13). Taking $\beta \simeq 114$ for diode A, values of the electric fields of 2×10^6 V/cm for $-V_R = 1$V and of 6.32×10^6 V/cm for $-V_R = 10$V were obtained. The actual field values are reduced somewhat since $v(y) \leq 1$, and since it is expected that $m^* < m_e$. Since these field values are one to two orders of magnitude larger than the avalanche breakdown field in a junction of approximately 5×10^5 V/cm, they have to be restricted within a small volume, otherwise localized charge multiplication due to impact ionization would take place giving rise to a discontinuous slope in the current-voltage characteristics whenever the multiplication factor reaches the value of one. Using the conditions invoked above, a field-enhancement factor of 9.4 corresponds to a c/b ratio of 3. For $\beta = 114$, the c/b ratio is approximately 20. Again, due to the unknown values of m^*, $q\Phi_B$, and $v(y)$, the c/b ratios have to be viewed more qualitatively than quantitatively. However, by comparing the c/b ratios of diodes A and B of Fig. 1 and 2, it can be concluded that the current contributing precipitates in diode A are more needle-like than the precipitates in diode B. Bearing in mind that the enhanced field at a precipitate can only occur over a small fraction of the junction area, Eq. [1] was used to check if the calculated current densities are consistent with this assumption. The emission area can be estimated from

$$I(V_R) = J(T = 0, V_R)A_p \quad [7]$$

where I is the measured temperature-independent current at a given reverse bias voltage, J is the current density given in Eq. [1], and A_p is the emission area at a precipitate. The results are: $A_p \simeq 10^{-10}A_j$ for diode A, and $A_p \simeq 10^{-3}A_j$ for diode B. Here A_j is the junction area. The value for diode B seems quite large, but since these junctions were intentionally contaminated, it is conceivable that in some cases quite a few precipitates of similar emissivity formed during the cooling cycle.

From Fig. 2 it can be seen that for diode A deviations from a straight line occur at voltages below 3V. This is expected since according to Eq. [4] the electric field is only proportional to $V_R^{1/2}$ for $V_R > V_{bi}$. Incorporating V_{bi} and plotting $\ln I/(V_{bi} + V_R)^{3/2}$ *vs.* $(V_{bi}$

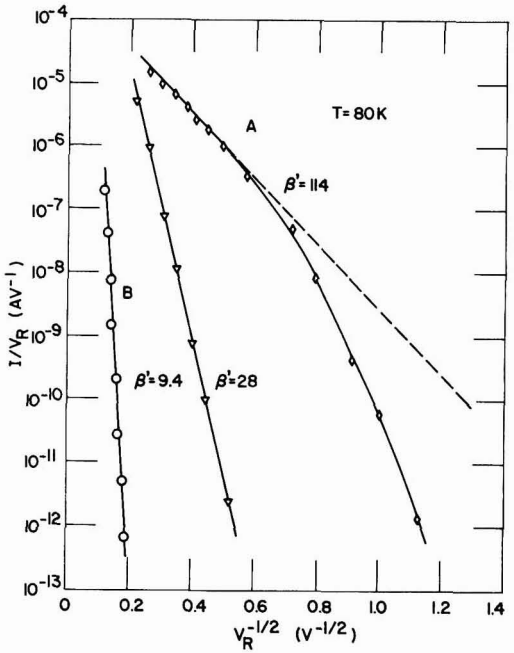

Fig. 2. Log I/V_R vs. $V_R^{-1/2}$ plots of the temperature-independent soft leakage component of several diodes.

$+ V_R)^{-1/2}$, however, did not result in a straight line fit at voltages below 3V.

Detection and distribution of SRH generation centers.—During the early stages of this work, the possibility was considered that the soft leakage component might be due to nonuniform distribution of generation centers or due to field-enhanced emission rates. To investigate this, DLTS measurements were taken at different voltage ranges. Examples of such measurements are given in Fig. 3 and 4. Figure 3 shows the *I-V* characteristics of a soft diode which was contaminated with tantalum. DLTS 1 was obtained for a quiescent reverse bias of -3V which was momentarily reduced to 0V. DLTS 2 was obtained for a quiescent reverse bias of -10V which was momentarily reduced to -6V. The width of the bias reduction pulse was 400 μsec. These two spectra are shown in Fig. 4. From the analysis of the data, the concentration of the near midgap levels were $N_t(\text{DLTS 1}) = 1.2 \times 10^{13}$ cm^{-2} and $N_t(\text{DLTS 2}) = 1.5 \times 10^{13}$ cm^{-3}, respectively. This moderate increase in N_t from DLTS 1 to DLTS 2 cannot be the cause of the sharp increase in the leakage current from -3 to -10V. From Fig. 4 it can be seen that the maxima of the near midgap peaks of the two spectra occur at the same temperature. This means that the emission rate in the two cases is the same. Therefore the observed large leakage current cannot be explained by a field-enhanced emission rate. The soft leakage component measured at 80°K was subsequently fitted to the precipitation model. From the analysis, a field-enhancement factor of 28 was obtained. It should be mentioned that the near midgap peak in Fig. 4 is due to gold contamination. This was established from control measurements. Therefore only the low temperature peak (0.21 eV, Table I) is associated with tantalum.

DLTS measurements were also used to measure the lateral distribution of generation centers. For this purpose, gate-controlled diodes and in some cases MOS capacitor structures, were employed. In some cases it was observed that up to 40 times more impurities in the form of generation centers were present in the depletion region of the field-induced junction of a gate-controlled diode as compared to the depletion region associated with the metallurgical junction. This was seen for iron- and tantalum-doped diodes, both of which showed soft *I-V* characteristics. Either gettering effects in the p$^+$ region or formation of precipitates near the metallurgical junction might be responsible for the depletion of generation centers near the metallurgical junction. In the case of the tungsten-doped diodes, an almost uniform distribution of the near midgap impurities in those two regions was observed. An example of such a measurement is given in Fig. 5. It shows the I-V_R characteristics of the metallurgical junction and of the field-induced junction of a tungsten-doped gate-controlled diode. Over most of the

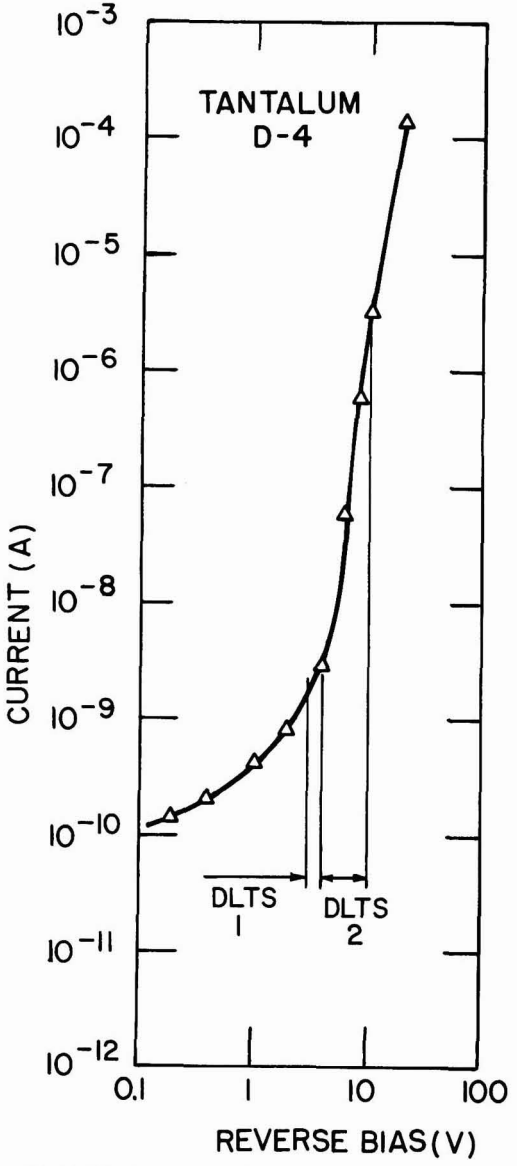

Fig. 3. I-V_R characteristics of the tantalum-doped diode C-4 of lot 4321, W-8, chip D-4, measured at room temperature. Indicated by DLTS 1 and DLTS 2 are the two voltage ranges for which DLTS spectra were obtained in order to measure possible nonuniform impurity distributions and/or field-enhanced emission rates.

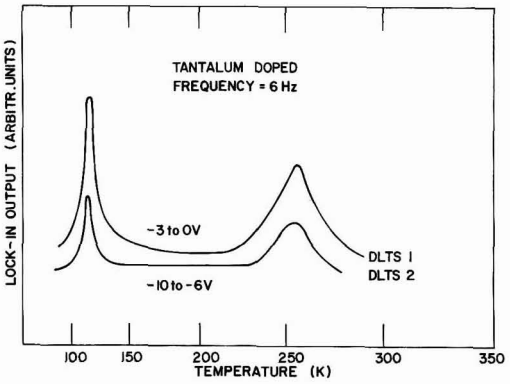

Fig. 4. DLTS spectra of the tantalum-doped diode C-4 of lot 4321, W-8, chip D-4. The spectra were measured at different reverse bias voltages and at different pulse heights.

voltage range the current of the metallurgical junction and of the field-induced junction varies as $V_R^{1/2}$. The current of the metallurgical junction was measured at a gate voltage $V_G = 0$. The current of the field-induced junction was obtained by taking the difference of the currents measured at strong inversion and at $V_G = 0$ (or for weak accumulation). V_R was held at a constant value. The measured current change $I_{FIJ}/(I_{FIJ} + I_{MJ})$ at $V_R = -1V$ is 23.2%. Assuming that the leakage is caused by the near midgap center, a similar change in the height of the DLTS peak should be expected. The DLTS spectra are shown in the insert of Fig. 5. The observed change in the amplitude of the signals is 22.2%. This is in excellent agreement with the above value. It should be mentioned that none of the observed soft leakage currents of gate-controlled diodes could be accounted for by surface generation-recombination centers. The surface recombination velocity s_0 of the diodes investigated ranged from 5 to 100 cm/sec.

In the usual treatment of junction leakage it is assumed that the entire contribution of SRH leakage comes from the depletion region which is associated with the lighter doped side of a junction. In practical cases, however, there is a nonzero depletion width which extends into the more heavily doped side of a junction. An indication that SRH centers lying in the p^+ regions contribute to diode leakage was obtained for copper-doped diodes. Figure 6 shows the DLTS spectra of a copper-doped diode and of a MOS capacitor lying adjacent to the diode. (Copper was filament

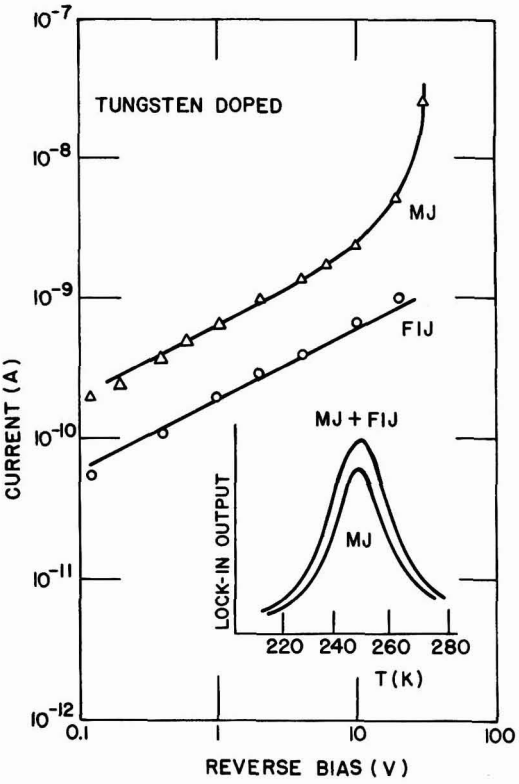

Fig. 5. I-V_R characteristics of the tungsten-doped diode D-1 of lot 4521, W-7, chip G-17. The insert shows the near midgap DLTS spectra for gate voltages $V_G = 0$ (designated as MJ) and for $V_G = -100V$ (designated as MJ + FIJ), respectively.

evaporated on the backs of the wafers and diffused at 1050°C in N_2 for 2 hr. The wafers were then fast pulled to room temperature.) Three peaks are discernible for the p^+n junction. Only one peak is obtained for the MOS capacitor. The increase of the signal of the MOS capacitor spectrum above 200°K is due to the fact that at the temperature where reemission of the trapped electrons would occur, thermal bulk and/or surface generation of minority carriers can invalidate the deep

Table I. Deep energy levels in silicon

Impurity	This work* (DLTS)	A. G. Milnes (15)**		
Au	0.55(c)	0.54(c) 0.35(v)	0.54(c) 0.35(v)	0.30(c) 0.83(v)
Fe	0.57(c)	0.40(v)	0.55(c) 0.40(v)	0.14(c) 0.51(c) 0.40(v)
Cu	0.20(c) 0.49(v)) or process in- 0.41(v)) duced, (c)?	0.52(v) 0.37(v) 0.24(v)	0.52(v) 0.37(v) 0.24(v)	0.26(c) 0.53(v) 0.40(v)
Ni	0.19(c) 0.36(c)	0.35(c) 0.23(v)	0.35(c) 0.22(v)	
Ta	0.21(c)	<0.14(c) 0.43(c)		
W	0.25(c) 0.28(c)	0.22(c) 0.30(c) 0.37(c) 0.34(v) 0.31(v)		

* Measurements by DLTS methods.
** Conventional techniques and surface capacitance studies.
(c) Measured from the conduction bandedge.
(v) Measured from the valence bandedge.

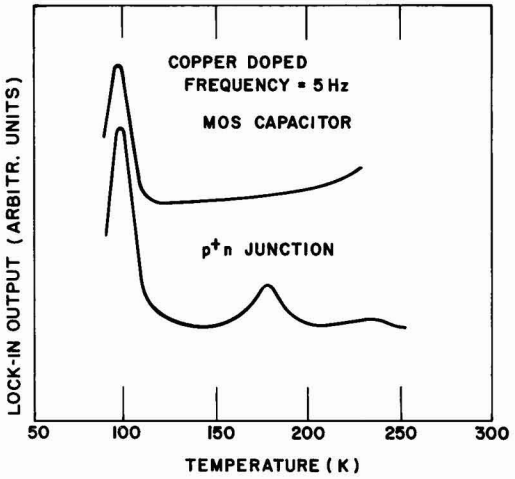

Fig. 6. DLTS spectra of the MOS capacitor C-3 and p+n junction C-4 of lot 5173, chip M-15. The wafer was doped with copper.

depletion condition by forming an inversion layer near the insulator-semiconductor interface. The two extra signals in the diode spectrum could also be process-induced defects (3, 14), but since the measured energy values are close to the published values for copper (see Table I), it is believed that these signals come from generation centers which are located in the more heavily doped p region. In principle, soft leakage currents could be explained by assuming a highly nonuniform distribution of SRH centers in the p^+ region. However, the experimentally observed temperature-independent current component does not agree with the exponentially dependent temperature dependence of the emission rates of SRH centers. It should be mentioned that for the chosen biasing conditions of the DLTS measurements (no minority carrier injection), only traps lying in the upper half of the bandgap can be observed with p^+n junction structures, assuming that the signals come from the more lightly doped side of the junction. For n^+p diodes and the same assumptions, only traps lying in the lower half of the bandgap can be detected. Therefore, the energy values of the additional signals coming from the p region of the p^+n diodes have to be measured from the valence band. Table I summarizes the energy values obtained by the DLTS method and compares them to published values (15).

Summary

The effects of impurities such as gold, iron, copper, nickel, tantalum, and tungsten on junction reverse *I-V* characteristics were investigated. In all cases, excluding gold, the reverse *I-V* characteristics consisted of two components; a normal Shockley-Read-Hall (SRH) generation component and a soft leakage component which dominates the SRH component above a given onset voltage. Only the SRH component can be detected with the DLTS and TSCAP methods. In many cases, when the soft leakage component dominated over almost the entire voltage range, only weak DLTS signals were observed ($N_t \simeq 10^{11}$-10^{13} cm^{-3}). In none of the cases investigated could soft leakage currents be associated with SRH centers. They were ascribed to the presence of impurity precipitates lying near the metallurgical junction of the devices. These currents, measured at 80°K, were fitted to a tunneling or field-emission model. It was found that the onset voltage of the soft leakage current depends on the magnitude of the field-enhancement factors and on the magnitude of the SRH component. Assuming that the precipitates are in the form of prolate spheroids and other conditions with regard to their position within a junction, information about the geometry (sphere-like to needle-like) could be obtained from the field-enhancement factors. Local electric fields of the order of 10^6-10^7 V/cm were obtained by this analysis.

DLTS measurements were used to obtain the distribution of the SRH centers within the active region of the devices by employing gate-controlled diode structures and MOS-capacitor structures. Activation energies of the emission rates of electrons and, in some cases, of holes, were measured. Hole emission was observed from impurities lying in the heavily doped p regions of the junctions.

It is expected that soft leakage currents will arise whenever conditions exist in fabrication where impurities are introduced in quantities exceeding the solid solubility at temperatures where sufficient impurity mobility permits precipitation. Clearly, the nature of impurity introduction, stresses, kinetics of precipitation, density, and location of nucleation sites will influence the effects of a given precipitate on junction leakage. For these reasons it has not been possible to systematically determine the relative effects of various contaminants with respect to precipitate-induced leakage.

Acknowledgments

Certain individuals and institutions contributed to the completion of this work. Numerous discussions pertaining to the DLTS and TSCAP measurements with D. V. Lang, L. C. Kimerling (both of Bell Laboratories, Murray Hill, New Jersey) and M. G. Buehler (National Bureau of Standards, Gaithersburg, Maryland) are sincerely appreciated. Thanks go to the staff members of Department 9133 and to the personnel of the Microelectronic Model Shop and the production MOS facility. Thanks are also due to C. Allen, S. Ostrowski, and V. Kosmas for their special packaging efforts.

Manuscript submitted July 13, 1976; revised manuscript received May 16, 1977. This was Paper 127 presented at the Washington, D.C., Meeting of the Society, May 2-7, 1976.

Any discussion of this paper will appear in a Discussion Section to be published in the June 1978 JOURNAL. All discussions for the June 1978 Discussion Section should be submitted by Feb. 1, 1978.

Publication costs of this article were assisted by Teletype Corporation.

REFERENCES

1. R. N. Hall, *Phys. Rev.*, **83**, 228 (1951), **87**, 387 (1952). W. Shockley and W. T. Read, Jr.; *ibid.*, **87**, 835 (1952).
2. M. G. Buehler, *Solid-State Electron.*, **15**, 69 (1972).
3. C. T. Sah and C. T. Wang, *J. Appl. Phys.*, **46**, 1767 (1975).
4. D. V. Lang, *ibid.*, **45**, 3014, 3023 (1974).
5. L. D. Yau and C. T. Sah, *Solid-State Electron.*, **17**, 193 (1974).
6. H. Sue and H. A. Waggener, Paper 108 presented at The Electrochemical Society Meeting, Washington, D.C., May 2-7, 1976.
7. A. Goetzberger and W. Shockley, *J. Appl. Phys.*, **31**, 1821 (1960).
8. S. M. Sze, "Physics of Semiconductor Devices," Chapter 2, Wiley-Interscience (1969).
9. R. H. Good and E. W. Müller, "Handbuch der Physik," 21, 176 (1956).
10. I. Brodie, *J. Appl. Phys.*, **35**, 2324 (1964).
11. A. S. Grove, "Physics and Technology of Semiconductor Devices," Chapter 6, John Wiley & Sons, Inc., New York (1967).
12. Oleg D. Jefimenko, "Electricity and Magnetism," Chapter VIII, Appleton-Century-Crofts, New York (1966).
13. J. L. Moll, "Physics of Semiconductors," p. 253, McGraw-Hill Book Co., New York (1964).
14. M. G. Buehler, in "Semiconductor Silicon 1973," H. R. Huff and R. R. Burgess, Editors, p. 549, The Electrochemical Society Softbound Symposium Series, Princeton, N.J. (1973).
15. A. G. Milnes, "Deep Impurities in Silicon," p. 14, John Wiley & Sons, New York (1973)

Properties of CdS Films Prepared by Spray Pyrolysis

Yale Y. Ma[1] and Richard H. Bube*

Department of Materials Science and Engineering, Stanford University, Stanford, California 94305

ABSTRACT

A detailed investigation has been made of the properties of CdS films deposited on amorphous glass substrates by the technique of spray pyrolysis. The variation of the electrical transport properties of these films as a function of substrate temperature has been correlated with variations in orientation, cubic/hexagonal phase ratio, and morphology. Additional effects of cooling rate, spraying rate, heat-treatment in hydrogen, and variations in substrate are also considered. By heat-treatment in hydrogen it is possible to produce films on amorphous glass substrates with an electron density in excess of 10^{18} cm^{-3} and an electron mobility of 90 cm^2/V-sec at 300°K.

The method of spray pyrolysis (or solution spraying) is a convenient and economical method for the deposition of materials suitable for this technique. The production of CdS films by spraying a solution of $CdCl_2$ and thiourea was described by Chamberlin and Skarman (1) following a patent by Hill and Chamberlin (2). The electrical properties of films produced by spray pyrolysis (SP) have been investigated by Micheletti and Mark (3), and by Wu and Bube (4). Solar cells have been produced by the deposition of n-CdS films by SP on p-CdTe single crystal substrates with a solar efficiency of over 6% (5), and SP films of n-CdS are also being used in p-Cu_2S/n-CdS heterojunctions for solar energy conversion (6). The SP technique is convenient for the deposition of ternaries involving sulfides and selenides, and the properties of CdS_xSe_{1-x} and $Zn_xCd_{1-x}S$ films prepared by this method have been described (7).

There is therefore ample motivation to understand the deposition of CdS films by the SP technique. We report here the results of a detailed investigation of the preparation and properties of such films as a function of substrate temperature, cooling rate, spraying rate, postdeposition heat-treatment in hydrogen, and choice of a substrate. By combining measurements of film orientation, cubic/hexagonal phase ratio, morphology, and optical transmission with analysis of electrical transport through thermoelectric and photothermoelectric measurements, it is possible to define some of the correlations between structure and electrical properties of these films.

Preparation of Films

All the films prepared in this paper were prepared by spraying an equimolar (0.1M) solution of $CdCl_2$ and thiourea onto a heated substrate. The solution was sprayed by an atomizer spray nozzle and the liquid spray rate was controlled by a flow meter and the air pressure applied to the nozzle. After the solution is sprayed onto the substrate, thermal decomposition of the complex ion $Cd(CN_2H_4S)_2Cl_2$ takes place, and uniform CdS films are grown on the substrate.

For most of the experiments described in this paper, amorphous glass substrates were used. In order to have a systematic investigation of the effect of substrate temperature on the properties of the films, a series of CdS films was prepared with all the parameters fixed except the substrate temperature. The spray rate used was fixed at 4.2 cm^3/min, and the films were removed from the substrate heater immediately after deposition of a 2 μm thick film. Subsequent portions of the investigation involved using crystalline substrates, changing the spraying rate, or allowing the films to cool slowly on the substrate heater. All spraying was done under air pressure and in an air environment.

It is well known that the electrical properties of CdS films prepared by SP can be affected by chemisorbed oxygen (3, 4). Our previous work, however, has shown that heat-treatment in air lowers the conductivity compared to an as-deposited film, and that subsequent heat-treatment in vacuum restores the conductivity to approximately the same as the as-deposited condition (4). Measurements reported here are primarily on as-deposited films, rapidly cooled and without subsequent heat-treatment in air, and measured by thermoelectric power in 10^{-5} Torr vacuum. For such films oxygen adsorption effects should be minimized.

Effect of Substrate Temperature

A series of films was deposited for substrate temperatures between 320° and 570°C. The room temperature electrical conductivity of these films is shown in Fig. 1a. The dark conductivity is a striking function of substrate temperature, exhibiting fluctuations by three orders of magnitude for differences in substrate temperature of 20°-30°C. Although this conductivity is so strongly temperature dependent, it is still possible to

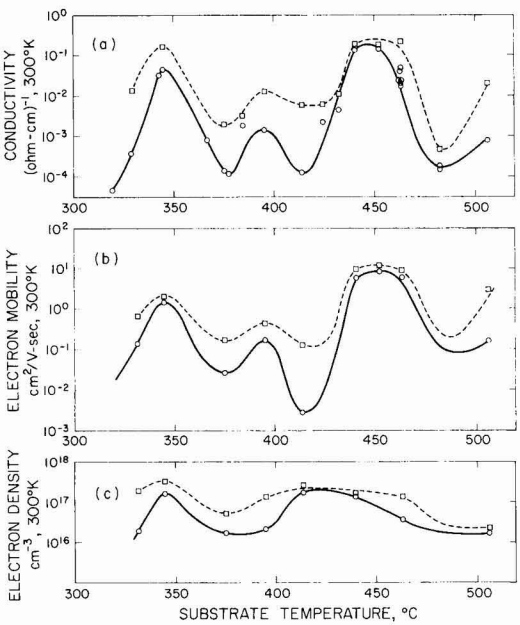

Fig. 1. Dependence of electrical conductivity, electron density, and electron mobility at 300°K on the substrate temperature during CdS film deposition. Solid curves are in dark; dashed curves are under illumination.

* Electrochemical Society Active Member.

[1] Present address: Optical Coating Laboratory, Inc., Santa Rosa, California 95400.

Key words: cadmium sulfide, films, spray pyrolysis, solution spraying, transport in films, thermoelectric power of films.

prepare highly reproducible films by carefully controlling substrate temperature, spraying rate, film thickness, cooling rate, etc. Most of the maximum and minimum conductivity points of Fig. 1a have been repeated several times in order to establish that the variations shown are not the consequence of uncontrolled preparation variables. Films prepared at 461°C, for example, have been repeated many times under the same spraying conditions; the reproducibility in conductivity in these films is within a factor of two.

In order to determine the relative contributions to these conductivity variations by changes in electron density and electron mobility, thermoelectric power measurements were made as a function of temperature in the dark and under photoexcitation. Samples subjected to this measurement were mounted on a sample holder, which consisted of two aluminum strips with heaters inserted into each strip. The heaters were used not only to heat the sample above room temperature, but also to establish a temperature gradient across the sample. Cooling of the sample below room temperature was controlled by a Joule-Thomson cryotip system. The temperature gradient and the thermoelectric voltage were measured by thermocouples and electrical leads mounted at the ends of the sample. The electron density n and the electron mobility μ of the CdS films were calculated from the equations

$$\alpha = -\frac{k}{e}[A + \ln(N_c/n)] \qquad [1]$$

$$\mu = \sigma/ne \qquad [2]$$

where α is the thermoelectric power obtained from the slope of the thermoelectric voltage *vs.* temperature gradient curve at each sample temperature, A is a constant taken equal to 2.5 for CdS (4), N_c is the effective density of states in the conduction band, and σ is the measured conductivity of the film.

The variation of the measured electron mobility at 300°K as a function of substrate temperature during deposition is given in Fig. 1b, and the variation of the electron density at 300°K in Fig. 1c. It is evident that the dependence of the electron mobility on substrate temperature is the determining factor in the dependence of the electrical conductivity on substrate temperature. All of the films have relatively high electron densities because of chlorine donors incorporated during preparation from the $CdCl_2$.

Typical light and dark electron density and mobility values as a function of temperature are shown in Fig. 2 as calculated from thermoelectric power measurements for the 441° and the 507°C samples. For both samples the electron density is relatively independent of temperature in both dark and light, as would be expected for totally ionized chlorine donors. The dark electron mobility for both samples is thermally activated with a larger activation energy in the higher temperature range than in the lower, and the activation energies are larger for the lower conductivity 507°C film than for the 441°C film. Under photoexcitation the electron mobility for the 507°C sample ceases to be temperature dependent.

These measured mobility variations can be described at least formally by the fairly universal expression (3 ,4)

$$\mu = \mu_0 \exp(-\phi/kT) \qquad [3]$$

where ϕ can be physically interpreted as the barrier height to electron transport between grains of the film. A summary of values of ϕ as a function of substrate temperature is given in Fig. 3a, and a summary of values of μ_0 in Fig. 3b. Comparison of Fig. 1b with Fig. 3a shows that large values of mobility are in general associated with small values of barrier height ϕ. The major conductivity maxima near 350° and 450°C are associated with values of ϕ approaching zero.

The higher temperature portion of the mobility curves of Fig. 2 can be interpreted as resulting from thermal excitation over the intergrain barriers, and the lower temperature portion of these curves can be

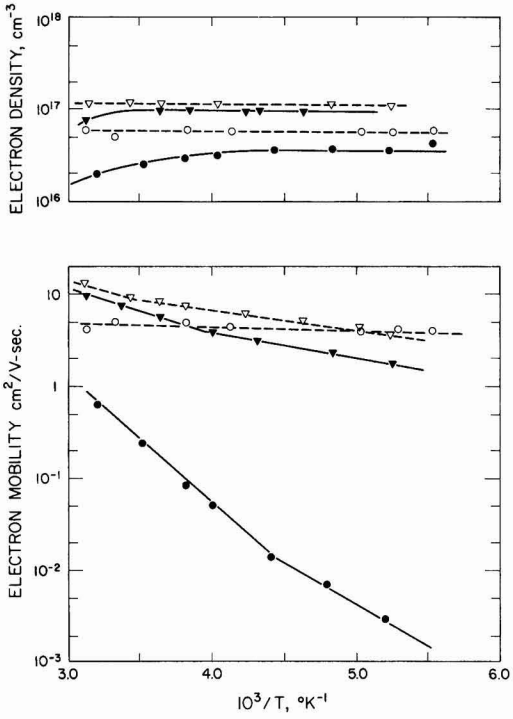

Fig. 2. Temperature dependence of the electron density and electron mobility in CdS films sprayed at 441°C (▼, ▽) and 507°C (●, ○). Solid curves are in dark; dashed curves are under illumination.

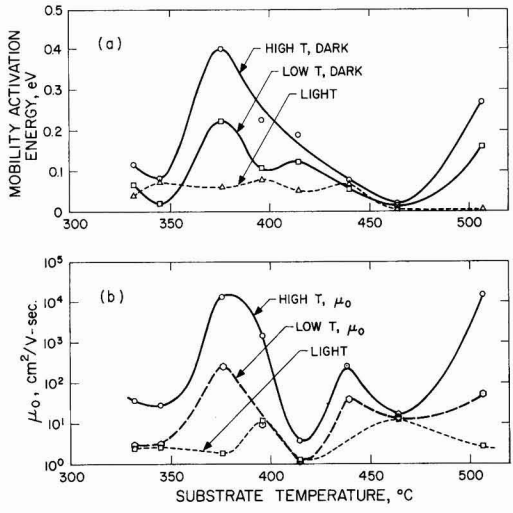

Fig. 3. Values of mobility activation energy ϕ and preexponential term μ_0 as a function of substrate temperature during deposition of CdS films, assuming $\mu = \mu_0 \exp(-\phi/kT)$. Where different values are found at high and low temperatures, both are indicated. Solid curves are in dark; dashed curves are under illumination.

interpreted as caused by thermally assisted tunneling through these intergrain barriers. Under photoexcitation, tunneling without thermal activation dominates in the 507°C film of Fig. 2.

The effect of photoexcitation is to make the variation with substrate temperature less pronounced, in every case causing variations that tend to equalize differences in conductivity, electron density, electron mobility, mobility activation energy, and μ_0 over the whole substrate temperature range explored. Such behavior is consistent with the effect of photoexcitation being both to decrease the barrier height and to enhance tunneling through the barrier, as previously reported (3, 4).

A correlation between the physical properties of the various films produced at different substrate temperatures and these electrical transport properties has been sought with results described as follows.

Orientation effects.—The structure of these films was analyzed by x-ray diffraction techniques. The preferred orientation of the films was determined by using the modified Debye-Scherrer x-ray camera (8) for qualitative analysis, to be compared with the quantitative data obtained from diffractometer patterns. These diffractometer patterns indicate that for substrate temperatures between 322° and 414°C, (11,2) and (10,1) reflections increase in intensity with substrate temperature, whereas (00,2) reflections decrease. Above 441°C the reverse trend is seen with (00,2) reflections increasing and (11,2) and (10,1) decreasing. The Debye-Scherrer patterns of films prepared below 350°C show uniform intensity in (00,2), (11,2), and (10,1) reflections, indicating that the crystallites in the films are randomly oriented. Preferred orientation occurs in the films deposited above 350°C, the degree of preferred orientation depending on the substrate temperature during deposition.

The intensities of the major x-ray reflections, I(10,1), I(00,2), and I(11,2), measured from diffractometer patterns, are plotted as a function of substrate temperature, and are compared with the electrical conductivity of the films, in Fig. 4. It is convenient to divide the temperature range into four regions as indicated. Orientation effects appear to be strongly correlated with conductivity variations in regions II, III, and IV. Between 400° and 483°C, the variation of the conductivity is similar to the variation of the I(10,1), and almost exactly inverse to the variation of I(11,2). In region II between 346° and 376°C, it can be speculated that the inverse variation of conductivity according to I(11,2) dominates over the direct variation according to I (10,1) because of the larger variation of the former with substrate temperature. In region IV, only the (00,2) orientation remains at 507°C; in this range the presence of the cubic phase also affects the conductivity, as described in the following section.

Cubic-hexagonal phase ratio.—CdS can exist in an hexagonal (wurtzite) structure or in either zincblende or rocksalt cubic structures. Cubic phases may be expected in films produced by SP for two reasons: The cubic phase is stable below about 400°C, and may therefore be expected in the films prepared with lower substrate temperatures; and the fast-cooling process can induce stacking faults with cubic structure because of the difference in thermal expansion coefficients of the CdS and the substrate. Such stress-induced stacking faults have been found in the films by observation of the (220) rocksalt cubic reflection in the x-ray diffractometer patterns for films prepared at 397°, 414°, 483°, and 490°C. These rocksalt reflections can also be observed in the modified Debye-Scherrer patterns. The probability of finding the zincblende structure reflections in the diffraction patterns is small since most of the zincblende reflections are superimposed on reflections of the hexagonal hcp phase.

The proportionality of hexagonal hcp phase in the films, called "hexagonality" H, can be calculated from the intensity ratio R of (10,1) to (00,2) reflections in the x-ray pattern, according to

$$H(\%) = \frac{15.9R - 8.1}{13.5R + 25.1} + \frac{33.2 - 2.5R}{32.5 + 71.2R} \qquad [4]$$

This equation was derived by following the suggestions of Smith (9) and Short and Steward (10) in their derivations of the proportion of cubic phase in ZnS and CdS powders. The constants in Eq. [4] are calculated by using the x-ray diffractometer patterns of the SP

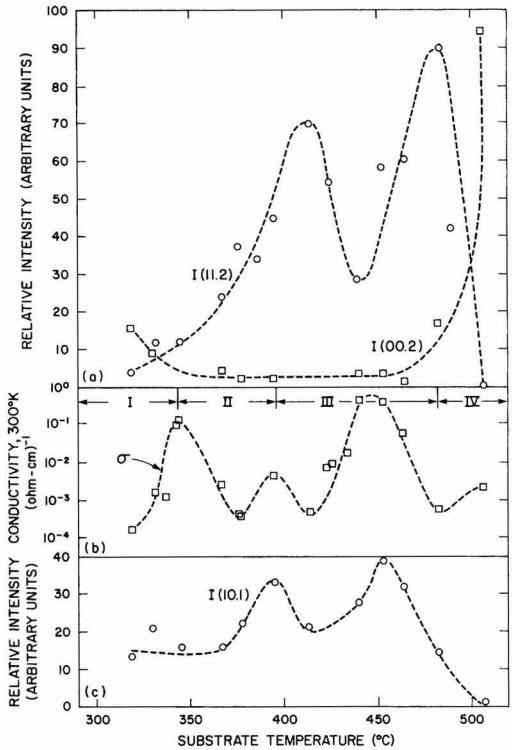

Fig. 4. Relative intensity of (11,2), (10,1), and (00,2) reflections in films of CdS as a function of the substrate temperature during deposition, compared with the electrical conductivity variation with substrate temperature.

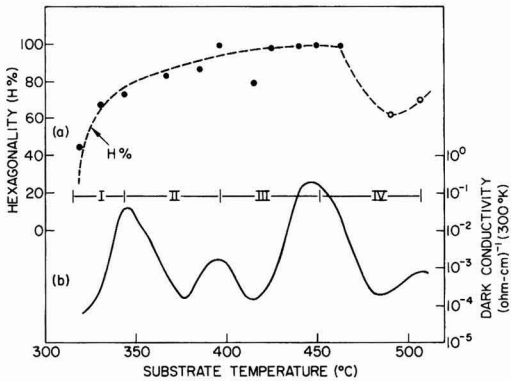

Fig. 5. Hexagonality (as defined in Eq. [4]) as a function of substrate temperature during deposition of CdS films, compared with the electrical conductivity variation with substrate temperature.

films prepared from 322° to 507°C. Detailed derivation of the equation is given elsewhere (11).

Values of H from Eq. [4] are plotted in Fig. 5 as a function of the substrate temperature. In the range of substrate temperatures between 322° and 346°C, H increases from 46 to 71%. Since there is no large change in crystallite orientation in this region the increase of conductivity appears to be associated with this change in phase composition. In region IV, the decrease of conductivity is again associated with an increase in cubic phase. Since the 507°C films are highly oriented in the (00,2) direction, the energy required to generate stacking faults in the close-packed (00,2) plane is small, and thermal or internal stress in the film can generate large proportions of cubic phase.

Surface morphology.—The surface morphology of films prepared at different substrate temperatures was investigated by TEM replica techniques. Figure 6 shows photographs of the surface microreliefs of films prepared at four different substrate temperatures, with different values of H. For the films prepared at 397° and 441°C, for which $H \sim 100\%$, the microreliefs show distinct grains with uniform size. For the films prepared at 332° and 507°C, however, with appreciable proportions of the cubic phase, the microreliefs show a range of grain sizes from less than 0.1 μm to 0.5-0.9 μm. By comparing the electron diffraction patterns of evaporated CdS films to x-ray diffraction patterns of the same samples, Shalimova *et al.* (12) and Galkin *et al.* (13) discovered that the larger grains were hexagonal, while the smaller grains were a mixture of cubic and hexagonal phases. The microreliefs of Fig. 6 are consistent, therefore, with the conclusion that relatively high proportions of the cubic phase are present even at the higher substrate temperature of 507°C.

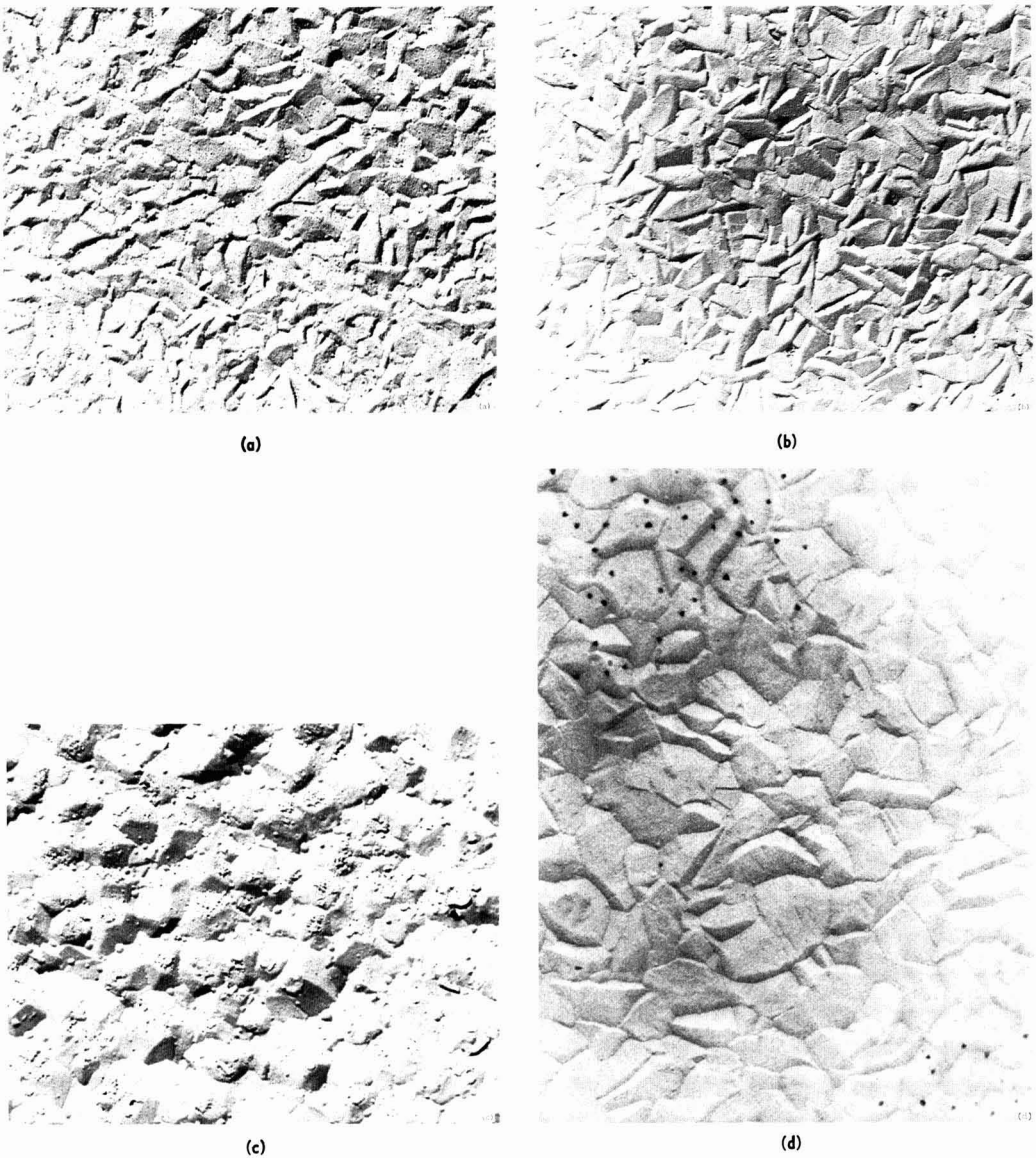

Fig. 6. TEM microreliefs showing surface morphology of CdS films deposited on substrates at (a) 332°C, (b) 397°C, (c) 507°C, and (d) 441°C. Magnification: X44,000.

Optical transmission.—Optical transmission measurements as a function of substrate temperature are summarized in Fig. 7. The film prepared at 332°C has the lowest optical transmittance as well as the lowest electrical conductvviity. Auger analysis (14) of this film shows a high concentration of chlorine inside the film, which may contribute to the low optical transmission. Alisoukas *et al.* (15) have also reported that the spectral distribution of photoconducting CdS sintered layers depends on the concentration of $CdCl_2$ used in the sintering and on the sintering temperature. The highest values of optical transmission are for the films prepared at 441° and 451°C, which also exhibit the highest values of electrical conductivity.

Effect of Cooling Rate

The effect of cooling rate was investigated for films prepared at 461°C. One sample was fast-cooled as described above, a second sample was cooled slowly from 461° to 100°C in 80 min, and a third was cooled slowly from 461° to 100°C in 115 min.

Figure 8 compares the electron density and mobility as a function of temperature for these three samples. The slower cooling decreases both the electron density and the mobility compared to the faster cooling, and increases the intergrain barrier height as determined from the mobility activation energy.

X-ray diffraction patterns indicate that the slow-cooled films have a reduced intensity for the (11,2) and (10,1) reflection, and an increase in the intensity of (00,2) reflections, indicating growth of (00,2) crystallites at the expense of others during slow cooling. Since the slow-cooled samples were exposed to air during the long period of cooling, it is likely that the slow-cooling procedure is equivalent to an air bake, causing the chemisorption of oxygen as discussed in the previous section on preparation of films, with related decrease in electron density and increase in intergrain barrier heights.

Effect of Spray Rate

Sensitivity of film properties to the spray rate appears to vary critically with substrate temperature. At 322°C, for example, the conductivity is relatively independent of changes in spray rate from 1.6 to 8.4 cm^3/min. At 464°C, the effect is small but detectable; a variation in the spray rate from 4.2 to 10.3 cm^3/min produced a decrease in conductivity by a factor of four, attributable to a decrease in mobility by a factor of four because of an increase in the barrier height between grains from 0.016 to 0.049 eV. At 346°C, however, the effect of spraying rate is very strong; the conductivity increases from 5.8×10^{-5} to 6×10^{-2} $(\Omega\text{-cm})^{-1}$ as the spray rate is increased from 1.6 to 4.0 cm^3/min, and then decreases again to 4.7×10^{-6} $(\Omega\text{-cm})^{-1}$ as the spray rate is increased further to 8.3 cm^3/min.

The major effect of a fast spraying rate is to introduce defects, such as stacking faults, dislocations, and vacancies into the films. Since 350°C is reported to be the phase transition temperature from cubic CdS to hcp (16), these defects generated by the fast spraying rate may increase the internal stress in the films and hence affect the phase transformation, particularly for films deposited at 346°C, close to this critical temperature. The hexagonality for these films shows a dramatic decrease from 83 to 43% as the spray rate is increased from 4.0 to 8.3 cm^3/min. Increased spray rate also causes a decrease in grain size observed in TEM micrographs, and a slight peak broadening in x-ray diffraction patterns indicating decreased crystallinity.

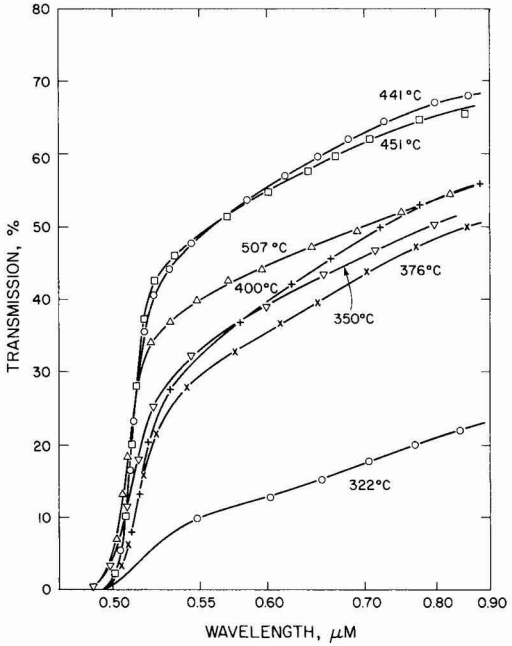

Fig. 7. Optical transmission of CdS films for various substrate temperatures during deposition.

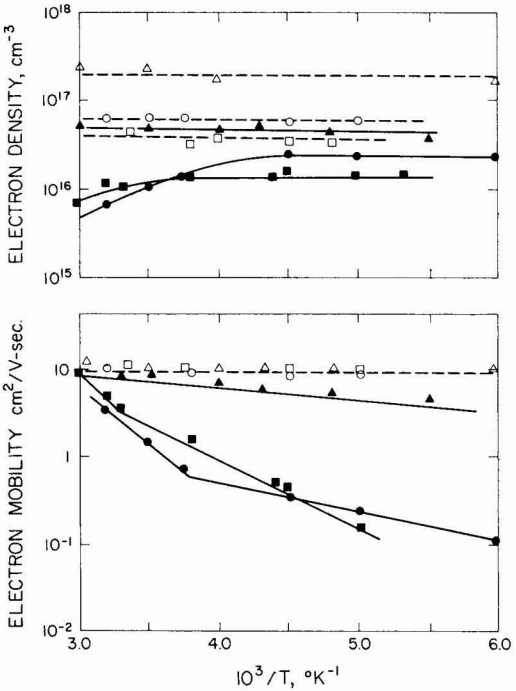

Fig. 8. Temperature dependence of the electron density and the electron mobility of CdS films deposited at a substrate temperature of 461°C for a fast-cooled sample (▲, △), and two slow-cooled samples (●, ○) and (■, □). Solid curves are in the dark; dashed curves are under illumination.

Effect of Heat-Treatment in Hydrogen

Heat-treatment of SP CdS films after deposition can increase their conductivity by as much as three orders of magnitude. The results of thermoelectric power measurements on films prepared under the same conditions with and without heat-treatment are given in Fig. 9. After 5 min heat-treatment in H_2 at 400°C, the films become partially degenerate with an electron

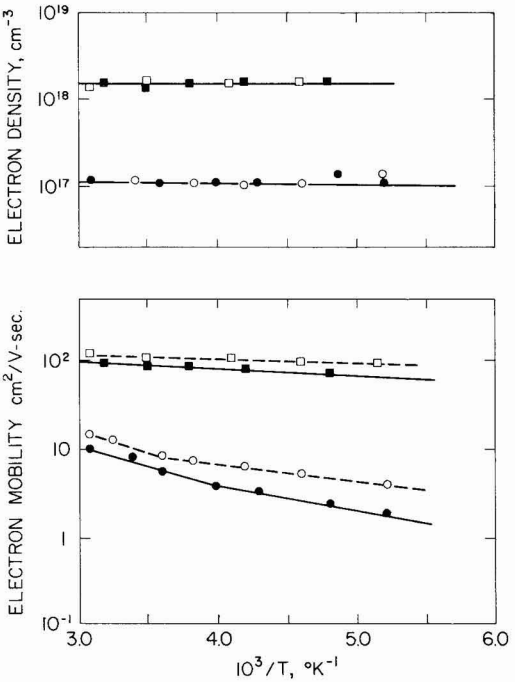

Fig. 9. Temperature dependence of the electron density and the electron mobility of CdS films before and after heat-treatment in H_2 for 5 min at 400°C. Before heat-treatment (●, ○), and after heat-treatment (■, □). Solid curves are in the dark; dashed curves are under illumination. No effects of illumination on the electron density are observed in these films.

density of 1.5×10^{18} cm^{-3}. The electron mobility is also increased by about an order of magnitude to a value of 90 cm^2/V-sec in the dark at 300°K. The dark mobility activation energy decreases from 0.083 eV to 0.015 eV as a consequence of the H_2 heat-treatment. X-ray diffraction patterns indicate both a growth in crystallites with the same orientation as in the non-heated film, and a growth of certain orientations at the expense of others. Heat-treatment in hydrogen is also expected to increase the nonstoichiometry of the film, producing excess cadmium donors, increasing the free electron density in the grains, and reducing intergrain barrier heights. Heat-treatment in H_2 should also remove any vestige of chemisorbed oxygen with similar consequences.

Effect of Substrates

A very limited survey was made of the electrical properties of CdS films deposited on a variety of crystalline substrates, to compare with those prepared on amorphous substrates and described at some length above. In this comparison a single deposition temperature of 461°C was used, together with a fixed spraying rate, cooling rate, etc. Substrates chosen included single crystal CdTe with (110) and (111) orientations, single crystal sapphire with (0001) and (1102) orientations, single crystal quartz, and a (100) oriented polycrystalline film of indium-tin oxide.

All of these films deposited on single crystal substrates have a strong (00,2) orientation, indicating that the c-axis of the film is perpendicular to the substrate, regardless of the specific orientation of the substrate. In spite of this difference, the measured 300°K conductivity of the films sprayed at 461°C was about the same on the crystalline substrates as on the amorphous substrates.

The only additional investigation carried out to date has been the preparation of n-CdS/p-CdTe heterojunctions by the SP deposition of CdS films on single crystalline p-CdTe substrates. As described more fully elsewhere (5), SP-deposited CdS films on substrates at 450°C had an as-deposited conductivity of about 10^{-2} $(\Omega\text{-cm})^{-1}$: This conductivity could be increased to 10^2 $(\Omega\text{-cm})^{-1}$ by heating for 5 min in H_2 at 420°C.

Conclusions

The method of spray pyrolysis for the deposition of thin films of materials like CdS is attractive for its technological ease and economy. This investigation shows that the optical and electrical properties of these films can be strongly influenced by substrate temperature, cooling rate, spraying rate, and postdeposition heat-treatments. It is therefore essential to have carefully controlled preparation conditions in order to achieve reproducible high quality films. With such care it is possible to prepare a wide variety of films with 300°K conductivity between 10^{-4} and 10^2 $(\Omega\text{-cm})^{-1}$, corresponding to electron mobilities between 10^{-3} and 10^2 cm^2/V-sec.

Acknowledgment

This research was supported by the National Science Foundation.

Manuscript submitted Feb. 8, 1977; revised manuscript received April 29, 1977.

Any discussion of this paper will appear in a Discussion Section to be published in the June 1978 JOURNAL. All discussions for the June 1978 Discussion Section should be submitted by Feb. 1, 1978.

Publication costs of this article were assisted by Stanford University.

REFERENCES

1. R. R. Chamberlin and J. S. Skarman, *This Journal*, **113**, 86 (1966).
2. J. E. Hill and R. R. Chamberlin, U.S. Pat. 3,148,084 (1964).
3. F. B. Micheletti and P. Mark, *Appl. Phys. Lett.*, **10**, 136 (1967).
4. C. Wu and R. H. Bube, *J. Appl. Phys.*, **45**, 648 (1974).
5. Y. Y. Ma, A. L. Fahrenbruch, and R. H. Bube, *Appl. Phys. Lett.*, **30**, 423 (1977).
6. J. F. Jordan and G. A. Samara, Proceedings of the 2nd ERDA Semiannual Solar Photovoltaic Conversion Program Review, 299 (1976).
7. R. S. Feigelson, A. N'Diaye, S.-Y. Yin, and R. H. Bube, *J. Appl. Phys.*, **48**, 3162 (1977).
8. M. H. Read and C. Altman. *Appl. Phys. Lett.*, **7**, 51 (1965).
9. F. G. Smith, *Am. Mineral.*, **40**, 658 (1955).
10. M. A. Short and E. G. Steward, *Phys. Chem.* **13**, 298 (1957).
11. Y. Y. Ma, Ph.D. dissertation, Stanford University (1977).
12. K. V. Shalimova, A. F. Andrushko, and V. A. Dmitriev, *Sov. Phys. Crystallogr.*, **8**, 618 (1964).
13. B. D. Galkin. N. V. Troitskaya, and R. D. Ivanov, *ibid.*, **12**, 766 (1968).
14. Y. Y. Ma and R. H. Bube, Unpublished.
15. A. Alisoukas, J. Jakimouicius, B. Alksiejunas, and A. Sirvoitis, *Liet. Fiz. Rin. Kimys.*, **13**, 427 (1973).
16. H. Holloway and E. Wilkes, *J. Appl. Phys.*, **39**, 5087 (1968).

Photoelectrolysis of Water with Semiconductor Materials

Micha Tomkiewicz and Jerry M. Woodall*

IBM Thomas J. Watson Research Center, Yorktown Heights, New York 10598

ABSTRACT

In an effort to find a semiconductor electrode with a bandgap in the visible part of the spectrum that can serve in the catalytic photodecomposition of water, different systems were explored. The first was sputtered thin films of wide bandgap semiconductor materials such as TiO_2, SnO_2, Nb_2O_3, Al_2O_3, and Si_3N_4 on low bandgap, n-type semiconductors such as GaAs and GaAlAs. Scanning electron micrographs showed that corrosion is greatly reduced but continues by diffusion of the electrolyte through the film, undermining the film by pit formation in the low bandgap semiconductor. There was no evidence for hole conduction through the film. The second system employed p-type GaP as the cathode and Pt as the anode. It was observed that this cell catalytically photoelectrolyzes water with conversion efficiency of 0.1%. The efficiency of the device is a strong function of crystal orientation, surface treatment, and purity of the crystal. The results are explained in terms of an energy diagram of the entire system. Areas for possible improvement are mentioned.

Photoassisted electrolysis of water using illuminated semiconductor electrodes has been demonstrated recently in several systems (1-14). In order for such devices to make significant contributions in the conversion and storage of solar energy they must meet two criteria. First, it is essential that a significant fraction of the solar radiation be absorbed by the semiconductor and efficiently converted to electrical energy in the form of charge separation. Second, this electrical energy must be converted into chemical energy that can be stored and then used in any required mode. The first reported photoassisted electrolysis by Fujishima and Honda (1) employed n-type TiO_2 as the anode and Pt as the cathode using either a two-compartment or single compartment device. Since then, many other n-type materials have been tried as anodes.

Two other basic configurations have also been studied. In the first one, a p-type semiconductor is used as the cathode and Pt as the anode (15). This is discussed in the last part of this paper. The other configuration employs n-type semiconductor anode and p-type semiconductor cathode (6, 14, 16) with light being absorbed by both semiconductor electrodes. This last configuration seems very attractive at first glance, since it avoids the highly restrictive condition of matching the flatband potential and the bandgap energies with the potentials of both the hydrogen and the oxygen electrodes. However, it appears that the efficiency of such a device is going to be limited to the lower efficiency of the separate electrodes. This is due to a charge imbalance and, hence, a loss which occurs as a result of the different efficiencies of the two electrodes.

In this paper, we describe some experiments in which we attempted to identify semiconductor systems which absorb visible light, photoelectrolyze water, and will not photocorrode. Our experiments involved both n- and p-type semiconductors. We discuss separately devices based on each kind of semiconductor.

n-type materials.—It has been observed that most small bandgap n-type materials (smaller than 3 eV) tend to corrode in a photoelectrolytic cell, whereas some large bandgap n-type semiconductors will photoelectrolyze water and remain stable. Recently, Fe_2O_3 (9) and WO_3 (13), both with bandgaps smaller than 3 eV, have been shown not to photocorrode. A natural consequence of this is to try to coat the low bandgap semiconductor with a thin protecting film to prevent direct contact between the semiconductor and the electrolyte, and thus prevent corrosion (7). At the same time, it was hoped that such a film would not prevent holes from reaching the aqueous interface.

One choice for such a film is a thin, inert, semitransparent metal film. This approach was tried, (17) and the main conclusion was that light was converted to electrical energy by providing a "negative overpotential" (18) to various electrochemical reactions including water electrolysis. The stability of this electrode system was vaguely mentioned and details about testing this aspect were not given. In our opinion the main drawback in this solution is that it does not appear to offer any advantage over the combination of two already well-established techniques, namely, a standard electrolytic cell connected to Schottky diode photovoltaic device. The reported (17) negative overvoltage is well within the capacity of the direct voltage delivery of metal/semiconductor junctions.

Another choice and the device we investigated will be called the semiconductor insulator electrolyte (SIE) device. This device employs a thin film of photoelectrolytically stable insulator or wide bandgap semiconductor on an efficiently solar absorbing material, with the hope that photogenerated holes, created by illuminating the solar absorbing material, can be transported to the electrode-electrolyte interface.

p-type materials.—Photoinduced hydrogen evolution on p-type semiconductor electrodes has been previously observed (19). However, the potential of this phenomenon in solar energy utilization was realized only recently (14-16). In solar-absorbing n-type materials, photogenerated holes are expected to migrate through the interface to interact with water. Instead they usually break up the crystal structure and form the thermodynamically very stable oxygen-metal bonds that will eventually cause dissolution in the electrolyte and corrosion of the surface. If a chemical change is to take place on p-type materials it will be through reduction of the surface by the minority carriers generated in the conduction band. Those reduction products are in most cases less stable than the parent semiconductor, and the electrons have a greater probability of interacting on the semiconductor electrolyte interface without permanent damage to the crystal lattice.

Experimental

A standard three-electrode electrochemical cell was used with a switch to monitor separately the current-potential and the current-voltage curves. The samples, which were usually in the form of thin wafers, were etched and cleaned. An ohmic contact was then applied. Au-In alloy was used for the n-type materials

* Electrochemical Society Active Member.

Key words: photoelectrolysis, semiconductor electrolyte, interface, photocorrosion.

and Zn-Au was used for the p-type samples. The contacts were alloyed at $\sim 400°C$ under a forming gas atmosphere. A copper wire was attached to the ohmic contact with silver epoxy. All the nonilluminated areas were masked with polyvinyl ketone. This mask proved to be resistant to both chemical attack and photochemical degradation. This material maintained also constant density even after prolonged exposure to highly basic or acidic solutions. The sample thus prepared was mounted on a Teflon holder and placed in the cell. A 4 cm^2 platinum sheet was used as the counterelectrode, and calomel electrode was used as reference. The light source was a water filtered 75W xenon lamp. Calibrated neutral density filters were used to change the light intensity. Corning, 300Å bandpass intereference filters were used for the spectral measurements. After each measurement, an Eppley thermopile was placed at the same position as the working electrode to monitor the light intensity.

The SIE devices were prepared by either sputtering the insulator (or the high bandgap semiconductor) on the low bandgap material (TiO_2, Al_2O_3, and Si_3N_4 on GaAs and GaAlAs) or by anodic deposition (SnO_2 and Nb_2O_5 on GaAs). The ohmic contact was made to the low bandgap material. The samples were washed with ethanol and distilled water prior to use.

The bulk GaP wafers used throughout this work were prepared by the liquid encapsulation method (20), cleaned with $HF:HNO_3:H_2O$ in the ratio of 1:3:4, and polish etched by mechanical polish in Br_2-methanol solution. The epitaxial GaP was grown on n-type GaP by liquid phase epitaxy. Orientations were determined by x-ray and doping levels by Hall measurements.

Results and Discussion

SIE devices.—The small bandgap, solar absorbing semiconductors that were studied were n-type GaAs and GaAlAs, and the wide bandgap semiconducting films were SnO_2, Nb_2O_5, Al_2O_3, TiO_2, or Si_3N_4. In all cases except TiO_2, the corrosion, as measured by photocurrent of the low bandgap semiconductors (a few $\mu A/cm^2$ for 500 mW/cm^2 xenon lamp illumination), was reduced by a few orders of magnitude compared with unprotected samples. For TiO_2, the photocurrent was about 100-200 $\mu A/cm^2$. However, corrosion was never completely eliminated. At first we believed that the corrosion was initiated by pinholes in the film which enabled the electrolyte to diffuse through localized spots. Corrosion could then continue through lateral diffusion of the electrolyte. However, optical microscopy revealed that the corrosion sites were not localized around presumed pinholes but were scattered uniformly all across the semiconductor surface. In order to reduce the contribution of pinholes to the corrosion, we took special care to prepare films which were pinhole free. This was done by sputtering multilayers of the films and checking them by SEM at magnifications up to 20,000 times.

After determination that within a 300Å resolution, there were no pinholes, the sample was put in the electrolytic cell and the current-voltage characteristics measured. If oxygen and hydrogen were observed, the system was kept electrolyzing water for a short time. Then the electrode was taken out, washed with distilled water, and examined with SEM. The results at two different magnifications are shown in Fig. 1. These pictures suggest that the corrosion can be explained by a mechanism involving diffusion of some species in the electrolyte through the intact film, which then corrodes the surface underneath the film by forming pits in the low bandgap semiconductor. This occurs while the film above the pit is still intact. Eventually the film forms a bubble above the pit which collapses due to surface pressure with the collapsed film hanging toward the interior of the pit. This finding indicates that more care and sophistication in the deposition of the film are not likely to eliminate this problem. Next, it was determined whether or not photogenerated holes were actually being transported to the electrolyte from the small bandgap material. This was done by comparing the photoinduced electrolytic current, using light with photon energies higher than the bandgap of the insulator film with that produced by photon energies less than the bandgap of the film. Specifically, for a 400Å TiO_2 film on GaAs and GaAlAs a cutoff filter of 480 nm was used to distinguish between direct absorption by the film and charge transport due to absorption of light by the low bandgap semiconductor. We found that except for a small corrosion photocurrent, all the observed photocurrent is produced by direct absorption of light by the film. This does not preclude the possibility that a pair might be found with band matching that will allow minority carriers to diffuse through much thicker films than 400Å.

p-type materials.—Current-potential and current-voltage curves were studied on a number of p-type

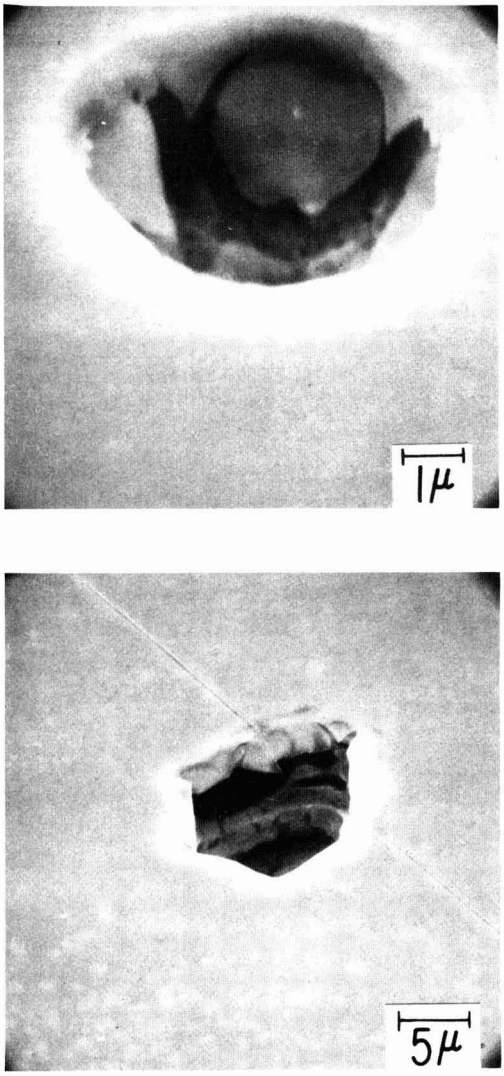

Fig. 1. SEM photomicrograph at two different magnifications of a 400Å TiO_2 film, sputtered on n-type GaAs, after 3 hr of photoelectrolysis in 0.33M phosphate buffer at pH = 7 at an average current density of 0.1 mA/cm^2.

semiconductors which included GaAs, GaAsP, GaP, and InP. It was found that in all cases except GaP the external bias which was needed to start photoelectrolysis exceeded the 'thermoneutral potential' (21), thus making the energy conversion efficiency negative regardless of the generated photocurrent. Only in the case of GaP did we find positive energy conversion efficiency. Thus, this discussion is limited to this semiconductor.

The current voltage behavior of a cell with a p-type $(\bar{1}\bar{1}\bar{1})$ GaP wafer as the cathode and platinum foil as anode in cell with 0.5M Na_2SO_4 + 10^{-2}M NaOH is shown in Fig. 2. When current is flowing through the cell, hydrogen and oxygen could be seen bubbling from the electrode/electrolyte interface for a light intensity as low as 50 mW/cm^2. Figure 2 also shows the conversion efficiency of such a cell when the conversion efficiency is defined as (15)

$$\eta = \frac{I_c \times (1.48 - V) \times 100}{I_a} \quad [1]$$

where I_c is the current flowing in the system, expressed in mA/cm^2, V is the cathodic bias on the GaP electrode, 1.48 is the "thermoneutral potential" (21), and I_a is the intensity of the light incident on the sample, expressed in mW/cm^2.

The current voltage behavior of a GaP (111) wafer from the same crystal is shown in Fig. 3. In this case,

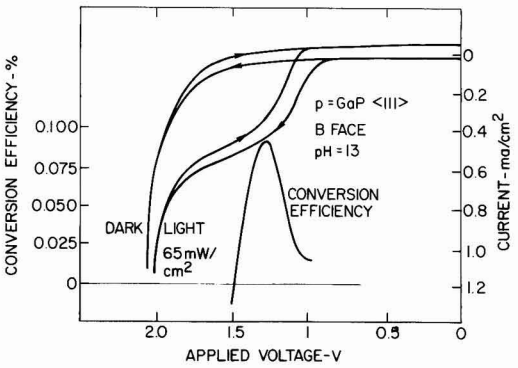

Fig. 2. Current-voltage and conversion-efficiency-voltage diagram for a cell made of Zn-doped GaP $(\bar{1}\bar{1}\bar{1})$ as cathode and Pt foil as the anode. The electrolyte was 10^{-2}M NaOH + 0.5M Na_2SO_4.

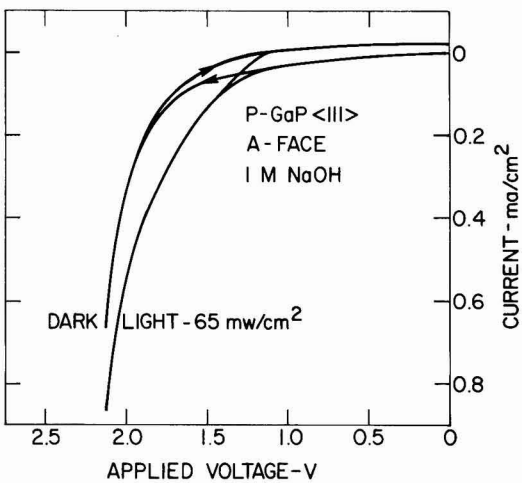

Fig. 3. The same as Fig. 2 except that the (111) surface was exposed. The electrolyte is 1M NaOH.

the bias voltage needed to produce current under illumination is somewhat higher than that needed for $(\bar{1}\bar{1}\bar{1})$ wafers, and, hence, according to Eq. [1], the efficiency will be lower.

The dependence of the light-induced current with light intensity at two different bias conditions is shown in Fig. 4. Above the saturation voltage the current is proportional to the light intensity, while at lower bias the current tends to saturate with light intensity.

Figure 5 shows the spectral response of the quantum efficiency of the photocurrent. The quantum efficiency peaks near 40% at a wavelength which is ~150 nm shorter than the bandgap. We have normalized this spectrum to the condition where only those photons that are absorbed within the first 0.2 μm from the electrolyte interface will lead to charge separation. Any photon that will be absorbed deeper than that will be lost, presumably due to charge recombination. This behavior is not an inherent property of GaP but a very strong function of the particular crystal that is being used.

Figure 6 shows normalized spectrum of two different samples of GaP, one grown by the liquid encapsulation technique and the other epitaxially on GaP. There is a shift of 70 nm in the action spectrum in those two samples. The decline in efficiency at shorter wavelengths is probably caused by increased surface recombination of carriers generated near the surface. If this is so, then the action spectrum should be time dependent, because hydrogen diffusion through the surface is known to have strong effects on the surface recombination rate in semiconductor electrodes (26).

Stability.—The stability of the electrode was checked by passing 100C of electricity through a 1 cm^2 sample

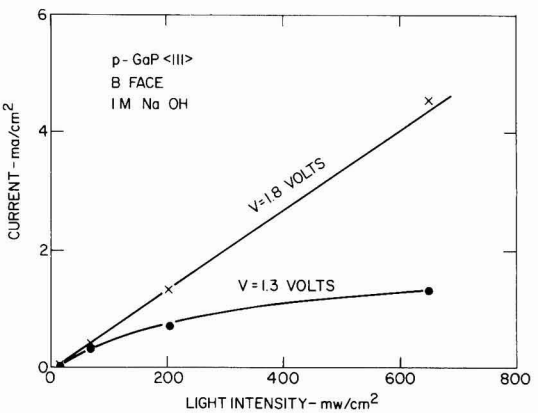

Fig. 4. Dependence of the photocurrent on the light intensity under two different bias conditions.

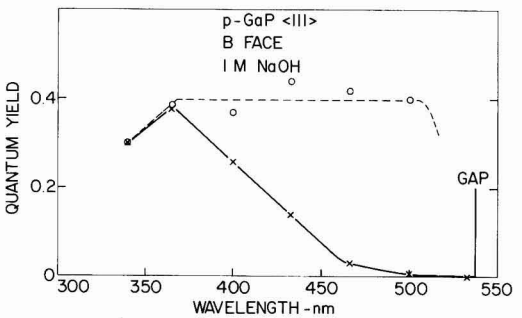

Fig. 5. Solid-line, the spectral response of the quantum yield of the photocurrent; dashed line, calculated spectral response, assuming charge separation in the first 0.2 μm from the electrolyte interface.

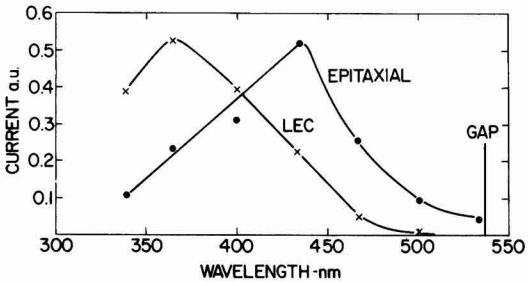

Fig. 6. Normalized spectral response of the photocurrent for two different GaP crystals. One was grown epitaxially on GaP and the other is a liquid encapsulation grown (LEC) wafer.

at an average current density of 5 mA/cm^2 in 0.5M H_2SO_4. Under these conditions the sample did not show any signs of dissolution or corrosion. Optical microscopy did not show any visual change in the surface, and atomic absorption spectroscopy of the electrolyte did not detect any presence of gallium with sensitivity better than 1.5×10^{-7} moles. One additional criterion for the stability of the semiconductor electrode is the stability of the photocurrent with time (14). Figure 7 shows the variation of the photocurrent with time of illumination, under potentiostatic conditions, and under constant bias conditions. It can be seen that under potentiostatic conditions the current is stable, at least for the time period shown here. We found some irregular variations with time over longer periods of illumination. These variations were caused mainly by accumulation of hydrogen bubbles on the electrode. The situation is different when we work under constant bias conditions. The time variation is evident there, but the current could be restored to its original value by turning the light off for a short period of time and then on again. Surface conditions and surface treatment have strong influence on this time behavior. The reversibility of the process indicates that it is not due to any permanent damage to the electrode. The probable cause is formation of surface states due to the hydrogen or metal impurities (22, 23). More studies are needed to explore this important aspect in the performance of the cell.

Energy diagram.—The current potential curve of GaP was measured against standard calomel electrode and agrees with results published earlier (24, 25). The current potential of the platinum electrode was measured and found to be independent of the light. The value of the flatband potential was taken from the work of Memming (24) after correction for the pH. Based on this information, a simplified energy diagram of the cell, under short-circuit conditions and under cathodic bias at the maximum conversion efficiency, was drawn and is shown in Fig. 8. From an examination of Fig. 8,

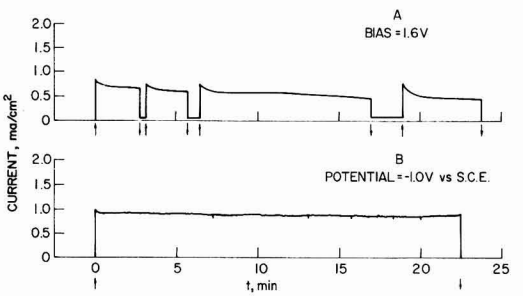

Fig. 7. Variation of the photocurrent with time, at a standard calomel electrode potential of 1.0V. A. under constant bias; B. under potentiostatic conditions. Conditions similar to Fig. 2: ↑ indicates light on; ↓ indicates light off.

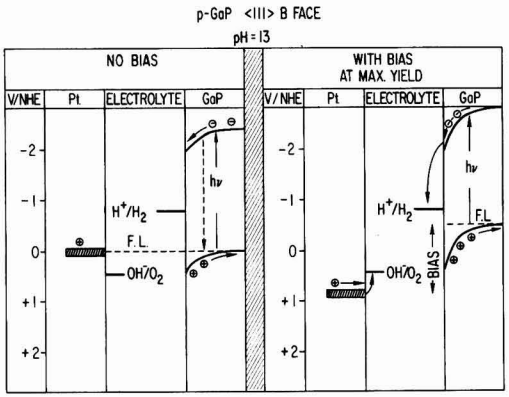

Fig. 8. Energy diagram of the combined cell. All energies are with respect to a standard hydrogen electrode. F.L. is the GaP Fermi Level. 1) under no bias and no photoelectrolysis conditions; 2) under conditions for which the maximum conversion efficiency was obtained.

it appears that the bias which is needed to get the maximum conversion efficiency is divided between the need to raise the potential of the platinum electrode from rest around 0.0V *vs.* a standard hydrogen electrode (SHE) to +0.9V *vs.* SHE. The position of the reversible oxygen electrode is ~ +0.5V *vs.* SHE and the difference is the overvoltage which is required for the evolution of oxygen. This overvoltage could be reduced by platinizing the platinum. The rest of the bias is being applied to increase the band bending of GaP from ~ 0.5V at zero bias to 1V when the light limiting quantum conversion is observed. This relatively high band bending is required to ensure efficient charge separation. A considerable increase in efficiency should be realized if efficient charge separation would occur with smaller band bending.

Conclusions

Two photoelectrolytic devices were discussed in this paper. The first one employed n-type semiconductors as anodes which were embodied in a structure that involved a thin film of insulator or a large bandgap semiconductor, deposited on a solar absorbing n-type wafer. It was shown that in this configuration, even intact films as thick as 400Å could not prevent corrosion of the semiconductor. Furthermore, it was found that these films did not transport charges which were created by absorption of light in the lower bandgap material. It was also shown that p-type semiconductors can serve as stable photocathodes in a photoelectrolytic device. However, among the materials that were studied only p-type GaP showed a positive energy conversion efficiency. The maximum yield that was found was 0.1%. The yield is limited largely by the minority carriers diffusion length and the quality of the crystals used, and by the large overvoltage on the oxygen electrode.

Manuscript submitted Oct. 5, 1976; revised manuscript received May 2, 1977.

Any discussion of this paper will appear in a Discussion Section to be published in the June 1978 JOURNAL. All discussions for the June 1978 Discussion Section should be submitted by Feb. 1, 1978.

Publication costs of this article were assisted by IBM Corporation.

REFERENCES

1. A. Fujishima and K. Honda, *Nature (London)* **238**, 37 (1972).
2. A. Fujishima, K. Kohayakawa, and K. Honda, *This Journal*, **122**, 1437 (1975).

3. M. S. Wrighton, D. S. Ginley, P. T. Wolczanski, A. B. Ellis. D. L. Morse, and A. Linz, *Proc. Nat'l. Acad. Sci. U.S.A.*, **72**, 1518 (1975).
4. M. S. Wrighton, D. L. Morse, A. B. Ellis, D. S. Ginely, and H. B. Abrahamson. *J. Am. Chem. Sco.*, **98**, 44 (1976).
5. A. J. Nozik, *Nature (London)*, **257**, 383 (1975).
6. J. G. Mavroides, D. I. Tchernev, J. A. Kafalas, and D. F. Kolesar, *Mater. Res. Bull.*, **10**, 1023 (1975).
7. P. A. Kohl, S. N. Frank, and A. J. Bard, Submitted to *This Journal*.
8. K. L. Hardee and A. J. Bard, *ibid.*, **122**, 139 (1975).
9. K. L. Hardee and A. J. Bard, *ibid.*, **123**, 1024 (1976).
10. J. Keeney, D. H. Weinstein, and G. M. Haas, *Nature (London)*, **253**, 719 (1975).
11. J. G. Mavroides, J. A. Kafales, and D. F. Kolesar, *Appl. Phys. Lett.*, **28**, 241 (1976).
12. J. H. Carey and B. G. Oliver, *Nature (London)*, **259**, 554 (1976).
13. G. Hodes, D. Cahen, and J. Manassen, *ibid.*, **260**, 312 (1976).
14. H. Yoneyama, H. Sakamoto, and H. Tamura, *Electrochim. Acta*, **20**, 341 (1975).
15. M. Tomkiewicz and J. M. Woodall, 443RNP, *This Journal*, **123**, 189C (1976); To be published.
16. A. J. Nozik, To be published.
17. Y. Nakato, T. Ohnishi, and H. Tsubomura, *Chem. Lett.*, 883-886 (1975).
18. D. Laser and J. Bard, *Chem. Phys. Lett.*, **34**, 605 (1975).
19. A. K. Vijh, "Electrochemistry of Metals and Semiconductors," Chapters 3 and 4, Marcel Dekker Inc., New York (1973).
20. S. E. Blum, R. J. Chicotka, and B. K. Bischoff, *This Journal*, **115**, 324 (1968).
21. D. Gregory, in "The Hydrogen Energy System," p. III-4, prepared for American Gas Association by I.G.T. (1973).
22. P. J. Boddy and W. H. Brattain, *This Journal*, **109**, 812 (1962).
23. A. Many, Y. Goldstein, and N. B. Grover, "Semiconductor Surfaces," North Holland, Amsterdam (1965).
24. R. Memming, *This Journal*, **116**, 785 (1969).
25. R. Memming and H. Tributsch, *J. Phys. Chem.*, **75**, 562 (1971).

Variation of GaAs Epitaxial Growth Rate with Distance along Substrate within a Constant Temperature Zone

J. Komeno, S. Ohkawa, A. Miura, K. Dazai, and O. Ryuzan

Fujitsu Laboratories, Limited, Kamikodanaka 1015, Nakahara, Kawasaki, Japan

ABSTRACT

On the basis of a model which assumes a laminar boundary layer, a rate equation is derived for the vapor phase epitaxial growth of GaAs within a constant temperature zone. The equation can be used to predict the variation of growth rate with distance along the substrate. The predictions of the equation are shown to be in excellent agreement with the experimental results obtained with the open-tube $AsCl_3$-Ga-N_2 system. It is also shown both theoretically and experimentally that the variation of growth rate decreases with increasing gas velocity and also with decreasing substrate temperature, whereas the initial $AsCl_3$ mole fraction has no effect on the growth rate variation.

One of the requirements for many GaAs devices is to prepare epitaxial layers uniform in thickness. Since a vapor phase epitaxial (VPE) growth method for GaAs was first proposed by Effer (1), many investigations have been reported on VPE growth of GaAs (2-6). However, very little has been published on the variation of growth rate with distance along the substrate. It is of considerable importance for preparing uniform thickness epitaxial layers to understand the growth rate at various positions on the substrate. In order to understand this in the case of growth in a graded temperature zone, which is usually employed in the VPE growth of GaAs, it is convenient to investigate the growth rate variation on the substrate in the gas flow direction in a constant temperature zone.

In the present study, a rate equation for epitaxial growth is obtained from a model based on a laminar boundary layer, and is applied to the calculation of the rate of GaAs epitaxial growth. The epitaxial growth within a constant temperature zone was carried out in the diffusion-limited region using the $AsCl_3$-Ga-N_2 system (7). Good agreement between calculated and experimental values is obtained.

Theory

In the VPE growth of a binary semiconductor, the growth rate, R, can be written as (8, 9)

$$R = [k_s h_g/(k_s + h_g)](C_t/N_1)nM_f \quad [1]$$

where k_s is the surface-reaction rate constant, h_g is the mass transfer coefficient, n is the number of crystal component atoms in a molecule of the rate-limiting reacting species, M_f is the mole fraction of the rate-limiting species, C_t is the total number of molecules per cubic centimeter in the gas, and N_1 is the number of gallium or arsenic atoms incorporated into unit volume of the epitaxial layer. The value of N_1 for GaAs is 2.22×10^{22} cm^{-3}.

The mass transfer coefficient h_g is defined as

$$h_g = D/\delta \quad [2]$$

where D is the diffusion coefficient of the reacting species and δ is the thickness of the boundary layer (9, 10).

Substitution of Eq. [2] into Eq. [1] leads to

$$R = k_s D C_t n M_f/(k_s\delta + D)N_1 \quad [3]$$

Figure 1 shows a schematic diagram of a horizontal reactor with a boundary layer. According to Schlichting (11), the thickness of the boundary layer along a thin flat plate, $\delta(x)$, is given by

$$\delta(x) = 5.0\ (\mu x/\rho V)^{1/2} \quad [4]$$

where x is the distance from the leading edge of the substrate, μ and ρ are the viscosity and density of the

Key words: VPE, binary semiconductor, reacting species, boundary layer, diffusion coefficient.

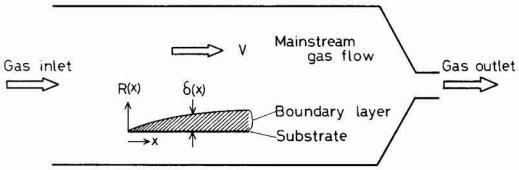

Fig. 1. Schematic diagram of a horizontal reactor with a boundary layer.

gas, respectively, and V is the velocity of the gas outside the boundary layer.

Substitution of Eq. [4] into Eq. [3] yields

$$R(x) = k_s D C_t n M_f / [5.0\, k_s N_1 (\mu x/\rho V)^{1/2} + N_1 D] \quad [5]$$

In order to apply this equation to the actual growth, it is necessary to obtain the temperature dependences of D and k_s.

The temperature dependence of the gaseous diffusion coefficient can be expressed as

$$D_s = D_o (T_s/T_o)^m \quad [6]$$

where T_s and T_o are the substrate temperatures (°K) and 273°K, respectively, D_s and D_o are the diffusion coefficients of the reacting species in nitrogen at T_s and T_o, respectively, and m has a value between 1.75 and 2 (12). In the present study, a value of $m = 2$ is used because most gases diffuse in nitrogen with this m value (13, 14). Thus, Eq. [6] is expressed by

$$D_s = D_o (T_s/T_o)^2 \quad [7]$$

In the low temperature region, the growth rate increases with increasing substrate temperature. This region is identified as a kinetically or surface-reaction limited region where the over-all epitaxial growth rate is limited by some slow surface process (15). In the case of present system, the apparent activation energy measured in the kinetically limited region is about 1.2 eV. Therefore, the surface-reaction rate constant k_s can be written as

$$k_s = A \exp(-1.2\ \text{eV}/kT_s) \quad [8]$$

where A is a frequency factor and k is the Boltzmann constant (9).

Using Eq. [7] and [8], Eq. [5] can be rewritten as

$$R(x) = n M_f K_1 / [(x/V)^{1/2} + K_2] \quad [9]$$

where

$$K_1 = C_t D_o (T_s/T_o)^2 \rho^{1/2}/5.0\, N_1 \mu^{1/2} \quad [10]$$

and

$$K_2 = D_o (T_s/T_o)^2 \rho^{1/2}/5.0\, \mu^{1/2} A \exp(-1.2\ \text{eV}/kT_s) \quad [11]$$

Normalizing $R(x)$ by dividing by the growth rate at the point $x = L$ cm, it follows that

$$R(x)/R(L) = [(L/V)^{1/2} + K_2]/[(x/V)^{1/2} + K_2 \quad [12]$$

Experimental

Figure 2 shows the growth apparatus and the temperature profile used for this series of experiments. The apparatus consists of a quartz reactor tube, a Ga source boat, an $AsCl_3$ bubbler, a substrate holder, and a doping tube. The reactor tube had an inside diameter of 44 mm. The purity of Ga and $AsCl_3$ was seven nines and six nines, respectively. The nitrogen gas was purified by a USD nitrogen purifier.

The temperature of the $AsCl_3$ bubbler was varied from 293° to 303°K. The Ga source temperature was held at 1123°K. Constant temperature growth zones of 973°, 987°, and 998°K were employed in the study. The flow rate of nitrogen through the $AsCl_3$ bubbler was kept to 300 cm³/min, and that of nitrogen through the bypass tube was varied from 300 to 1500 cm³/min. It was confirmed that the nitrogen carrier gas was saturated with $AsCl_3$ for the flow rate of 300 cm³/min.

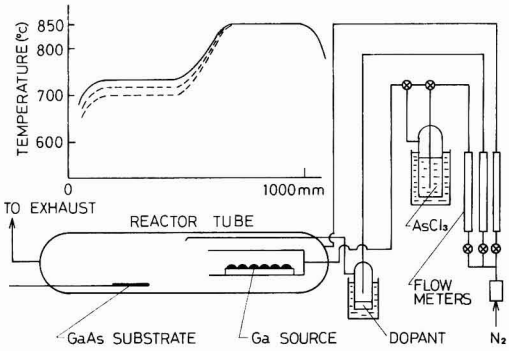

Fig. 2. Schematic diagram of the apparatus and the temperature profile for the epitaxial growth of GaAs.

The substrates used were tellurium-doped GaAs with a resistivity of approximately 2×10^{-3} Ω-cm. Their surfaces were oriented 2° off (100) toward <110>, and the area was 20 × 30 mm. The substrate was placed on a substrate holder in a direction parallel to the gas flow, with a distance between the source and substrate of 20 cm.

The thickness of the grown layer was measured by the infrared interference method (16, 17). The infrared spectrophotometer used was a Beckman IR-18 with a wavelength range of 2.5-16 μm.

Results and Discussion

Diffusion coefficient of reacting species.—In the case of epitaxial growth of GaAs, both gallium- and arsenic-bearing reacting species must arrive at the GaAs surface before the reaction can take place. In the present study, it is assumed that the reacting species bearing both components diffuse through the boundary layer and react at the surface. If, however, one is transported to the surface at a significantly slower rate, it will control the over-all growth rate. Since As_4 is the principal arsenic species and is the largest molecular species in the present GaAs epitaxial growth system, it is reasonable to assume that its diffusion through the boundary layer will be the rate-limiting process. In the present system, GaCl, As_2, and As_4 are considered as the principal reacting species. However, the fluxes of these molecules are in the order

$$F_{GaCl} > F_{As_4} > F_{As_2} \quad [13]$$

over the entire range of growth conditions (18, 19). It is apparent that the process is limited principally by arsenic transport. Thermodynamic considerations (20), however, indicate that F_{As_4} is approximately fifty times as great as F_{As_2} over the range of temperatures employed. Thus, it is reasonable to assume that the over-all growth rate is limited by the process of As_4 diffusion through the boundary layer. Therefore, in order to apply Eq. [9] to the actual growth, the mole fraction of As_4 in the reaction tube must be calculated. The As_4 mole fraction can be calculated from the initial $AsCl_3$ mole fraction; assuming that above approximately 970°K complete reduction of $AsCl_3$ occurs according to the following reaction (20, 21)

$$2AsCl_3 = \tfrac{1}{2}\, As_4 + 3Cl_2 \quad [14]$$

A typical plot of growth rate *vs.* distance along the substrate under a diffusion-limited growth condition is shown in Fig. 3. Values of K_1 and K_2 in Eq. [9] are calculated, by least squares analysis of this plot, to be 7.441×10^{-5} cm/sec$^{1/2}$ and 1.535 sec$^{1/2}$, respectively. The gas viscosity μ and its density ρ at 973°K are taken to be 3.19×10^{-4} g/cm sec and 3.51×10^{-4} g/cm³, respectively (13). Using these values, the diffusion coefficient D_o and the frequency factor A are calculated as follows

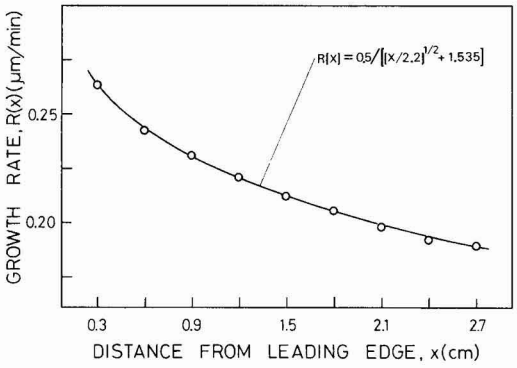

Fig. 3. Growth rate as a function of distance from the leading edge of the substrate. Initial $AsCl_3$ mole fraction 11.20×10^{-3}, growth temperature 973°K, gas velocity 2.2 cm/sec.

$$D_o = 0.083 \text{ cm}^2/\text{sec} \quad \text{and} \quad A = 2.34 \times 10^5 \text{ cm/sec}$$

It is evident that the value of D_o obtained approximately represents the diffusion coefficient of As_4 in nitrogen. On the basis of the molecular weight of As_4, this value of D_o seems reasonable (13, 22).

Effect of initial $AsCl_3$ mole fraction.—Figure 4 shows the experimental and the calculated results of $R(x)/R(0.3)$ *vs.* distance x for different initial $AsCl_3$ mole fractions (M_f) at fixed substrate temperature and gas velocity. Variations in the initial $AsCl_3$ mole fraction were obtained by varying the $AsCl_3$ temperature. As can be seen in the figure, there is good agreement between the experimental results and the curve calculated from Eq. [12].

Figure 4 also shows that the variation of growth rate with distance along the substrate is independent of the initial $AsCl_3$ mole fraction M_f. This is because both mass transfer coefficient h_g and surface-reaction rate constant k_s are independent of M_f, since the thickness of the boundary layer is insensitive to variations in M_f, as is evident from Eq. [4]. However, it should be noted here that according to Eq. [9], the growth rate is proportional to the initial $AsCl_3$ mole fraction.

Effect of gas velocity.—The experimental and the calculated results of $R(x)/R(0.3)$ *vs.* x for different gas velocities (V) at a fixed substrate temperature are shown in Fig. 5. The gas velocity was varied by changing the bypass flow so that the efficiency of source

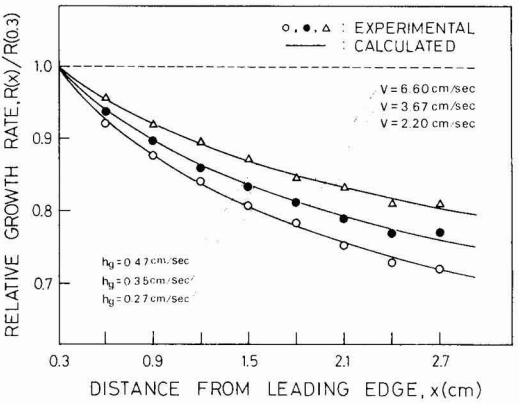

Fig. 5. Comparison of calculated and experimental results of $R(x)/R(0.3)$ as a function of distance from the leading edge of the substrate for different gas velocities (V). Growth temperature 973°K.

reaction did not change. Also given in the figure are the values of h_g at $x = 1.5$ cm for each gas velocity and, as can be clearly seen, there is good agreement between the experimental results and the predictions of Eq. [12].

Figure 5 also reveals that the variation of growth rate along the substrate decreases as the gas velocity is increased. This can be explained by the fact that the mass transfer coefficient h_g increases in proportion to the square root of the gas velocity, which is evident from Eq. [2] and [4], while the surface-reaction rate constant k_s is independent of the gas velocity. It is also evident that further increase in h_g would lead to the kinetically limited region where the growth rate is limited by some relatively slow surface process (adsorption, surface reaction, or desorption). In the kinetic region the growth rate is independent of distance x, as shown by the broken line in Fig. 5. It should also be noted here that the growth rate at each distance x increases as the gas velocity is increased, due to a reduction in the thickness of the boundary layer, provided that the initial $AsCl_3$ mole fraction is held constant.

Effect of substrate temperature.—In Fig. 6 the experimental and the calculated results of $R(x)/R(0.3)$ *vs.* x for different substrate temperatures (T_s) at fixed initial $AsCl_3$ mole fraction and gas velocity are shown. As is evident from the figure, the agreement between

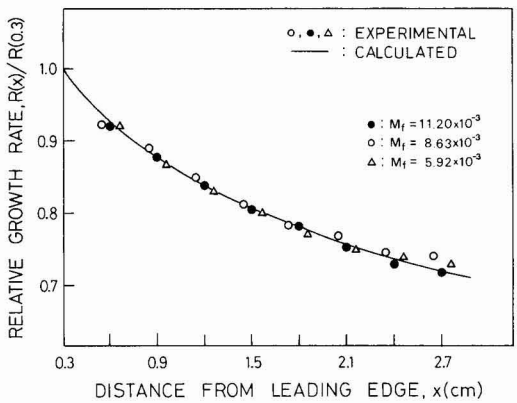

Fig. 4. Comparison of calculated and experimental results of $R(x)/R(0.3)$ as a function of distance from the leading edge of the substrate for different initial $AsCl_3$ mole fractions (M_f). Growth temperature 973°K, gas velocity 2.2 cm/sec.

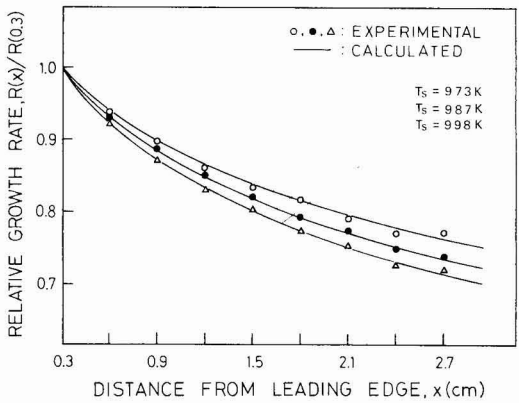

Fig. 6. Comparison of calculated and experimental results of $R(x)/R(0.3)$ as a function of distance from the leading edge of the substrate for different substrate temperatures (T_S). Initial $AsCl_3$ mole fraction 6.71×10^{-3}, gas velocity 3.67 cm/sec.

the experimental and the calculated values is very good.

In the figure the variation of growth rate along the substrate is observed to decrease as the substrate temperature is decreased. This tendency is due to the fact that, according to Eq. [8], the surface-reaction rate constant k_s rapidly decreases with decreasing substrate temperature while the mass transfer coefficient h_g is nearly independent of the substrate temperature. Further decrease in k_s would also lead to the kinetically limited region where the growth rate is independent of distance x.

Conclusions

The present investigation has resulted in the following:

1. A rate equation for the epitaxial growth of GaAs has been derived from a model based on a laminar boundary layer. Use of this equation permits the description of the variation of growth rate with distance along the substrate in a constant temperature growth zone. The validity of this equation has been demonstrated by comparison of the calculated growth rate variation with that obtained experimentally.

2. The effects of the initial $AsCl_3$ mole fraction, gas velocity, and substrate temperature on the variation of growth rate with distance along the substrate, in a constant temperature growth zone, have been determined. The variation of growth rate is dependent on the gas velocity and on the substrate temperature, but not on the initial $AsCl_3$ mole fraction.

Acknowledgment

The authors would like to thank Messrs. A. Shibatomi, K. Nakai, and K. Ogasawara for their helpful comments and suggestions.

Manuscript submitted Nov. 3, 1976; revised manuscript received April 29, 1977.

Any discussion of this paper will appear in a Discussion Section to be published in the June 1978 JOURNAL. All discussions for the June 1978 Discussion Section should be submitted by Feb. 1, 1978.

Publication costs of this article were assisted by Fujitsu Laboratories, Limited.

REFERENCES

1. D. Effer, *This Journal*, **112**, 1020 (1965).
2. M. Rubenstein and E. Myers, *ibid.*, **113**, 365 (1966).
3. R. C. Taylor, *ibid.*, **114**, 410 (1967).
4. D. W. Shaw, *J. Cryst. Growth*, **8**, 117 (1970).
5. P. Rai-Choudhury, *ibid.*, **11**, 113 (1971).
6. H. Seki, H. Eguchi, and H. Kobayashi, *ibid.*, **24/25**, 225 (1974).
7. M. Ihara, K. Dazai, and O. Ryuzan, *J. Appl. Phys.*, **45**, 528 (1974).
8. A. S. Grove, *Ind. Eng. Chem.*, **58**, 48 (1966).
9. A. S. Grove, "Physics and Technology of Semiconductor Devices," John Wiley & Sons, Inc., New York (1967).
10. R. E. Treybal, "Mass-Transfer Operations," McGraw-Hill Book Co., New York (1955).
11. H. Schlichting, "Boundary Layer Theory," 4th ed., chap. 7, McGraw-Hill Book Co., New York (1960).
12. W. Jost, "Diffusion in Solids, Liquids and Gases," Academic Press, New York (1960).
13. "Amercian Institute of Physics Handbook," 3rd ed., McGraw-Hill Book Co., New York (1972).
14. P. C. Rundle, *J. Cryst. Growth*, **11**, 6 (1971).
15. D. W. Shaw, *This Journal*, **115**, 405 (1968).
16. M. P. Albert and J. F. Combs, *ibid.*, **109**, 709 (1963).
17. P. A. Schumann, Jr., R. P. Phillips, and P. J. Olshefski, *ibid.*, **113**, 368 (1966).
18. B. G. Secrest, W. W. Boyd, and D. W. Shaw, *J. Cryst. Growth*, **10**, 251 (1971).
19. A. Boucher and L. Hollan, *This Journal*, **117**, 932 (1970).
20. D. J. Kirwan, *ibid.*, **117**, 1572 (1970).
21. R. R. Fergusson and T. Gabor, *ibid.*, **111**, 585 (1964).
22. W. H. Shepherd, *ibid.*, **112**, 988 (1965).

Oxygen Sensing with $Co_{1-x}Mg_xO$ Ceramics

Kwansuh Park and E. M. Logothetis

Ford Motor Company, Dearborn, Michigan 48121

ABSTRACT

Use of $Co_{1-x}Mg_xO$ ceramics for fabrication of oxygen sensors is reported. The phase stability, electrical conductivity, and thermoelectric power of these solid solutions with $x < 0.85$ have been investigated in the range 700°-1100°C and for oxygen partial pressures in the range $1\text{-}10^{-20}$ atm. The nonstoichiometric defects appear to be singly and doubly ionized cobalt vacancies and give rise to a p-type conductivity. These materials have properties, including stability over a wide range of oxygen pressures and temperatures, that make the $Co_{1-x}Mg_xO$ oxygen sensors particularly suited for monitoring and control of combustion processes. Some results on sensor performance in an internal combustion engine are presented.

In recent years there has been an increased interest in oxygen sensors, particularly those that can be used for the monitoring and control of the combustion process in an internal combustion (IC) engine or a furnace (1-4). The objective of this control is the optimization of the combustion process with respect to fuel economy, emissions, and system performance. Monitoring of the combustion process by means of oxygen sensing is possible because there is a direct relationship between the equilibrium oxygen partial pressure in the exhaust from an engine or furnace and the air-to-fuel ratio (A/F)[1] of the burned mixture. Sensor characteristics that are necessary or desirable for these applications, especially the control of IC engines, include fast response time (generally 1 sec or less), the ability to operate at high temperatures, and the ability to withstand corrosive or contaminating environments. For most furnaces and several IC engine systems, optimization of the combustion process is achieved with air-to-fuel mixtures corresponding to "lean-burn" combustion, *i.e.*, there is more than enough oxygen in the mixtures to convert all the hydrocarbons of the fuel to

Key words: oxygen sensing, combustion process control, ceramics, electrical properties, oxide solid solutions.

[1] A/F is defined as the ratio of the mass of air to the mass of fuel that make up the mixture before combustion.

water and carbon dioxide. Under these conditions, the oxygen partial pressure (P_{O_2}) of the exhaust gas from an engine or furnace is generally in the range of 10^{-3} to 10^{-1} atm.

In a previous publication (5) we reported the use of CoO ceramics as oxygen sensors for lean-burn applications. Pure, stoichiometric CoO is a wide-gap semiconductor with very high resistivity. However, deviations from stoichiometry result in structural defects (cobalt vacancies) that strongly influence electronic conductivity. These properties make the conductivity of CoO at high temperatures depend on the ambient P_{O_2} (5-8). Although CoO ceramic sensors heated at temperatures 900°-1000°C were shown (5) to possess characteristics that make them well suited for lean-burn applications, their usefulness is limited by the fact that CoO decomposes to metallic Co at low P_{O_2}; for example, at 1000°C, the CoO/Co phase boundary occurs at $P_{O_2} \approx 10^{-12}$ atm (Fig. 1); this corresponds to an equivalent air-to-fuel ratio (A/F) of about 14, *i.e.*, a value slightly rich of the stoichiometric A/F ratio. The CoO decomposition does not allow the prolonged exposure of the sensors to very low P_{O_2} such as those corresponding to very rich air-to-fuel mixtures. In the present paper we report the use of solid solutions of CoO with MgO to obtain oxygen sensors with characteristics similar to CoO but without the rich-mixtures-exposure limitation. Since systems operating at high P_{O_2} (lean A/F mixtures) may experience prolonged exposures to very low P_{O_2} (*e.g.*, those corresponding to very rich A/F mixtures) either accidentally or as the result of a certain normal operating mode, the use of $Co_{1-x}Mg_xO$ materials greatly increases the usefulness of these oxygen sensors. Furthermore, the $Co_{1-x}Mg_xO$ sensors can be operated at temperatures lower than CoO.

Properties of $Co_{1-x}Mg_xO$ Materials

The $Co_{1-x}Mg_xO$ materials have been prepared by high temperature reaction of CoO and MgO. Powders of the two oxides were milled together and then fired at temperatures in the range 1400°-1600°C for a few hours. This process was repeated several times until x-ray diffraction measurements indicated that a single phase material was obtained. Ceramic specimens of $Co_{1-x}Mg_xO$ were prepared by standard ceramic techniques involving cold pressing, with or without binder and subsequent sintering.

Figure 1 shows a portion of the P_{O_2}-T phase diagram for the Co-Mg-O system (9). This diagram is

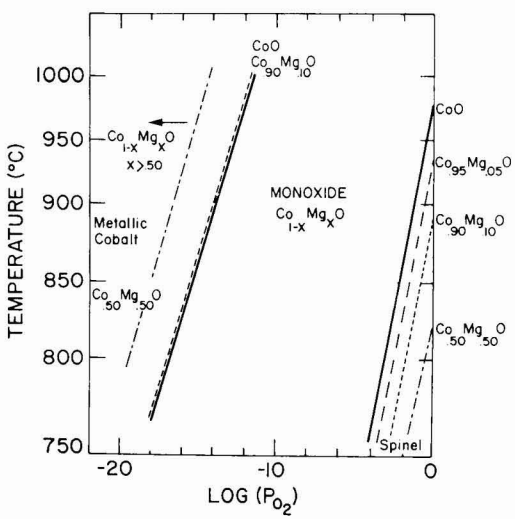

Fig. 1. Approximate P_{O_2}-T phase diagram for the Co-Mg-O system.

only approximate because of difficulties arising from hysteresis phenomena at each phase change; for example, at a given P_{O_2}, the temperature of the phase change from monoxide to spinel is lower than the temperature for the reverse change. The hystereses become more pronounced at lower temperatures and higher rates of change of T (or P_{O_2}). The transition temperature (or P_{O_2}) from one phase to another was determined by monitoring the electrical resistance; this is possible because all three phases (metallic, monoxide, and spinel) have very different resistivities. As Fig. 1 shows, the addition of small amounts of MgO (*e.g.*, $x < 0.10$) into CoO increases the stability range of the monoxide phase by a corresponding suppression of the spinel phase without a noticeable shift in the CoO/Co phase boundary; this boundary, however, shifts substantially to lower P_{O_2} (at a given temperature) for large MgO content (*e.g.*, $x > 0.50$). The wider stability range of the $Co_{1-x}Mg_xO$ materials allows safe exposure of those with $x > 0.5$ to P_{O_2} considerably lower than that for which CoO is decomposed; in addition, at high P_{O_2} (*e.g.*, 0.1 atm) these materials can be maintained at lower temperatures than CoO without transforming to spinel. The spinel composition derived from pure CoO is Co_3O_4; however, when MgO is added, the spinel phase appears to be generally a two phase region consisting of $Co_{1-y}Mg_yO$ and $(Co_{1-z}Mg_z)_3O_4$ (spinel).

The high temperature electrical properties of $Co_{1-x}Mg_xO$ were investigated in the 700°-1100°C temperature range and at P_{O_2} between 1 and 10^{-20} atm. Electrical connections to the ceramic specimens were made by attaching Pt wires with Pt paste. The specimens were mounted inside a quartz vessel that was placed in a furnace. The oxygen partial pressure was established by a continuous flow through the vessel of gas mixtures at a total pressure of 1 atm, O_2 in CO_2 or O_2 in N_2 for high P_{O_2} and CO in CO_2 for low P_{O_2}. At high temperatures, nonohmic behavior and polarization phenomena were absent and 2-probe and 4-probe measurements gave the same results. Figure 2 shows some results on the dependence of the electrical resistivity of the $Co_{1-x}Mg_xO$ ceramics on P_{O_2} at 1000°C. On the high P_{O_2} side the data terminate at approximately the monoxide-to-spinel phase boundary, whereas on the low P_{O_2} side the data terminate at the metal-to-monoxide phase boundary; (for materials with $x > 0.40$, the latter phase boundary extends beyond 10^{-14} atm; see Fig. 1). Complete results on the dependence of the electrical conductivity and the thermoelectric power of $Co_{1-x}Mg_xO$ materials on P_{O_2} and temperature (700°-1100°C) for $0 \leq x < 1$ will be published elsewhere (10).

The behavior of the electrical resistivity of the $Co_{1-x}Mg_xO$ materials appears to be generally the same as that of CoO. In the temperature range of 700°-1100°C, the resistivity is approximately proportional to $P_{O_2}^{-1/4}$ at high P_{O_2} and tends toward a $P_{O_2}^{-1/6}$ dependence for the lower P_{O_2}. These dependences are consistent with a simple model of point defects (most likely Co vacancies) that are predominantly singly ionized at high P_{O_2} and predominantly doubly ionized at low P_{O_2} (6-8, 10). The P_{O_2} range with a $P_{O_2}^{-1/6}$ dependence (doubly ionized defects) widens as the Mg content in the materials increases. At very low P_{O_2}, the resistivity of the materials with $x > 0.5$ tends to saturate. The saturation becomes more pronounced at the lower temperatures and is probably due to donor impurities in the specimens (10). The absolute value of the resistivity increases slowly with x for small x, becoming a strong function of x for large x. The activation energy for the conductivity remains close to that of CoO ($\approx$ 0.5 eV) for $x < 0.20$ and increases strongly for larger x, attaining a value of 1.2 eV for $x = 0.85$. These results in the range 700°-1000°C appear to be generally consistent with the results of thermogravimetric and conductivity studies by Von G. Schwier *et al.* (11, 12)

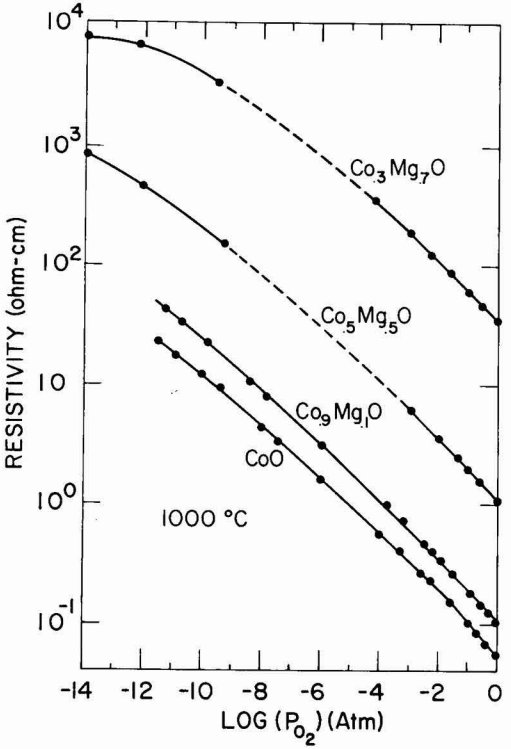

Fig. 2. Dependence of the resistivity of $Co_{1-x}Mg_xO$ alloys on the oxygen partial pressure at 1000°C.

at higher temperatures (900°-1300°C) and at P_{O_2} in the range $1\text{-}10^{-4}$ atm.

For the thermoelectric power measurements, temperature differences ΔT between the two ends of a $Co_{1-x}Mg_xO$ ceramic were established with a small platinum heater near one end of the specimen. Values of ΔT were measured with two Pt/Rh thermocouples, attached to the two ends of the ceramic specimen with platinum paste. The thermoelectric voltage was measured with the platinum legs of the two thermocouples. The sign of the thermoelectric power S shows that the conductivity in all $Co_{1-x}Mg_xO$ solid solutions studied here ($x \leq 0.85$) is p-type, *i.e.*, the charge carriers are holes; this is consistent with the interpretation that the intrinsic defects in these materials are Co vacancies. Furthermore, for materials with $x < 0.5\text{-}0.7$, a plot of S *vs.* $1/T$ gives a straight line having a slope E_S that is equal to the activation energy E_C of the conductivity. This suggests that the exponential increase in the conductivity with temperature results from a similar increase in the carrier concentrations and not from an activated mobility. It thus appears that, as for CoO, the holes in $Co_{1-x}Mg_xO$ with $x < 0.5\text{-}0.7$ are not small polarons but rather itinerant carriers. For $x > 0.5\text{-}0.7$, it was found that $E_C > E_S$ which suggests that the mobility becomes activated. A change from band conduction to hopping conduction is thus indicated at high Mg content. These preliminary results are in disagreement with those of Von G. Schwier *et al.* (11, 12); from combination of mass loss and conductivity measurements these authors concluded that the mobility is activated for all x. It is pointed out that similar discrepancy on the nature of the carrier mobility deduced from mass/loss conductivity and thermoelectric power/conductivity data exists for pure CoO (6-8, 10-13). Experimental uncertainties do not appear to be the source for this discrepancy, since such results for CoO have been obtained consistently by many investigators (6-8, 10-13).

Oxygen Sensor Characteristics

Experimental $Co_{1-x}Mg_xO$ sensors have been fabricated with a configuration similar to that of CoO sensors (5). The ceramic sensing element is in the form of a small bar or disk with two imbedded platinum wires as resistance sensing electrodes. The temperature of the sensor is maintained at some approximately constant value in the range 700°-1000°C by means of a small furnace surrounding the ceramic element.

Figure 3 shows some results on the performance of these oxygen sensors from the specific application of sensing the air-to-fuel ratio of an IC engine. Several sensors were inserted into the exhaust from an 8-cylinder 351 CID (cubic inch displacement) engine and the dependence of the d-c resistance of the $Co_{1-x}Mg_xO$ elements on A/F ratio was investigated. The A/F ratio was determined by conventional gas analysis techniques (14). Figure 3 shows the resistance of the ceramic element of a sensor with composition $Co_{0.3}Mg_{0.7}O$ as a function of the A/F ratio in the range A/F = 15-18 (lean region). The temperature of the sensor was 900°C. The approximate P_{O_2} of the exhaust is also shown at the top of the figure.

Figure 3 shows an approximate two-to-one change in resistance over the range of A/F measured. This change is large enough to be useful in practical applications, provided the materials properties are stable and extraneous changes in resistance (*e.g.*, those due to temperature fluctuations) are small. The resistance *vs.* P_{O_2} relationship and the activation energy of the $Co_{1-x}Mg_xO$ ceramics were found to be very reproducible at least for $T > 800$°C and $P_{O_2} > 10^{-6}$ atm. In addition, they were independent of the porosity of the ceramics in the range 0-50%. These characteristics as well as the absolute value of the resistance remained unchanged after more than 1000 hr of operation at temperatures in the range 800°-1000°C. The tempera-

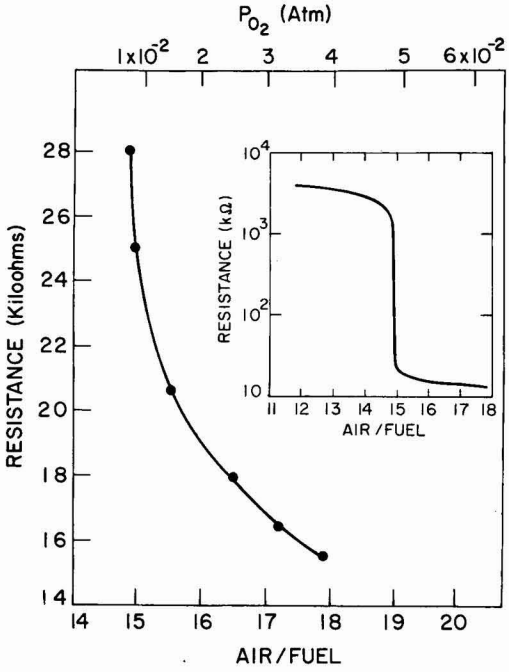

Fig. 3. Dependence of the resistance of a $Co_{0.3}Mg_{0.7}O$ sensor on air-to-fuel ratio (A/F) of an IC engine for A/F > $(A/F)_{stoichiometric}$, and on oxygen partial pressure P_{O_2}. The temperature of the sensor was 900°C. The inset shows the behavior of the sensor resistance for an extended A/F range including the stoichiometric A/F ratio.

ture coefficient of resistance increases with x from 0.3% per °C for CoO to 0.6% per °C for $Co_{0.3}Mg_{0.7}O$ in the neighborhood of 1000°C. These coefficients become about 0.4% and 0.7% per °C respectively in the neighborhood of 800°C.

An important characteristic of an oxygen sensor is its response time. The requirements on response time depend on the application. Sensors made from porous $Co_{1-x}Mg_xO$ ceramics have shown response times similar to the CoO sensors, *i.e.*, of the order of 1 sec or less (5). Shorter response times are expected by optimization of the ceramic structure. It appears that for $P_{O_2} > 10^{-6}$ atm, the response time of the $Co_{1-x}Mg_xO$ sensors is determined by a combination of gas transport through the pores (gas exchange) and the equilibration kinetics (diffusion) within the individual grains.

Since $Co_{1-x}Mg_xO$ materials with $x > 0.5$ do not decompose at very low P_{O_2} (*e.g.*, very rich air-fuel mixtures such as those with A/F = 11), oxygen sensors made from these compositions can be used not only for sensing lean A/F mixtures but also for sensing passage through the stoichiometric A/F mixture. Such "stoichiometric" A/F sensors are presently of considerable interest for the control of engine systems that use a 3-way catalytic converter for the simultaneous removal of all three pollutants (hydrocarbons, CO, NO_x) from the exhaust. Figure 3 (inset) shows the dependence of the resistance of a $Co_{0.3}Mg_{0.7}O$ sensor on A/F ratio for a wide range of A/F ratios, from very rich (A/F = 11) to very lean (A/F = 18). The large step-wise change in the resistance at A/F $\approx$ 14.8 signifies the passage through the stoichiometric A/F mixture and arises from a corresponding large change in the P_{O_2} of the exhaust gas. When the $Co_{1-x}Mg_xO$ is used as an indicator of passage through stoichiometry, the requirements for temperature control are greatly reduced.

Conclusions

Our initial laboratory measurements indicate that oxygen sensors made from $Co_{1-x}Mg_xO$ have electrical properties as well as materials stability over a wide range of P_{O_2} and temperatures, that make them attractive for a variety of applications. The reproducibility and stability of the resistance *vs.* P_{O_2} (or A/F) relationship, the absence of drifts and polarization effects, the relatively small temperature coefficient of resistance, and the fast speed of response, all combine to give a sensor with good performance at high P_{O_2} (lean air-fuel mixtures). More complete evaluation of these sensors for the application of monitoring and control of combustion processes is in progress.

Acknowledgment

We thank G. Beaudoin for the assistance in the fabrication and testing of the oxygen sensors.

Manuscript submitted March 1, 1977; revised manuscript received May 5, 1977.

Any discussion of this paper will appear in a Discussion Section to be published in the June 1978 JOURNAL. All discussions for the June 1978 Discussion Section should be submitted by Feb. 1, 1978.

Publication costs of this article were assisted by the Ford Motor Company.

REFERENCES

1. R. Zechnall, G. Baumann, and H. Eisele, Paper No. 730566, SAE National Automotive Engineering Meeting, Detroit, May 1973.
2. T. Y. Tien, H. L. Stadler, E. F. Gibbons, and P. J. Zacmanidis, *J. Am. Ceram. Soc.*, **54**, 280 (1975).
3. E. M. Logothetis, Proceedings of the International Conference on Electronic Properties of Oxides, Purdue University, May 1974; *J. Solid State Chem.*, **12**, 331 (1975).
4. H. E. Hendler, *Chem. Eng. Prog.*, **71**, 39 (1975).
5. E. M. Logothetis, K. Park, A. H. Meitzler, and K. R. Laud, *Appl. Phys. Lett.*, **26**. 209 (1975).
6. B. Fisher and D. S. Tannhauser, *J. Chem. Phys.*, **44**, 1663 (1965).
7. N. G. Eror and J. B. Wagner, *J. Phys. Chem. Solids*, **29**, 1597 (1968).
8. I. Bransky and J. M. Wimmer, *ibid.*, **33**, 801 (1972).
9. See also, "Phase Diagrams for Ceramicists." E. M. Levin, C. R. Robbins, and H. F. McMurdie, The American Ceramic Society (1964).
10. Some results have already been reported: E. M. Logothetis and K. Park, *Bull. Am. Phys. Soc.*, **20**, 469 (1975); K. Park and E. M. Logothetis, *Am. Ceram. Soc. Bull.*, **55**, 416 (1976).
11. Von G. Schwier, R. Dieckmann, and H. Schmalzried, *Ber. Bunsenges. Physik. Chem.*. **77**, 402 (1973).
12. Von G. Schwier and H. Schmalzried, *ibid.*, **77**, 721 (1973).
13. A. J. Bosman and C. Crevecoeur, *J. Phys. Chem. Solids*, **30**, 1151 (1969).
14. N. A. Henein and D. J. Patterson, "Emission from Combustion Engines and Their Control," Chap. 9, Ann Arbor Science Pub., Inc., Ann Arbor, Mich.

Technical Notes

Vapor-Phase Etching and Polishing of GaAs Using Arsenic Trichloride

Rajaram Bhat*,[1] and Sorab K. Ghandhi*

Electrical and Systems Engineering Department, Rensselaer Polytechnic Institute, Troy, New York 12181

A study of the vapor-phase etching and polishing of GaAs substrates using hydrogen chloride gas was presented in a previous paper (1). In that study, it was observed that the etching process critically depended on the purity of the etchant. Arsenic trichloride is readily available in purities better than six nines, and is less expensive compared to HCl gas on the basis of the number of moles of available chlorine. It is, therefore, an attractive alternative for *in situ* etching of GaAs substrates. Knight, Effer, and Evans (2), Hirao and Nakashima (3), and Nozaki and Saito (4) have investigated the etching of gallium arsenide substrates in a $Ga/AsCl_3/H_2$ vapor deposition reactor. Further, DiLorenzo (5) has studied the etching of GaAs substrates with $AsCl_3$ in a helium ambient. However, a detailed information on the effect of temperature, substrate orientation, and $AsCl_3$ mole fraction on the etching and polishing of GaAs substrates, in a H_2 atmosphere, is not available. In this paper, we present results obtained for $AsCl_3$ etching of GaAs substrates in a cold-wall reactor, and compare them with those obtained using HCl gas in the same system. Throughout these etching experiments, a flow of arsine gas was maintained to prevent decomposition of the GaAs. The apparatus and experimental procedure were similar to those used in (1), and the etch rate was defined and determined as in (1).

Experimental Results

Temperature.—The effect of temperature on etch rate was determined for (100) and ($\bar{1}\bar{1}\bar{1}$) oriented, Te-doped GaAs substrates[2] using a flow of 5 liters/min of hydrogen, 30 ml/min of arsine, and 70 ml/min of hydrogen through the $AsCl_3$ bubbler, which was kept at 25°C. Under these conditions, as seen in Fig. 1, the activation energies of the etching reaction and the temperatures at which the etching reaction became mass-transport (type II) limited (6) and independent of crystallographic orientation, were found to be the same as those reported for HCl gas (1). Again, as in (1), GaAs substrate surfaces of both (100) and ($\bar{1}\bar{1}\bar{1}$) orientation were featureless when etched above 870°C, and were faceted with the simultaneous formation of etch pits or hillocks when etched below this temperature. Further, etching experiments with $AsCl_3$ and HCl gas conducted under otherwise identical conditions resulted in equal etch rates for an HCl gas mole fraction which was three times that of $AsCl_3$ in the input gas stream. This indicates that $AsCl_3$ completely dissociates within the reactor before reaching the substrate. The dissociation of $AsCl_3$ produces HCl gas since chlorine is unstable in an atmosphere of hydrogen at the etching temperature (7).

$AsCl_3$ concentration.—Figure 2 shows the etch rate of (100) Te-doped GaAs substrates as a function of the hydrogen flow through the $AsCl_3$ bubbler. These experiments were conducted at a temperature of 900°C, using a total hydrogen flow of 5 liters/min and an arsine flow of 30 ml/min in a reactor tube of 50 mm ID. The etch rate was found to vary superlinearly with HCl concentration. Similar nonlinear dependence of the etch rate on etchant gas flow, under mass-transport (type II) limited conditions, was observed in the etching of Si (8, 9), Ge (10), and GaAs (1). This result differs from the findings of Hirao and Nakashima (3), who observed a linear variation of etch rate with $AsCl_3$ concentration during experiments performed in a hot wall reactor.

Arsine flow.—The effect of arsine flow on etch rate and surface quality under mass-transport (type II)

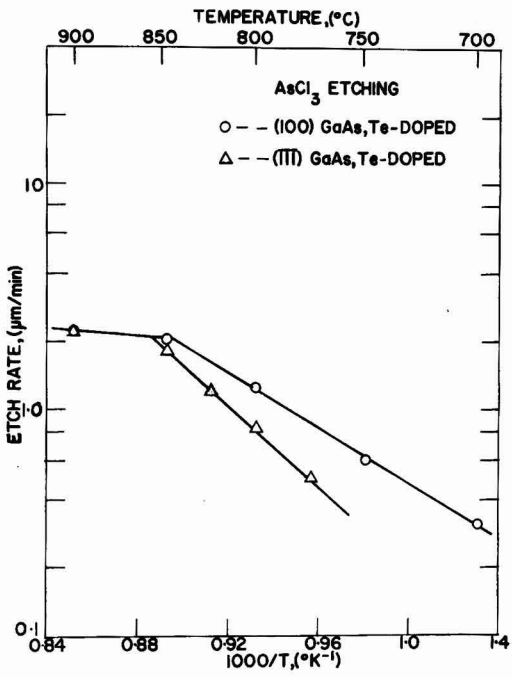

Fig. 1. Variation of etch rate with temperature

* Electrochemical Society Active Member.

[1] Present address: General Electric Company, Advanced Technology Group, Semiconductor Products Department, Syracuse, New York 13201.

Key words: gallium arsenide, arsenic trichloride, etching, polishing.

[2] All (100) substrates mentioned in this paper were misoriented 2° from (100) towards (110).

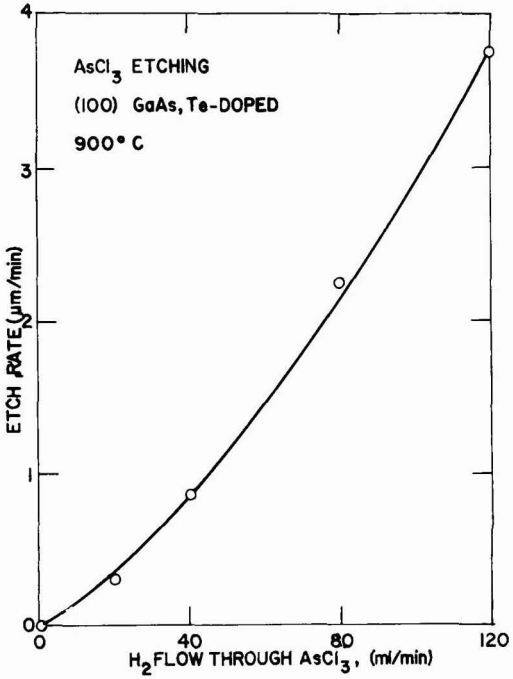

Fig. 2. Variation of etch rate with $AsCl_3$ concentration

limited conditions was investigated at 900°C using a hydrogen flow of 5 liters/min. It was found that at least 15 ml/min of arsine were required to prevent decomposition of the substrate. There was no appreciable change in surface quality for arsine flows between 15 and 30 ml/min, and the etch rate did not change within experimental error. These results are in agreement with those obtained with HCl gas (1).

Orientation and dopant type.—Investigations of the etch rate under mass-transport (type II) limited and kinetically controlled conditions for (100) Cr- and Zn-doped GaAs indicated that it was the same as for their Te-doped counterparts. Therefore, as in (1), the etch rate for $AsCl_3$ etching of GaAs substrates is also independent of dopant type.

It was possible under mass-transport (type II) limited conditions to obtain specular surfaces for (100) Cr- and Zn-doped and $(\bar{1}\bar{1}\bar{1})$ Cr-, Si-, and Zn-doped substrates. In agreement with results obtained in (1), the quality of $(\bar{1}\bar{1}\bar{1})$ Cr- and Si-doped substrates was inferior to that obtained with Te- and Zn-doped GaAs substrates. However, unlike the HCl gas etching study (1), no difference was observed in the quality of (100) oriented Te- and Cr-doped substrates etched with $AsCl_3$. This result is in contrast to that obtained by Hirao and Nakashima (3), who failed to obtain specular etched surfaces for Cr-doped GaAs.

It was noted during the etching of GaAs using HCl gas that the use of a less pure etchant resulted in nonspecular surfaces. Since the $AsCl_3$ was considerably purer than the HCl gas used, we conclude that the difference in the quality of Cr-doped GaAs substrate surfaces etched with HCl gas or $AsCl_3$ was mainly due to the difference in purity of the etchant.

Dopant segregation.—Auger spectra taken on etched and unetched Te-, Si-, and Cr-doped GaAs substrates showed no segregation of dopants on the surface within the limits of detectability.[3] This is in agreement with the results obtained by Moon and James (11) for Te- and Si-doped substrates.

Conclusion

The etching reaction of $AsCl_3$ with GaAs in a hydrogen ambient at temperatures above 700°C has been shown to be identical to that of HCl gas. The ability to obtain equally good specular etched surfaces for both Te- and Cr-doped GaAs substrates makes $AsCl_3$ more attractive than HCl gas in the choice of an etchant.

Acknowledgment

The authors would like to thank R. Rafun for assistance in manuscript preparation. This work was supported by Grant No. DAAG29-76-G-0127 from the U.S. Army Research Office, Durham, North Carolina.

Manuscript submitted Feb. 24, 1977; revised manuscript received May 6, 1977.

Any discussion of this paper will appear in a Discussion Section to be published in the June 1978 JOURNAL. All discussions for the June 1978 Discussion Section should be submitted by Feb. 1, 1978.

Publication costs of this article were assisted by Rensselaer Polytechnic Institute.

[3] 0.1% of the atoms in the first monolayer.

REFERENCES

1. R. Bhat, B. J. Baliga, and S. K. Ghandhi, *This Journal*, **122**, 1378 (1975).
2. J. R. Knight, D. Effer, and P. R. Evans. *Solid-State Electron.*, **8**, 178 (1965).
3. M. Hirao and H. Nakashima, *J. Jpn. Soc. Appl. Phys., Suppl.*, **40**, 46 (1971).
4. T. Nozaki and T. Saito, *Jpn. J. Appl. Phys.*, **11**, 110 (1972).
5. J. V. DiLorenzo, Proceedings of the 5th International Symposium on GaAs and GaAs Related Compounds. p. 362, Institute of Physics, Deauville, France (1976).
6. D. W. Shaw, in "Crystal Growth Theory and Techniques," Vol. 1, C. H. L. Goodman, Editor, Chapter 1, Plenum Press, New York (1974).
7. D. J. Kirwan, *This Journal*, **117**, 1573 (1970).
8. G. A. Lang and T. Slavish, *RCA Rev.*, **24**, 488 (1963).
9. W. H. Shepherd, *This Journal*, **112**, 988 (1965).
10. J. A. Amick, E. A. Roth, and H. Gossenberger, *RCA Rev.*, **24**, 473 (1963).
11. R. L. Moon and L. W. James, *This Journal*, **120**, 581 (1973).

Lifetime Degradation in Silicon by Emitter Diffusion

R. N. Ghoshtagore*

Westinghouse Research Laboratories, Pittsburgh, Pennsylvania 15235

The electrical characteristics of silicon devices are critically dependent on wafer processing parameters. Most of these device characteristics are directly derived both from such high temperature process-induced gross internal changes in silicon as resistivity type and level, resistivity gradients and thicknesses of different layers, and such subtle changes in the bulk as heavy metal, vacancy, and oxygen precipitations, minority carrier lifetimes in each doped layer, etc. In this work, the effects of different techniques of one such processing step, namely, $POCl_3$ emitter diffusion, on the minority carrier recombination lifetime of the starting material was investigated.

The starting material in all these experiments was (111) $\pm$ 1° orientation, boron-doped, 20-30 Ω-cm, 1-1/4 in. diam, 8 $\pm$ 1 mil thick, one-side chem-mechanically polished, $<$ 500/cm² dislocation density, p-silicon, with photoconductivity lifetime of ~225 μsec. The wafers were cleaned by standard techniques with the peroxide process used just before diffusion. They were blown dry with nitrogen before loading into the diffusion furnace. All $POCl_3$ diffusions were done with 4 wafer batches at 1200°C in a 50 mm ID quartz tube for 1-59-1 m (1 preheat time; 59 deposition time; 1 flush time). $POCl_3$ bubbler temperature was controlled to 20° $\pm$ 0.5°C by a thermocooler. The carrier gas flow was uniformly N_2 at 2 liters/m. N_2 flow through the bubbler and oxygen flow into the furnace were controlled directly as percentages of the main-line nitrogen carrier gas flow rates. After the emitter diffusion cycle the wafers were cooled by either quenching (by pulling the boat out of the furnace) or slow cooling the furnace (with a programmer) at fixed rates to 600°C and then pulling the boat out of the furnace.

After diffusion, the phosphosilicate glass thicknesses were measured as SiO_2 equivalents, glass stripped in HF, and sheet resistivity and junction depths (angle lap and stain) recorded. The n layer was then lapped off the polished side, and 1/16 in. diam mesa n^+p diodes (1/4 in. apart) fabricated (on the lapped side). Evaporated Al contacts were used on both sides. Open-circuit voltage decay (OCD) lifetime was measured for corresponding diodes under low injection conditions (1 mA forward current) using the relationship (1)

$$\tau = \frac{kT}{q}\left(\frac{dv}{dt}\right)^{-1}$$

All the OCD measurements were made in the dark at room temperature under flowing nitrogen ambients with no further surface passivation of the mesa diodes (1). Surface leakage currents were not a problem in these measurements.

For any particular type of cooling cycle, the phosphosilicate glass thickness on the wafers increased more than linearly with increasing $POCl_3$ concentration in the gas stream, the thicknesses being higher with slower cooling rates. In the entire range of experiments reported here no "bubbles" were observed in the glass. For the experiments where the wafers were pulled out of the furnace after diffusion (quench), junction depths were 6.9 $\pm$ 0.8μ. In the slow cool runs, junction depths increased uniformly with decreasing rates of cooling with a 90 $\pm$ 5% increase of x_j (over quench) for 0.5°C/min cool rate. Gas phase reactant concentrations (in the range used) had no detectable effect on x_j. Similarly, measured sheet resistivities were primary functions of $POCl_3$ gas phase concentration. Variation of oxygen concentration produced second-order effect that was almost masked by experimental perturbation. All the sheet resistivities were in the range of 0.70-1.33 Ω/□ in. Surface concentrations, calculated from spreading resistance profiles, were also the direct function of only $POCl_3$ gas phase concentration. They ranged from 1×10^{20} to 1.9×10^{20} cm^{-3} in all these experiments. From the spreading resistance profiles, the run conditions with >3.25% $POCl_3$ were difficult to distinguish mainly due to wafer-to-wafer and run-to-run variations.

As we present the OCD lifetime data in Fig. 1-3, the following processing questions will be specifically addressed: (*i*) What is the best $POCl_3$ gas phase concentration for the maximum lifetime preservation? (*ii*) Is there a corresponding O_2:$POCl_3$ ratio? (*iii*) From the same point of view, what is the best range of cooling rates? (*iv*) What deleterious effect, if any, does the thermal preoxidation of wafers have? For a direct basis of comparison of the measured OCD lifetimes, some of the same wafers were used to fabricate 750°C Sb-Au alloyed-in 1/8 in. diam n^+p diodes. The OCD lifetime of such diodes averaged about 60 μsec. The diode size has never been found to have any effect on such measurements.

Minority carrier lifetimes measured by the low injection OCD technique were plotted as a histogram

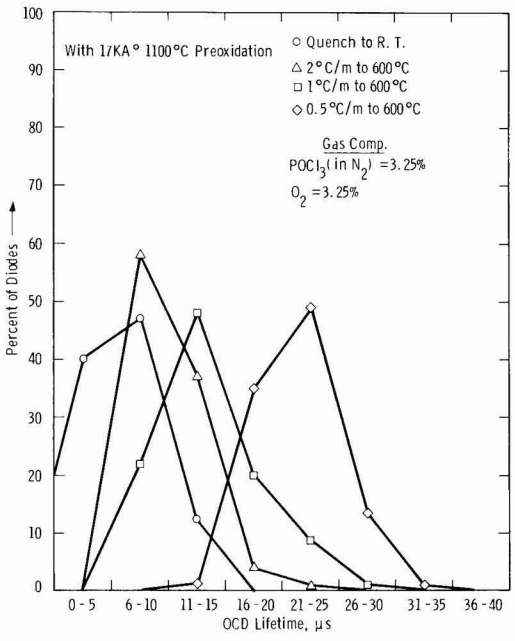

Fig. 1(a). OCD lifetime spectra of 1100°C 17 kÅ preoxidized wafers after the medium concentration emitter diffusion at different slow cooling rates (diffusions at 1200°C).

* Electrochemical Society Active Member.

Key words: silicon, lifetimes, phosphorus, diffusion, degradation, slow cooling.

of the percent of the measured diodes (~100 in each run) as a function of the lifetime divided into 5 μsec groups. Examination of the statistical data in such a form is expected to indicate only the trend of the effect of processing variables experimented. Emitter diffusions were performed for $POCl_3$ gas phase concentrations of 1-10%; O_2:$POCl_3$ ratios of 0.5-3.0 at each $POCl_3$ concentration, and at four primary slow cool rates under any fixed O_2 plus $POCl_3$ concentration condition. Figure 1(a) shows one such set of OCD data illustrating the deleterious effect of wafer preoxidation on the peak OCD lifetime value. Similar effects were observed with unoxidized wafers [Fig. 1(b)]. It should be noted that the maximum programmed slow cool rate of 2°C/min is about equivalent to furnace shut-off condition. Figure 2 shows the peak OCD lifetime data as a function of $POCl_3$ gas phase concentration under two primary O_2:$POCl_3$ ratios. From the trend curves drawn through the data points, it is clear that for the maximum possible lifetime preservation at $\leq$ 2°C/min, cooling rates emitter diffusion must be performed at ~6% $POCl_3$ concentration condition. Under these conditions, peak OCD lifetime initially increases with increasing $POCl_3$ gas phase concentration up to ~6.5%, probably due to heavy metal gettering. But the subsequent drop in each τ value with further increase of gas phase phosphorus concentration must be due to defect generation in the undiffused bulk (2). Both of these gettering and bulk defect generation phenomena become neutralized by the opposing kinetics at low cooling rates (*i.e.*, < 1° C/min). Although Fig. 2 shows that the effect of O_2:$POCl_3$ ratio on the peak τ_{OCD} is very minor, a detailed examination of all the data indicate that the optimum emitter processing should be done at O_2:$POCl_3$ = 2.5-3.0:1.

The topic of the effect of slow cool rate on peak τ_{OCD} is the most controversial one. It has been generally considered to provide considerable time (at different temperatures) for gettering of heavy metals, dissolution of appropriate precipitate centers, annihilation of planar and line-type lattice defects, etc., and thus enhance minority carrier recombination lifetime in heat-treated silicon. As shown in the typical data sets of Fig. 1, all the results obtained in this study

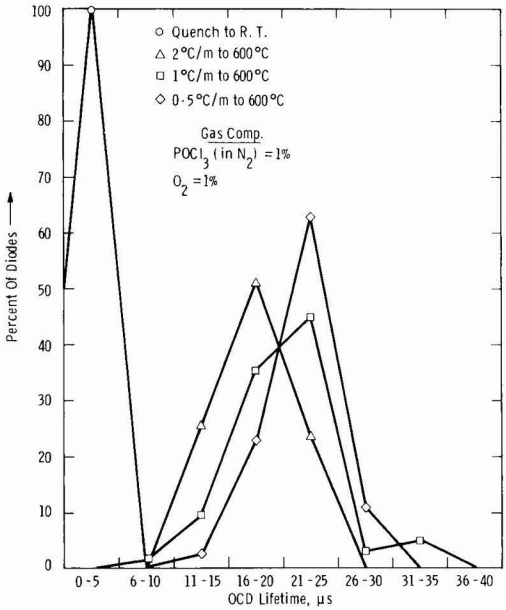

Fig. 1(b). OCD lifetime spectra after low concentration emitter diffusion at 1200°C for different slow cooling rates (no preoxidation).

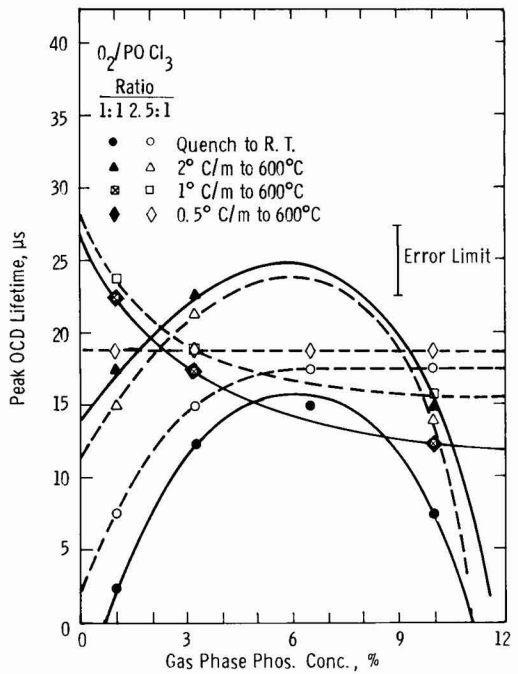

Fig. 2. The dependence of peak τ_{OCD} on the gas phase diffusion conditions at different postdiffusion cooling rates from 1200°C (no preoxidation).

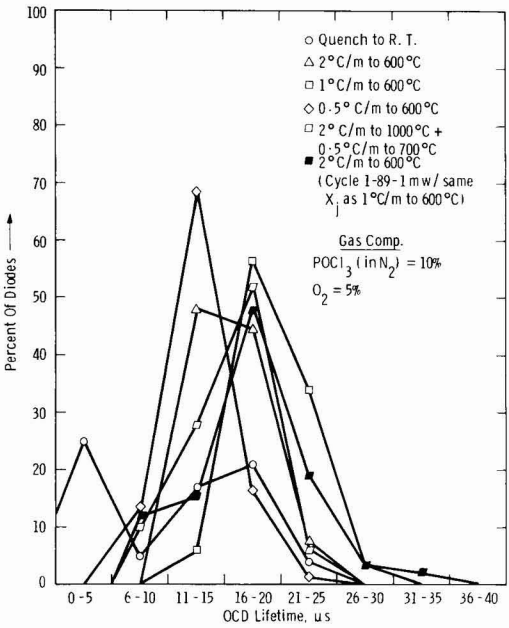

Fig. 3. The effects of low oxygen concentration, junction depth, and different cooling rates at different temperatures on the OCD lifetime spectra of 1200°C emitter diffusion (no preoxidation).

unequivocally indicate longer lifetimes under slow cool conditions, within the aforementioned constraints of gas phase reactant concentrations. As can be seen from Fig. 2, in the case of bare silicon under increasing gas phase phosphorus concentrations, the effects of different slow cool rates on peak τ_{OCD} become minimal. Emitter diffusions under different slow cool rates also drastically alter the distribution of τ_{OCD} values obtainable in any one run. It should be pointed out that in all the data obtained in this study, the trends of the maximum lifetime as a function of slow cooling rates are not monotonically varying. However, with oxidized wafers, the slower the cooling rate the higher is the peak τ_{OCD} [Fig. 1(a)]. Lifetime degradation in preoxidized wafers, being the most relevant to device processing, should determine the best cooling rate (i.e., 0.5°C/min). Slowest cooling rate being equivalent to the maximum x_j immediately raises the question of x_j dependence on τ_{OCD}. Figure 3 attempts to answer that question for an O_2:$POCl_3$ ratio of 0.5:1.0. The set of data with 2°C/min cooling rate (to 600°C) with a 1-89-1 min diffusion cycle is equivalent to that with 1°C/min cooling rate (to 600°C) with a 1-59-1 min diffusion cycle insofar as x_j is concerned (11.0μ). Their lifetime spectra are also nearly identical. This is also approximately the case with that set of data where the slow cool rate was changed from 2° to 0.5°C/min at 1000°C. This latter set of data indicate the importance of the slowest possible cooling rate under 1000°C (0.5°C/min data being anomalous). It has also been observed that the x_j dependence on peak τ_{OCD} ceases to exist after $\sim x_j = 12$-14μ. Finally, it should be mentioned that all the lifetime data were highly reproducible in the general shape of the spectra. Over 50% of the runs were repeated twice at different times, with some 5-10% being repeated several times.

It is probably appropriate at this point to speculate on the possible mechanisms operating to degrade minority carrier lifetime by emitter diffusion alone. From the clear trend of the data presented, it is not unreasonable to assume that heavy metal contamination is not involved in general, and the wafer cleaning procedure was consistent enough. The presence of optimum $POCl_3$ and O_2 gas phase concentrations probably is consistent with that of least SiP-type precipitation center density production (2). Such incoherent precipitation within the diffused layer is normally associated with dislocation-type recombination centers extending well into the base material. Slow cooling quite possibly could anneal out a fraction of such centers (sessile dislocations). The major effects of slow cooling must, however, be either vacancy annealing (3) and/or oxygen evolution in the silicon lattice as SiO_4-polyhedra. To obtain a clearer idea of the type of thermally induced centers introduced, their densities and locations in the bandgap should be established. Other methods of lifetime determinations could also be usefully employed.

Manuscript submitted Feb. 22, 1977; revised manuscript received May 16, 1977. This was Paper 338 presented at the Las Vegas, Nevada, Meeting of the Society, Oct. 17-22, 1976.

Any discussion of this paper will appear in a Discussion Section to be published in the June 1978 JOURNAL. All discussions for the June 1978 Discussion Section should be submitted by Feb. 1, 1978.

Publication costs of this article were assisted by Westinghouse Research Laboratories.

REFERENCES

1. Y. C. Kao and J. R. Davis, *IEEE Trans. Electron Devices*, **ed-17**, 652 (1970).
2. P. Negrini, D. Nobili, and S. Solmi, *This Journal*, **122**, 1254 (1975).
3. C. T. Sah and C. T. Wang, *J. Appl. Phys.*, **46**, 1767 (1975).

Electrolytic Etching of Aluminum from an Al-Al_3Ni Two-Phase Matrix in Aluminum Chloride Containing Molten Salts

C. L. Hussey,* J. C. Nardi, L. A. King,* and J. K. Erbacher

The Frank J. Seiler Research Laboratory (AFSC), United States Air Force Academy, Colorado 80840

The growth of an aligned microstructure of a controlled eutectic alloy trialuminum nickelide (Al_3Ni) has been investigated by several workers as a means of providing tensile strength enhancement in aluminum (1, 2). A practical method of producing Al_3Ni whiskers in an aluminum matrix utilizes a unidirectional solidification technique (1, 2). In order to properly evaluate the quality of the filament network that has been produced with this growth procedure, it is necessary to remove the solid aluminum phase without causing damage to the filaments. Small diameter fibers composed of Al_3Ni are also expected to find useful application in industrial and military microelectronics if they can be removed undamaged from the aluminum matrix in which they are imbedded. Thus, a practical means of removing aluminum from a two-phase Al-Al_3Ni matrix without damage to the Al_3Ni fibers would be useful to investigators studying the two-phase Al-Al_3Ni system.

Previous attempts using aqueous electrolytes or acid etches for removing or dissolving aluminum from an Al-Al_3Ni matrix have almost always been accompanied by gas evolution, resulting in disordering of the fiber bundles as they are exposed (3). A problem also encountered with aqueous acid etches is low selectivity of attack; i.e., the Al_3Ni fibers are dissolved as well as the bulk aluminum. An electrolyte that would sustain aluminum electrolysis without gas evolution while permitting selective attack on the bulk aluminum phase would be a potential way to circumvent these problems.

Aluminum has been anodized in aprotic media (4, 5), but generally the rate of removal of aluminum is limited by the low electrical conductivity of these media. Application of molten salt media, particularly those containing aluminum chloride, to the anodization of

* Electrochemical Society Active Member.

Key words: aluminum chloride, 1-ethylpyridinium, thin filaments, electrolytic etching, anodization.

aluminum has been demonstrated in both alkali chloride-aluminum chloride (6, 7) and organic salt-aluminum chloride (8, 9) mixtures. Separation procedures using these types of materials provide a number of advantages. Foremost, the method is electrolytic in nature, and therefore provides a great deal of control in the attack. Secondly, the process is not accompanied by gas evolution provided the electrode is not made so anodic as to decompose the melt. Finally, because the electrolyte used is a molten salt the conductivity is high, allowing a rapid removal of material.

King, Brown, and Frayer (6) showed that the anodic dissolution of aluminum proceeds at 100% efficiency at 175°C in a 3:2 molar ratio $AlCl_3$-NaCl melt over the current range 63-500 mA/cm^2. Recently, Gale and Osteryoung (7) found similar results in a 1:1 molar ratio $AlCl_3$-NaCl melt over the current range 0.03-6.30 mA/cm^2 at 175°C. Anodization of aluminum in an organic room temperature molten salt such as 2:1 molar ratio $AlCl_3$-1-ethylpyridinium bromide was also reported to occur with 100% current efficiency (8, 9).

This investigation was undertaken to examine the practicability of using these types of electrolytes to remove the bulk aluminum from a two-phase Al-Al_3Ni matrix.

Experimental

Melts were prepared and maintained and experiments were conducted in a nitrogen filled glove box (Vacuum/Atmospheres Corporation, Model HE 43-6 DRI-LAB). The moisture content was maintained below 10 ppm.

1-ethyl pyridinium bromide (EPB) was prepared by refluxing ethyl bromide (Baker A.R. Grade) with 10% excess pyridine (Baker A.R. Grade) in acetone (Eastman). The resulting white hygroscopic crystals were washed with anhydrous diethyl ether (Baker A.R. Grade) and vacuum dried at 34°C. The melting point of the dried EPB was 121°C and compared favorably with published values of 120°-121°C (10).

A 2:1 molar ratio room temperature melt of $AlCl_3$-EPB was prepared by adding aluminum chloride (Fluka, A.G., iron free) to the EPB. A melt of $AlCl_3$-NaCl saturated with NaCl [49.75 mole percent (m/o) $AlCl_3$] was prepared by fusing aluminum chloride with excess sodium chloride (Baker A.R. Grade) at 175°C. Both melts were purified utilizing a constant current electrolysis procedure (7), and after at least 10 days of electrolysis were clear. They exhibited no evidence of impurities with cyclic voltammetry at a glassy carbon electrode (Fig. 1). The importance of removing impurities from the melt was demonstrated by Gale and Osteryoung (7), who reported that a black deposit forms on aluminum anodes during electrolysis in impure aluminum chloride containing melts.

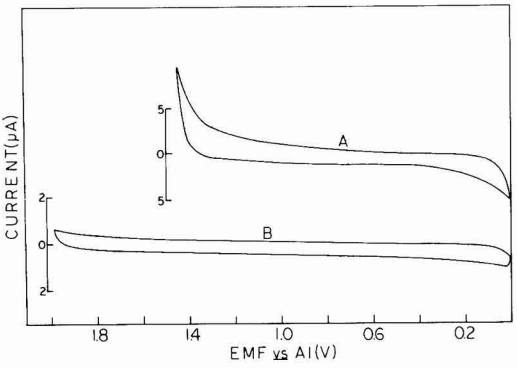

Fig. 1. Cyclic voltammograms at a glassy carbon electrode (A ~ 0.2 cm^2). A is the $AlCl_3$-EPB melt at 23°C and B is the $AlCl_3$-NaCl melt at 175°C. Sweep rate was 100 mV/sec.

Samples of the Al-Al_3Ni matrix were obtained as 3.20 by 0.32 cm diam rods. In addition, a pure sample of Al_3Ni alloy was furnished which had been produced by fusing stoichiometric quantities of aluminum and nickel. This was shaped into a rod of similar dimensions.

Electrodes were fashioned from the samples by wrapping aluminum wire around the ends of the specimens that were not immersed in the melt to provide electrical contact. The immersed area of the Al-Al_3Ni specimen was determined from geometry to be 0.6 cm^2. The Al_3Ni electrode was quite porous, resembling felt metal. A geometrical area, 1 cm^2, was estimated.

Constant current and controlled potential electrolyses were accomplished with a potentiostat/galvanostat (Princeton Applied Research Corporation, Model 173). A voltage programmer (Princeton Applied Research Corporation, Model 175) was coupled to the potentiostat/galvanostat for linear sweep or cyclic voltammetry.

For voltammetry experiments, either a glassy carbon electrode, a pure aluminum wire, or the Al_3Ni electrode was used as the working electrode in a three-electrode cell. The Al_3Ni rod was the working electrode in selective etching experiments. The counter-electrode was a cup-shaped piece of aluminum foil (Research Organic/Inorganic Company, m5n purity), and the reference electrode was a spiral aluminum wire (Alfa-Ventron, m5n purity) isolated from the melt by a 10 mm fine porosity Pyrex frit. The composition of melt in the reference compartment was identical to that of the bulk melt. All potentials described during this investigation were measured against this electrode, *i.e.*, the Al(III)/Al couple.

Cell temperature was maintained at 175°C with a platinum resistance element controlled furnace for experiments with the $AlCl_3$-NaCl melt. Experiments with the $AlCl_3$-EPB melt were conducted at 23°C.

Cyclic voltammograms to determine the melt purity and the $AlCl_3$-EPB anodic limit were constructed by sweeping the glassy carbon electrode between the anodic limit of the melt and the point at which aluminum deposition occurs, *i.e.*, 0.0V at a sweep rate of 100 mV/sec. Linear sweep voltammograms with Al_3Ni or aluminum electrodes were accomplished by sweeping the electrode from 0.0V to the desired anodic potential at a sweep rate of 20 mV/sec.

Results and Discussion

The anodic potential limit of $AlCl_3$-NaCl molten mixtures has been established at *ca.* 2.2V *vs.* Al (11), and was attributed to the oxidation of chloride-containing species to chlorine gas. For the 2:1 $AlCl_3$-EPB melt the limit was determined in this study to be about 1.50V (Fig. 1). Repeated anodization of a glassy carbon electrode in this melt at potentials exceeding 1.50V imparted an orange coloration, suggesting the formation of bromine.

In order that the best electrolysis conditions might be determined, *i.e.*, maximum rate of aluminum removal with minimum fiber attack, it was necessary to know the approximate potential at which significant electrolysis of Al_3Ni took place. For this reason anodic linear sweep voltammograms of aluminum and Al_3Ni were run in both melts. The open-circuit potential of Al_3N was about 0.35V *vs.* Al in both melts.

Linear sweep voltammograms of aluminum and Al_3Ni in the $AlCl_3$-NaCl melt at 175°C (Fig. 2) show that aluminum anodization begins approximately 0.5V before appreciable anodization occurs at the Al_3Ni sample. Therefore, aluminum can be removed in this melt without appreciable attack at the Al_3Ni whiskers, providing the potential of the matrix rod sample is kept below 0.9V. Since this potential is considerably more cathodic than the melt limit, no gas evolution was observed.

The onset of aluminum anodization in this melt is preceded by a reproducible 0.3V overpotential. This

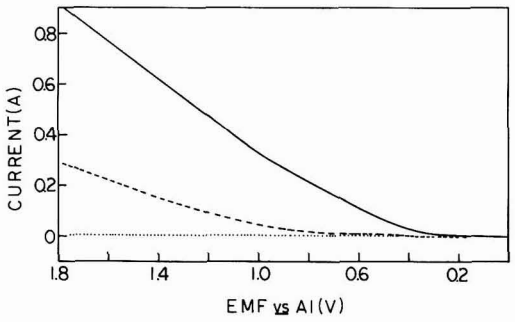

Fig. 2. Anodic linear sweep voltammograms for aluminum and Al_3Ni electrolysis in the $AlCl_3$-NaCl melt at 175°C. Sweep rate was 20 mV/sec. Initial potential was 0.0V *vs.* Al. —— pure aluminum wire ($A \sim 1$ cm^2); ---- Al_3Ni electrode ($A \sim 1$ cm^2); .... glassy carbon electrode ($A \sim 0.2$ cm^2).

overpotential was not affected by pretreatment of the aluminum electrode. An overpotential of similar magnitude was also observed during steady-state current-potential experiments made in this laboratory. This phenomena is in contrast to the behavior of aluminum in $AlCl_3$ rich $AlCl_3$-KCl-NaCl reported in the literature (12) and in $AlCl_3$ rich $AlCl_3$-NaCl melts observed in this laboratory. Unfortunately a detailed discussion of this phenomena is outside the scope of the present investigation.

A similar experiment in the $AlCl_3$-EPB melt at 23°C (Fig. 3) revealed different behavior for the aluminum electrode than in the previous case. Anodization begins almost immediately and a linear rise in current with increasing potential is evident to about 1.1V. At this point the current fell to a constant value, suggesting the formation of a partially insulating film of $AlCl_3$ (12). Attack of the Al_3Ni electrode was negligible until a potential of about 1.0V was attained. Thus, at potentials below 1.0V aluminum can be removed without significant attack on the Al_3Ni fibers. All electrolysis experiments demonstrating the selective removal of aluminum from the Al-Al_3Ni matrix in $AlCl_3$-EPB were carried out in a stirred melt in an attempt to limit the formation of the passivating film at the electrode. The results of these experiments are given below.

Photomicrographs of a portion of an Al-Al_3Ni rod prior to its electrolysis revealed no discernible exposed fibers (Fig. 4). Examination of the rod end surface at greater magnification (Fig. 5) showed Al_3Ni rods which protrude slightly from the Al-Al_3Ni matrix surface where the rod was saw cut. After electrolysis for 1 hr at a potential of 0.9V in an unstirred solution of $AlCl_3$-NaCl at 175°C, a photomicrograph (Fig. 6) revealed myriad-exposed Al_3Ni fibers. During electrolysis the current progressed from an initial value of 0.3 A/cm^2 to a final value of 0.02 A/cm^2. Similar results were obtained after 2 and 5 mA/cm^2 (Fig. 7) constant current electrolysis in the stirred $AlCl_3$-EPB melt at 23°C. During this experiment the potential did not exceed 0.5V.

There appeared to be no discernible difference in the appearance of Al_3Ni fibers exposed by electrolysis in the $AlCl_3$-NaCl melt and those produced in the $AlCl_3$-EPB melt. This was true in spite of the significant differences in the media used for anodizing the Al-Al_3Ni matrix. However, more extensive studies will be required before the extent of damage to the Al_3Ni fibers can be fully assessed. The fibers do appear to be suffi-

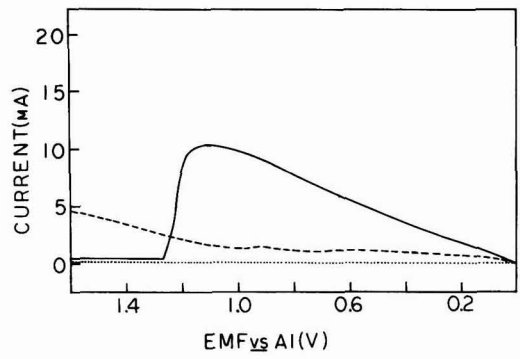

Fig. 3. Anodic linear sweep voltammograms for aluminum and Al_3Ni electrolysis in the $AlCl_3$-EPB melt at 23°C. Sweep rate was 20 mV/sec. Initial potential was 0.0V *vs.* Al. —— pure aluminum wire ($A \sim 1$ cm^2); ---- Al_3Ni electrode ($A \sim 1$ cm^2); .... glassy carbon electrode ($A \sim 0.2$ cm^2).

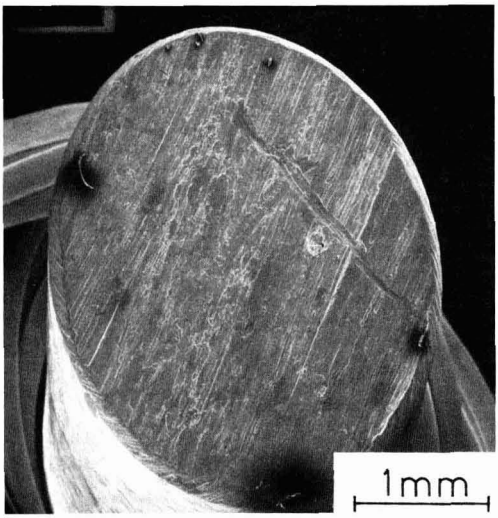

Fig. 4. End-on view of two-phase Al-Al_3Ni matrix rod prior to electrolysis.

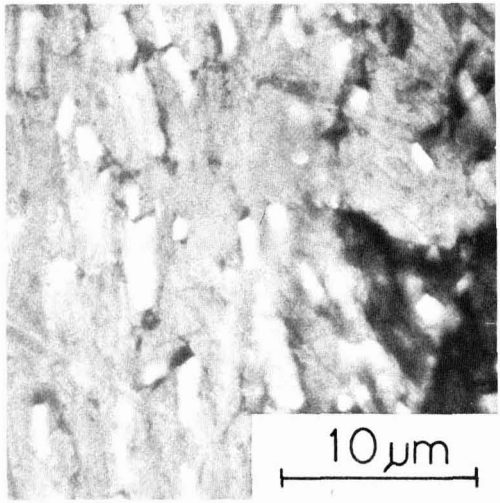

Fig. 5. Al-Al_3Ni matrix rod surface prior to electrolysis

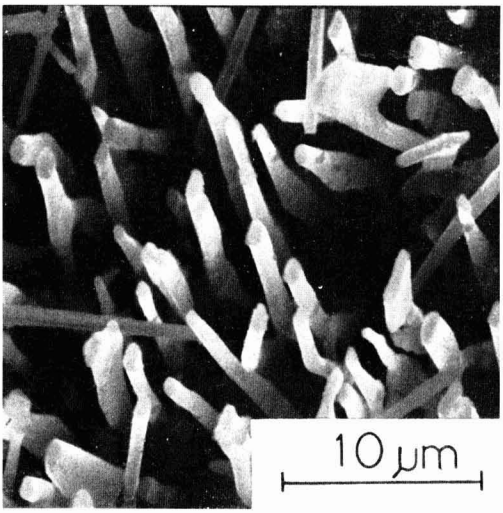

Fig. 6. Al_3Ni filaments exposed with controlled potential electrolysis in $AlCl_3$-NaCl at 175°C. Electrolysis potential was 0.9V.

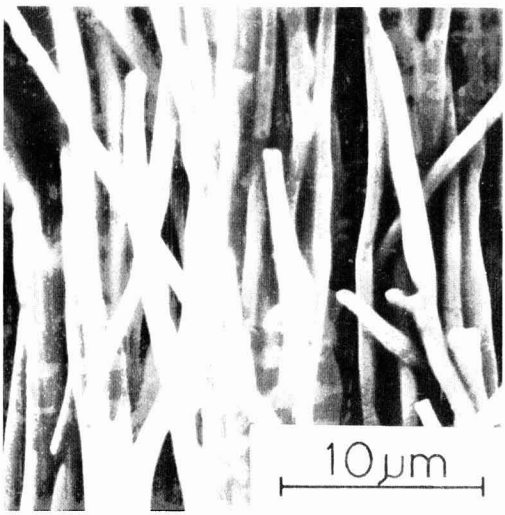

Fig. 7. Al_3Ni filaments exposed with constant current electrolysis in $AlCl_3$-EPB at 23°C. Current density was 5 mA/cm^2.

ciently intact to provide information about the quality of growth techniques used to produce them.

Conclusion

The selective electrolytic etching of aluminum from a two-phase Al-Al_3Ni matrix has been shown to be feasible in aluminum chloride containing molten salts. The molten salts chosen for this study, NaCl saturated $AlCl_3$-NaCl and 2:1M ratio $AlCl_3$-1-ethylpyridinium bromide represent wide extremes in conductivity and liquidus temperature available in aluminum chloride containing molten salts. It should be possible to employ almost any aluminum chloride containing molten salt whose properties lie within these extremes for the selective electrolytic etching of aluminum from an Al-Al_3Ni matrix providing the selectivity constraints are predetermined. In addition, the procedure demonstrated in this study appears promising for scale-up separation operations in which it is desired to produce free, intact, Al_3Ni filaments.

Acknowledgments

Financial assistance in this investigation was provided by the Rome Air Development Center (AFSC), Hanscom AFB, Massachusetts. We would like to thank Dr. J. Hutta and Dr. N. Klausutis of that organization for furnishing samples and for their helpful discussions of the work. We wish to express our appreciation to Dr. J. Clifford and Dr. R. Swedenburg of the Department of Physics, United States Air Force Academy, Colorado, for SEM photographs, and to Dr. J. Robinson and Dr. R. A. Osteryoung, Colorado State University for the gift of a glassy carbon electrode.

Manuscript submitted Jan. 1, 1977; revised manuscript received April 25, 1977.

Any discussion of this paper will appear in a Discussion Section to be published in the June 1978 JOURNAL. All discussions for the June 1978 Discussion Section should be submitted by Feb. 1, 1978.

Publication costs of this article were assisted by the U.S. Air Force Systems Command.

REFERENCES

1. B. J. Bayles, J. A. Ford, and M. J. Salkind, *Trans. Metall. Soc. AIME*, **239**, 844 (1967).
2. F. D. Lemkey, R. W. Hertzberg, and J. A. Ford, *ibid.*, **233**, 334 (1965).
3. J. Hutta, Personal communication.
4. A. W. Davidson and F. Jirik, *J. Am. Chem. Soc.*, **72**, 1700 (1950).
5. W. E. Bennett, A. W. Davidson, and J. Kleinberg, *ibid.*, **74**, 732 (1952).
6. L. A. King. A. D. Brown, and F. H. Frayer, Proc. OAR Res. Appl. Conf., 21 March 1968, p. J-1.
7. R. J. Gale and R. A. Osteryoung, *This Journal*, **121**, 983 (1974).
8. F. H. Hurley and T. P. Wier, *ibid.*, **98**, 203 (1951).
9. W. H. Safranek, W. C. Schickner, and C. L. Faust, *ibid.*, **99**, 53 (1952).
10. J. Willems and J. Nys, *Bull. Soc. Chim. Belg.*, **66**, 502 (1957).
11. Iu K. Delimarskii and B. F. Markov, "Electrochemistry of Fused Salts," p. 145, The Sigma Press, Publishers, Washington D.C. (1961).
12. G. L. Holleck and J. Giner, *This Journal*, **119**, 1161 (1972).

Sputter Deposition of a Metastable Equiatomic Tin-Nickel Alloy

J. A. Augis and J. E. Bennett

Bell Laboratories, Columbus, Ohio 43213

The equiatomic metastable tin-nickel alloy, "Sn-Ni", used for protective and decorative purposes and in electronic components, shows a remarkable resistance to most corrosive agents (1). It is a metastable single phase alloy which has been made only by electrodeposition (2, 3).

Thin film deposition (including electrodeposition) of metals and alloys often leads to phases which cannot be obtained by standard metallurgical techniques. Due to the different rates of nucleation and growth encountered in thin film deposition, it is possible to "quench-in" microstructures (4) which would evolve toward different equilibrium structures during typical metallurgical processing. Two important parameters ruling the microstructures and the kinetics of transformation during film deposition are the flux of impinging atoms and the temperature of the substrate.

While the impinging flux is more easily controlled during electrodeposition, the substrate temperature is more easily controlled during vacuum deposition. It seems reasonable then to expect that a metastable phase could also be produced by sputtering methods. The motivation behind sputtering tin-nickel is twofold: firstly, can certain undesirable properties of the electrodeposited alloy (*e.g.*, brittleness) be improved by the sputtering process; secondly, can the comparisons in physical properties of the two kinds of deposits (sputtered and plated) help to elucidate the nature of the metastable phase? This paper will simply confirm that a metastable tin-nickel alloy can be prepared by sputtering.

Experimental

The equiatomic "Sn-Ni" alloy was deposited using a MRC sputtering head mounted on a Veeco oil-diffusion pumping system. The sputtering gas was argon.

The deposition was made on a substrate of either molybdenum or copper placed on a platen assembly which could be either water cooled or heated and kept at a predetermined temperature. The temperature of the upper face of the substrate was monitored by a compensated thermocouple.

A target having a composition close to equiatomicity was needed. The mixture of equilibrium phases corresponding to the equiatomic composition (Ni_3Sn_4 and Ni_3Sn_2) is extremely brittle, and this precluded the manufacturing of a 5 in. thin disk by melting, forming, and homogenizing nickel and tin. Consequently, the target was prepared by electroplating 10 ml of the metastable phase from the bath previously described in Ref. (3) on a 254 μm thick layer of the 12.7 cm diam copper plate.

Sputter depositions were made under various conditions: the d-c voltage was kept at 3800V; the argon pressure was varied from 10 to 40 mTorr, corresponding to deposition rates ranging from 100 to 325 Å/min; and the substrate temperatures were fixed at values from 40° to 220°C.

Results

The metastable phase can be identified by x-ray diffraction and thermal analysis (3). The equilibrium system (5) corresponding to equiatomicity is a mixture of Ni_3Sn_4 and Ni_3Sn_2. The tin-rich phase Ni_3Sn_4 crystallizes in the monoclinic system; the phase Ni_3Sn_2 crystallizes in the hexagonal system and has the NiAs ($B8_2$) structure. The $B8_2$ structure was also assigned to the electroplated metastable phase by Rooksby (6). However, the x-ray diffraction patterns for two of the three phases are quite similar, suggesting analogous atomic arrangements. In particular, both "Sn-Ni" and Ni_3Sn_2 structures can be described by hexagonal cells with dimensions which are almost equal. The main difference between the two cells concerns the lattice spacings of the (110) and (102) planes. While in Ni_3Sn_2, the spacings are sufficiently different to give two resolvable diffraction peaks for this region of 2θ; the x-ray diffraction pattern shows only one peak for both the 110 and 102 reflections in the case of the electroplated metastable phase. Ni_3Sn_4 shows a somewhat different x-ray pattern in the same region of 2θ where 3 peaks can be resolved. Because only the x-ray pattern of Ni_3Sn_4 is sufficiently distinctive, we checked primarily for the presence of Ni_3Sn_4 diffraction lines in the sputtered deposit.

Table I shows the various sputtering conditions that were used, along with the nature of the film obtained. The compositions of the films were determined with energy-dispersive x-ray analysis (EDAX) using ingot Ni_3Sn_2, ingot Ni_3Sn_4, and electroplated "Sn-Ni" as standards. The latter sample had been previously analyzed by a wet chemistry method (3). It is generally observed during sputtering of alloys that the composition of the deposit is close to the composition of the target. Within the limits of the compositional analysis technique (EDAX), the sputtered films show Ni to Sn ratios comparable to that observed in typical electroplated films. In the two cases where copper substrates were used and sputtering was made at high temperatures (190° and 220°), the lower concentration of tin in the deposit is probably the result of its interdiffusion with the substrate. An evolved gas analysis (EGA) was run on a few samples. The plated samples evolved some water, oxygen, and chlorine. The sputtered samples showed mostly water and argon.

The next to last column of Table I indicates either the absence or the presence of x-ray lines characteristic of Ni_3Sn_4. The equilibrium equiatomic alloy should contain approximately 50% of the Ni_3Sn_4 phase. Only for the three cases where the substrate temperature was at 180°, 190°, or 220°C were any Ni_3Sn_4 x-ray lines observed. It was concluded that for all the runs where the substrate temperature was 100°C or below, a metastable deposit similar to the electroplated alloy was obtained.

Upon heating, the electroplated metastable phase reverts exothermically (3) to the equilibrium mixture presumably by the following reaction

$$6\ \text{"Sn-Ni"} \rightarrow Ni_3Sn_4 + Ni_3Sn_2 + \text{heat}$$

As in Ref. 3, a heat-treatment was given to some of the sputtered films. Substrates were etched away and the films (10 μm thick) were ground to a fine powder. Figure 1a shows the x-ray pattern obtained from unheated powder, and it is similar to the pattern of the as-plated "Sn-Ni" (ASTM x-ray diffraction file card 7-256). In Fig. 1b, which is the pattern given by the heat-treated powder (500°C, 1 hr), lines corresponding to Ni_3Sn_4 and Ni_3Sn_2 can be observed (ASTM

Key words: alloy surfaces, sputtering films, phase transformation stoichiometry.

Table I. Occurrence of the metastable "Sn-Ni" phase under varied sputtering conditions

Identification	Type of substrate	Substrate temperature (°C)	Deposition rate (Å/min)	Composition, atomic percent	Ni_3Sn_4 x-ray lines	Structure
Mo I	Mo unpolished	36	100	53Ni, 47Sn	none	metastable
Mo II	Mo unpolished	100	180	53Ni, 47Sn	none	metastable
Mo III	Mo unpolished	180	220	51.5Ni, 48.5Sn	yes	stable
Cu V	Cu unpolished	50	160	52Ni, 48Sn	none	metastable
Cu VI	Cu polished	190	150	55.25Ni, 44.75Sn	yes	stable
Cu VII	Cu polished	220	370	55.25Ni, 44.75Sn	yes	stable
Cu VIII	Cu polished	84	380	52.25Ni, 47.75Sn	none	metastable
Cu X	Cu polished	80	330	53Ni, 47Sn	none	metastable
Cu XI	Cu polished	80	330	52Ni, 48Sn	none	metastable

cards 4-0845 and 6-0141), showing that transformation to the equilibrium structures takes place during heat-treatment of the sputtered deposit also. These results were confirmed using the technique of differential thermal analysis (DTA) [see Ref. (3)]. Similar to the as-plated alloy, the sputtered material exhibits a broad exothermic peak. In Fig. 2, three DTA traces are shown. It is apparent that the exothermic peaks for the sputtered samples occur at a substantially higher temperature and are much larger than was observed for the plated sample. This indicates somewhat different kinetics of transformation, possibly linked to a different microstructure.

Discussion

From both the x-ray and thermal analyses results we can conclude that sputtering, just as electroplating, produces films of "Sn-Ni" having a different phase structure than equilibrium alloys of the same composition. Both types of films (plated and sputtered) are close to being equiatomic and, following heat-treatment, both have x-ray diffraction patterns corresponding to a mixture of the equilibrium phases Ni_3Sn_4 and Ni_3Sn_2. We have already mentioned in the preceding paragraph that the DTA results for the sputtered films indicate somewhat different kinetics of transformation. The x-ray data, besides showing strong similarities between the two types of films, also reveal some differences.

As explained in the results section, the main difference between the x-ray patterns of Ni_3Sn_2 and "Sn-Ni" is that the 110 and 102 reflections coalesce into a single broad peak in electroplated "Sn-Ni", while they are easily resolved in Ni_3Sn_2. The corresponding 2θ regions of the x-ray patterns for the sputtered samples were carefully examined. For the as-deposited sputtered films, which were believed to be the metastable phase, a small shoulder was always present on the lower 2θ side of the main peak when the sample was actually in film form. Sputtered and electroplated films often show strong preferred orientation. The main reflection which was enhanced by the preferred orientation in the as-sputtered films was found to be 110 using the Laue transmission pinhole technique, and the small shoulder corresponded to the 102 reflection. Effects of preferred orientations were minimized by using powder samples, and there is evidence of peak splitting (102, 110) in Fig. 1a. The x-ray spectra for powder smears of sputtered "SnNi", plated "SnNi", and Ni_3Sn_2 are shown in Fig. 3 with an extended 2θ scale. Note that for the sputtered sample in powder form the 102 peak is now more intense than the 110 peak which is the reverse of that observed for the film samples.

Table II shows the calculated d_{110} and d_{102} values for some of the films. Even when metastable character is attributed to the sputtered films, d_{102} is separated

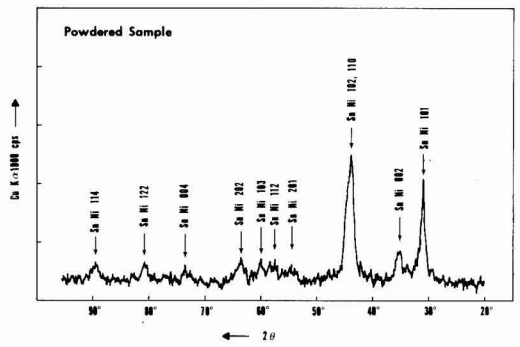

Fig. 1a. Full x-ray diffraction pattern of sputtered tin-nickel in powder form, (sample Cu X) before heat-treatment. Filtered copper radiation 50 kV, 30 mA.

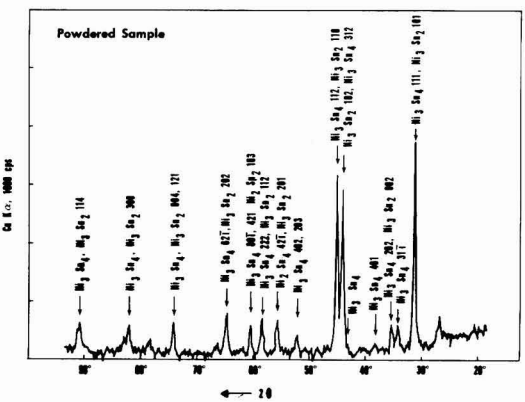

Fig. 1b. Same as above, after 1 hr-500°C heat-treatment of the sample Cu X.

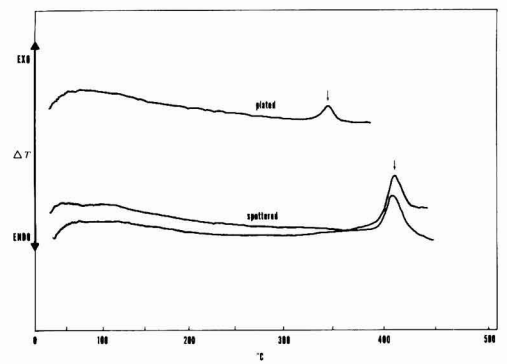

Fig. 2. DTA curves for heating of plated and sputtered tin-nickel alloy. Atmosphere, flowing Ar (0.035 liter/min); heating rate, 5°C/min; reference, α Al_2O_3; sample weight = reference weight = 0.007g.

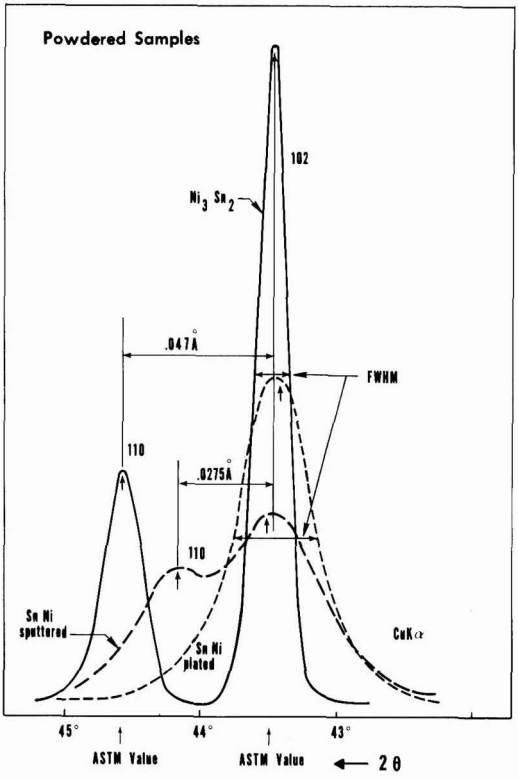

Fig. 3. X-ray diffractometer peaks 110 and 102 for powder samples of plated "Sn-Ni," sputtered "Sn-Ni," and ingot Ni_3Sn_2. The peaks have been normalized to unit area. Filtered Cu radiation 50 kV, 30 mA.

from d_{110} by a Δd ranging from 0.02 to 0.033Å. It should be noted that with increasing substrate temperature, Δd tends toward the value observed for Ni_3Sn_2 of 0.041Å. The last four entries of Table II show the data on powder samples in which preferred orientation did not exist. The results for powders are also illustrated by Fig. 3. In this figure the x-ray traces for the 110 and 102 peaks (normalized to unit area) are shown for equilibrium Ni_3Sn_2, electroplated "Sn-Ni", and sputtered "Sn-Ni". The 102 peaks have been arbitrarily centered at the ASTM value for better illustration. In spite of a rather large broadening effect, two separate peaks can be resolved for the sputtered sample, while no such separation is observed for the plated sample. The extent of the peak broadening is also recorded in Table II as the corrected full width at half-maximum (FWHM). The correction was made by using the gaussian approximation and taking as instrument broadening the width observed for the equilibrium Ni_3Sn_2 sample. X-ray line broadening is known to be due to small grain size, internal microstresses, and/or lattice defects. While it is not possible in the present case to separate these three factors, the line breadth is still a semiquantitative measure of the lattice "irregularities." Results in Table II indicate that the amount of "irregularities" observed in the sputtered sample was comparable to that observed in the plated sample. It is also significant that the line breadth decreased with increasing substrate temperature, and increased with deposition rate. If the line breadth was due only to small crystallite size, the Scherrer formula (7) predicts crystallite main dimensions of roughly 100-150Å for the samples showing the most line broadening.

From these results we can reasonably conclude that both electroplating and sputtering deposit a seemingly homogeneous and equiatomic phase of tin-nickel, the lattice cell of which bears strong resemblance to the cell of the equilibrium phase Ni_3Sn_2. Both methods of deposition, due to the slow rates of growth and migration at low substrate temperature, lead to fine-grained and highly distorted structures. On the other hand, the NiAs-Ni_2In structure, in which both Ni_3Sn_2 and the metastable phase crystallize, is known to accommodate defects and a wide range of composition (8). It is possible then that the metastable "Sn-Ni" is not a new phase as thought by Clarke (9), but the result of a distorted Ni_3Sn_2 lattice as suggested originally by Rooksby (6). In this light, the differences exhibited by plating and sputtering can be attributed to differences in the levels of microstress and deformation produced in the two processes or minor differences in microstructure.

In the first approximation, the microstructure of thin films is primarily fixed by the substrate temperature, but the flux of impinging species in electroplating was almost two orders of magnitude greater than the rate observed in sputtering. Also, plating is a charged process while sputtering is neutral. These differences can lead to a greater "quenching" effect in plating than in sputtering. Also there is the possibility that the difference in impurity levels and impurity species stabilizes differently the plated and sputtered structures. As a consequence, plating may deposit a film with the Ni_3Sn_2 lattice having enough anisotropic deformation and microstresses to make d_{110} and d_{102} equal. Sputtering, however, may allow enough relaxation to produce a lattice in which deformation is not as severe, and thus d_{110} and d_{102} are different. This difference is not as much as in the equilibrium Ni_3Sn_2 compound.

Unfortunately, the dissimilarity in the DTA results, *i.e.*, the apparent shift in the transformation temperature and larger heat of reaction, do not lend themselves to a ready explanation. The DTA results in-

Table II. Differences in lattice spacing and line broadening for the (110) and (102) planes in "Sn-Ni" and Ni_3Sn_2

Sample	State of sample	d_{110} (Å)	d_{102} (Å)	Δd (Å)	Corrected FWHM (degrees)	Structure
Mo I	film	2.070	2.090	0.02	0.38	metastable
Mo II	*film*	*2.060*	*2.09*	*0.03*	0.38	metastable
Mo III	film	2.066	2.093	0.033	0.22	stable
Cu V	film	2.057	2.085	0.028	0.75	metastable
Cu VI	film	2.044	2.085	0.041	0.19	stable
Cu VII	film	2.047	2.088	0.041	0.22	stable
Cu VIII	film	2.055	2.088	0.033	1.16	metastable
Cu X	powder	2.056	2.089	0.033	0.80	metastable
Cu XI	powder	2.058	2.083	0.025	0.85	metastable
Electroplated	powder	2.076*	2.076*	0	0.69-1.10	metastable
Ingot Ni_3Sn_2	powder	*2.036**	2.077*	0.041	0	stable

* ASTM values.

dicate that the sputtered films are stable to a higher temperature and release more energy upon decomposition. Both a thermal kinetic study and an electron microscope study are in progress to clarify these observations and ascertain the causes for these differences.

Conclusion

By using sputtering, we have been able to deposit a metastable equiatomic tin-nickel alloy which is in many ways similar to that which previously has been obtainable only by electrodeposition. Results show that the sputtered alloy has the same basic crystal structure and composition as the electroplated alloy and undergoes the same transformation to equilibrium compounds upon heating. The observed minor differences in x-ray results and stability of the two types of deposits are possibly linked to differences in microstructures and/or microstresses.

Acknowledgments

The authors extend their sincere appreciation to G. V. McIlhargie for his special expertise and effort in preparation of the electroplated sputtering target, T. M. Paskowski for his diligence in obtaining the DTA data, and P. K. Gallager who conducted the E.G.A. study.

Manuscript submitted April 4. 1977; revised manuscript received May 26, 1977.

Any discussion of this paper will appear in a Discussion Section to be published in the June 1978 JOURNAL. All discussions for the June 1978 Discussion Section should be submitted by Feb. 1, 1978.

Publication costs of this article were assisted by Bell Laboratories.

REFERENCES

1. M. Antler, *IEEE Trans. Parts, Hybrids, Packag.*, **php-11**, 216 (1975).
2. N. Parkinson, *J. Electrodepositors Tech. Soc.*, **27**, 129 (1951).
3. J. E. Bennett and H. G. Tompkins, *This Journal*, **123**, 999 (1976).
4. K. L. Chopra, "Thin Film Phenomena," Chapter IV, McGraw-Hill Book Co., New York (1969).
5. M. Hansen, "Constitution of Binary Alloys," p. 1042, McGraw-Hill Book Co., New York (1958).
6. H. P. Rooksby, *J. Electrodepositors Tech. Soc.*, **27**, 153 (1951).
7. H. Klug and L. Alexander, "X-Ray Diffraction Procedures," p. 491, John Wiley & Sons, New York (1967).
8. A. Kjekshus and W. B. Pearson, "Progress in Solid State Chemistry," Vol. 1, Chapter 3, Pergamon Press, New York (1964).
9. M. Clarke and P. K. Dutta, *J. Phys. D*, **4**, 1652 (1971).

Brief Communication

Passivation of Silicon p-n Junctions by Slightly Conductive Chalcogenide Films

E. T. J. M. Smeets, J. Dieleman, F. H. M. Sanders, and D. de Nobel

Philips Research Laboratories, Eindhoven, The Netherlands

Edge breakdown and excessive surface leakage are two well-known hazards of reverse-biased p-n junctions. As a result of numerous studies about the properties of thermal SiO_2 and its interface with silicon, the semiconductor technologist has learned how to avoid these hazards in most cases. Nevertheless, edge breakdown and excessive leakage remain a problem in devices with features that make them prone to these failures. Such features are, for instance, high internal fields, a shallow p-n junction (sharp edges), or a technology that precludes the use of high-temperature oxidation to passivate the critical region where the p-n junction intersects the surface.

The present contribution gives some results of an investigation aimed at exploring the merits of passivation by means of slightly conducting films directly applied to the silicon at a low temperature. With a proper conductivity such a film will cause a gradual voltage drop at the surface of the silicon and thus extend the depletion layer parallel to the surface, thereby reducing the curvature of the depletion layer at the edge of the p-n junction. It is shown that thin chalcogenide films can effectively suppress edge breakdown. Although this goes at the expense of some increase in reverse current because of the additional leakage path created by the chalcogenide film, it has nevertheless proved possible to keep reverse currents in the low nanoampere range and, what is also important, the currents were observed to stay in this range during operation.

The semiplanar mesa-type avalanche photodiode sketched in Fig. 1 was chosen as a vehicle for this study. This device is hard to passivate (1), and it shows all the awkward features mentioned above. The n^+ layer is a shallow ion-implanted layer (0.5 μm), and therefore the critical edges (A and A′ in Fig. 1) are sharp and for this reason prone to edge breakdown. The device is designed for operation slightly below the intrinsic breakdown voltage of the active central part. $V_{BD}{}^{i} = 135$V, which is rather high. Moreover, the use of oxidation at high temperature and the use of a diffused guard ring is impracticable because of the risk of spoiling the critical doping profile at the interface between the p- and the π-layer, which was grown epitaxially in an earlier processing step. Attempts to passivate this device by thermal oxidation at or below 900°C or by applying oxide films with low temperature CVD or sputtering met with no success. Edge breakdown remained or the dark current was high and/or increased with time.

Key words: passivation, chalcogenide films, p-n junctions.

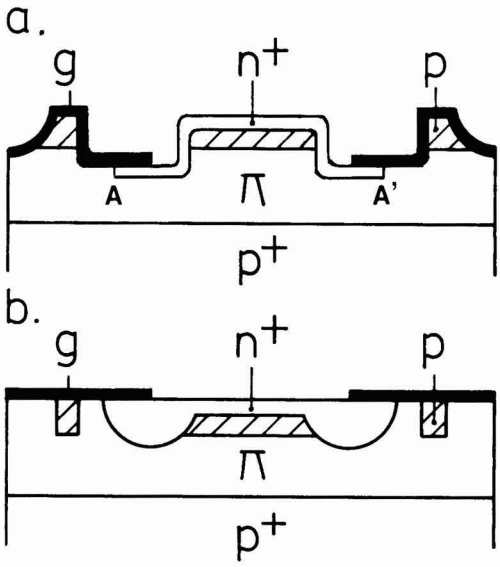

Fig. 1. Main Si APD structures: a. semiplanar mesa type; b. planar type. Both types have the $n^+pp^-p^+$ structure with the circular, active n^+p region surrounded by a concentric annular p-type channel stopper. The planar APD contains an additional n^+ guard ring at the edge of the active n^+p region. The film indicated by "g" is the chalcogenide film applied for edge breakdown suppression and/or passivation.

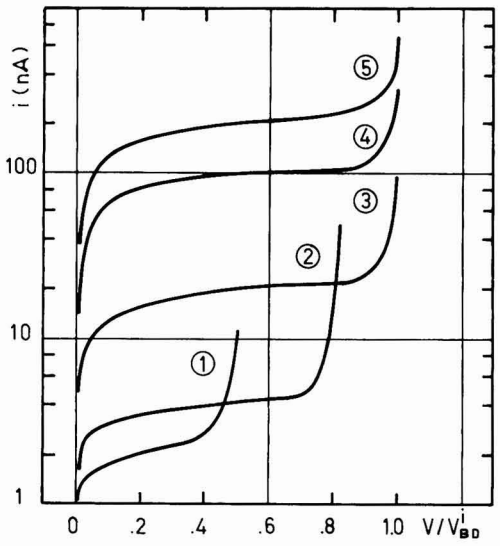

Fig. 2. I-V characteristics of the mesa-type APD for various conductivities of the chalcogenide film g. Curve 1 for a 0.1μ thick GaSe film; curve 2 for $GaSe_{1-x1}Te_{x1}$ with x_1 a few percent; curve 3 for $GaSe_{1-x2}Te_{x2}$ with $x_2 > x_1$ and just sufficient to suppress edge breakdown; curve 4 for a 0.5μ thick CdTe film heat-treated for 2 hr at 150°C in air; curve 5 for the as-deposited CdTe film.

Subsequently, chalcogenide films were examined, with particular emphasis on glassy films based on GaSe. These films are inert against corrosion in air and have high crystallization temperature of up to 450°C. Moreover, GaSe-based films, for instance, can be made over a large range of conductivities. The conductivity of these films increases with increasing substitution of Te for Se or of In for Ga (2, 3).

Figure 2 shows the reverse characteristics for such semiplanar mesa diodes (diameter n^+ region 400 μm) passivated with thin chalcogenide films. The conductivity of the films increases in the sequence 1-5. Curves 4 and 5 refer to diodes with a polycrystalline CdTe film, whereas curves 1, 2, and 3 give results for the glassy chalcogenide films.

The curves show that with increasing conductivity of the passivating film the breakdown voltage quickly rises up to the intrinsic breakdown voltage $V_{BD}{}^i$ (135V); apparently the passivation works satisfactorily. As expected, the reverse current increases with increasing conductivity of the film. This might suggest that the increased reverse current of the diodes is simply due to a resistive parallel leakage path. If this were the case, however, one would expect incomplete saturation of the reverse current with rising conductivity of the passivating film, which is not observed in Fig. 2. Apparently the assumption of simple parallel leakage is an oversimplification of the actual situation.

In Fig. 2 the switch towards intrinsic breakdown occurs somewhere between curves 2 and 3, *i.e.*, between diodes with leakage currents with, say, 4 and 20 nA. By proper adjustment of the Te content, films were deposited which gave diodes with intrinsic breakdown (135V) and a leakage current of only 5 nA at $V = 0.9\ V_{BD}{}^i$.

Another test was made on planar devices [see Fig. 1b and Ref. (1)], where, owing to the presence of a diffused guard ring, edge breakdown was no problem. Here films with even lower conductivities could be used satisfactorily. After stripping the oxide passivation of planar devices and deposition of a glassy GaSe film instead, good planar APD's (diam 450 μm) were obtained with stable dark currents as low as 2 nA at $V = 0.9\ V_{BD}{}^i$ ($V_{BD}{}^i = 250$V), *i.e.*, only about a factor of two higher than that of the original devices with standard high temperature thermal-oxide passivation. In summary, the present work shows that in cases where the well-established passivation with high temperature thermal oxide cannot be used, chalcogenide films of the kind described offer interesting possibilities.

Manuscript submitted April 19, 1977.

Any discussion of this paper will appear in a Discussion Section to be published in the June 1978 JOURNAL. All discussions for the June 1978 Discussion Section should be submitted by Feb. 1, 1978.

Publication costs of this article were assisted by Philips Research Laboratories.

REFERENCES

1. L. J. M. Bollen, J. J. Goedbloed, and E. T. J. M. Smeets, *Philips Tech. Rev.*, 36, 205-210 (1976).
2. J. Dieleman and A. M. E. Hoeberechts, U.S. Pat. 3,982,149.
3. C. Wood, L. R. Gilbert, C. M. Garner, and J. C. Shaffer, "Proceedings of the 5th International Conference on Amorphous and Liquid Semiconductors," J. Stuke and W. Brenig, Editors, p. 285, Taylor and Francis, London (1974).

Comparison of the Erosion of Vitreous Carbon and High Density Graphite in Molten Silicon

R. E. Chaney*

Motorola Incorporated, Semiconductor Group, Phoenix, Arizona 85008

Materials compatibilty problems have seriously affected the development of new silicon ribbon crystal growth technologies. One of the most notable problems has been the degradation of forming dies used for the edge-defined film-fed growth (EFG) process (1), the capillary action shaping technique (CAST) (2), and the inverted Stepanov technique (3). In an effort to understand the materials interaction phenomena, an investigation was undertaken to study the erosion processes of several materials in molten silicon (4, 5). In the previously reported work the materials studied were chosen because of possibly very low erosion, negligible contamination effects, and low porosity. Vitreous carbon[1] was selected as the most promising candidate of the various carbon products. However, many investigators use high density graphite for die fabrication. The purpose of this note is to compare the erosion characteristics of the two carbon products.

The experimental procedure was to immerse rods of the test materials in molten silicon. The rod was either withdrawn or immersed, in stages, to yield a sample with several segments which had been exposed to the melt for various lengths of time. At the top of each section, at the liquid-solid-ambient interface, a groove was produced by the combined effects of surface erosion and surface tension driven flow (6). That this effect is at least partially responsible for severe degradation of the edges of forming dies is a reasonable assumption. The radius change of the lower portion of the segment gives a measure of the surface erosion rate of the test material in silicon. The ambient was one atmosphere of helium while the temperature was maintained at the melting point plus 5°C.

Figure 1 graphically shows the surface erosion *vs.* exposure time for high density graphite.[2] Sample 1 gave very poor results. Several of the zones were so badly pitted that radius measurements were not possible. Sample 2 shows an offset from the axis indicating that the initial melt temperature was too close to the melting point, allowing a protective coating of silicon to be frozen onto the sample initially. Samples 3 and 4 gave reproducible results. All samples were polished prior to testing. The erosion rates for the surface of the rod and for the groove (near the liquid-solid-ambient interface) are tabulated in Table I for high density graphite and vitreous carbon. Fused silica is given as a reference.

The plot of groove depth *vs.* exposure time yields the erosion rate (groove) listed in Table I. Samples 1 and 3 were eroded severely, consequently the results were nonuseable. Samples 2 and 4 did yield a linear relationship similar to that for erosion of the rod surface.

Based only on the data in Table I it is not apparent that there is much difference in the behavior of the two carbon materials in molten silicon. However, investigation of cross sections of the interface between the test rods and the silicon adhering to the rod tip gives an insight into the erosion process. Results for vitreous carbon are given elsewhere (5). The nonporous material erodes by a simple dissolution mechanism involving the formation of a continuous and uniform SiC boundary layer. The presence and effects of this layer are discussed by Swartz *et al* (7).

Figure 2 shows the interface between the high density graphite and silicon. The boundary layer is thin but apparent. The broad light colored band, indicated by the arrow, between the interface and the bulk material is the region of penetration of the graphite by the melt after a 4 hr exposure. It consists of graphite, Si, and SiC in the pores of the bulk material. It is approximately 0.5 mm thick, and contrasts with the absence of penetration of vitreous carbon by the melt (5).

A closer view of the boundary layer is shown in Fig. 3. The layer is irregular and noncontinuous. The arrows indicate particles of SiC which appear to have been released from the layer and frozen into the melt at the termination of the experiment. During ribbon crystal growth such particles which are swept to the crystal growth interface cause twinning and polycrystalline ribbons (2, 3).

It is apparent that high density graphite undergoes erosion by a complex mechanism involving the formation and dissolution of a second phase compound (SiC) and intergranular corrosion.

From these results and those of previously reported work, it can be concluded that while the two carbon materials erode at approximately the same rate, the mechanism is more complex for high density graphite. Intergranular attack appears to result in SiC particles in the melt which affect the ribbon crystallinity and will produce irregular die surface geometry. Thus, forming dies fabricated from vitreous carbon, where

* Electrochemical Society Active Member.

Key words: silicon, crystal growth, vitreous carbon, graphite, erosion.

[1] Beckwith Carbon Corporation.

[2] DFP-2, Poco Graphite.

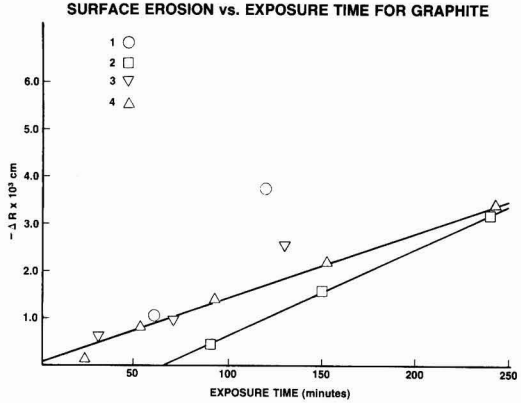

Fig. 1

Table I. Erosion results

Sample	Erosion rate (surface)	Erosion rate (groove)
Graphite		
1	—	—
2	1.8×10^{-5} cm/min	11.3×10^{-5} cm/min
3	1.4	—
4	1.4	3.3
Vitreous carbon (5)	1.7	0 to 44
SiO_2 (4)	1.15	3.4

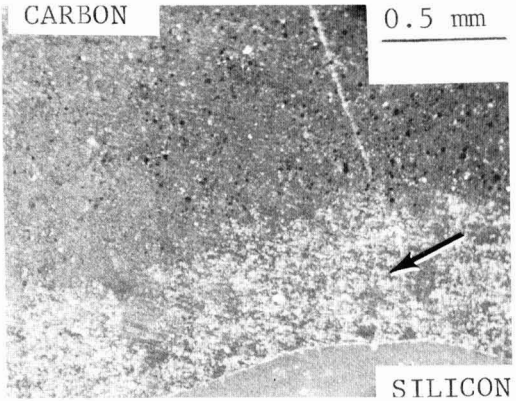

Fig. 2. Photomicrograph of a cross section of the silicon-graphite interface. The SiC boundary layer is apparent between the carbon and silicon. The arrow indicates the penetration region of silicon into the bulk graphite.

intergranular corrosion is not a factor, should yield a superior crystal product.

Acknowledgments

The author would like to thank C. J. Varker for many valuable discussions and for the SEM photographs, and F. R. Garcia for technical assistance.

Manuscript submitted April 13, 1977; revised manuscript received June 6, 1977.

Any discussion of this paper will appear in a Discussion Section to be published in the June 1978 JOURNAL. All discussions for the June 1978 Discussion Section should be submitted by Feb. 1, 1978.

Publication costs were assisted by Motorola Incorporated.

REFERENCES

1. A. D. Morrison, K. V. Ravi, C. V. Hari Rao, T. Surek, D. F. Bliss, L. C. Garone, and R. W. Hogencamp, "Large Area Silicon Sheet by EFG," Fourth Quarterly Report, ERDA/JPL 954355 (1976).

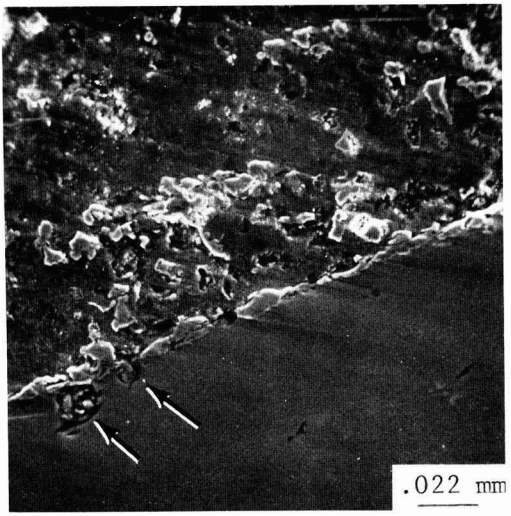

Fig. 3. A closer view of the SiC boundary layer. The arrows indicate particles which have broken away from the boundary layer into the melt. Note the SiC particles formed in the bulk due to penetration of the graphite by the melt.

2. G. H. Schwuttke, T. F. Ciszek, and A. Kran, "Silicon Ribbon Growth by a Capillary Action Shaping Technique," Sixth Quarterly Report, ERDA/JPL 954144 (1976).
3. K. M. Kim, G. W. Cullen. S. Berkman, and A. E. Bell, "Silicon Sheet Growth by the Inverted Stepanov Technique," Third Quarterly Report, ERDA/JPL 954465 (1976).
4. R. E. Chaney and C. J. Varker, *J. Cryst. Growth*, **33**, 188 (1976).
5. R. E. Chaney and C. J. Varker, *This Journal*, **123**, 846 (1976).
6. R. A. Laudise, "The Growth of Single Crystals," p. 187, Prentice-Hall, Inc., Englewood Cliffs, N.J. (1970).
7. J. C. Swartz, T. Surek, and B. Chalmers, *J. Electron. Mater.*, **4**, 255 (1975).

A Technique for Fabricating Oxide Passivated BARITT Diodes

B. M. Armstrong, R. A. Moore, H. S. Gamble, and J. Wakefield

Department of Electrical and Electronic Engineering, The Queen's University of Belfast, Belfast, BT7 1NN, Northern Ireland

It is well known that oxide passivation as used in the "Planar" process greatly improves the reliability, life and yield of semiconductor devices. However, mesa diodes as used in microwave devices such as IMPATTs and BARITTs are not normally oxide passivated. It has been observed with such devices, particularly when Schottky barriers are employed, that degradation of the d.c. characteristic can occur leading to premature failure of the device.

This note reports on a fabrication technique for producing oxide passivated silicon BARITT mesa diodes. These may have either platinum silicide Schottky injecting contacts (M-N-P^+ BARITT) or diffused P^+ injecting contacts (P^+-N-P^+ BARITT). Particular features of this process are the method of production of the self-aligned contacts and the simple method of chip separation.

Experimental Procedure.-- Silicon nitride, because of its slow rate of oxidation (1) and resistance to silicon etch is ideally suited to the processes described below. Following an initial boron diffusion the wafers are coated with C.V.D. silicon nitride and silicon dioxide layers. These layers are then patterned with a scribe-line type network using standard photolithographic techniques the silicon dioxide layer acting as a mask during etching of the nitride in hot orthophosphoric acid. The line network is then chemically etched into the silicon to a depth of about 10μm forming a matrix of squares which define the individual chips and aid device separation.

The remaining layers of silicon dioxide and nitride are re-patterned into an array of dots and 10μm tall mesas are formed by chemical etching. After removal of the masking oxide the wafers are thermally oxidised in water vapor at 1000°c for 20 minutes giving approximately 0.2μm of oxide on the mesa sides. The remaining nitride is easily removed in hot orthophosphoric acid leaving oxide passivated mesas with exposed silicon

Keywords: transit-time devices, passivation, silicon nitride, Schottky barrier.

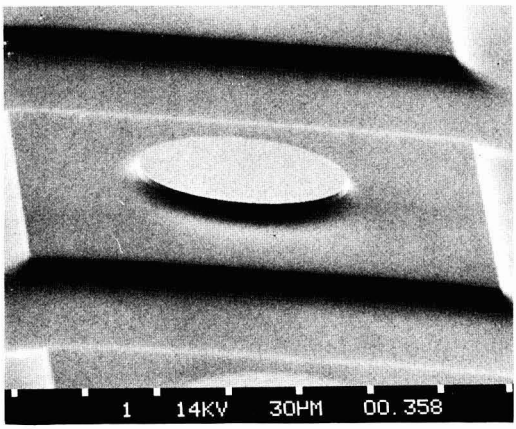

Fig. 1. Scanning electron micrograph of a mesa prior to thinning and separation X500.

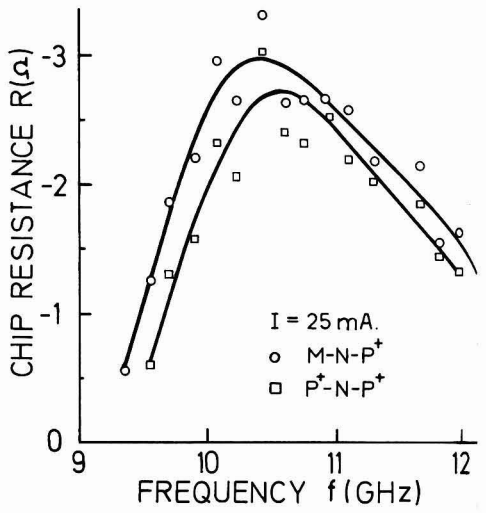

Fig. 2. Small signal chip resistance versus frequency.

top.

Platinum is sputtered over the whole wafer and annealed in nitrogen at 600°c to form platinum silicide on the mesa tops only. For bonding purposes the platinum is covered with evaporated layers of chromium and gold. The unalloyed platinum over the oxide is removed in an ultrasonic bath and this lifts off the chromium-gold leaving self-aligned contacts on the mesa tops. Fig. 1 shows a scanning electron micrograph of a typical mesa, with self-aligned contact, surrounded by etched channels.

The wafers are thinned from the back by mounting them face down on a float which is placed in a chemical bath (2). The process is stopped once the wafers have been thinned down to the scribe lines giving an overall device thickness of about 20μm. The individual chips remain fixed on the float and are coated with evaporated layers of chromium and gold. This chromium-gold layer is then copper plated to a reasonable thickness for handling. At this stage the copper plated chips are removed from the float as a unit and fine lines are scribed in the chromium-gold exposing the underlying copper which is then etched through in dilute nitric acid to produce isolated chips.

In the fabrication of M-N-P^+ BARITT diodes the initial diffusion is omitted and the platinum silicide layer becomes a rectifying Schottky barrier contact to the N-layer.

Results.-- Diodes manufactured using this technique exhibit excellent current-voltage characteristics. Schottky barrier and diffused BARITTs were fabricated from the same wafer to operate at approximately 10.5GHz. The N layer doping was $3 \times 10^{15} cm^{-3}$ and the respective active lengths were 4.4μm and 4.1μm giving punch-through voltages of 40.5V and 35.5V which are in good agreement with theoretical predictions.

The small signal r.f. impedance of these diodes was measured using a Hewlett Packard network analyser. Both types of diode, of area $1.8 \times 10^{-4} cm^2$, produced about 3 ohms of chip negative resistance at 10.5GHz as shown in Fig. 3. When operated in a triple slug-tuned coaxial circuit the P^+-N-P^+ diode produced a maximum power of 8mW and 0.82% efficiency while the M-N-P^+ diodes produced 13mW with 1% efficiency. These results were in good agreement with a computer analysis (3) assuming a diode series resistance of 0.5 ohms indicating that the oxide passivation does not appear to degrade the microwave performance of these diodes.

Conclusions.-- We have found with our oxide-passivated structures that failure due to metal contamination deposited on the mesa sides during top-cap welding is no longer a problem, and in general, oxide passivation reduces the loss of devices during handling and packaging. It has also been found that the technology outlined above produces high yields of good operating devices. Some devices have been operated for several months without a top-cap (i.e. exposed to the room atmosphere) and have shown no degradation, making them suitable for unpackaged insertion into microstrip. In conclusion these BARITT diodes have the advantages associated with semiconductor devices made by the "Planar" process.

Acknowledgements.-- Thanks are due to E. Duffin and J.A.C. Stewart for carrying out the microwave measurements. The financial support of the Science Research Council is gratefully acknowledged.

REFERENCES

1. J.A. Appels, E. Kooi, M. Paffen, J.H. Schatorje, and W. Verkuylen, Philips Res. Repts., 25, 118 (1970)
2. S. Opresko, R.F. Speers and A.I. Stoller, RCA Review, 30, 265 (1970)
3. J.A.C. Stewart, Electron Lett., 9, 345 (1975)

Manuscript received May 17, 1977.

Publication costs of this article were assisted by The Queen's University of Belfast.

THE ELECTROCHEMICAL SOCIETY, INC.

The Electrochemical Society is an international organization of individuals and companies concerned with or interested in materials sciences.

OBJECTIVES

1. The advancement of the theory and practice of electrochemistry, electrometallurgy, electrothermics, electronics, solid state, and allied subjects.
2. To encourage research and the reporting of such research for the dissemination of knowledge in the field of electrochemistry and solid state.
3. To insure the availability of adequate training in the field of electrochemistry for chemists, engineers, metallurgists, physicists, and solid-state investigators.

BENEFITS OF MEMBERSHIP

1. Assurance of keeping abreast of the latest scientific developments in your particular fields of interest.
2. Enjoyment of personal association with fellow scientists and engineers in the professions.
3. Opportunity to contribute to the advancement of the science and application of electrochemistry and solid state in your areas of interest.
4. Stimulation of interdisciplinary exchanges.

DIVISIONS

The activities of the Society are carried on by its nine Divisions and Group as follows:

Battery
Corrosion
Dielectrics and Insulation
Electrodeposition
Electronics
General Materials and Processes
Luminescence
Semiconductors
Electrothermics and Metallurgy
Energy Technology Group
Industrial Electrolytic
Organic and Biological Electrochemistry
Physical Electrochemistry

SECTIONS

Local Sections of the Society have been organized in the following cities and regions:

Boston
Chicago
Cleveland
Columbus
Detroit
Indianapolis
Metropolitan New York
Midland (Michigan)
National Capital Area
Niagara Falls
North Texas
Ontario-Quebec
Pacific Northwest
Philadelphia
Pittsburgh
Rocky Mountain
San Francisco
Southern California-Nevada

JOURNAL OF THE ELECTROCHEMICAL SOCIETY

REVIEWS AND NEWS — SEPTEMBER 1977

Candidates for ECS Officers for 1978

The following material consists of biographical sketches and photographs of the nominated candidates for the annual election of the Society.

Ballots will be mailed by the Secretary to all Active Members in October 1977.

Offices not affected by this election are those of the two other Vice-Presidents, Joan B. Berkowitz and Erik M. Pell, that of Secretary, Paul C. Milner, and that of Treasurer, John L. Griffin.

Dennis R. Turner

Presidential Candidate

Dennis R. Turner is Supervisor of Electrochemical Process Development at Bell Laboratories, Murray Hill, New Jersey. He was born in London, England, in 1920 and came to the United States via Canada at the age of three. After attending public schools in Chicago, Illinois, he enrolled at Lake Forest College and received a B.A. degree in 1942. From 1942 to 1945, Dr. Turner worked as a research engineer at the Research Laboratories of the Westinghouse Electric Corporation, East Pittsburgh, Pennsylvania, doing research and development work on radar components and electrochemical processes. He was involved in the early development of the periodic reverse current plating process and the electropolishing of silver by an anodic pulsing technique.

Dr. Turner did graduate work in the evenings at the University of Pittsburgh and in 1945 he enrolled at the University of Michigan. He worked as a teaching assistant in electrochemistry in 1947-1949 and was awarded the degrees M.S. in chemistry in 1947 and Ph.D. in 1950. Dr. Turner returned to Westinghouse Research Laboratories in 1949 where he did research on electroplating processes.

In 1952, Dr. Turner joined the Electrochemical Research Department of Bell Laboratories. He did research work on the electrochemistry of semiconductor materials, electroplating, and batteries. In 1961, he transferred to the Device Development Area of Bell Laboratories to work on sealed nickel-cadmium batteries for satellite relay and other communication applications. Appointed Supervisor of Basic Development of Batteries in 1963, his supervisory responsibility was expanded in 1967 to include electroless and electroplated copper and gold and semiconductor device chemical processing. Since 1972, Dr. Turner has concentrated on electrochemical problems associated with printed wiring board development and manufacture. His work has brought him in close contact with practical problems in several plants of the Western Electric Company. He also continues his interest and work on the fundamental aspects of electroplating as it applies to innovative ideas for printed wiring board fabrication.

Dr. Turner has published more than 31 papers and review articles and is the author of four book chapters. He has been awarded thirteen patents.

A member of The Electrochemical Society since 1945, Dr. Turner has been active in the Electrodeposition, Electronics, Corrosion, and Physical Electrochemistry Divisions. He has served as Secretary-Treasurer, Vice-Chairman, and during 1963-1964, as Chairman of the Electrodeposition Division. He was a member of the Publication Committee for two years before becoming Society Secretary. Dr. Turner served two three-year terms as Society Secretary from 1967 to 1974, during which time he was responsible for the Society Headquarters Office and served as a member of the Publication, Finance, Society Meeting, and Executive Committees of the Society. He also served on the Nominating Committee on two occasions and on the Young Author's Awards Committee three times. He was active in the Metropolitan New York Section of the Society and served as Vice-Chairman of that Section from 1966 to 1967.

Dr. Turner has been active in the American Electroplaters' Society for many years. He served as a member, Director, and Supervisor of AES Research Project Committees (1960-1972), a member and Chairman of the AES Research Board (1964-1967), a member of the AES Technical Education Board (1970-1972), and a member and Chairman of the AES Paper Awards Committee (1967-1972). Dr. Turner is also a member of the International Society of Electrochemistry and Sigma Xi.

Manfred W. Breiter

Vice-Presidential Candidate

Manfred W. Breiter is a physical chemist at the General Electric Research and Development Center in Schenectady, New York. He was born in Langenbielan (then part of Germany) in 1925. He is an alumnus of the Technical University at Munich, where he received his M.S. degree in 1951 and his Ph.D. in physics in 1953. After working as a postdoctoral fellow for several years on fundamental problems of electrode kinetics at the Institute of Physical Chemistry and Electrochemistry, he was appointed "Dozent" at the Technical University of Munich in 1957. From 1957 to 1958, he spent a year as a visiting assistant professor at the Chemistry Department of Louisiana State University in Baton Rouge. From 1958 to the end of 1960, he directed graduate research in studies related to electrochemical processes on solid electrodes at the Technical University

Con't on p. 344C, Col. 1

Ralph J. Brodd

Vice-Presidential Candidate

Ralph J. Brodd is technical manager of the General Scientific function of Battery Products Technology Laboratory in Parma, Ohio. He was born in Moline, Illinois. He obtained the B.A. in chemistry from Augustana College (Rock Island), and the M.A. and Ph.D. in physical chemistry from the University of Texas in 1953 and 1955, respectively. He won the Corrosion Division Student Essay Contest (ECS) in 1954.

Dr. Brodd joined the National Bureau of Standards in 1955 and worked in the areas of standard cells, kinetics of battery-related reactions, and internal impedance of batteries. He taught physical chemistry in the U.S. Department of Agriculture Graduate School from 1956 to 1961, and lectured in electrochemistry at Georgetown University (1960) and American University (1958). In 1961 Dr. Brodd joined LTV Research Center as

Con't on p. 344C, Col. 2

M. W. Breiter
Vice-Presidential Candidate
Con't.

at Munich, and also taught courses in basic physics at the Munich Branch of Maryland University.

In January, 1961, Dr. Breiter immigrated to the United States to accept his present position on the staff of the General Electric Research and Development Center. He became a U.S. Citizen in 1964. At the Center, he has carried out investigations of both a fundamental and practical nature on electrocatalysis, metal dissolution and oxidation, passivation, electrochemical machining, and solid electrolytes. During the last five years, he has contributed to the development of a sodium-sulfur battery for energy storage.

Dr. Breiter has written more than one hundred technical papers and a book on his research. In addition, he is the editor of the Proceedings of the Symposium on Electrocatalysis, which was organized by the Physical Electrochemistry Division of The Electrochemical Society. Two years ago, he served as chairman of the Gordon Research Conference on Electrochemistry. From 1966 until the present, he served as an adjunct professor of chemistry at Rensselaer Polytechnic Institute in Troy, New York, where he has participated in teaching graduate courses in electrochemistry.

Dr. Breiter has been an Active Member of The Electrochemical Society since 1956, during which time he has served the Society in such functions as officer, including Division Chairman, of the Physical Electrochemistry Division (1965-1975); Divisional Editor of **This Journal** for the Physical Electrochemistry Division (1962-1973); Electrochemical Society Lecturer (1970); Member of the Palladium Award Committee (1968-1971); Member of the Honors and Awards Committee (1971-1974). Chairman of the Palladium Award Subcommittee (1972-1973); and Chairman of the Symposium on Electrocatalysis (1974).

R. J. Brodd
Vice-Presidential Candidate
Con't.

senior scientist, and was appointed head of the Energy Sources Section in 1962 which included fuel cell and plasma physics. In 1963 Dr. Brodd joined Union Carbide. In 1965 he was group leader there, and in 1966 technical manager. His areas of assignments have included rechargeable batteries, porous electrodes, exploratory new concepts, separator, lithium batteries, oxygen electrodes, and zinc-air batteries of analytical and fundamental electrode properties. His technical work has resulted in publication of 25 technical articles, three book chapters, and one patent.

Dr. Brodd has held offices in the Washington Capital and Cleveland Local Sections of the Society. In 1971 he received the Heise Award from the Cleveland Section. He was general chairman of the MnO_2 Symposium sponsored by the International Common Sample Office in 1975. He has been chairman of the Council of Local Sections and the Battery Division, as well as of the Honor and Awards Committee. He has served on the Education and the Contributing Membership Committees, and was Chairman of the 75th Year Anniversary Celebration ad hoc committee. He is presently serving on the Technical Affairs Committee as Technical Advisor for the Battery, Industrial Electrolytic, and Electrodeposition Divisions, and the Energy Technology Group. He is the Society representative to the Intersociety Energy Commerce and Engineering Conference, and also serves as a Battery Divisional Editor.

Dr. Brodd presently is the national secretary to the International Society of Electrochemistry. He also is chairman-elect of the Gordon Conference in Electrochemistry and secretary of the National Advisory ad hoc Battery Committee to ERDA. Finally, Dr. Brodd is a member of the International Society of Electrochemistry, American Chemical Society, American Association for the Advancement of Sciences, Chemical Society (London), American Institute of Chemists, Sigma Xi, New York Academy of Science, and the Ohio Academy of Science.

SECTION NEWS

Rocky Mountain Section

The Rocky Mountain Local Section held its final meeting of the season on May 7, 1977. This meeting, the Section's 3rd Annual Mile High Symposium on Electrochemistry, was held at Colorado State University in Fort Collins, Colorado. Janet G. Osteryoung of the National Science Foundation, Washington, D.C., gave the keynote address which was followed by papers presented by members from the Rocky Mountain area.

This meeting also included the Section's annual business meeting with election of officers being held for 1977-1978.

Jim Howard
Secretary

Columbus Section

The May luncheon meeting of the Columbus Local Section was held on May 25, 1977, at the Battelle's Columbus Cafeteria. Curtis R. Watts of the Materials Application Section of Battelle's Columbus Laboratories presented two films of NASA's Skylab experiments on the behavior of liquids under microgravity conditions. As one would expect, the behavior of fluids under orbital conditions is in many respects different from that in a 1-G environment. Implications for the study and use of electrochemical phenomena in orbital environments were discussed.

The Annual Business Meeting was held on June 27, 1977, at Battelle's Columbus Laboratories. Officers were elected to serve during the 1977-1978 year. Following the business session, John E. Clifford of the Corrosion and Electrochemical Technology Section of Battelle gave a presentation on the "Development of the Water Battery for Bulk Energy Storage." The water battery concept developed by Battelle's Columbus Laboratories is a reversible, water electrolyzer (operates as a hydrogen-oxygen fuel cell in the reverse mode) with external storage of hydrogen, oxygen, and water. It is an advanced energy conversion device for electric utility load leveling applications.

The results of a two-year research effort provided by the Battelle Energy Program, on both electrolysis and fuel cell modes, substantiate the feasibility of long life and high efficiencies at operating temperatures in the range of 200°-250°C. Plans for the further development of the concept were outlined.

Bryan L. McKinney
Secretary-Treasurer

NEWS ITEM

28th Power Sources Symposium

Call for Papers

The 28th Power Sources Symposium will convene June 12-15, 1978, at the Howard Johnson's Regency Hotel in Atlantic City, New Jersey. The Symposium is sponsored by the U.S. Army Electronics Command, with other DOD Agencies, COMSAT, NASA, and ERDA.

Five unclassified technical sessions will be held, these being, alternate power sources, lithium batteries, high temperature and advanced systems primary batteries, and secondary batteries. Scientific and engineering papers describing recent and new developments and advances in these fields are solicited.

For further information, please contact the Chairman: David Linden, Power Sources Technical Area, ATTN: DRSEL-TL-P, U.S. Army Electronics Command, Fort Monmouth, New Jersey 07703; telephone, (comm) 201-544-2084, (autovon) 995-2084.

Nominations Invited for Edward Goodrich Acheson Award and Prize

The Edward Goodrich Acheson Award and Prize was established in 1928 to recognize a person who, in the judgment of the directors of the Society, has made contributions to the advancement of any of the objects, purposes, or activities of The Electrochemical Society as to merit the award. Such contributions may consist of, but shall not be limited to, (a) a discovery pertaining to electrochemistry, electrometallurgy, or electrothermics, (b) an invention of a plan, process, or device, or research evidenced by a paper embodying information useful, valuable, or significant in the theory or practice of electrochemistry, electrometallurgy, or electrothermics, and/or (c) distinguished services rendered to the Society.

The Award consists of a gold medal, a bronze replica, and two thousand dollars ($2000). The following have received the Award:

1929—Edward G. Acheson
1931—Edwin F. Northrup
1933—Colin Garfield Fink
1935—Frank J. Tone
1937—Frederick M. Becket
1939—Francis C. Frary
1942—Charles F. Burgess
1944—William Blum
1946—H. Jermain Creighton
1948—Duncan A. MacInnes
1951—George W. Vinal
1953—J. W. Marden
1954—George W. Heise
1956—Robert M. Burns
1958—William J. Kroll
1960—Henry B. Linford
1962—C. L. Faust
1964—Earl A. Gulbransen
1966—Warren C. Vosburgh
1968—Francis L. LaQue
1970—Samuel Ruben
1972—Charles W. Tobias
1974—Cecil V. King
1976—N. Bruce Hannay

Nominations for the next Award to be presented at the Fall Meeting of the Society in 1978 in New Orleans, Louisiana, are invited. Nominees do not have to be members of the Society to be considered. Furthermore, there are no distinctions, restrictions, or reservations regarding age, sex, race, citizenship, or place of origin or residence.

Please send nominations with supporting documents to G. W. Cullen, RCA Laboratories, Princeton, New Jersey 08540 no later than March 1, 1978.

PEOPLE

David E. Carlson has been appointed head of photovoltaic device development at RCA Laboratories in Princeton, New Jersey. A native of Weymouth, Massachusetts, Dr. Carlson received a B.S. degree from Rensselaer Polytechnic Institute in 1963 and a Ph.D. degree in physics from Rutgers University in 1968. He worked in the Army Nuclear Effects Laboratory in 1968 and 1969, and in 1969 received the Bronze Star Medal while serving as an army captain in Vietnam. Dr. Carlson joined RCA Laboratories as a member of the technical staff in 1970. He received an RCA Laboratories Outstanding Achievement Award in 1973 for his work on ion depletion of glasses, and a second Award in 1976 for the development of amorphous silicon devices. The American Ceramic Society awarded him the Ross Coffin Purdy Award "in recognition of this outstanding contribution to ceramic literature in 1974."

Dr. Carlson is a member of The Electrochemical Society, the American Physical Society, the American Ceramic Society, and Sigma Xi. He has published more than 20 technical papers, and has been issued 5 U.S. patents.

PEOPLE

N. Bruce Hannay, Vice-President, Research and Patents, Bell Laboratories, has been named one of the 60 new members in the National Academy of Sciences. The basis of selection for membership has always been "actual scientific labor in the way of original research; that is, in making positive additions to the sum of human knowledge, connected with unimpeachable moral character. It is not social position, popularity, extended authorship or success as an instructor in science, which entitle to membership, but actual new discoveries." This spring, the National Academy has thus honored 60 American scientists and engineers. We are pleased that Mr. Hannay, an Active Member and Past President of the Society, is one of them.

NEW MEMBERS

It is a pleasure to announce the following new members of The Electrochemical Society as recommended by the Admissions Committee and approved by the Board of Directors in July 1977.

Active Members

Baird, S. L., San Jose, Ca.
Borky, J. M., Dayton, Oh.
Bryant, W. A., Pittsburgh, Pa.
Elwell, D., Stanford, Ca.
Fahidy, T. Z., Waterloo, Ont., Canada
Gutzler, D. E., Aloha, Or.
Kramer, D. E., Trenton, N.J.
Lin, H. C., College Park, Md.
Secco D'Aragona, F., Scottsdale, Az.
Sequeda O., F., San Jose, Ca.
Shah, P. M., Warminster, Pa.
Sigmon, T. W., Corvallis, Or.
Steiner, R. R., Rolling Meadows, Il.

Student Members

Bayraktaroglu, B., Newcastle upon Tyne, England
Dillinger, T. E., Madison, Wi.
Hannah, S. J., Newcastle upon Tyne, England
Johnson, J. F., Cincinnati, Oh.
Pollard, R., Berkeley, Ca.

Reinstatement

Gilliland, J. L., San Jose, Ca.

Transfer

deBernardy-Sigoyer, R. C., Neuilly, France

NEW BOOKS

We continue here a new feature of the **Journal:** synopses of current books thought to be of interest to readers of the **Journal.** Except where noted, these have been prepared by the staff of The Engineering Societies Library, and were selected for inclusion in the **Journal** by Dr. Daniel Cubicciotti of Stanford Research Institute. The Electrochemical Society does not have copies available for sale or loan. Orders for the books should be forwarded directly to the publishers. We will be interested in reader reaction to this new feature and will welcome submission of additional reviews or recommendations of items that should be included.

J. H. Westbrook
News Editor

Thin and Thick Films for Hybrid Microelectronics, by Z. H. Meiksin.

1976, Lexington Books, D. C. Heath and Co., 125 Spring St., Lexington, MA 02173. 453 pages, bound. $29.95.

This volume gives comprehensive coverage of thin and thick films for hybrid electronics. The author has drawn together the physics of thin films, mathematical analysis of distributed networks, and practical step-by-step design procedures for thick and thin film hybrid circuits with new applications. The necessary background in vacuum theory, quantum physics, and semiconductor and surface physics is provided. This book will be of interest to scientists and engineers.

Lasers and Their Applications, 2nd ed., by M. J. Beesley.

1976, Halsted Press, 605 Third Ave., New York, NY 10016. 253 pages, bound. $19.50.

The aim of this book is to explain the mechanism of laser action, to describe the various types of laser which are commercially available, and to describe some applications of the laser, both immediate and potential. This latest edition reflects the developments in devices, particularly microelectronic devices, and in techniques since 1972. On the industrial uses, the experience of four more years has improved our judgment of which applications are likely to be of real use.

Nonemissive Electrooptic Displays, by A. R. Kmetz and F. K. von Willisen.

1976, Plenum Publishing Corp., 227 W. 17th St., New York, NY 10011. 360 pages, bound. $35.00.

This volume provides comprehensive coverage of the materials, phenomena, and technology of the field of nonemissive electro-optic displays. The contributors relate results of recent research to display applications and compare the various approaches currently under development by scientists and engineers. Topics covered include: liquid crystal displays; electrochromic displays; electrophoretic and ferroelectric displays; addressing techniques for nonemissive flat-panel displays.

Applied Solid State Science: Advances in Materials and Device Research, Vol. 6, edited by R. Wolfe.

1976, Academic Press Inc., Publishers, 111 Fifth Ave., New York, N.Y. 10003. 263 pages, bound. $27.00.

Each of the reviews in this volume deals with a different type of composite: composite materials consisting of finely dispersed mixtures of metals and insulators; composite devices in which two distinct semiconductor devices are combined in one package; and composite glass fibers with the core and cladding differing in their optical properties. These composites are all beginning to fulfill their promise of expanding areas of application in electronic systems.

Halbleitermesstechnik, by S. Pfüller.

1976, VEB Verlag Technik, DDR-102 Berlin, Oranienburger, Strasse 13/14, Germany. 284 pages, bound.

Following a short introduction, the chapter on the determination of structural parameters is concerned with optical and electron optical methods. Chapter 3 is on the determination of circuit types, followed by a chapter detailing the various measurement methods for specific resistances. Chapter 5 discusses the measurement of the lifetime of minority carriers, followed by an evaluation of the Hall effect. Chapter 7 is concerned with the measurement of semiconductor surfaces. A short chapter on the determination of optoelectronic characteristics is followed by the concluding, extensive treatment of determination of thin film parameters. A lengthy bibliography is included.

Physics of Semiconductors, edited by F. G. Fumi.

1976, Istituto di Fisica dell'Università, P.le delle Science 5, Rome, Italy. 1328 pages, bound.

Sessions were held on: the role of semiconductors in applications; band structure; lattice dynamics; electron-phonon interaction; phase transitions; one- and two-dimensional effects; layer compounds; small gap materials; new materials; disordered semiconductors; impurities; surfaces; space-charge layers; excitons; biexcitons; exciton condensation; optical properties; magneto-optics; recombination and luminescence; transport and magnetotransport; hot electrons; and spin-dependent properties.

Fuel Cells, (Energy Alternatives Series), by A. McDougall.

1976, Halsted Press, 605 Third Ave., New York, N.Y. 10016. 147 pages, bound. $11.95.

In these days of the "energy crisis," attention has been turned to ways of using our present resources of energy more efficiently, that is to say with less waste. The direct conversion of chemical energy into electricity by means of the fuel cell is an example of such a process, and much research effort has been expended in recent years in an attempt to develop the fuel cell for commercial use. This book provides a discussion of the background to the use of the fuel cell as a source of electrical power, showing the advantages and constraints of the system and illustrating the attempts that have been made to produce commercially viable fuel batteries. Emphasis has been placed on general principles, which are discussed in the first four chapters, and on their application to particular designs of cell, described in the remainder of the book. Economic considerations are outlined briefly in Chapter 12, and a review of future prospects appears as Chapter 13. Although detailed descriptions, both of the scientific basis of fuel cell operation and of the technological development of fuel battery construction, have been reduced to a minimum, references are made to suitable sources of information on these points.

Thermodynamics of Seawater as a Multicomponent Electrolyte Solution, (Marine Science, Vol. 3, Pt. 1), by J. V. Leyendekkers.

1976, Marcel Dekker, Inc., 270 Madison Ave., New York, N.Y. 10016. 496 pages, bound. $28.50.

In this book seawater is treated as a mixture of salts and water of fixed composition, representative of the solution in the open ocean. The individual components of the seawater solution have been treated separately; the salts in terms of the respective binary solution, and the water as the pure liquid. In addition, the properties of many other aqueous salt solutions have been considered, allowing the extension of the general equations to cover compositional variations of many types. Part I covers entropy, volume, expansibility, and compressibility, including equations of state and some optical properties of water and seawater. Special emphasis has been placed on the effect of the solute on the solvent, water, and interesting new facts concerning the properties of this fascinating liquid emerge.

Korrosion und Korrosionsschutz Metallischer Werkstoffe im Hoch- und Ingenieurbau, edited by D. Grimme et al.

1976, Verlag Stahleisen M.B.H., Breite Strasse 27, Postfach 8229, 4000 Duesseldorf, Germany. 325 pages, paper.

These 21 papers are concerned with the many practical aspects of corrosion and its prevention in the various metals used in construction. There is a general paper on the fundamentals of atmospheric corrosion. Subsequent papers discuss corrosion prevention in plain steel, low alloy steel, stainless steels, etc. Corrosion of reinforcing rods in reinforced concrete is discussed. A group of papers is devoted to corrosion prevention using nonferrous metals, including aluminum, zinc, lead, and copper.

Aufarbeitung Von Kupferendelektrolyten durch Dialyse und Elektrodialyse, by H. Winterhager and J. Krüger.

1976, Westdeutscher Verlag GmbH, Gustav-Stresemann-Ring 12-16, 6200 Wiesbaden 1, Germany. 98 pages, paper.

Following a short introduction there is a short survey of dialysis and electrodialysis of electrolytes. A short chapter on membranes and their properties is included, followed by a chapter on material transport through membranes. The final two chapters are devoted specifically to the regeneration of copper refinery electrolytes by dialysis and electrodialysis.

Trends in Electrochemistry, edited by J. O'M. Bockris et al.

1977, Plenum Press, 227 W. 17th St., New York, N.Y. 10011. 408 pages, bound. $35.00.

This book discusses current research and applications of electrochemical technology. The authors emphasize the changes in technological perspective necessitated by the depletion of natural resources, focusing on the problem of preventing future energy shortages. The papers illustrate the potentialities of electrochemical technology in a solar/hydrogen economy; chemical and mineral processing industries, recycling processes corrosion control, and sewage and waste disposal biology. Particular emphasis is placed on the diverse ways in which the development and improvement of energy sources will depend on electrochemical research.

Encyclopedia of Electrochemistry of the Elements, Vol. VII: Carbon-Vanadium, edited by A. J. Bard.

1976, Marcel Dekker, Inc., 270 Madison Ave., New York, N.Y. 10016. 483 pages, bound. $75.00.

The aim of the series is to provide a critical, systematic, and comprehensive review of the electrochemical behavior of the elements and their compounds. This volume is devoted to vanadium and carbon. Chapters cover standard and formal potentials, voltammetric characteristics for vanadium only; double layer properties; electrochemical studies; applied electrochemistry; and inorganic carbon compounds. References are included.

Electrochemical Stripping Analysis, by F. Vydra et al.

1976, Ellis Horwood Ltd., England. Distributed in the U.S. by Halsted Press, 605 Third Ave., New York, N.Y. 10016. 283 pages, bound. $40.00.

This book presents a thorough treatment of all aspects of electrochemical (voltammetric) stripping analysis. This method has been applied successfully in trace analysis for monitoring pollutants in food, water, soil, and other substances, and is important because of its low cost and instrumental simplicity combined with precision. The book is mainly practical and describes the design and construction of simple inexpensive equipment, emphasizing methods and ex-

perimental techniques. An instrumentation section is based on operational amplifier circuitry, circuits for nonstationary electrochemical methods, and their automation. Procedures described include analyses of pure salts, metals, alloys, minerals, rocks, the atmosphere and waters, and clinical analyses. Extensive references are included.

Point Defects in Crystals, by R. K. Watts.

1977, John Wiley & Sons, 605 Third Ave., New York, N.Y. 10016. 312 pages, bound. $21.95.

This book is an introduction to the spectroscopic properties of point defects in crystals. It is intended for materials scientists, physicists, chemists, and students. The book is divided into two parts. The first six chapters deal with theoretical models of defect structure and general discussions of spectra, and the last four chapters survey the experimental situation with regard to defects in a variety of elemental and binary crystals. Many references are included for each chapter.

Aspects Physiques et Chimiques de la Combustion, by G. De Soete and A. Feugier.

1976, Editions Technip, 61, blvd. Saint-Germain, Paris 5e, France. 166 pages, bound. 110F.

Neutral Current Sheets in Plasmas, edited by N. G. Basov.

1976, Plenum Publishing Corp., 227 W. 17th St., New York, NY 10011. 163 pages, paper. $39.50.

Molecular Fluids: Les Houches Lectures 1973, edited by R. Balian and G. Weill.

1976, Gordon and Breach, 1 Park Ave., New York, NY 10016. 459 pages, bound. $48.00.

Electrical and Electronics Trades Directory, 94th ed.

1976, Peter Peregrinus Ltd., U.K., distributed in the U.S. by International Scholarly Book Services, Inc., P.O. Box 555, Forest Grove, OR 97116. 647 pages, bound. $52.50.

Arbeitsgemeinschaft Magnetismus Conference, 1975, edited by A. J. Freeman and K. Schüler.

1976, Elsevier, 52 Vanderbilt Ave., New York, NY 10017. 317 pages, bound. $61.50.

Rare Earth Research Conference.

1976, Rare Earth Research Conference Committee, Denver Research Institute, Denver, CO 80212. 1120 pages, paper. Price not available.

Best's Safety Directory—1977: Safety, Industrial Hygiene, Security, 17th ed.

1976, A. M. Best Co., Inc., Ambest Rd., Oldwick, NJ 08858. 1083 pages, softcover. Price not available.

BOOK REVIEWS

"Vapour Growth and Epitaxy," Proceedings of the Third International Conference on Vapour Growth and Epitaxy, Amsterdam, The Netherlands, August 18-25, 1975, edited by G. W. Cullen, E. Kaldis, R. L. Parker, and C. J. M. Rooymans. Published by North-Holland Publishing Co., Amsterdam (1975). 398 pages; $71.25.

This volume, reprinted from the Journal of Crystal Growth [JCG 31 (1975)], contains 55 of the approximately 100 papers presented at the Third Vapour Growth and Epitaxy Conference. Other papers, which apparently missed the publication deadline, have appeared subsequently in the JCG.

Reprinting the papers in this form was presumably done to make available a desk copy of the Conference Proceedings, and although the information is valuable and owning a personal copy of the book is desirable, the price is prohibitive. Further, there appears to be no incentive for a library to purchase a copy if they already subscribe to the JCG. The Conference Committee would be well advised in the future to use photo offset from author-submitted camera-ready copy, to make the full Proceedings available at a reasonable cost either at the Conference or shortly thereafter. Subsequent publication of the fully reviewed papers in JCG would then provide for wider circulation and archival preservation. On the positive side, the volume is of superior quality. It is a credit to the editors and the publisher. However, if such quality is obtainable only at high cost, one must question whether the publication is viewed as an end in itself or a means to an end.

Those working in the area are already familiar with the contents of the volume, either through attendance at the Conference or via JCG. The casual reader of **This Journal** will want to know that this group of papers, as those of the First and Second Conferences, represents a good cross section of current activity. It would be unfair to the authors to single out papers for comment. All are significant contributions to the field, as ensured by careful selection of invited papers, and from the papers submitted to the Conference. However, it should be noted that they reflect an increasing awareness of, and attention to, the fundamentals of thermodynamics, kinetics, and mass transport in the fluid medium (papers on epitaxial growth from both liquid and vapor phases are included). Significant new techniques are the use of in situ sampling of the vapor phase by mass spectrometry, and by raman scattering and resonance fluorescence spectroscopy to elucidate deposition mechanisms.

John M. Blocher, Jr.
Battelle Columbus Laboratories
Columbus, Ohio

"Multicomponent Chromatography— Theory of Interference," Vol. 4 of Chromatographic Science Series, by F. Helferich and G. Klein. Published by Marcel Dekker, Inc., New York (1970). 419 pages; $24.50.

The high level of scientific presentation shown in the first three volumes of the series is continued here. The strong mathematical bent and its emphasis on a rather narrow part of chromatographic theory will not lead to a wide audience, particularly among electrochemists. However, the authors wish to use chromatography in a larger connotation than that of analytical separations in providing a general system for multicomponent flow through porous media. Thus, those electrochemists concerned with flooded electrodes or flow in restricted channels may find this book useful.

The book should be viewed as presenting original research rather than as a synopsis or review. The concluding chapter presents an excellent overview. There are no references in the book to the electrochemical literature, and a check of the Science Citation Index and recent articles in **This Journal** revealed no citations, but it does seem apparent from SCI that the normal separation science literature has made good use of "Multicomponent Chromatography."

Richard C. Carlston
General Monitors, Incorporated
Costa Mesa, California

"Modern Aspects of Solid State Chemistry," edited by C.N.R. Rao. Published by Plenum Press, New York (1970). 589 pages; $35.00.

The topics covered in 22 chapters by 20 different sets of authors (lecturers at the 1969 Winter School at the Indian Institute of Technology, Kanpur) do justice to the title. Since much of Rao's own research has been directed towards transition metal oxides, there is understandable bias in the coverage of the field in this book, but with a benefit of supplying a focal point. Rao covers this criticism in the preface where he explains some of the factors that dictated the choice of material. As a graduate level text it would have to be supplemented by some elementary crystallography, materials preparation, characterization, and fabrication, as well as the chemistry of covalent semiconductors in order to present a balanced view of current solid-state, crystalline, inorganic chemistry. By inference one can determine what is covered.

Generally each chapter stands on its own and except for some referrals by Rao in the concluding chapter, the material is not cross referenced by the authors. This leads to the awkward situation where zirconia is discussed under defect chemistry (p. 51), anion conductivity (p. 65), and phase transformations (p. 596), but not acknowledged as an ion conductor (Chapter 15). This monograph approach limits its value as a textbook. The sequence of chapters does not make much sense in developing a graduate course. I would prefer to see an arrangement like Chapters 1-4, 18-22, 13-17, and 5-12.

The book's value is not diminished in seven years. In fact, some topics like Magneli-Wadsley defect oxide phases and perovskite materials are even more timely now. The book does have competition provided, among others, by a similar rendition of the 1973 Winter School (at a higher price). On its own merits it can be recommended for every serious student of the solid state.

Richard C. Carlston
General Monitors, Incorporated
Costa Mesa, California

CALL FOR PAPERS

TOPICAL CONFERENCE ON CHARACTERIZATION TECHNIQUES FOR SEMICONDUCTOR MATERIALS AND DEVICES
MAY 21-26, 1978

A topical conference on characterization techniques for semiconductor materials and devices, sponsored by the Electronics Division of The Electrochemical Society, is scheduled for the May 1978 meeting in Seattle, Washington. The purpose of this symposium is to provide a forum for those workers committed to the characterization of semiconductor materials and processes as they relate to device function, performance, and yield. Conversely, those device evaluation techniques which correlate with or produce unique information on materials properties are solicited. All semiconductor materials, including Group IV, III-V, II-VI, IV-VI, etc. are of interest. However, the papers will be grouped according to diagnostic technique rather than by materials in order to stimulate cross-fertilization among workers in elemental and compound semiconductors.

Papers will be grouped into the four general classifications listed below, with an invited paper scheduled as the lead paper in each topic area. Authors contributing papers should specify to which topic area they would prefer to have their paper assigned.

1. **Electrical Methods:** Hall effect, capacitance measurements (C-V, C-t), spreading resistance, minority carrier lifetime, deep level spectroscopy
2. **Chemical Methods:** Auger, SIMS, Rutherford scattering, neutron activation analysis, optical and x-ray spectroscopy
3. **Structural:** Optical and electron microscopy (TEM, SEM), x-ray topography, and etch pit techniques
4. **Device Measurements:** I-V characteristics, derivative techniques, junction leakage, MOS storage time, MTBF

Contributed papers will be screened to ensure that they adequately reflect the interdisciplinary and device-oriented theme of the symposium. This will be accomplished by setting a December 1, 1977, deadline for both the 75-word short abstract and the 500-1000 word extended abstract. Those abstracts considered outside the scope of this topical conference will be automatically submitted to the Electronics General Session. The 500-1000 word abstract submitted should be in a form suitable for use in the extended abstracts volume. Instructions for preparation of the 75- and 500-1000 word abstracts can be found in the July 1977 issue of **This Journal**, pp. 241C-244C. All abstracts should be sent directly to the conference Co-Chairmen, Peter Barnes and George Rozgonyi, Bell Laboratories, Murray Hill, New Jersey 07974. A symposium volume may be published if sufficient interest develops.

Special attention is called to the meeting format. In addition to reviewing prospective papers, each session will consist of oral presentations plus a poster discussion period. Each presentation will be 12 minutes in length. Speakers are asked to bring key figures to be used in a one-hour poster session to immediately follow the oral presentations, allowing for an extended discussion period. Time will be scheduled so that speakers may visit other poster booths.

The session Co-Chairmen would appreciate suggestions, inquiries, and especially comments on the novel aspects of this symposium.

ADVERTISERS' INDEX

POSITIONS WANTED

Please address replies to the box number shown, c/o The Electrochemical Society, Inc., P.O. Box 2071, Princeton, N. J. 08540.

Crystal Grower/Inorganic Chemist—Ph.D., extensive background in the research, R&D, and production of semiconducting (including III-V's), luminescent, optical, acoustooptical, laser, and bubble materials. More than 25 published papers. Will relocate; available immediately. Reply Box C-201.

Electrochemist—Ph.D. Several years of experience in industrial corrosion problems, development of inhibitors and protective coatings, performance of battery elements, etc. Seeks R&D or teaching position. Available immediately. Will relocate anywhere in North America. Reply Box C-202.

Ph.D. Electrochemist—Extensive experience in all phases of plating and metal finishing. Seeks a responsible position in process/product development, production, production supervision, technical service, trouble shooting, or consulting in plating and metal finishing. Reply Box C-203.

Chemical/Electrochemical Engineer, M.S. sc. 8 years experience. Process and product development in semiconductor devices, plating, anodizing, and waste treatment. Reply Box C-204.

Positions Wanted

Society members of any class may, at no cost and for the purposes of professional employment, place not more than three identical insertions per calendar year, not to exceed 8 lines each. Count 43 characters per line, including box number, which the Society will assign.

The Electrochemical Society, Inc.
P.O. Box 2071, Princeton, New Jersey 08540 • 609/924-1902

Instructions to Authors of Papers

Revised July 1, 1972

JOURNAL OF THE ELECTROCHEMICAL SOCIETY is the official journal of the Society and contains three sections totaling some 2500 editorial pages annually: Electrochemical Science and Technology, Solid-State Science and Technology, and Reviews and News.

GENERAL

Manuscripts submitted to the Journal should be sent in **triplicate** (one original and two clear copies) to the Editorial Office, P.O. Box 2071, Princeton, New Jersey 08540. They must be typewritten, double-spaced, on one side only of white bond 8½ x 11 in. paper, 2½-4 cm (1-1½ in.) margins. Illustrations should also be sent in triplicate, with one original and two copies that are clear enough for easy review.

Titles should be brief and properly descriptive, followed by the author's name, professional connection and complete address, including city, state, and zip code. **Text** should be as brief as is consistent with clarity and should omit introductory or explanatory material which may be regarded as familiar to specialists in the particular field. Papers should be written in concise and **good** English and authors are urged to ensure they have been carefully edited and proofread before they are submitted. Suitable headings and subheadings should be included but sections should not be numbered. For current form and style, papers in recent issues should be consulted. Proprietary and trade names should be generally avoided; if used with discretion, they should be capitalized to protect the owners' rights.

If a paper was presented at a meeting of the Electrochemical Society, it should be mentioned in the covering letter sent with the original manuscript.

Under present Society policy, the review procedure is handled by the various Divisional Editors, with final acceptance or rejection by the Editor. Manuscripts are usually reviewed in several weeks and those returned to the author for revision should be resubmitted promptly to the appropriate Divisional Editor. This generally allows publication in five months or less from date of original receipt.

Authors are encouraged to suggest qualified reviewers for their manuscripts, with the editors reserving the right to final choice. It is helpful if the author tells which ECS division (listed in the front of each issue of the Journal) would be most interested in his paper.

Inquiries concerning submitted manuscripts should be addressed to the Editor, President's Office, Rice University, Houston, Texas 77001.

TYPES OF ARTICLES

Articles of wide diversity of interest are acceptable, but subjects primarily covered in the other specialized journals (e.g., analytical or nuclear chemistry) are not considered appropriate.

Technical Papers are divided into two categories: fundamental and applied. The former describes original research of basic nature and must have scientific depth. The latter may deal with any practical aspect of the fields of interest to the Society, e.g., plant design or operation, production and control methods, economics. Each paper should be introduced by an abstract stating the scope of the paper and summarizing fully its results and contents.

Review Papers furnish a current and critical analysis of the subject with citation only of truly pertinent references, and normally should not exceed 20 manuscript pages. An abstract is required.

Technical Notes are used for reporting brief research, developmental work, process technology, new or improved devices, materials, techniques, processes which do not involve more extensive basic scientific study. No abstract is required.

Brief Communications are used to report information of scientific or technological importance which warrants rapid dissemination, even though not necessarily a completed research. Length should be limited to 1000 words or less, with no more than two illustrations. No abstract is required. Publishing time is normally less than three months.

KEY WORDS

Authors are responsible for supplying a list of from three to five single key words to facilitate information retrieval. No paper will be published without them. Generic terms generally are to be avoided as are terms already contained in the title. Key words acceptable to **Chemical Abstracts** are also generally acceptable in Society publications. List key words at the bottom of the first page of the manuscript.

EQUATIONS

Mathematical equations should be written on a single line if possible, and parentheses, brackets, the solidus (/), negative exponents, etc., may be used freely for this purpose. Authors are urged to consult Chapter VI of the "Style Manual" of the American Institute of Physics (available for $2.50 at the American Institute of Physics, 335 East 45 Street, New York, N. Y. 10017) and to follow the patterns described there.

SYMBOLS

Authors are encouraged to use symbols extensively. These should be defined in a list at the end of the paper, with units given. For example:

$a, b \ldots$ = empirical constants of Brown equation
f_i = fugacity of pure ith component, atm
D_v = volume diffusion coefficient, cm²/sec

ABBREVIATIONS UNITS

The AIP "Style Manual" referred to here gives a suitable list of common **Abbreviations.** Units usually will be abbreviated without periods throughout the text, as sec, min, hr, cm, mm, etc. **Metric Units** should be used throughout, unless English units are clearly more appropriate in the area of discussion.

POTENTIAL SIGNS

Electrode potentials: Authors are urged to state and make use of the polarity of test electrodes with respect to the reference electrode used, **i.e.,** Zn is normally negative, Cu normally positive with respect to the standard hydrogen electrode. The sign for the emf of a cell should conform to the free energy change of the chemical reaction as written or implied, in accordance with the definition $\Delta G = -nFE$. These suggestions agree with the IUPAC conventions adopted in 1953.

REFERENCES

Literature References should be listed on a separate sheet at the end of the paper in the order in which they are cited in the text. Authors' initials must be given, and the style and abbreviations adopted by **Chemical Abstracts** should be used. Any recent issue of Society journals may be consulted. Literature cited should be readily available; consequently personal communications, Department of Defense (DOD), and Office of Technical Services (OTS) citations should be minimized. When references are not readily accessible, **Chemical Abstracts** citation numbers must be supplied.

TABLES

Tables should be typed on separate sheets.

ILLUSTRATIONS

Photographs should be used sparingly, must be glossy prints, and should be mailed with protection against folding. **Micrographs** should have a labeled length unit drawn or pasted on the picture. On both, label "top" where any uncertainty might arise. **Captions** for figures (including photographs) must be included on a separate sheet. Figure numbers must **not** appear in the body of the figure; they will be removed if they do. **Numerical Data** should not be duplicated in tables and figures.

Drawings and **Graphs** ordinarily will be reduced to 8.3 cm (3¼ in.) column width, and after such reduction should have lettering no less than 0.15 cm high. Lettering must be of letter-guide quality. India ink on tracing cloth or paper is preferred, but India ink on coordinate paper with blue ruling is acceptable. Line weight 2 is used for borders and zero lines. When several curves are shown, each may be numbered and described in the caption. Lettering shown is approximately ⅛ in. In plotting current or potential as ordinate, increasing negative values should go down.

PUBLICATION CHARGE

To cover part of the cost of publication a page charge of $50.00 per printed page is requested for the publication of technical material. A 10% reduction is allowed if at least one author of an article is an ECS member or an employee of a Patron or Sustaining Member firm. However, acceptance of a manuscript is on the basis of merit and is in no way dependent on such payment. The charge may be waived in individual cases.

Printed in U.S.A.

Call for Papers

153rd Meeting, Seattle, Washington, May 21-26, 1978

Divisions which have scheduled sessions are listed on the overleaf, along with symposium topics.

1. Symposium Papers.

Authors desiring to contribute papers to a symposium listed on the overleaf should check first with the symposium chairman to ascertain appropriateness of the topic.

2. General Session Papers.

Each of the several Society Divisions which will meet in Seattle, Washington, can plan a general session. If your paper does not fit readily into a planned symposium, you should specify "General Session."

3. To Submit a Meeting Paper.

Each author who submits a paper for presentation at a Society Meeting must do three things:

A—Submit one original 75-word abstract of paper to be delivered. **Use the form printed on the overleaf or a facsimile. Deadline for receipt of 75-word abstract is December 1, 1977.**

B—Submit original and one copy of an Extended Abstract of the paper. **Deadline for receipt of Extended Abstract is January 1, 1978.** See (5) below for details.

C—Determine whether the meeting paper is to be submitted to the Society Journal for publication. See (6) below for details.

Send all material to The Electrochemical Society, Inc., P.O. Box 2071, Princeton, N.J. 08540.

Unless the 75-word and required Extended Abstracts are received at Society Headquarters by stated deadlines, the papers will not be considered for inclusion in the program.

4. Meeting Paper Acceptance.

Notification of acceptance for meeting presentation, along with scheduled time, will be mailed to authors with general instructions no earlier than two months before the meeting. Those authors who require more prompt notification are requested to submit with their abstracts a self-addressed postal card with full author-title listing on the reverse.

5. Extended Abstract Volume Publication.

All scheduled papers will be published in the EXTENDED ABSTRACTS volume of the meeting. The volume is published by photo-offset directly from typewritten copy submitted by the author. Therefore, special care should be given to the following instructions to insure legibility.

A—Abstracts are to be from 500 to 1000 words in length and should not exceed two pages, single spaced. The abstract should contain to whatever extent practical all significant experimental data to be presented during oral delivery.

B—Abstracts should be typed single spaced on the typing guide forms which are sent to each author after the submission of a short abstract. If it is necessary to use white bond paper, it should be 8½ x 11 inches with 1¼ inch margins on all sides. Submit all copy in black ink. Do not use handwritten corrections.

C—Title of paper should be in capital letters. Author(s) name and affiliation and address should be typed immediately below in capital and lower case letters. Please include zip code in address. It is not necessary to designate paper as "Extended Abstract" or to quote the divisional symposium involved.

D—If figures, tables, or drawings are used, they should follow the body of the text and should not exceed one page. Submit only the important illustrations and avoid use of halftones. Lettering and symbols should be no smaller than ⅛ inch in size. Figure captions should be typed beneath the figure and be no wider than the figure. Table titles should be typed above, and the same width as, the table.

E—Mail original and one copy of the abstract to: The Electrochemical Society, Inc., P.O. Box 2071, Princeton, N.J. 08540, unfolded.

Abstracts exceeding the stipulated length will be returned to author for condensation and retyping.

6. Manuscript Publication in Society Journal.

All meeting papers upon presentation become the property of The Electrochemical Society, Inc. However, presentation incurs no obligation to publish. If publication in Journal is desired, papers should be submitted as promptly as possible in full manuscript form in order to be considered. If publication elsewhere after presentation is desired, written permission from Society Headquarters is required.

Seattle, Washington, Meeting Symposia Plans—Spring 1978
May 21-26, 1978

a.) For receipt no later than December 1, 1977, submit a 75-word abstract of the paper to be delivered on the form overleaf.
b.) For receipt no later than January 1, 1978, submit two copies of an extended abstract, 500-1000 words.
c.) Send all abstracts to The Electrochemical Society, Inc., P.O. Box 2071, Princeton, N.J. 08540. See details on preceding page.

CORROSION

General Session

All aspects of low temperature and high temperature corrosion will be considered. Techniques for the study of corrosion phenomena are of interest. Suggestions and inquiries should be sent to the Symposium Chairman: J. Kruger, National Bureau of Standards, Rm. B254, Bldg. 223, Washington, D.C. 20234.

CORROSION/ELECTROTHERMICS & METALLURGY

Oxidation of Metals and Alloys

Fundamental and applied papers are solicited to promote a thorough interdisciplinary approach to the following topics of high temperature gas-metal reactions and the associated industrial problems: 1. Theoretical advances in metal and alloy oxidation mechanisms. 2. Experimental methods and techniques for determining physicochemical properties of the metal-reaction product composite system. 3. Metal and alloy oxidation in pure and mixed gaseous oxidants. 4. Investigations on development of more effective oxidation resistant alloys. 5. Other topics in the gaseous degradation of materials.

Suggestions and inquiries should be sent to the Symposium Co-Chairmen: R. A. Rapp, Dept. of Metallurgical Engineering, The Ohio State University, Columbus, Ohio 43210; or W. W. Smeltzer, Dept. of Metallurgy and Materials Science, McMaster University, Hamilton, Ont., Canada L8S 4M1.

CORROSION/INDUSTRIAL ELECTROLYTIC/ PHYSICAL ELECTROCHEMISTRY

Characterization of Current, Potential, and Mass Distributions in Corrosion and Passivation Phenomena

This symposium is intended to provide an opportunity for electrochemists and electrochemical engineers to present results of modeling and mathematical treatments of corrosion-related problems. Investigations of the behavior of electrolytes and thin films and their impact on corrosion and passivation phenomena are invited. Particular fields of interest for treatment include: 1. Anodic and cathodic protection. 2. Pitting corrosion. 3. Crevice corrosion. 4. Differential concentration cell corrosion. 5. Stress corrosion cracking. 6. Breakdown and repair of passive films. 7. Transport phenomena in thin oxide films. 8. Corrosion under applied organic films. 9. Atmospheric corrosion.

Suggestions and inquiries should be sent to the Symposium Co-Chairmen: W. H. Smyrl, Sandia Laboratories, Div. 5831, Albuquerque, N.M. 87115; R. C. Alkire, Dept. of Chemical Engineering, University of Illinois, Urbana, Ill. 61801; or M. J. Dignam, Dept. of Chemistry, University of Toronto, Toronto, Ont., Canada M5S 1A1.

DIELECTRICS & INSULATION

Solid-State Chemical Sensors

The use of solid-state devices for measuring chemical composition is truly interdisciplinary, involving chemistry, physics, electronics, biological, and health sciences. This symposium will consider the many opportunities for significant practical products, as well as the principles of device design and operation.

Papers are requested on the following subjects: 1. Chemically sensitive transistors. 2. Semiconductor materials and devices for chemical detection. 3. Solid-state electrochemical cells. 4. Piezoelectric sorption detectors. 5. Specific-ion electrodes. 6. Catalytic combustion sensors. 7. Miscellaneous methods.

There is no special emphasis on fundamental or applied work, or on a particular group of materials. Papers that cover the full range of topics in environmental monitoring, chemical process control, personal monitoring, and medical and biological analyses are welcome.

Suggestions and inquiries should be sent to the Symposium Chairman: L. D. Locker, Solid State Sensors Co., 5600 Peach Blossom Pl., Fort Lauderdale, Fla. 33319.

General Session

Papers are especially solicited on the following topics: 1. High temperature and special polymer materials for solar thermal applications, including selective absorbers. 2. Thin film dielectric materials; their formation and characterization. 3. Packaging and encapsulation materials and techniques for semiconductor devices, including solar cells.

Suggestions and inquiries should be sent to the Symposium Chairman: J. A. Amick, Exxon Research and Engineering Co., Box 8, Linden, N.J. 07036.

DIELECTRICS & INSULATION/ ELECTRONICS

Thin Films of Tunneling Dimensions

The potential for devices employing thin films of tunneling dimensions appears to be on the rise. Thus, papers are solicited for a symposium focusing on properties and applications of such films. Examples of topics of interest are:

Chemical and Physical Properties: 1. Film preparation, growth, deposition, multilayered structures. 2. Film characterization, interfacial and bulk composition, defects, uniformity. 3. Electrical characterization, tunneling phenomena. 4. Electronic and electrical behavior of surfaces.

Applications: 1. New tunneling devices. 2. Solar cells. 3. Superconductive tunneling. 4. Interfacial layer devices.

The purpose of this symposium is to promote a dialogue between those scientists interested in surface physics and the physics of interfacial layers and those working in the field of device physics. A symposium volume will be published if sufficient interest develops.

Suggestions and inquiries should be sent to the Symposium Co-Chairmen: J. Shewchun, Dept. of Engineering Physics and Institute of Materials Research, McMaster University, Hamilton, Ont., Canada L8S 4M1; or S. I. Raider, IBM Thomas J. Watson Research Center, P.O. Box 218, Yorktown Heights, N.Y. 10598.

DIELECTRICS & INSULATION/ ELECTRONICS/ELECTROTHERMICS & METALLURGY

Defect Chemistry of Semiconductors and Dielectrics

This symposium will deal with the generation and interactions of defects and with defect-related properties in semiconductors and dielectrics. Both experimental and theoretical papers are solicited. Subjects within the scope of the symposium include isolated point defects, impurity centers, defect associates, and defect ordering in elemental and compound semiconductors. Experimental results are invited which involve such techniques as electrical conductivity, resonance techniques, optical methods, phase diagram determinations, preparation of crystals and films containing controlled deviations from stoichiometry, dielectric breakdown, and mobility determinations.

Suggestions and inquiries should be sent to the Symposium Co-Chairmen: D. M. Smyth, Materials Research Center, Lehigh University, Bethlehem, Pa. 18015; J. A. van Vechten, IBM Thomas J. Watson Research Center, P.O. Box 218, Yorktown Heights, N.Y. 10598; or J. B. Wagner, Jr., Center for Solid State Science, Arizona State University, Tempe, Ariz. 85281.

DIELECTRICS & INSULATION/ ELECTROTHERMICS & METALLURGY

Fundamentals of Film Growth Processes in Anodic and Thermal Oxides

The main thrust of this symposium is to discuss the processes responsible for the thickening of uniform oxide films on metal surfaces. The anodic oxides of metals such as Ta, Zr, Al, and Si, and of alloys such as GaAs fall into this category, as do certain films formed by plasma anodization or thermal oxidation. Contributions are solicited on various features of such oxides, particularly: 1. Growth kinetics. 2. Atom movements. 3. Structure and composition. 4. Ionic conduction and dielectric properties. 5. Related topics.

Suggestions and inquiries should be sent to the Symposium Co-Chairmen: (for anodic oxides) J. P. S. Pringle, Chalk River Nuclear Labs, Atomic Energy of Canada Ltd., Chalk River, Ont., Canada K0J 1J0 ; or (for plasma oxides or thermal oxides) P. F. Schmidt, Bell Laboratories, 555 Union Blvd., Allentown, Pa. 18103.

ELECTRONICS

Semiconductors

Multilayer Epitaxy

Invited and contributed papers will address the state-of-the-art and current problems associated with growth of epitaxial layers with complex compositional variations. Of particular interest will be the factors that limit compositional transitions between sequential layers during growth by diverse epitaxial processes, e.g., liquid phase, vapor phase, and molecular beam epitaxy. Examples of appropriate topics include: 1. Abrupt doping level transitions. 2. Growth of superlattice structures. 3. Evaluation of abrupt compositional transitions. 4. Autodoping control. 5. Solid-state diffusion during epitaxial growth. 6. Growth of layers with controlled compositional variations, e.g., hyperabrupt or graded profiles.

Suggestions and inquiries should be sent to the Symposium Chairman: D. W. Shaw, Texas Instruments Inc., P.O. Box 5936, M/S 118, Dallas, Texas 75222.

Topical Conference on Characterization Techniques for Semiconductor Materials and Science

The purpose of this symposium is to provide a forum for those workers committed to the characterization of semiconductor materials and processes as they relate to device function, performance, and yield. Conversely, those device evaluation techniques which correlate with or produce unique information on materials properties are solicited. The papers will be grouped according to diagnostic technique, e.g., chemical (metallurgical), structural, or electrical, rather than by material in order to stimulate cross-fertilization among workers in elemental and compound semiconductors. Also, a device characteristics/materials session, possibly relating starting material, processing, and aging perturbations to device performance would be desirable.

A symposium volume may be published if sufficient interest develops. Speakers are asked to bring key figures to be used in a one-hour poster session to immediately follow the oral presentation allowing for an extended discussion period.

Suggestions, inquiries, and especially comments on the novel aspects of this symposium should be sent to the Symposium Co-Chairmen: P. Barnes and G. Rozgonyi, Bell Laboratories, Murray Hill, N.J. 07974.

General Sessions

The Semiconductor General Sessions will cover a broad range of topics related to semiconductor device fabrication and materials characterization. Original papers representing work related to the following topics are requested: 1. Thin film deposition techniques for device fabrication, characterization of thin films, and process monitoring techniques. 2. Photolithography and etching techniques for small geometry devices, device characterization, and monitoring techniques. 3. Influence of materials defects and impurities on device operation, reliability, measurement techniques, and correlation of such defects with yield. 4. Amorphous semiconductor materials and devices, preparation, characterization, and device modeling. 5. Fabrication and processing technology for LED's, lasers, solar cells, and thin film electroluminescent devices and thin film transistors. 6. Characterization of process techniques using the high pressure, low temperature, partial vacuum, or other innovative fabrication techniques.

Suggestions and inquiries should be sent to the Symposium Chairman: P. L. Castro, Hewlett-Packard Labs, 3500 Deer Creek Rd., Palo Alto, Calif. 94304.

Luminescence

Improved Energy Conversion for Lighting Fluorescent Lamps and Phosphors

Suggested areas for papers include:
1. Fluorescent lamp color and luminosity characteristics which permit high light out-

put for a given energy input, permit lower power input to match or improve existing lighting norms, and show improved utilization of light for specialized purpose.

2. Phosphor design and application which permits their use under new and different lamp conditions, i.e., excitation course, ambient temperature, atmosphere, or discharge characteristics, such as higher power loading.

3. Lamp designs of improved energy conversion which utilize phosphors as a light source.

Suggestions and inquiries should be sent to the Symposium Chairman: M. V. Hoffman, General Electric Co., Nela Park No. 136, East Cleveland, Ohio 44112.

Phosphor Screening

This symposium will emphasize properties of phosphors which relate directly to the performance or fabrication of phosphor-containing devices, such as fluorescent lamps, x-ray screens, cathode-ray picture or specialty tubes, and flat discharge panels. Examples of subjects for papers include among others: 1. Phosphor efficiencies as a function of excitation density. 2. Optical properties of phosphors as they relate to device performance, examples, emission color, persistence, and reflectivity. 3. Screening properties of phosphors, examples, wettability, dispersibility, bulk density, screen cohesion, and substrate adherence. 4. Synthesis considerations related to phosphor screening.

Suggestions and inquiries should be sent to the Symposium Co-Chairmen: M. Royce, *RCA Corp., New Holland Ave., Lancaster*, Pa. 17604; or H. Forest, Zenith Radio Corp., Rauland Tube Div., 2407 North Avenue, Melrose Park, Ill. 60160.

General Sessions

General sessions will be held covering all topics of luminescence in inorganic solids. Twenty-five minutes will be allotted for each paper, including discussions. Review or survey papers requiring a longer time will also be considered.

Suggestions and inquiries should be sent to the Symposium Chairman: F. F. Mikus, GTE Sylvania Inc., Chemical and Metallurgical Div., Towanda, Pa. 18848.

General Materials and Processes

General Session

Papers are encouraged in emerging areas of materials science; new generic concepts in the processing of electronics devices or circuits; follow-up papers in areas recently covered by other Electronics Division symposia; papers in areas such as devices and *materials for energy generation*, materials for magnetic bubbles, integrated optics, optimized or new microwave materials, thermodynamic properties of electronic materials, thermodynamics and kinetics of growth and processing, and other areas of interest.

Suggestions and inquiries should be sent to the Symposium Chairman: M. B. Panish, Bell Laboratories, Room 1C-321, Murray Hill, N.J. 07974.

ELECTRONICS/ELECTROTHERMICS & METALLURGY

Eighth International Conference on Electron and Ion Beams in Science and Technology

The following topics will be included in the program of this eighth conference: 1. Progress in the physics of electron and ion beams. 2. Novel electron and ion beam applications. 3. High power electron beam applications for materials processing including welding, heat-treatment, evaporation, melting, and refining. Papers dealing with advanced high throughput industrial systems and computer-controlled systems are of particular interest. Papers dealing with mechanisms and betterment of understanding of the physics of the processes involved are welcomed. 4. Applications of electron and ion beams to microelectronics including x-ray and electron lithography systems for IC and device manufacture and control, manufacturing processes and characteristics of advanced IC's, and unusual devices of all types, ion implantation and ion implantation systems. 5. Electron beam recording and information storage. 6. Irradiation processing activities including sterilization and polymer curing. 7. Extreme power systems for triggering fusion reactions and related activities.

Suggestions and inquiries should be sent to the Symposium Chairman: R. Bakish, Bakish Materials Corp., 171 Sherwood Pl., Englewood, N.J. 97631.

ELECTRONICS/ENERGY TECHNOLOGY GROUP/PHYSICAL ELECTROCHEMISTRY

Photoelectrochemical Energy Conversion

The symposium will cover advances in semiconductor liquid junction solar cells, photoelectrolysis of water, and properties of illuminated junctions between semiconductors and electrolytic solutions. Papers on both fundamental and practical aspects of these topics are invited.

Suggestions and inquiries should be sent to the Symposium Co-Chairmen: A. Heller, Bell Laboratories, Murray Hill, N.J. 07974; or A. J. Bard, Dept. of Chemistry, University of Texas, Austin, Texas 78712.

ELECTROTHERMICS & METALLURGY

Industrial Slags, Fluxes, and Fused Salts

The first day of the symposium will consist of invited papers on: 1. Fluxes used in aluminum extraction and refining, 2. Fluxes used in electroslag melting and welding, 3. Fluxes used in the molten salt reactor, 4. Fluxes used in heat treatment baths, 5. Iron and steelmaking slags, 6. Non-ferrous slags, 7. Arc-welding slags and fluxes.

Contributed papers in related areas are solicited for the second day of the symposium.

Suggestions and inquiries should be sent to the Symposium Chairman: D. Cubicciotti, Stanford Research Institute, Room B222, Menlo Park, Calif. 94025.

General Session

Papers dealing with materials reactivity and stability, particularly at high temperature, will be considered. Experimental techniques for study of such properties are also of interest. Suggestions and inquiries should be sent to the Symposium Chairman: H. S. *Spacil, General Electric Co., Research and* Development, P.O. Box 8, Schenectady, N.Y. 12301.

INDUSTRIAL ELECTROLYTIC

Chlorine and Chlorate Cell Technology

The purpose of this symposium is to review recent improvements now in commercial use, emerging technology that is applicable in today's economy, and long-range developments that will make an impact on the industry. Areas of interest will not be limited to, but may include energy conservation and environmental considerations.

Suggestions and inquiries should be sent to the Symposium Co-Chairmen: T. C. Jeffrey, *PPG Industries, Chemical Div., P.O. Box 1000*, Lake Charles, La. 70601; or M. P. Grotheer, Hooker Chemical Co., Electrochemical Div., Niagara Falls, N.Y. 14302.

General Session

Suggestions and inquiries should be sent to the Symposium Chairman: R. C. Alkire, Dept. of Chemical Engineering, University of Illinois, Urbana, Ill. 61801.

INDUSTRIAL ELECTROLYTIC/ ENERGY TECHNOLOGY GROUP

Industrial Water Electrolysis

Specific topics of interest for the symposium are: 1. Current technology, including aspects such as hardware designs, advantages and disadvantages of different designs, problems such as time variation of performance, material problems, life, etc. 2. High pressure water electrolyzers; their present and future applications. 3. Future technological developments, e.g., water electrolyzers using solid polymer electrolytes, alkaline electrolytes at elevated temperatures, or solid oxide electrolytes. 4. Prospects for photoelectrolysis of water or production of hydrogen using hybrid thermochemical-electrochemical cycles. 5. Economic analysis of hydrogen production by water electrolysis and prospective users of the hydrogen thus produced.

Contributed papers are solicited on the topics outlined above.

Suggestions and inquiries should be sent to the Symposium Co-Chairmen: S. Srinivasan or F. J. Salzano, Brookhaven National Laboratories, Dept. of Applied Science, Upton, N.Y. 11973; or A. R. Landgrebe, U.S. Energy Research and Development Administration, *Div. of Energy Storage Systems*, Washington, D.C. 20545.

ORGANIC & BIOLOGICAL ELECTROCHEMISTRY

Behavior of Electrochemical Acidic/Electrophilic and Basic/Nucleophilic Species

The emphasis of this symposium will be electrochemical generation of the titled species as reagents in chemical reactions. It is directed toward, but not limited to, papers in which such species are used advantageously in organic synthesis, especially in *cases where* the electrogenerated reagents prove to be superior to traditional chemical reagents.

Suggestions and inquiries should be sent to the Symposium Co-Chairmen: R. C. Hallcher or R. D. Goodin, Monsanto Co., Corporate Research Dept., Mail Zone Q1A, 800 N. Lindberg Blvd., St. Louis, Mo. 63166.

Electrochemical Processes at Biological Membranes

This symposium will consider a broad range of phenomena involving biological membranes, i.e., ion transport, redox processes, adsorption, and effects of charge on structure.

Suggestions and inquiries should be sent *to the Symposium Chairman: M. Blank, Dept.* of Physiology, Columbia University, 630 West 168th St., New York, N.Y. 10032.

Present Methods for Elucidating the Mechanisms of Organic Electrode Reactions

This symposium will deal with modern methods of studying organic electrode reactions, how these have been applied to actual systems, and the current status of the field. Papers are requested on: 1. A review of modern methods (electrochemical, optical, etc.), their strengths and limitations. 2. Representative case histories. 3. What is now known and what remains to be discovered about the general path of organic electrode reactions.

Suggestions and inquiries should be sent to the Symposium Co-Chairman: A. J. Bard, Dept. of Chemistry, University of Texas, Austin, Texas 78712. Contributed papers are also solicited; these should be sent to the Symposium Co-Chairman: J. T. Maloy, Dept. *of Chemistry, West Virginia University*, Morgantown, W.Va. 26506.

General Session

Suggestions and inquiries should be sent to the Symposium Chairman: J. H. Wagenknecht, Monsanto Co., 800 N. Lindbergh Blvd., St. Louis, Mo. 63166.

PHYSICAL ELECTROCHEMISTRY

Electrochemical Stability of Nonaqueous Solvents

This symposium will consider the stabilities of various organic and inorganic nonaqueous electrolytes, particularly in the contexts of batteries, electro-organic synthesis, passive alphanumeric displays (e.g., electrochromics, liquid crystals, electrophoretics), active alphanumeric displays (e.g., electrochemiluminescence), and electrodeposition. Specific topics to be included are: 1. Anodic/cathodic decomposition rates and mechanisms for pure solvents and electrolytes. 2. Impurity-related decomposition processes. 3. Purification techniques and analytical methods. 4. Electrode-catalyzed decomposition. 5. Active electrode protection via passivation. 6. Related device failure modes and device failure rates.

Suggestions and inquiries should be sent to the Symposium Chairmen: R. J. Jasinski, Texas Instruments Inc., P.O. Box 5936, M/S 147, *Dallas*, Texas 75222; or *M. Salomon*, U.S. Army ECOM, Fort Monmouth, N.J. 07703.

General Session

Suggestions and inquiries should be sent to the Symposium Chairman: S. Bruckenstein, Dept. of Chemistry, State University of New York at Buffalo, Buffalo, N.Y. 14214.

MULTISPONSORED

Strategies for Environmental Planning: Reduction at Source, Recycling, and New Processes

The intent of the symposium is to broaden the current outlooks to pollution control. Starting from conventional methods, usually add-on processes to existing technologies, it will cover the development of new approaches that stress source reduction, recycling, and conservation.

It is hoped that the discussions will reflect the ways in which new technologies can be integrated with our increasing understanding of environmental systems. This will assist the development of planning and regulatory processes that support the requirements of both profitability and sound environmental management.

Invited and contributed papers will deal with all aspects of industrial production and processing, particularly: 1. Opportunities presented by existing technologies. 2. Energy costs, nonconventional sources, and conservation. 3. Materials scarcity and substitution as technological and economic constraints. 4. Recycling and closed-cycle processing. 5. Acceptable emission tolerances, environmental safety, and monitoring techniques. 6. Durability and acceptability of products and resource conservation as societal goals.

Suggestions and inquiries should be sent to the Symposium Chairman: M. C. B. Hotz, Office of the Science Advisor, Dept. of the Environment, Ottawa, Ont., Canada K1A 0H3.

75-Word Abstract Form

(Deadline for receipt—December 1, 1977)

SEATTLE, WASHINGTON, MEETING—MAY 21-26, 1978

Submit to: **The Electrochemical Society, Inc.**
P.O. Box 2071, Princeton, N.J. 08540

Schedule for .....
Symposium **ECS Division**

Abstract No. .....
(do not write in this space)

(Title of paper) .....

.....

(Authors) (Underline name of author presenting paper) .....

.....

(Business Affiliation and Address) .....

.....

.....
(ZIP Code) **(Tel. No.)**

(Type abstract in this area—double spaced.)

Do you require any audiovisual equipment?
☐ **35 mm (2 x 2 in.) slide projector**
☐ **vugraph**
☐ **other (specify)**
Is a full length paper on this work to be submitted for Society Journal publication?
☐ **Yes** ☐ **No**

Papers presented before a Society technical meeting become the property of the Society and may not be published elsewhere without written permission of the Society. Papers presented at Society technical meetings must be authored by a member or sponsored by an active member.

.....
Insert name of Society member author or sponsor

THE ELECTROCHEMICAL SOCIETY PATRON MEMBERS

Bell Telephone Laboratories, Inc.
Murray Hill, N.J.

Dow Chemical Co.
Inorganic Chemicals Dept., Midland, Mich.

General Electric Co.
Battery Business Department, Gainesville, Fla.
Chemical Laboratory, Knolls Atomic Power Laboratory, Schenectady, N.Y.
Electronic Capacitor Products Section, Irmo, S.C.
Lamp Div., Cleveland, Ohio
Materials & Process Laboratory, Large Steam Turbine-Generator Dept., Schenectady, N.Y.
Research and Development Center, Physical Chemistry Laboratory & Power Systems Laboratory, Signal Processing & Communication Laboratory, Schenectady, N.Y.
Semiconductor Products Dept., Syracuse, N.Y.

International Business Machines Corp.
New York, N.Y.

The International Nickel Co., Inc.
New York, N.Y.

Olin Corporation
Chemicals Div., Research Dept., New Haven, Conn.

Philips Research Laboratories
Eindhoven, Holland

Union Carbide Corp.
Battery Products Div., Corporate Research Dept., New York, N.Y.

Westinghouse Electric Corp.
Electronic Tube Div., Elmira, N.Y.
Lamp Div., Bloomfield, N.J.
Semiconductor Div., Youngwood, Pa.
Research Laboratories, Pittsburgh, Pa.
K. W. Battery Co., Westinghouse Subsidiary, Skokie, Ill.

THE ELECTROCHEMICAL SOCIETY SUSTAINING MEMBERS

The Aerospace Corporation
Los Angeles, Calif.

Airco Industrial Gases
Murray Hill, N.J.

Airco Speer Carbon-Graphite
St. Marys, Pa.

Allied Chemical Corp.
Industrial Chemicals Division
Solvay, N.Y.

Aluminum Co. of America
New Kensington, Pa.

Aluminum Co. of Canada, Ltd.
Montreal, P.Q., Canada

AMAX Inc.
New York, N.Y.

AMP Incorporated
Harrisburg, Pa.

Analog Devices, Inc.
Norwood, Mass.

Applied Materials, Inc.
Santa Clara, Calif.

ASARCO Incorporated
South Plainfield, N.J.

BASF Wyandotte Corporation
Wyandotte, Mich.

Battelle Memorial Institute
Columbus, Ohio

Beckman Instruments, Inc.
Fullerton, Calif.

Bell-Northern Research
Ottawa, Ont., Canada

Bethlehem Steel Corp.
Bethlehem, Pa.

Boeing Co.
Seattle, Wash.

The Borg-Warner Corp.
Roy C. Ingersoll Research Center
Des Plaines, Ill.

Brown, Boveri & Co., Ltd.
Research Center
Baden, Switzerland

Canadian Industries Ltd.
Montreal, P.Q., Canada

Carborundum Co.
Niagara Falls, N.Y.

Cominco Ltd.
Trail, B.C., Canada

Corning Glass Works
Corning, N.Y.

Crawford & Russell Inc.
Stamford, Conn.

Diamond Shamrock Corp.
Painesville, Ohio

Dow Corning Corporation
Hemlock, Mich.

E. I. du Pont de Nemours and Co.
Central Research Department
Wilmington, Del.

Duro-Test Corp.
North Bergen, N.J.

Eastman Kodak Co.
Rochester, N. Y.

Electrochemical Technology Corp.
Seattle, Wash.

Electrode Corporation
Chardon, Ohio

Eltra Corp.
Prestolite Div., Toledo, Ohio
C&D Batteries, Conshohocken, Pa.

Energy Conversion Devices Inc.
Troy, Mich.

ESB Incorporated
Ray-O-Vac Div., Madison, Wisc.
Technology Center, Yardley, Pa.

SUSTAINING MEMBERS (CONTINUED)

Ever Ready Co. (Holdings) Ltd.
Whetstone, London, England

Exmet Corporation
Bridgeport, Conn.

Exxon Research and Engineering Co.
Corporate Research Battery Unit
Linden, N.J.
Engineering Technology Div.
Florham Park, N.J.

Fairchild Camera & Instrument Corp.
Research and Development Laboratory
Palo Alto, Calif.

FMC Corp.
Inorganic Chemicals Div.
Buffalo, N.Y.

Foote Mineral Co.
Exton, Pa.

Ford Motor Co.
Dearborn, Mich.

GAF Corporation
Inorganic Chemicals Department
Glens Falls, N.Y.

General Motors Corporation
Delco Electronics Div., Kokomo, Ind.
Delco-Remy Div., Anderson, Ind.
Research Laboratories Div., Warren, Mich.

Globe-Union, Inc.
Milwaukee, Wisc.

GTE Laboratories
Waltham, Mass.

GTE Sylvania Incorporated
Chemical & Metallurgical Division
Towanda, Pa.

B. F. Goodrich Chemical Co.
Cleveland, Ohio

Gould Inc.
Gould Laboratories, Rolling Meadows, Ill.
Gould Laboratories—Energy Research, St. Paul, Minn.
Gould Laboratories—Materials Research, Cleveland, Ohio

Great Lakes Carbon Corp.
New York, N.Y.

The Harshaw Chemical Co.
Cleveland, Ohio

Hill Cross Co., Inc.
West New York, N.J.

Honeywell, Inc.
Power Sources Center
Horsham, Pa.

Hooker Chemical Corp.
Niagara Falls, N.Y. (2 memberships)

HP Associates
Palo Alto, Calif.

Hughes Research Laboratories
Div. of Hughes Aircraft Co.
Malibu, Calif.

Industrial Innovation Center
Tehran, Iran

Kaiser Aluminum & Chemical Corp.
Pleasanton, Ca.

Kawecki Berylco Industries, Inc.
Boyertown, Pa.

Kennecott Copper Corp.
New York, N.Y.

Kerr-McGee Corporation
Technical Center
Oklahoma City, Okla.

Arthur D. Little, Inc.
Cambridge, Mass.

Lockheed Missiles & Space Co., Inc.
Research Laboratory
Palo Alto, Calif.

Mallory Battery Company
Tarrytown, N.Y. (2 memberships)

Marathon Battery Co.
Waco, Texas

Marston Bermuda
Hamilton, Bermuda

Matsushita Electric Industrial Co., Ltd.
Osaka, Japan

Microwave Associates, Inc.
Burlington, Mass.

Molycorp, Inc.
New York, N.Y.

Monsanto Company
St. Louis, Mo.

Motorola Inc.
Phoenix, Ariz.

M&T Chemicals Inc.
Detroit, Mich.

NL Industries, Inc.
New York, N.Y.

Olin Corporation
Metals Research Laboratories
New Haven, Conn.

Owens-Illinois Inc.
Toledo, Ohio

Oxy Metal Industries Corp.
Warren, Mich.

The Parker Company
Madison Heights, Mich.

Perkin-Elmer Corp.
Norwalk, Conn.

Phelps Dodge Refining Corp.
Maspeth, N.Y.

Philips Laboratories. Inc.
Briarcliff Manor, N.Y.

PPG Industries, Inc.
Chemical Div.
Pittsburgh, Pa.

RCA Corporation
Color Picture Tube Division
Lancaster, Pa.

Reynolds Metals Co.
Reduction Research Div.
Sheffield, Ala.

Rockwell International
El Segundo, Calif.

SAFT America, Inc.
Valdosta, Ga.

Sandia Laboratories
Albuquerque, N. M.

J. C. Schumacher Co.
Oceanside, Calif.

Siemens Aktiengesellschaft
Munich, Germany

Signetics Corp.
Sunnyvale, Ca.

Sobin Chemical Co.
Orrington, Maine

Sperry Research Center
Sudbury, Mass.

Sprague Electric Co.
North Adams, Mass.

Stackpole Carbon Co.
St. Marys, Pa.

Standard Telecommunication Laboratories Ltd.
Essex, England

Stauffer Chemical Co.
Dobbs Ferry, N.Y.

St. Joe Minerals Corp.
Monaca, Pa.

Teletype Corp.
Skokie, Ill.

Texas Instruments Inc.
Attleboro, Mass.
Dallas, Texas

Tokyo Shibaura Electric Co., Ltd.
Toshiba Research and Development Center
Kawasaki, Japan

United States Steel Corp.
Research Laboratory
Monroeville, Pa.

Varian Associates
Palo Alto, Calif.

Wacker Chemitronic
Burghausen, Germany

Xerox Corporation
Rochester, N.Y.

Yardney Electric Corporation
Pawcatuck, Conn.

Zenith Radio Corp.
Chicago, Ill.